THE UNIVERSITY OF HULL

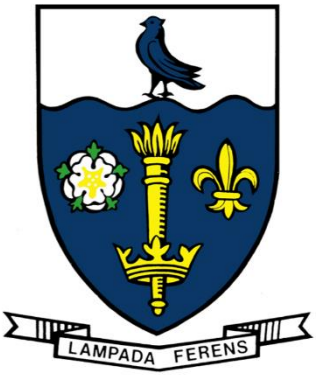


# NOVEL NANOPARTICLE FORMULATIONS FOR ANTIMICROBIAL ACTION

being a Thesis submitted for the Degree of Doctor of Philosophy

in the University of Hull

by

**Ahmed Fawzi Halbus Al-Mamoori**

BSc (University of Babylon, Iraq, 2005)

MSc (University of Babylon, Iraq, 2012)

**June 2019**

## Acknowledgement

I would like to take this opportunity to give my acknowledgement to all who helped in the successful completion of my PhD project.

Firstly, I will give my highest appreciation to my supervisors, Professor Vesselin N Paunov and Dr. Tommy S. Horozov. The thanks to them are not only for giving me a chance to work on the interesting project, but also for their effective instruction, broad knowledge, free discussion and encouragement for me.

Secondly, I am grateful to all members of Paunov Research Group and all PhD students in the Department of Chemistry and Biochemistry, both past and present, for their support and friendship. Special thanks to Mrs A. Lowry and Mr A. Sinclair for helping with transmission electron microscopy and scanning electron microscopy imaging.

Thirdly, I would like to thank the Iraqi Government/ The Higher Committee for Education Development in Iraq (HCED-Iraq), the Iraqi Ministry of Higher Education and Scientific Research and the University of Babylon for supporting me financially. Last but not least, I would like to thank the Iraqi attaché in London and Ireland, for their help and support.

Finally, I would like to thank my wife (Zahraa), my daughter (Malak), my parents and to my brothers and sisters for the help and support throughout writing this thesis and my life in general.

# List of Publications, Posters and Certificates

The work contained within this thesis has given rise to the following publications, posters and certificates:

1. **Ahmed F. Halbus**, Tommy S. Horozov, Vesselin N. Paunov, Colloid particle formulations for antimicrobial applications, *Adv. Colloid Interface Sci.*, 249 (2017) 134-148.
2. **Ahmed F. Halbus**, Tommy S. Horozov, Vesselin N. Paunov, Strongly enhanced antibacterial action of copper oxide nanoparticles with boronic acid surface functionality, *ACS Applied Materials and Interfaces*, 11 (2019) 12232–12243.
3. **Ahmed F. Halbus**, Tommy S. Horozov, Vesselin N. Paunov, Self-grafting copper oxide nanoparticles show a strong enhancement of their anti-algal and anti-yeast action, *Nanoscale Advances*, 1 (2019) 2323 – 2336.
4. **Ahmed F. Halbus**, Tommy S. Horozov, Vesselin N. Paunov, Controlling the antimicrobial action of surface modified magnesium hydroxide nanoparticles, *Biomimetics*, 4 (2019**)** 41.1-20.
5. **Ahmed F. Halbus**, Tommy S. Horozov, Vesselin N. Paunov, 'Ghost' silica nanoparticles with host-inherited antibacterial action, *ACS Applied Materials and Interfaces*, 11 (2019) 38519−38530.
6. **Ahmed F. Halbus**, Tommy S. Horozov, Vesselin N. Paunov, Controlling the anti-algal and anti-yeast properties of surface modified zinc oxide nanoparticles, *ACS Applied Nano Materials, under review.*
7. Poster presentation in the 8$^{th}$ PhD Experience Conference at the University of Hull on 12 July 2017. The poster entitled "Controlling the Antimicrobial Action of Surface Modified Magnesium Hydroxide Nanoparticles".
8. Poster presentation in PhD Colloquium on 24$^{th}$ Jan 2018 which was held in the department of chemistry and Biochemistry at the University of Hull. The poster entitled "Controlling the Antimicrobial Action of Surface Modified Magnesium Hydroxide Nanoparticles".
9. I attended of MERCIA meeting at Liverpool John Moores University in 14$^{th}$ December 2016.
10. I studied research and communication skills and chemistry related modules and got **110 credits**.

## Abstract

Colloidal particles are being extensively studied in various antimicrobial applications due to their small size, enormous surface area to volume ratio and ability to exhibit a wide spectrum of antibacterial, antifungal, antialgal and antiviral action. This thesis aims to develop novel nanoparticle formulations for antimicrobial action.The present work focuses on various nanoparticles (NPs) of inorganic materials and discusses some of the methods for their preparation as well as mechanisms of their antimicrobial action. The antimicrobial applications of metal oxide nanoparticles (zinc oxide and copper oxide) and metal hydroxide nanoparticles such as magnesium hydroxide were studied. Recent advances in the functionalization of nanoparticles and their potential antimicrobial applications were also studied as a viable alternative of conventional antibiotics and antiseptic agents which can help to tackle antimicrobial resistance.

The synthesis and characterisation of a range of surface modified zinc oxide (ZnONPs, Chapter 3 and 4), magnesium hydroxide $Mg(OH)_2$NPs (Chapter 5 and 6) and copper oxide (CuONPs, Chapter 7 and 8) have been described including particle size distribution, crystallite size, zeta potential, isoelectric point, X-ray diffraction (XRD), dynamic light scattering (DLS), scanning electron microscopy (SEM), etc. The antibacterial, anti-algal and anti-yeast activity of the modified nanoparticles on microalgae (*C. reinhardtii*), yeast (*S. cerevisiae*) and *Escherichia coli* (*E.coli*) were explored. The viability of these cells was evaluated for various concentrations and exposure times with nanoparticles. It was discovered that the antimicrobial activity of uncoated nanoparticles on the viability of *C. reinhardtii* occurred at considerably lower particle concentrations than for *S. cerevisiae* and *E.coli*. The results indicate that the antimicrobial activity of polyelectrolyte-coated nanoparticles alternates with their surface charge. The anionic nanoparticles (ZnONPs/PSS, ZnONPs/ZnS, ZnONPs/$SiO_2$, CuONPs/PSS and $Mg(OH)_2$NPs/PSS) have much lower antibacterial activity than the cationic ones (NPs/PSS/PAH and uncoated NPs). These findings have been explained by the lower adhesion of the anionic nanoparticles to the cell wall because of electrostatic repulsion and the enhanced particle-cell adhesion due to electrostatic attraction in the case of cationic nanoparticles. The results can potentially be applied to control the cytotoxicity and the antimicrobial activity of other inorganic nanoparticles.

A novel type of antimicrobial formulation of CuONPs has been developed and tested. This has been achieved by functionalizing CuONPs with (3-glycidyloxypropyl)-trimethoxysilane (GLYMO) and subsequent covalent coupling of 4-hydroxyphenylboronic acid (4-HPBA). As the boronic acid (BA) groups on the surface of CuONPs/GLYMO/4-HPBA can form reversible covalent bonds with the diol groups of glycoproteins on the bacterial cell surface, they can strongly bind to the cells walls resulting in a very strong enhancement of their antibacterial, anti-algal and anti-yeast action which is not based on electrostatic adhesion. This work (Chapter 8) demonstrates that the CuONPs with boronic acid surface functionality are far superior antibacterial agents compared to bare CuONPs. The results showed that the antibacterial, anti-algal and anti-yeast impact of the 4-HPBA-functionalized CuONPs on *Rhodococcus rhodochrous* (*R. rhodochrous*), *E.coli*, *C. reinhardtii* and *S. cerevisiae* is one order of magnitude higher than that of bare CuONPs or CuONPs/GLYMO. It was also observed a marked increase of the 4-HPBA-functionalized CuONPs antibacterial action on these microorganisms at shorter incubation times compared with the bare CuONPs at the same conditions. Significantly, the results show that the cytotoxicity of CuONPs functionalized with 4-HPBA as an outer layer can be controlled by the concentration of glucose in the media, and that the effect is reversible as glucose competes with the sugar residues on the bacterial cell walls for the BA-groups on the CuONPs. The experiments with human keratinocyte cell line exposure to CuONPs/GLYMO/4-HPBA indicated lack of measurable cytotoxicity at particle concentrations which are effective as an antibacterial agent for both *R. rhodochrous*, *E. coli*, *C. reinhardtii* and *S. cerevisiae*. This suggests that formulations of CuONPs/GLYMO/4-HPBA can be used to drastically reduce the overall CuO concentration in antimicrobial formulations while strongly increasing their efficiency.

The role of surface roughness in the antimicrobial activity of oxide nanoparticles has been studied (Chapter 9). This has been achieved by comparing the antimicrobial action of non-porous silica nanoparticles ($SiO_2$NPs) with smooth surface and mesoporous surface-rough $SiO_2$NPs, both functionalized with GLYMO and 4-HPBA. Surface-rough mesoporous silica nanoparticles ('ghost' $SiO_2$NPs) have been fabricated by using composite mesoporous copper oxide nanoparticles ('host' CuONPs) as templates which allowed the $SiO_2$NPs to copy their surface morphology. It was demonstrated that the functionalized 'ghost' $SiO_2$NPs with GLYMO and 4-HPBA ($SiO_2$NPs/GLYMO/4-HPBA) show a very significant antibacterial effect compared to smooth $SiO_2$NPs of the

same surface coating and particle size. This was attributed to the 'ghost' $SiO_2$NPs surface morphology which mimics to certain extent the surface of the original CuONPs used as templates for their preparation. It can be envisaged that the 'ghost' $SiO_2$NPs effectively acquire some of the antibacterial properties from the 'host' CuONPs, with the same functionality, despite being completely free of copper. Antibacterial tests showed that the 'ghost' $SiO_2$NPs/GLYMO/4-HPBA have much higher antibacterial action than the non-functionalized 'ghost' $SiO_2$NPs or GLYMO functionalized 'ghost' $SiO_2$NPs for *R. rhodochrous*. The results indicate that the combination of rough surface morphology and strong adhesion of the particle surface to the bacteria can make even benign material as silica act as a strong antimicrobial.

# Contents

# List of abbreviations

| | |
|---|---|
| NMs | Nanomaterials |
| NPs | Nanoparticles |
| DLS | Dynamic Light Scattering |
| UV | Ultraviolet |
| ROS | Reactive Oxygen Species |
| VB | Valence Band |
| CB | Conduction Band |
| XRD | X-Ray Diffraction |
| QDs | Quantum Dots |
| DNA | Deoxyribonucleic Acid |
| TAP | Tris-Acetate-Phosphate |
| EDTA | Ethylenediaminetetraacetic Acid |
| Tris | Tris(hydroxymethyl)-aminomethane |
| ZnONPs | Zinc oxide nanoparticles |
| CuONPs | Copper oxide nanoparticles |
| $Mg(OH)_2$NPs | Magnesium hydroxide nanoparticles |
| ZnS | Zinc sulfide |
| $SiO_2$ | Silica |
| PSS | Poly (sodium-4-styrenesolfonate) |
| PAH | Poly (allylamine hydrochloride) |
| TGA | Thermogravimetric analysis |
| EDX | Energy dispersive X-ray spectroscopy |
| BET surface area | Brunauer-Emmett-Teller surface area |

| | |
|---|---|
| SEM | Scanning electron microscopy |
| TEM | Transmission electron microscopy |
| Z.P. | Zeta potential |
| LbL | Layer by Layer |
| APTES | (3-Aminopropyl) triethoxysilane |
| GLYMO | (3-Glycidoxypropyl) trimethoxysilane |
| Boronic acid | BA |
| 4-FPBA | 4-Formylphenylboronic acid |
| 4-HPBA | 4-Hydroxyphenylboonic acid |
| 4-TPBA | 4-Mercaptophenylboronic acid |
| 4-CPBA | 4-Carboxyphenylboronic acid |

# Chapter 1

# 1. Introduction

## 1.1 Nanotechnology

Conventional antimicrobial agents are usually low molecular weight species that attack and selectively kill microbial cells or suppress their growth. Due to their excessive use, many microbial strains develop resistance and their effective treatment often requires a continuous pipeline of novel antiseptic and antibiotic agents to be developed.[1] This calls for new alternative approaches to antimicrobials or unconventional protection strategies that can potentially bypass antimicrobial resistance.[1-5] Nanotechnology provides us with alternative approaches for development of novel antimicrobials that do not rely on the existing pathways of antibiotic action. Over the last few years there is an increasing interest in developing colloid particles with antimicrobial functionality which exhibit strong and universal antibacterial, antifungal or antiviral action towards which pathogens have not yet been able to develop resistance. Synthetic colloids with engineered antimicrobial action designed to target specific microorganisms could be deployed to address this challenge as they can potentially have high antimicrobial activity at very low particle concentrations.[6] Nanoparticles are widely used for biological and medical applications as contrast agents for medical imaging, labelling of cells, targeting of tumours and in therapeutic drug delivery.[7] Nanoparticles have attracted significant interest for applications as antimicrobials due to their unique photoactive, electronic, optical, catalytic and thermal properties, suitable particle size and morphologies[8-10] that can be prepared with high degree of control.[11-20] Recently, inorganic nanoparticles have been broadly researched for their nanotoxicity and potential antimicrobial action[21-23] which is enhanced by their highly developed surface area. There are several metal oxides and hydroxides in the form of nanoparticles that act as antimicrobial agents which have very different mechanisms of action against microbial cells.[21-23] Inorganic nanoparticles are usually found in a vast number of consumer products that interact with our skin, GI tract, and mucus membranes,[24, 25] and thus have the potential to cause unintentional changes to the microbiome (see Figure 1.1).[26] This chapter will summarize the antimicrobial properties of various metal oxides and hydroxides and their NPs, and discuss the possible mechanisms by which they can eliminate and inhibit the growth of

potentially harmful microorganisms.[21] This chapter will also consider several applications of complex colloids and inorganic nanoparticles with selective antimicrobial action.

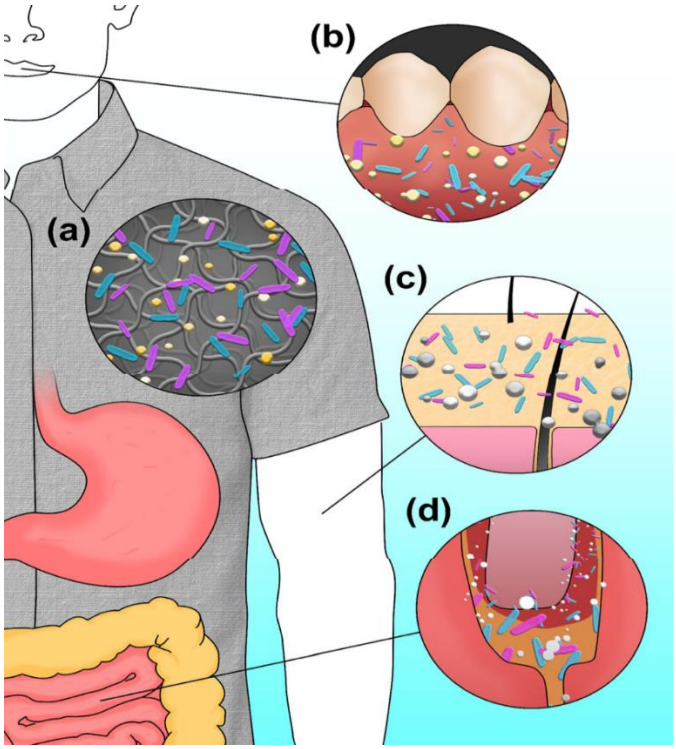


**Figure 1.1.** Inorganic NPs contained in consumer products can interact with the local microbiome. (a) AgNPs, which are, at times, included in the clothing fabric to reduce the bacterial odor associated with sweating, can interact with our skin microbiome. (b) $TiO_2$NPs, included as a whitening agent in toothpastes, can interact with the oral microbiome. (c) ZnONPs, included in sunscreen products as a coloring agent, can interact with the skin microbiome. (d) $SiO_2$NPs, often used as a bulking agent in foods and pharmaceuticals, can interact with the GI microbiome. Reproduced with permission from Ref.[26]

## 1.2 Colloid particles as antimicrobials

The present understanding of the possible mechanisms by which specific colloid particles kill microbial cells is still patchy and incomplete. Although a range of mechanisms of their antimicrobial activity have been explored, most of the research in this area is still ongoing. Recent studies have been concentrated on antimicrobial inorganic nanoparticles, for example, metal oxide nanoparticles, like ZnO, MgO, CuO, $Cu_2O$, $Al_2O_3$, $TiO_2$,$CeO_2$ and $Y_2O_3$; metals, e.g. copper, silver, gold etc., metal hydroxides such as $Mg(OH)_2$ as well as colloids made from biodegradable materials, such as chitosan, lignin and dextran, loaded with antimicrobial agents. The metal oxides nanoparticles are divided into two different groups based on the mechanisms involved in the growth inhibition of

microorganisms (Figure 1.2). Metal oxide nanoparticles are among the most utilised NPs having applications in the different fields, for example, cosmetics, textile and medicine. Zinc oxide nanoparticles (ZnONPs) have already been utilised in antimicrobial agents, sunscreens, and electronics. [2, 27, 28]

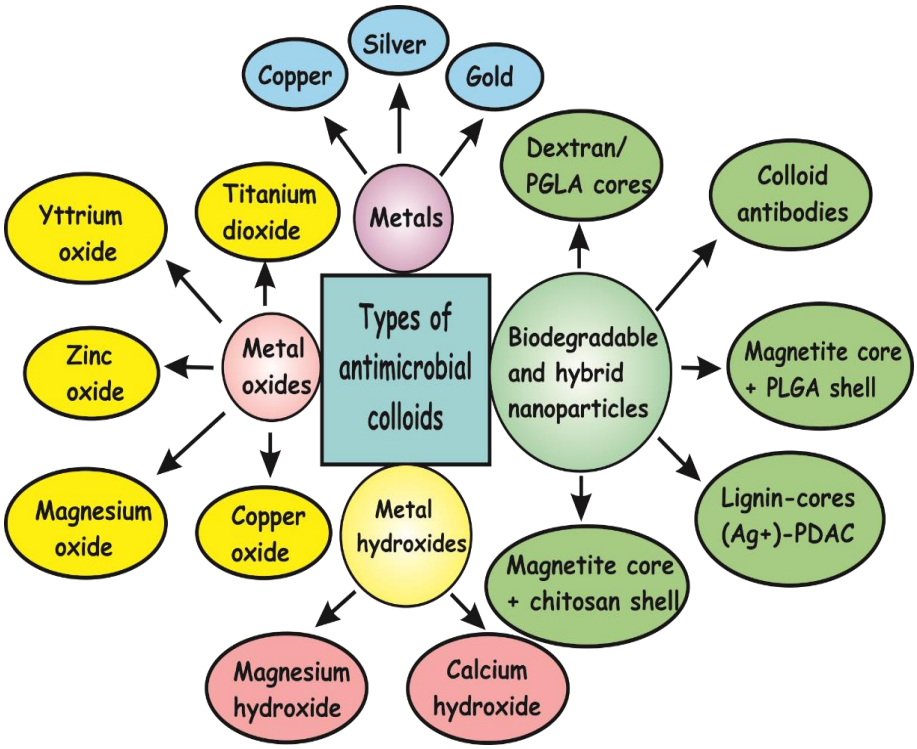


**Figure 1.2.** Classification of colloid particles as antimicrobial agents. [2, 28]

## 1.3 Types of nanoparticles

Nanoparticles are commonly classified based either on their structure, morphology or size. Nevertheless, as for their structure, they can be extensively sorted as carbon nanotubes, fullerenes, quantum dots and metal oxide NPs etc., as shown in Figure 1.3. [29, 30] In 1992 Japanese researcher Sumio Lajima discovered Carbon nanotubes (CNTs); CNTs are fibrous fullerenes comprised of moved graphine sheets and have pulled a lot of consideration. CNTs are utilised in many fields, for example, high thermal conductivity, electronics, and optics because of their exceptional electrical properties, hydrophobicity and mechanical quality. Fullerenes are mainly comprised of pure carbon and instances incorporate endofullerenes and bucky balls. Quantum dots are fluorescent semiconductor nano dots essentially having PbSe, CdS and CdSe cores. These can broadly utilised as a part of medicinal applications and transmit light as their size is smaller than Bohr excitation radius. [29]

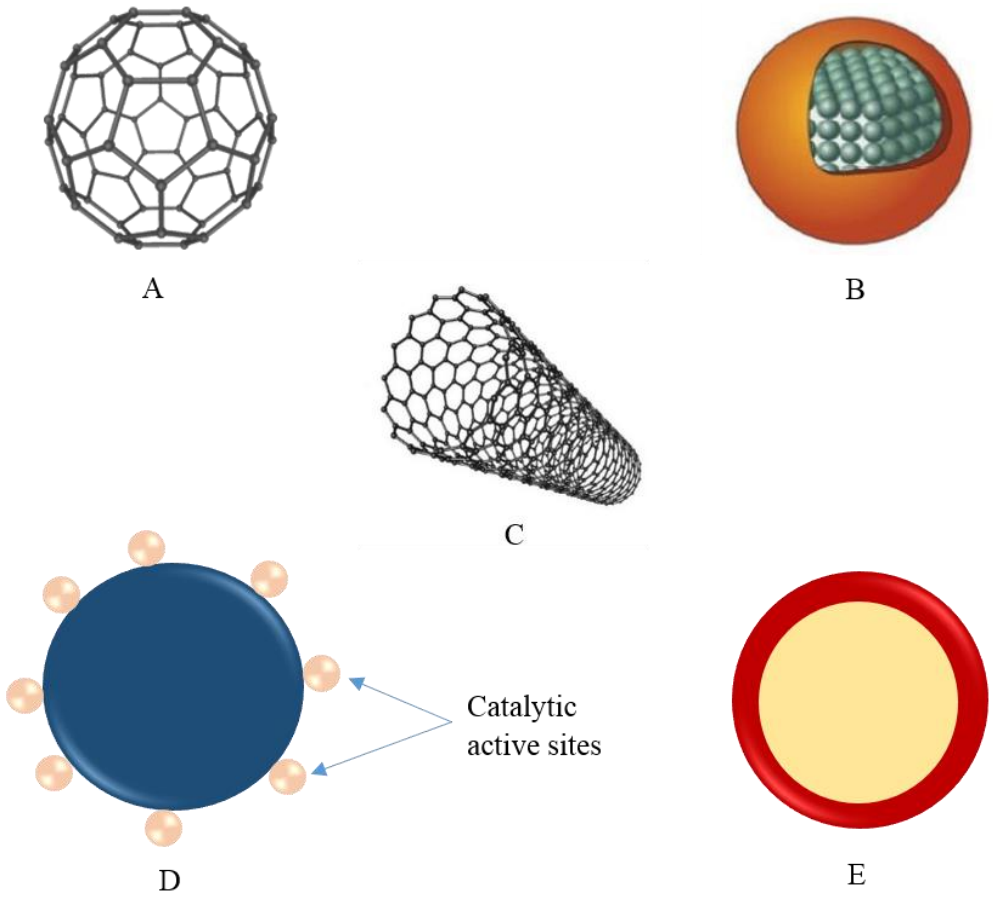


**Figure 1.3.** Types of nanoparticles (A) fullerene (B) quantum dots (C) nanotubes (D) surface functionalised nanoparticles and (E) ceramic nanoparticles. [30]

## 1.4 Physicochemical properties of nanoparticles

The chemical and physical properties of nanosized particles are not the same as bulk materials of the same chemical component, due to their small size, reactivity and great surface area, prompting potential poisonous impacts.[31]The toxicity of ZnO was because of solubilized $Zn^{2+}$ ions as demonstrated with a recombinant Zn-sensor cell. While Cu formulations had various toxicities, copper oxide NPs (CuONPs) are 50-fold more lethal than bulk CuO particles against crustaceans, [32] protozoa[33], yeast[34] and algae. [35]

Otherwise, $Al_2O_3$ and $TiO_2$ nanoparticles are around twice as toxic than bulk $Al_2O_3$ and $TiO_2$ particles towards nematodes.[36] Furthermore, the action of NPs changes the shape of the particles changes, prompting variety in their toxicity. Silver nanoparticles (Ag NPs) for instance, have been indicated to have antibacterial impact depending upon their shape.[37]

The chemical formulations of the particle surface have substantial impacts on nanoparticles. A large type of metal nanoparticles has toxic impacts, expanding the level

of receptive oxygen species (ROS) such as superoxide ($^{\cdot}O_2^-$), hydrogen peroxide ($H_2O_2$) and hydroxyl radical ($^{\cdot}OH$) in free cell framework. It is predicted that the surface modification of NPs can lessen the toxicity by covering their surface.[38, 39]

Free radicals delivered by numerous toxic NPs *in vivo*, may bring about an oxidative stress, which prompts inflammation, genotoxicity, and cell degradation.[40, 41] Moreover, the charge of the surface of the NP dispersions shows toxicity because of the size of the NPs variation with the change in the pH and the ionic strength.[41]

Aggregation and agglomeration of NPs have a huge effect on sample production for toxicological examinations. Warheit et al., (2004) have demonstrated that using aggregated and precarious NP scatterings in an *in vitro or in vivo* test cause inaccurate evaluation of NP toxicity.[42] Consequently, it is essential to identify whether these NPs are in an aggregated (strong attraction between primary particles) or agglomerated (weak attraction between primary particles) state, as this infers various toxicological impacts.[43, 44]

## 1.5 Post-utilisation fate of engineered nanopartciles

Recently, engineered NPs have been utilised in a number of consumer products, due to their specific properties.[18] With the large consumption of nanoparticles, there is a high probability of their discharge into the environment through production, transport, and use. This can bring about adverse environmental and health problems.[45] Once released, these new particles can endure various modifications as shown in Figure 1.4. Moreover, these NPs can enter soil framework and atmosphere, and their existence in the environment lead to a higher level of human exposure.[45] For instance, it has been discovered from many of studies that air contains 10,000 – 15,000 particles for every cubic centimetre which are in the nanoscale size range.[29] Likewise, soil contains a lot of NPs, where high surface area and a wealth of charged and hydrophobic adsorption locales make soil a good store for NPs. [29]

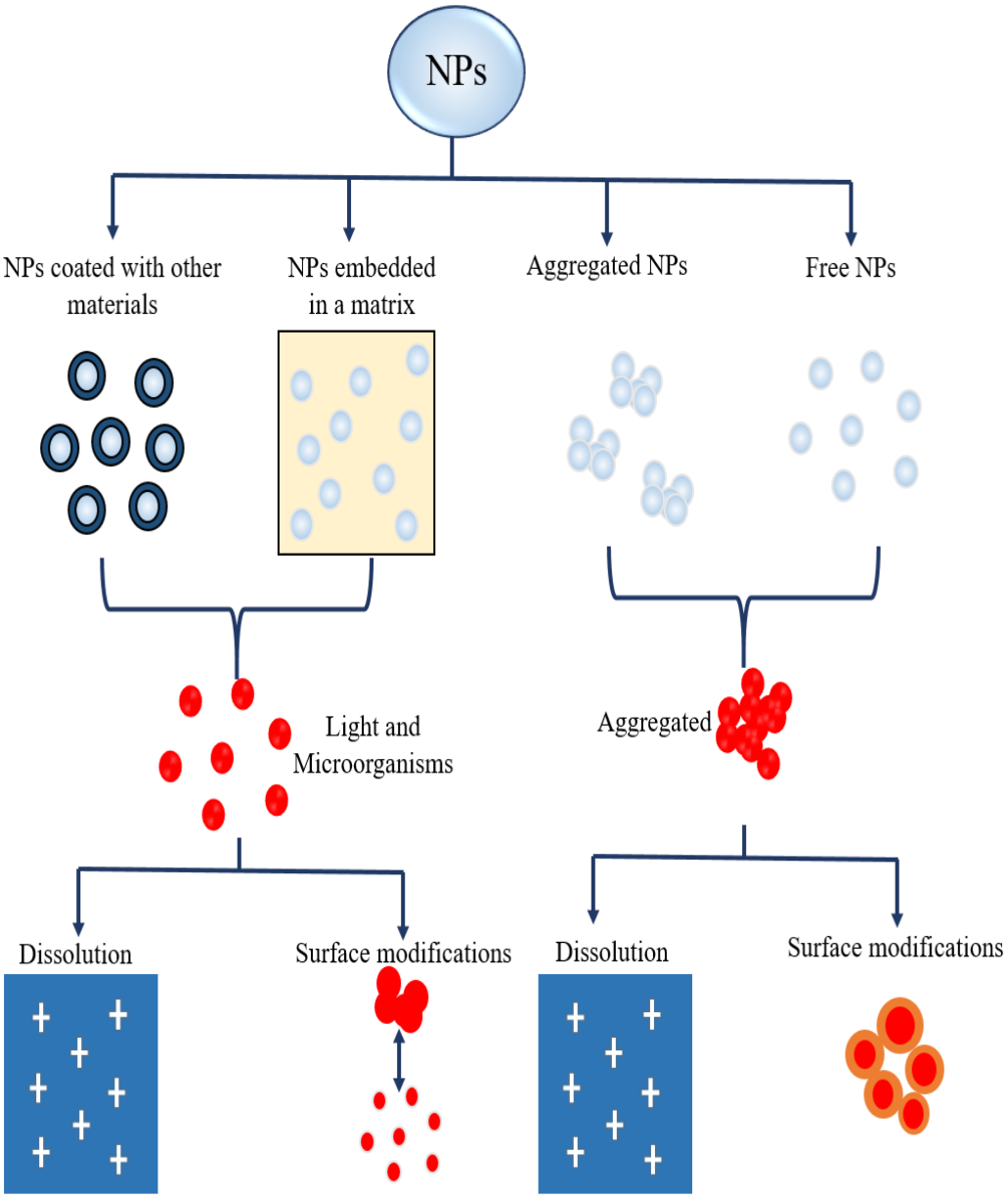


**Figure 1.4.** Fate of engineered NPs once they are released in the environment. Redrawn from ref.[45]

## 1.6 Aggregation of NPs

Aggregation is defined as the NPs have a tendency to pull with each other through chemical bonds or physical interaction strengths at interfaces forming bigger particles so as to decrease high surface energy. [43] This is an essential point in the vast majority of industrial applications where aggregation can diminish the effectiveness of certain reactions. Subsequently reagents, for example, dispersants are added to NPs suspensions to forestall aggregation. The total interaction energy $U_{total}$ between two particles can be

expressed as the sum of the van der Waals attraction energy $U_{vdw}$ and the electrostatic repulsion energy $U_{el}$.

$$U_{total} = U_{vdw} + U_{el} \qquad (1.1)$$

The DLVO (Derjaguin, Landdau, Verwey and Overbeek) theory successfully describes the electrostatic interaction. [43, 46, 47]As indicated by the DLVO theory when the distance between the surfaces of the two particles is bigger than the consolidated thickness of the electrical twofold layers of the two particles, there would be no interference of the dissemination twofold layers. At the point when particles approach each other, two electric double layers (EDLs) can interfere, and a repulsion occurs as shown in Figure 1.5.

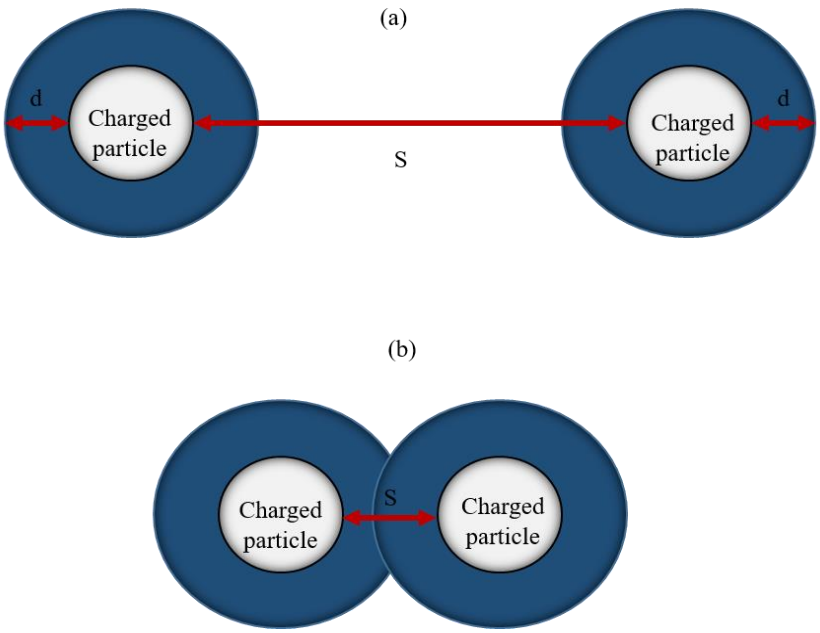


**Figure 1.5.** Schematic diagram of NP-NP interactions. (a) The distance between particles is bigger than the electric double layer thickness and no overlap. (b) When the NPs EDLs overlap the electrostatic interaction can oppose the Van der Walls attraction.

Particles having enough energy to conquer the energy barrier which is made by the counterplay of repulsive and attractive interactions will shape the formation of NP aggregates. NPs aggregation plays a huge part in deciding the transport and destiny of NPs where constrained bio availability is produced upon aggregation.

## 1.7 Properties and applications of ZnONPs

Zinc oxide (ZnO) is an inorganic compound which is utilised in various applications and occurs as a white powder called "Zincite". [48-51] Properties, such as heat capacity, melting point and high thermal conductivity have made ZnO a suitable applicant in the ceramic

industry.[48, 49]As a consequence of high band gap, ZnO is utilised in the electronics. Table 1.1 shows some of the essential properties of ZnO.[20, 52]

**Table 1.1.** Properties of ZnONPs.

| Property | Value |
|---|---|
| Molar mass | 81.408 g/mol |
| Band gap | 3.37 eV |
| Odor | odorless |
| Binding energy | 60-80 meV |
| Density | 5.606 g/cm$^3$ |
| Melting point | 1975 °C |
| Solubility in water | 0.16 mg/100 ml (30 °C) |
| Refractive index | 2.0041 |
| Boiling point | 2360 °C |

ZnO nanoparticles are of particular interest due to their potential application as a part of various consumer products, for example, dye-sensitized photovoltaic cells, cosmetics, electronics and plastic additives because of its optical, distinct thermal and electronic properties.[18, 53-57] ZnO nanostructures are prepared in a range of morphologies, for example, nanoparticles, tetrapods, nanorods and nanowires using, for instance, hydro thermal, template induced methods and wet chemical processes.[58] In the cosmetics industry, ZnONPs are utilised as antimicrobial agents and sunscreen creams. ZnONPs acts as a good UV blocking agent because its band gap is in the UV range. The antimicrobial activity of ZnONPs is accomplished using the production of reactive oxygen species. Also, nanorod arrays of ZnONPs are utilised in different photoelectric methods such as solar cells, schottky diodes, nanolasers and biosensors. [59] Moreover, thin films of ZnONPs play a significant part in medicinal applications and drug delivery. Furthermore, ZnO nanotubes are utilised in dye-sensitized solar cells. So, ZnO can be named as one of the most broadly utilised classes of nanomaterials. [60] ZnONPs have huge numbers of applications in different fields due to their distinct properties such as large

binding energy, wide bandgap and chemical stability. [61] Figure 1.6 demonstrates uses of ZnO nanoparticles in various areas.

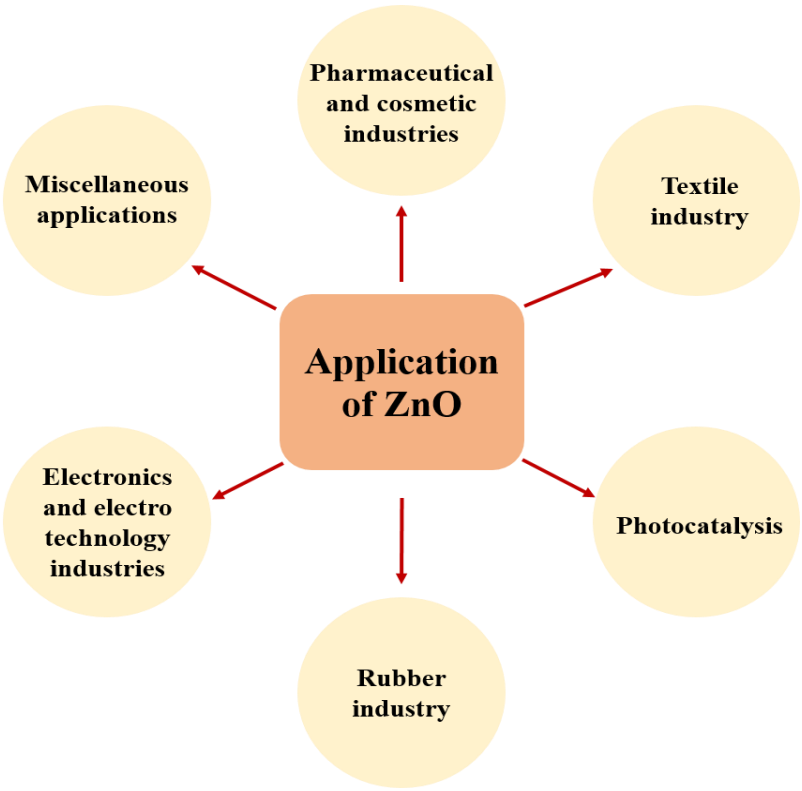


**Figure 1.6.** Schematic diagram of all the application of ZnONPs.

## 1.8 Properties and applications of $Mg(OH)_2$NPs

Magnesium hydroxide is an inorganic compound with the chemical formula $Mg(OH)_2$. $Mg(OH)_2$ is a very simple mineral, named brucite, regularly viewed as a very good example of a material with structurally bound OH group.[62, 63] Brucite has been the topic of several experimental[64-70] and theoretical studies in previous research.[68, 71-73] In spite of its simple structure, its physical properties are unexplored in actuality even its crystallographic symmetry has not yet been completely settled[74], while its structure has been addressed many times previously.[68, 71-73] The crystal structure of $Mg(OH)_2$ is a simple, layered, [75] hexagonal structure with layers of Mg interlaced with layers of OH groups.[75] $Mg(OH)_2$ is a white solid with low solubility in water ($K_{sp} = 5.61\times10^{-12}$)[76]. $Mg(OH)_2$ is a common component of antacids, for example milk of magnesia, in addition to laxatives. Table 1.2 illustrates some of the essential properties of $Mg(OH)_2$.

**Table 1.2.** Properties of $Mg(OH)_2$.

| Property | Value |
|---|---|
| Molar mass | 58.3197 g/mol |
| Odor | Odorless |
| Density | 2.3446 g/cm$^3$ |
| Melting point | 350 °C (662 °F; 623 K) decomposes |
| Solubility in water | 0.00064 g/100 mL (25 °C) 0.004 g/100 mL (100 °C) |
| Refractive index | 1.559 |

$Mg(OH)_2$NPs have been widely applied in many fields, from neutralizing acidic wastewaters to artificial reef construction[77], antibacterial agents[78], as well as environmental processes[79-81] and pharmaceutical formulations[82-85]. There are various morphologies of $Mg(OH)_2$ for example, the lamella, needle, rod, wire morphologies (see Figure 1.7), have been obtained by different synthesis methods at different temperatures (see Figure 1.8) or in various preparation conditions.[86-93]

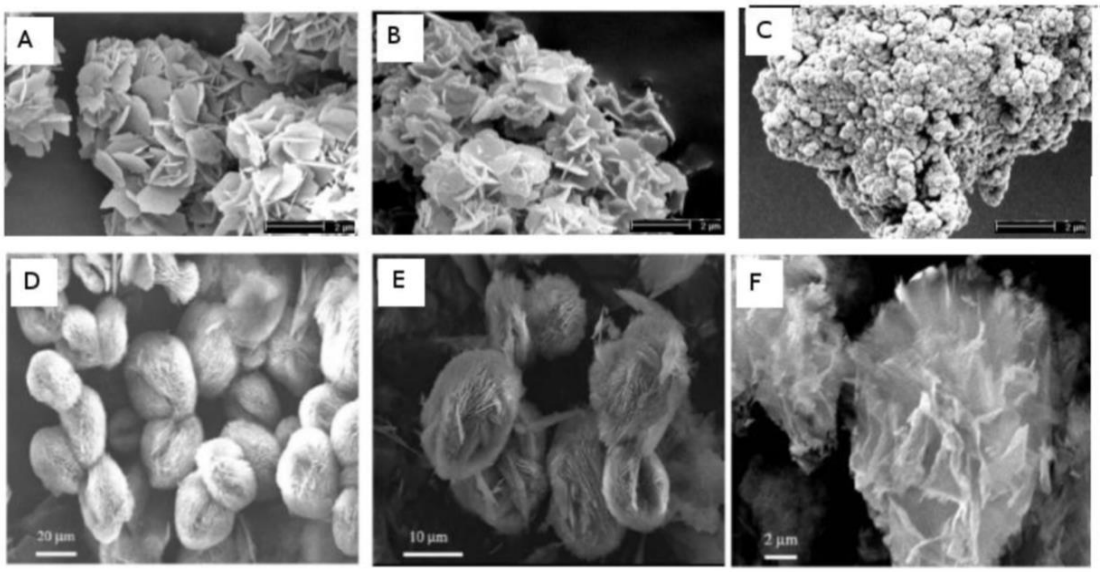


**Figure 1.7.** SEM images of various 3D shapes of $Mg(OH)_2$NPs (A) Typical 3D shape of $Mg(OH)_2$NPs named "sand rose" (B) and (C) display globular aggregation. (D) and (E) demonstrate examples of spherical particles that are uniform (D) and irregular (E). (F) displays an example of "nanoflower" synthesized at 115°C and pH 9.5. (A-C) were taken from[89] and (D-F) were taken from.[93]

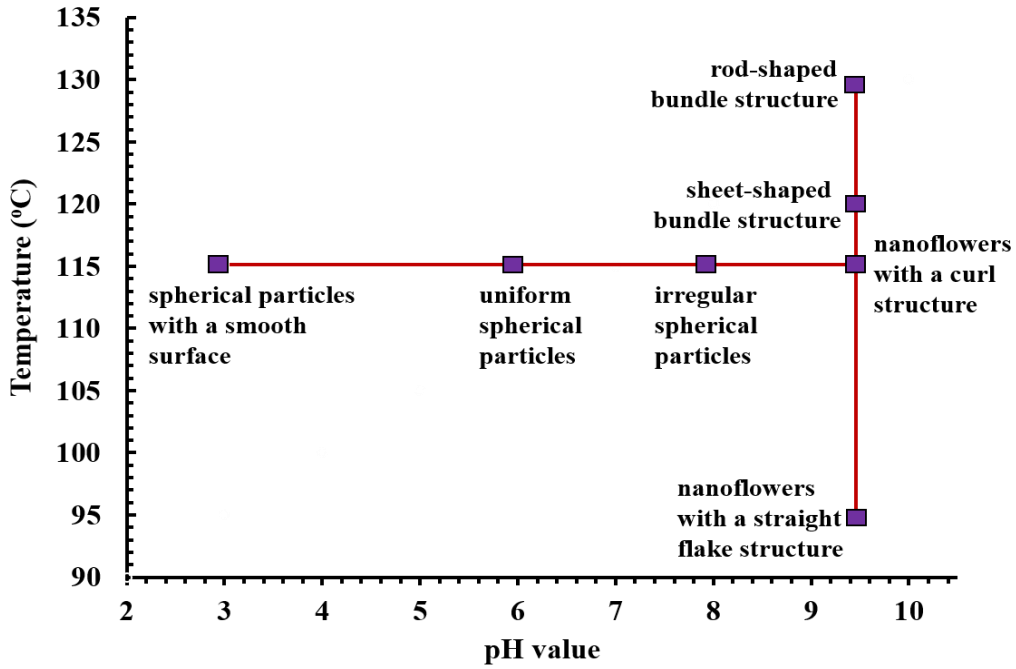


**Figure 1.8.** Diagram of $Mg(OH)_2$NP morphologies at different pH values and temperatures of the hydrothermal growth method. [93]

## 1.9 Properties and applications of CuONPs

Copper (II) oxide is an inorganic compound with the formula CuO. CuO is the simplest member of the family of Cu compounds and illustrations a series of potential physical properties, for example, electron correlation effects, spin dynamics, and high-temperature superconductivity.[94, 95] CuONPs is a black solid, it is one of the two stable oxides of copper, the other being $Cu_2O$ or cuprous oxide. As a mineral, it is famous as paramelaconite and tenorite. It is a form of copper ore and the precursor to several other copper-containing chemical compounds.[96] The Cu atom is coordinated by 4 O atoms in an approximately square planar configuration.[97] In addition to that, CuONPs are semiconducting compounds with a monoclinic crystal system. [97] CuONPs have attracted particular interest in different fields. They possess useful photoconductive and photovoltaic properties due to CuO crystal structures displaying a slight band gap of 1.2 eV.[98] Table 1.3 shows some of the essential properties of CuONPs.

**Table 1.3.** Properties of CuONPs.

| Property | Value |
|---|---|
| Molar mass | 79.545 g/mol |
| Appearance | black to brown powder |
| Density | 6.315 g/cm$^3$ |
| Melting point | 1.326 °C (2.419 °F; 1.599 K) |
| Solubility in water | insoluble |
| Refractive index | 2.63 |
| Solubility | soluble in ammonium chloride, potassium cyanide insoluble in alcohol, ammonium hydroxide, ammonium carbonate |

CuONPs have been applied in various areas depending on the different properties they display, which are extremely influenced by their surface properties, size, optical and magnetic traits, the preparation method being a significant parameter for controlling all these and therefore, their biological properties.[99] Some of these applications include doping materials in semiconductors, for example, antimicrobial agents, chemical sensors, catalyst for various cross coupling reactions, coating materials and anti-cancer formulations.[100] Lazary and co-workers have stated that CuONPs have been widely used in hospitals as anti-microbial agents due to their ability to kill more than 99.9% of both Gram-negative and Gram-positive bacteria within 2 hours of treatment of various surfaces. It has been found that the use of CuO in this way has radically decreased the occurrence of hospital-acquired infections and the costs associated with health care. A non-intravenous approach to utilizing CuONPs in bed sheets is a very exciting innovation as the particles can decrease microbial attachment and therefore limit hospital acquired infections (see Figure 1.9).[101]

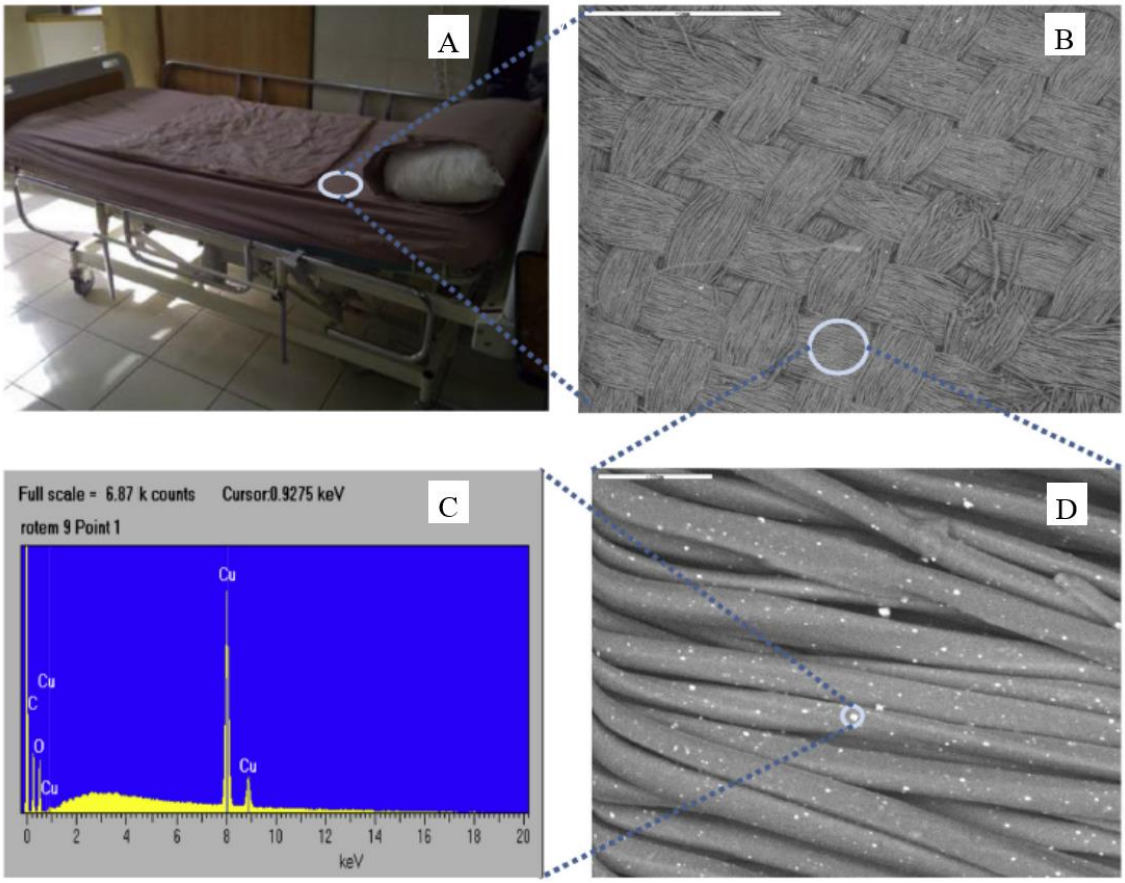


**Figure 1.9.** (B and D) scanning electronic microscope images (taken with a Jeol JMS 840 scanning electron microscope) of a representative pillowcase (A) are presented. The white dots in image D are the CuONPs embedded in the polyester fibers. (C) The chart is an X-ray photoelectron spectra analysis (done with a Shimadzu XRD 6000, TN-5500 X-ray analysis system) of the encircled white dot, displaying a peak at 8 keV corresponding to Cu these images were taken from.[101]

## 1.10 Characterisation of inorganic NPs

Several techniques can be applied for examining the size distribution, the surface charge and structure of inorganic nanoparticles. For example, Dynamic Light Scattering (DLS), zeta potential, X-Ray Diffraction, Scanning Electron Microscopy (SEM) and Transmission Electron Microscopy (TEM) which are as follows:

### 1.10.1 Dynamic Light Scattering (DLS)

A Zetasizer Nano ZS (Malvern) was used to examine the hydrodynamic diameter by DLS. DLS relies on upon illuminating the sample with a monochromatic beam of laser light which is scattered into an indicator situated at an angle (θ) relating to the transmitted light, which allows the measurement of the size distribution of suspended particles.[102] Figure 1.10 shows a schematics diagram of the Zetasizer Nanoseries NanoZS instrument.

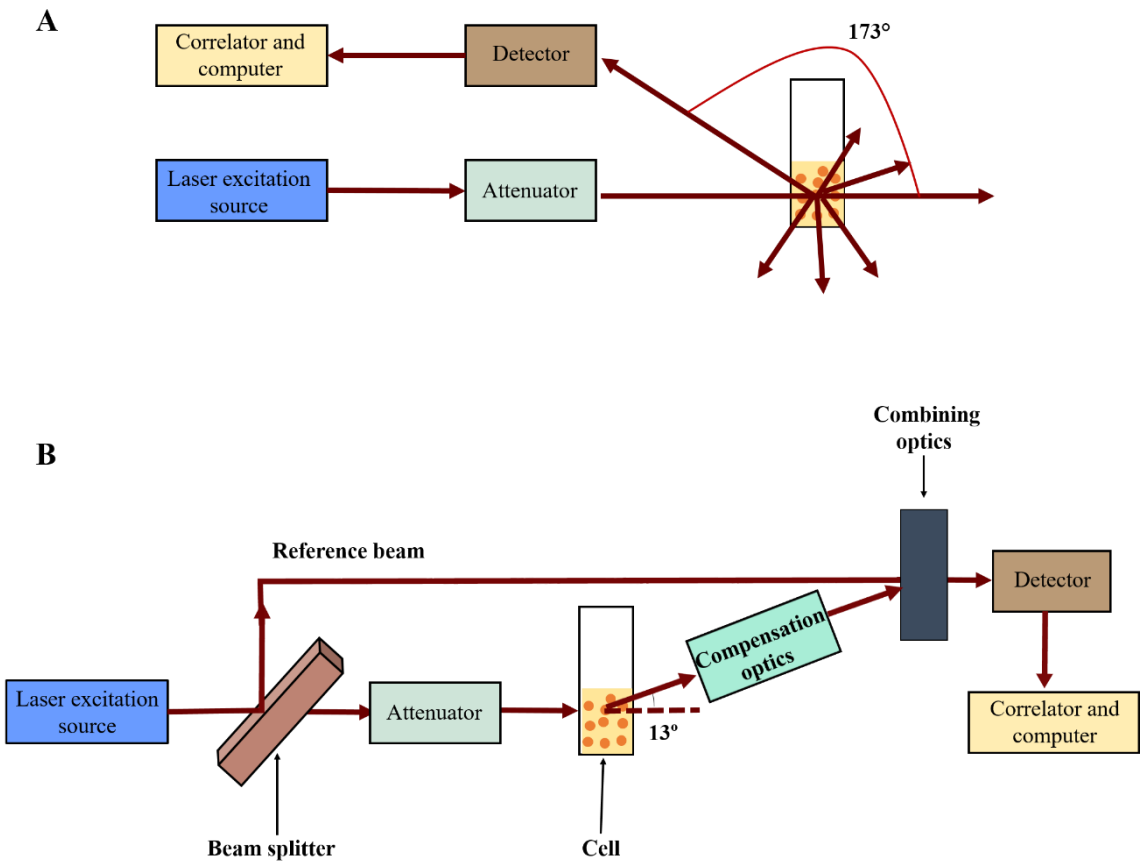


**Figure 1.10.** Schematic representation of the Zetasizer Nanoseries NanoZS (Malvern instruments) for the measurement of the (A) average diameter and (B) zeta potential. Redrawn from ref. [102, 103]

## 1.10.2 Zeta potential

Zeta potential (Z.P.) is a parameter that can be utilised for examining and anticipating colloid stability and surface morphology. [104] It can be characterized as the electric potential (ψ) in the electric double layer at the shear plane between a moving charged particles and the stable liquid phase in which the particle is suspended. [105] At the point when particles are put in an aqueous suspensions, an electric double layer is formed around them with one layer comprised of ions unequivocally adsorbed on the surface of the particles and this layer is named the Stern layer. On the other hand, the other layer is enveloped of diffusely distributed ions, as shown in Figure 1.11. The last part of the potential variance is known as the zeta potential, and it is measured at the shear plane; thus, the zeta-potential is an estimation of the amount of charge present on the particle surface on the shearing part of the dispersing media. [106]

The Z.P. of any dispersion is impacted by the surface chemistry. The surface chemistry can be varied by any number of means involving a variation in the salt concentration, pH,

surfactant concentration, and other formulation choices. It is, consequently, frequently desirable to examine how pH influences the Z.P. of dispersion. An isoelectric point estimation concentrates how pH impacts Z.P. and determines at which pH the Z.P. equals zero. In addition to that, the size of the NPs can be changed by varying the pH of a solution. [107]

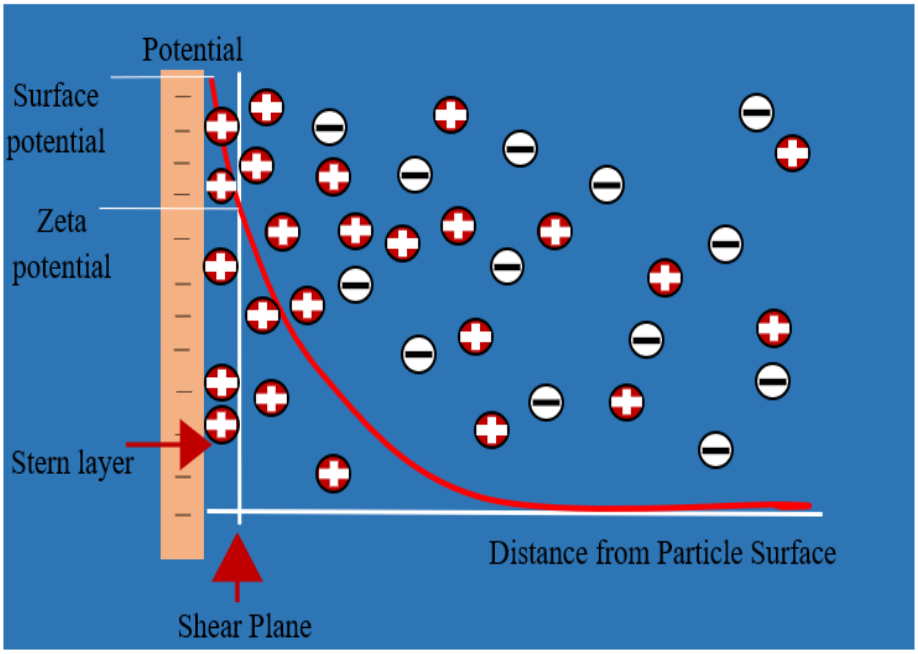


**Figure 1.11.** Schematic diagram of zeta potential which demonstrates the distribution of ions around the charged particle.[106]

### 1.10.3 X-RAY Diffraction of inorganic nanoparticles

XRD is an important characterisation technique that gives detailed information about the crystallographic structure of solid materials and chemical composition. The essential work of X-ray diffraction relies on constructive interference of a crystalline sample and monochromatic X-rays. Figure 1.12 shows Bragg's angle diffraction. The average crystal domain size (D) can be calculated using the Scherrer equation. Equation (1.2) was utilized to calculate the size of the crystallite of the inorganic nanoparticles.

$$D = \frac{K\lambda}{\beta \cos\theta} \qquad \text{Equation (1.2)}$$

$K$ is a dimensionless shape constant taken as 0.94

$2\theta$ is the diffraction angle,

$\lambda$ is the wavelength of the X-ray radiation (CuKα = 0.15406 nm), and

$\beta$ is the full width at half-maximum (FWHM) of the diffraction peak. [108, 109]

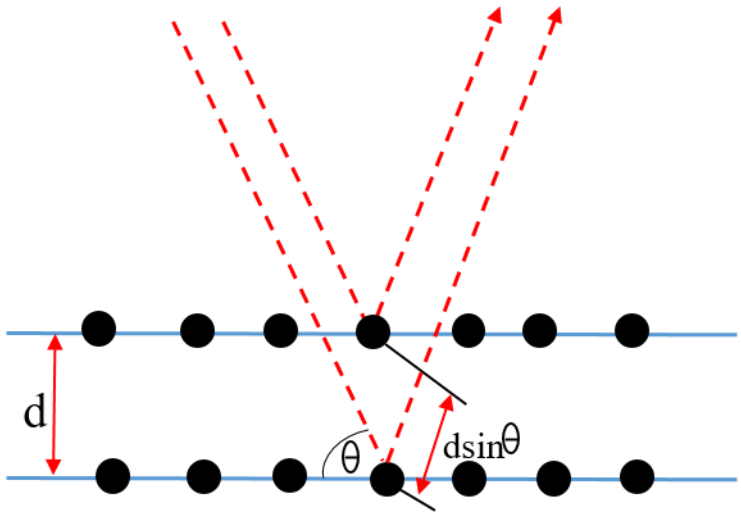


**Figure 1.12.** Bragg diffraction occurring by the interaction between X-rays and a crystalline sample. [108]

### 1.10.4 Scanning Electron Microscopy (SEM)

A scanning electron microscope is a type of electron microscope that creates images of a sample by scanning it with a concentrated beam of electrons. The electrons interact with atoms in the sample, reflecting at different angles that can be noticed and that contain data about the sample's surface topography and structure (see Figure 1.13). The most widely recognised method of analysis is by secondary electrons radiated by atoms energised by the electron beam. The signals are produced from connections of the electron beam with atoms at or close to the surface of the sample. The types of signals created by an SEM involve secondary electrons (SE), back-scattered electrons (BSE), characteristic X-rays, light (cathodoluminescence) (CL), specimen current and transmitted electrons. [110]

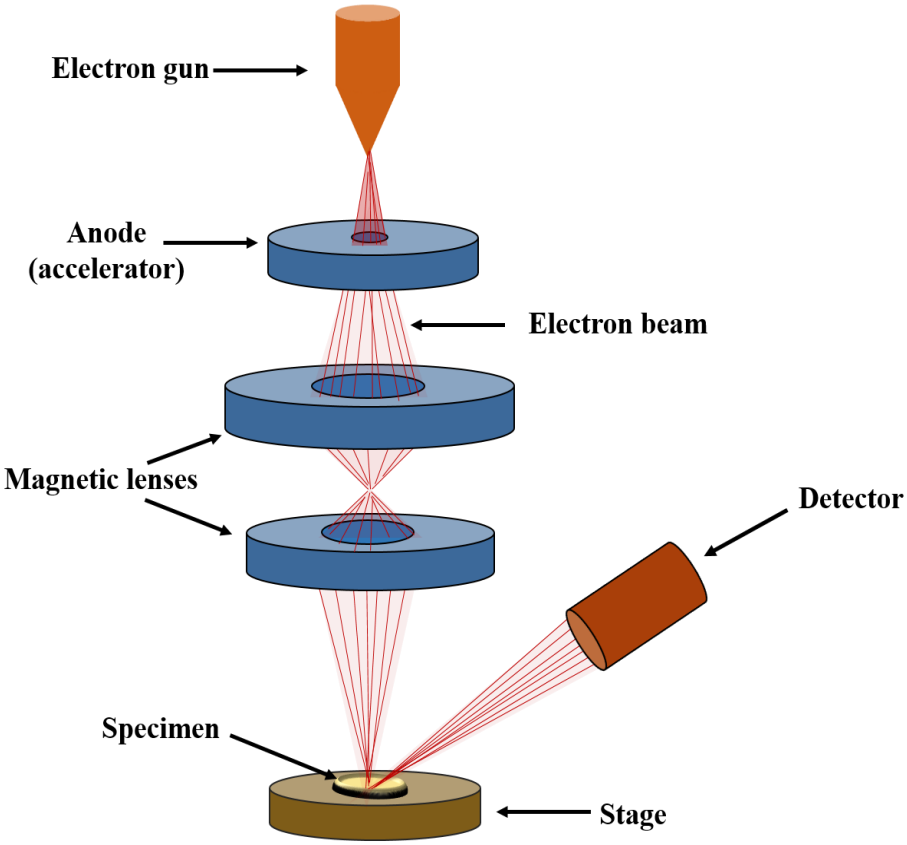


**Figure 1.13.** Schematic diagram of the components of scanning electron microscopy. Redrawn from ref.[111]

### 1.10.5 Transmission Electron Microscopy (TEM)

Transmission electron microscopy is a microscopy method whereby a beam of electrons is transmitted through an ultra-thin specimen, reacting with the specimen as it goes through. A TEM image is created by the interaction of the electrons transmitted through the specimen; the picture is magnified and centered onto an imaging device, for example, a fluorescent screen, a layer of photographic film, or a sensor, for instance, a CCD camera. It is generally used to examine crystal structures, chemical compositions, and sample orientations (see Figure 1.14). [110, 112]

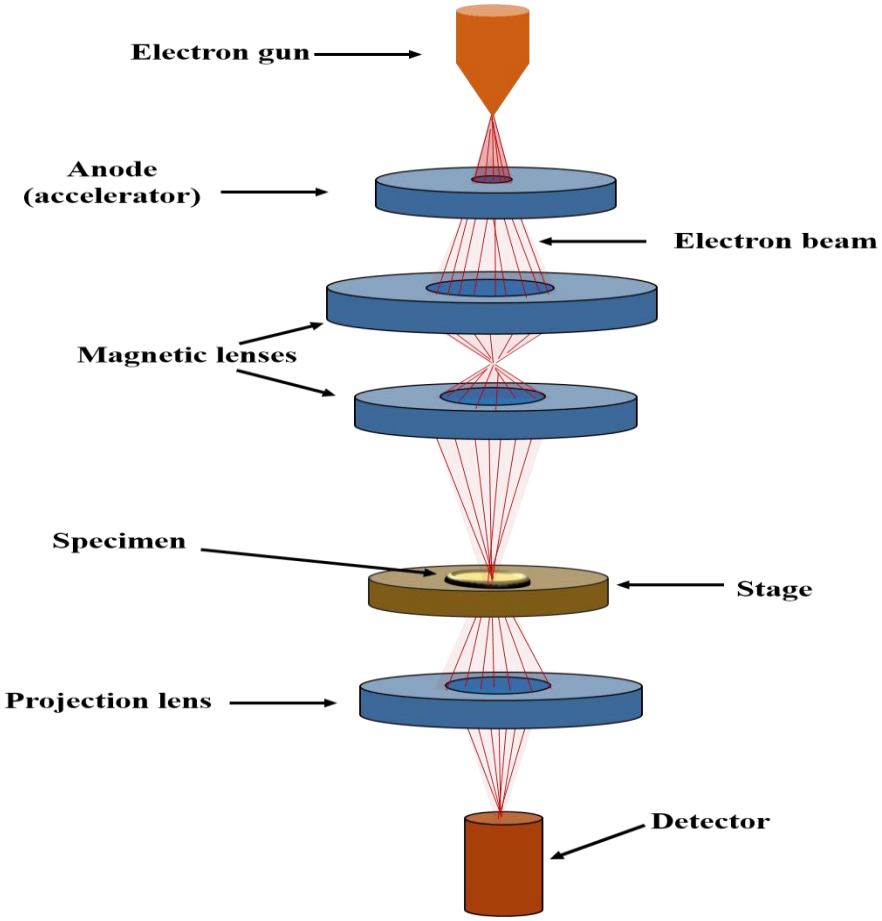


**Figure 1.14.**Schematic diagram of the components of transmission electron microscopy. Redrawn from ref.[111]

## 1.11 Antimicrobial activity of zinc oxide nanoparticles (ZnONPs) and titania nanoparticles ($TiO_2$NPs)

Although bulk ZnO is not considered a biologically hazardous material, recent studies focus on highlighting potential biological toxicities of ZnO in a nanoparticulate form (ZnONPs).[113] ZnO is found to have a high photocatalytic effectiveness and is reported as more biocompatible than $TiO_2$.[114, 115] ZnONPs and $TiO_2$NPs can both strongly absorb UV light [116] which activates them to interact with the cells in their vicinity. Their photocatalytic effect continues long after illumination with UV light, and it has been ascribed to surface electron depletion region strongly related to adsorbed negative oxygen species ($O_2^{\cdot-}$ , $O_2^{2-}$) on the particle surface.[117]

Aqueous suspensions of ZnONPs and $TiO_2$NPs under illumination with UV light and oxygen have a phototoxic impact due to generating reactive oxygen species (ROS), for example, superoxide ions ($O_2^{\cdot-}$) and hydrogen peroxide ($H_2O_2$) which is fundamental for their applications as antimicrobial agents.[118] The produced reactive species can enter into the microbial cells by diffusion and consequently, kill them or damage their cell

membranes and interior which inhibits microbial growth. This mechanism utilises the photocatalytic activity of ZnONPs for their antibacterial applications in bionanomedicine and bionanotechnology. Accordingly, improvement of ZnONPs bioactivity was considered as a consequence of the created free radicals, as ZnONPs is activated by UV illumination.[119] Seven *et al*.[120] and Padmavathy and Vijayaraghavan [121] have proposed a detailed reaction mechanism of this phenomenon. Both ZnO and $TiO_2$ as semiconductor materials contain a valence band (VB) and a conduction band (CB). Incident illumination with photons of energy more than 3.3 eV is directly absorbed and consequently causes an electron transfer from the VB to the CB. The transfer of electron starts a series of conceivable photoreactions with positive holes (h+) created in the VB while at the same time free electrons ($e^-$) are produced within the CB.[120, 122, 123] The positive holes ($h^+$), an immediate oxidant fundamental for the production of reactive hydroxyl radicals ($OH^\bullet$), serve as important oxidants in the photocatalytic process.[122-124] The free electrons in the CB reduce oxygen molecules, which are adsorbed on the surface of the photocatalyst.[124] Padmavathy and Vijayaraghavan proposed a relationship between photon reaction of the photocatalytic particles and their antibacterial activity in a progression of interactions resulting in the generation of hydrogen peroxide ($H_2O_2$) molecules which can easily penetrate the membrane of cells, creating deadly harm.[121] Sawai *et al*. have ascribed the damage of the cell membrane to peroxidation of the unsaturated phospholipids as a consequence of photo-catalytically produced free radicals and $H_2O_2$. [125] The researchers expressed the created ROS by chemical equations which are as follows:

$$ZnO \text{ or } TiO_2 + h\nu \longrightarrow e^- + h^+$$

$$h^+ + H_2O \longrightarrow {}^{\cdot}OH + H^+$$

$$e^- + O_2 \longrightarrow {}^{\cdot}O_2^-$$

$${}^{\cdot}O_2 + H^+ \longrightarrow HO_2^{\cdot}$$

$$HO_2^{\cdot} + H^+ + e^- \longrightarrow H_2O_2$$

Al-Awady *et al.* studied the antimicrobial effect of titania nanoparticles ($TiO_2$NPs) of various hydrodynamic diameters and crystallite sizes towards *C. reinhardtii* and *S. cerevisiae* upon illumination with UV and visible light for a range of nanoparticle concentrations and incubation times.[126] They also confirmed that bare $TiO_2$NPs affect the *C. reinhardtii* cell viability at much lower particle concentrations than for *S. cerevisiae.* The $TiO_2$NPs antimicrobial action increased upon illumination with UV light compared with that in dark conditions due to the oxidative stress of the produced ROS. However, they found that $TiO_2$NPs have also affected *C. reinhardtii* upon illumination with visible

light which indicates that they may also interfere with the microalgae's photosynthetic system leading to decreased chlorophyll content upon exposure to $TiO_2$NPs. Their results indicate that the larger the hydrodynamic diameter of the $TiO_2$NPs the lower is their antimicrobial effect, with anatase $TiO_2$NPs generally being more effective than rutile $TiO_2$NPs.[126] Some of the mechanisms of particle attachment to the microbial cells and pathways of cell damage are illustrated in Figure 1.15.

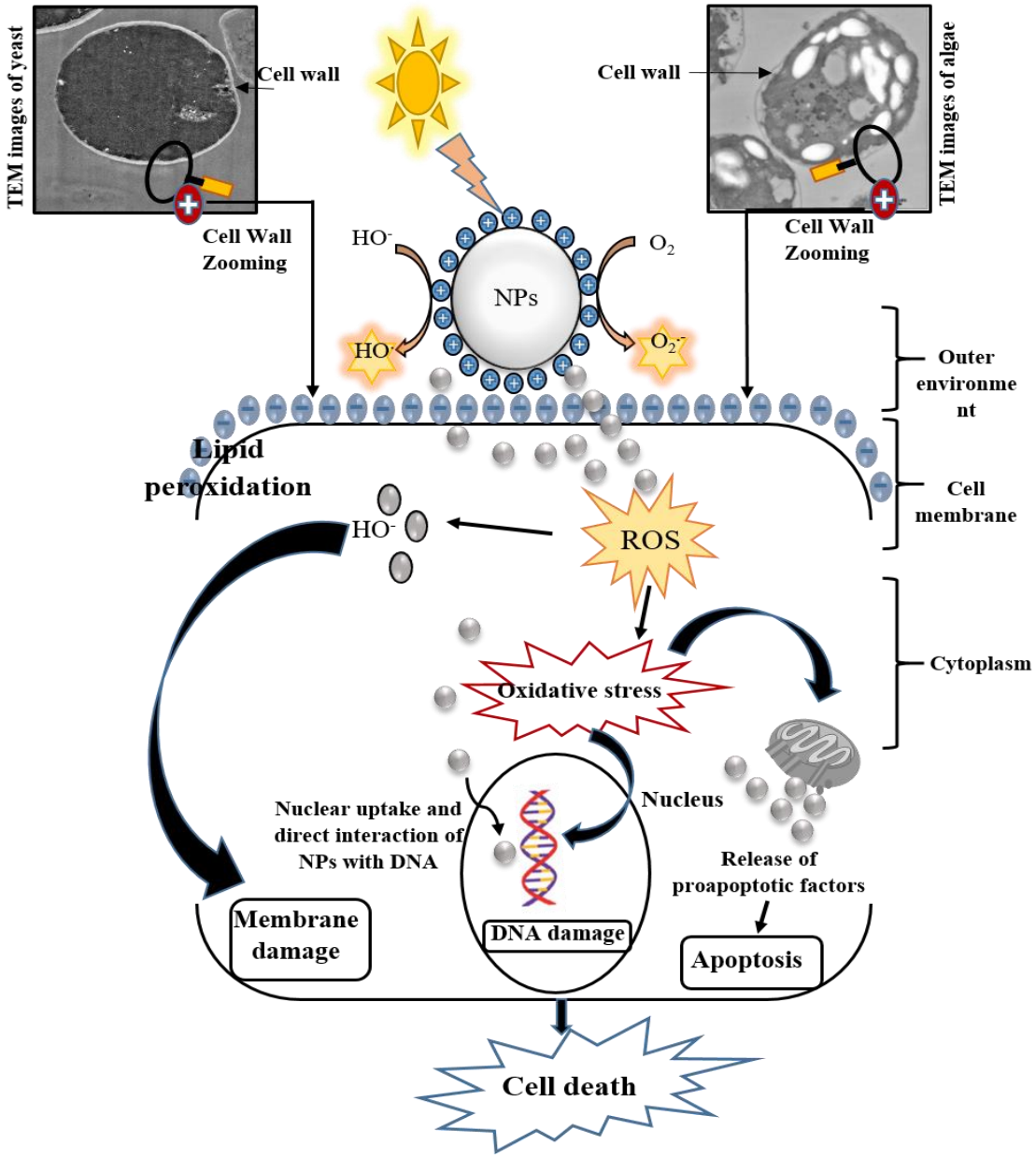


**Figure 1.15.** The interaction between nanoparticles and microalgae and yeast cell walls, leading to generating of ROS in the presence of light which in turn would destroy the cell wall because of oxidation of organic compounds such as carbohydrate, lipid, and protein. Some components were taken from references.[126, 127]

Due to their negative charge the generated $\cdot O_2^-$ and $\cdot OH^-$ species cannot easily penetrate through the negatively charged cell membrane.[128] Consequently, these species have been found to accumulate on the external surface of the microorganisms cell wall, while $H_2O_2$ molecules can also enter much easier through the cell membrane, leading to oxidation and damage of the cell interior (see Figure 1.15).[126, 129, 130] Thus, photo-oxidations may illustrate the photocatalytic action of ZnO on cells and its possible impact on their DNA.[131] Dunford *et al*. have examined the impact of ZnO samples as well commercial $TiO_2$ samples with various proportions of anatase/rutile on DNA upon UV irradiation *in vivo*. The work uncovers that DNA in human cells is also damaged by UV irradiation in the presence of ZnO.[132] Reddy *et al*. have used flow cytometry and viability tests to study ZnONPs toxicity toward *S. aureus* and *E. coli*.[133] Other researchers have studied the antibacterial action of ZnONPs to determine the bacterial growth through the viable cell percentage and the culture turbidity by the colony counts assay. They found that ZnONPs can significantly effect on the viability of bacteria. [134]

Yamamoto improved the antibacterial activity of ZnONPs by modifying the viability assessment method.[135] They believed that the antibacterial action rate was greatly enhanced by diminishing the start number of bacterial cells from $10^2$ to $10^6$ colony forming units. Nair *et al*. believed that the determination of the initial number of bacterial cells is essential in the assessment of the particles antibacterial action.[136] Aruoja *et al*. have studied the efficiency of three metal oxide nanoparticles (CuONPs, ZnONPs and $TiO_2$NPs) in inhibiting the growth of microalgae *Pseudokirchneriella subcapitata*.[35] Heinlaan and others have used the same three types of nanoparticles and found that CuONPs and ZnONPs have a toxic impact on *Thamnocephalus platyurus*, the bacteria *Vibrio fischeri* and crustaceans *D. magna*, while $TiO_2$NPs were apparently non-toxic.[32] Therefore, the toxicity of NPs depends on the size, particle morphology, synthesis method, and test organism species, and other factors as described in Figure 1.16. [32, 117, 126]

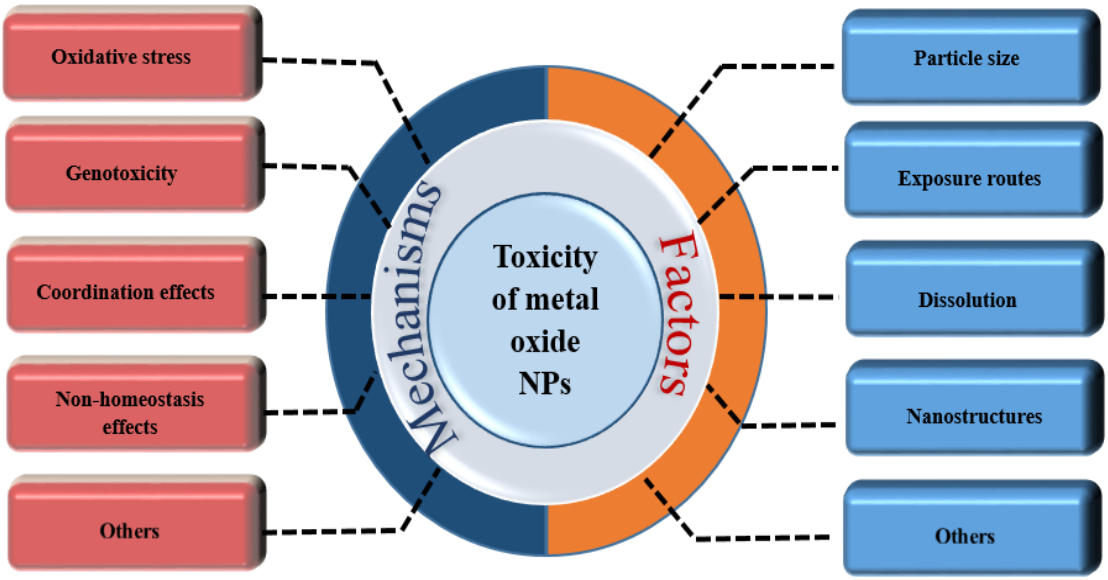


**Figure 1.16.** Schematic overview of the nanotoxic impact of metal oxide NPs. The essential factors that result in toxicity towards microbial cells include nanoparticle size, dissolution, structure and morphology, exposure routes, etc. The cell destroying mechanisms include oxidative stress, genotoxicity, coordination effects and non-homeostasis.[117, 127]

Hu *et al*. exposed earthworms *Eisenia fetida* in soil samples to different concentrations of ZnONPs and $TiO_2$NPs for up to seven days to assess their toxicity. They found that these NPs can significantly harm and kill the earthworms at particle concentrations higher than than 1.0 g $kg^{-1}$, influencing the cellulase enzyme activity, mitochondria and the cell DNA.[137] Kasemet *et al*. examined the toxicity of CuONPs, $TiO_2$NPs and ZnONPs on *S. cerevisiae* – a unicellular eukaryotic microorganism for 24 hours of incubation. It was found that for *S. cerevisiae* both ZnONPs and bulk ZnO were of equivalent toxicity, while, CuONPs showed nearly 60-fold increase in toxicity compared to the bulk CuO. It was discovered that both $TiO_2$NPs and bulk $TiO_2$ were non-toxic even at 20000 μg $L^{-1}$.[34]
Al-Awady *et al.* produced polyelectrolyte-coated $TiO_2$NPs with up to 4 layers of polyelectrolytes of alternating charge (PSS and PAH) using the layer-by-layer technique. They showed that the antimicrobial properties of polyelectrolyte-coated titania nanoparticles alternate with the surface charge for the particles with cationic outer layer (or bare titania) being much more effective antimicrobials than the ones with an outer layer of anionic polyelectrolyte. The anionic nanoparticles ($TiO_2$NPs/PSS and $TiO_2$NPs/PSS/PAH/PSS) showed much lower activity than the cationic ones,

$TiO_2$NPs/PSS/PAH and the bare $TiO_2$NPs, respectively.[126] These authors suggest that the decrease of antimicrobial action can be explained by the poor adhesion of the anionic nanoparticles ($TiO_2$NPs/PSS and $TiO_2$NPs/PSS/PAH/PSS) to the cell walls due to their electrostatic repulsion and the enhancement of the antimicrobial effect for cationic nanoparticles ($TiO_2$NPs and $TiO_2$NPs/PSS/PAH) is due to the amplification of the particle-cell electrostatically driven adhesion (Figure 1.17). They illustrate that the cationic nature of the titania nanoparticles at the conditions of the experiment (pH 5) has a much higher disrupting effect on the microorganisms cell wall than the photocatalytic effect and the production of ROS.

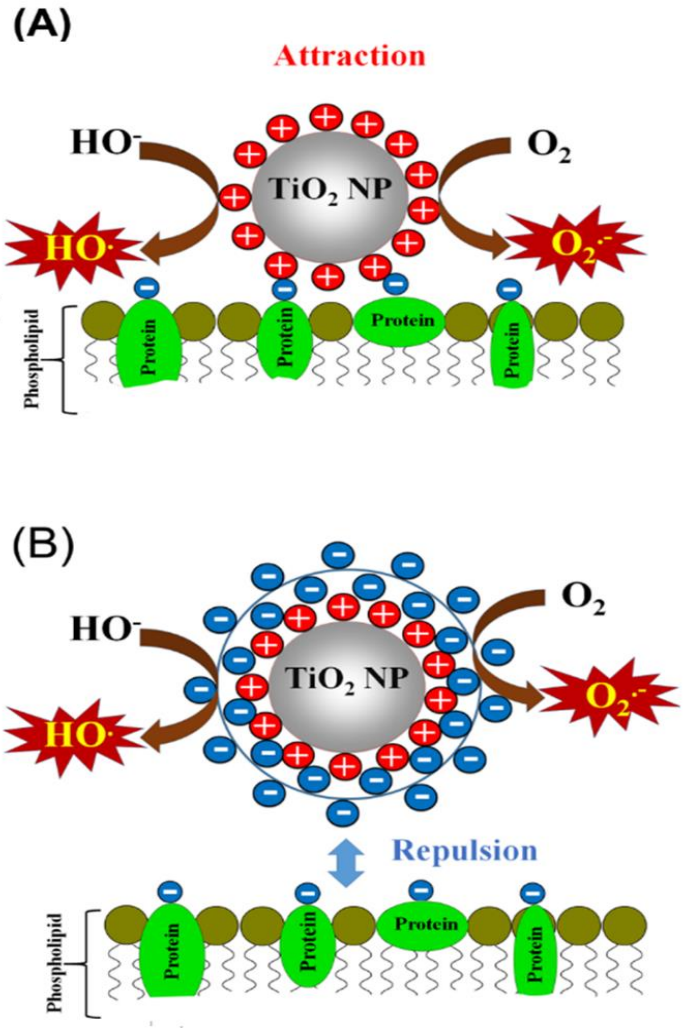


**Figure 1.17.** (A) Mechanism of cytotoxic action of $TiO_2$NPs due to the generation of reactive oxygen species (ROS) in the presence of sunlight and oxygen which can lead to cell damage. (B) The adhesion of the uncoated $TiO_2$NPs to the cell wall surfaces is favoured due to their opposite surface charges. (C) The interaction between the anionic surface of the cell membrane and $TiO_2$NPs coated with anionic polyelectrolyte is repulsive. The cationic $TiO_2$NPs and $TiO_2$NPs/PSS/PAH nanoparticles are expected to be

more toxic to the cells than the anionic $TiO_2$NPs/PSS particles. Reproduced with permission from Ref..[126]

Adams *et al*. have researched the eco-toxicity impacts of ZnONPs, $SiO_2$NPs and $TiO_2$NPs on Gram-negative bacteria (*E.coli*) and Gram-positive bacteria (*Bacillus subtilis*). These authors demonstrated that all three nanomaterials were destructive to both bacteria to variable degrees, with their antibacterial action increasing with the nanoparticle concentration. Also, the antibacterial impact of those nanoparticles normally increased from $SiO_2$NPs to $TiO_2$NPs to ZnONPs.[138] Jong *et al*. examined the antialgal action of four oxide NPs namely ZnO, $Al_2O_3$, $TiO_2$, and $SiO_2$ to microalgae *Chlorella sp*. From this study, it was found that ZnONPs (20 mg $L^{-1}$) and $TiO_2$NPs (HR3, anatase, 30 mg $L^{-1}$) mainly inhibited the growth of the algae at an exposure time for six days EC30, while $TiO_2$NPs (DJ3, rutile), $Al_2O_3$NPs and $SiO_2$NPs had practically no measurable toxicity to algae. In general, nanoparticles showed higher toxicity than that of bulk materials of the same chemical composition and polymorphic form. [139]

## 1.12 Magnesium hydroxide ($Mg(OH)_2$NPs) and magnesium oxide nanoparticles (MgONPs)

$Mg(OH)_2$NPs have attracted much attention over the years due to their wide applications in different fields as an environmentally friendly material with low cost of production [79-81] and may potentially be used in pharmaceutical formulations.[82-85] However, a limited number of studies have investigated the antimicrobial effects of $Mg(OH)_2$NPs and reported that *in vivo* toxicity values are low, thus demonstrating that it has a non-toxic effect on humans in sensible amounts.[140] Recently, it has been reported that $Mg(OH)_2$NPs were effective as antibacterial agents towards several bacteria, including *E. coli*, *S. aureus*, *P. aeruginosa* and *B. phytofirmans* [76, 141-145] and a number of studies have been focused on this new and effective antimicrobial agent.[78] Dong *et al*. have investigated the antibacterial action of $Mg(OH)_2$NPs on *Burkholderia phytofirmans* and *Escherichia coli*.[76] Their results indicated that $Mg(OH)_2$NPs suspensions are effective towards *B. phytofirmans* and *E. coli.* Their study has also examined the role of the $OH^-$ and $Mg^{2+}$ ions, which are naturally present in the $Mg(OH)_2$NPs suspension, on the antimicrobial action. They showed that an alkaline medium of pH 10.4 as well as an equivalent amount of $Mg^{2+}$ ions in the aqueous solution could not kill the bacteria.[76] They have also indicated that $Mg(OH)_2$NPs can kill *E. coli* even in dark conditions, suggesting that no photocatalytic properties are involved in their antibacterial action.[141] Hence, the

antibacterial mechanism of $Mg(OH)_2$NPs seems to be very different to those of other metal and metal-based compounds.[145-148]

Pan *et al*. synthesised $Mg(OH)_2$NPs from three different precursors (e.g. $MgCl_2$, $MgSO_4$ and MgO) and tested their antibacterial efficiency towards *E. coli* as a model Gram-negative bacteria.[78] Bactericidal examinations indicated that the antibacterial activity of $Mg(OH)_2$NPs was inversely related to the particle size. Their results also revealed that the ability of $Mg(OH)_2$NPs to adhere on the bacterial cell walls decreased in the order: $Mg(OH)_{2\_MgCl_2}$ > $Mg(OH)_{2\_MgSO_4}$ > $Mg(OH)_{2\_MgO}$, showing that the toxicity of the produced $Mg(OH)_2$NPs may be caused by the electrostatic interaction induced by secondary adsorption of counter-ions (Figure 1.18).

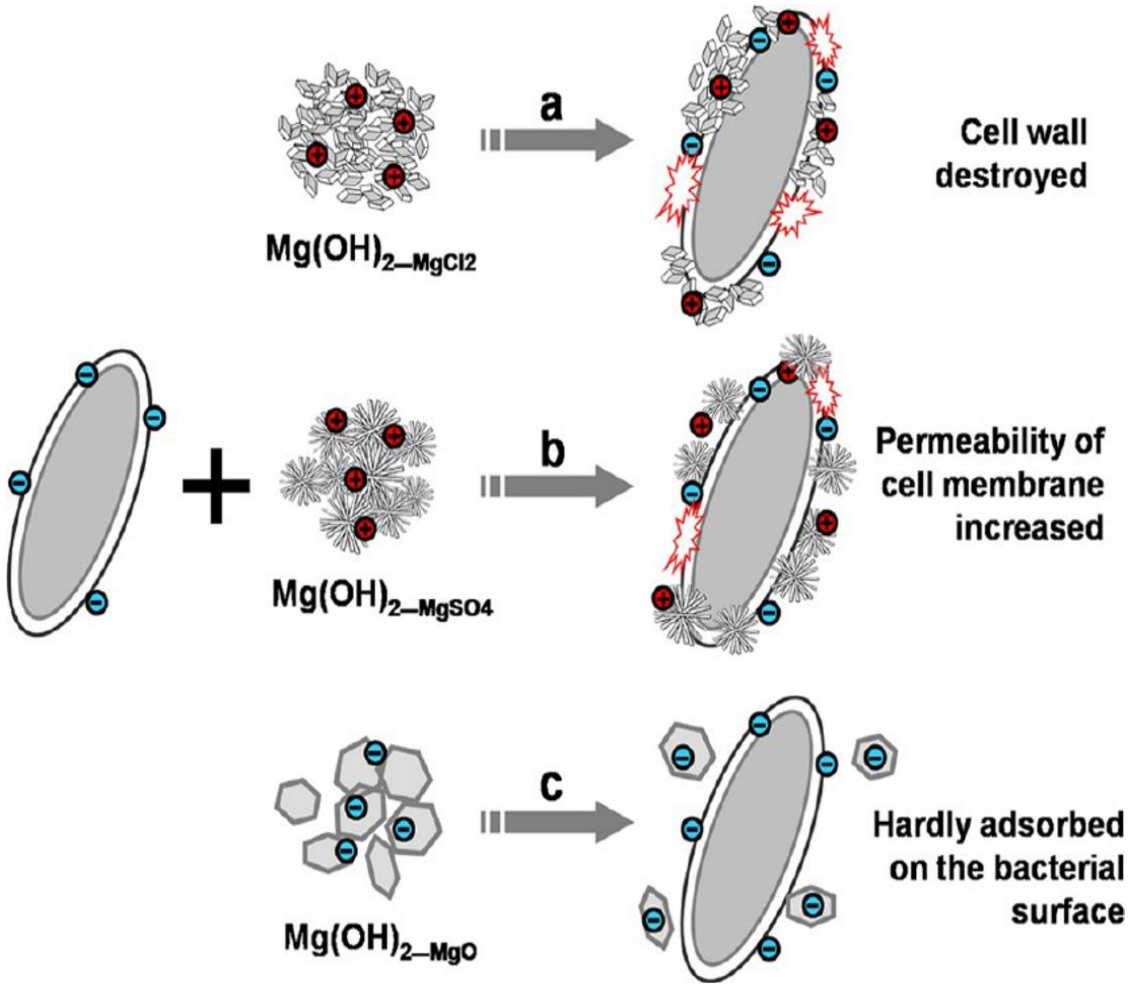


**Figure 1.18.** Schematic diagram showing the different contacting patterns between bacterial cells and $Mg(OH)_2$NP aggregates produced from different magnesium precursors ($MgCl_2$, $MgSO_4$ and MgO). [78]

This means that the type of precursor magnesium salt used to produce the $Mg(OH)_2$NPs by hydrolysis can greatly influence their antimicrobial properties by secondary absorption of counter-ions on the particles surface. These authors propose that $Mg(OH)_2$NPs adsorb on the negatively charged bacterial cell wall and somehow disrupt its integrity and increase its permeability which kills the bacteria as illustrated in Figure 1.19.[78]

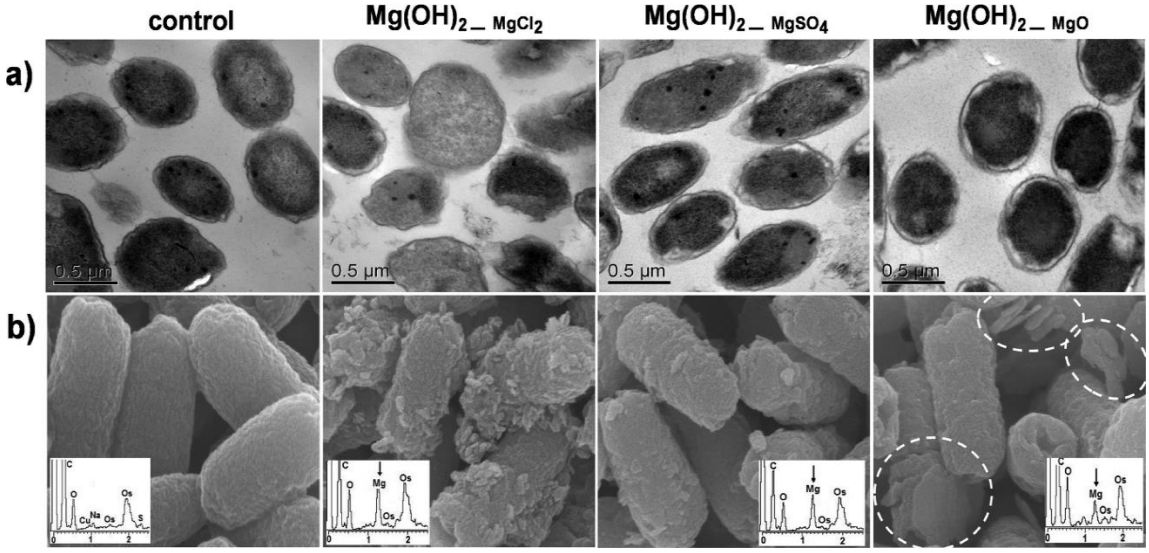


**Figure 1.19.** (a) TEM and (b) SEM images of *E. coli* treated with 0.5 mg/mL $Mg(OH)_2$ colloidal slurries for 4 h. Inset images of (b) show the EDS analysis of bacteria. The size of all SEM images is 6.0 µm. Reproduced with permission from Ref..[78]

Magnesium oxide nanoparticles (MgONPs) are very stable and biocompatible material and are strong antibacterial agents due to their alkalinity and generation of active oxygen species. It has been confirmed that the antibacterial mechanism of MgONPs is achieved by the production of superoxide on the surface of the MgONPs as well as a local increase in the pH by the hydration of the MgONPs surface with water.[149, 150] According to published reports, MgONPs disrupt the cell membrane and then cause the leakage of intracellular contents, which results in the bacterial cell death.[151] Hewitt *et al*. have evaluated the effects of three ceramic powders MgO, ZnO and CaO on *E. coli*. They indicated that MgONPs initiated the sensitivity changes in *E. coli* produced by active oxygen.[152] However, Leung *et al*. have described that very efficient antibacterial action of the MgONPs could be observed in the absence of any ROS generation. They showed that the mechanism of antimicrobial action might be because of the damage of cell

membrane. They reported that the toxicity of MgONPs, similar to other metal oxide NPs, is commonly due to the generation of ROS.[153]

## 1.13 Copper nanoparticles (CuNPs) and Copper oxide nanoparticles (CuONPs)

CuNPs have exceptional biological, physical and chemical properties, and due to the low cost of their preparation have become very popular to researchers developing novel antimicrobial agents.[100, 154, 155] By synthesizing a hybrid inorganic/organic species in the form of a Cu-chitosan nanoparticle, Usman *et al.*[155] have found that their antimicrobial action is highly effective when the coated particles have a size range of 2–350 nm. The same research team has evaluated the antibacterial and antifungal activities of these nanoparticles on different microorganisms, including methicillin-resistant *Staphylococcus aureus*, *Salmonella choleraesuis*, *Candida albicans*, *Pseudomonas aeruginosa*, and *Bacillus subtilis*. The results from their work have shown that the highly effective Cu-chitosan particles are very active as antimicrobial agents in anaerobic conditions. Note that Cu nanoparticles have the ability to rapidly oxidize, which limits their applications as antimicrobials when used in aerobic conditions.[100, 155, 156] Katwal and others have developed a new CuONPs preparation route by using electrochemical methods and demonstrated that they can control the CuONPs morphologies.[157] CuO particles can be produced in various shapes and sizes, and can provide enhanced antibacterial and antifungal activity against several pathogenic strains (Figure 1.20). Limited research has so far been undertaken on the anti-yeast activity of copper, however, it is widely accepted that its usability against yeast is similar to that against bacterial species.[158, 159] The mechanism of 'contact killing' in *S. cerevisiae* and *C. albicans* cells has been investigated when in contact with Cu-based particles (C11000 99.9% Cu and C75200 62% Cu).[158] By modifying Cu homeostasis, it was found that the elimination of *C. albicans* was 4 – 6 times faster, when compared to Cu ATPase export and *S. cerevisiae* deficient for Cu uptake transporters. Both scenarios involved the intracellular regulation of Cu rather than wild-type cells due to a large accumulation of Cu. This research group showed that the initial damage is localized on the cellular membranes, hence it action is similar to the 'contact killing' mechanism previously mentioned for bacteria. Characterization of the cell via mutation detection assays proved that there was an absence of DNA damage after treatment with Cu in this way. This did show extensive cytoplasmic membrane damage when the yeast was exposed to Cu surfaces. For the case

of *C. albicans* strains, there were very high levels of the *CRP1* P1-type ATPase copper transporter gene. By altering the intracellular uptake of Cu, there is a greater resistance against the Cu itself. An alternative resistance mechanism in place of the 'contact killing' scenario is suggested through the ALS1 and ALS3. This is a cluster of genes that encode the cell surface-associated glycoproteins, this could regulate the CRP1.[158, 159]

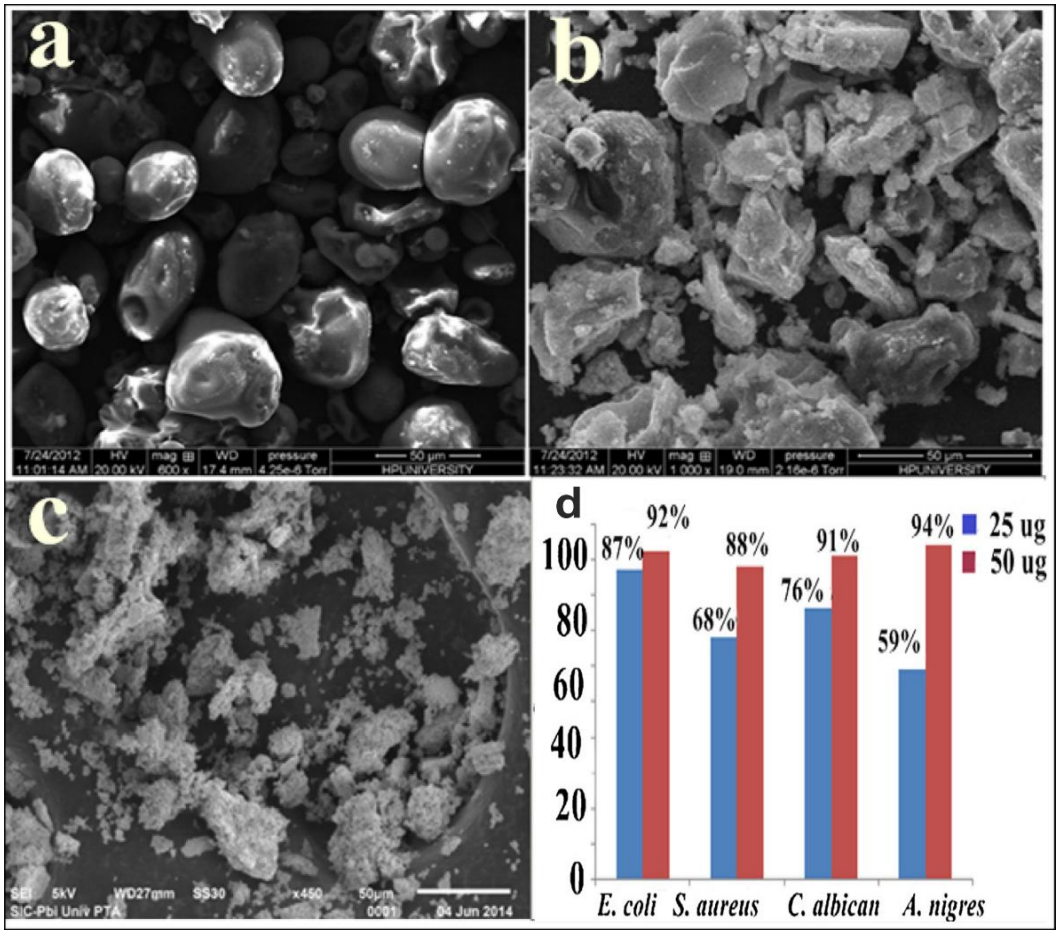


**Figure 1.20.** SEM micrographs of CuONPs prepared in the presence of (a) water, (b) water–methanol, (c) water–acetonitrile. (d) Inhibition rate (%) of *E. coli*, *S. aureus*, *C. albicans* and *A. nigres* after being exposed to 25 and 50 concentration (mg $mL^{-1}$) of CuONPs. Reproduced with permission from Ref..[157]

Mahapatra *et al.*[156] tested the antibacterial action of CuONPs towards *Klebsiella pneumoniae*, *Salmonella paratyphi*, *Shigella strains* and *Pseudomonas aeruginosa* and showed that the nanoparticles are efficient against these bacteria. They envisaged that CuONPs can cross through the bacterial cell membrane and affect vital enzymes in the bacteria cytoplasm leading to their death. It has also been shown that CuONPs are not cytotoxic on some human cells (e.g. HeLa cell line). Azam *et al.*[160] have also reported

that the activity of CuO based nanoparticles is dependent on their particle size when used as an antibacterial agent. In their study, they examined two Gram-negative bacteria (*E. coli* and *P. aeruginosa*) and two Gram-positive bacteria (*B. subtilis* and *S. aureus*). It was found that CuONPs exhibited inhibitory effects towards both groups of bacteria, which clearly depended on their stability, particle size and concentration when incubated with the bacterial culture. They concluded that the CuONPs can limit the bacterial growth by interacting with nanometric pores that exist on the cell membranes of most microorganisms. Ahamed and co-workers discovered that CuONPs with a size of ~23 nm had significant antimicrobial action towards various bacterial strains (*Klebsiella pneumoniae, Pseudomonas aeruginosa, Escherichia coli, Enterococcus faecalis, Shigella flexneri, Salmonella typhimurium, Staphylococcus aureus,* and *Proteus vulgaris*). *Escherichia coli* and *Enterococcus faecalis* showed the highest sensitivity to CuONPs while *Klebsiella pneumoniae* was resistant to this treatment.[100]

The mechanisms of toxicity of CuONPs might be mainly dependent on the contact between NPs and biomolecules, and toxicity essentially involves protein unfolding[161] , enzymatic activity loss, fibrillation, and thiol cross-linking. Below, we talk about three mechanisms that possibly clarify why CuONPs exert toxic impacts: oxidative stress, non-homeostasis impacts, and coordination impacts (see Figure 1.21).

The mechanism of CuONPs entry into cells appears in Figure 1.21a. CuONPs diffusion across the membrane happens directly when the size is small enough, there are positive ions on the surface of CuONPs, or when different factors are available.[162, 163] In the meantime, ion channels and transporter proteins allow very small CuONPs to cross the plasma membrane. Some CuONPs can go in cells via “endocytosis”: the membrane wraps around them, and vesicles transport CuONPs into cells. $Cu^{2+}$ solute from CuONPs can enter cells by transport and ion/voltage-gated channels.[127, 164, 165] Intracellular reactive oxygen species impact induced by CuONPs is shown in Figure 1.21b. CuONPs can directly interrelate with oxidative organelles for example mitochondria, redox active proteins stimulate reactive oxygen species production in cells, and ions $Cu^{2+}$ created by CuONPs can induce reactive oxygen species by different chemical reactions. Reactive oxygen species can induce DNA strand breaks, and affect gene expression. Furthermore, it can be seen from Figure 1.21c that $Cu^{2+}$ ions have the ability to form chelates with biomolecules or dislodge the metal ions in specific metalloproteins, which may result in functional protein inactivation. In addition to that, $Cu^{2+}$ released by CuONPs increase their local concentration and disrupt cellular metal cation homeostasis to result in cell toxicity as shown in Figure 1.21d.

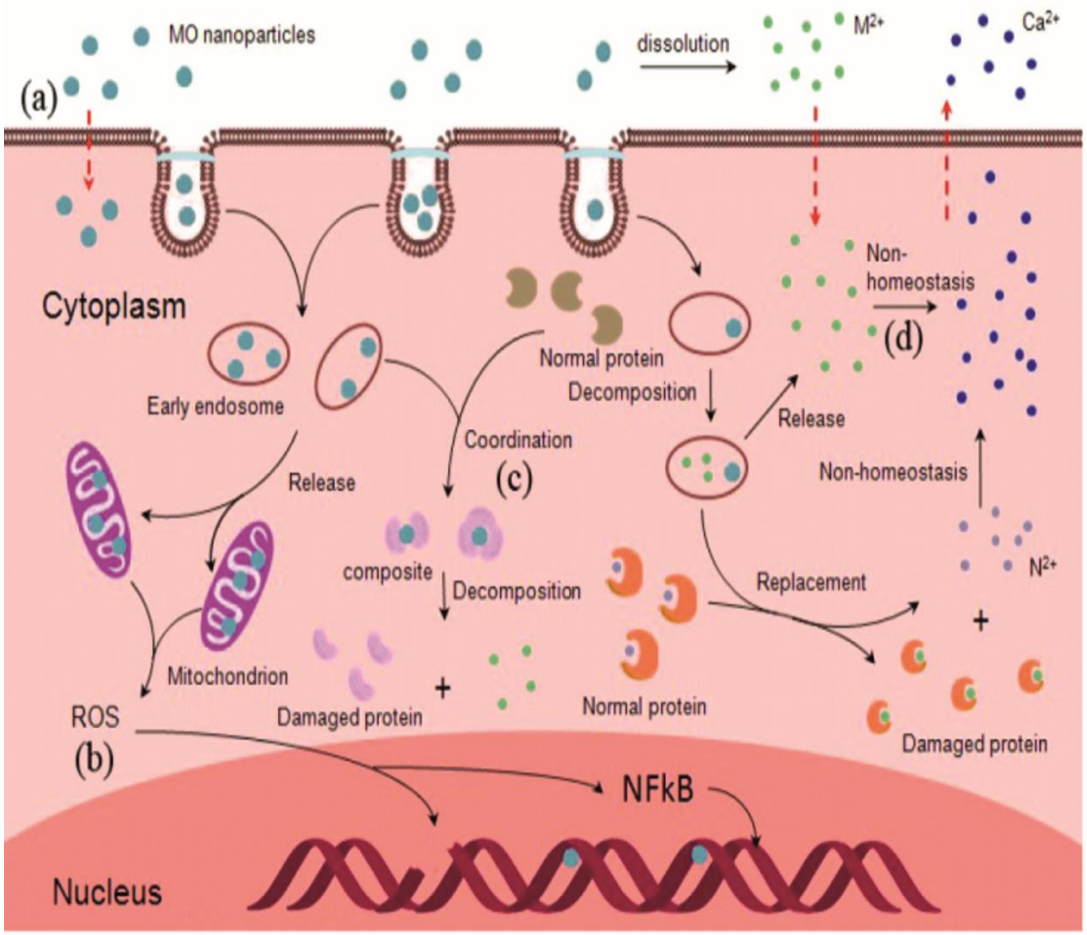


**Figure 1.21.** Schematic overview of the various pathways inducing cellular toxicity by CuONPs. (a) Potential mechanisms of CuONPs entry into cells; (b) The ROS impact of intracellular CuONPs; (c) The coordination impact of $Cu^{2+}$ released from CuONPs in cell; (d) The non-homeostasis impact disrupted by $Cu^{2+}$.[127]

## 1.14 Silver nanoparticles (AgNPs) and silver oxide nanoparticles ($Ag_2ONPs$)

AgNPs are one of the most studied inorganic nanoparticles utilized as antimicrobial agents [166-169]. AgNPs find antimicrobial applications in the production of injection mould plastics, textiles and coating-based usages [170] and they are also widely used in biomedical applications.[171, 172] Jo *et al*. have discovered that AgNPs show a good antimicrobial activity comparable to silver in its ionic form.[173] Allahverdiyev *et al*. have demonstrated that AgNPs have significant antimicrobial activity towards drug-resistant bacteria.[174] Lok *et al*. have reported that the antibacterial activity of AgNPs results from destroying the bacterial outer membrane.[175] A number of studies have suggested that AgNPs can cause

pits and gaps in the bacterial membrane and after that can fragment the cell.[176, 177] Egger *et al*. have also shown that $Ag^+$ ions emitted by AgNPs interact with disulfide or sulfhydryl groups of enzymes that lead to damage of metabolic processes which causes the bacterial cell death. [170]

According to Sintubin *et al.,* AgNPs release silver ions (Ag+) which can damage the target cells through several different pathways: (i) $Ag^+$ ions binding to DNA and RNA which result in their loss of biological function; (ii) AgNPs can also react with sulphur containing peptides inside the cells and on the cell membrane which in affects their viability. (iii) AgNPs can potentially destabilise cell membrane proteins and inhibit various intracellular enzymes. (iv) at high AgNPs concentration, the released $Ag^+$ ions affect the cytoplasm components and nucleic acids whereas at lower concentrations they tend to inhibit respiratory chain enzymes and impair membrane permeability to proton and phosphates.[178]

Mie *et al*. have examined the antibacterial action of their custom-synthesized AgNPs of particle size 19 nm towards eight different microorganisms utilizing the disk diffusion method. Their results showed that such AgNPs synthesized using *Parmotrema praesorediosum* have potential antibacterial action towards Gram-negative bacteria. Therefore, the authors recommended that such synthesized AgNPs could be used in the pharmaceutical and biomedical industries.[179] Hernández-Sierra *et al*. have studied the bactericidal action of AgNPs, ZnONPs, and AuNPs against *Streptococcus mutans*. The authors demonstrated that AgNPs displayed the most effective antibacterial action for controlling *S. mutans*, suggesting that AgNPs could be utilized in fighting dental caries since it usually is caused by *S. mutans*.[180] Besinis *et al*. have also examined the toxicity effect of AgNPs towards *S. mutans* and showed that the antibacterial activity of AgNPs towards *Streptococcus mutans* was higher than that of chlorhexidine.[181] Zarei *et al*. have studied toxicities of AgNPs against four foodborne pathogens namely *Escherichia coli, Vibrio parahaemolyticus, Listeria monocytogenes* and *Salmonella typhimurium*. As indicated by their results, AgNPs had the strongest antibacterial impact against the mentioned pathogens. Thus, the authors concluded that AgNPs could be a good option for cleaning and disinfection of equipment and surfaces in the food-related environments.[182] Additionally, AgNPs have been reported to be less toxic than numerous different disinfectants. Marambio-Jones and Hoek had reviewed the antibacterial effects of the AgNPs and their implications for the environment and human health.[183] Kim *et al.* reported strong antifungal effect of AgNPs against pathogenic yeast.[184]

$Ag_2$ONPs have been found to have very strong antimicrobial properties and may be considered as an alternative of most modern antiseptic agents.[174, 185] Sondi and Salopek-Sondi have tested the antimicrobial activity of $Ag_2$ONPs towards *E. coli*. These authors believed that when *E. coli* were exposed to $Ag_2$ONPs nanoparticles, they can end the cell cycle at the $G_2$/M phase because of the DNA damage through oxidative stress.[186] Such nanoparticles would be promising substitutes for various broad spectrum antibiotics.

## 1.15 Gold nanoparticles (AuNPs)

AuNPs are thought to be so important in the development of antibacterial action because of their photothermal activity, nontoxicity, polyvalent impacts, high ability for surface functionalization and ease of detection.[187-190] Cui *et al*. have reported that the antimicrobial action of AuNPs does not include any ROS-related mechanism rather than the adhesion of the AuNPs to the bacterial membrane followed by membrane potential modification and ATP level decline. In addition, AuNP have been found to inhibit tRNA by binding to the ribosomes.[191] Tiwari *et al*. have tested the antibacterial and antifungal effects of the AuNPs functionalized with 5-fluorouracil towards *Staphylococcus aureus*, *Escherichia coli*, *Pseudomonas aeruginosa*, *Aspergillus fumigatus*, *Aspergillus niger* and *Micrococcus luteus*. Their results revealed that the AuNPs had higher antibacterial activity towards Gram-negative bacteria than Gram-positive bacteria because of the easier nanoparticle transfer into the Gram-negative bacteria. Likewise, they indicated antifungal activity against *Aspergillus fumigatus* and *Aspergillus niger*.[188]

Zhou *et al*. have investigated antibacterial effects of Au and AgNPs on bacillus Calmette-Guérin (BCG) and *E. coli*. According to their results, AgNPs showed excellent antibacterial activity on both the Gram-positive bacteria BCG and the Gram-negative bacteria *E. coli*. They also investigated AuNPs with a weakly bound capping agent (citrate) and a strongly bound capping agent (poly-allylamine hydrochloride, PAH). The researchers showed that the PAH could strongly interact with the bacterial cell membrane because of its positively charged nature. The authors commented on the mechanisms of interaction between AuNP and AgNPs and *E. coli*.[189] These bacterial cells were found to take up single citrate-coated AuNPs or aggregates of AuNPs complexes. The PAH-coating facilitated the AuNPs uptake into the bacterial cells followed by lysis. However, most of the AgNPs were trapped on the cell walls.[189]

## 1.16 Aluminium oxide nanoparticles ($Al_2O_3$NPs)

Aluminium oxide nanoparticles have a wide range of applications in different fields such as personal care products as well as industrial sorbents and fillers. Alumina forms very stable nanoparticles which are impervious to temperature changes and have a hexagonal close packing structure, including the $O_2^-$ and the $Al^{3+}$ ions that fill 65% of all the octahedral sites existing in the structural network.[192-195] Sadiq *et al*. have studied the action of $Al_2O_3$NPs as anti-oxidants that block the generation of reactive oxygen species (ROS), indirectly blocking apoptosis, which starts the ROS defence system, before finishing the cell death program.[195] Furthermore, they have reported the growth inhibition of the pathogen *E. coli* by alumina nanoparticles with a particle size of approximately 179 nm in the concentration range of 10-1000 µg $mL^{-1}$. The majority of the metal oxides act as antimicrobials by using the processes of production of ROS, which leads to damage of the bacterial cell wall. However, $Al_2O_3$NPs can likewise act as a radical scavenging agent which have non-toxic effect to the human cell. [195] The method of action of $Al_2O_3$NPs towards *E. coli* can be explained by an initial adhesion of positively charged alumina nanoparticles to the negatively charged bacterial cell surface. When a bacterial cell influences a human cell, it leads to the generation of ROS, which can be very damaging to human health, as it can cause DNA damage that could be a probable cause of cancer. Since, $Al_2O_3$NPs have a radical scavenging property, they block the production of ROS, which leads to bacterial cell death, before the human cells are damaged. [195, 196]

## 1.17 Cerium oxide nanoparticles ($CeO_2$NPs)

$CeO_2$ is a technologically significant material because of its properties and applications in different fields ranging from engineering to biological sciences [112].[197, 198] Santos *et al*. have found that at lower temperatures the $CeO_2$NPs have antimicrobial action towards different bacteria, including *Shewanellaoneidensis, Pseudokirchneriella subcapitata, E. coli* and *B. subtilis*, due to damaging of the microorganisms cell walls.[197, 198] Many studies state that the concentration of $Ce^{3+}$ increases compared to $Ce^{4+}$ as the size of the nanoparticles decreases, with the concentration of $Ce^{3+}$ is under 1% in suspension of 10 nm $CeO_2$NPs, while it increases to 6% for $CeO_2$NPs. There are $O_2$ gaps present in the oxidation states of these two $CeO_2$NPs. The production of an $O_2$ vacancy is accompanied by the reduction of the $Ce^{4+}$ formula to the $Ce^{3+}$, resulting in the loss of $O_2$ molecule. This distinctive radical scavenging property of $CeO_2$ (IV) nanoparticles makes them an attractive option for applications in wound healing dressings. Moreover, $CeO_2$NPs have

an important antimicrobial action, as they can act as radical scavengers and block the ROS generation which can also eliminate microorganisms.[197-199]

## 1.18 Yttrium oxide nanoparticles ($Y_2O_3$NPs)

$Y_2O_3$NPs have multiple applications in mechanical polishing, chemical synthesis and as additives to drugs, varnishes, food and cosmetics.[200] $Y_2O_3$NPs have one of the highest free energy of formation of their oxide structure [201] and do not deviate from their stoichiometry under the normal temperature and pressure conditions or by the impact of atmospheric $CO_2$ and $H_2O$ vapours. $Y_2O_3$NPs have two polymorphs, which are A and B form of hexagonal close-packing structure (hcp). Atou *et al*. have indicated that the antioxidant properties of the $Y_2O_3$NPs prevent the cell death because of excessive oxidative stress.[202] Furthermore, Schubert *et al*. have shown that the properties of $Y_2O_3$NPs are dependent on their structure but independent of the particle size in the range of 6-1000 nm. The researchers also showed that the $Y_2O_3$NPs act as direct antioxidants to limit the amount of reactive oxygen species required to kill the cells.[203] The $Y_2O_3$NPs are relatively non-toxic to neutrophils and macrophages which is a very beneficial wound healing property. [199, 203]

## 1.19 Colloid antibodies for microbial cells shape and surface recognition

Conventional antimicrobial nanoparticles have one major drawback as they cannot specifically differentiate between microbial and human cells, which is why they could potentially have a toxic effect on human health. This is the reason why direct replacement of common antibiotics with antimicrobial nanoparticles formulations can be challenging. This can be partially overcome by functionalising antimicrobial nanoparticles with antibodies. An interesting alternative was recently proposed by Borovicka *et al.* where a combination of antimicrobial nanoparticles with inorganic shells imprinting the shape of target microbes [204] was used in their cell shape-selective recognition and killing in a mixture with microbial cells of different cell shape and size. These "colloidal cell imprints" were prepared by depositing silica on microbial cells pre-coated with AuNPs. These composite shells were then partially fragmented by ultrasound and the fragments were recovered after removing the templated cells with a bleaching solution (see Figure 1.22).[205]

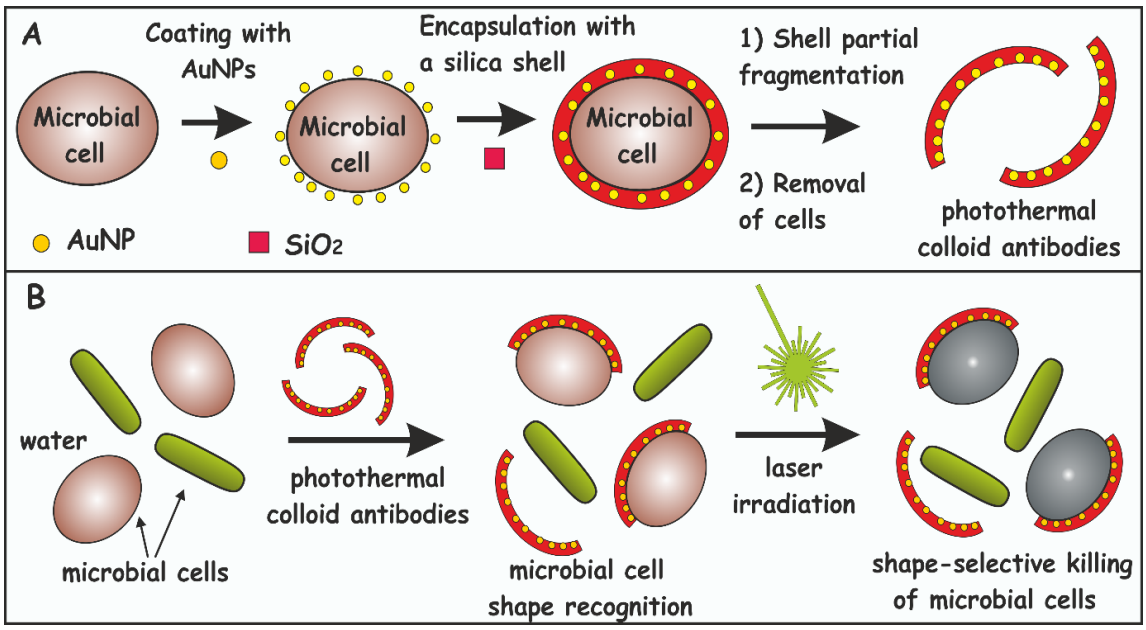


**Figure 1.22.** (A) Fabrication of the photothermal colloid antibodies (PCAs) by templating AuNP-coated cells with silica and subsequent silica shell fragmentation and bleaching of the cell templates with Piranha solution. (B) Experimental setup illustrating the principle of action of PCAs with integrated AuNPs on their inner surface in a suspension of two types of microbial cells of different morphology. PCAs recognize and bind only to bacteria of matching shape, which are killed selectively by the photothermal effect after laser irradiation while the other bacteria in the mixture remain viable. Grey colour signifies dead cells. Redrawn from Ref.[205]

The incubation of these AuNPs-functionalised colloidal cell imprints in a mixture of microbial cells of various shapes (Figure 1.22) showed that they attach only to cells matching the imprinted cell shape and deliver antimicrobial agent (gold nanoparticles) directly to their membranes. Since the AuNPs have photothermal properties, irradiation with laser led to cell shape selective killing of microbial cells due to overheating of their surface in contact with the imprint (see Figure 1.22b and Figure 1.23).

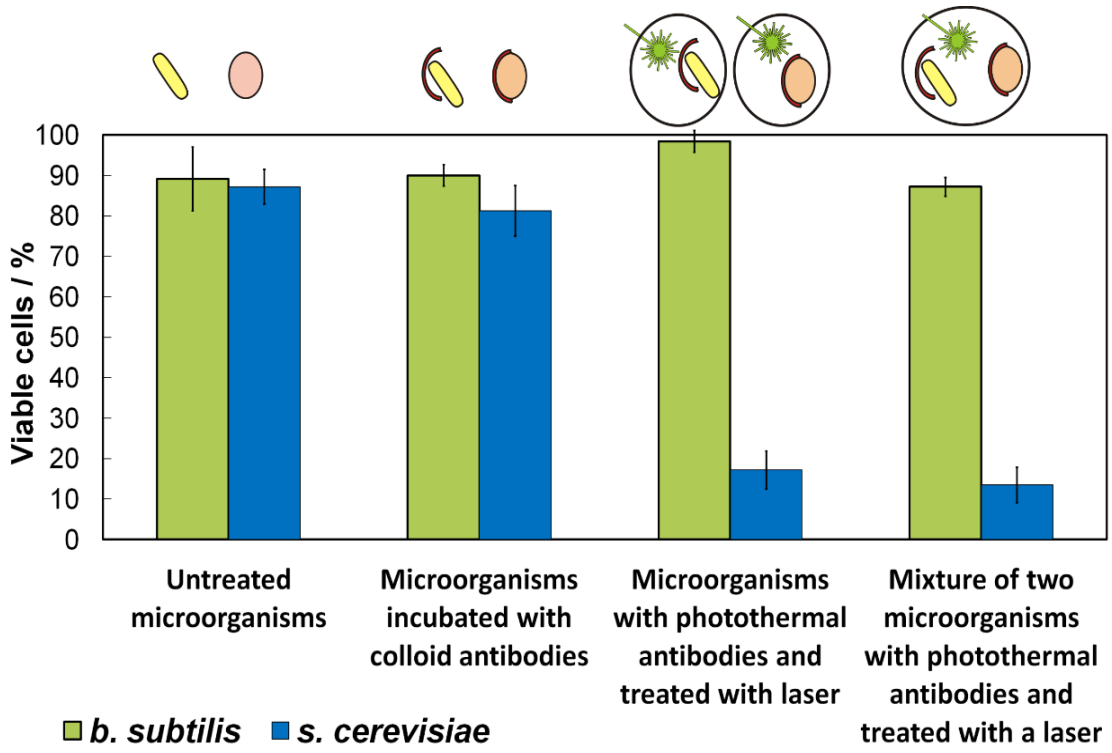


**Figure 1.23.** Graphical summary of the selective yeast cell recognition and killing experiments by PCAs in a mixture of yeast and B. subtilis. Reproduced with permission from Ref.[205]

The same approach can be applied with many other antimicrobial nanoparticles. This cell shape recognition of the microbial cell imprints minimises the direct exposure of other cells to antimicrobial nanoparticles .[205] Generally, the size recognition of the target cell and its colloid imprint amplifies the magnitude of the interaction energy between their surfaces. When the free interaction energy (sum of electrostatic, van der Waals and biospecific interactions) between the surfaces of the target microbial cell and its colloid imprint is attractive, the cell size and shape matching amplifies the attraction. For micrometre-sized target cells and moderate ionic strength this can result in more than three orders of magnitude difference in the interaction energy.[206] Rahma *et al.* developed similar approach by using hemispherical silica shell particles produced by templating yeast cells with silica followed by their fragmentation, bleaching and surface functionalisation with N-chloramines. Antimicrobial testing was carried out on Gram-negative (*E. coli*) and Gram-positive (*B. cereus*) bacteria and confirmed their superior antimicrobial efficacy compared with small molecule antiseptic agents.[207] This approach opens a number of new avenues for building powerful selective biocides based on combinations of colloid antibodies and cell killing strategies based on nanoparticles which can be applied in new antibacterial therapies.

## 1.20 Environmentally benign antimicrobial nanoparticles

Biodegradable antimicrobial nanoparticles with cores prepared from renewable materials could be used as sustainable delivery system for active payloads in molecular or ionic form, such as metal ions and other useful bioactive components.[208] Lignin is the most abundant aromatic biopolymer in nature.[209] It has an amorphous 3D structure,[210, 211] and it is naturally degradable and biocompatible.[212, 213] Biodecomposition of lignin in the environment [214, 215] transforms it in soil humus.[216] Frangville *et al.* [217] and Richter *et al.* [218, 219] proposed two alternative methods for preparation of environmentally biodegradable lignin nanoparticles from Kraft and Organosolv lignin which can be loaded with hydrophilic [217] and hydrophobic [217, 218] antimicrobial payloads. Their work was extended by Richter *et al*. by synthesizing environmentally-benign antimicrobial nanoparticles from lignin cores infused with silver-ion (see Figure 1.24 and Figure 1.25).[219]

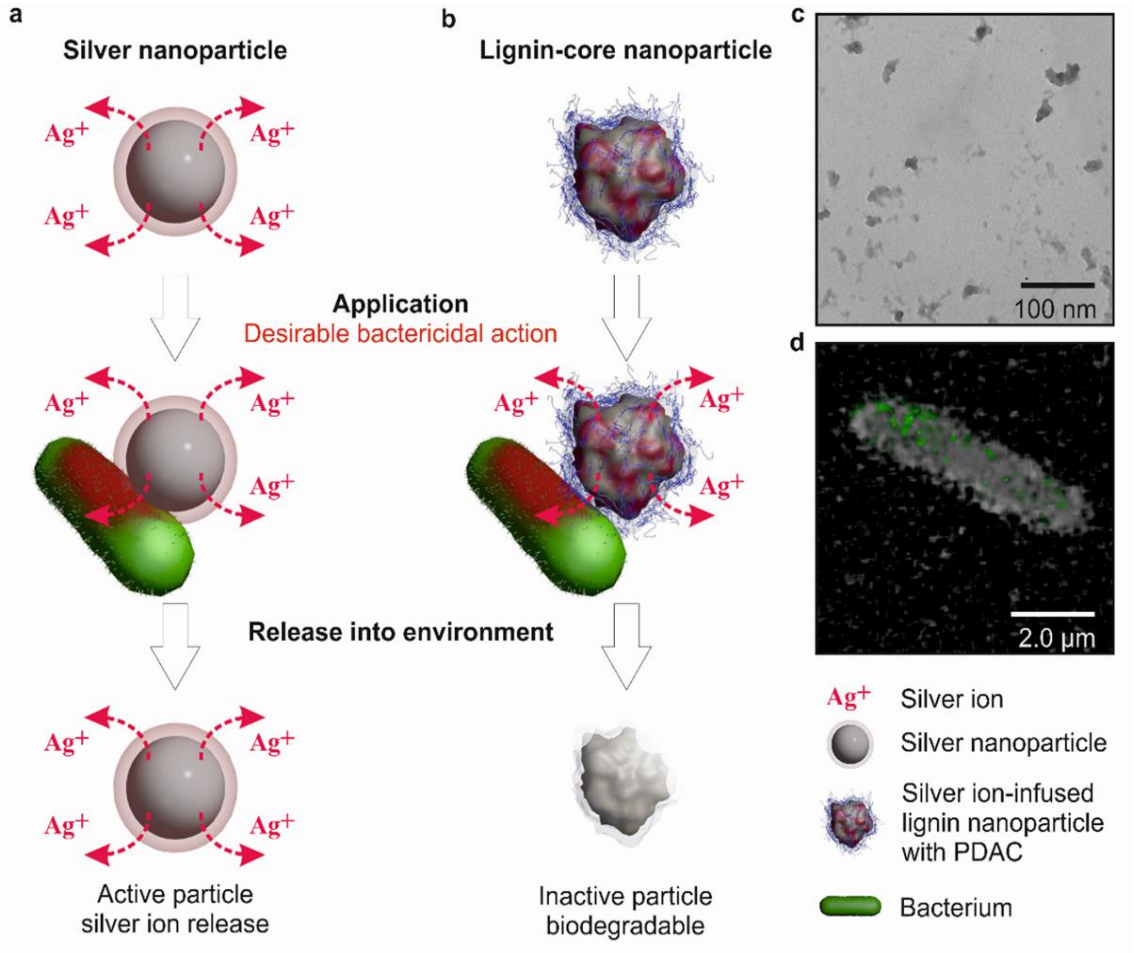


**Figure 1.24.** Schematics of the general use cycle and principle of bactericidal action of the environmentally-benign lignin-core nanoparticles (EbNPs) compared to the presently used silver nanoparticles (AgNPs). (a) General mechanism of antimicrobial action of

common AgNPs via release of $Ag^+$ ions, which continues post utilization. (b) Antimicrobial action mechanism of $Ag^+$ ion-infused EbNPs with cationic polyelectrolyte coating, which facilitates electrostatic attraction between the EbNPs and the negatively charged cell walls. In contrast to AgNPs, EbNPs are depleted of silver ions during application, minimizing their post-utilization activity. (c), TEM micrograph of as-synthesized EbNPs in the size range of 40 to 70 nm. (d), Confocal microscopy image of EbNPs with polyelectrolyte coating adhering to the cell membrane of *E. coli*. Reproduced with permission from Ref..[219]

These lignin nanoparticles were turned cationic by adsorption of a cationic polyelectrolyte, polydiallyldimethylammonium chloride (PDAC) to give $Ag^+$-loaded environmentally benign nanoparticles (EbNPs-$Ag^+$-PDAC). The cationic nature of these particles facilitated the targeted adhesion of the nanoparticles to negatively-charged cell membranes of a range of bacteria. These particles exhibit broad-spectrum antimicrobial activity during application, while offering an environmentally friendly alternative to metallic silver nanoparticles (Figure 1.26). The EbNPs-$Ag^+$-PDAC exhibit broad spectrum biocide action and are capable of killing common Gram-negative and Gram-positive human pathogens as well as quaternary amine-resistant bacteria, while using 10× less silver when compared with conventional branched poly ethylene imine–coated AgNPs (BPEI-AgNPs) and $AgNO_3$ aqueous solution. The array of high-throughput screening tests on mammalian cells and zebrafish embryos indicate that the EbNPs have decreased impact on the majority of biological endpoints, when compared with equivalent mass of AgNPs and $Ag^+$. However, the EbNPs-$Ag^+$-PDAC were showed to have time-limited antimicrobial action after they can release their residual silver ions.[219]

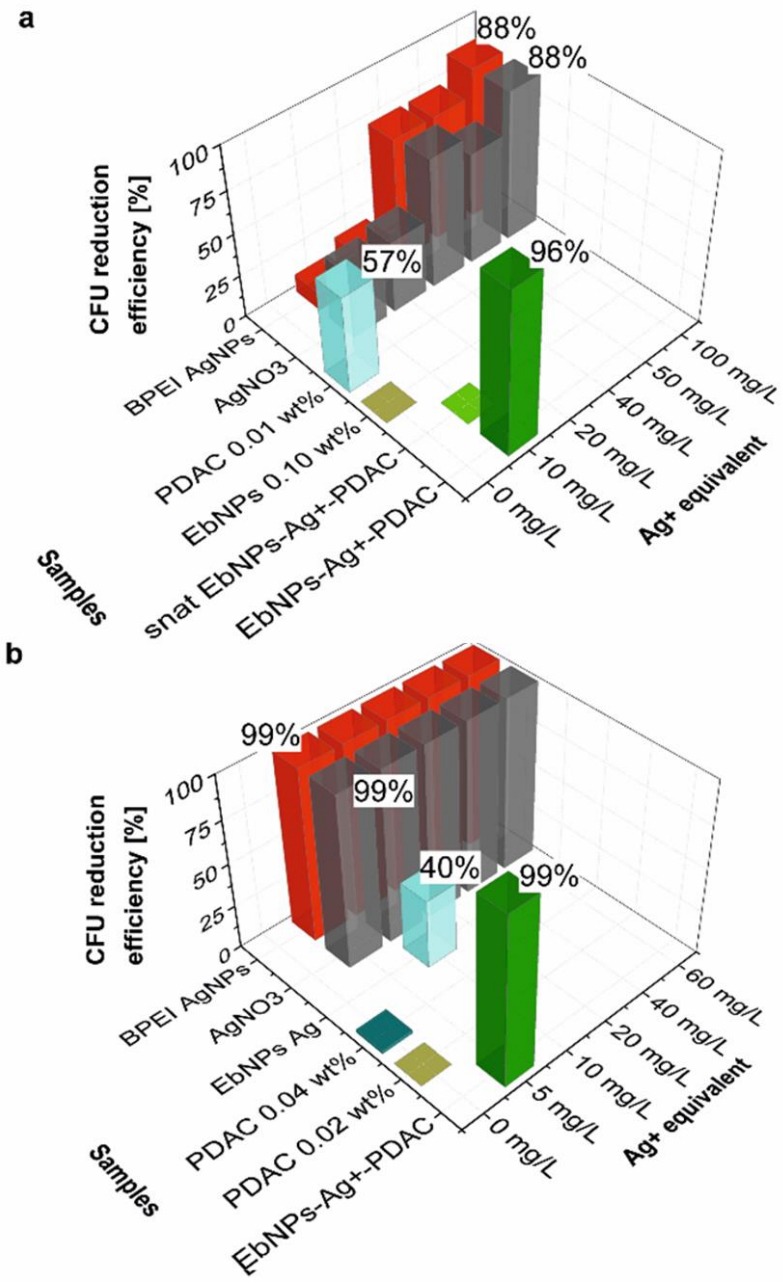


**Figure 1.25.** Quantification of Colony Forming Unit (CFU) reduction efficiency as a function of mg $L^{-1}$ $Ag^{+}$ equivalent of EbNPs and control samples on *E. coli*, *P. aeruginosa*, and *Ralstonia sp*. (a), *E. coli* test – 1 min contact time. The fully functionalized sample is EbNPs-$Ag^{+}$-PDAC. It is compared to a number of controls, EbNPs without $Ag^{+}$, PDAC polyelectrolyte solution, $AgNO_3$ solution and BPEI-coated AgNPs. EbNPs-$Ag^{+}$-PDAC achieved the highest CFU reduction of all samples with the smallest amount of silver. (b) PDAC-resistant *Ralstonia* test: For these bacteria EbNPs-$Ag^{+}$-PDAC, BPEI-AgNPs and $AgNO_3$ solutions outperformed PDAC samples. Note that EbNPs-$Ag^{+}$-PDAC is the only sample that is consistently efficient at very low $Ag^{+}$ loading. Reproduced with permission from Ref. [219]

Different methods for characterisation of the nanoparticle antimicrobial action have been employed, e.g. growth inhibition method,[220] the estimation of the minimum inhibitory particle concentration,[178] and the minimum bactericidal concentration.[221] Nanoparticles have also been used to encapsulate and deliver antibacterial. Martins *et al.* has encapsulated violacein poly-(D,L-lactide-co-glycolide) (PLGA) nanoparticles to deliver it as bactericidal agent. This minimum inhibitory concentration of PGLA NPs-loaded violacein has been found to be five times lower than free violacein in solution.[222] Biodegradable nanoparticles made of dextran loaded with silver carbene complex have also been shown by Ornelas-Megiatto *et al.* to have higher antibacterial activity compared to the free silver complex.[223] Hybrid nanoparticles (e.g. magnetite), whose surfaces are coated by polymers (chitosan/PGA) of high affinity for the microbial cells have shown a boost in their antimicrobial efficiency.

Qi *et al.* demonstrated that the vancomycin-modified mesoporous silica nanoparticles (MSNs⊂Van) can efficiently target and kill Gram-positive bacteria over macrophage-like cells (Figure 1.26). Owing to the specific hydrogen bonding interactions of vancomycin toward the terminal D-alanyl-D-alanine moieties of gram-positive bacteria, the MSNs⊂Van exhibited enhanced recognition for Gram-positive bacteria due to the multivalent hydrogen binding effect.[224] Table 1.4 shows commonly used nanoparticles as antimicrobial agent, their surface properties and the cell-nanoparticle interactions.

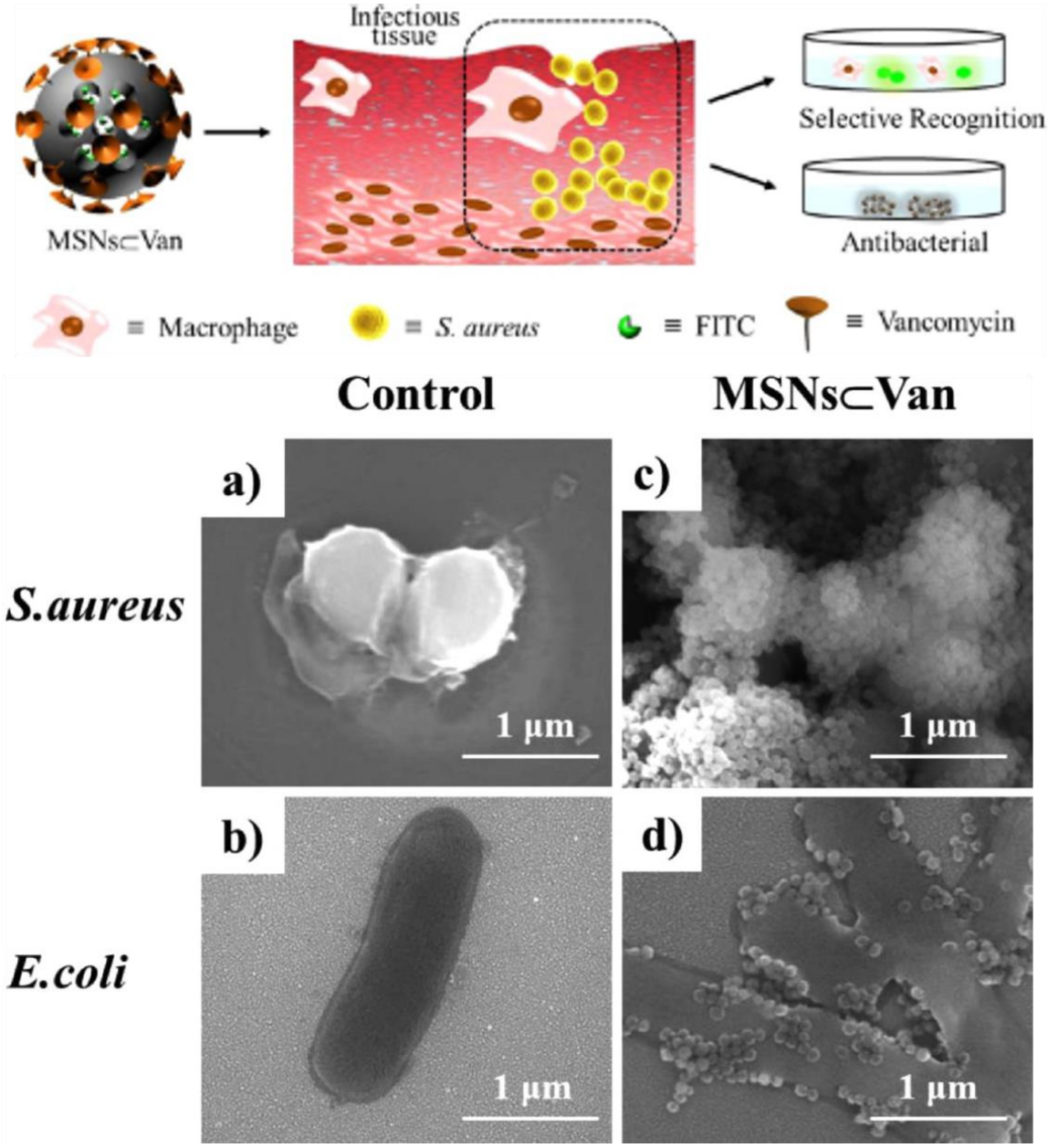


**Figure 1.26.** Top: Schematic representation of MSNs⊂Van for selective recognition and killing pathogenic Gram-positive bacteria over macrophage-like cells. Bottom: SEM images of *S. aureus* and *E .coli*. (a, b) *S. aureus* and *E.coli* ($1 \times 10^5$ CFU $mL^{-1}$) suspended in PBS as control groups; (c, d) Images of S. aureus and E .coli treated by MSNs⊂Van with a concentration of 200 μg $mL^{-1}$ for 2 h, respectively. Reproduced with permission from Ref..[224]

**Table 1.4.** Commonly used nanoparticles as antimicrobial agent, their surface properties and the cell-nanoparticle interactions.

| Type of nanoparticles | Surface properties at pH 7 | Cell-particle interactions | Refs. |
|---|---|---|---|
| ZnONPs | Cationic, IEP 9.7 | Bacterial attachment by electrostatic interactions, ROS generation on the surface of the particles; zinc ion release, membrane dysfunction; and nanoparticles internalization into cell. | 225-230 |
| MgONPs | Cationic IEP 9.8-12.7 | Electrostatic interactions, Damaging the cell membrane and then causing the leakage of intracellular contents and death of the bacterial cells. | 149, 151-153 |
| CuNPs and CuONPs | Cationic IEP 9.5-10 | Release of $Cu^{2+}$, electrostatic interactions, Crossing of nanoparticles from the bacteria cell membrane and then damaging the vital enzymes of bacteria. | 100, 156, 228, 231 |
| $Al_2O_3$NPs | Cationic IEP 8-9 | Bacterial attachment (electrostatic interaction) damage to the bacterial cell wall and increase the permeability. | 232 |
| $TiO_2$NPs | Cationic IEP 6.8 | Electrostatic interactions, oxidative stress via the generation of ROS; lipid peroxidation that cause to enhance membrane fluidity, disrupt the cell integrity. | 126, 174, 229, 233-235 |
| $CeO_2$NPs | Cationic IEP6.7-8.6 | There are oxygen gaps present in the oxidation states of these two $CeO_2$ NPs. The creation of an oxygen vacancy is accompanied by the reduction of the $Ce^{4+}$ form to the $Ce^{3+}$, resulting in the loss of an oxygen molecule. This unique radical scavenging property of ceria makes them an attractive option in wound healing. $CeO_2$ nanoparticles have a good antimicrobial activity, as they can act as radical scavengers and block the ROS production to eliminate bacteria. | 197, 199, 203, 236 |

| | | | |
|---|---|---|---|
| $Y_2O_3$NPs | Cationic IEP7.2-8.9 | The $Y_2O_3$ nanoparticles act as direct antioxidants to limit the amount of reactive oxygen species required to kill the cells. | 203 |
| AgNPs and $Ag_2O$NPs | Cationic IEP 9.4 | Release of $Ag^+$, electrostatic interactions, Ion release; induction of pits and gaps in the bacterial membrane; interact with disulfide or sulfhydryl groups of intracellular enzymes that lead to disruption of metabolic processes. DNA loses its replication ability and the cell cycle halts at the $G_2$/M phase owing to the DNA damage (in the case of $Ag_2O$). | 37, 170, 176, 177, 231, 237 |
| AuNPs | Cationic IEP 5.5-6.8 | Electrostatic interactions, attachment of these nanoparticles to membrane which change the membrane potential and then cause the decrease the ATP level; and inhibition of tRNA binding to the ribosomes. | 187, 188, 190, 191 |
| $Mg(OH)_2$NPs | Cationic IEP 10-12.7 | Electrostatic interactions, Firstly, the cationic $Mg(OH)_2$NPs adsorb on the negatively charged bacterial cell wall by electrostatic attraction. Secondly, the adsorbed $Mg(OH)_2$NPs disrupts the integrity of the cell wall which then increases the permeability of bacterial cell membrane and finally causes the bacteria's death. | 78 |

## 1.21 Biomedical and industrial applications of antimicrobial nanoparticles

Nanoparticles have offered great possibilities for applications as antimicrobial agents. Metal and metal oxide based nanoparticles with antimicrobial action could find many applications in health related and industrial products, like food preservation, cosmetics, home and personal care, water treatment and crop protection as shown in Figure 1.27.[2, 28]

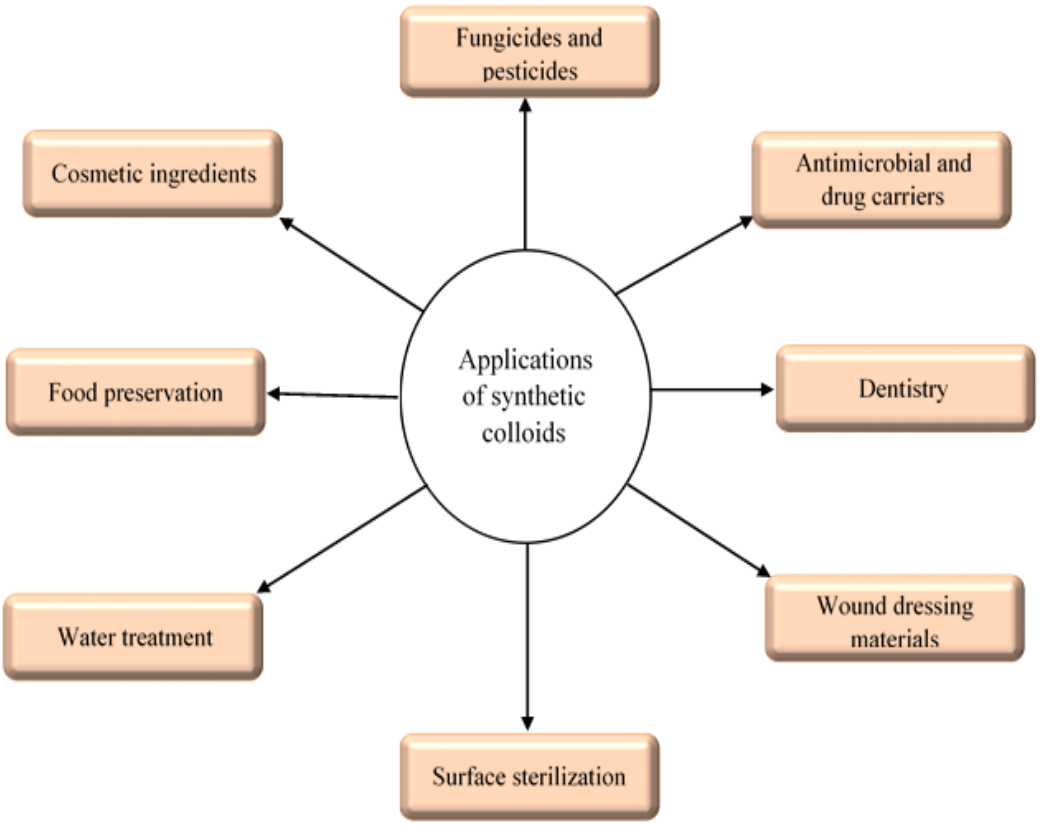


**Figure 1.27.** Different antimicrobial practical applications of nanoparticles. Redrawn from Ref..[2, 28]

ZnONPs and colloidal size ZnO powders have numerous applications in pharmaceutical and cosmetic formulations, textile industry, electronics and electro technology industries and photocatalysis due to their distinct properties such as large binding energy, wide bandgap and chemical stability.[61] Moreover, ZnONPs are used as antimicrobial agents for surface coatings on walls and wallpapers. $Mg(OH)_2$NPs are approved as additives in a number of foods and drugs.[238] Furthermore, the MgONPs can be utilized in medical treatments as well as in environmental preservation and food processing.[239] $TiO_2$NPs have already been utilized in cosmetics, waste water treatment and foods. AgNPs have also been used in textiles and other consumer goods for surface sterilization.[2] The antifungal and antiviral activity of nanoparticles has not yet been studied extensively but it is a very promising area with a huge potential. Silver nanoparticles ware recently used by Lara *et al.* as antiviral agents against HIV-1 strain at non-cytotoxic levels. It showed good efficiency at the early stage of viral replication (see Table 1.5).[240]

**Table 1.5.** A brief list of advantages and drawbacks of inorganic antimicrobial nanoparticles.

| Type of antimicrobial nanoparticles | Advantages and applications | Drawbacks |
|---|---|---|
| ZnONPs | Antimicrobial, photocatalytic activity; high stability; bactericidal effects on both Gram-positive and Gram-negative bacteria; antibacterial activity against spores which are resistant to high temperature treatment.[225-230] | Cannot specifically differentiate between microbial and human cells. |
| MgONPs | Effective against both Gram-positive and Gram-negative bacteria; high stability; low cost; availability, flame re-tardant, UV protection.[149, 151-153] | Non-specific antimicrobial action. |
| CuNPs and CuONPs | Effective against Gram-positive and Gram-negative bacteria; high stability; antifungal activity.[100, 156, 228, 231] The [antibacterial and antifungal activities of these nanoparticles on different microorganisms, including methicillin-resistant *Staphylococcus aureus*, *Salmonella choleraesuis*, *Candida albicans*, *Pseudomonas aeruginosa*, and *Bacillus subtilis*.[155] | Could potentially have a toxic effect on human health. This is the reason why direct replacement of common antibiotics with antimicrobial nanoparticles formulations can be challenging. |
| $Al_2O_3$NPs | Antimicrobial, catalyst support, $Al_2O_3$NPs can act as a radical scavenging agent which have non-toxic effect to the human cell.[195] | Could potentially have a toxic effect upon dissolution in acidic environment. |
| $TiO_2$NPs | Antimicrobial, Suitable photocatalytic properties; high stability; effective antifungal for fluconazole resistant strains, no toxicity in dark condition.$TiO_2$NPs affect the *C. reinhardtii* cells viability at much lower particle concentrations.[126, 174, 229, 233-235] | Non-specific antimicrobial action. |
| $CeO_2$NPs | Antimicrobial, catalyst support, radical scavenger[199] at lower temperatures the $CeO_2$NPs have antimicrobial action towards different bacteria, including *Shewanellaoneidensis*, *Pseudokirchneriella subcapitata*, *E. coli* and *B. subtilis*, due to damaging of the microorganisms cell walls.[197] | Non-specific antimicrobial action; expensive to make in large quantities. |

| | | |
|---|---|---|
| $Y_2O_3$NPs | Antimicrobial, UV protection, radical scavenger.[199, 203] | Non-specific antimicrobial action; expensive to make in large quantities. |
| AgNPs and $Ag_2O$NPs | High antimicrobial activity against both bacteria and drug-resistant bacteria, antifungal activity on spore-producing fungal plant pathogens, high stability, nontoxicity, disinfectant, electrical conductive, UV protection.[37, 170, 176, 177, 231, 237] | Non-specific antimicrobial action; this can be partially overcome by functionalizing antimicrobial nanoparticles with antibodies. (see Fig. 1.22) [204, 205] |
| AuNPs | Nontoxicity, not inducing any ROS-related process; high ability to functionalization, polyvalent effects; ease of detection; photothermal activity.[187, 188, 190, 191] The antibacterial and antifungal effects of the AuNPs functionalized with 5-fluorouracil towards *Staphylococcus aureus*, *Escherichia coli*, *Pseudomonas aeruginosa*, *Aspergillus fumigatus*, *Aspergillus niger* and *Micrococcus luteus*. Their results revealed that the AuNPs had higher antibacterial activity towards Gram-negative bacteria than Gram-positive.[188] | Expensive to make in large quantities. |
| $Mg(OH)_2$NPs | Antibacterial, environmental processes, pharmaceutical formulations. Due to its non-toxicity and low cost, $Mg(OH)_2$ is an approved drug and food additive.[78-85, 141] $Mg(OH)_2$NPs were effective antibacterial agents towards several bacteria, like *E. coli*, *S. aureus*, *P. aeruginosa* and *B. phytofirmans*.[76, 141-145] | Moderately efficient as antimicrobial agents; require relatively high particle concentrations to act as antimicrobials; sensitive to pH of the environment. |
| Environmentally benign nanoparticles (EBNPs) | Biodegradable environmental friendly can outperform inorganic antimicrobial.[218, 219, 222-224] | Complexity of fabrication; non-specific antimicrobial action. |
| Colloid antibodies | Cell shape specific better selectivity.[204-206] | Cost of production; complexity of fabrication. |

## 1.22 Functionalization of nanoparticles

Surface functionalization of nanoparticles is vital for controlling their properties and interactions with molecules and ligands of relevance for biomedical applications, in addition to their susceptibility to undergo a transformation in environmental and biological systems. Considerable efforts have been devoted to the development of surface modifiers that can offer not only stability but also better control of the interaction between nanoparticles and biological membranes to obtain more biocompatible materials.[3]

One of the potential surface modifications is the addition of hydroxyl functional groups which can react with carboxyls in organic or inorganic molecules. This can occur if they are produced in aqueous or non-hydrolytic solutions, through oxygen atoms or with silane groups through a -O-Si bond. This type of surface modification is used for hydrophobic superparamagnetic iron oxide nanoparticles (SPIONs), enabling them to be hydrophilic through a covalent linkage (Fe-S) with the bi-functional molecule, 3-mercaptopropionic acid. The nanoparticles can then be enhanced further by esterifying the carbonyl group with dextran, this makes the structure biocompatible which is important for clinical applications.[241]

Amine and oxysilane are other common functional groups that are useful for the functionalization of nanoparticles. These can provide various properties which on their own have a benefit for a wide range of biological applications.[242] Specifically for drug delivery applications, semiconducting nanoparticles such as quantum dots (QDs), can be used through surface modification with mercapto groups using thiolate polymers.[243] Examples of metals that are used for this application are Pt, Ag and Au. In some cases, pre-requisite surface based molecules are essential in order to graft and activate the surface for further modifications with other chemical or bioactive molecules.

Silane coupling agents are materials with dual functional groups, one for tethering to the surface of a nanoparticle and the second acting as a platform active site for chemical reactions.[244]

None chemical based enhancements in the form of electrostatic interactions[245] and Van der Waals interactions[246] (physical adsorption) are also considered to be useful methods for functionalizing nanoparticles because of improvements for their stability, hydrophilicity in suspensions and simple synthetic conditions at room temperature, the downside to these benefits are that they tend to be weak. A probe molecule Human Serum Albumin (HAS) was used to monitor the physical adsorption of a protein on the surface of a nanoparticle for biodistribution.[247]

Self-assembly is another method which has the ability to generate large multifaceted arrays nanomaterials.[248] The main forces that control self-assembly are electrostatic interactions, surface tension, capillary forces, hydrophobic interactions and bio-specific recognition.[249] Electrostatic interactions are a driving force for layer-by-layer self-assembly of polyelectrolyte shells.[250] The shell thickness can be controlled by repeating the depositing procedure with oppositely charged polyelectrolytes or nanomaterials. The opposing charges attach the electrolytes to the surface through electrostatic interactions.[251] Polyelectrolytes (PEs) are either anionic or cationic polymers with chargeable monomer units. In polar solvents such as water, ion pairs are able to dissociate, producing the charges on the surface of the polymer while the counter ions are released into solution. PEs are classified as either strong or weak. Strong polyelectrolytes involve permanent charges and can fully dissociate in water. On the other hand, weak PEs are strongly dependent on pH.[252] An example of this was when Gittens and co-workers synthesised, 35 nm gold nanoparticles and were able to create a surface coating of up to eight layers of polyelectrolytes using electrostatic interactions.[253] The method used has also been used for manufacturing ultra-thin films with desirable properties for corrosion control through cationic and anionic polyelectrolyte multilayers coating of stainless steel wires. [251, 254]

More precisely, anionic titanium(IV) bis(ammonium lactate)dihydroxide (TALH) as a titania precursor can be electrostatically assembled with the cationic polyelectrolyte poly(allylamine hydrochloride) (PAH), allowing the formation of multilayers. Metal nanoparticles can then be given a surface charge and deposited into the titania network, an example of this was when negatively charged Pt nanoparticles were inserted into TALH/PAH multilayers. This was completed using the layer by layer (LbL) method to produce a titania nanocomposite.[255, 256]

LbL films can be prepared from an anionic and a cationic polymer through the electrostatic affinity between them. The adsorption of charged polymers onto an oppositely charged surface produces an entirely new platform with an opposite charge, this is due to an overall overcompensation of the net surface charge. The new surface enables the deposition of the next layer of an oppositely charged polymer. In a typical procedure, the solid substrate is immersed in aqueous solutions of the polymers, followed by solvent rinsing to remove non-specific or weakly adsorbed polymers (Figure 1.28a). By varying the number of deposited layers, the overall thickness of the film can be easily regulated. Biopolymers, such as proteins,[257, 258] polysaccharides,[259, 260] and DNA[261, 262]

can also be used as building blocks when constructing films by the LbL approach. This is because the various biopolymers contain their own net charges.[263]

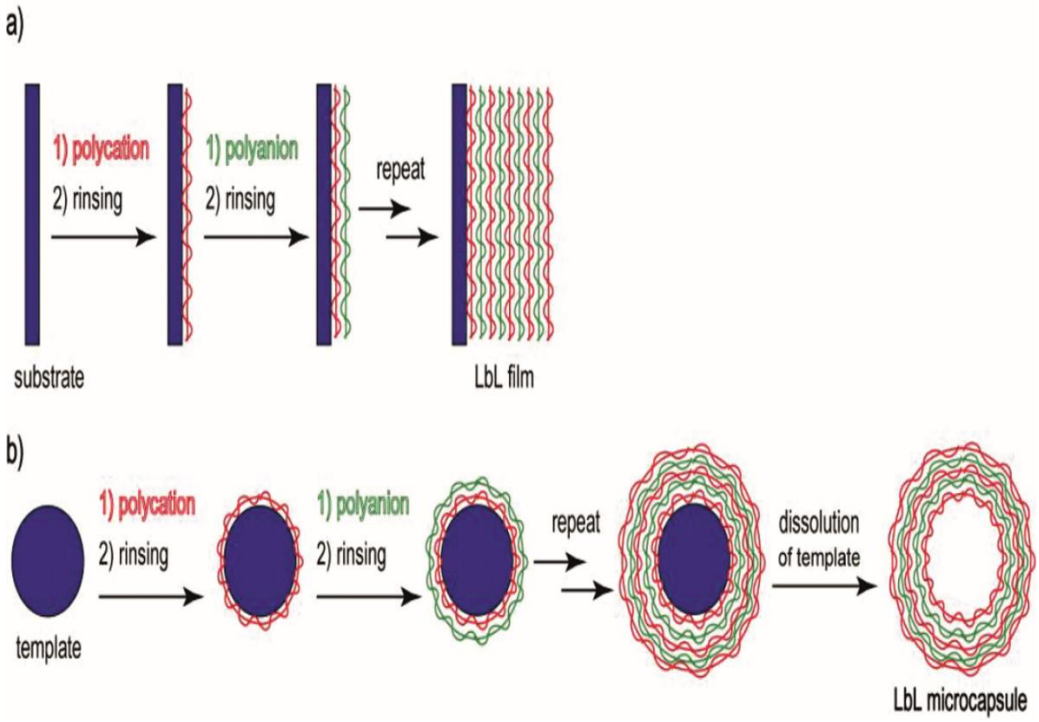


**Figure 1.28.** Preparation of LbL films (a) and microcapsules (b).[263]

Hydrogen bonding can likewise be used as a driving force for constructing LbL films. Poly(acrylic acid) (PAA) and poly(methacrylic acid) (PMA) are often used as hydrogen bonding donor polymers in combination with hydrogen bonding acceptors, for example poly(ethylene glycol).[264, 265] A key feature of the LbL hydrogen-bonded films is their pH-dependent stability. LbL films consisting of both PAA and PMA are stable in acidic solutions, whereas these films will decompose through a deprotonation pathway when the carboxylic acid residues lose their hydrogen bonding in a neutral or basic environment. Molecules with biological affinity such as proteins can be used as components of LbL films. Examples of this are, concanavalin A and avidin, which specifically bind sugars and biotin, respectively, thus constructing a LbL film.[266-268]

Hollow microcapsules can be constructed by LbL deposition of polymers on the surfaces of colloidal particles, for instance $CaCO_3$ microspheres, followed by dissolution of the core (Figure 1.28b). These microcapsules are stable over a wide pH range, this means that this structure could be considered and studied as a potential drug carrier. [269, 270] A major advantage of the LbL microcapsule is that the structure of the shell membrane can be tailored at the molecular level by using suitable materials to suit its desired role.[263]

The synthetic approach for a polyelectrolyte multilayer coating is illustrated in Figure 1.29a. The primary strategies were developed to prepare antimicrobial coatings and anti-adhesive films. Their purpose was to prevent bacterial adhesion by using a hydrophilic polymer base to inhibit the contact of bacteria with the surface. This species is called a contact-killing film and can be constructed by adsorbing antimicrobial agents onto the surface. Most bacteria cell membranes are negatively charged, this can be easily combated by utilising a positively charged antimicrobial interaction between the bacteria and polymer film. The antimicrobial agents can be released and will penetrate the microbial cells and destroy the structure, leading to cell death (Figure 1.29b).[271]

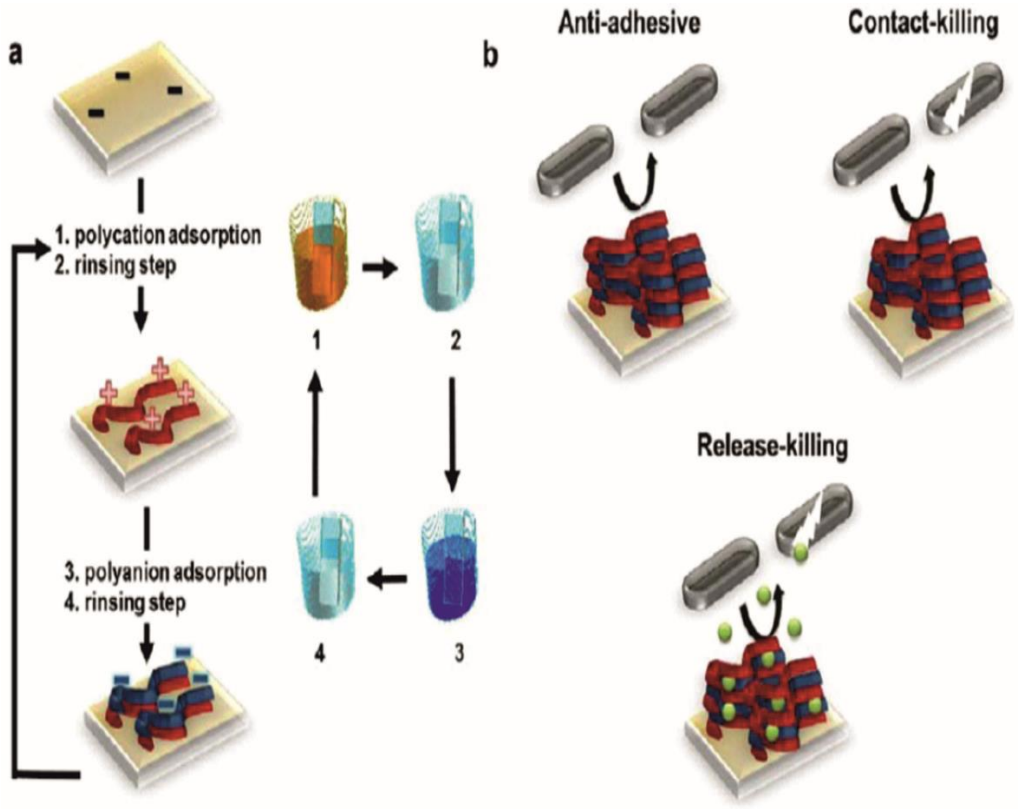


**Figure 1.29.** (a) Schematic representation of a polyelectrolyte multilayer (PEM) film build up by successive adsorption steps of polycations and polyanions followed by rinsing steps using the dipping method. (b) Three main strategies were followed to design antimicrobial PEM: antiadhesive films inhibiting the close approach of pathogens, contact killing films by exposing antimicrobial agents on the surface, and release-killing films delivering antimicrobial agents in the supernatant, with the last two strategies leading to the death of pathogens.[271]

Amphoteric crystalline $TiO_2$NPs with PEs have been used to manufacture a dye-sensitized solar cell through assembling a polyion/$TiO_2$ nanocomposite multilayered films. This was generated by using an electrostatic layer-by-layer deposition method with two weak PEs, poly(allylamine hydrochloride) and poly(acrylic acid), as well as two strong PEs, poly(dimethyldiallylammonium chloride) (PDAC) and poly(sodium 4-styrenesulfonate).[272]

Martin and co-workers conducted a wet LbL self-assembly method to fabricate reforming junctions on metal nanowires, originating from individual nanoparticles ($TiO_2$/ZnO)/polymers thin films.[273]. Metal supported (Pd, Ni, Co and Ag) doped titania heterogeneous catalysts enabled the degradation of Rhodamine B by means of photo catalysis under visible light. This process was carried out by deposition on glass slides via the LbL self-assembly method using a poly(styrene sulfonate sodium salt) (PSS) and poly(allylamine hydrochloride) (PAH) polyelectrolyte system. Deposition of metal doped $TiO_2$NPs on a thin film gave robust adhesion properties with high stability and the same efficiency over a very recyclable process (5 cycles).[274] Stable and super-hydrophilic NPs based thin films have also exhibited biocompatibility and suitability for successful cell culturing and attachment to human dermal fibroblast through LbL coating on substrates such as glass, poly(methyl methacrylate) (PMMA) and poly(dimethyl siloxane) (PDMS) with poly(styrene sulfonate) to procedure films with various thicknesses.[275] The PEs coated photocatalyst (NPs) was also utilized for coating polyester textiles and producing photo active antibacterial textiles. Again, this was constructed via an LbL assembly by coating a cationic polyethylenimine (PEI) with negatively charged NPs. These entities were dispersed by polyanionic poly(styrene sulfonate) (PSS), switching the net charge of the nanoparticles.[276]

The typical procedure for LbL self-assembly proceeds as follows: Initially, A charged substrate is immersed in a solution of an oppositely-charged colloid to adsorb the first monolayer. Next, a washing cycle follows to remove any unbound material and lessen the potential contamination of the subsequent oppositely-charged colloid. Finally, the coated substrate is submerged to deposit a second layer and a multi-layered structure is generated (Figure 1.30).[277, 278] However, there are some LbL processes that do not require a washing cycle, this dramatically expedites the assembly process.[279]

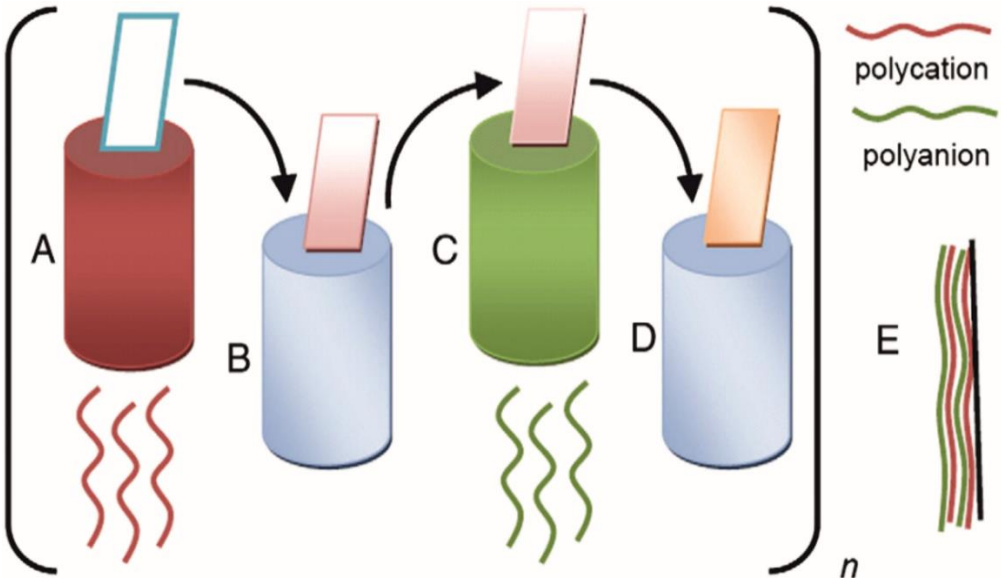


**Figure 1.30.** A schematic illustration of the alternate adsorption of the polyelectrolyte species to produce a multilayered structure. (A) Dipping in a polycation (example) followed by B) rinsing in a solvent for the polycation with (C) dipping in a polyanion and (D) rinsing in a solvent for the polyanion. The process is repeated n times to produce (E) the multilayered construct.[277]

Figure 1.30 shows the LbL adsorption process includes a rinsing step at this time the coated substrate is solvent washed to ensure the removal of any unbound PEs and to prevent the cross-contamination of solutions.[280] Strong PE layers (with high surface charge density) are not significantly altered by the washing process since the layer is secured by strong interactions. Nevertheless, the weakly bound PEs (low surface charge density) may be stripped off, this hampers the LbL assembly process being successful.[277, 281] Hollow nano-spheres or capsules can also be formed by utilising a LbL self-assembly procedure by using a templating method to generate core-shell structures.[282] The PEs and functionalized nanoparticles were accomplished by polymerization and silanization methods. Hollow capsules can be produced stripping away the templating agent *via* calcination or by using chemical etching agent such as ammonium hydroxide. The completed hollow structures can then be used as potential transporters for drug delivery.[283, 284] The most frequently used cation-anion PE pairs to generate this type of system include poly(styrene sulfonate) (PSS) and poly(diallyldimethylammonium chloride) (PDADMAC) [253, 285], PSS and PAH[282, 284], PSS and poly(diallydimethyl-ammonium) (PDDA) or poly(pyrrole) and poly(N-methylpyrrole).[286, 287] These combinations and subsequent coating procedures could prove to be useful in generating a variety of different nanomaterials.[283, 288]

## 1.23 Boronic acids functionality

Boronic acids have been extensively studied and present in the literature since 1860, these have enabled us to develop organic molecules over the years into a very popular and current hot topic of interest in chemistry. [289] Their ease of synthesis and stability has led to their use in a variety of important synthetic reactions, from hydroboration (C–H, C–OH bonds),[290] Suzuki–Miyaura coupling (C–C bonds), for which a Nobel prize was awarded in 2010 [291] and the Chan–Lam coupling (C–N and C–O bonds).[292] Boron can form reversible covalent complexes with substances such as, sugars and amino acids, these form vicinal (1,2) or (1,3) di-Lewis base donors (alcohols or amines). The pKa range of BA is about 8–10, thereby, allowing them to remain protonated under physiological conditions. BA are remarkably stable despite their high reactivity and have long been established as presenting a very low toxicology profile.[293] These reagents are considered a bioisotere of carboxcylic acids, occupying the same period as carbon.[294] BA have received attention recently for their ability to act as sugar unit binders,[295] for both probing biological systems and as potential indicators for identifying metabolites in the disease pathology of such afflictions as diabetes.[296] A number of excellent reviews exist in this area, in particular a review by Wang *et al.* detailing design considerations for the construction of such binding agents.[297] Recently, the use of carbohydrate binding agents has been proposed as a potential therapeutic route to the treatment of infections attributed to viruses possessing a highly glycosylated envelope such as HIV.[298] Kitano and co-workers described a glucose responsive polymer complex containing a phenylboronic acid moiety that acted as a novel drug delivery polymer.[299, 300] Figure 1.31 shows a wide array of applications for the boronic acid chemosensor.

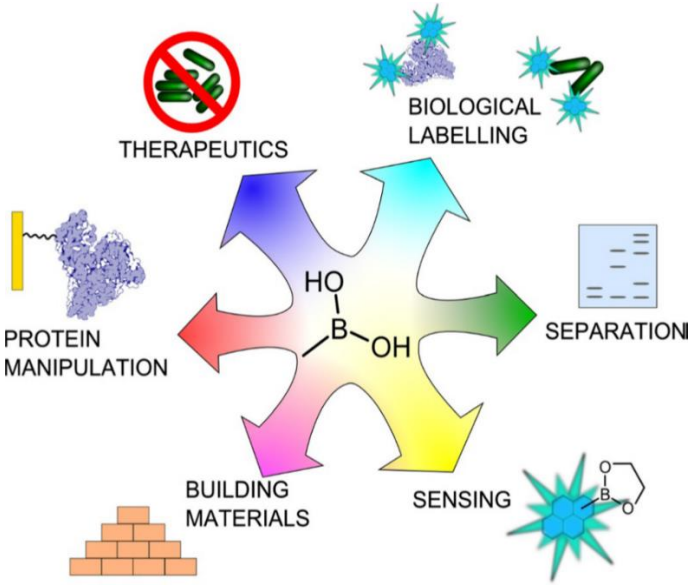


**Figure 1.31.** Different applications and usage of boronic acids.[301]

The combination of the acid-diol interaction has found many applications. A few of them are highlighted here, some of which are illustrated in Figure 1.32. Many BA-based sensors for sugars have been developed, with efforts in making these sensors selective for specific sugars. Particular attention has been given to the selective and sensitive detection of glucose for the monitoring of glucose levels in the blood of diabetic patients. Also the development of glucose-responsive materials that automatically release insulin when glucose levels are too low.[302-304] Glycoproteins are proteins which contain oligosaccharide chains (glycans) covalently attached to amino acid side-chains. This type of molecule has been found to be reversibly captured by utilising various BA moieties from complex mixtures, facilitating their detection, detailed analysis or purification. Functionalised BA surfaces have been found in the past to immobilize glycoproteins, this enables the user to utilise the protein based molecule for a variety of other applications, e.g., detection of antigens through the use of surface-bound antibodies. Furthermore, as glycans are also found on cell surfaces, BA-containing materials are being developed for the detection or capture of cancer cells, which overexpress specific glycans at their surface.[305-308] Benkovic and others have reported a novel class of boronic- quinoline esters, targeted against bacterial methyltransferases. By using a mechanism-based approach, this research group developed inhibitors against the *Caulobacter crescentus* cell cycle regulated methytransferase (CcrM) an essential DNA methyltransferase enzyme, found in most a-proteobacteria, exerting a key role in cell progression and the ability to infect or cause damage to others. [300, 309] The solid phase extraction of glycopeptides and glycoproteins has been explored by using several materials immobilized with BA. BA-based agarose resins have been found to provide quick, efficient, and specific enrichment of glycoproteins from complex samples such as human serum and commercial maminophenylboronic acid-agarose resin has been widely used for glycoprotein enrichment and immobilization.[310, 311]

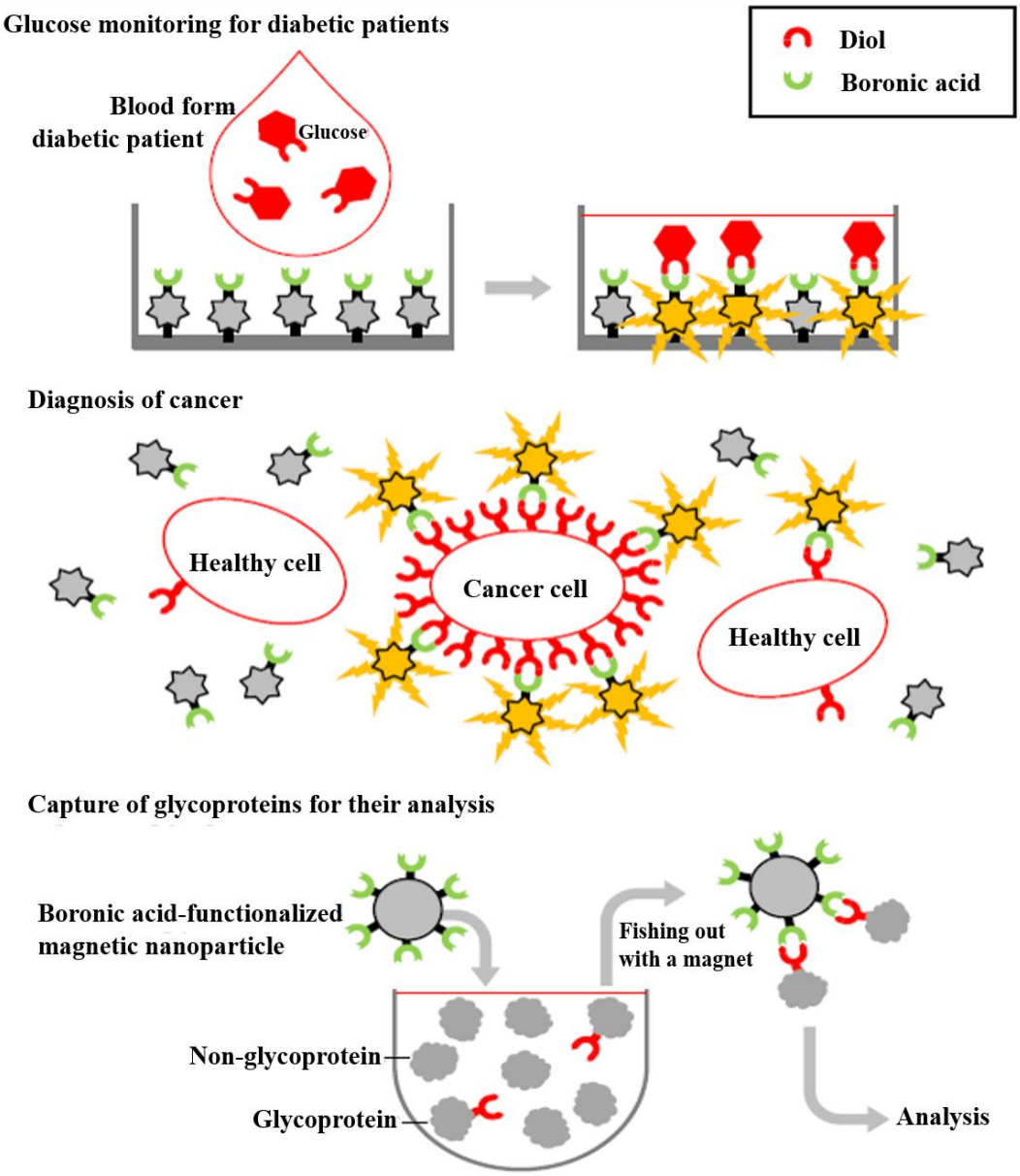


**Figure 1.32.** Some known applications of the boronic acid-diol interaction.[308]

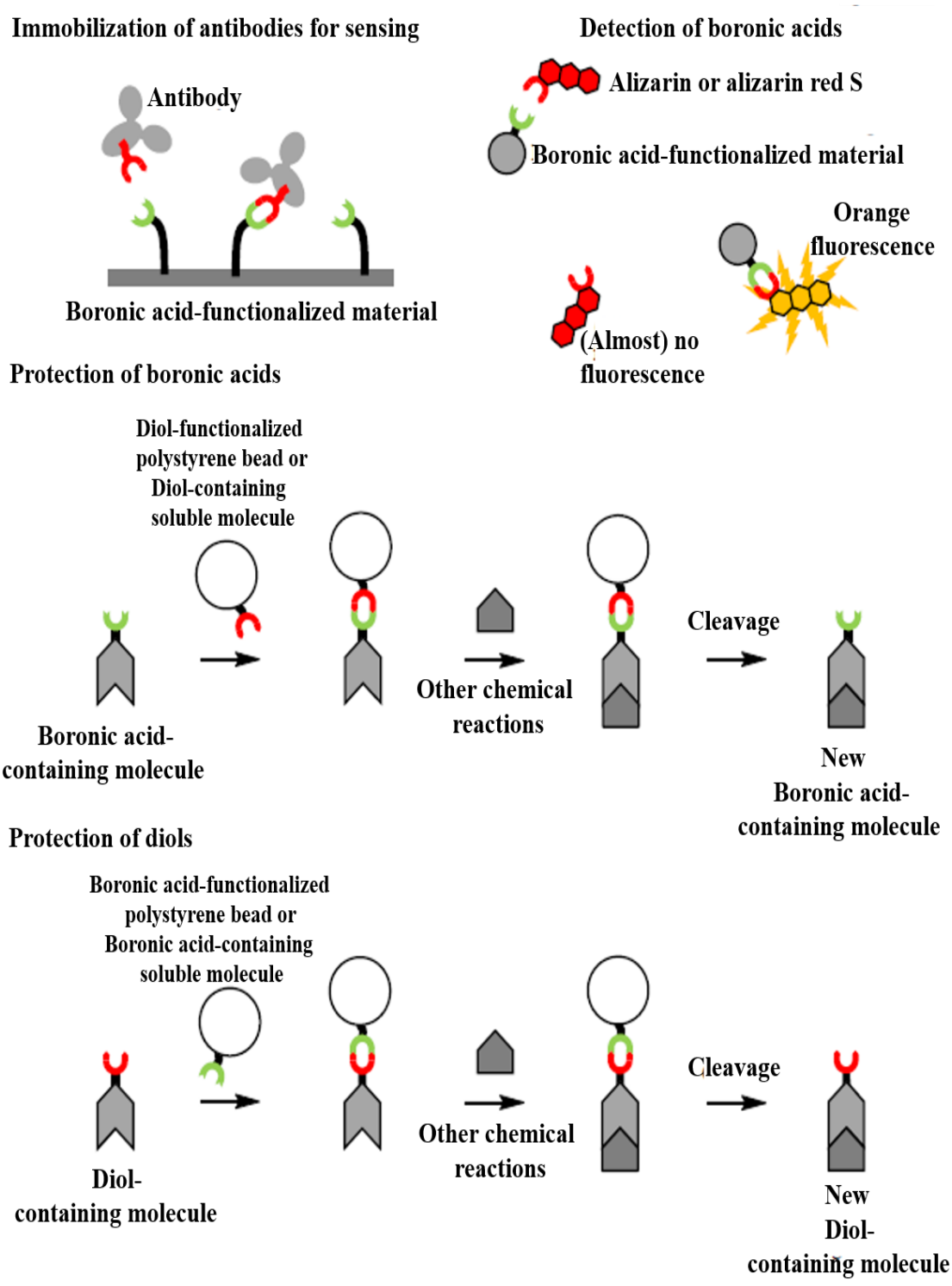


**Figure 1.32.** *(Continued).*[308]

Qu and co-workers reported that polymer microspheres with a hydrophilic core and a boronic acid-functionalized shell constructed from poly (N,Nmethylenebisacrylamide-co-methacrylic acid and poly (4-vinylphenylboronic acid) (P(MBA-co-MAA)PVPBA). The shell was polymerised using a free-radical reaction, where upon the BA was

introduced and tethered instead of applying a standard solid− liquid grafting reaction. The microspheres were added to enrich the glycosylated peptides for glycoproteome analysis with good selectivity.[312, 313]

Qi *et al.* prepared iron oxide based magnetic microspheres ($Fe_3O_4$-C-Au) with a mercaptophenylboronic acid-functionalized shell. The core−shell-structures were found to be successful for the selective enrichment of glycoproteins.[311, 314]

The unique abilities of micron sized and especially nanoparticles can be enhanced by the incorporation of BA on to the surface (Figure 1.33). The ability to prepare diverse sensor materials by modifying carbon nanotubes (CNTs) has been reviewed.[315] Au nanoparticles are the subject of a large array of works over the past few decades. Specifically, for this branch of research very recently, the combination of mercaptophenylboronic acid, Au nanoparticles, graphene and the enzyme glucose oxidase has resulted in a material able to detect glucose.[316] Au nanoparticles modified with 4-mercaptophenylboronic acid were also found to detect tyrosinase activity. The system was used to quantify surface bound catechol which was produced by the enzymatic oxidation of phenol initially present in the system.[301, 317, 318]

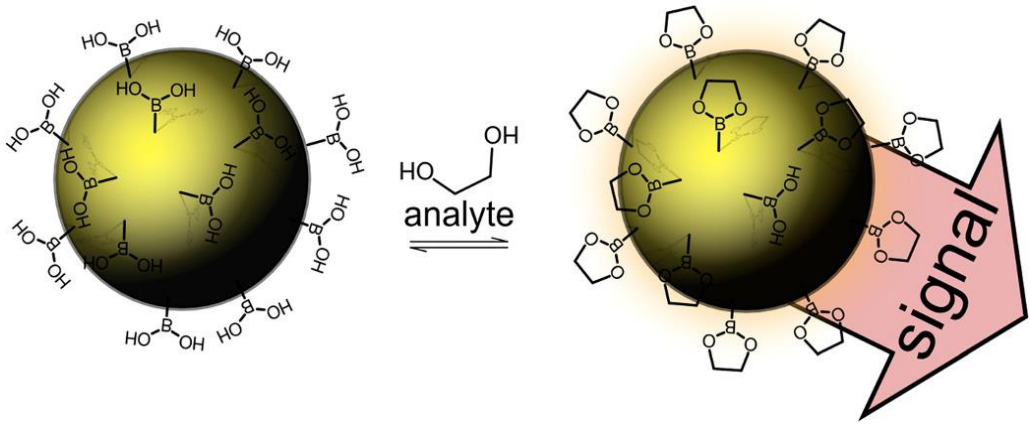


**Figure 1.33.** Selective detection of diols using nanoparticles modified with boronic acids.[301]

## 1.24 Surface roughness nanoparticles and modification

Design and preparation of surface-rough nanoparticles have attracted much attention because of their special structure and wide applications.[319] Surface modification of nanoparticles can be used to improve the stability and antimicrobial potential of the nanomaterial. Conjugation of various compounds, such as surfactants, polyethylenimine,

polymers, amoxicillin, peptides, and polysaccharides to nanoparticles can result in synergistic antimicrobial effects. Improved antimicrobial activity is detected for antibiotics and antimicrobial peptides when conjugated to metal nanoparticles: for example, Ag nanoparticles conjugated to the cationic antimicrobial peptide ubiquicidin have increased antibacterial activity against Gram-negative bacteria, providing a promising alternative therapy for topical infections.[320] $TiO_2$NPs modified with pericarp extract of *Garcinia zeylanica* showed enhanced antimicrobial activity against methicillin resistant *S. aureus*.[321] Capping of nanoparticles to obtain enhanced stability leads to the alteration of the surface chemistry and biological properties. Capping agents such as chitosan, polyethylenimine, citrate, polysaccharides, hydrocarbons, polyvinylpyrrolidone (PVP), peptides, carbon, starch, and bovine serum albumin can all have an effect on inducing oxidative stress, DNA damage, and apoptosis of mammalian cells.[322, 323] Karaman and others have developed mesoporous silica nanoparticles (MSPs) of different size and shape, and the surface coatings were utilized to study their differential effects in enhancing antibacterial activity. They have stated the antibacterial effect of MSPs with three different aspect ratios (1, 2 and 4), doped with silver ions and finally coated with the polymer chitosan against Gram-positive and Gram-negative bacteria. Their results indicated that silver ion doped and chitosan coated MSPs with the aspect ratio of 4 (Cht/MSP4:Ag+) have the highest antimicrobial activity among the prepared series. Their findings showed that both shape and surface engineering contribute positively towards killing bacteria, and the newly developed silver ion-doped and chitosan-coated MSPs have good potential as antimicrobial nanomaterials.[324]

## 1.25 Aims of current research

The aim of the research presented in this thesis is to investigate the role of the polymer coating in the antimicrobial activity of ZnO, $Mg(OH)_2$ and CuO nanoparticles synthesized by the direct precipitation method. Four different types of microorganisms, *C. reinhardtii*, *S.cerevisiae* cells, Gram-negative *E.coli* and Gram-positive *R. rhodochrous* were used to examine the antimicrobial activity of the surface modified nanoparticles. The working hypothesis is that coating the nanoparticles with cationic polyelectrolytes may enhance their antimicrobial activity while coating them with anionic polyelectrolytes as an outer layer may lead to decreased antibacterial activity because of their electrostatic repulsion from the bacterial cell wall (Figure 1.34A). The aim of this research was also to study the surface functionalized CuONPs with GLYMO and 4-HPBA as innovative anti-algal, anti-fungal and antibacterial agents. Since *C. reinhardtii* is a typical representative of the algae genre and *S. cerev*isiae is a fungal microorganism, they are a good proxy for these assessments. The results shed light on the possible mechanisms of their anti-algal, anti-yeast and antibacterial activity.

The novelty of the work is that CuONPs/GLYMO/4-HPBA targets the cells by covalently binding to the glycoproteins expressed on their membranes which does not rely on electrostatic interactions (Figure 1.34B and 1.34C).[3] Such self-grafting mechanism of attachment to cells is expected to amplify their antimicrobial action. The toxicity of both bare CuONPs and 4-HPBA -functionalized CuONPs on human keratinocytes is also examined.

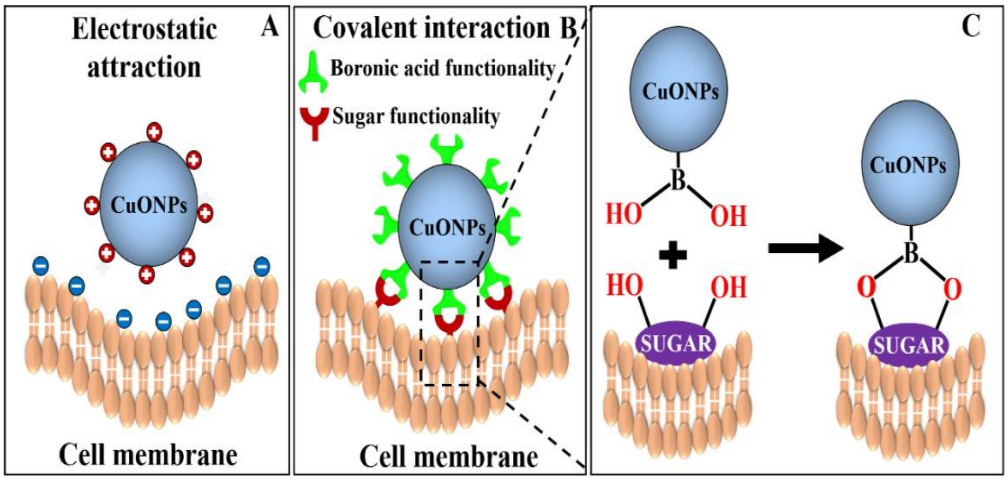


**Figure 1.34.** The perceived attachment mechanisms of CuONPs to the bacterial cell membranes. (A) Electrostatic attraction between bare CuONPs and the cells; (B) covalent bonding between CuONPs/GLYMO/4-HPBA and the cells. (C) The interaction between the CuONPs with boronic acid surface functionality and the sugar groups on the surface of the bacterial cell wall.

The final objective was to explore the role of the silica particle surface roughness on their antimicrobial action. The surface-rough $SiO_2$NPs were prepared by using mesoporous shaped CuONPs as templates (host), which are reported to have strong antimicrobial action.[3, 4] In order to explore the effect of the particle surface roughness and morphology we effectively created 'ghost' $SiO_2$NPs which copy the morphology of the templated 'host' CuONPs (Figure 1.35). The 'ghost' $SiO_2$NPs were functionalized with boronic acid surface groups in an attempt to design a non-electrostatic mechanism for their attachment to bacteria surfaces which is expected to accumulate them on the cell walls despite the presence of other anionic species in the aqueous solution.

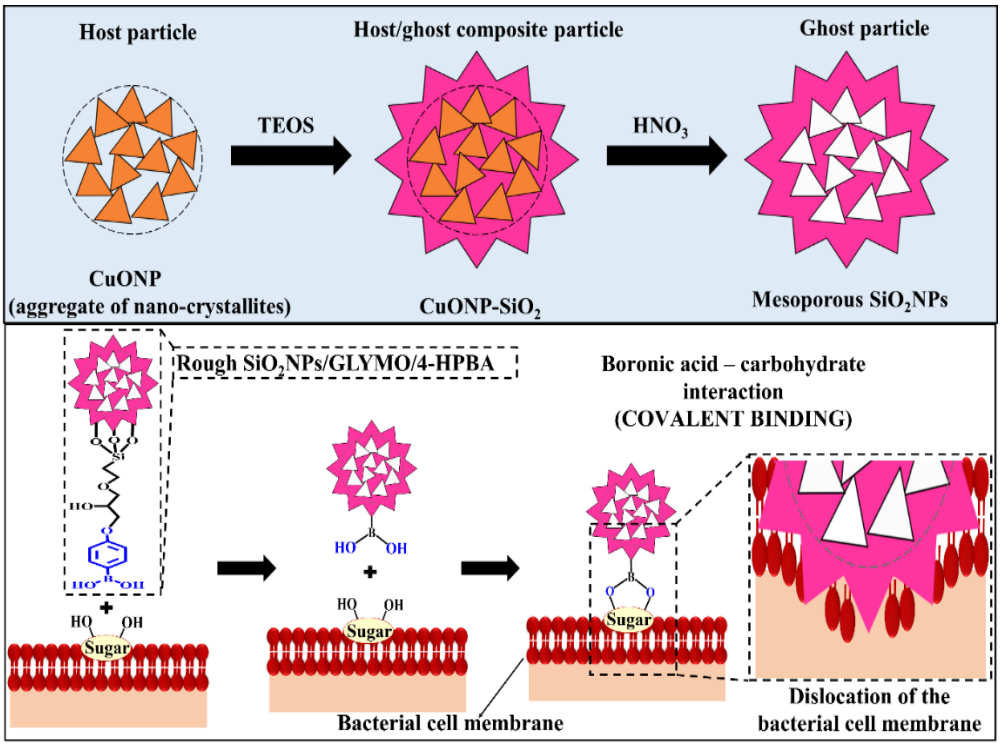


**Figure 1.35.** Schematics to show the synthesis of 'ghost' $SiO_2$NPs and the mechanism of self-grafting/covalent attachment of HPBA-functionalized 'ghost' $SiO_2$NPs and the sugar groups on the surface of the bacterial cell membrane.

## 1.26 References


1. M. Moritz and M. Geszke-Moritz, *Chemical Engineering Journal*, 2013, **228**, 596-613.
2. A. F. Halbus, T. S. Horozov and V. N. Paunov, *Advances in Colloid and Interface Science*, 2017, **249**, 134-148.
3. A. F. Halbus, T. S. Horozov and V. N. Paunov, *ACS Applied Materials & Interfaces*, 2019, **11**, 12232–12243.
4. A. F. Halbus, T. S. Horozov and Vesselin N. Paunov, *Nanoscale Advances*, 2019, **1**, 2323 – 2336.
5. S. S. M. Al-Obaidy, A. F. Halbus, G. M. Greenway and V. N. Paunov, *Journal of Materials Chemistry B*, 2019, **7**, 3119-3133.
6. J. Davies and D. Davies, *Microbiology and molecular biology reviews*, 2010, **74**, 417-433.
7. H. Palza, *International journal of molecular sciences*, 2015, **16**, 2099-2116.
8. R. Brayner, S. A. Dahoumane, C. Yepremian, C. Djediat, M. Meyer, A. Coute and F. Fievet, *Langmuir*, 2010, **26**, 6522-6528.
9. H. Zhang, B. Chen and J. F. Banfield, *The Journal of Physical Chemistry C*, 2010, **114**, 14876-14884.
10. J. Liu, D. M. Aruguete, M. Murayama and M. F. Hochella Jr, *Environmental science & technology*, 2009, **43**, 8178-8183.
11. Y. Zhang, Y. Chen, P. Westerhoff, K. Hristovski and J. C. Crittenden, *Water research*, 2008, **42**, 2204-2212.
12. A. R. Petosa, D. P. Jaisi, I. R. Quevedo, M. Elimelech and N. Tufenkji, *Environmental science & technology*, 2010, **44**, 6532-6549.
13. K. Tiede, M. Hassellöv, E. Breitbarth, Q. Chaudhry and A. B. Boxall, *Journal of Chromatography A*, 2009, **1216**, 503-509.
14. V. H. Grassian, *The Journal of Physical Chemistry C*, 2008, **112**, 18303-18313.
15. Z. Abbas, C. Labbez, S. Nordholm and E. Ahlberg, *The Journal of Physical Chemistry C*, 2008, **112**, 5715-5723.
16. C. Rao, G. Kulkarni, P. J. Thomas and P. P. Edwards, *Chemistry–A European Journal*, 2002, **8**, 28-35.
17. J.-P. Jolivet, C. Froidefond, A. Pottier, C. Chanéac, S. Cassaignon, E. Tronc and P. Euzen, *Journal of Materials Chemistry*, 2004, **14**, 3281-3288.
18. Q. Zhao, T. Xie, L. Peng, Y. Lin, P. Wang, L. Peng and D. Wang, *The Journal of Physical Chemistry C*, 2007, **111**, 17136-17145.
19. S. E. McNeil, *Journal of Leukocyte Biology*, 2005, **78**, 585-594.
20. S.-W. Bian, I. A. Mudunkotuwa, T. Rupasinghe and V. H. Grassian, *Langmuir*, 2011, **27**, 6059-6068.
21. S. Parham, D. H. Wicaksono, S. Bagherbaigi, S. L. Lee and H. Nur, *Journal of the Chinese Chemical Society*, 2016, **63**, 385-393.
22. G. Fu, P. S. Vary and C.-T. Lin, *The Journal of Physical Chemistry B*, 2005, **109**, 8889-8898.
23. S. Makhluf, R. Dror, Y. Nitzan, Y. Abramovich, R. Jelinek and A. Gedanken, *Advanced Functional Materials*, 2005, **15**, 1708-1715.
24. D. J. McClements and H. Xiao, *npj Science of Food*, 2017, **1**, 6.

25. M. E. Vance, T. Kuiken, E. P. Vejerano, S. P. McGinnis, M. F. Hochella Jr, D. Rejeski and M. S. Hull, *Beilstein journal of nanotechnology*, 2015, **6**, 1769.
26. K. Qiu, P. G. Durham and A. C. Anselmo, *Nano Research*, 2018, 1-19.
27. R. A. French, A. R. Jacobson, B. Kim, S. L. Isley, R. L. Penn and P. C. Baveye, *Environmental science & technology*, 2009, **43**, 1354-1359.
28. A. A. K. Das, Paunov, V.N., *Microbiologist*, 2004, pp. 16-19.
29. E. Joner, T. Hartnik and C. Amundsen, *Final Report. TA*, 2008, **2304**, 2007.
30. W. Cai and X. Chen, *Small*, 2007, **3**, 1840-1854.
31. A. Nel, T. Xia, L. Mädler and N. Li, *Science*, 2006, **311**, 622-627.
32. M. Heinlaan, A. Ivask, I. Blinova, H.-C. Dubourguier and A. Kahru, *Chemosphere*, 2008, **71**, 1308-1316.
33. M. Mortimer, K. Kasemets and A. Kahru, *Toxicology*, 2010, **269**, 182-189.
34. K. Kasemets, A. Ivask, H.-C. Dubourguier and A. Kahru, *Toxicology in vitro*, 2009, **23**, 1116-1122.
35. V. Aruoja, H.-C. Dubourguier, K. Kasemets and A. Kahru, *Science of the total environment*, 2009, **407**, 1461-1468.
36. H. Wang, R. L. Wick and B. Xing, *Environmental Pollution*, 2009, **157**, 1171-1177.
37. S. Pal, Y. K. Tak and J. M. Song, *Applied and environmental microbiology*, 2007, **73**, 1712-1720.
38. S. Singh, T. Shi, R. Duffin, C. Albrecht, D. van Berlo, D. Höhr, B. Fubini, G. Martra, I. Fenoglio and P. J. Borm, *Toxicology and applied pharmacology*, 2007, **222**, 141-151.
39. J. Ai, E. Biazar, M. Jafarpour, M. Montazeri, A. Majdi, S. Aminifard, M. Zafari, H. R. Akbari and H. G. Rad, *Int J Nanomedicine*, 2011, **6**, 1117-1127.
40. S. Hussain, S. Boland, A. Baeza-Squiban, R. Hamel, L. C. Thomassen, J. A. Martens, M. A. Billon-Galland, J. Fleury-Feith, F. Moisan and J.-C. Pairon, *Toxicology*, 2009, **260**, 142-149.
41. A. Hoshino, K. Fujioka, T. Oku, M. Suga, Y. F. Sasaki, T. Ohta, M. Yasuhara, K. Suzuki and K. Yamamoto, *Nano Letters*, 2004, **4**, 2163-2169.
42. D. B. Warheit, B. R. Laurence, K. L. Reed, D. H. Roach, G. A. M. Reynolds and T. R. Webb, *Toxicological Sciences*, 2004, **77**, 117-125.
43. J. Jiang, G. Oberdörster and P. Biswas, *Journal of Nanoparticle Research*, 2009, **11**, 77-89.
44. N. B. Hartmann, *Unpublished doctoral dissertation, Department of Environmental Engineering, Technical University of Denmark*, 2011.
45. B. Nowack and T. D. Bucheli, *Environmental Pollution*, 2007, **150**, 5-22.
46. J. M. Pettibone, D. M. Cwiertny, M. Scherer and V. H. Grassian, *Langmuir*, 2008, **24**, 6659-6667.
47. I. A. Mudunkotuwa and V. H. Grassian, *Journal of the American Chemical Society*, 2010, **132**, 14986-14994.
48. A. Degen and M. Kosec, *Journal of the European Ceramic Society*, 2000, **20**, 667-673.
49. S. Yamabi and H. Imai, *Journal of Materials Chemistry*, 2002, **12**, 3773-3778.

50. S. George, S. Pokhrel, T. Xia, B. Gilbert, Z. Ji, M. Schowalter, A. Rosenauer, R. Damoiseaux, K. A. Bradley and L. Mädler, *Acs Nano*, 2009, **4**, 15-29.
51. Ü. Özgür, Y. I. Alivov, C. Liu, A. Teke, M. Reshchikov, S. Doğan, V. Avrutin, S.-J. Cho and H. Morkoc, *Journal of applied physics*, 2005, **98**, 041301.
52. Z. L. Wang, *Journal of Physics: Condensed Matter*, 2004, **16**, R829.
53. D. Zhou and A. A. Keller, *Water research*, 2010, **44**, 2948-2956.
54. P. Zhang, F. Xu, A. Navrotsky, J. S. Lee, S. Kim and J. Liu, *Chemistry of Materials*, 2007, **19**, 5687-5693.
55. X. Peng, S. Palma, N. S. Fisher and S. S. Wong, *Aquatic Toxicology*, 2011, **102**, 186-196.
56. Z. Hu, G. Oskam and P. C. Searson, *Journal of colloid and interface science*, 2003, **263**, 454-460.
57. R. Brayner, R. Ferrari-Iliou, N. Brivois, S. Djediat, M. F. Benedetti and F. Fiévet, *Nano Letters*, 2006, **6**, 866-870.
58. L. Guo, Y. L. Ji, H. Xu, P. Simon and Z. Wu, *Journal of the American Chemical Society*, 2002, **124**, 14864-14865.
59. T. Y.-J. Han, M. A. Worsley, T. F. Baumann and J. H. Satcher Jr, *Journal of Materials Chemistry*, 2011, **21**, 330-333.
60. K. Yang, G.-W. She, H. Wang, X.-M. Ou, X.-H. Zhang, C.-S. Lee and S.-T. Lee, *The Journal of Physical Chemistry C*, 2009, **113**, 20169-20172.
61. A. Kołodziejczak-Radzimska and T. Jesionowski, *Materials*, 2014, **7**, 2833-2881.
62. L. Finger and C. Prewitt, *Geophysical Research Letters*, 1989, **16**, 1395-1397.
63. M. Kanzaki, *Physics of the Earth and Planetary Interiors*, 1991, **66**, 307-312.
64. M. Kruger, Q. Williams and R. Jeanloz, *The Journal of Chemical Physics*, 1989, **91**, 5910-5915.
65. T. S. Duffy, T. J. Ahrens and M. A. Lange, *Journal of Geophysical Research: Solid Earth*, 1991, **96**, 14319-14330.
66. S. Redfern and B. Wood, *The American mineralogist*, 1992, **77**, 1129-1132.
67. Y. Fei and H. K. Mao, *Journal of Geophysical Research: Solid Earth*, 1993, **98**, 11875-11884.
68. J. B. Parise, K. Leinenweber, D. J. Weidner, K. Tan and R. B. V. Dreele, *American Mineralogist*, 1994, **79**, 193-196.
69. M. Catti, G. Ferraris, S. Hull and A. Pavese, *Physics and Chemistry of Minerals*, 1995, **22**, 200-206.
70. T. S. Duffy, C. Meade, Y. Fei, H.-K. Mao and R. J. Hemley, *American Mineralogist*, 1995, **80**, 222-230.
71. D. M. Sherman, *American Mineralogist*, 1991, **76**, 1769-1772.
72. P. D'Arco, M. Causà, C. Roetti and B. Silvi, *Physical Review B*, 1993, **47**, 3522.
73. S. Raugei, P. L. Silvestrelli and M. Parrinello, *Physical Review Letters*, 1999, **83**, 2222.
74. M. Mookherjee and L. Stixrude, *American Mineralogist*, 2006, **91**, 127-134.
75. P. T. Jochym, A. M. Oleś, K. Parlinski, J. Łażewski, P. Piekarz and M. Sternik, *Journal of Physics: Condensed Matter*, 2010, **22**, 445403.
76. C. Dong, J. Cairney, Q. Sun, O. L. Maddan, G. He and Y. Deng, *Journal of Nanoparticle Research*, 2010, **12**, 2101-2109.

77. R. B. Stone, *Marine Fisheries Review*, 1982, **44**, 2-3.
78. X. Pan, Y. Wang, Z. Chen, D. Pan, Y. Cheng, Z. Liu, Z. Lin and X. Guan, *ACS applied materials & interfaces*, 2013, **5**, 1137-1142.
79. E. Sada, H. Kumazawa, Y. Sawada and T. Kondo, *Industrial & Engineering Chemistry Process Design and Development*, 1982, **21**, 771-774.
80. H. Gui, X. Zhang, W. Dong, Q. Wang, J. Gao, Z. Song, J. Lai, Y. Liu, F. Huang and J. Qiao, *Polymer*, 2007, **48**, 2537-2541.
81. H. Cao, H. Zheng, J. Yin, Y. Lu, S. Wu, X. Wu and B. Li, *The Journal of Physical Chemistry C*, 2010, **114**, 17362-17368.
82. P. D. Martin, D. W. Schneck, A. L. Dane and M. J. Warwick, *Current medical research and opinion*, 2008, **24**, 1231-1235.
83. G. Scott, C. V. Reynolds, S. Milosavljev, W. Langholff, M. Shenouda and C. Rordorf, *Clinical pharmacokinetics*, 2004, **43**, 341-348.
84. J. Kang and S. P. Schwendeman, *Biomaterials*, 2002, **23**, 239-245.
85. K. Tong, X. Song, G. Xiao and J. Yu, *Industrial & Engineering Chemistry Research*, 2014, **53**, 4755-4762.
86. Y. Ding, G. Zhang, H. Wu, B. Hai, L. Wang and Y. Qian, *Chemistry of materials*, 2001, **13**, 435-440.
87. W. Fan, S. Sun, X. Song, W. Zhang, H. Yu, X. Tan and G. Cao, *Journal of Solid State Chemistry*, 2004, **177**, 2329-2338.
88. H. Wu, M. Shao, J. Gu and X. Wei, *Materials Letters*, 2004, **58**, 2166-2169.
89. C. Henrist, J.-P. Mathieu, C. Vogels, A. Rulmont and R. Cloots, *Journal of Crystal Growth*, 2003, **249**, 321-330.
90. J. C. Yu, A. Xu, L. Zhang, R. Song and L. Wu, *The Journal of Physical Chemistry B*, 2004, **108**, 64-70.
91. Y. Li, M. Sui, Y. Ding, G. Zhang, J. Zhuang and C. Wang, *Advanced materials*, 2000, **12**, 818-821.
92. L. Yan, J. Zhuang, X. Sun, Z. Deng and Y. Li, *Materials Chemistry and Physics*, 2002, **76**, 119-122.
93. C. Yan, D. Xue, L. Zou, X. Yan and W. Wang, *Journal of Crystal Growth*, 2005, **282**, 448-454.
94. R. Cava, *Science*, 1990, **247**, 656-662.
95. J. Tranquada, B. Sternlieb, J. Axe, Y. Nakamura and S. Uchida, *nature*, 1995, **375**, 561.
96. H. Wayne, *Wiley-VCH, Weinheim*, 2002, 273-298.
97. J. Forsyth and S. Hull, *Journal of Physics: Condensed Matter*, 1991, **3**, 5257.
98. J. Xu, W. Ji, Z. Shen, S. Tang, X. Ye, D. Jia and X. Xin, *Journal of Solid State Chemistry*, 1999, **147**, 516-519.
99. M. E. Grigore, E. R. Biscu, A. M. Holban, M. C. Gestal and A. M. Grumezescu, *Pharmaceuticals*, 2016, **9**, 75.
100. M. Ahamed, H. A. Alhadlaq, M. Khan, P. Karuppiah and N. A. Al-Dhabi, *Journal of Nanomaterials*, 2014, **2014**, 17.
101. A. Lazary, I. Weinberg, J.-J. Vatine, A. Jefidoff, R. Bardenstein, G. Borkow and N. Ohana, *International Journal of Infectious Diseases*, 2014, **24**, 23-29.

102. B. J. Berne and R. Pecora, *Dynamic light scattering: with applications to chemistry, biology, and physics*, Courier Corporation, 1976.
103. S. Bhattacharjee, *Journal of Controlled Release*, 2016, **235**, 337-351.
104. R. Xu, C. Wu and H. Xu, *Carbon*, 2007, **45**, 2806-2809.
105. W. Chesworth.
106. S. Ramanathan, K. K. Kumar, P. De and S. Banerjee, *Bulletin of Materials Science*, 2005, **28**, 109-114.
107. R. Marsalek, *APCBEE Procedia*, 2014, **9**, 13-17.
108. A. Patterson, *Physical review*, 1939, **56**, 978.
109. G. Oskam, A. Nellore, R. L. Penn and P. C. Searson, *The Journal of Physical Chemistry B*, 2003, **107**, 1734-1738.
110. J. M. Hancock, *Brigham Young University*, 2013.
111. M. J. Walock, *University of Alabama at Birmingham*, Paris, ENSAM, 2012.
112. J. Ye, *University of Sheffield*, 2014.
113. R. Rupasinghe, *University of Iowa*, 2011.
114. J. Zhang, *International Coriference on Electronics and Optoelectronics*, 2011.
115. F. H. Hussein and A. F. Halbus, *International Journal of Photoenergy*, 2012, **2012**.
116. M. Nirmala, M. G. Nair, K. Rekha, A. Anukaliani, S. Samdarshi and R. G. Nair, *Afr J Basic Appl Sci*, 2010, **2**, 161-166.
117. A. Sirelkhatim, S. Mahmud, A. Seeni, N. H. M. Kaus, L. C. Ann, S. K. M. Bakhori, H. Hasan and D. Mohamad, *Nano-Micro Letters*, 2015, **7**, 219-242.
118. H. Zhang, B. Chen, H. Jiang, C. Wang, H. Wang and X. Wang, *Biomaterials*, 2011, **32**, 1906-1914.
119. J. T. Seil, E. N. Taylor and T. J. Webster, 2009.
120. O. Seven, B. Dindar, S. Aydemir, D. Metin, M. Ozinel and S. Icli, *Journal of Photochemistry and Photobiology A: Chemistry*, 2004, **165**, 103-107.
121. P. Nagarajan and V. Rajagopalan, *Science and Technology of Advanced Materials*, 2008, **9**, 035004.
122. S. Ahmed, M. Rasul, W. N. Martens, R. Brown and M. Hashib, *Desalination*, 2010, **261**, 3-18.
123. P. Espitia, *Food Bioprocess Technol*, 2012, **5**, 1447.
124. Y. Zhang, M. K. Ram, E. K. Stefanakos and D. Y. Goswami, *Journal of Nanomaterials*, 2012, **2012**, 20.
125. J. Sawai, S. Shoji, H. Igarashi, A. Hashimoto, T. Kokugan, M. Shimizu and H. Kojima, *Journal of Fermentation and Bioengineering*, 1998, **86**, 521-522.
126. M. J. Al-Awady, G. M. Greenway and V. N. Paunov, *RSC Advances*, 2015, **5**, 37044-37059.
127. Y.-N. Chang, M. Zhang, L. Xia, J. Zhang and G. Xing, *Materials*, 2012, **5**, 2850-2871.
128. Y. Xie, Y. He, P. L. Irwin, T. Jin and X. Shi, *Applied and environmental microbiology*, 2011, **77**, 2325-2331.
129. L. Zhang, Y. Jiang, Y. Ding, M. Povey and D. York, *Journal of Nanoparticle Research*, 2007, **9**, 479-489.
130. J. Sawai, E. Kawada, F. Kanou, H. Igarashi, A. Hashimoto, T. Kokugan and M. Shimizu, *Journal of chemical engineering of Japan*, 1996, **29**, 627-633.

131. A. Lipovsky, Y. Nitzan, A. Gedanken and R. Lubart, *Nanotechnology*, 2011, **22**, 105101.
132. R. Dunford, A. Salinaro, L. Cai, N. Serpone, S. Horikoshi, H. Hidaka and J. Knowland, *FEBS letters*, 1997, **418**, 87-90.
133. K. M. Reddy, K. Feris, J. Bell, D. G. Wingett, C. Hanley and A. Punnoose, *Applied physics letters*, 2007, **90**, 213902.
134. K. R. Raghupathi, R. T. Koodali and A. C. Manna, *Langmuir*, 2011, **27**, 4020-4028.
135. O. Yamamoto, *International Journal of Inorganic Materials*, 2001, **3**, 643-646.
136. S. Nair, A. Sasidharan, V. D. Rani, D. Menon, S. Nair, K. Manzoor and S. Raina, *Journal of Materials Science: Materials in Medicine*, 2009, **20**, 235-241.
137. C. Hu, M. Li, Y. Cui, D. Li, J. Chen and L. Yang, *Soil Biology and Biochemistry*, 2010, **42**, 586-591.
138. L. K. Adams, D. Y. Lyon and P. J. Alvarez, *Water research*, 2006, **40**, 3527-3532.
139. J. Ji, Z. Long and D. Lin, *Chemical Engineering Journal*, 2011, **170**, 525-530.
140. S. L. Waaijers, D. Kong, H. S. Hendriks, C. A. de Wit, I. T. Cousins, R. H. Westerink, P. E. Leonards, M. H. Kraak, W. Admiraal and P. de Voogt, in *Reviews of environmental contamination and toxicology*, Springer, 2013, pp. 1-71.
141. C. Dong, D. Song, J. Cairney, O. L. Maddan, G. He and Y. Deng, *Materials Research Bulletin*, 2011, **46**, 576-582.
142. C. Dong, G. He, H. Li, R. Zhao, Y. Han and Y. Deng, *Journal of membrane science*, 2012, **387**, 40-47.
143. Z. Wang, C. Li, Y. Mu, Z. Lin, A. Yi, Q. Zhang and B. Yan, *Journal of hazardous materials*, 2015, **287**, 296-305.
144. A. Pilarska, K. Bula, K. Myszka, T. Rozmanowski, K. Szwarc-Rzepka, K. Pilarski, Ł. Chrzanowski, K. Czaczyk and T. Jesionowski, *Open Chemistry*, 2015, **13**.
145. C. Dong, G. He, W. Zheng, T. Bian, M. Li and D. Zhang, *Materials Letters*, 2014, **134**, 286-289.
146. Q. Li, S. Mahendra, D. Y. Lyon, L. Brunet, M. V. Liga, D. Li and P. J. Alvarez, *Water research*, 2008, **42**, 4591-4602.
147. A. F. Mendonca, T. L. Amoroso and S. J. Knabel, *Applied and Environmental Microbiology*, 1994, **60**, 4009-4014.
148. A. Kumar, P. K. Vemula, P. M. Ajayan and G. John, *Nature materials*, 2008, **7**, 236-241.
149. O. Yamamoto, T. Ohira, K. Alvarez and M. Fukuda, *Materials Science and Engineering: B*, 2010, **173**, 208-212.
150. J. H. Lee, K. Ahn, S. M. Kim, K. S. Jeon, J. S. Lee and I. J. Yu, *Journal of Nanoparticle Research*, 2012, **14**, 1-10.
151. T. Jin and Y. He, *Journal of Nanoparticle Research*, 2011, **13**, 6877-6885.
152. C. J. Hewitt, S. R. Bellara, A. Andreani, G. Nebe-von-Caron and C. M. McFarlane, *Biotechnology Letters*, 2001, **23**, 667-675.
153. Y. H. Leung, A. Ng, X. Xu, Z. Shen, L. A. Gethings, M. T. Wong, C. Chan, M. Y. Guo, Y. H. Ng and A. B. Djurišić, *Small*, 2014, **10**, 1171-1183.
154. H.-Q. Wu, X.-W. Wei, M.-W. Shao, J.-S. Gu and M.-Z. Qu, *Chemical physics letters*, 2002, **364**, 152-156.

155. M. sani Usman, *International journal of nanomedicine*, 2013, **8**, 4467-4479.
156. O. Mahapatra, M. Bhagat, C. Gopalakrishnan and K. D. Arunachalam, *Journal of Experimental Nanoscience*, 2008, **3**, 185-193.
157. R. Katwal, H. Kaur, G. Sharma, M. Naushad and D. Pathania, *Journal of Industrial and Engineering Chemistry*, 2015, **31**, 173-184.
158. D. Quaranta, T. Krans, C. E. Santo, C. G. Elowsky, D. W. Domaille, C. J. Chang and G. Grass, *Applied and environmental microbiology*, 2011, **77**, 416-426.
159. M. Vincent, R. E. Duval, P. Hartemann and M. Engels-Deutsch, *Journal of applied microbiology*, 2018, **124**, 1032-1046.
160. A. Azam, A. S. Ahmed, M. Oves, M. Khan and A. Memic, *Int. J. Nanomed*, 2012, **7**, 3527-3535.
161. T. Chatterjee, S. Chakraborti, P. Joshi, S. P. Singh, V. Gupta and P. Chakrabarti, *The FEBS journal*, 2010, **277**, 4184-4194.
162. A. Verma, O. Uzun, Y. Hu, Y. Hu, H.-S. Han, N. Watson, S. Chen, D. J. Irvine and F. Stellacci, *Nature materials*, 2008, **7**, 588-595.
163. A. E. Nel, L. Mädler, D. Velegol, T. Xia, E. M. Hoek, P. Somasundaran, F. Klaessig, V. Castranova and M. Thompson, *Nature materials*, 2009, **8**, 543-557.
164. C.-L. Ho, S.-S. Teo, R. A. Rahim and S.-M. Phang, *Asia-Pacific Journal of Molecular Biology and Biotechnology*, 2010, **18**, 315-319.
165. R. A. Colvin, C. P. Fontaine, M. Laskowski and D. Thomas, *European journal of pharmacology*, 2003, **479**, 171-185.
166. S. S. Zinjarde, *Chronicles of Young Scientists*, 2012, **3**, 74.
167. M. Rai, A. Yadav and A. Gade, *Biotechnology advances*, 2009, **27**, 76-83.
168. A. El-Batal, B. M. Haroun, A. A. Farrag, A. Baraka and G. S. El-Sayyad, *British Journal of Pharmaceutical Research*, 2014, **4**, 1341.
169. V. K. Sharma, R. A. Yngard and Y. Lin, *Advances in colloid and interface science*, 2009, **145**, 83-96.
170. S. Egger, R. P. Lehmann, M. J. Height, M. J. Loessner and M. Schuppler, *Applied and environmental microbiology*, 2009, **75**, 2973-2976.
171. C. Malarkodi, S. Rajeshkumar, K. Paulkumar, M. Vanaja, G. Gnanajobitha and G. Annadurai, *Bioinorganic chemistry and applications*, 2014, **2014**.
172. K. Chaloupka, Y. Malam and A. M. Seifalian, *Trends in biotechnology*, 2010, **28**, 580-588.
173. Y.-K. Jo, B. H. Kim and G. Jung, *Plant Disease*, 2009, **93**, 1037-1043.
174. A. M. Allahverdiyev, E. S. Abamor, M. Bagirova and M. Rafailovich, *Future microbiology*, 2011, **6**, 933-940.
175. C.-N. Lok, C.-M. Ho, R. Chen, Q.-Y. He, W.-Y. Yu, H. Sun, P. K.-H. Tam, J.-F. Chiu and C.-M. Che, *Journal of Proteome research*, 2006, **5**, 916-924.
176. H. Yun, J. D. Kim, H. C. Choi and C. W. Lee, *Bulletin of the Korean Chemical Society*, 2013, **34**, 3261-3264.
177. I. Iavicoli, L. Fontana, V. Leso and A. Bergamaschi, *International journal of molecular sciences*, 2013, **14**, 16732-16801.
178. L. Sintubin, B. De Gusseme, P. Van der Meeren, B. F. Pycke, W. Verstraete and N. Boon, *Applied microbiology and biotechnology*, 2011, **91**, 153-162.

179. R. Mie, M. W. Samsudin, L. B. Din, A. Ahmad, N. Ibrahim and S. N. A. Adnan, *International journal of nanomedicine*, 2014, **9**, 121.
180. J. F. Hernández-Sierra, F. Ruiz, D. C. C. Pena, F. Martínez-Gutiérrez, A. E. Martínez, A. d. J. P. Guillén, H. Tapia-Pérez and G. M. Castañón, *Nanomedicine: Nanotechnology, Biology and Medicine*, 2008, **4**, 237-240.
181. A. Besinis, T. De Peralta and R. D. Handy, *Nanotoxicology*, 2014, **8**, 1-16.
182. M. Zarei, A. Jamnejad and E. Khajehali, *Jundishapur Journal of Microbiology*, 2014, **7**.
183. C. Marambio-Jones and E. M. Hoek, *Journal of Nanoparticle Research*, 2010, **12**, 1531-1551.
184. K.-J. Kim, W. S. Sung, S.-K. Moon, J.-S. Choi, J. G. Kim and D. G. Lee, *J Microbiol Biotechnol*, 2008, **18**, 1482-1484.
185. M. B. Sathyanarayanan, R. Balachandranath, Y. Genji Srinivasulu, S. K. Kannaiyan and G. Subbiahdoss, *ISRN microbiology*, 2013, **2013**.
186. I. Sondi and B. Salopek-Sondi, *Journal of colloid and interface science*, 2004, **275**, 177-182.
187. E. Lima, R. Guerra, V. Lara and A. Guzmán, *Chemistry Central Journal*, 2013, **7**, 1.
188. P. M. Tiwari, K. Vig, V. A. Dennis and S. R. Singh, *Nanomaterials*, 2011, **1**, 31-63.
189. Y. Zhou, Y. Kong, S. Kundu, J. D. Cirillo and H. Liang, *Journal of Nanobiotechnology*, 2012, **10**, 1.
190. S. Lokina and V. Narayanan, *Chemical Science Transactions*, 2013, **2**, S105-S110.
191. Y. Cui, Y. Zhao, Y. Tian, W. Zhang, X. Lü and X. Jiang, *Biomaterials*, 2012, **33**, 2327-2333.
192. P. ZielińAski, R. Schulz, S. Kaliaguine and A. Van Neste, *Journal of materials research*, 1993, **8**, 2985-2992.
193. P. Ganguly and W. J. Poole, *Materials Science and Engineering: A*, 2003, **352**, 46-54.
194. F. W. Dynys and J. W. Halloran, *Journal of the American Ceramic Society*, 1982, **65**, 442-448.
195. I. M. Sadiq, B. Chowdhury, N. Chandrasekaran and A. Mukherjee, *Nanomedicine: Nanotechnology, Biology and Medicine*, 2009, **5**, 282-286.
196. M. Ansari, H. Khan, A. Khan, S. Cameotra, Q. Saquib and J. Musarrat, *Journal of applied microbiology*, 2014, **116**, 772-783.
197. A. Shabrandi, S. Azizi, R. Hobbenaghi, A. Ownagh and S. Keshipour, *Iranian Journal of Veterinary Surgery*, 2017, **12**, 9-20.
198. C. C. L. dos Santos, I. A. P. Farias, A. d. J. dos Reis Albuquerque, P. M. d. F. e Silva, G. M. da Costa One and F. C. Sampaio, 2014.
199. S. Becker, J. Soukup and J. Gallagher, *Toxicology in vitro*, 2002, **16**, 209-218.
200. S. Bodapati, 2011.
201. P. Kofstad, *Nonstoichiometry, diffusion, and electrical conductivity in binary metal oxides*, Wiley-Interscience New York, 1972.
202. T. Atou, K. Kusaba, K. Fukuoka, M. Kikuchi and Y. Syono, *Journal of Solid State Chemistry*, 1990, **89**, 378-384.

203. D. Schubert, R. Dargusch, J. Raitano and S.-W. Chan, *Biochemical and biophysical research communications*, 2006, **342**, 86-91.
204. J. Borovička, S. D. Stoyanov and V. N. Paunov, *Nanoscale*, 2013, **5**, 8560-8568.
205. J. Borovička, W. J. Metheringham, L. A. Madden, C. D. Walton, S. D. Stoyanov and V. N. Paunov, *Journal of the American Chemical Society*, 2013, **135**, 5282-5285.
206. J. Borovička, S. D. Stoyanov and V. N. Paunov, *Physical Review E*, 2015, **92**, 032730.
207. H. Rahma, S. Asghari, S. Logsetty, X. Gu and S. Liu, *ACS applied materials & interfaces*, 2015, **7**, 11536-11546.
208. F. A. Aouada and M. R. de Moura, in *Nanotechnologies in Food and Agriculture*, Springer, 2015, pp. 103-118.
209. J. H. Lora and W. G. Glasser, *Journal of Polymers and the Environment*, 2002, **10**, 39-48.
210. M. Norgren and H. Edlund, *Current Opinion in Colloid & Interface Science*, 2014, **19**, 409-416.
211. F. J. Ruiz-Dueñas and Á. T. Martínez, *Microbial biotechnology*, 2009, **2**, 164-177.
212. A. Leonowicz, A. Matuszewska, J. Luterek, D. Ziegenhagen, M. Wojtaś-Wasilewska, N.-S. Cho, M. Hofrichter and J. Rogalski, *Fungal genetics and biology*, 1999, **27**, 175-185.
213. M. Tuomela, M. Vikman, A. Hatakka and M. Itävaara, *Bioresource technology*, 2000, **72**, 169-183.
214. K. Lundquist, T. K. Kirk and W. J. Connors, *Archives of Microbiology*, 1977, **112**, 291-296.
215. T. D. Bugg, M. Ahmad, E. M. Hardiman and R. Rahmanpour, *Natural product reports*, 2011, **28**, 1883-1896.
216. C. H. Ludwig and K. Sarkanen, *Lignins: occurrence, formation, structure and reactions*, Wiley-Interscience New York, 1971.
217. C. Frangville, M. Rutkevičius, A. P. Richter, O. D. Velev, S. D. Stoyanov and V. N. Paunov, *ChemPhysChem*, 2012, **13**, 4235-4243.
218. A. P. Richter, B. Bharti, H. B. Armstrong, J. S. Brown, D. Plemmons, V. N. Paunov, S. D. Stoyanov and O. D. Velev, *Langmuir*, 2016, **32**, 6468-6477.
219. A. P. Richter, J. S. Brown, B. Bharti, A. Wang, S. Gangwal, K. Houck, E. A. C. Hubal, V. N. Paunov, S. D. Stoyanov and O. D. Velev, *Nature nanotechnology*, 2015, **10**, 817.
220. X. Wang, S. Zhang, L. Zhu, S. Xie, Z. Dong, Y. Wang and W. Zhou, *The Veterinary Journal*, 2012, **191**, 115-120.
221. M. Valodkar, A. Bhadoria, J. Pohnerkar, M. Mohan and S. Thakore, *Carbohydrate Research*, 2010, **345**, 1767-1773.
222. D. Martins, F. Costa, M. Brocchi and N. Duran, *Journal of Nanoparticle Research*, 2011, **13**, 355-363.
223. C. Ornelas-Megiatto, P. N. Shah, P. R. Wich, J. L. Cohen, J. A. Tagaev, J. A. Smolen, B. D. Wright, M. J. Panzner, W. J. Youngs and J. M. Fréchet, *Molecular pharmaceutics*, 2012, **9**, 3012-3022.

224. G. Qi, L. Li, F. Yu and H. Wang, *ACS applied materials & interfaces*, 2013, **5**, 10874-10881.
225. V. Ravishankar Rai and A. Jamuna Bai, *A Méndez-Vilas A, editor. Mysore: Formatex*, 2011.
226. R. Saraf, *International Journal of Advances in Applied Sciences*, 2013, **2**, 85-88.
227. Q. Liu, M. Zhang, Z. x. Fang and X. h. Rong, *Journal of the Science of Food and Agriculture*, 2014, **94**, 2547-2554.
228. A. Azam, A. S. Ahmed, M. Oves, M. S. Khan, S. S. Habib and A. Memic, *International journal of nanomedicine*, 2012, **7**, 6003.
229. M. Rai, A. Yadav and N. Cioffi, in *Nano-Antimicrobials*, Springer, 2012, pp. 211-224.
230. J. W. Rasmussen, E. Martinez, P. Louka and D. G. Wingett, *Expert opinion on drug delivery*, 2010, **7**, 1063-1077.
231. J. P. Ruparelia, A. K. Chatterjee, S. P. Duttagupta and S. Mukherji, *Acta biomaterialia*, 2008, **4**, 707-716.
232. W. Jiang, H. Mashayekhi and B. Xing, *Environmental pollution*, 2009, **157**, 1619-1625.
233. F. Haghighi, S. Roudbar Mohammadi, P. Mohammadi, S. Hosseinkhani and R. Shipour, *Infection, Epidemiology and Microbiology*, 2013, **1**, 33-38.
234. A. S. Roy, A. Parveen, A. R. Koppalkar and M. A. Prasad, *Journal of Biomaterials and Nanobiotechnology*, 2010, **1**, 37.
235. G. Carré, E. Hamon, S. Ennahar, M. Estner, M.-C. Lett, P. Horvatovich, J.-P. Gies, V. Keller, N. Keller and P. Andre, *Applied and environmental microbiology*, 2014, AEM. 03995-03913.
236. C. C. L. dos Santos, I. A. P. Farias, A. d. J. dos Reis Albuquerque, P. M. d. F. e Silva, G. M. da Costa One and F. C. Sampaio, 2014.
237. C. Buzea, I. I. Pacheco and K. Robbie, *Biointerphases*, 2007, **2**, MR17-MR71.
238. C. Jiao, Z. Wang, Z. Ye, Y. Hu and W. Fan, *Journal of fire sciences*, 2006, **24**, 47-64.
239. J. Sawai and H. Igarashi, *FOODS AND FOOD INGREDIENTS JOURNAL OF JAPAN*, 2002, 47-57.
240. H. H. Lara, L. Ixtepan-Turrent, E. N. G. Treviño and D. K. Singh, *Journal of nanobiotechnology*, 2011, **9**, 38.
241. W. Kyoungja and J. Hong, *Magnetics, IEEE Transactions on*, 2005, **41**, 4137-4139.
242. R. Shen, P. H. Camargo, Y. Xia and H. Yang, *Langmuir*, 2008, **24**, 11189-11195.
243. J. M. Bergen, H. A. von Recum, T. T. Goodman, A. P. Massey and S. H. Pun, *Macromolecular Bioscience*, 2006, **6**, 506-516.
244. L. M. Liz-Marzán, M. Giersig and P. Mulvaney, *Langmuir*, 1996, **12**, 4329-4335.
245. A. M. De Campos, A. Sánchez, R. Gref, P. Calvo, M. Alonso, amp, x and J. a, *European Journal of Pharmaceutical Sciences*, 2003, **20**, 73-81.
246. D. Jian-Fang and J. Ji-Sen, *Journal of Inorganic Materials*, 2007, **22**, 859-863.
247. T. I. Armstrong, M. C. Daves and L. Dium, *Journal of Drug Targeting*, 1997, **4**, 389-398.

248. D. E. Bergbreiter, *Angewandte Chemie International Edition*, 1999, **38**, 2870-2872.
249. F. Caruso, M. Spasova, V. Salgueiriño-Maceira and L. Liz-Marzán, *Advanced Materials*, 2001, **13**, 1090-1094.
250. F. Caruso, E. Donath and H. Möhwald, *The Journal of Physical Chemistry B*, 1998, **102**, 2011-2016.
251. G. Decher, *science*, 1997, **277**, 1232-1237.
252. A. Ciferri, *Chemistry-A European Journal*, 2010, **16**, 10930-10945.
253. D. I. Gittins and F. Caruso, *Advanced Materials*, 2000, **12**, 1947-1949.
254. T. R. Farhat and J. B. Schlenoff, *Electrochemical and solid-state letters*, 2002, **5**, B13-B15.
255. C. Lee, I. Kim, H. Shin, S. Kim and J. Cho, *Nanotechnology*, 2010, **21**, 185704.
256. R. A. Caruso, A. Susha and F. Caruso, *Chemistry of Materials*, 2001, **13**, 400-409.
257. J.-i. Anzai, Y. Kobayashi, Y. Suzuki, H. Takeshita, Q. Chen, T. Osa, T. Hoshi and X.-y. Du, *Sensors and Actuators B: Chemical*, 1998, **52**, 3-9.
258. H. Shi, Y. Yang, J. Huang, Z. Zhao, X. Xu, J.-I. Anzai, T. Osa and Q. Chen, *Talanta*, 2006, **70**, 852-858.
259. B. Wang and J.-i. Anzai, *Langmuir*, 2007, **23**, 7378-7384.
260. T. Crouzier, T. Boudou and C. Picart, *Current Opinion in Colloid & Interface Science*, 2010, **15**, 417-426.
261. H. Sato and J.-i. Anzai, *Biomacromolecules*, 2006, **7**, 2072-2076.
262. C. M. Jewell and D. M. Lynn, *Advanced drug delivery reviews*, 2008, **60**, 979-999.
263. U. Akiba and J.- ichi. Anzai, *AIMS Materials Science*, 2017, **4(4)**, 832-846.
264. S. A. Sukhishvili and S. Granick, *Macromolecules*, 2002, **35**, 301-310.
265. S. Pavlukhina and S. Sukhishvili, *Advanced drug delivery reviews*, 2011, **63**, 822-836.
266. S. V. Rao, K. W. Anderson and L. G. Bachas, *Biotechnology and bioengineering*, 1999, **65**, 389-396.
267. K. Sato, D. Kodama, Y. Naka and J.-i. Anzai, *Biomacromolecules*, 2006, **7**, 3302-3305.
268. T. Hoshi, S. Akase and J.-i. Anzai, *Langmuir*, 2002, **18**, 7024-7028.
269. E. Donath, G. B. Sukhorukov, F. Caruso, S. A. Davis and H. Möhwald, *Angewandte Chemie International Edition*, 1998, **37**, 2201-2205.
270. L. L. del Mercato, M. M. Ferraro, F. Baldassarre, S. Mancarella, V. Greco, R. Rinaldi and S. Leporatti, *Advances in colloid and interface science*, 2014, **207**, 139-154.
271. L. Séon, P. Lavalle, P. Schaaf and F. Boulmedais, *Langmuir*, 2015, **31**, 12856-12872.
272. J.-A. He, R. Mosurkal, L. A. Samuelson, L. Li and J. Kumar, *Langmuir*, 2003, **19**, 2169-2174.
273. N. I. Kovtyukhova, B. R. Martin, J. K. Mbindyo, P. A. Smith, B. Razavi, T. S. Mayer and T. E. Mallouk, *The Journal of Physical Chemistry B*, 2001, **105**, 8762-8769.

274. M. M. Mahlambi, A. K. Mishra, S. B. Mishra, A. M. Raichur, B. B. Mamba and R. W. Krause, *Journal of Nanomaterials*, 2012, **2012**, 1.
275. D. S. Kommireddy, A. A. Patel, T. G. Shutava, D. K. Mills and Y. M. Lvov, *Journal of nanoscience and nanotechnology*, 2005, **5**, 1081-1087.
276. G. Carré, L. Garnier, J. Moeller-Siegert, J.-P. Gies, V. Keller, P. André and N. Keller, *RSC Advances*, 2015, **5**, 38859-38867.
277. M. M. De Villiers, D. P. Otto, S. J. Strydom and Y. M. Lvov, *Advanced drug delivery reviews*, 2011, **63**, 701-715.
278. Y. Lvov, K. Ariga, M. Onda, I. Ichinose and T. Kunitake, *Colloids and Surfaces A: Physicochemical and Engineering Aspects*, 1999, **146**, 337-346.
279. G. Bantchev, Z. Lu and Y. Lvov, *Journal of nanoscience and nanotechnology*, 2009, **9**, 396-403.
280. N. G. Hoogeveen, M. A. Cohen Stuart, G. J. Fleer and M. R. Böhmer, *Langmuir*, 1996, **12**, 3675-3681.
281. M. R. Linford, M. Auch and H. Möhwald, *Journal of the American Chemical Society*, 1998, **120**, 178-182.
282. Y. Wang, A. S. Angelatos and F. Caruso, *Chemistry of Materials*, 2008, **20**, 848-858.
283. F. Caruso, *Chemistry – A European Journal*, 2000, **6**, 413-419.
284. Y. Wang, V. Bansal, A. N. Zelikin and F. Caruso, *Nano letters*, 2008, **8**, 1741-1745.
285. F. Caruso and H. Möhwald, *Langmuir*, 1999, **15**, 8276-8281.
286. A. B. Artyukhin, O. Bakajin, P. Stroeve and A. Noy, *Langmuir*, 2004, **20**, 1442-1448.
287. T. Cassagneau and F. Caruso, *Journal of the American Chemical Society*, 2002, **124**, 8172-8180.
288. F. Caruso, R. A. Caruso and H. Möhwald, *Science*, 1998, **282**, 1111-1114.
289. E. Frankland and B. Duppa, *Justus Liebigs Annalen der Chemie*, 1860, **115**, 319-322.
290. H. C. Brown and B. S. Rao, *Journal of the American Chemical Society*, 1956, **78**, 5694-5695.
291. N. Miyaura, K. Yamada and A. Suzuki, *Tetrahedron Letters*, 1979, **20**, 3437-3440.
292. P. Y. Lam, C. G. Clark, S. Saubern, J. Adams, M. P. Winters, D. M. Chan and A. Combs, *Tetrahedron Letters*, 1998, **39**, 2941-2944.
293. A. Michaelis and P. Becker, *Berichte der deutschen chemischen Gesellschaft*, 1880, **13**, 58-61.
294. M. Philipp and M. Bender, *Proceedings of the National Academy of Sciences*, 1971, **68**, 478-480.
295. T. D. James, M. D. Phillips and S. Shinkai, *Boronic acids in saccharide recognition*, Royal Society of Chemistry, 2006.
296. R. N. Fedorak, M. D. Gershon and M. Field, *Gastroenterology*, 1989, **96**, 37-44.
297. J. Yan, H. Fang and B. Wang, *Medicinal research reviews*, 2005, **25**, 490-520.
298. J. Balzarini, *The Lancet Infectious Diseases*, 2005, **5**, 726-731.
299. S. Kitano, Y. Koyama, K. Kataoka, T. Okano and Y. Sakurai, *Journal of Controlled Release*, 1992, **19**, 161-170.

300. P. C. Trippier and C. McGuigan, *MedChemComm*, 2010, **1**, 183-198.
301. K. Lacina, P. Skládal and T. D. James, *Chemistry Central Journal*, 2014, **8**, 60.
302. S. Jin, Y. Cheng, S. Reid, M. Li and B. Wang, *Medicinal research reviews*, 2010, **30**, 171-257.
303. J. S. Fossey, F. D'Hooge, J. M. van den Elsen, M. P. Pereira Morais, S. I. Pascu, S. D. Bull, F. Marken, A. T. A. Jenkins, Y. B. Jiang and T. D. James, *The Chemical Record*, 2012, **12**, 464-478.
304. J. S. Hansen, J. B. Christensen, J. F. Petersen, T. Hoeg-Jensen and J. C. Norrild, *Sensors and Actuators B: Chemical*, 2012, **161**, 45-79.
305. H. Li and Z. Liu, *TrAC Trends in Analytical Chemistry*, 2012, **37**, 148-161.
306. X. Wang, N. Xia and L. Liu, *International journal of molecular sciences*, 2013, **14**, 20890-20912.
307. C.-C. Chen, W.-C. Su, B.-Y. Huang, Y.-J. Chen, H.-C. Tai and R. P. Obena, *Analyst*, 2014, **139**, 688-704.
308. F. Duval, *New applications of the interaction between diols and boronic acids*, Wageningen University, 2015.
309. S. J. Benkovic, S. J. Baker, M. Alley, Y.-H. Woo, Y.-K. Zhang, T. Akama, W. Mao, J. Baboval, P. R. Rajagopalan and M. Wall, *Journal of medicinal chemistry*, 2005, **48**, 7468-7476.
310. X. C. Liu and W. H. Scouten, *Journal of Molecular Recognition*, 1996, **9**, 462-467.
311. M. Pan, Y. Sun, J. Zheng and W. Yang, *ACS applied materials & interfaces*, 2013, **5**, 8351-8358.
312. Y. Qu, J. Liu, K. Yang, Z. Liang, L. Zhang and Y. Zhang, *Chemistry–A European Journal*, 2012, **18**, 9056-9062.
313. W. Zhou, N. Yao, G. Yao, C. Deng, X. Zhang and P. Yang, *Chemical Communications*, 2008, 5577-5579.
314. D. Qi, H. Zhang, J. Tang, C. Deng and X. Zhang, *The Journal of Physical Chemistry C*, 2010, **114**, 9221-9226.
315. K. Yum, T. P. McNicholas, B. Mu and M. S. Strano, *Journal*, 2013.
316. V. K. Gupta, N. Atar, M. L. Yola, M. Eryılmaz, H. Torul, U. Tamer, İ. H. Boyacı and Z. Üstündağ, *Journal of colloid and interface science*, 2013, **406**, 231-237.
317. N. Xia, L. Zhang, Q. Feng, D. Deng, X. Sun and L. Liu, *Int J Electrochem Sc*, 2013, **8**, 5487-5495.
318. N. Xia, L. Zhang, G. Wang, Q. Feng and L. Liu, *Biosensors and Bioelectronics*, 2013, **47**, 461-466.
319. X. Du and J. He, *ACS applied materials & interfaces*, 2011, **3**, 1269-1276.
320. E. Morales-Avila, G. Ferro-Flores, B. E. Ocampo-García, et al., *J Nanomater*, 2017, **2017**, Article ID 5831959 *doi: https://doi.org/10.1155/2017/5831959*.
321. U. L. Senarathna, S. S. Fernando, et al., *Chem Cent* J, 2017, **11**, 7.
322. S. Kim and D.Y. Ryu, *J Appl Toxicol*, 2013, **33**(2), 78-89.
323. SSN Fernando, TDCP Gunasekara and J Holton, *Sri Lankan Journal of Infectious Diseases*, 2018, **8** (1), 2-11.
324. D. Sen Karaman, S. Sarwar, D. Desai, E. M. Bjo¨rk, M. Ode´n, P. Chakrabarti, J. M. Rosenholm and S. Chakraborti, *J. Mater. Chem. B,* 2016, **4**, 3292.

# Chapter 2

# 2. Experimental

This chapter describes the materials and experimental methods used for the preparation of nanoparticles and outlines the protocols for preparation of surface modified nanoparticles. In addition to that, it contains the protocols utilized for the preparation of different inorganic nanoparticles and impacts of pH on the zeta potential and particle size measurement. Furthermore, procedures for the examining of the anti-algal, anti-yeast and antibacterial activities of non-functionalized and functionalized nanoparticles are described. All the techniques used for characterisation and analysis of the surface modified nanoparticles are also detailed in this chapter.

## 2.1 Materials

Zinc nitrate (99%, Sigma Aldrich, UK), copper (II) chloride (99%, Sigma Aldrich, UK) and magnesium chloride (98%, Sigma Aldrich, UK) were used as a precursor in the synthesis of nanoparticles by the direct precipitation method. Sodium hydroxide (99.6%, Fisher, UK) and potassium hydroxide (85%, Sigma Aldrich, UK) were used as a precipitating agent to synthesis nanoparticles. (3-glycidyloxypropyl) trimethoxysilane (GLYMO) and 4-hydroxyphenylboronic acid (4-HPBA) were purchased from Sigma Aldrich. Fluorescein diacetate (FDA, 98%) for cell viability assays was purchased from Fluka, UK. BacTiter-Glo (BTG) microbial cell viability assay was delivered by Promega, UK. Deionized water purified by reverse osmosis and ion exchange with a Milli-Q water system (Millipore, UK) was used in all our studies. Its surface tension was 71.9 $mNm^{-1}$ at 25°C, with measured resistivity more than 18 $M\Omega\ cm^{-1}$. Types of various reagents that were utilized as a part of this study are arranged in Table 2.1.

**Table 2.1.** The chemicals that were utilized in this project.

| Material | Purity | Supplier |
|---|---|---|
| Ethanol | Absolute | Fisher, UK |
| Hydrochloric Acid | 37 % | Fisher, UK |
| Ammonia Solution | 35 % | Prime, UK |
| Tetraethylorthosilicate | 98 % | Fisher, UK |
| Acetone | Absolute | Fisher, UK |
| Sodium Chloride | 99.5 % | Fisher, UK |
| Sodium Sulfide | 60 % | Sigma Aldrich, UK |

### 2.1.1 Anionic and cationic polyelectrolytes

Polyelectrolytes were utilized for LbL coating of ZnONPs, $Mg(OH)_2$NPs and CuONPs to get negatively or positively surface charged ZnONPs, $Mg(OH)_2$NPs and CuONPs were Poly (sodium-4-styrene sulfonate) (PSS) (supplied from Sigma Aldrich, UK) as the first layer with molecular weight 70 kDa. In addition to that, Poly (allylamine hydrochloride) (PAH) (supplied from Sigma Aldrich, UK) as the second layer with molecular weight 15 kDa. Figure 2.1 illustrations the chemical formulas of PSS and PAH.

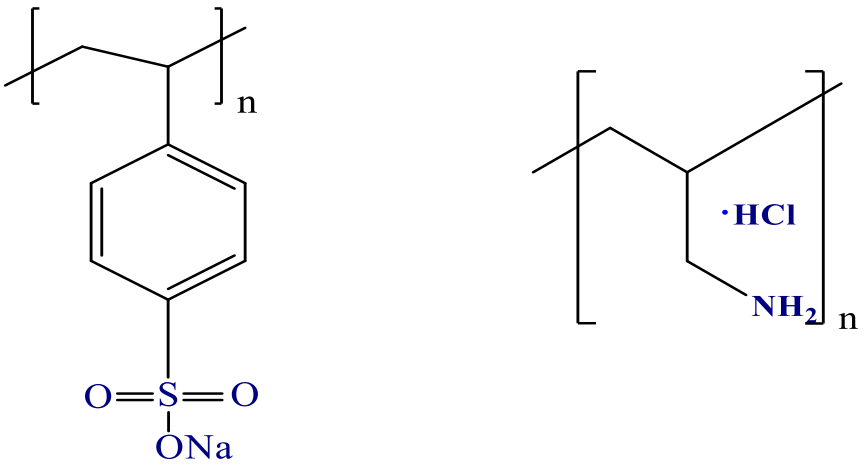


A B

**Figure 2.1.** The chemical structures of (A) Poly (sodium-4-styrene sulfonate) and (B) Poly (allylamine hydrochloride).

### 2.1.2 (3-Aminopropyl)triethoxysilane (APTES)

APTES is an aminosilane frequently utilized in the process of silanization, the functionalization of surfaces with alkoxysilane molecules. It can also be used for covalent attaching of organic films to metal oxides such as silica, ZnO and CuO. APTES was supplied from Sigma Aldrich, UK and the chemical formulas of APTES is shown in Figure 2.2.

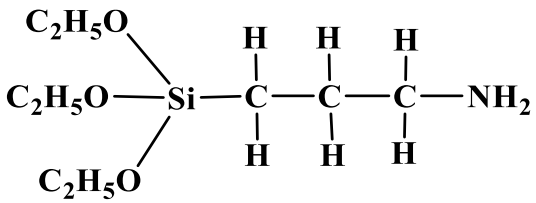


**Figure 2.2.** The chemical structures of APTES.

### 2.1.3 (3-Glycidoxypropyl) trimethoxysilane (GLYMO)

GLYMO is the first commonly utilized coupling agent. One end of its structure with reactive groups such as vinyl and amino, can react with epoxy, polyester, phenolic and other synthetic resin molecules. The other end is alkoxy for example, ethoxy, methoxy etc. or chlorine atoms which is linked with silicon. These groups can be transformed into silanol in the hydrolysis in water solution or damp air. Also the formed silanol is able to react with surface hydroxyl of glass, minerals and inorganic filler. Thus, silane coupling agent is usually used in silicate-filled epoxy, phenolic, polyester resin and other systems. In our work we utilized GLYMO for functionalizing of CuONPs. Figure 2.3 shows the chemical formulas of GLYMO.

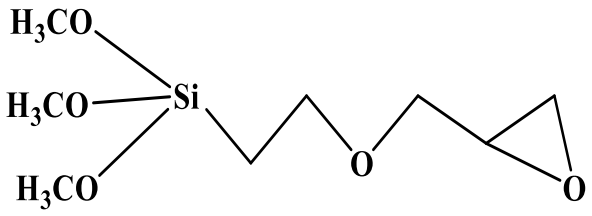


**Figure 2.3.** The chemical structures of GLYMO.

### 2.1.4 Boronic acid functionality

4-Formylphenylboronic acid (4-FPBA), 4-Hydroxyphenylboonic acid (4-HPBA), 4-Mercaptophenylboronic acid (4-TPBA) and 4-Carboxyphenylboronic acid (4-CPBA) were used for functionalizing of GLYMO and nanoparticles. These compounds were

purchased from Sigma Aldrich, UK. Figure 2.4 shows the chemical structures of 4-FPBA, 4-HPBA, 4-TPBA and 4-CPBA.

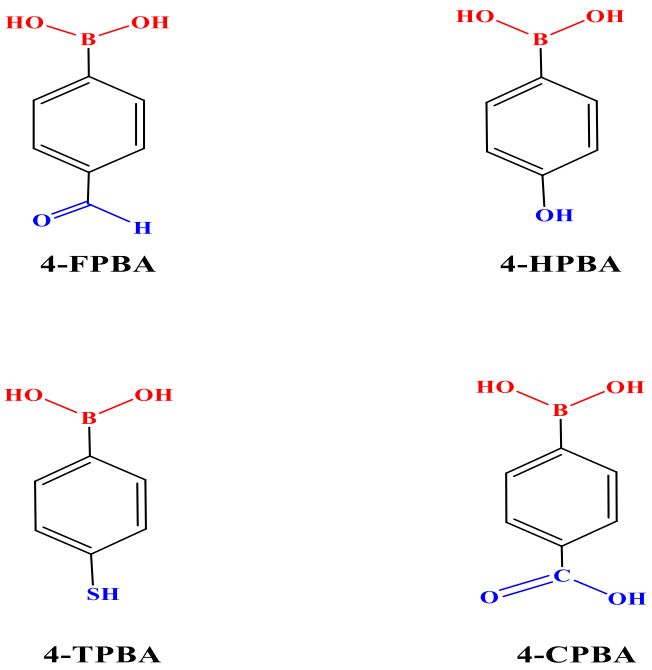


**Figure 2.4.** The chemical formulas of 4-FPBA, 4-HPBA, 4-TPBA and 4-CPBA.

### 2.1.5 Fluorescein Diacetate (FDA)

FDA solution is synthesised by dissolving 5 mg of fluorescein diacetate in 1 ml of acetone. [1, 2] Figure 2.5 shows the converting of FDA via intracellular esterase enzyme to fluorescein. FDA is a simple test which is delicate and quick for examining a microbial action by calculating the cells number in relation to the membrane integrity. [3, 4]

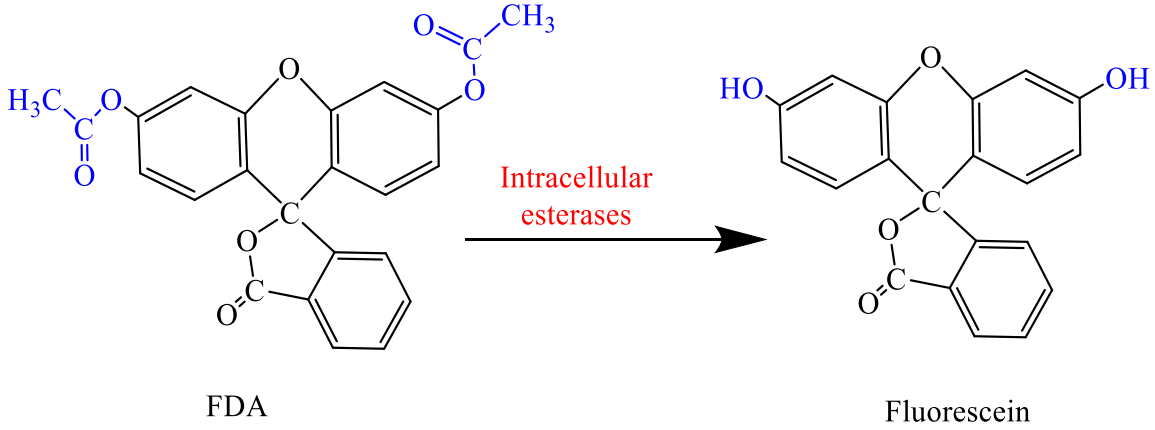


FDA Fluorescein

**Figure 2.5.** The hydrolysis of fluorescein diacetate (colorless) via intracellular esterase enzyme to fluorescein (colored acid yellow) visible at 490 nm.[2]

### 2.1.6 Culture Medium for *C. reinhardtii* Growth

*C. reinhardtii* cc-124 microalgae strain was kindly provided by Prof Flickinger's group at North Carolina State University, USA. This microalgae culture was grown in Tris-Acetate-Phosphate (TAP) culture medium and incubated at 30°C. The *C. reinhardtii* culture media consisted of TAP salts ($NH_4Cl$; $MgSO_4.7H_2O$ and $CaCl_2.2H_2O$), phosphate buffer solution (PBS) and Hutner's trace elements solution (EDTA disodium salt, $ZnSO_4.7H_2O$, $H_3BO_3$, $MnCl_2.4H_2O$, $CoCl_2.6H_2O$, $CuSO_4.5H_2O$, $FeSO_4.7H_2O$, $(NH_4)_6Mo_7O_{24}.4H_2O$), all purchased from Sigma-Aldrich, UK. The microalgae batch was grown in the TAP media at pH 7 while being illuminated for 72 hours with a white luminescent lamp with a light intensity of 60 W $m^{-2}$ under constant stirring with a magnetic stirrer.[5-9] The stock cultures of *C.reinhardtii* were with a typical concentration of $4 \times 10^5$ cells $mL^{-1}$ determined by a cell counter (Nexcelom Cellometer Auto X4).

### 2.1.7 Culture Medium for *S. cerevisiae* Growth

*S. cerevisiae* (Baker's yeast), was purchased from Sigma-Aldrich. It was cultured by hydrating 10 mg of lyophilized yeast cells in 10 mL of deionized water. Then 1 mL of this hydrated yeast cell suspension was added to 100 mL of autoclaved YPD culture media consisting of peptone (Sigma Aldrich, UK), D-glucose, (Fisher Scientific, UK), and yeast extract, (Oxoid ltd, UK.), then incubated at 30°C for 24-48 hours.[10] The chemicals for the culture media of yeast are listed in Table 2.2 as follows:

**Table 2.2.** Preparation method of culture media for growing *S. cerevisiae* cells.

| Reagent | Quantity (for 100 mL) |
|---|---|
| Peptone | 2.0 g |
| Yeast extract | 1.0 g |
| Dextrose (D-Glucose) | 2.0 g |
| Deionized water | 100 mL in a 250 mL conical flask |

### 2.1.8 BacTiter-Glo (BTG) microbial cell viability assay

Figure 2.6 illustrations the luminescence reaction among the adenosine triphosphate (ATP) and reagent in the presence of molecular oxygen. The BTG is a homogenous luminescence-based reaction for determining the viable bacteria number, depending on the amount of adenosine triphosphate presented in viable bacteria. The chemical reaction

is established on the properties of a thermostable luciferase and a proprietary formulation for removing adenosine triphosphate from bacteria. The examine procedure is completed via the addition of the BTG reagent straight to the solution and then examining of luminescence. The luminescent signal produced is relational to the quantity of adenosine triphosphate which deliberated as an indicator of the bacteria viability.

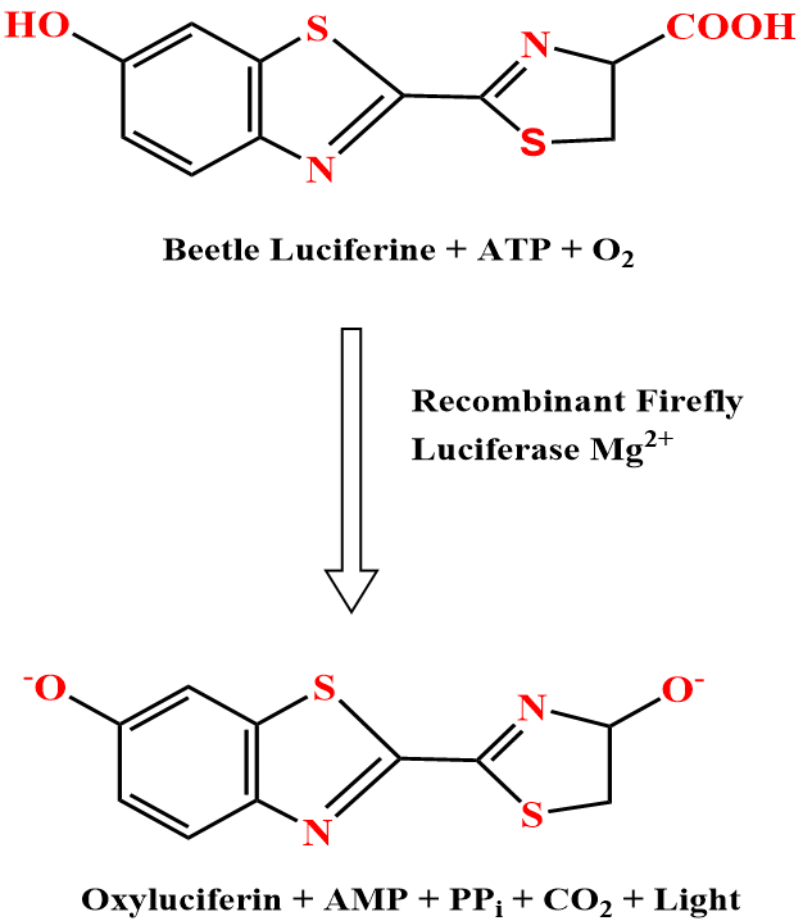


**Figure 2.6.** The luciferase reaction. Mono-oxygenation of luciferin is catalysed by luciferase in the existence of $Mg^{2+}$, molecular O and ATP.

### 2.1.9 Culture medium for *E. coli* growth

*E. coli*, sourced from Thermofisher (Invitrogen MAX Efficiency™ DH10B™) was kindly provided for our antibacterial tests by Prof J. Rotchell's group at the University of Hull, UK. The chemicals for the culture media of *Escherichia coli* are listed in Table 2.3 as follows:

**Table 2.3.** Preparation method of culture media Luria-Bertani medium (LB medium) for growing *E. coli*.[11]

| Reagent | Quantity (for 100 mL) |
|---|---|
| Tryptone | 1.0 g |
| Yeast extract | 0.5 g |
| Sodium chloride | 0.5 g |
| Deionized water | 100 mL in a 250 mL conical flask |

Then, these components were autoclaved for one hour at 1.5 bar at 125$^{o}$C. Once the culture media was cooled down to room temperature, a few microlitres of stock suspension of *E.coli* was dispersed in the autoclaved culture media near Bunsen burner. The cultured *E.coli* was incubated with shaking at 25$^{o}$C for 48 hours.

### 2.1.10 Culture medium for *R. rhodochrous* growth

*R. rhodochrous* was supplied by Blades Biological Ltd., UK. The culture media of *R. rhodochrous* was prepared by adding 13 g of nutrient broth to 1 L of deionized water. It was mixed well and transferred into the final containers after autoclaving at 125 $^{o}$C and 1.5 bar for 1 hour. Once the culture media was cooled down to 30 $^{o}$C, a few microliters of a stock solution of *R. rhodochrous* were dispersed in the autoclaved culture media beside the Bunsen burner. The *R. rhodochrous* was incubated with shaking at 30 $^{o}$C for 5-7 days.

## 2.2 Characterisation

The nanoparticle size distribution and the zeta potential were characterised by Zetasizer nano ZL (Malvern, UK). A digital sonicator (Branson LTD) was utilized for dispersing the nanoparticle samples at 40% amplitude for 15 minutes at 2.0 sec ON/2.0 sec OFF pulse time. Thermogravimetric analysis (TGA) of nanoparticle was done using a Mettler Toledo TGA/DSC instrument under $N_2$ atmosphere. The specific surface area of the nanoparticles was measured using a Micromeritics instrument (USA) by the BET method. The crystallite size of nanoparticle at various temperatures was studied by X-ray diffraction (Siemens D5000 X-Ray Diffractometer at 0.15418 nm wavelength). FT-IR spectroscopy measurements were acquired to explore the surface functional groups

present on nanoparticles. FT-IR spectra of nanoparticles were recorded at room temperature using Thermo Scientific Nicolet 380 FT-IR (Themo Scientific, Hemel Hempstead, UK), equipped with attenuated total reflectance (ATR) where the samples were in direct contact with the ATR diamond crystal. A JEM 2011 (JEOL, Japan) Transmission Electron Microscopy (TEM) machine was used to characterise the particle size and morphology of nanoparticle on the microbial cells surface. JEOL JSM-6480 LV SEM instrument was utilized to characterise the morphology of nanoparticle with bacterial. UV light illumination was carried out with the radiation source type 11868010, UVP™ Fraud Detection Lamp with 6W (Fisher Scientific, UK). Aqueous suspensions of the nanoparticles containing cells, under magnetic stirring, were irradiated in light of wavelength 365 nm with an irradiation intensity of (161 ± 5 Lux). Visible light illumination was carried out using lamp type Maxibright T5 (Germany) in all our studies. The distance from the source (both UV and visible lamp) was 14 cm. Table 2.4 below shows the general instruments utilised in this study.

**Table 2.4.** General instrumentations

| Instrument | Provider and Model |
|---|---|
| pH-meter | Fisher Brand Hydrous 300, UK |
| Micropipettes | Eppendorff, UK |
| Muffle Furnace | Carbolite, UK |
| Hotplate with Magnetic Stirrer | IKA C-MAG HS7, UK |
| Vortex Mixer | Stuart, UK |
| Balance | Precisa 125 ASC, UK |
| Mini-Centrifuge | Eppendorff mini spin plus, UK |
| Centrifuge | Thermo Biofuge Primo, UK |
| Cellometer Auto X4 | Nwxcelom Bioscience, USA |

### 2.2.1 Synthesis of ZnONPs

The direct precipitation method was used for the synthesis ZnONPs by using zinc nitrate as the precursor and potassium hydroxide as a precipitating agent. The aqueous solution 0.2 M of zinc nitrate and the solution 0.4 M of potassium hydroxide were prepared with deionized water, respectively. In the first step, 0.4 M of potassium hydroxide solution was added dropwise to the zinc nitrate solution with vigorous stirring at room temperature which led to the formation of a white suspension. The white product was centrifuged at

5000 rpm for 30 min and washed three times with deionized water, and washed with ethanol at last and dried under vacuum (Gallenkamp vacuum oven) at 60 °C for 3 h.[12] In the next step, for the production of ZnONPs of various size, the ZnO created was calcined at various temperatures from 100 °C to 600 °C for 3 h. The crystallite sizes of the synthesized ZnO in solid state were characterised via TEM, XRD, BET, SEM and FTIR. The ZnONPs were synthesized by dispersing of ZnO sample in deionized water at pH 7.37 via a digital sonicator. The characterisation of the ZnONPs was carried out using a Zetasizer Nano ZL (Malvern, UK). For examining the pH impact on the particle size and zeta potential of ZnONPs, the pH was adjusted from 5 to 12 utilizing 0.1 M HCl or 0.1 M NaOH. A schematic diagram of synthesis of ZnONPs is presented in Figure 2.7.

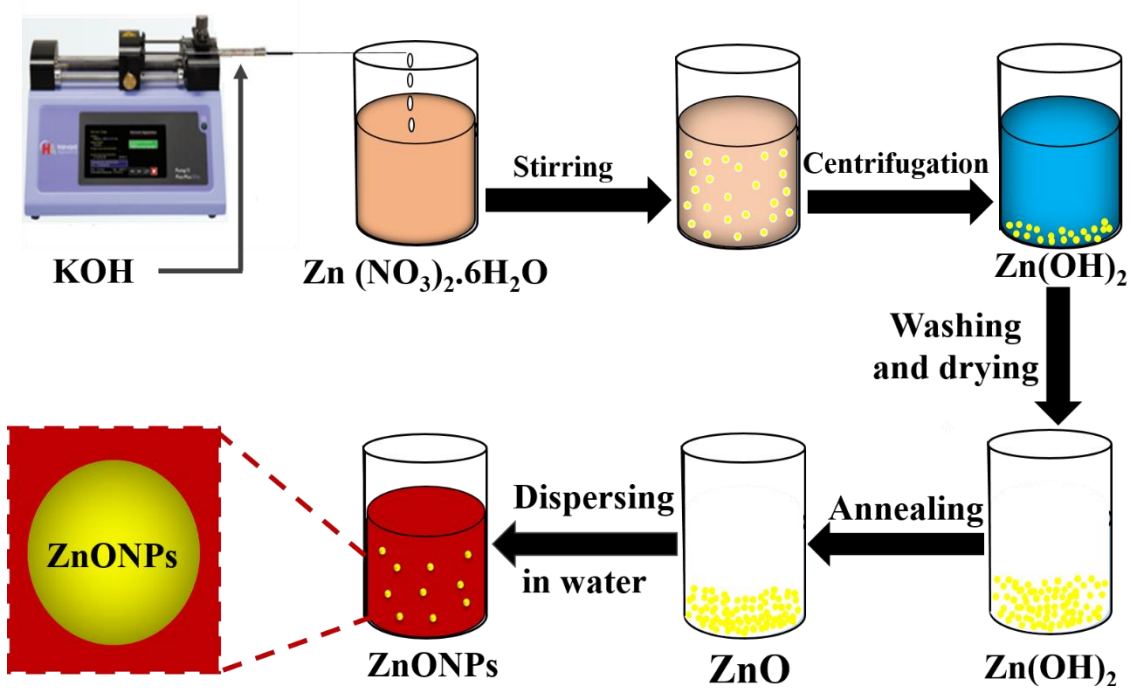


**Figure 2.7.** A schematic overview is summarizing of the synthesis method of ZnONPs.

## 2.2.2 Synthesis of $Mg(OH)_2$NPs

$Mg(OH)_2$NPs were prepared from magnesium chloride ($MgCl_2$) as a source of magnesium ions and sodium hydroxide (NaOH) aqueous solution Precipitation was induced by dropwise addition of 0.4 M NaOH into the 0.2 M $MgCl_2$ solution under continuous stirring at different reaction temperatures (*i.e.* 25°C, 50°C, 75°C and 100 °C) for 1 hour. The white product was centrifuged and washed with copious amounts of high purity water and ethanol for the effective removal of impurities. The final product was dried at 80°C for 24 hours.[13] Aqueous dispersions of the $Mg(OH)_2$NPs were then prepared

by dispersing 0.025 g of $Mg(OH)_2$ sample in 100 ml deionized water by using a digital sonicator (Branson Ltd.) at 40% of the maximum power for 15 minutes at 2 sec ON/2 sec OFF pulse time. Figure 2.8 shows a schematic diagram of synthesis method of Mg $(OH)_2$NPs.

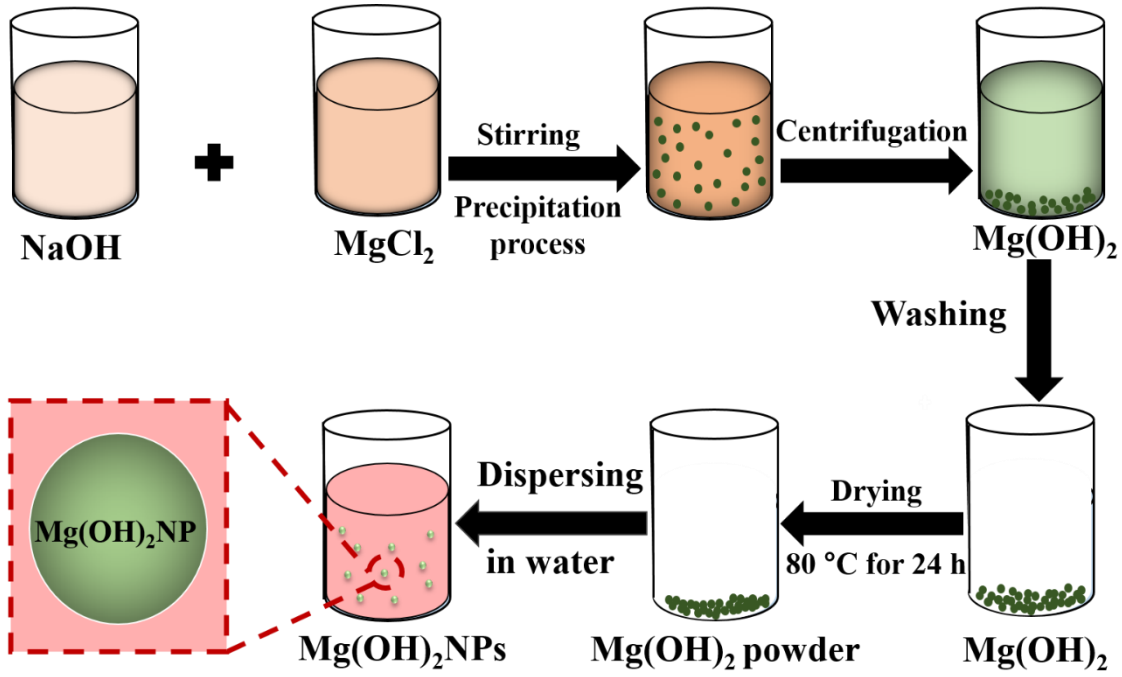


**Figure 2.8.** A schematic overview is summarizing of the synthesis method of $Mg(OH)_2$NPs.

## 2.2.3 Synthesis of CuONPs

In first stage of the preparation, 3.0 g of copper (II) chloride ($CuCl_2$) was dissolved in 160 mL of ethanol. 1.8 g of sodium hydroxide (NaOH) was dissolved in 50 mL ethanol. The NaOH solution was added dropwise to $CuCl_2$ solution under constant stirring at room temperature. During the course of the reaction, the color of the solution turned from green to greenish blue and lastly to black. This black precipitate was copper hydroxide, $Cu(OH)_2$ (see Figure 2.9) which was centrifuged, washed with ethanol and deionized water, and dried at 60 $^oC$ in the electric furnace. In order to produce CuONPs, the sample of dry $Cu(OH)_2$ was annealed at different temperatures, 100 $^oC$, 200 $^oC$, 300 $^oC$, 400 $^oC$, 500 $^oC$ and 600 $^oC$ followed by grinding to obtain CuO in powdered form.[14] CuONPs were produced by dispersing CuO in deionized water at pH 6 via a sonication (Branson

450, 5 mm tip, 400 W maximum power) at 40% of the maximum power for 10 minutes (2 s ON - 2 s OFF pulse time).

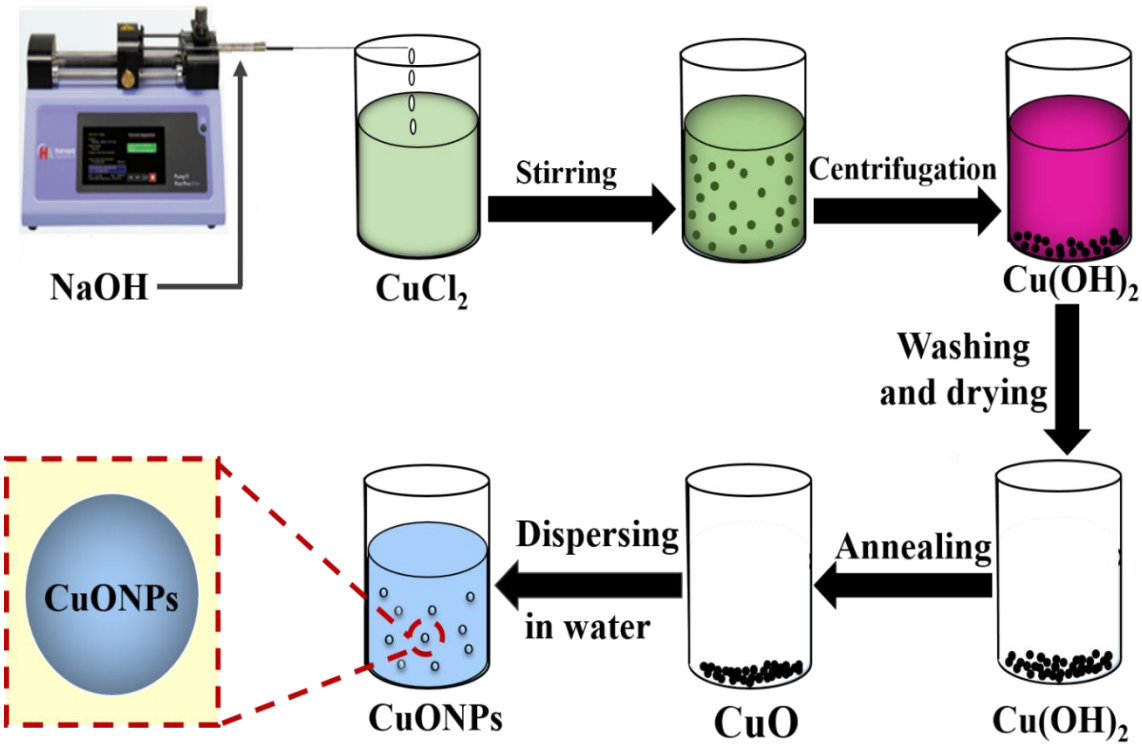


**Figure 2.9.** A schematic overview is summarizing of the synthesis method of CuONPs.

### 2.2.4 Characterization of the surface functionalized nanoparticles.

The particle size and the zeta potential of the surface functionalized nanoparticles was examined by dynamic light scattering (DLS) using the Malvern Zetasizer Nano ZL instrument. The zeta potential values of the surface functionalized nanoparticles were determined after dispersing the nanoparticles samples in deionized water using an ultrasonic probe. After that, a range of nanoparticles suspensions with different pH was made by using 0.1 M HCl and 0.1 M NaOH and adding two drops of 0.01 M NaCl into each sample (10 mL). All measurements have been done at room temperature and the results reported are an average of 3 runs.

### 2.2.5 Anti-algal and anti-yeast activity of surface-grafted nanoparticles.

UV lamp and white light lamp were used to illuminate the samples in this study. UV light illumination was carried out with the radiation source type 11868010, UVP™ Fraud Detection Lamp with 6W (Fisher Scientific, UK). Aqueous suspensions of the

nanoparticles containing cells, under magnetic stirring, were irradiated with 365 nm UV light at an irradiation intensity of 161 ± 5 Lux. Visible light illumination was carried out using a Maxibright T5 lamp (Germany) in all our studies. The distance from the source (both UV and visible lamp) was 14 cm. 50 mL of *C. reinhardtii* cells were washed three times from the culture media and re-dispersed in 30 mL deionized water. 5 mL aliquots of the washed *C. reinhardtii* cells suspension were incubated with a series of 5 mL aliquots of the aqueous dispersions of nanoparticle (bare or surface-grafted) at different particle concentrations. After that, these samples were split into three equal parts which were illuminated for various exposure times under visible light or UV light, or kept in dark conditions, respectively. Likewise, a control sample of the cells was treated at the similar conditions without exposure to nanoparticle. After that, 1 mL of the *C. reinhardtii* suspension was taken from each tested sample, washed with deionized water to remove the excess of nanoparticle by centrifugation at 3500 rpm for 4 minutes and re-suspended in 1 mL of deionized water. Two drops of 1 mM FDA solution in acetone was added to each sample and mixed together for 15 minutes. After that, these samples were washed three times with deionized water by centrifugation at 3500 rpm for 4 minutes to remove the excess of FDA. Finally, the cell viability was tested by using automatic cell counter. The same methodology was used to test the impact of surface functionalized nanoparticle on the cell viability of *C. reinhardtii*, which were incubated with different concentrations for various exposure times. The effect of nanoparticle on *S. cerevisiae* was also examined, by the following procedure. A 30 mL aliquot of the *S. cerevisiae* culture was washed three times with deionized water via centrifugation and after that re-dispersed in 30 mL deionized water. Then, 5 mL of *S. cerevisiae* dispersion were mixed with 5 mL of nanoparticle aqueous suspension at various total particle concentrations. After that, the tested suspensions were exposed separately for various incubation times under UV light or visible light, or kept in dark condition. 1 mL of each sample was taken from each tested sample with nanoparticle, and the cells were washed with deionized water via centrifugation at 3500 rpm for 4 minutes to remove the excess of nanoparticle. The *S. cerevisiae* cells were re-suspended in 1 mL of deionized water and then 2 drops of FDA solution were added to each sample and mixed together for 15 minutes with a magnetic stirrer. After that, the samples were washed three times with deionized water via centrifugation at 3500 rpm for 4 minutes. Finally, the viable percentage of cells was examined by using 20 μL of the cell suspension with an automatic cell counter Cellometer Auto X4 fitted with a fluorescein filter set.

### 2.2.6 Determination of the chlorophyll content of microalgae cells

Hartmut K., (1983) have used method for the determination of the total chlorophyll content of microalgae cells.[15] 2.4 ml of acetone was added to 0.6 ml of the microalgae samples which had been exposed ZnONPs at different particle concentration (0, 1, 10, 50,100, and 250 μg $ml^{-1}$) in dark conditions, visible light condition, and UV light condition. Then, the chlorophyll content of the microalgae cells was extracted for 1 minute by utilising vortex mixer followed by centrifugation at 14000 rpm for 5 minutes. After that, UV-Vis Spectrophotometer was used to measure the absorbance at 646 nm and 663 nm for the determination of chlorophyll a and chlorophyll b, respectively. The equations for the determination of total chlorophyll content of microalgae cells are as follows:

$$C_a = (12.21A_{663} - 2.81A_{646}) \text{ x Dilution Factor} \quad (2.1)$$

$$C_b = (20.13A_{646} - 5.03A_{663}) \text{ x Dilution Factor} \quad (2.2)$$

$$C_a + C_b = \text{Total chlorophyll concentration} \quad (2.3)$$

### 2.2.7 Antibacterial assay of polyelectrolyte-coated $Mg(OH)_2$NPs on *E.coli*.

10 mL of the *E.coli* culture grown in LB medium was washed, centrifuged three times with deionized water at 5000 rpm for 3 minutes and redispersed in 100 mL deionized water. Then, 5 mL of the washed *E.coli* suspension were incubated with a series of 5 mL aliquots of aqueous dispersions of $Mg(OH)_2$NPs of different concentrations (0, 250, 500, 750, 1000, 2500, 5000 and 6000 μg $mL^{-1}$). After each incubation, 1 mL of each *E.coli* suspension sample was washed and re-suspended in 1 mL deionized water. Then 100 μL of culture media free *E.coli* bacteria was incubated with 100 μL of BacTiter-Glo Microbial cell viability reagent in a white opaque 96-well solid flat bottom microplate, shaken for 30 seconds, and incubated for 5 minutes at 25 $^oC$. The relative luminance was measured as a function of incubation time to find out the cell viability upon incubation with different concentration of $Mg(OH)_2$NPs. The same experiments were also repeated with polyelectrolyte-coated $Mg(OH)_2$NPs. This was done by incubating an aliquot of the *E.coli* suspension (diluted 10 times) with $Mg(OH)_2$NPs coated with poly(sodium-4-styrenesolfonate and poly(allylamine hydrochloride) for up to 24 hours.

### 2.2.8 MIC of non-modified and PSS/PAH-coated $Mg(OH)_2$NPs on microbial cells.

The following protocol was used to determine the Minimal Inhibitory Concentration (MIC) of $Mg(OH)_2$NPs and PSS/PAH-coated $Mg(OH)_2$NPs on cells. A negative control of 100 µL of LB medium was added to the first line of wells of a 96 well plate. 50 µL of LB medium was added to the treatment wells and the positive bacteria control wells. A stock solution of $Mg(OH)_2$NPs and PSS/PAH-coated $Mg(OH)_2$NPs was created in fresh LB medium to a total volume of 10 mL. 50 µL of this formulation was added to the first line of treatment wells, and serial diluted 1:2 across the 96 well plate, ensuring it was mixed by pipetting up and down within each well. An overnight culture of *E.coli* was diluted into sterilised 0.85% saline until an absorbance reading of between 0.08–0.12 at 625 nm was obtained on a spectrophotometer (0.5 Mcfarland Standard). The saline diluted bacteria was diluted further 1 : 150 into LB (10 mL LB + 66.67 µL of bacteria in saline solution) yielding a 10 mL stock containing $5 \times 10^5 – 1 \times 10^6$ per mL cells. 50 µL from this bacteria stock was added to each treatment and positive bacteria control wells, seeding with $2.5 \times 10^4 – 5 \times 10^4$ cells per well. Each well contained a final volume of 100 µL with decreasing concentrations of treatment on equal amounts of bacteria. The plate was incubated for 24 h at 37 °C. After incubation, 20 µL of resazurin solution was added to each well. The MIC was determined from the lowest concentration treatment which inhibited growth.

### 2.2.9 Antibacterial activity of bare and surface functionalized CuONPs on *E.coli* and *R. rhodochrous*.

10 mL of the bacteria culture was centrifuged and washed three times with deionized water for 4 minutes at 4000 rpm, and re-dispersed in 100 mL deionized water. Then, 5 mL of the washed bacteria were incubated with a series of 5 mL aliquots of the CuONPs suspension at various particles concentrations. The number of bacteria was measured directly after removing the excess nanoparticles from the bacteria dispersion. Then, 1 mL of each bacteria suspension was washed and re-suspended in 1 mL deionized water. 100 µL aliquot of the washed bacteria suspension was then incubated with 100 µL of BTG reagent in a white opaque 96-well microplate with solid flat bottom, and after that shaken for 30 seconds, and incubated at 30 ºC for 5 minutes. The relative luminance was measured as a function of the incubation time and used to calculate the fraction of viable bacteria upon exposure to various concentrations of CuONPs. We did the same

experiments with CuONPs functionalized with GLYMO as well as ones functionalized with GLYMO and 4-HPBA at various particle concentrations.[16-18]

### 2.2.10 Colony forming units assessment for antimicrobial assay.

The bacteria were grown overnight in sterilized LB medium at 37 $^{o}$C to produce viable colonies. Bacterial cells were pelleted down by centrifugation at 5000 rpm for 10 minutes followed by washing (twice) with 0.85 w/v% serial saline until an optical density of 0.08-0.12 at 625 nm was obtained using a spectrophotometer. These adjusted bacterial saline suspensions were then diluted 1:150 into LB to yield starting concentrations between $5 \times 10^5 - 1 \times 10^6$ colony forming units per mL (CFU/mL). Then flasks 250 mL containing LB medium 100 mL with different concentrations of the bare CuONPs and surface functionalized of CuONPs with GLYMO and 4-HPBA were inoculated with an equal volume of the bacterial suspension. Flasks containing bacterial cells and media without nanoparticles were used as control. All the flasks were incubated for 10 min, 1 hour and 6 hours in a shaker at 37 $^{o}$C with 140 rpm. After that, the serial dilutions were made of all the treated samples including control and 100 µL of each were homogeneously spread on LB agar plates for colony forming unit (CFU). The growth rate of bacterial cells interacting with the nanoparticles was determined from a plot of the CFU/mL versus concentrations. The time-kill assay was repeated in three independent experiments.

### 2.2.11 Preparation of polyelectrolyte-coated nanoparticles

Polyelectrolyte–coated NPs were prepared using NPs synthesised at an annealed temperature of 100 $^{o}$C. 50 mL of 1000 µg mL$^{-1}$ NPs dispersion in deionized water were added dropwise to an equal amount of 50 mg mL$^{-1}$ PSS (M.W. ~70kDa) solution in 1 mM NaCl. After shaking for 1 hour on orbital shaker, the samples were washed three times by centrifugation for 1 hour at 10000 rpm to remove the excess of PSS. Finally, the PSS-coated NPs were re-dispersed in 50 mL deionized water[19] and the particle size and zeta potential measured by Zetasizer Nano ZL. To prepare PAH-coated nanoparticles, the PSS-coated NP suspension was mixed dropwise with 50 mL of 50 mg mL$^{-1}$ PAH (M.W. 15 kDa) dissolved in 1 mM NaCl solution. The mixture was shaken for 20 minutes and centrifuged three times at 10000 rpm for 1 hour to yield NPs/PSS/PAH (see Figure 2.10).

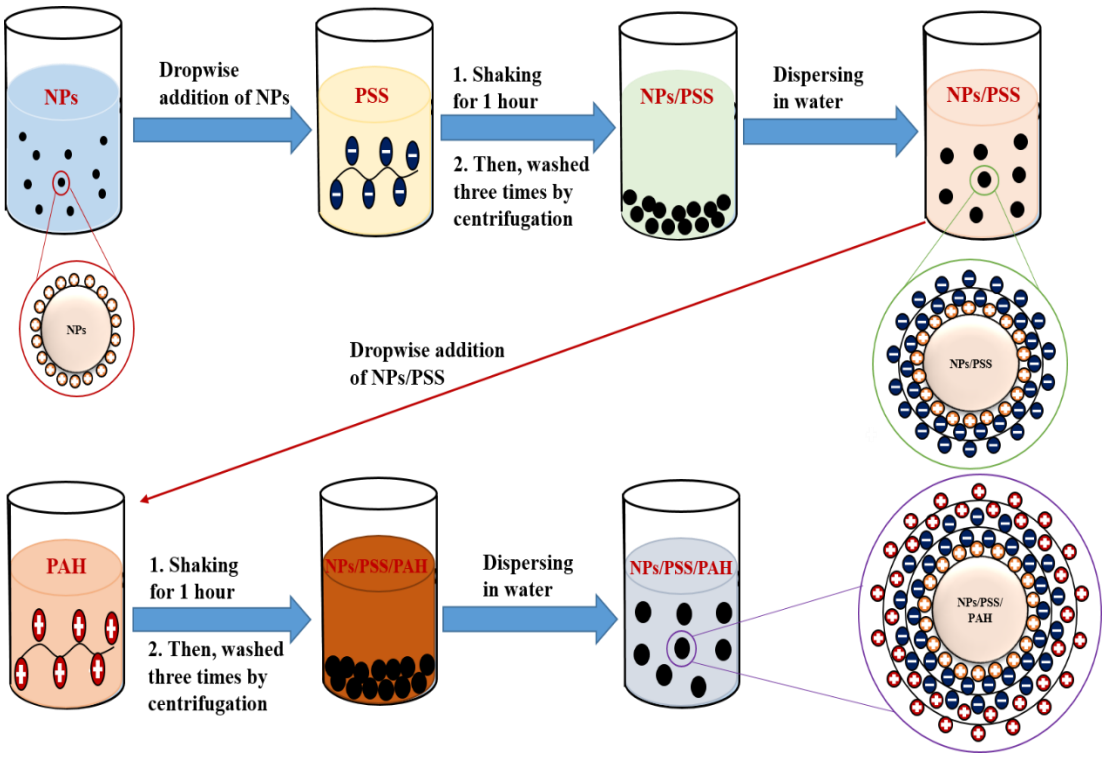


**Figure 2.10.** The schematic diagram of LbL polyelectrolytes coating of nanoparticles.[19]

### 2.2.12 Preparation of zinc sulfide-coated ZnONPs

ZnONPs were covered with the zinc sulphide using 0.05 g of the ZnONPs with 50 mL deionized water was sonicated for 10 min. After adjusting the pH to 7.37 using 0.1 M HCl or 0.1 M NaOH, a solution of 0.1 M sodium sulfide ($Na_2S$) was added dropwise to a suspension of ZnONPs. After that, these particles were kept under continuous stirring for 2 h at 60 $^oC$. The particles were washed three times by centrifugation with deionized water and was dried at 70 $^oC$. [20] The ZnS-coated ZnONPs were characterised by the Zetasizer to check the zeta potential and the particle size.

### 2.2.13 Preparation of silica-coated ZnONPs

ZnONPs were coated with the silica using 0.05 g of the ZnONPs with 50 mL deionized water was sonicated for 10 minutes. Silica particles were synthesised through a procedure depend on the Stöber method, using tetraethoxysilane (TEOS) and in the existence of ammonia ($NH_3$ 35 %) as a catalyst. [21-23] In the first step, 1 mL of $NH_3$ solution was added to the ZnONPs solution with stirring for 5 minutes to ensure complete mixing at room temperature. In the second step, 0.25 mL of TEOS as a starting material were dissolved in of 50 % ethanol and 50 % deionized water. Then, an amount of TEOS in ethanol and deionized water was added dropwise to the solution in the first step and the reaction

proceeded at room temperature for 24 h under continuous stirring. After that the particles in the colloidal solution were collected by centrifugation, and the particles were washed with absolute ethanol and deionized water for three times to remove undesirable particles. The Silica-coated ZnONPs were characterised by the Zetasizer to check the zeta potential and the particle size.

### 2.2.14 Grafting of CuONPs with APTES and 4-FPBA.

0.1 g of CuO was dispersed into 100 mL of deionized water of pH 6–6.5 by sonication followed by addition of 0.1 g APTES. The reaction mixture was stirred for a further 24 hours, then the unreacted APTES was removed by centrifugation and washing with deionized water three times. The process is analogous to the APTES functionalization of other inorganic nanoparticles.[24] This functionality has not been reported before for CuONPs. The APTES- functionalized CuONPs pellet was then re-dispersed in 100 mL of deionized water and mixed drop-wise with 0.1 g of 4-FPBA dissolved in 100 mL of ethanol solution. The mixture was shaken for 2 hours, then washed and centrifuged three times with ethanol at 10000 rpm for 30 minutes. The CuONPs/APTES/4-FPBA produced were finally re-dispersed in 100 mL of deionized water.[25-27] using a digital sonicator Branson 420 at 40% of the maximum power for 15 minutes (2 s ON - 2 s OFF pulse time). The particle size and the zeta potential of the APTES/FPBA grafted CuONPs was examined by dynamic light scattering (DLS) using the Malvern Zetasizer Nano ZL. The chemistry of the process of the APTES/FPBA grafted CuONPs is shown in Figure 2.11.

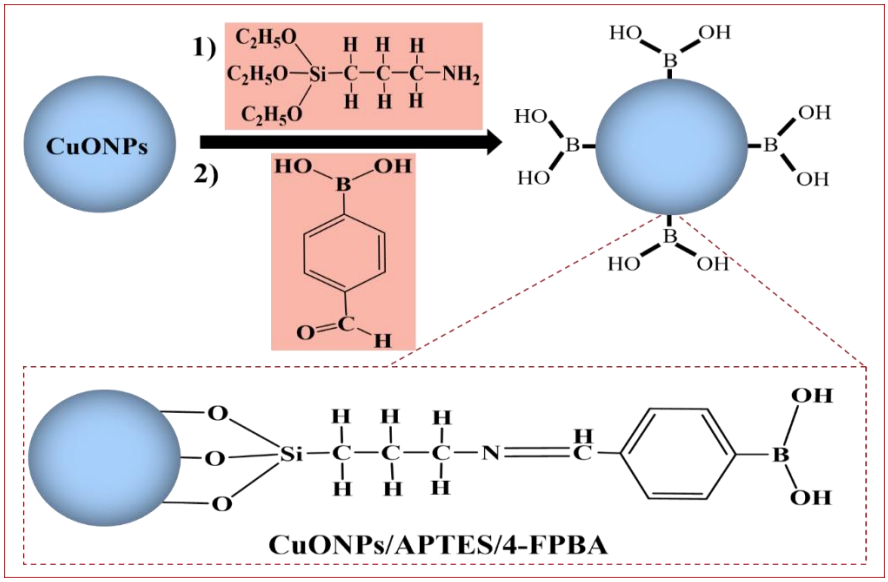


**Figure 2.11.** The schematic of the surface functionalized of CuONPs with APTES and 4-FPBA.

### 2.2.15 Surface functionalization of CuONPs by GLYMO and 4-HPBA.

A sample of 0.1 g of CuONPs was dispersed into deionized water (100 mL, pH 6–6.5). The suspension was stirred for 1 hour and 0.1 wt% of GLYMO were added. The reaction mixture was stirred for a further 24 hours, then the unreacted GLYMO was removed by centrifugation and washing with deionized water three times. The process is analogous to the APTES functionalization of other inorganic nanoparticles[24] but in our case GLYMO brings epoxy-ring as a terminal group. This functionality has not been reported before for CuONPs. The GLYMO- functionalized CuONPs pellet was then re-dispersed in 100 mL of deionized water and mixed drop-wise with 0.1 g of 4-HPBA dissolved in 100 mL of ethanol solution. The mixture was shaken for 2 hours, then washed and centrifuged three times with ethanol at 10000 rpm for 30 minutes. The CuONPs/GLYMO/4-HPBA produced were finally re-dispersed in 100 mL of deionized water.[25-27] The chemistry of the process of surface functionalization of CuONPs with phenyl boronic acid is shown in Figure 2.12.

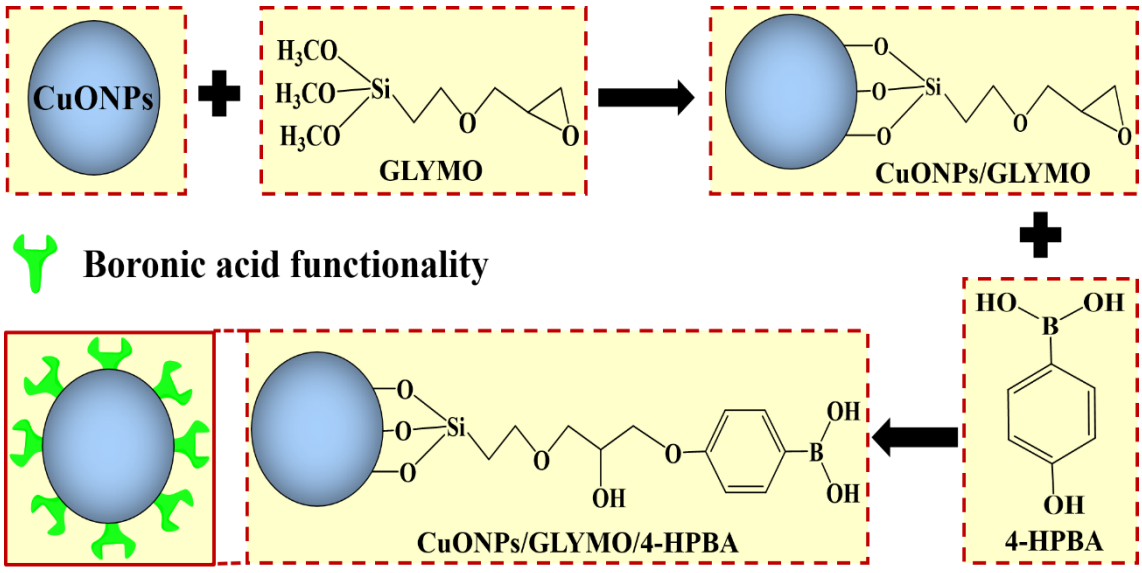


**Figure 2.12.** The schematic of the surface functionalized of CuONPs with GLYMO and 4-HPBA.

### 2.2.16 Surface functionalization of CuONPs by 4-CPBA.

A sample of 0.1 g of CuONPs was dispersed into deionized water (100 mL, pH 6–6.5). The suspension was stirred for 1 hour and 0.1 g of 4-CPBA was dissolved in 100 mL of ethanol solution were added. The reaction mixture was stirred for a further 24 hours, then the unreacted 4-CPBA was removed by centrifugation and washing three times with

ethanol and deionized water. The CuONPs/4-CPBA produced were finally re-dispersed in 100 mL of deionized water.

### 2.2.17 Surface coating of CuONPs with $SiO_2$.

The silica-coated copper oxide nanoparticles labelled as CuONPs/$SiO_2$ were prepared. The process is analogous to the $SiO_2$ functionalization of other inorganic nanoparticles, [28, 29] but in our case, the CuONPs were modified with $SiO_2$. Briefly, 0.1 g of CuONPs was dispersed in a mixture of ethanol (40 mL), deionized water (10 mL) and concentrated ammonia solution (35 %, 1.2 mL) or sodium hydroxide by ultrasonication for 1 hour. To the above mixture, 0.43 mL of Tetraethyl orthosilicate (TEOS) was added dropwise. After stirring for 6 hours, the product was collected and washed with ethanol and deionized water. [30]

### 2.2.18 Surface modification of CuONPs/$SiO_2$ by GLYMO and 4-HPBA.

The CuONPs/$SiO_2$ suspension was stirred for 1 hour and 0.1 wt% of GLYMO were added. The reaction mixture was stirred for a further 24 hours, then the unreacted GLYMO was removed by centrifugation and washing with deionized water three times. The process is analogous to the APTES functionalization of other inorganic nanoparticles[24] but in our case GLYMO brings epoxy-ring as a terminal group. This functionality has not been reported before for CuONPs/$SiO_2$. The GLYMO-functionalized CuONPs/$SiO_2$ pellet was then re-dispersed in 100 mL of deionized water and mixed drop-wise with 0.1 g of 4-HPBA dissolved in 100 mL of ethanol solution. The mixture was shaken for 2 hours, then washed and centrifuged three times with ethanol at 10000 rpm for 30 min. The CuONPs/$SiO_2$/GLYMO/4-HPBA produced were finally re-dispersed in 100 mL of deionized water. [16, 25-27]

### 2.2.19 Surface modification of smooth $SiO_2$NPs by GLYMO and 4-HPBA.

The silica nanoparticles with smooth surface and a nominal diameter of 100 nm were purchased from Fiber Optical Center, USA. A sample of 0.1 g of $SiO_2$NPs was dispersed into deionized water (100 mL, pH 7). Then, the same procedure used in the surface modification of CuONPs/$SiO_2$ described above was followed. [24] The $SiO_2$NPs/GLYMO/4-HPBA produced were finally re-dispersed in 100 mL of deionized water. [16, 25-27]

### 2.2.20 Synthesis of $SiO_2$NPs with rough surface.

The rough $SiO_2$NPs were prepared by using CuONPs as templates. CuONPs were first synthesized in aqueous solution. Silica layer was then coated on CuONPs to achieve CuONPs/$SiO_2$ nanostructures using $NH_3$ as a catalyst (labelled as rough $SiO_2$NPs-1) or NaOH as a catalyst (labelled as rough $SiO_2$NPs-2). The as-synthesized CuONPs/$SiO_2$ nanoparticles were collected by centrifugation. After centrifugation, the CuONPs/$SiO_2$ nanoparticles were treated with 1M of $HNO_3$ three times. After 24 hours, the products were centrifuged, washed with EDTA and deionized water to remove the CuO templates completely, producing rough $SiO_2$NPs. The rough $SiO_2$NPs were modified with GLYMO and 4-HPBA by the similar procedures reported above. Then, 5 mL of the washed cells were incubated with a series of 5 mL aliquots of the rough $SiO_2$NPs/GLYMO/4-HPBA suspension at various particles concentrations as shown in Figure 2.13.

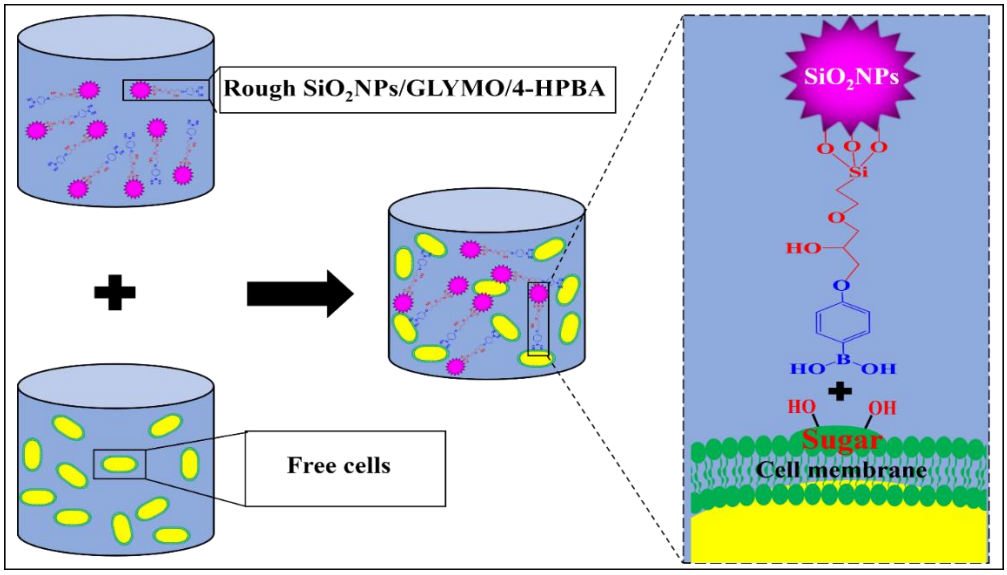


**Figure 2.13.** Schematics showing the mechanism of self-grafting/covalent attachment of HPBA-functionalized a surface-rough $SiO_2$NPs and the sugar groups on the surface of the R. rhodochrous cell membrane.

### 2.2.21 SEM and TEM sample preparation protocol for bacterial cells after exposure to surface-functionalized nanoparticles.

After incubation with the surface modified nanoparticles, the bacterial cells were fixed with 2.5% glutaraldehyde at room temperature for two hours in 0.1M cacodylate buffer pH 7.2. These samples were then post-fixed in 1% osmium tetroxide for one hour, and dehydrated in a range of ethanol-water mixtures with increasing ethanol content from 50 vol% up to 100 vol% followed by critical point drying. After incubation with

nanoparticles, the bacterial cells were prepared for TEM imaging using the following procedure. The bacteria were washed with deionized water to remove the excess of nanoparticles at 500 rpm and then fixed in 2 wt% glutaraldehyde for one hour at room temperature followed by treatment with 1 wt% osmium tetroxide for one hour. Then, the samples were incubated for one hour with 2.5 % uranyl acetate and washed with aqueous ethanol solutions of increasing concentration, as described above. After standard dehydration, the bacterial samples were embedded in fresh epoxy/Araldite at 60 $^{o}$C for 2 days, left for 2 days at room temperature and sectioned with an ultra-microtome. Bacteria samples before and after the nanoparticle treatment were imaged by SEM and TEM.

### 2.2.22 Zeta potential measurements of the *C. reinhardtii, S.cerevisiae and E.coli* after treatment with nanoparticles.

The changes of surface charge of *C. reinhardtii, S.cerevisiae* and *E.coli* after exposure to bare and the surface modified nanoparticles at different particle concentrations were determined by a Zetasizer Nano ZL (Malvern, UK). The cells were removed from the excess of nanoparticles in the aqueous phase by centrifugation and replaced with deionized water. For each sample, an appropriate amount of undiluted solution was placed into the cuvette, and an average zeta potential value was obtained from three individual measurements. The solution media was deionized water in all zeta potential measurements.

### 2.2.23 Cytotoxicity assay of bare and surface functionalized CuONPs on HaCaT cells.

HaCaT cell line culture (immortalized human keratinocytes) was kindly provided by the Skin Research Group at St James University Hospital at Leeds. The cells were cultured in high-glucose DMEM media supplemented with 10% Fetal Bovine Serum (FBS, Labtech, UK) and 1% antibiotics (Penicillin Streptomycin, Lonza, UK) and placed in an incubator (37°C, 5% $CO_2$). After reaching 70% confluence, HaCaT cells were carefully washed with PBS for 10 seconds then incubated with 0.25% Trypsin-EDTA (1X, Lonza, UK) to detach the cells from their support after 5 minutes. Its action was neutralized by adding complete DMEM medium before a centrifugation at 400×g for 4 minutes. An 25 mL aliquot of the HaCaT cells culture (~75000 cells $ml^{-1}$) were washed three times from the culture media via centrifuged, and re-dispersed with 25 mL PBS. Then, 2.5 mL aliquots of this HaCaT cells suspension were incubated with a series of 2.5 mL aliquots of aqueous dispersions of bare and surface functionalized CuONPs at different

concentrations. Likewise, a control sample of the HaCaT cells was treated at the similar conditions without exposure to any nanoparticles. After that, 1 mL of the solution HaCaT was taken from each addressed sample with nanoparticles, washed with PBS to remove the excess of nanoparticles via centrifuged at 400×g for 4 minutes. The HaCaT was re-suspended in 1 mL of PBS, then two drops of FDA solution in acetone was added to each sample and mixed together for 15 minutes followed by triple washing with PBS by centrifugation at 400×g for 4 minutes. Finally, a microplate reader was utilized to assay the HaCaT cell viability.

### 2.2.24 Cytotoxicity assay of bare- and HPBA-grafted CuONPs on Human Embryonic Kidney cells.

HEK 293 cell line culture was grown in high-glucose DMEM media supplemented with 10% Fetal Bovine Serum (FBS, Labtech, UK) and 1% antibiotics (Penicillin Streptomycin, Lonza, UK) inside an incubator (37°C, 5% $CO_2$). After reaching 70% confluence, HEK 293 cells were carefully washed with PBS for 10 seconds then incubated with 0.25% Trypsin-EDTA (1X, Lonza, UK) to detach the cells from their support after 5 minutes. The Trypsin-EDTA action was neutralized by adding complete DMEM medium before a centrifugation at 400×g for 4 minutes. A 25 mL aliquot of the HEK 293 cells culture (~70000 cells $mL^{-1}$) was washed three times from the culture media by centrifugation and re-dispersed in 25 mL PBS. Then, 2.5 mL aliquots of this HEK cells suspension were incubated with a series of 2.5 mL aliquots of aqueous dispersions of bare and HPBA-grafted CuONPs at different concentrations. Likewise, a control sample of the HEK cells was treated at the similar conditions without exposure to any nanoparticles. After that, 1 mL of the solution HEK was taken from each sample treated with nanoparticles, washed with PBS to remove the excess of nanoparticles by centrifugation at 400×g for 4 minutes. The HEK cells were re-suspended in 1 mL of PBS, then two drops of FDA solution in acetone were added to each sample, mixed together for 15 minutes and washed three times with PBS by centrifugation at 400×g for 4 minutes. A microplate reader was utilized to assay the HEK cell viability.

## 2.2.25 References


1. *Cold Spring Harbor Protocols*, 2008, **2008**, pdb.rec11277.
2. G. Adam and H. Duncan, *Soil Biology and Biochemistry*, 2001, **33**, 943-951.
3. G. G. Guilbault and D. Kramer, *Analytical Chemistry*, 1964, **36**, 409-412.
4. J. Schnürer and T. Rosswall, *Applied and environmental microbiology*, 1982, **43**, 1256-1261.
5. M. Tillhon, L. M. G. Ortiz, P. Lombardi and A. I. Scovassi, *Biochemical pharmacology*, 2012, **84**, 1260-1267.
6. C. V Diogo, N. G Machado, I. A Barbosa, T. L Serafim, A. Burgeiro and P. J Oliveira, *Current drug targets*, 2011, **12**, 850-859.
7. A. A. Das, M. M. Esfahani, O. D. Velev, N. Pamme and V. N. Paunov, *Journal of Materials Chemistry A*, 2015, **3**, 20698-20707.
8. D. S. Gorman and R. Levine, *Proceedings of the National Academy of Sciences of the United States of America*, 1965, **54**, 1665.
9. S. Hutner, L. Provasoli, A. Schatz and C. Haskins, *Proceedings of the American Philosophical Society*, 1950, **94**, 152-170.
10. *Cold Spring Harbor Protocols*, 2006, **2006**, pdb.rec8194.
11. *Cold Spring Harbor Protocols*, 2009, **2009**, pdb.rec11945.
12. H. R. Ghorbani, F. P. Mehr, H. Pazoki and B. M. Rahmani, *Oriental Journal of Chemistry*, 2015, **31**, 1219-1221.
13. B. Vatsha, P. Tetyana, P. M. Shumbula, J. C. Ngila, L. M. Sikhwivhilu and R. M. Moutloali, *Journal of Biomaterials and Nanobiotechnology*, 2013, **4**, 365.
14. V. Pandey, G. Mishra, S. Verma, M. Wan and R. Yadav, *Materials Sciences and Applications*, 2012, **3**, 664.
15. H. K. LICHTENTHALER and A. R. Wellburn, *Biochemical Society Transactions*, 1983, **11**, 591-592.
16. A. F. Halbus, T. S. Horozov and V. N. Paunov, *ACS applied materials & interfaces*, 2019, **11**, 12232–12243.
17. A. F. Halbus, T. S. Horozov and Vesselin N. Paunov, *Nanoscale Advances*, 2019, **1**, 2323 – 2336.
18. S. S. M. Al-Obaidy, A. F. Halbus, G. M. Greenway and V. N. Paunov, *Journal of Materials Chemistry B*, 2019, **7**, 3119-3133.
19. M. J. Al-Awady, G. M. Greenway and V. N. Paunov, *RSC Advances*, 2015, **5**, 37044-37059.

20. A. Sadollahkhani, I. Kazeminezhad, J. Lu, O. Nur, L. Hultman and M. Willander, *RSC Advances*, 2014, **4**, 36940-36950.
21. W. Stöber, A. Fink and E. Bohn, *Journal of colloid and interface science*, 1968, **26**, 62-69.
22. K. Tadanaga, K. Morita, K. Mori and M. Tatsumisago, *Journal of sol-gel science and technology*, 2013, **68**, 341-345.
23. H. Wang, *Development of silica based nanopigments*, Lehrstuhl für Textilchemie und Makromolekulare Chemie, 2013.
24. F. Grasset, N. Saito, D. Li, D. Park, I. Sakaguchi, N. Ohashi, H. Haneda, T. Roisnel, S. Mornet and E. Duguet, *Journal of Alloys and Compounds*, 2003, **360**, 298-311.
25. V. J. Cunningham, A. M. Alswieleh, K. L. Thompson, M. Williams, G. J. Leggett, S. P. Armes and O. M. Musa, *Macromolecules*, 2014, **47**, 5613-5623.
26. D. Zhang, K. L. Thompson, R. Pelton and S. P. Armes, *Langmuir*, 2010, **26**, 17237-17241.
27. R. Pelton, D. Zhang, K. L. Thompson and S. P. Armes, *Langmuir*, 2011, **27**, 2118-2123.
28. W. Zeng, Z. Wang, X.-F. Qian, J. Yin and Z.-K. Zhu, *Materials research bulletin*, 2006, **41**, 1155-1159.
29. I. M. El-Nahhal, J. K. Salem, S. Kuhn, T. Hammad, R. Hempelmann and S. Al Bhaisi, *Powder Technology*, 2016, **287**, 439-446.
30. I. M. El-Nahhal, J. K. Salem, S. Kuhn, T. Hammad, R. Hempelmann and S. Al Bhaisi, *Journal of Sol-Gel Science and Technology*, 2016, **79**, 573-583.

# Chapter 3

# 3. Synthesis and characterisation of surface modified ZnONPs

## 3.1 Introduction

This Chapter describes the preparation and characterisation of surface modified ZnONPs. ZnONPs were used because they play a vital role in many applications involving pharmaceutical, electronics and industrial. [1-3] Also, they have unique chemical and physical properties such as particle size, surface area and quantum effect which have a potential toxic impact upon release to the environment. [1, 4-7] Therefore, the aim of the present study was to reduce the toxicity of ZnONPs by coating them with a zinc sulfide (ZnS), silica ($SiO_2$) layer, anionic poly(sodium 4-styrene sulfonate) sodium salt (PSS) and cationic poly(allylamine hydrochloride) (PAH), which could be used in human applications, such as cosmetic preparations. In this chapter, ZnONPs were synthesised and characterised to study their behaviour upon incubation with some microorganisms as well as surface modifications of ZnONPs with zinc sulfide, silica, anionic and cationic polyelectrolytes to study the impact of surface charge on the microorganisms in the environment.

## 3.2 Characterisation of ZnONPs

Particle size distribution can be influenced in several ways: sonification, pH and adding a stabilizer. Dispersant also plays a very important role. The mean hydrodynamic diameter and zeta potential of the ZnONPs in deionized water was measured by DLS. For DLS measurements suspensions were prepared by dispersing 0.2 mg of ZnO sample in 10 ml of deionized water at pH 7.4. The average particle diameter of ZnONPs was found to be approximately 16 ± 5 nm using TEM and 82 ± 10 nm using Zetasizer with a surface charge around +32 ± 5 mV as shown in Figure 3.1 and Figure 3.2. The stability of ZnONPs suspensions can be monitored by measuring the zeta potential. Suspensions of ZnONPs are stable in the neutral pH range.

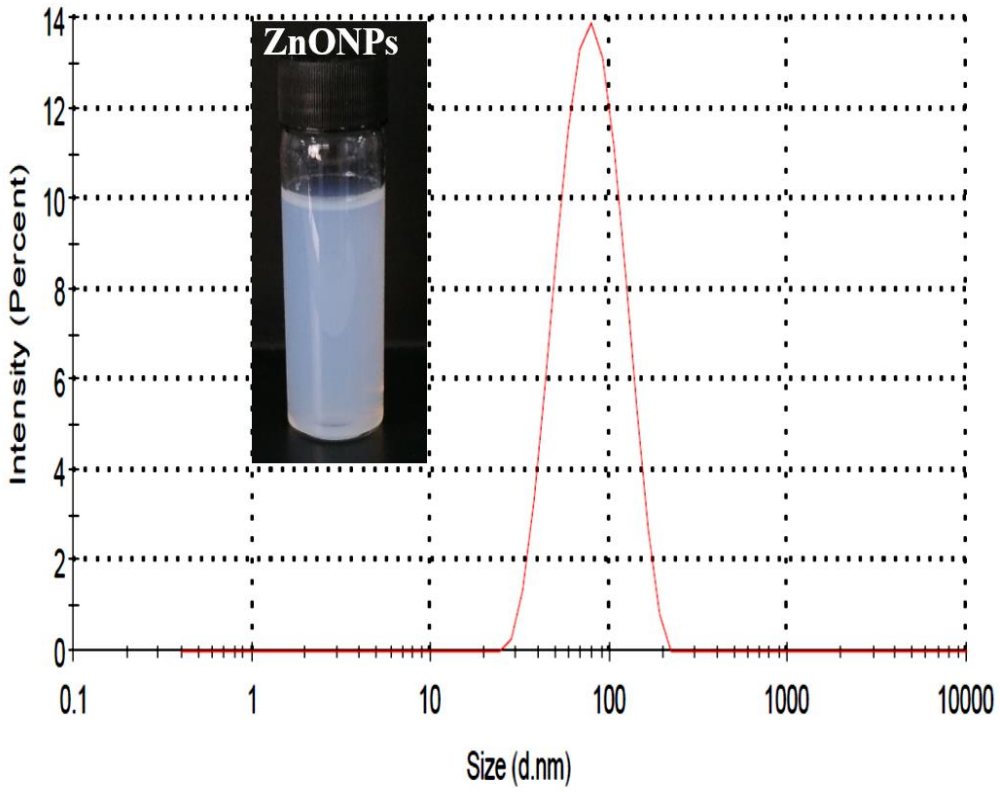


**Figure 3.1.** The particle size distribution of ZnONPs in deionized water at pH 7.4.

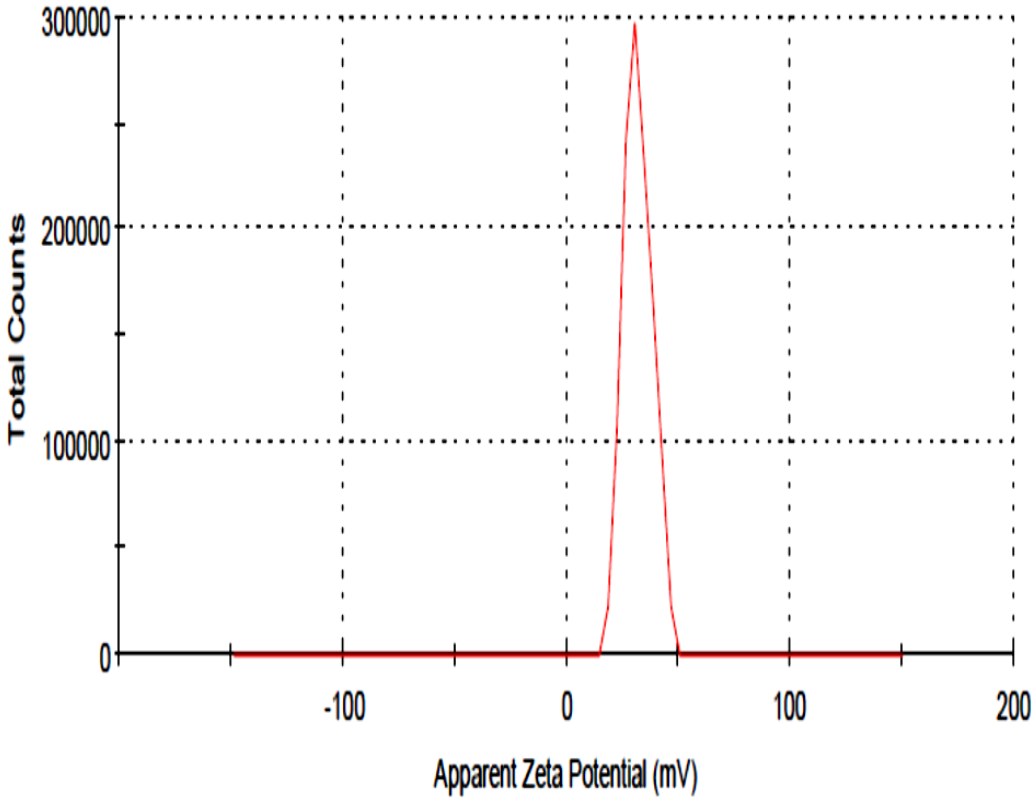


**Figure 3.2.** The zeta potential of ZnONPs prepared by dispersing ZnONPs in deionized water at pH 7.4.

## 3.3 Thermogravimetric analysis (TGA)

Figure 3.3 shows the TGA thermogram for the ZnO precursor. As can be seen from Figure 3.3, the weight loss of the precursor occurs in two stages with increasing temperature. The first weight loss appears in the range of 50 $^{o}$C to approximately 190 $^{o}$C because of the removal of absorbed water from the surface of the sample. The second stage is from 190 °C to 350 °C with no further weight loss, indicating the loss of $OH^-$ due to the dehydration and combustion of organic species, for example, residues of the precursor (zinc nitrate). TGA curve explains that the precursor can be totally decomposed to ZnO after calcining at approximately 350 °C. [8]

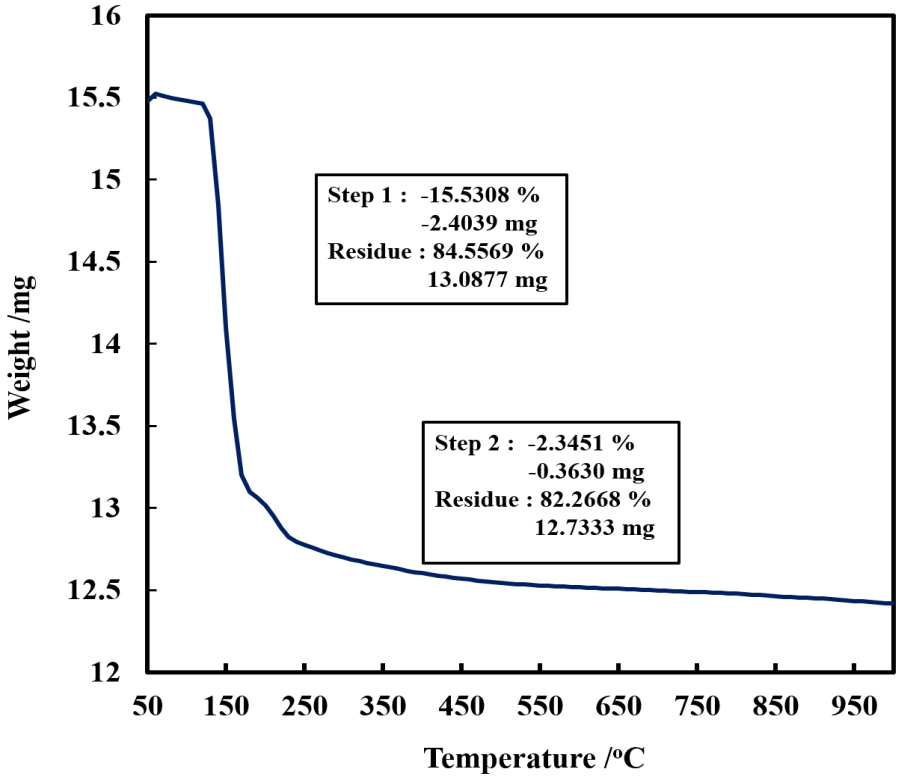


**Figure 3.3.** Thermal gravimetric analysis pattern of ZnONPs powder.

## 3.4 The absorption of UV-Vis spectroscopy of ZnONPs

The UV–Vis spectra of ZnONPs obtained from 0.2 M zinc nitrate and 0.4 M of potassium hydroxide and calcined at 100 $^{o}$C for 3 hours appeared in Figure 3.4. For measuring UV–Vis spectra, aqueous dispersions of the ZnONPs were prepared by dispersing of ZnO sample in milli-Q water using a digital sonicator. The absorption peak in Figure 3.4 corresponds to ZnO sample calcined at a temperature of 100 $^{o}$C demonstrating the strong absorption at the wavelength of 378 nm. This can be assigned to the intrinsic band gap absorption of ZnO because of electron movement from the valence band (VB) to the

conduction band (CB). [9] The band gap energy (Eg) of ZnONPs was calculated using the equation Eg=hc/λ [10, 11], where h is the Planks constant, 6.626 × $10^{-34}$ J s, $c$ is the speed of light, 3.0 × $10^{8}$ m/s and $\lambda$ is the wavelength (nm). The band gap energy was found to be 3.27 eV.

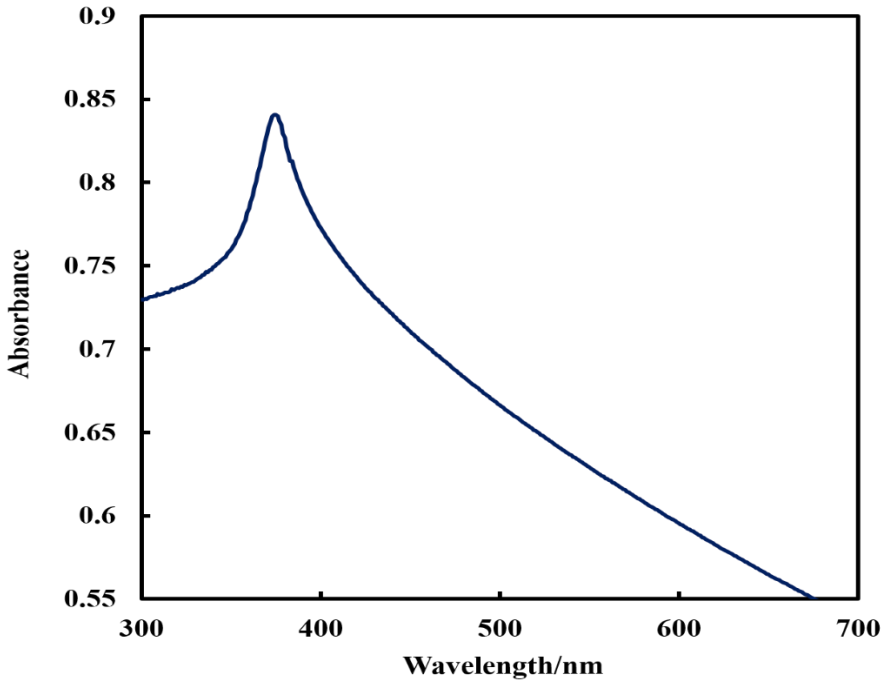


**Figure 3.4.** UV–vis absorption spectrum of ZnONPs.

## 3.5 Calcination of the synthesized ZnONPs

The XRD patterns of ZnONPs obtained from the calcining of ZnO precursor at various temperatures (100°C - 600°C) are shown in Figure 3.6, utilising the muffle furnace to find out the impact of temperature on the crystallite size of ZnONPs. All characteristic peaks observed for ZnONPs are in great agreement with similar results previously reported in the literature.[12] In the XRD pattern, no peaks related to impurities were identified, confirming the good purity of the synthesised product. These results showed that there is a change in the crystallinity of the ZnONPs by increasing the calcining temperatures from 100 to 600°C as shown in Figure 3.5. The results in Figure 3.6 also displays that the crystal size for ZnONPs annealed at 600$^{o}$C was highest and for ZnONPs annealed at 100$^{o}$C the value was the lowest. It was also discovered that with increasing the annealing temperature, the intensity of the diffraction peaks became sharper and the size of crystallinity of ZnONPs was also increased. The average crystalline size of ZnONPs was calculated using Scherer's equation and it is found to be in the range 35-85 nm for the different annealing temperature.

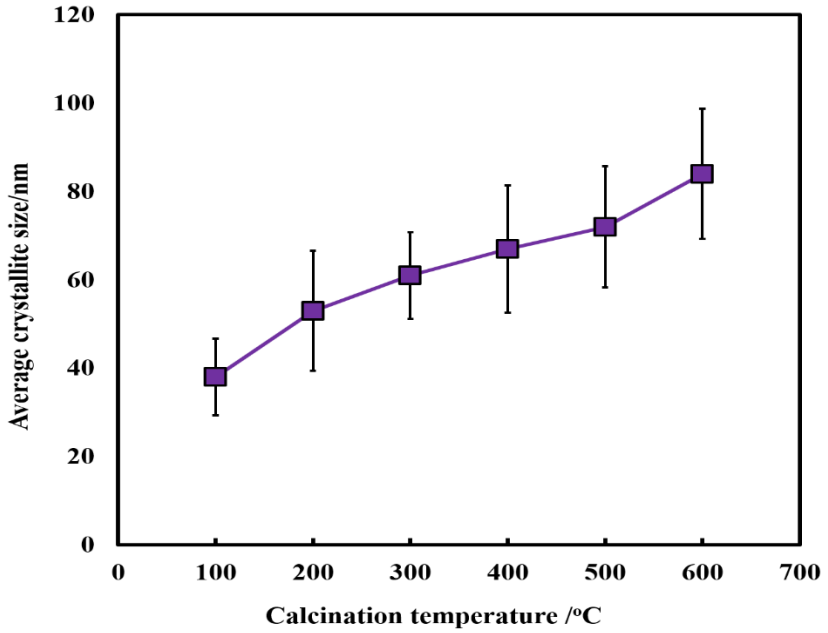


**Figure 3.5.** Average crystallite size of ZnONPs at calcination temperature.

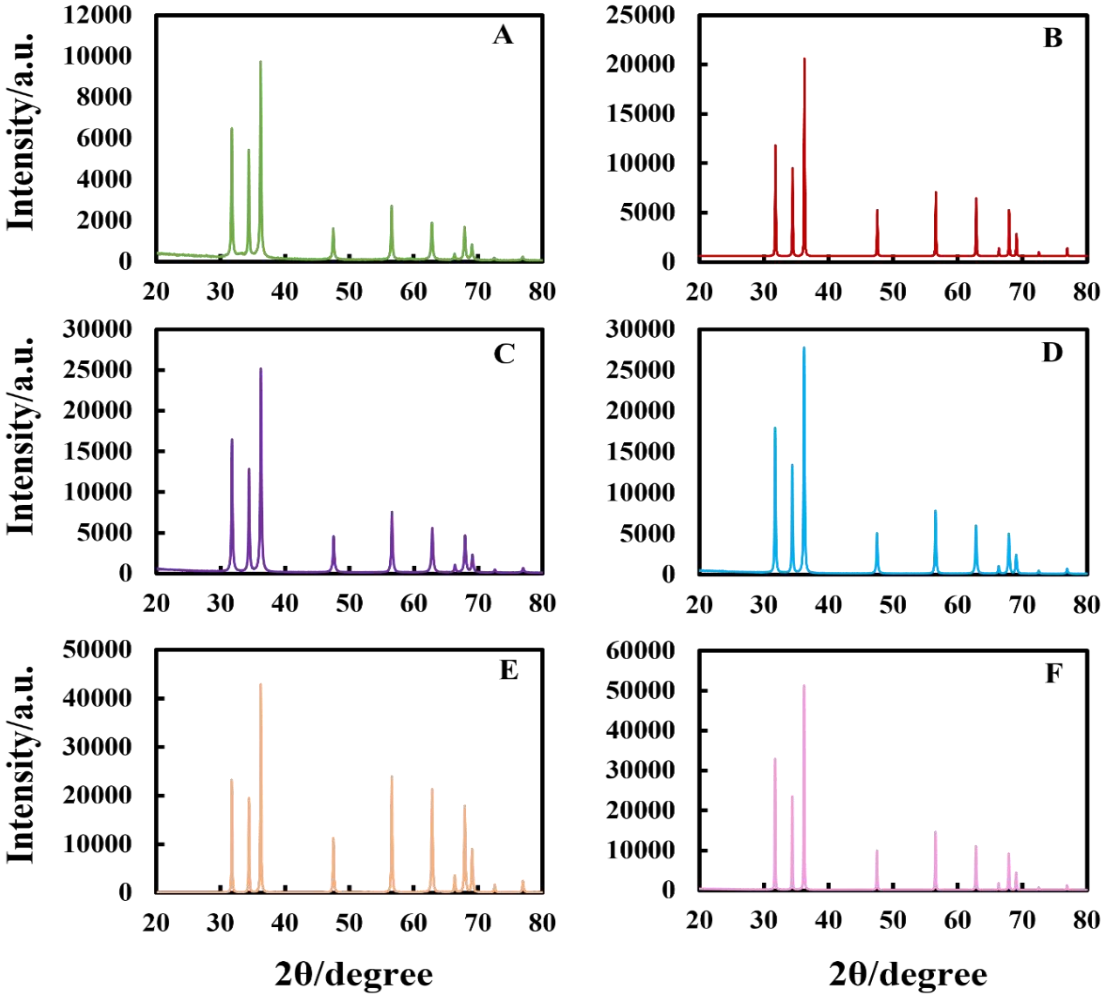


**Figure 3.6.** Powder XRD pattern of ZnO nanoparticles as synthesised calcined at different temperatures (A) 100°C, (B) 200°C, (C) 300°C, (D) 400°C, (E) 500°C, and (F) 600°C.

## 3.6 Effect of the temperature on the surface area, particles size, and zeta potential of the ZnONPs

The surface area of ZnONPs was measured at different calcination temperature as well as the particle size and zeta potential. Surface area measurements of ZnONPs at various calcination temperatures were carried out by nitrogen adsorption at 77K utilising the BET technique. Obviously, the surface area decreased as the temperature of calcining increased from 29 $m^2 g^{-1}$ for 82 ± 10 nm ZnONPs at 100 $^oC$ to 7 $m^2 g^{-1}$ for 265 ± 8 at 600 $^oC$ calcining temperature as appeared in Figure 3.7 and also was in agreement with previous studies.[13]

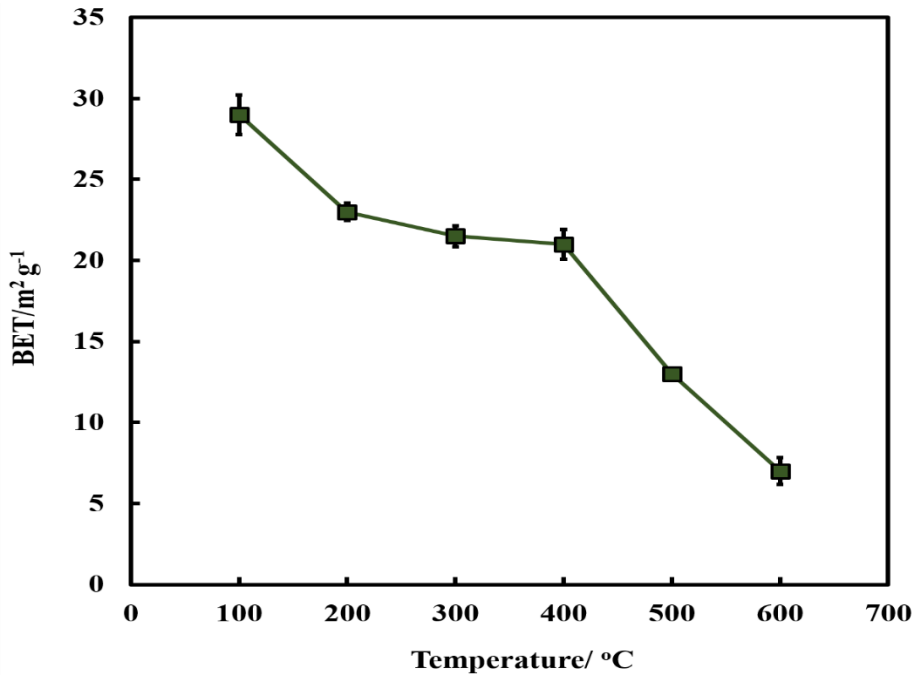


**Figure 3.7.** The effect of the annealing temperature during the ZnONPs synthesis on the BET surface area of ZnO nanoparticle from 100 to 600 $^oC$.

Also from Figure 3.8, it is clear that the hydrodynamic diameter is increasing with increasing annealing temperatures. Thus, it was found that ZnONPs with same crystal type but various particle size could be obtained by changing the calcination temperature and this also was in agreement with the previous studies.[14-16] These results might be explained that at higher calcination temperatures, agglomeration of ZnONPs begins to occur and hence the particle size increased. In addition to that, the zeta potential was measured for each calcined sample of ZnONPs, and it can be seen from Figure 3.9 that at 100 $^oC$, the zeta potential was +39 mV which means it was highly stable while, at 600 $^oC$, the zeta potential was +15 mV.

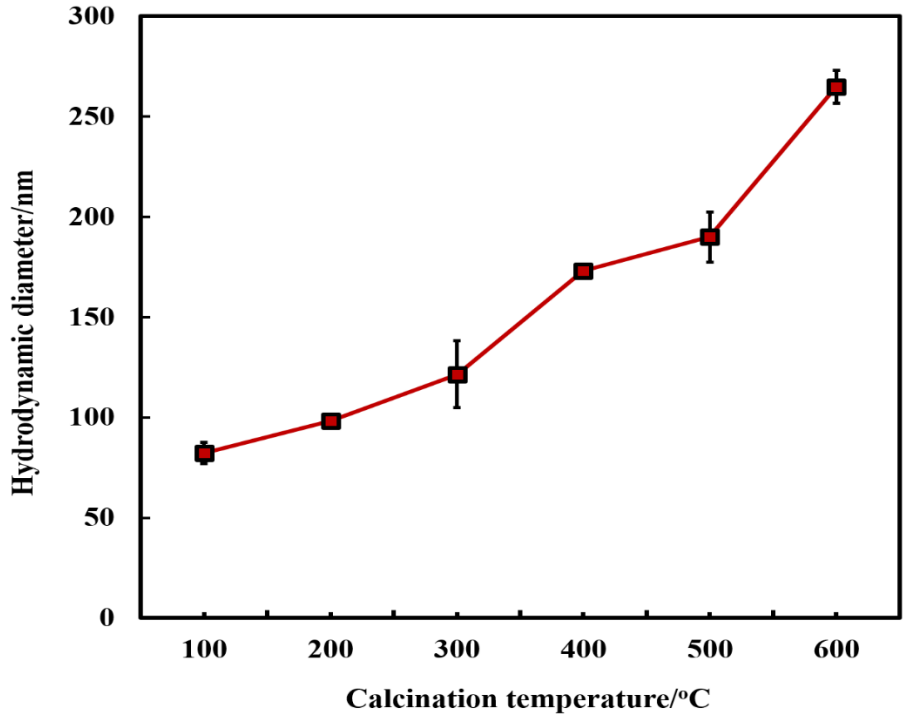


**Figure 3.8.** The hydrodynamic diameter of ZnONPs produced from ZnO calcinated at different temperatures.

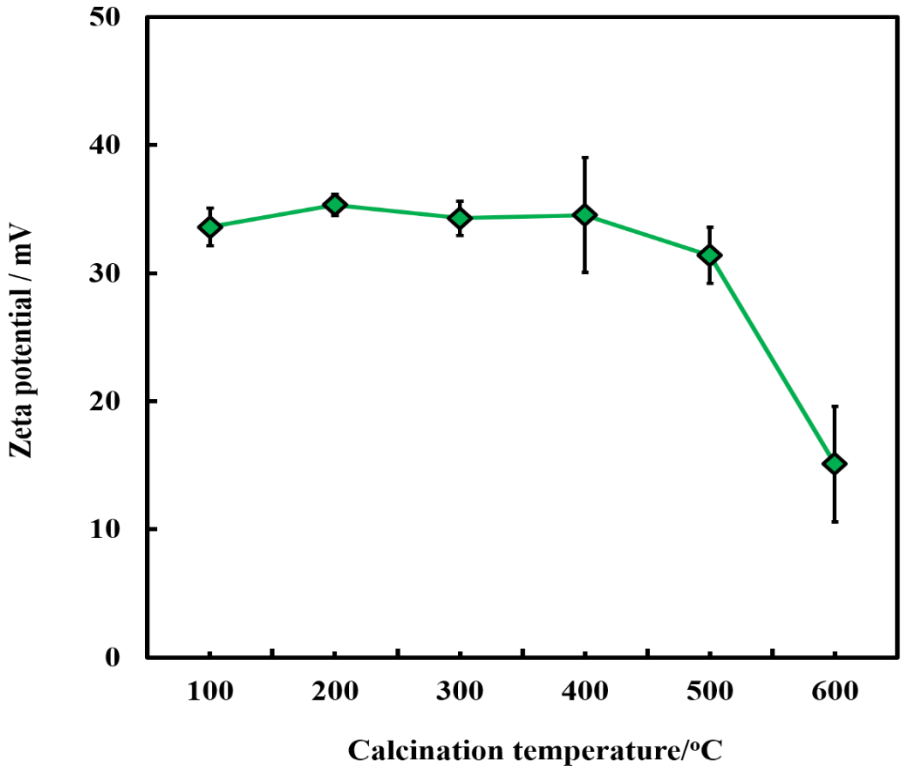


**Figure 3.9.** The zeta potential of ZnONPs produced from ZnO calcinated at different temperatures.

## 3.7 Isoelectric point of ZnONPs.

The isoelectric point of the ZnONPs is the pH at which the sample has a neutral zeta potential or surface charge of zero. At a neutral charge, the ZnONPs have very low stability and are very prone to aggregation and flocculation. In order to keep ZnONPs stable in solution, it is necessary to suspend them in a solution with a pH that is far away from their isoelectric point. The magnitude of the zeta potential provides information about particle stability, with particles with higher magnitude zeta potentials exhibiting increased electrostatic repulsion and therefore increased stability. A series of different pH values from 5-12 of ZnONPs were prepared in deionized water. Dilute HCl or NaOH was utilised for adjusting pH of each solution. Then, the zeta potential and particle size of the ZnONPs were measured to find out the impact of acidity and basicity on the surface charge of ZnONPs. Figure 3.10 shows the impact of pH on the zeta potential and particle size of the dispersed ZnONPs in the medium. The surface charge of ZnONPs is decreased gradually from a positive charge in the acidic medium to be negatively charged particles in the basic medium; the isoelectric point was about pH 10.1. As can be seen from Figure 3.10 the changes of the zeta potential and particle size during addition of 0.1 M NaOH. In other words, the addition of 0.1 M NaOH caused the increase of particle size and decrease of the zeta potential. Thus, the aggregation of ZnONPs start to happen.

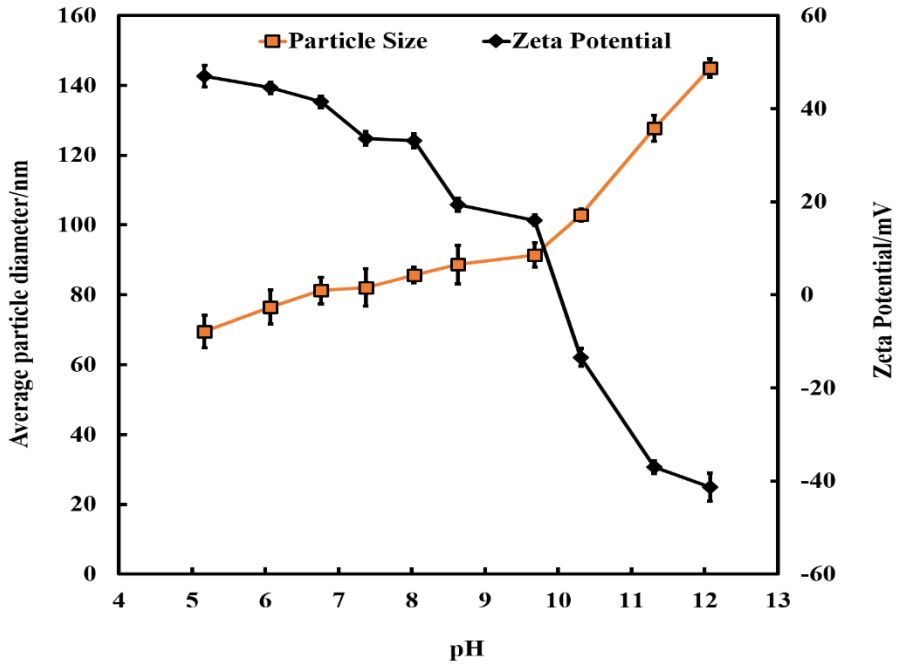


**Figure 3.10.** The variation the zeta potential and the particle diameter of dispersed ZnONPs in an aqueous solution, pH adjusted by addition of 0.1 M HCl or 0.1 M NaOH. The blue line shows the impact of pH on the average particle hydrodynamic diameter.

## 3.8 Energy dispersive X-ray diffractive (EDX) of ZnONPs

EDX analysis was carried out for the synthesised ZnONPs to find out about the elemental composition. It can be seen from Figure 3.11 that the EDX confirms the presence of zinc and oxygen signals of zinc oxide nanoparticle and this examination demonstrated the peaks that corresponded to the optical absorption of the created nanoparticle. The elemental analysis of the ZnONPs yielded 79% of zinc and 20% of oxygen which proves that the formed ZnONPs is in its highest purified form and likewise was in agreement with the previous studies.[17, 18]

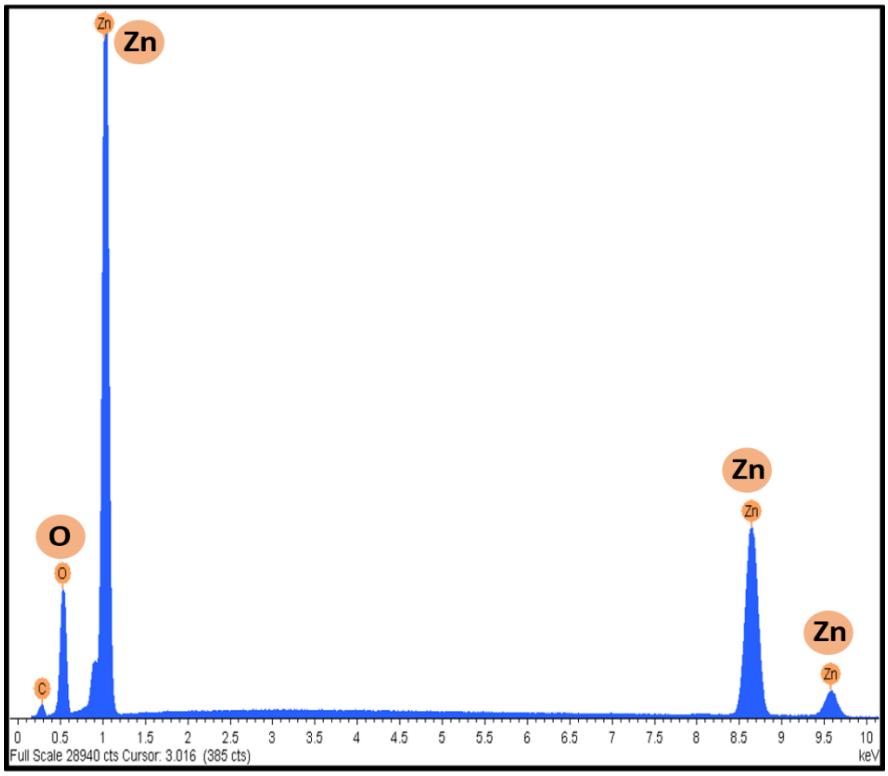


**Figure 3.11.** The EDX spectra of the ZnONPs sample was done by the SEM machine. The EDX reveals that both Zn and O is present in the sample.

## 3.9 Transmission electron microscopy analysis of ZnONPs at different temperatures.

Figures 3.12 (A, B and C), show TEM images of ZnONPs resulted from the calcining of ZnO at 100 °C, 500 °C and 600 °C for 3 hours. As can be seen from TEM images that the ZnONPs were a spherical shape. Obviously, the particle size is increasing with increasing calcining temperatures. For the sample calcined at 100°C (Figure 3.12A), it was found that the average diameter is 16 ± 5 nm. It is significant that the average crystal diameter

resulted from the Scherer's equation (38 nm) is in good agreement with the value produced from analysis of TEM images. While, for the sample calcined at 500 °C and 600 °C (Figure 3.12B, C), it was discovered that the average diameter is 25 ± 11 nm and 43 ± 16 nm, respectively.

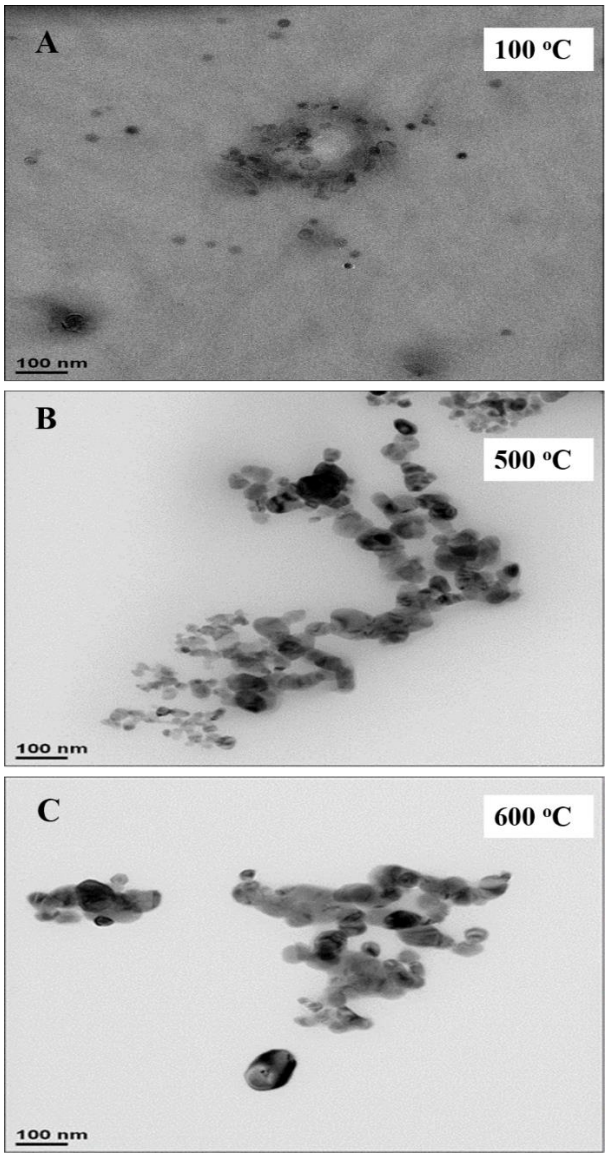


**Figure 3.12.** TEM image of synthesized ZnO nanoparticles calcined at different temperatures (A) 100 °C, (B) 500 °C, and (C) 600 °C.

## 3.10 Fourier transform infrared spectroscopy analysis of ZnONPs calcined at different temperatures.

FTIR spectrum was obtained for the calcined ZnO samples at 100, 200, 300, 400, 500 and 600 °C in the range 500-4000 $cm^{-1}$. Figure 3.13 demonstrates the FTIR spectra of ZnONPs calcined at different temperatures. It can be seen in Figure 3.13 A the peak at 3150-3620 $cm^{-1}$ correspond to the existence of hydroxyl groups (–OH). Moreover, The peaks at 1370

$cm^{-1}$ and 1504 $cm^{-1}$ correspond to the bending vibrations of $Zn(OH)_2$.[15, 19] After calcining of the precursor, a peak is shown at approximately 500 $cm^{-1}$, this is because of transverse optical stretching modes of ZnO. The peak at 3150-3620 $cm^{-1}$ has been decreased significantly after calcining (200-600 $^oC$) illustrating the decomposition of the hydroxyl group. These results were well matched with other studies reported in the literature. [12, 13, 19, 20]

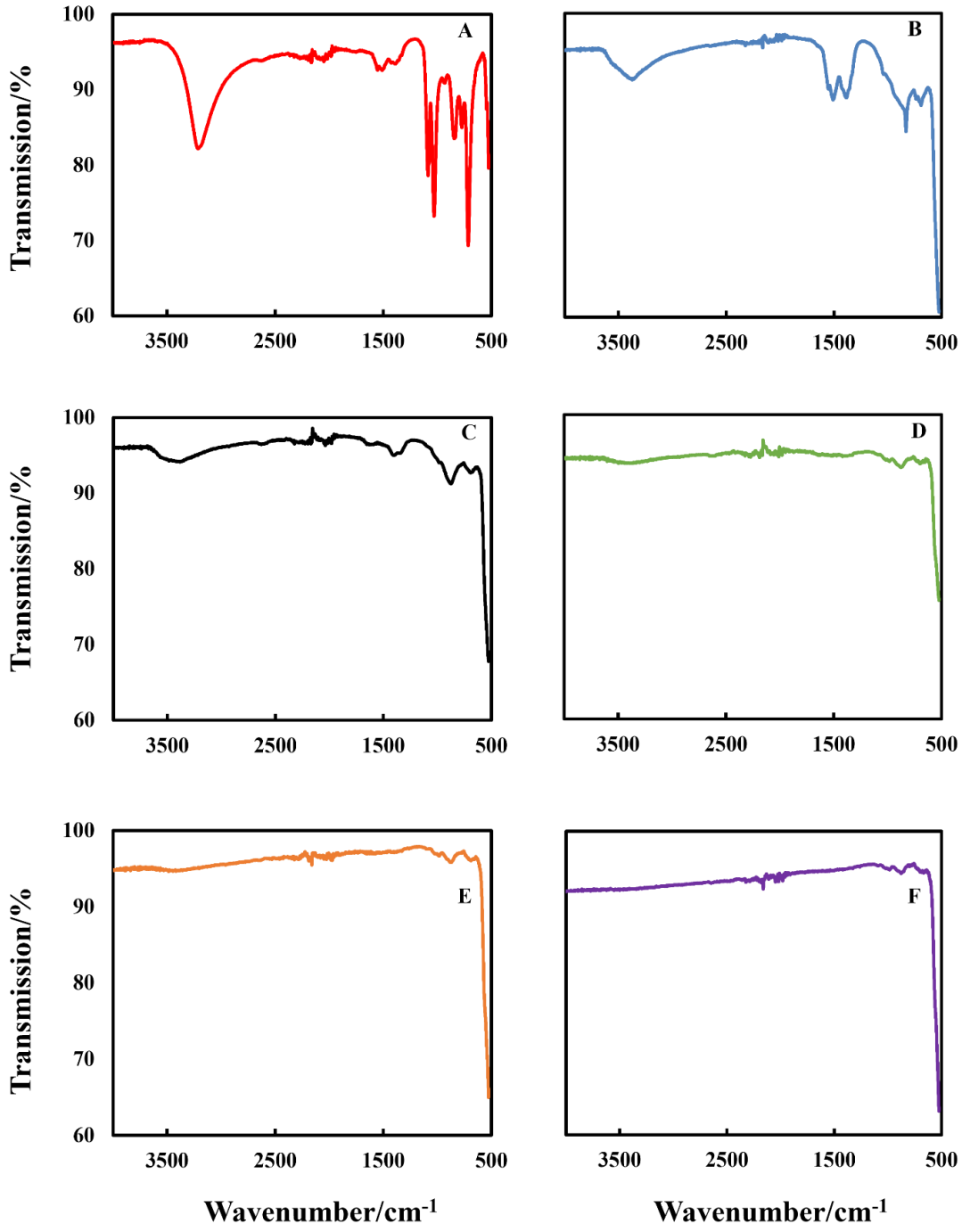


**Figure 3.13.** FTIR spectra of prepared ZnO nanoparticles at different calcination temperatures (A) 100 $^oC$, (B) 200 $^oC$, (C) 300 $^oC$, (D) 400 $^oC$, (E) 500$^oC$ and (F) 600$^oC$ in the range of 500– 4000 $cm^{-1}$.

## 3.11 Zinc sulfide, silica and polyelectrolyte -coating of ZnONPs

The formation mechanism of ZnONPs/ZnS is illustrated in Figure 3.14A. After dispersing the ZnONPs in deionized water, the pH of the solution was adjusted to approximately 7.4. 0.1 M $Na_2S$ was added dropwise to a suspension of ZnONPs, the surface of the nanoparticles will begin to dissolve, and the $S^{2-}$ freed from the $Na_2S$ will interact with the $Zn^{2+}$ and lead to create ZnS around the bare ZnONPs:

$$Zn^{2+} + S^{2-} \rightarrow ZnS$$

The presence of sulphur is confirmed by EDX analysis as shown in Figure 3.15. The particle size and zeta potential of the ZnONPs coated with ZnS were 112 ± 6 nm and -38 ± 4 mV as shown in Figure 3.16 and Figure 3.17.

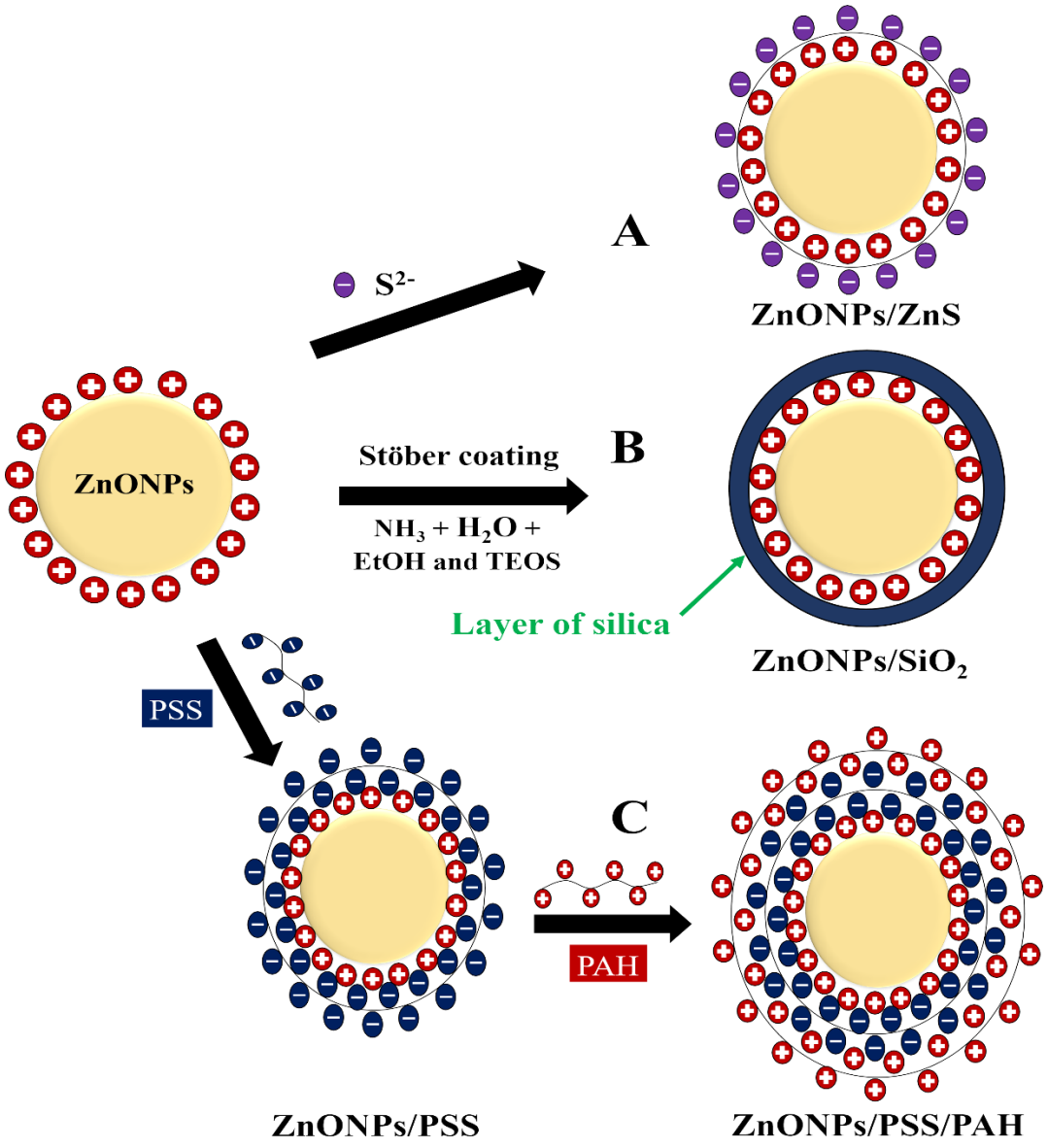


**Figure 3.14.** The schematic coating of bare ZnONPs with (A) ZnS, (B) $SiO_2$ and (C) two layers of anionic and cationic polyelectrolytes (10 kDa PSS and 15 kDa PAH) in 1 mM NaCl.

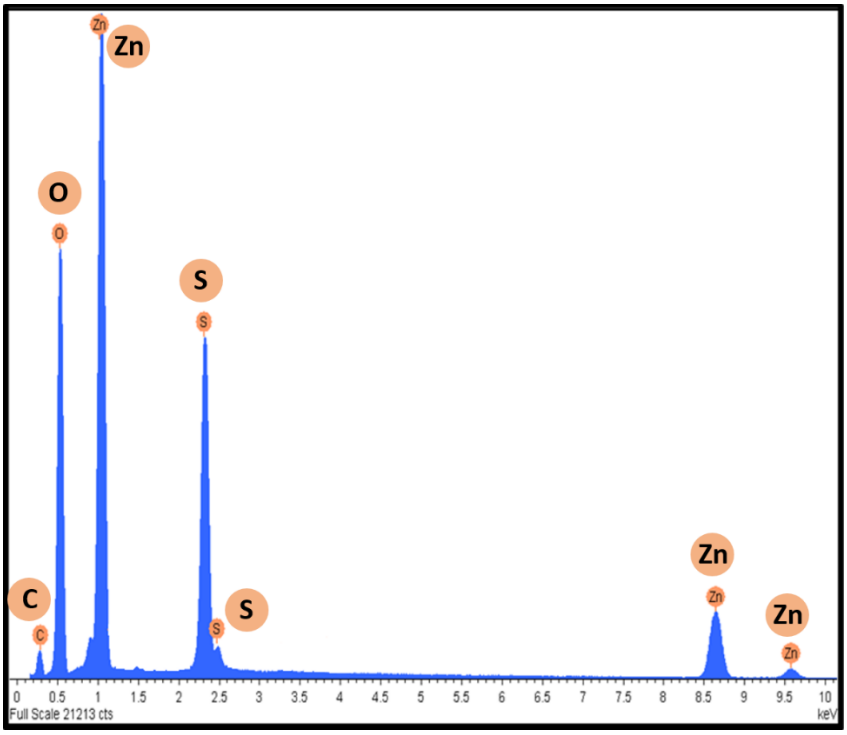


**Figure 3.15.** The EDX diagram of the ZnONP/ZnS sample was done by the SEM machine. The EDX shows that Zn, O and S is present in the sample.

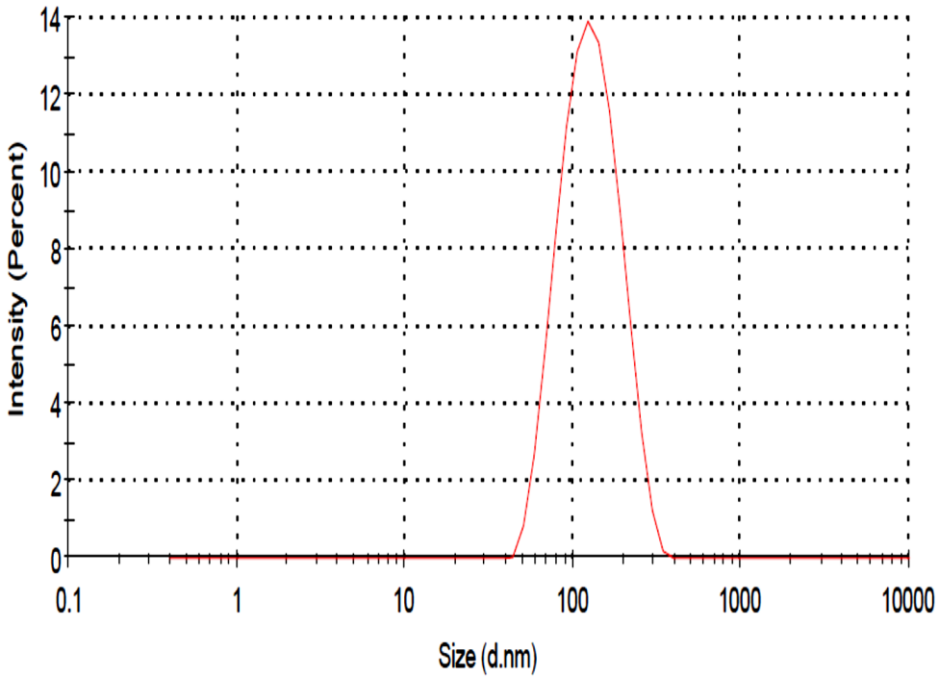


**Figure 3.16.** Particle size of ZnONPs/ZnS prepared by dissolving 0.4 g of sodium sulfide in 50 ml deionized water.

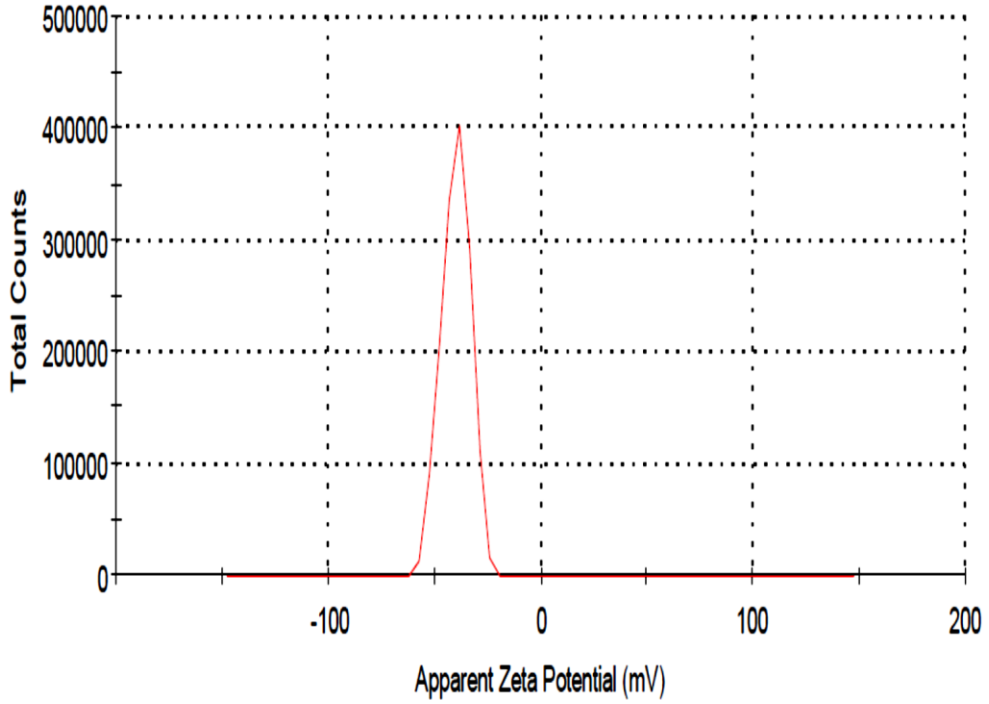


**Figure 3.17.** The zeta potential of ZnONPs/ZnS prepared by dissolving 0.4 g of sodium sulfide in 50 ml deionized water.

ZnONPs were coated with a layer of silica by Stöber method in the presence of ammonia together with ethanol and TEOS. After coating (ZnONPs/$SiO_2$), these particles were re-dispersed in deionized water. Figure 3.14B shows the schematic diagram of the silica coating of the bare ZnONPs. The silica layer created over the bare ZnONPs were checked further by the TEM, EDX, zeta potential and particle size measurements. The EDX data in Figure 3.18 confirm the presence of Zn, O and Si signals in the ZnONPs/$SiO_2$ sample. TEM images show that a layer of silica with thickness approximately 20~25 nm has been formed on the bare ZnONPs (Figure 3.19). The ZnONPs/$SiO_2$ were characterised by the Zetasizer to check the particle size and the zeta potential. It was found that the particle size of ZnONPs/$SiO_2$ was 134 ± 8 nm (Figure 3.20). In zeta potential study the bare ZnONPs demonstrated a value of +32 ± 5 mV. After coating, the surface charge reversal was -33 ± 3 mV for the ZnONPs/$SiO_2$ (Figure 3.21). A high negative charge of the ZnONPs/$SiO_2$ was attributed to the huge silica layer with many Si–OH groups at the surface. [21]

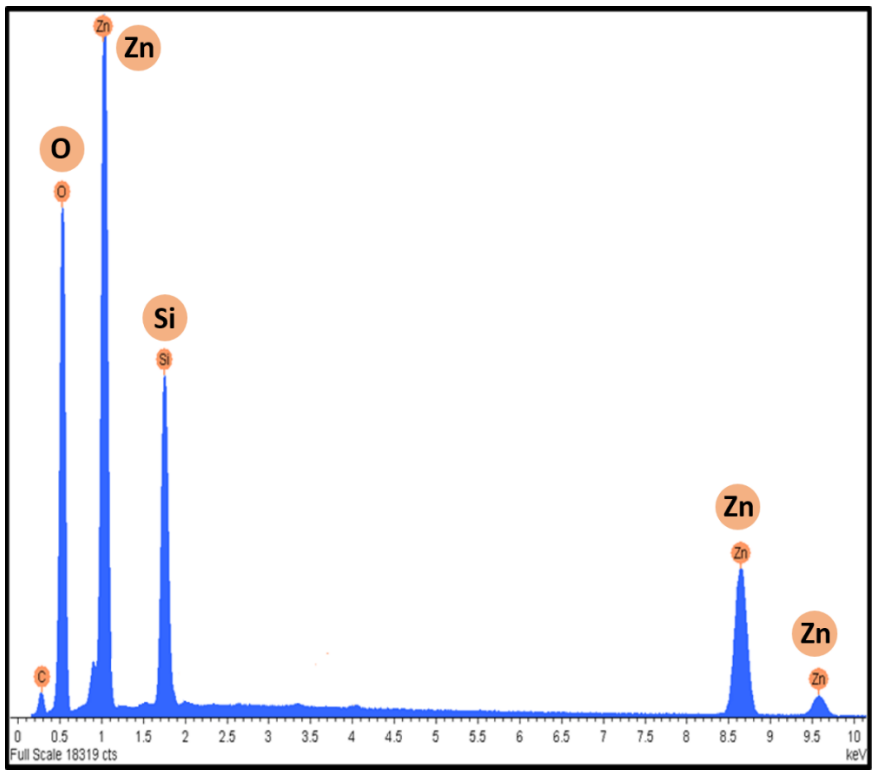


**Figure 3.18.** The EDX spectra of the ZnONPs/Silica sample was done by the SEM machine. The EDX shows that Zn, O and Si are present in the sample.

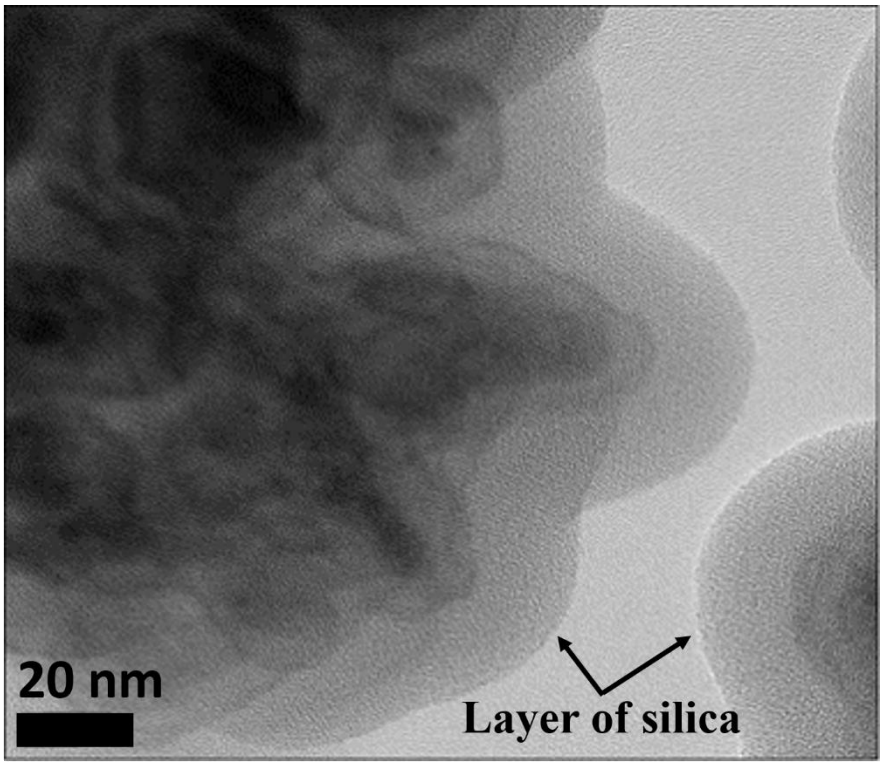


**Figure 3.19.** TEM image of ZnONPs/$SiO_2$. Note the silica layer in top of the ZnO cores.

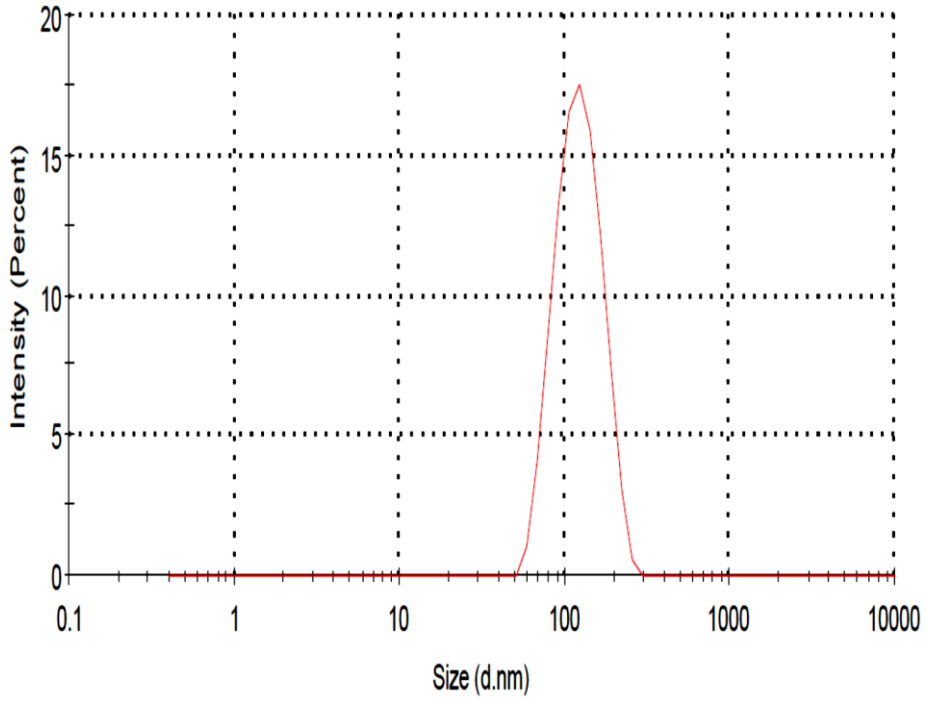


**Figure 3.20.** The particle size of ZnONPs/$SiO_2$.

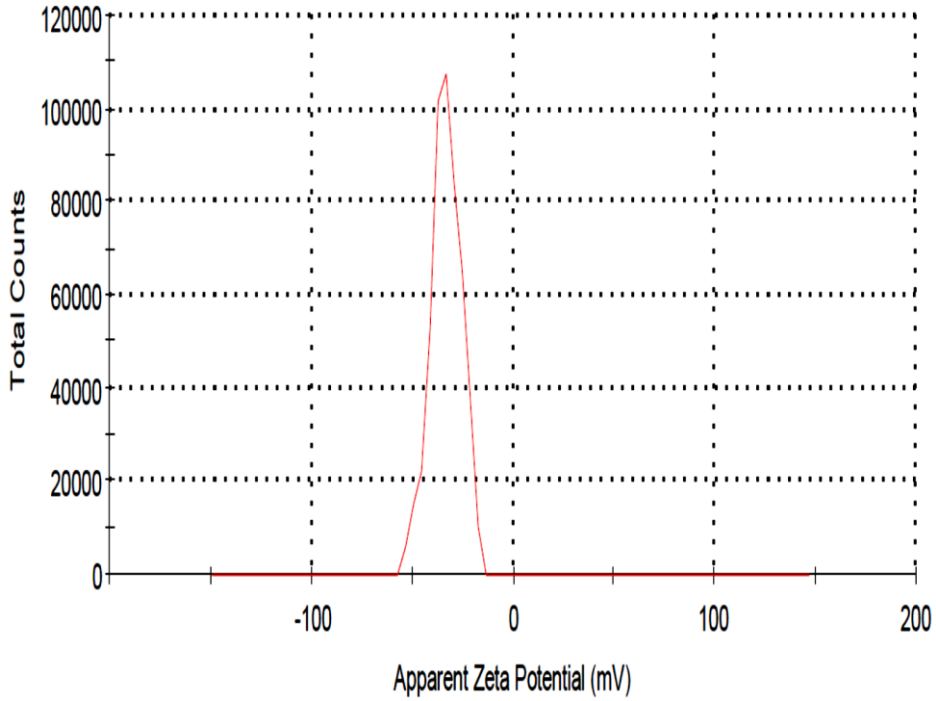


**Figure 3.21.** The zeta potential of ZnONPs/silica.

Figure 3.14C shows the ZnONPs coated with two subsequent layers of PSS and PAH. Figure 3.22 shows TEM image of ZnONPs coated with one layer of polyelectrolyte. The particle size and zeta potential of the ZnONPs coated with anionic polyelectrolyte were

106 nm and -41 mV as shown in Figures 3.23 and 3.24. The coating was influenced by many parameters such as the addition of ZnONPs which can cause the aggregation of particles.

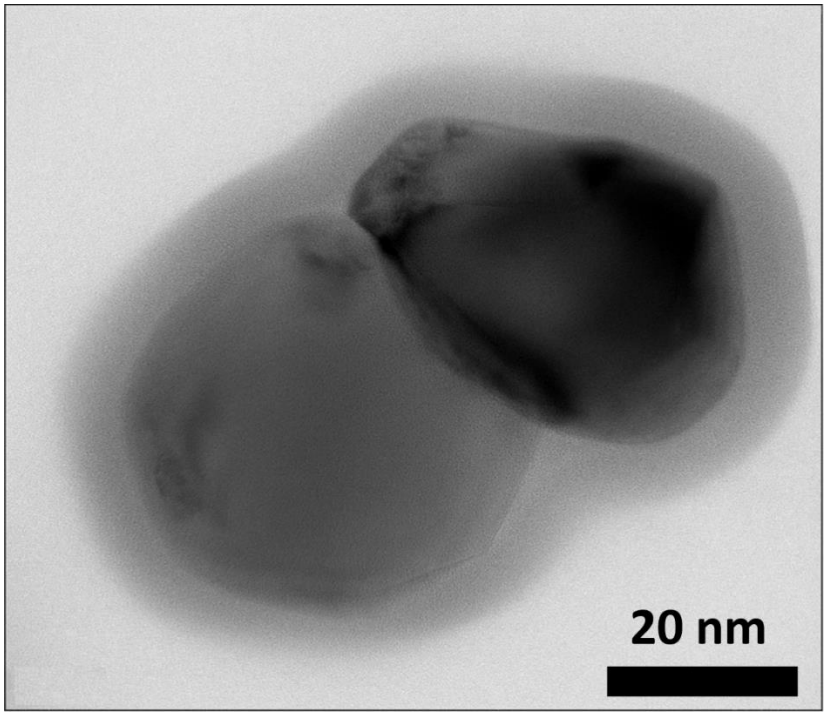


**Figure 3.22.** TEM image of ZnONPs coated with one layer of PSS.

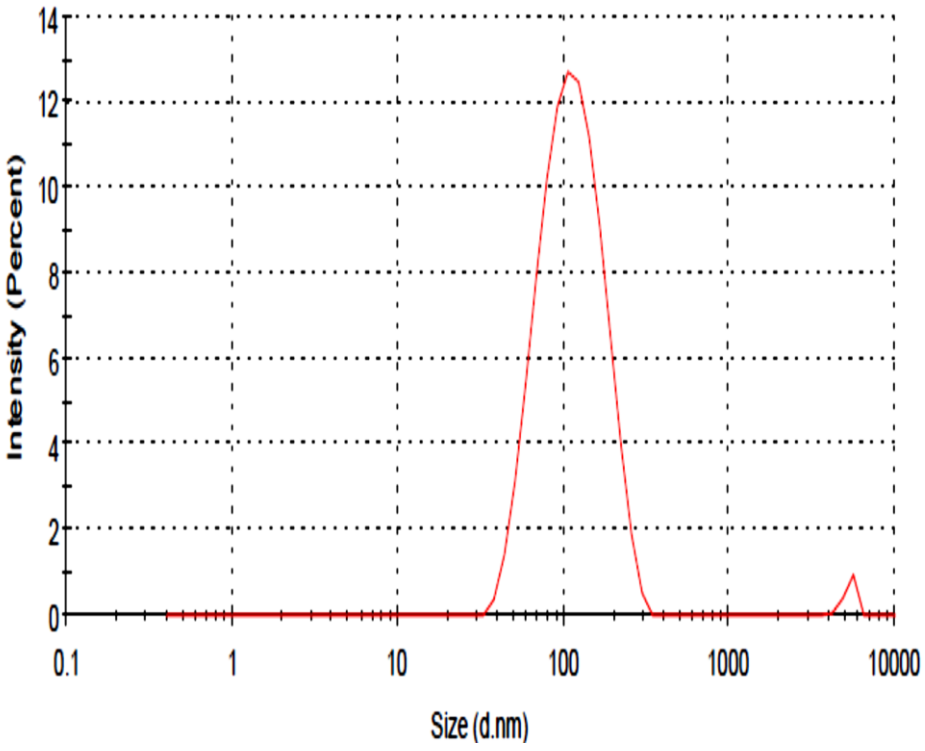


**Figure 3.23.** The particle size of ZnONPs/PSS using dropwise addition with ultra-sonication.

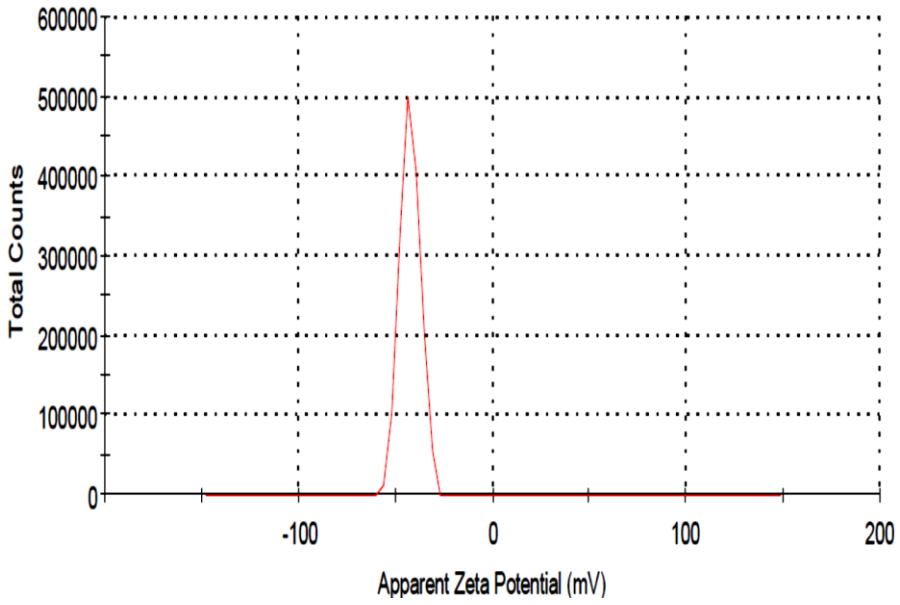


**Figure 3.24.** The zeta potential of ZnONPs/PSS using dropwise addition with ultra-sonication.

The particle size and zeta potential of the ZnONPs after each coating with PSS, silica, ZnS and PAH were measured as shown in Figure 3.25 and Figure 3.26. It can be seen from Figure 3.26 that the zeta potential of the bare ZnONPs was +32 mV. After each coating, the zeta potential reversal became -41 mV for the ZnONPs/PSS, -33 mV for the ZnONPs/silica and -38 mV for the ZnONPs/ZnS and then the ZnONPs/PSS coating with PAH was positively charged ZnONPs/PSS/PAH with +42 mV.

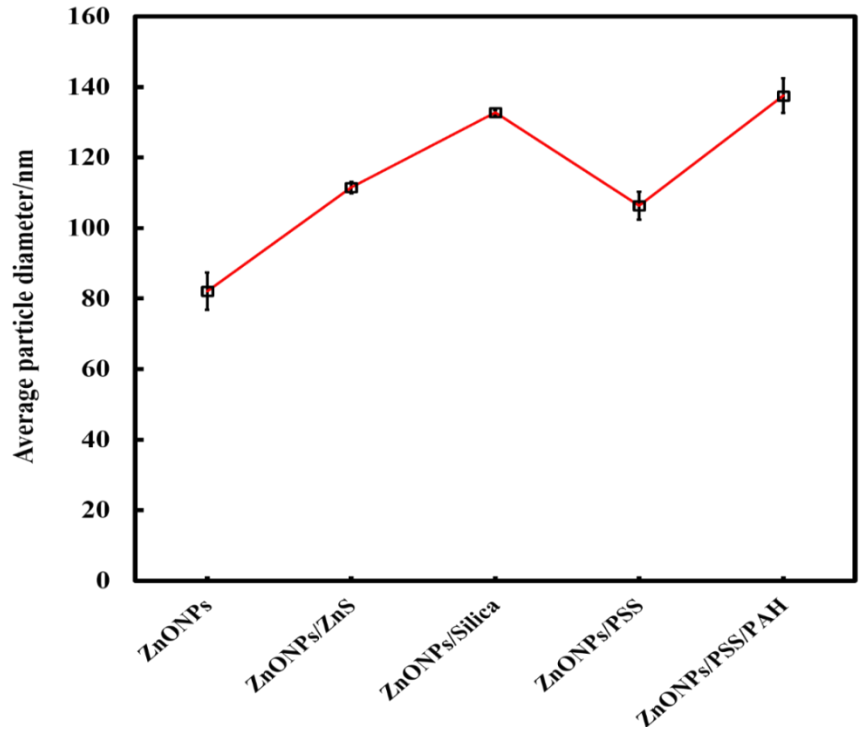


**Figure 3.25.** The particle size of bare ZnONPs, ZnONPs/PSS, ZnONPs/$SiO_2$, ZnONPs/ZnS and ZnONPs/PSS/PAH.

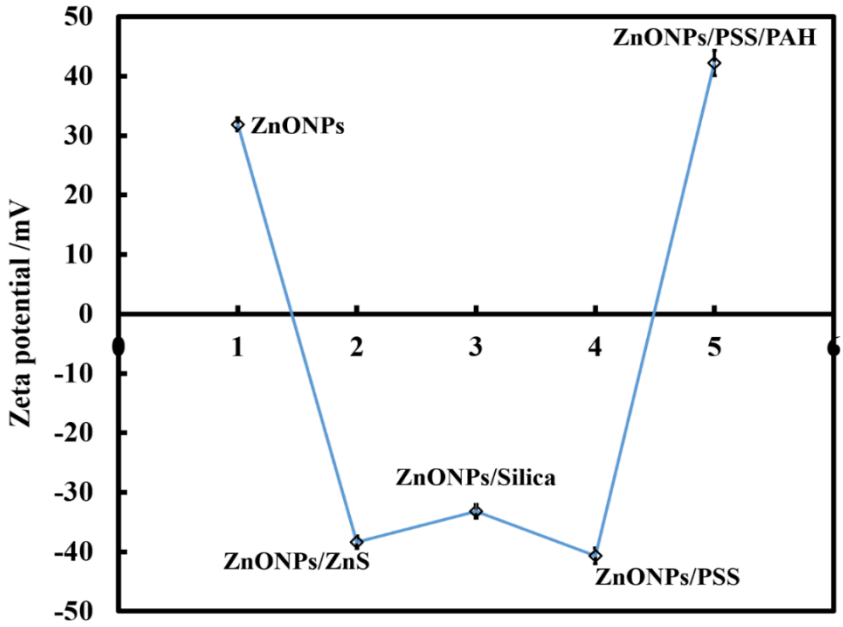


**Figure 3.26.** The zeta potential of bare ZnONPs, ZnONPs/PSS, ZnONPs/$SiO_2$, ZnONPs/ZnS and ZnONPs/PSS/PAH.

From Figure 3.25 it can be seen that the particle size of the PSS, $SiO_2$, ZnS and PAH coated ZnONP increased after each coating compared with the bare ZnONPs. The ZnONPs coated with PSS, $SiO_2$, ZnS and PAH will use in the next chapter to be incubated with individual microorganisms such as microalgae and yeast cells to assay the nanotoxicity impact of coated ZnONPs. Likewise, it useful to reveal the behaviour of bare ZnONPs, ZnONPs/PSS, ZnONPs/$SiO_2$, ZnONPs/ZnS and ZnONPs/PSS/PAH upon incubation in dark, under visible and UV light conditions.

### 3.11.1 The effect of addition of ZnONPs to PSS

The impact of utilising different techniques to add ZnONPs to PSS was investigated, including a dropwise addition with ultra-sonication, direct addition and drop by drop. Figure 3.27 shows how to affect the technique of addition of the ZnONPs to the PSS can influence the average particle diameter of ZnONPs. As can be noted from Figure 3.27, dropwise addition with vigorous shaking seemed to cause aggregation, with particle diameters approximately 228 nm. While, in the case of direct addition of ZnONPs to the PSS resulted a particle diameter about 162 nm. Nevertheless, dropwise addition with ultra-sonication was observed to be the best addition technique with the particle diameter around 106 nm. This may be explained that ultrasonic energy plays an essential role in dispersing the clustered ZnONPs upon utilising excess amount of PSS, allowing interaction with aggregated nanoparticles to give a good stability of the colloidal particles.

Thus, this technique provided good stability of PSS coated ZnONPs. Likewise, the zeta potential of ZnONPs was measured for each technique as shown in Figure 3.28.

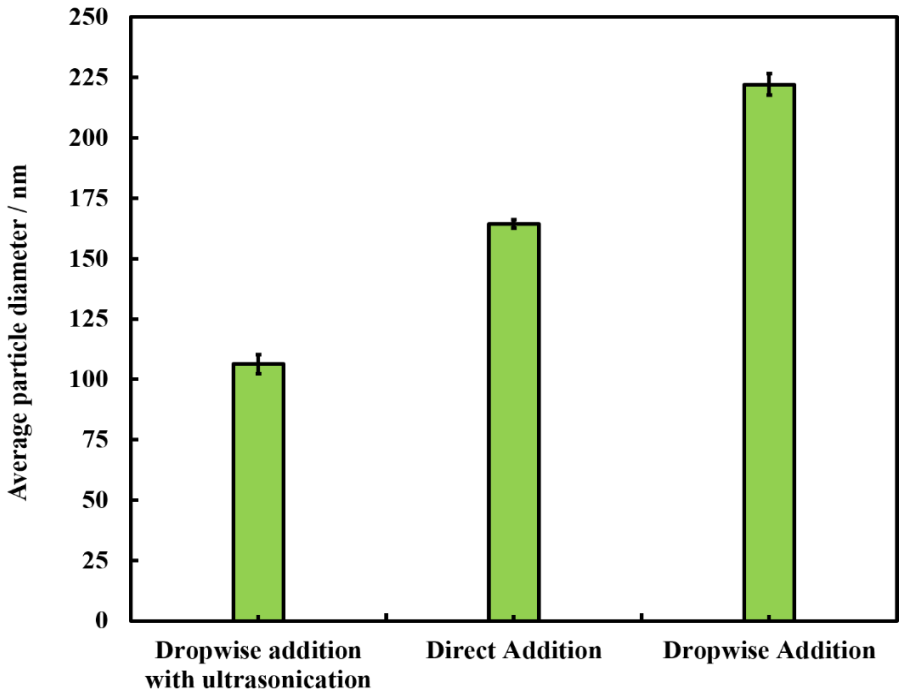


**Figure 3.27.** The impact of addition of ZnONPs to the PSS on the average particle diameter of coated ZnONPs. It was discovered that the drop-by-drop addition with ultra-sonication is the best technique with particle size106 ± 11 nm.

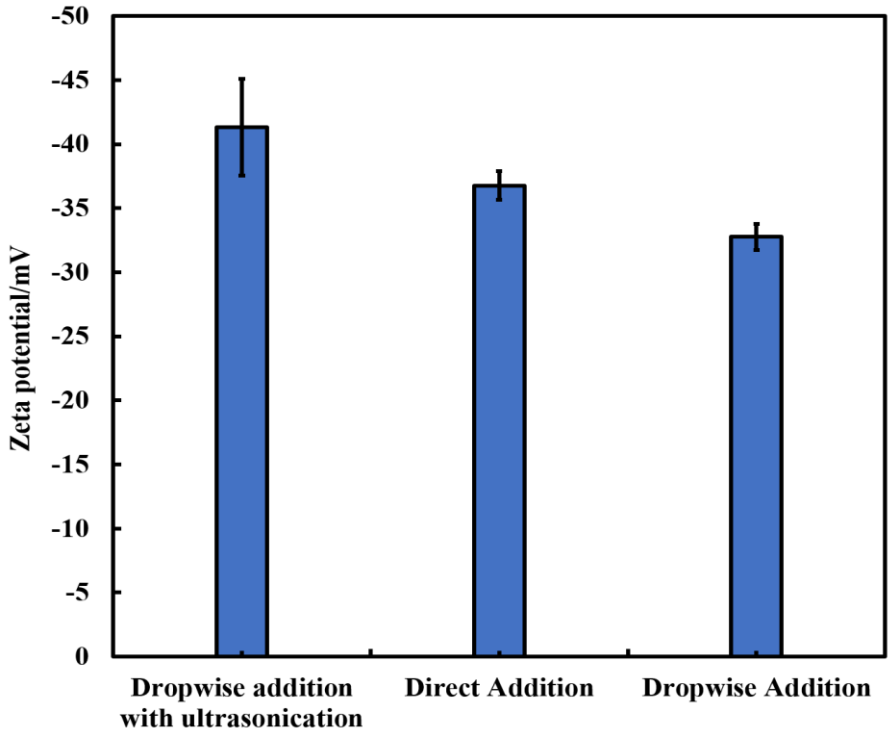


**Figure 3.28.** The impact of addition of ZnONPs to the PSS on the zeta potential of PSS-coated ZnONPs.

### 3.11.2 The zeta potential of PSS coated ZnONPs.

The zeta potential of the ZnONPs after coating with one layer of polyelectrolyte was measured in different conditions such as dark conditions, under visible and UV light as seen in Figures 3.29A, 3.29B and 3.29C. It can be concluded that the zeta potential of the polyelectrolyte-coated ZnONPs in three conditions after 24 h at different particle concentrations was stable. The purpose of these experiments was to study the stability of the coating.

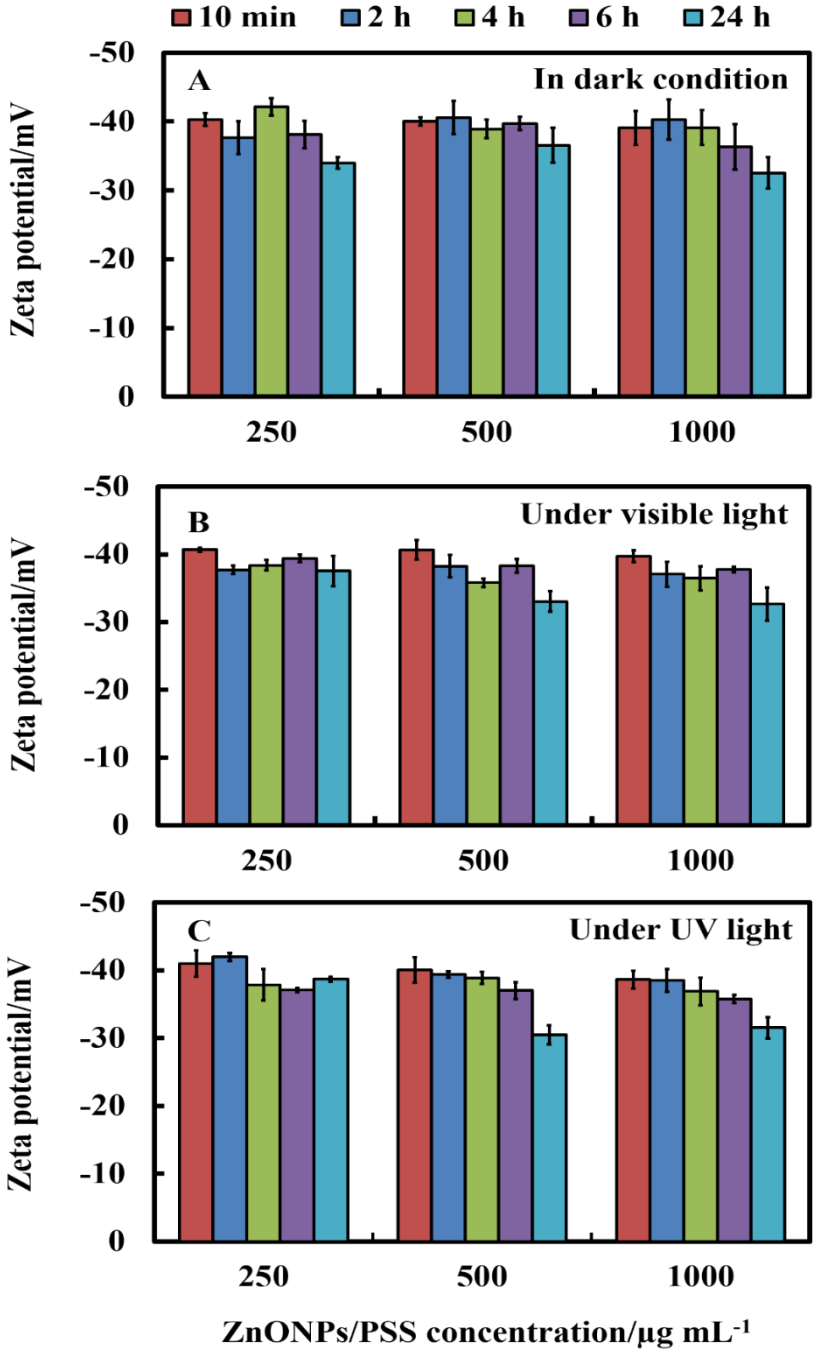


**Figure 3.29.** The zeta potential of ZnONPs coated with one layer of PSS at different concentrations (250, 500 and 1000 µg $mL^{-1}$) in (A) dark, (B) under visible and (C) UV light condition after 24 h.

## 3.12 Conclusions

This chapter mainly studied the synthesis and characterisation of surface modified zinc oxide nanoparticle. A range of ZnONPs of various crystallite size was prepared via direct precipitation method after calcining at various temperatures ranging from 100-600$^{o}$C and characterised in terms of their surface charge and average hydrodynamic diameter in aqueous suspensions. The average particle diameter of ZnONPs was found to be approximately 16 ± 5 nm using TEM and 82 ± 10 nm using Zetasizer with a surface charge around +32 ± 5 mV. The elemental composition and chemical composition of ZnONPs were confirmed by EDX and FTIR. EDX confirmed the presence of zinc and oxygen signals of zinc oxide nanoparticle which proves that the formed ZnONPs is in its highest purified form. The crystal planes of ZnONPs were determined by XRD. The results showed that there is a change in the crystallinity of the ZnONPs by increasing the calcining temperatures from 100 to 600°C. XRD spectrum revealed that no peaks related to impurities were identified, confirming the good purity of the synthesised product. The isoelectric point of ZnONPs was about pH 10.1.

Zinc sulfide, silica, anionic poly(sodium 4-styrene sulfonate) sodium salt and cationic poly(allylamine hydrochloride)-coated ZnONPs were fabricated, and convincing evidence for their surface modification was obtained through EDX, TEM and zeta potential analyses. After each coating, the zeta potential reversal became -38 mV for the ZnONPs/ZnS, -33 mV for the ZnONPs/silica and -41 mV for the ZnONPs/PSS and then the ZnONPs/PSS coating with PAH was positively charged ZnONPs/PSS/PAH with +42 mV. The hydrodynamic diameter of the ZnONPs after each coating with ZnS, silica, PSS and PAH were measured. It was found that the hydrodynamic diameter of the PSS, $SiO_2$, ZnS and PAH coated ZnONPs increased after each coating compared with the bare ZnONPs. The data indicate that surface modifications of ZnONPs, such as coating with silica layer, ZnS, PSS and PAH, may alter their biokinetics, toxicity, and thus potential medical applications.

## 3.13 References


1. A. F. Halbus, T. S. Horozov and V. N. Paunov, *Advances in colloid and interface science*, 2017, **249**, 134-148.
2. T. Dayakar, K. V. Rao, K. Bikshalu, V. Rajendar and S.-H. Park, *Materials Science and Engineering: C*, 2017, **75**, 1472-1479.
3. L. Ai, Y. Wang, G. Tao, P. Zhao, A. Umar, P. Wang and H. He, *Molecules*, 2019, **24**, 503.
4. S. Fernando, T. Gunasekara and J. Holton, *Sri Lankan Journal of Infectious Diseases*, 2018, **8**.
5. L. Zhang, Y. Jiang, Y. Ding, M. Povey and D. York, *Journal of Nanoparticle Research*, 2007, **9**, 479-489.
6. Y.-W. Wang, A. Cao, Y. Jiang, X. Zhang, J.-H. Liu, Y. Liu and H. Wang, *ACS applied materials & interfaces*, 2014, **6**, 2791-2798.
7. A. Lipovsky, Y. Nitzan, A. Gedanken and R. Lubart, *Nanotechnology*, 2011, **22**, 105101.
8. D. Raoufi, *Renewable Energy*, 2013, **50**, 932-937.
9. J. Yu and X. Yu, *Environmental science & technology*, 2008, **42**, 4902-4907.
10. M. R. Hoffmann, S. T. Martin, W. Choi and D. W. Bahnemann, *Chemical reviews*, 1995, **95**, 69-96.
11. S. Bagheri, K. Chandrappa and S. B. A. Hamid, *Der Pharma Chemica*, 2013, **5**, 265-270.
12. N. A. Salahuddin, M. El-Kemary and E. M. Ibrahim, *Nanoscience and Nanotechnology*, 2015, **5**, 82-88.
13. A. Bagabas, A. Alshammari, M. F. Aboud and H. Kosslick, *Nanoscale research letters*, 2013, **8**, 1.
14. J. Ye, R. Zhou, C. Zheng, Q. Sun, Y. Lv, C. Li and X. Hou, *Microchemical Journal*, 2012, **100**, 61-65.
15. Y. Wang, C. Zhang, S. Bi and G. Luo, *Powder Technology*, 2010, **202**, 130-136.
16. M. Thirumavalavan, K.-L. Huang and J.-F. Lee, *Materials*, 2013, **6**, 4198-4212.
17. S. Nagarajan and K. A. Kuppusamy, *Journal of nanobiotechnology*, 2013, **11**, 1.
18. L. Raj and E. Jayalakshmy, *Orient J Chem*, 2015, **31**, 51-56.
19. A. Askarinejad, M. A. Alavi and A. Morsali, *Iranian Journal of Chemistry and Chemical Engineering (IJCCE)*, 2011, **30**, 75-81.
20. G. Xiong, U. Pal, J. Serrano, K. Ucer and R. Williams, *physica status solidi (c)*, 2006, **3**, 3577-3581.
21. M. Ramasamy, Y. J. Kim, H. Gao, D. K. Yi and J. H. An, *Materials Research Bulletin*, 2014, **51**, 85-91.

# Chapter 4

# 4. Evaluation of anti-algal and anti-yeast properties of surface modified zinc oxide nanoparticles

## 4.1 Introduction

ZnO is a compound commonly recognized as safe by the Food and Drug Administration of the United States of America (21CFR182.8991). ZnO has anti-bacterial, anti-fungal and anti-viral actions and minimal toxicity to humans.[1-4] ZnONPs have a marked antibacterial ability with a high specific surface area to volume ratio. ZnONPs can inhibit the growth of both Gram negative and Gram positive bacteria. The anti-algal and anti-yeast activity of ZnONPs is related to nanoparticle size. The smaller the size is, the greater the probability for nanoparticles to have contact with the cells surface area. With the decrease of the particle size of ZnONPs, its anti-algal and anti-yeast properties increase.[5-8] Furthermore, ZnONPs have anti-corrosive and UV filtering properties. ZnONPs are easy to synthesise and have a kind of green nanomaterials that possess great biodegradability and biocompatibility.[9-11] ZnONPs have wide applications in the cosmetics industry and food packaging.[10, 12]

In this chapter, the anti-algal and anti-yeast properties of ZnONPs with different surface modifications, *i.e.*, ZnS, $SiO_2$, anionic (PSS) and cationic (PAH) were assessed. Two different types of microorganisms, *C. reinhardtii* and *S.cerevisiae* cells were used to test the antimicrobial activity of the surface modified ZnONPs in both dark, visible and UV light conditions. It was found that the ZnONP toxicity increased upon illumination with UV light compared to dark conditions because of the oxidative stress of the reactive oxygen species produced. It was observed that ZnONP nanotoxicity increased upon illumination with visible light which indicated that the nanoparticles might also interfere with the microalgae photosynthetic system leading to decreased chlorophyll content upon exposure to ZnONPs.

## 4.2 Anti-algal activity of bare ZnONPs

The anti-algal activity of ZnONPs towards *C. reinhardtii* cells upon illumination with visible and UV light as well as in dark conditions was studied. Aqueous suspensions of *C. reinhardtii* cells were exposed to an aqueous suspension of ZnONPs at varying concentrations in a range of 1-250 μg $mL^{-1}$ for several different periods of time. A control sample of *C. reinhardtii* was kept at the same conditions for the same period of time.

The number of viable *C. reinhardtii* cells was examined quickly after taking away the excess of ZnONPs from the *C. reinhardtii* suspension. Figure 4.1 shows the antimicrobial activity of bare ZnONPs on *C. reinhardtii* cells in dark, visible and UV light conditions at various exposure time up to 6 h.

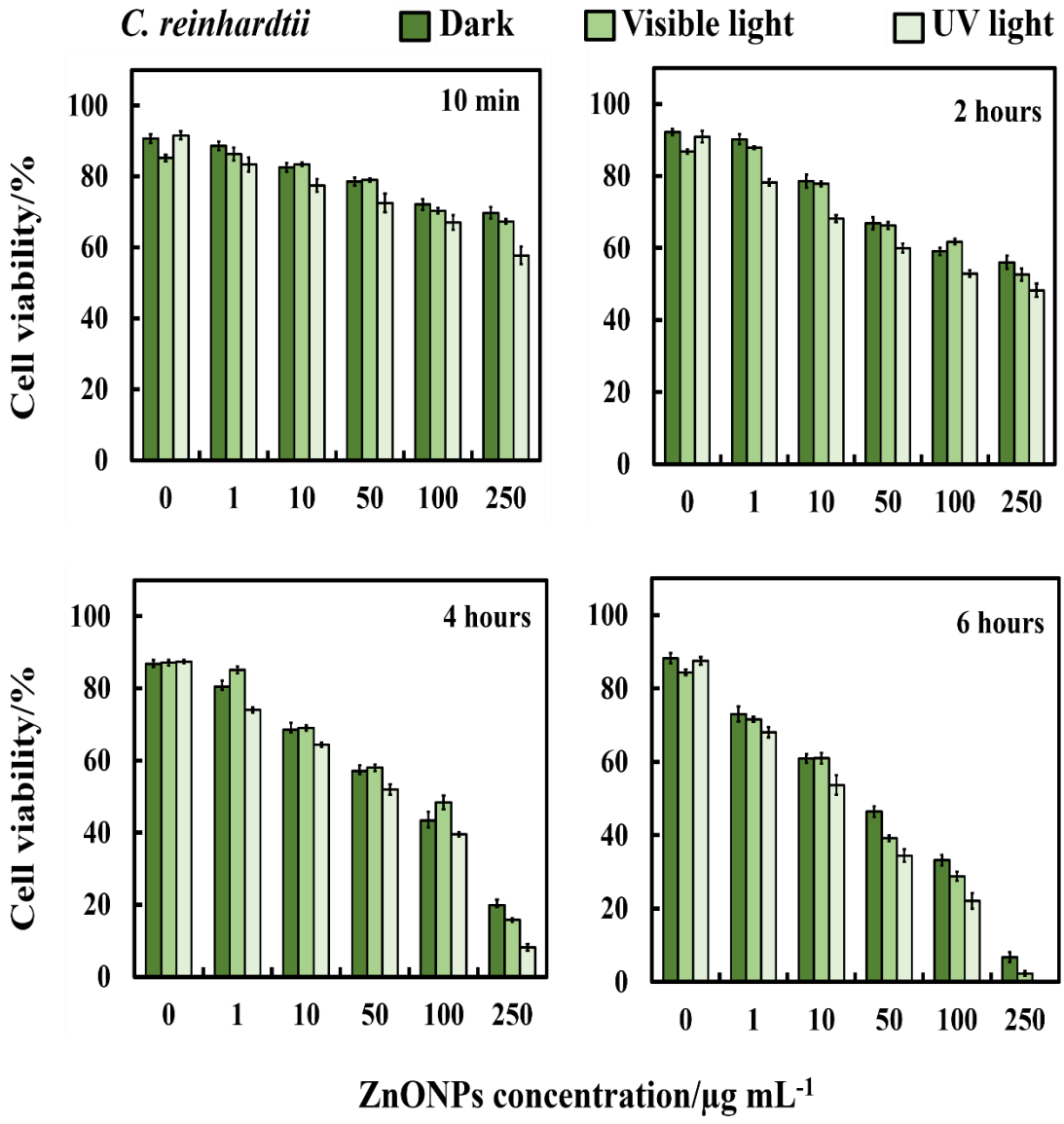


**Figure 4.1.** The anti-algal activity expressed as cell viability of ZnONPs on *C. reinhardtii* at various ZnONPs concentrations (0, 1, 10, 50, 100 and 250 μg $mL^{-1}$). The *C. reinhardtii*

was incubated with the ZnONPs at 10 min., 2 h, 4 h, and 6 h of exposure times in dark, under visible and UV light conditions.

The data in Figure 4.1 shows that immediately after incubation (10 minutes), the cell viability gradually declined with ZnONPs concentrations higher than 1 μg $mL^{-1}$. From 2 to 6 hours of exposure to visible and UV light, the number of viable *C. reinhardtii* cells also reduced. At low exposure times to visible and UV light, there was an apparent toxic impact for ZnONPs concentrations above 10 μg $mL^{-1}$. After 2 h of exposure, a sharp decline in the number of the viable *C. reinhardtii* cells was observed for ZnONPs concentrations from 10-250 μg $mL^{-1}$. At 250 μg $mL^{-1}$ ZnONPs concentration after 6 h of exposure that all *C. reinhardtii* lost their viability. The *C. reinhardtii* samples were sectioned and imaged with SEM. Figure 4.2 shows SEM images of *C. reinhardtii* cells after incubation with ZnONPs for up to 6 h. The images clearly show the adherent layer of ZnONPs which bind to the cells (Figure 4.2C, D).

Figure 4.1 shows that the antimicrobial activity of ZnONPs on the *C. reinhardtii* using UV light for 6 h is more than that with visible light and dark at similar conditions.

One possible explanation is that aqueous suspensions of ZnONPs under UV light can create ROS like $O_2^{\cdot-}$ and $H_2O_2$. [13, 14] The produced active radicals can kill or inhibit the microorganisms. The *C. reinhardtii* viability also declined in dark conditions. This can be explained that a positive surface charge leading to a strong interaction among ZnONPs and cell walls, that damages the integrity of cell membranes.

The results showed that the ZnONPs have a strong impact on viable *C. reinhardtii* above 1 μg $mL^{-1}$ for 6 h incubation time. Similar data have been presented by Vijayaraghavan and Padmavathy,[15] showing that the ZnONPs aqueous suspensions in lower concentrations (0.01-1 mM) no significant antibacterial activity towards *E. coli* was observed, and the presence of soluble $Zn^{2+}$ ions may even act as a nutrient for this microorganism. In contrast, at the highest particle concentration range (5-100 mM) the metals and ZnO are known to be toxic.[15-17]

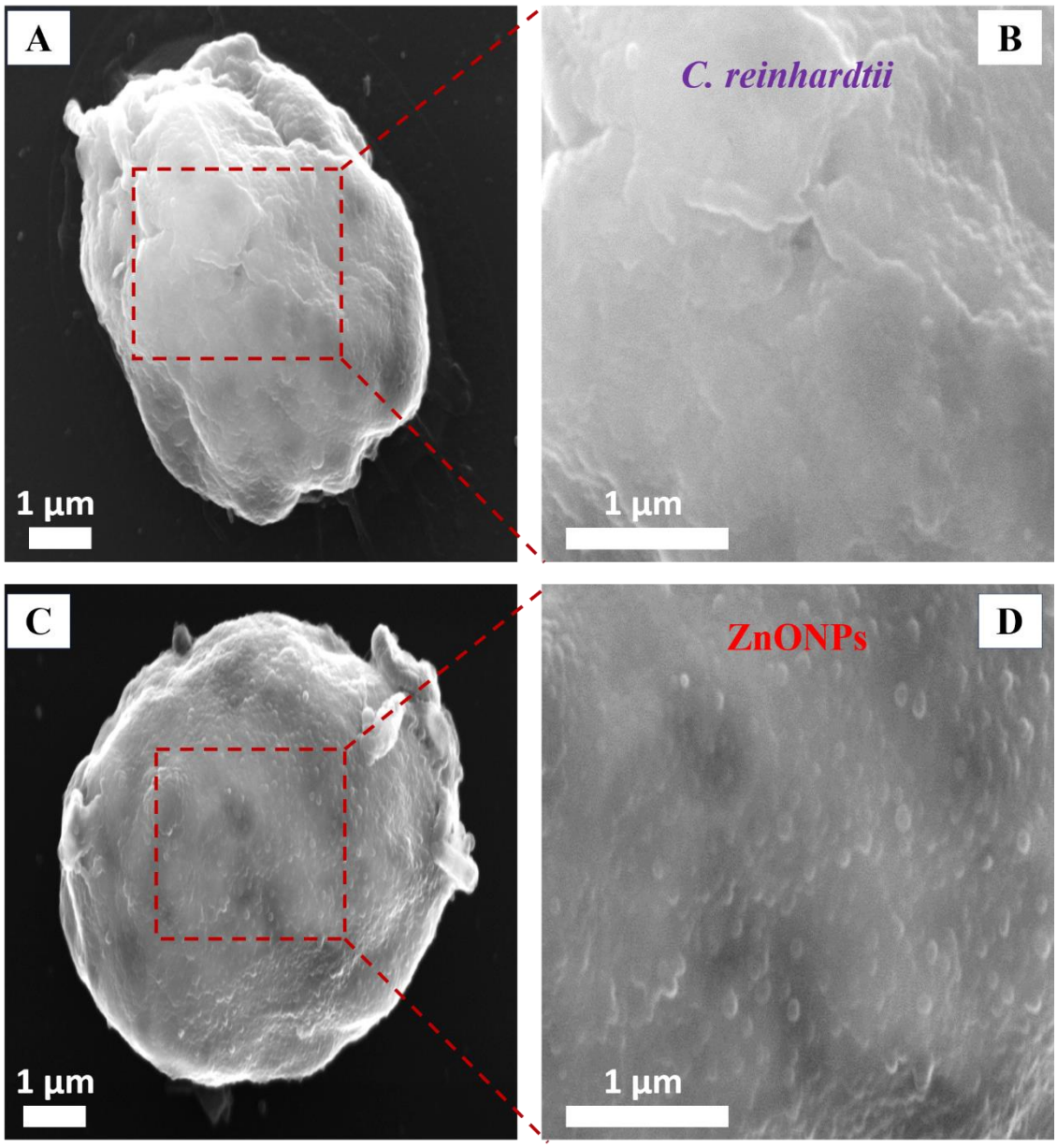


**Figure 4.2.** SEM images of *C. reinhardtii* after being incubated for 6 h with nanoparticles: (A and B) an untreated sample, (C and D) after treatment with bare ZnONPs.

Figure 4.3 shows a schematic diagram of the toxicity impact of the ZnONPs on *C. reinhardtii* cells which are as follows. Firstly, the ZnONPs adhere to the outer wall of the *C. reinhardtii*. Subsequently, ZnONPs enter *C. reinhardtii* causing disruption to the internal content of the cell and its organelles which leads to the death and destruction of these cells. Figure 4.3A shows surface-functionalized ZnONPs with cells in suspensions, the nanoparticles have attached to the outer wall of the cell in the beginning (Figure 4.3B), and further, they have entered the inner wall of the cell which can be seen in the images (Figure 4.3C and Figure 4.3D) resulting in damage of the bacterial cell. However, the exact mechanism is still under debate.

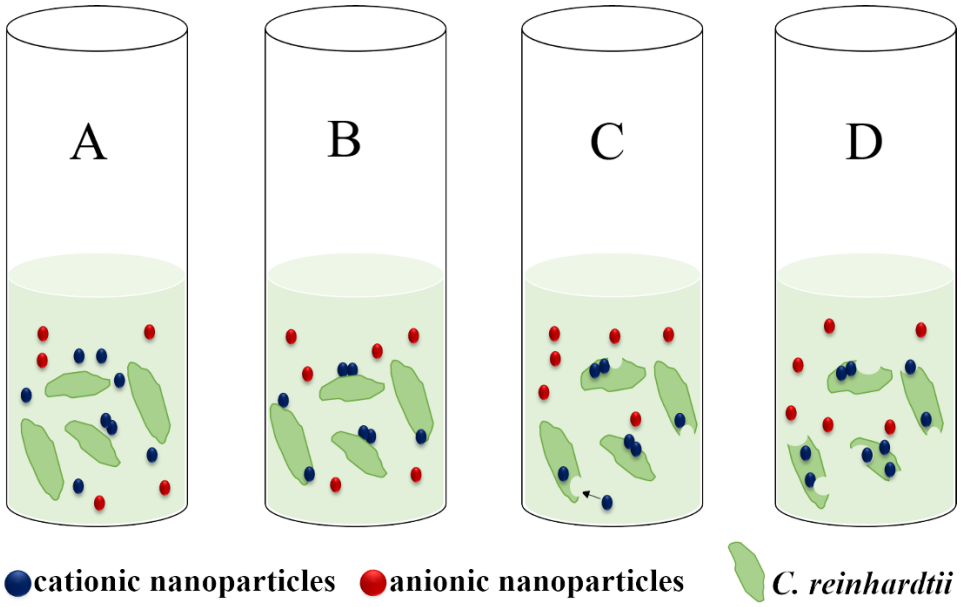


**Figure 4.3.** A possible mechanism of toxicity effect of the bare ZnONPs and surface functionalized ZnONPs on *C. reinhardtii* cells. (A) ZnONPs with cells in suspensions,(B) attachment of ZnONPs to *C. reinhardtii* membrane, (C) cleavage of *C. reinhardtii* membrane, and (D) *C. reinhardtii* lysis and death. [17]

## 4.3 Chlorophyll content of microalgae after exposure to ZnONPs

The impact of ZnONPs on *C. reinhardtii* was also indirectly assessed by determining the cells chlorophyll content as a measure of their photosynthetic ability. Figures 4.4, 4.5 and 4.7 show the UV–Vis spectra of total chlorophyll content (chlorophyll a and b) as a function of ZnONPs concentration after various exposure times and up to 6 h of in both dark, under visible and UV light conditions, respectively. It can be seen from Figures 4.6 and 4.8 that the *C. reinhardtii* apparently lose part of their chlorophyll content in the existence of ZnONPs not only upon exposure to UV light but also upon illumination with visible light.

The chlorophyll content of *C. reinhardtii* was also decreased in dark conditions in the presence of ZnONPs. Nevertheless, a sharp decrease of the cells chlorophyll content was observed upon illumination with visible and UV light above ZnONPs concentration of 1 μg $mL^{-1}$ which is near to the threshold concentration where the *C. reinhardtii* begin to decrease their viability as appeared in Figures 4.6 and 4.8. It can be concluded that the *C. reinhardtii* cells without ZnONPs did not lose their viability or discolour at the same conditions.

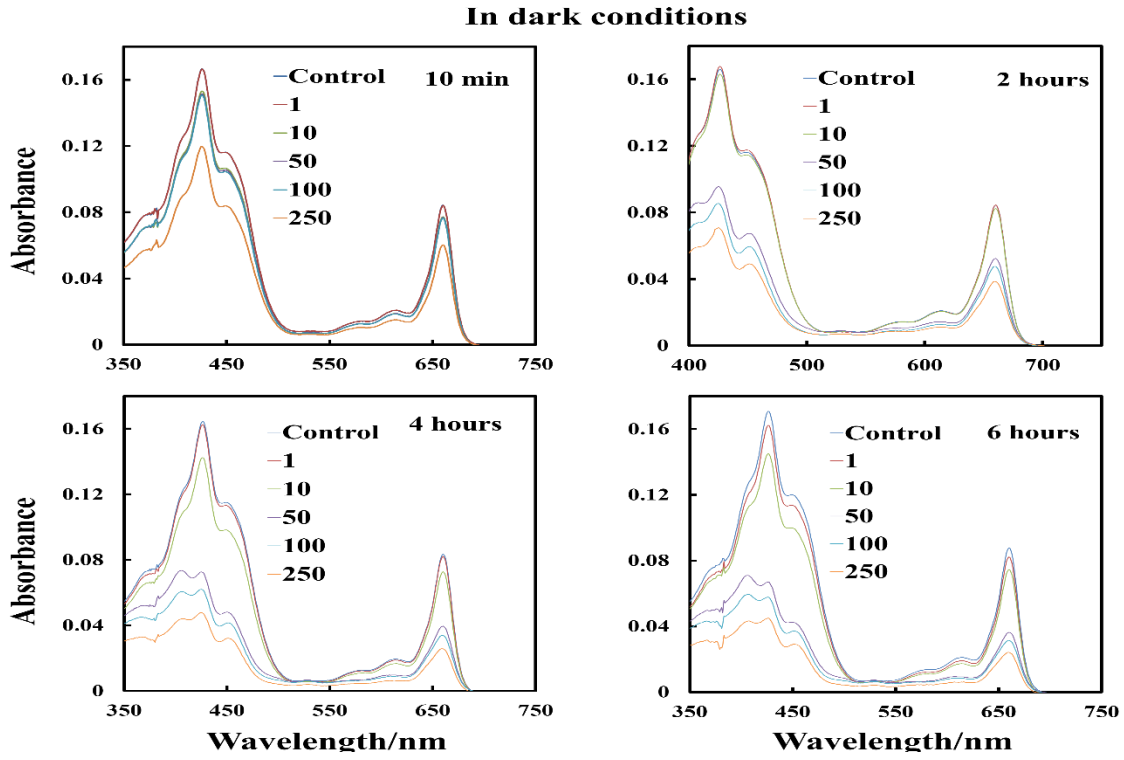


**Figure 4.4.** UV spectra of chlorophyll content in *C. reinhardtii*, the impact of the ZnONP concentration on the chlorophyll content of *C. reinhardtii* in dark conditions after 10 min., 2 h, 4 h, and 6 h.

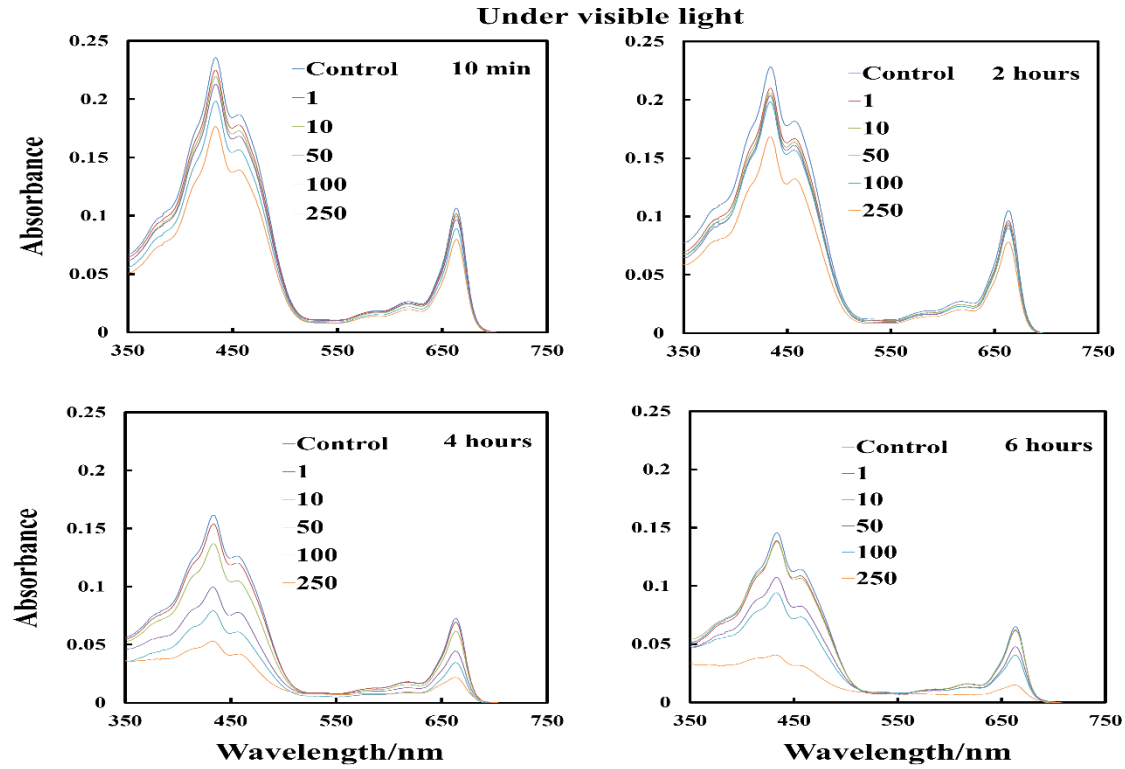


**Figure 4.5.** UV spectra of *C. reinhardtii*, the impact of the ZnONP concentration on the chlorophyll content of *C. reinhardtii* under visible light after 10 min., 2 h, 4 h, and 6 h of exposure time.

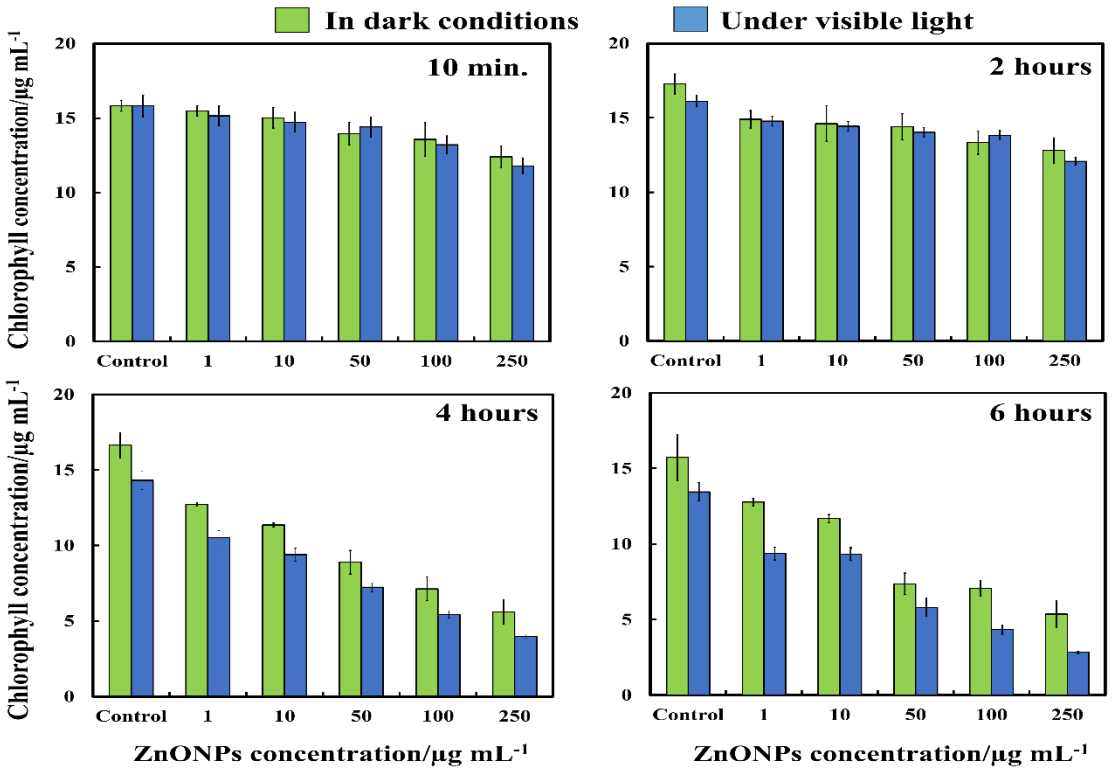


**Figure 4.6.** The impact of the ZnONPs concentration on the chlorophyll content of *C. reinhardtii* in dark and under visible light conditions after 10 min., 2 h, 4 h, and 6 h of exposure time.

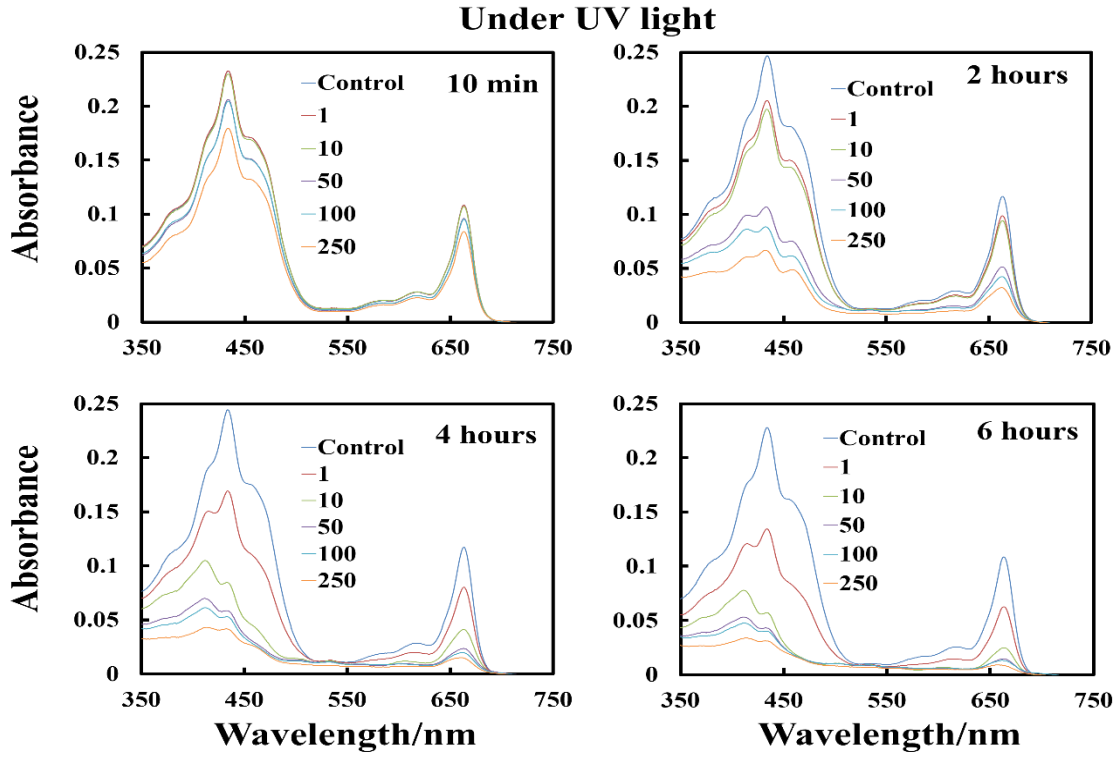


**Figure 4.7.** UV spectra of *C. reinhardtii*, the impact of the ZnONPs concentration on the chlorophyll content of *C. reinhardtii* under UV light after 10 min., 2 h, 4 h, and 6 h of exposure time.

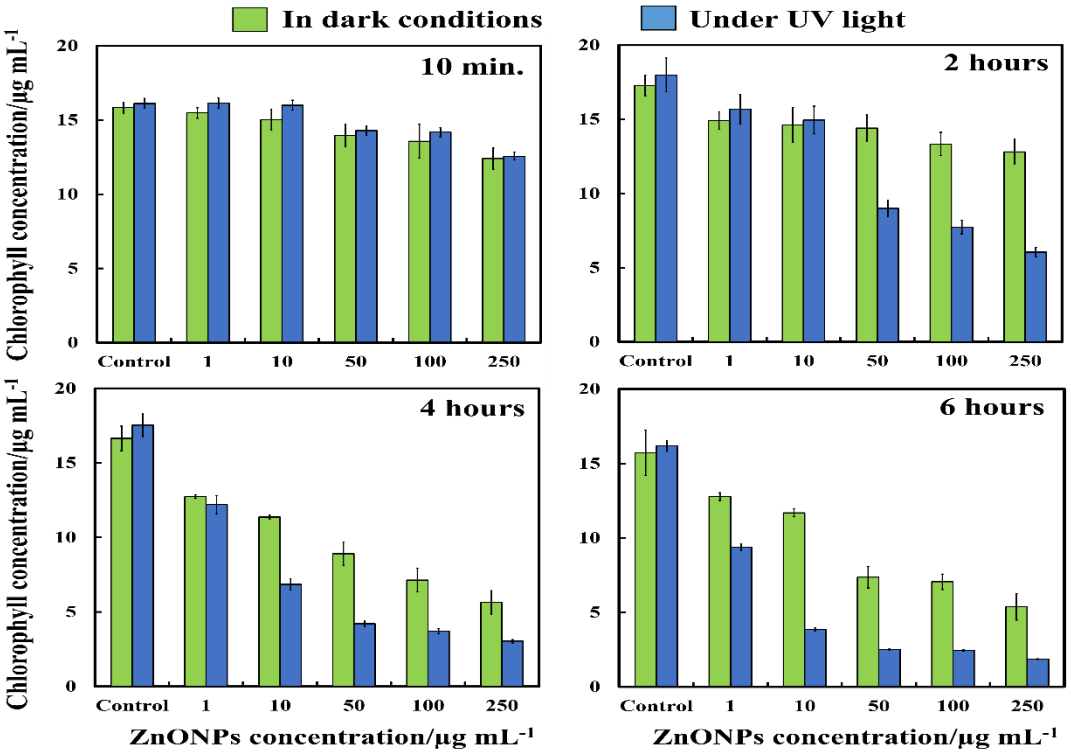


**Figure 4.8.** The impact of the ZnONPs concentration on the chlorophyll content of *C. reinhardtii* in dark and under UV light conditions after 10 min., 2 h, 4 h, and 6 h of exposure time.

Figure 4.9 exhibits optical images of the impact of ZnONPs on the *C. reinhardtii* which indicate that for the range of 0-250 $\mu$g mL$^{-1}$ particle concentrations, a different discoloration of the cells chloroplasts was noticed after 6 h of exposure to UV light.

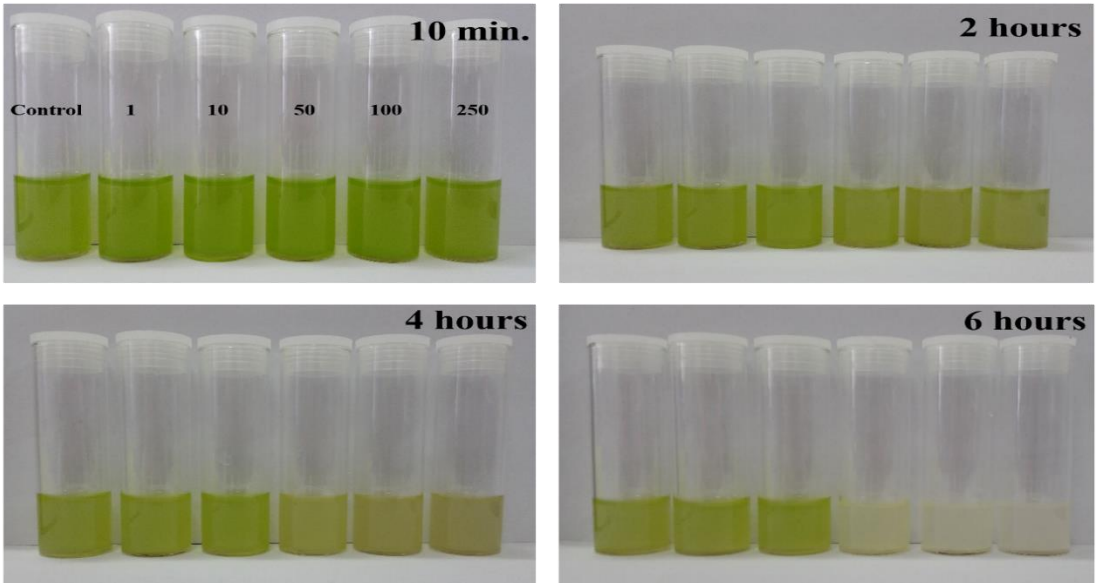


**Figure 4.9.** Optical images of *C. reinhardtii* samples after 10 min., 2h, 4h and 6 h of irradiation with UV light in the presence of ZnONPs at the particle concentration range (0-250 µg mL$^{-1}$).

## 4.4 Anti-yeast activity of bare ZnONPs

Toxicity assay of ZnONPs was conducted by incubating the nanoparticles with *S.cerevisiae* cells. An aliquot of every sample was taken to assay the number of viable *S.cerevisiae* cells after isolating the *S.cerevisiae* from the culture media by washing it 3 times with deionized water by centrifugation. Figure 4.10 shows that at 10 minutes exposure time, the number of viable *S.cerevisiae* cells gradually declined for ZnONPs concentrations above 10 μg $mL^{-1}$. After 6 h incubation time, the number of viable *S.cerevisiae* cells decreased from 10 - 750 μg $mL^{-1}$ under visible and UV light, however, in dark condition they were more than that for visible and UV light at the similar concentrations. These results are similar to previous results of *C. reinhardtii* cells of high concentrations of nanoparticles which can be explained with the positive surface charge of the ZnONPs which interact with the negatively charged of cell membranes, thus, killing the cells.

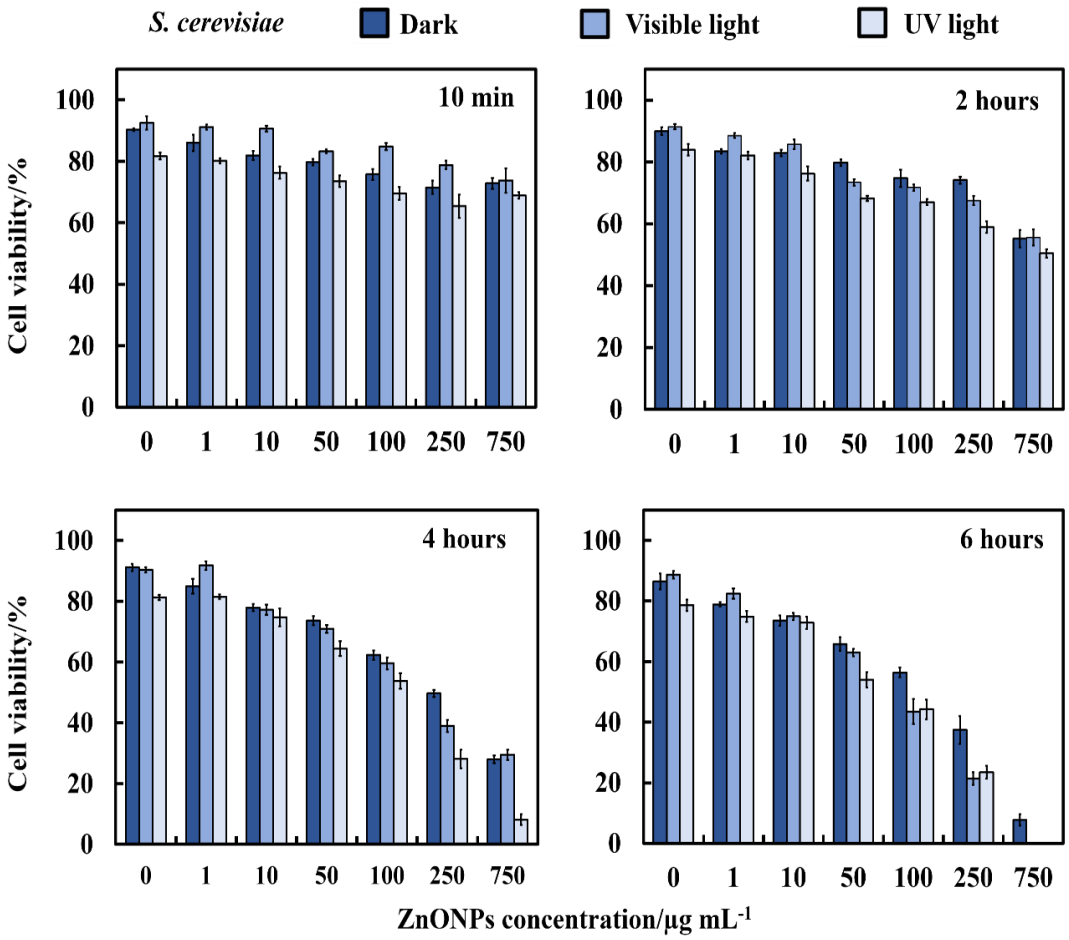


**Figure 4.10.** The anti-yeast activity of ZnONPs on *S.cerevisiae* at various ZnONPs concentrations (0, 1, 10, 50,100, 250 and 750 μg $mL^{-1}$). The *S.cerevisiae* was incubated into ZnONPs at 10 min., 2 h, 4 h, and 6 h of exposure times in dark, under visible and UV light conditions.

The data in Figure 4.10 showed that the ZnONPs have a strong impact on *S.cerevisiae* above 250 µg $mL^{-1}$ in both dark conditions, under visible and UV light. The cytotoxic impact of the ZnONPs on *C. reinhardtii* upon irradiation with visible and UV light is stronger and can be observed at much lower ZnONPs concentrations (above 10 µg $mL^{-1}$). The specific cytotoxicity of ZnONPs under visible and UV light probably occurs because of the generation of ROS on the ZnONPs surface as they are deposited on the cell wall which leads to local oxidation of phospholipids into the cell membrane. The internalisation of ZnONPs through the damaged cells walls hence may cause DNA damage, disruption of vital organelles and the electron transport chain, which leads to the death of the cells. It was found that the ZnONPs have a disruptive impact even in dark condition. These results were similar to recently reported results in the literature. [2, 13, 18-20] TEM images of *S.cerevisiae* treatment in the presence of bare ZnONPs solution showed initial results of cellular internalization of ZnONPs and cell wall disorder as shown in Figure 4.11 (B, C and D). The cell membrane in most of the *S.cerevisiae* was extensively destroyed and, most likely, the intracellular content has leaked out.

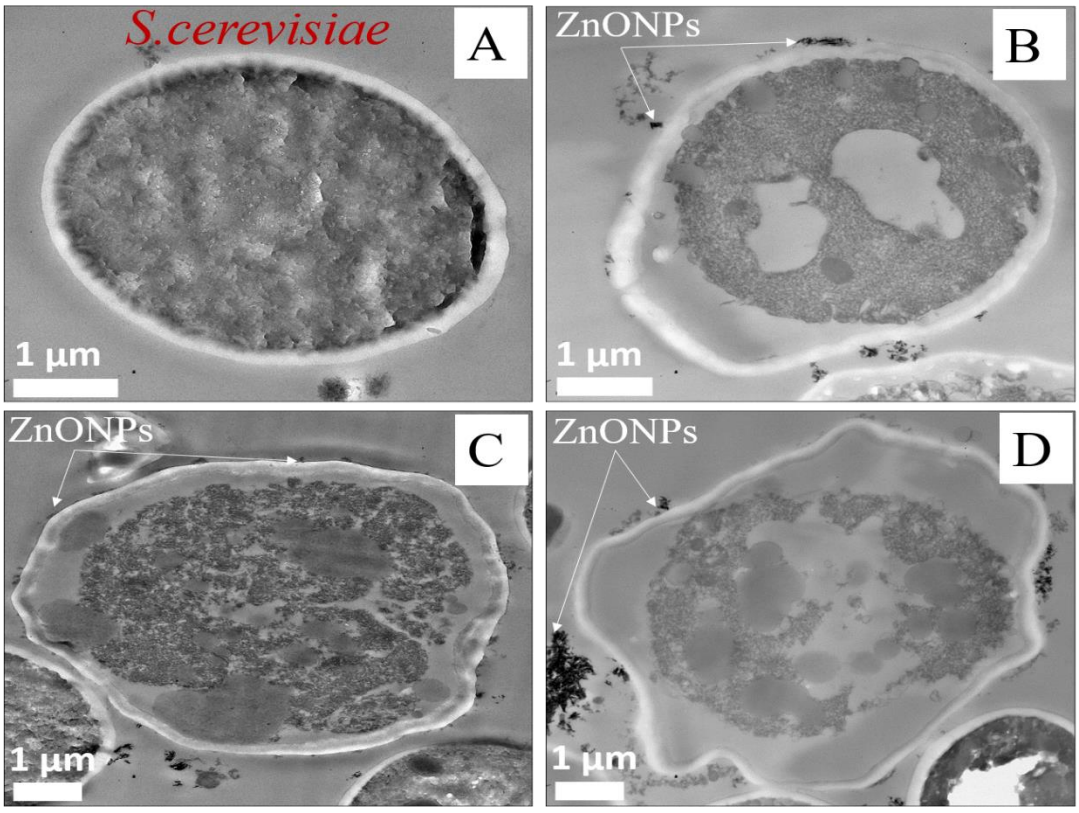


**Figure 4.11.** TEM images of *S.cerevisiae* after being exposed for 6 h with uncoated ZnONPs: (A) An untreated sample without ZnONPs (B) *S.cerevisiae* cells exposed into 100 µg $mL^{-1}$ of ZnONPs (C) *S.cerevisiae* cells exposed into 250 µg $mL^{-1}$ of ZnONPs and (D) *S.cerevisiae* cells exposed into 750 µg $mL^{-1}$ ZnONPs which displays the attachment of ZnONPs to the surface of cell.

## 4.5 Anti-algal activity of Polyelectrolyte-Coated ZnONPs

The anti-algal activity of ZnONPs coated with two layers of polyelectrolyte was studied and compared with the bare ZnONPs, due to the connection of the bare ZnONPs to the membrane of cells is largely driven by electrostatic forces. Figure 4.12 shows the cytotoxic impact of ZnONPs coated with one layer of anionic polyelectrolyte on the *C. reinhardtii* cells in dark, visible and UV light conditions. The data in Figure 4.12 shows that the toxic impact of ZnONPs/PSS on the *C. reinhardtii* viability in dark, visible and UV light conditions is much lower than the one of the bare ZnONPs (Figure 4.1).

After 6 h of incubation at higher particle concentrations of ZnONPs (250 μg $mL^{-1}$) there was remarkable difference between the viability of *C. reinhardtii* in dark condition and under UV light is solely because of the photoactivity of the ZnONPs. It can be concluded that the functionalization of the ZnONPs with PSS decreased its anti-algal activity perhaps due to the electrostatic repulsion of the coated ZnONPs from the surface of cells as both of ZnONPs/PSS and cell membranes have a negative surface charge.

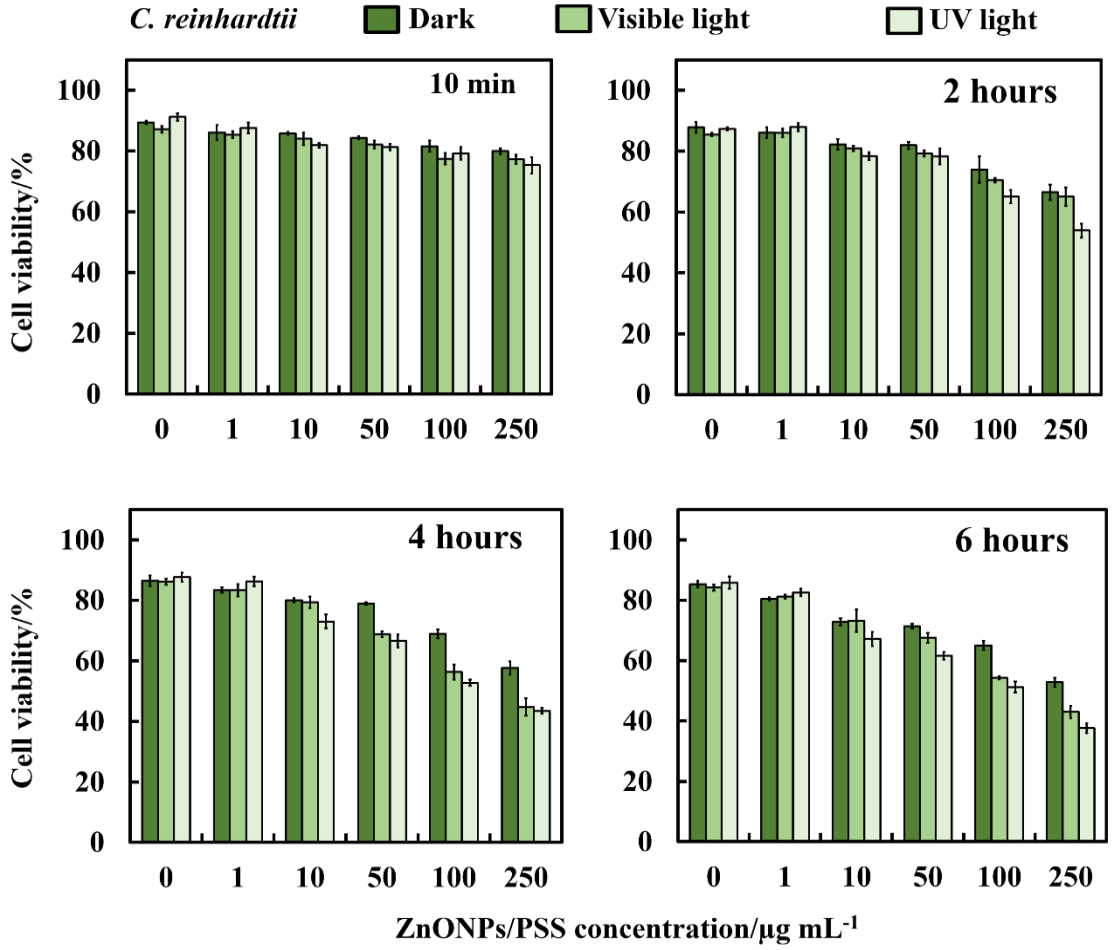


**Figure 4.12.** Comparison of the *C. reinhardtii* viability at various concentrations of the surface functionalized ZnONPs with PSS in dark, visible, and UV light conditions at different incubation times.

ZnONPs/PSS was coated with PAH which gives the overall positive charge of the nanoparticles ZnONPs/PSS/PAH to study the impact various charges on the *C. reinhardtii*. The data in Figure 4.13 where a next layer of the PAH was added the percentage of the *C. reinhardtii* cells decreases significantly. At the lower particle concentration of ZnONPs/PSS/PAH which is 250 µg $mL^{-1}$ after 6 h exposure time; 100 % of the *C. reinhardtii* were killed, i.e. these cationic coated particles are even more antimicrobial than the bare ZnONPs in both dark, visible light and UV light conditions. This form of alternating antimicrobial activity of the polyelectrolyte coated ZnONPs appears to be consistent with their surface charge and the resulting electrostatically driven adhesion to the negatively charged cells wall surface. These results indicated that the cationic NPs (the uncoated ZnONPs and ZnONPs/PSS/PAH) have more antimicrobial activity than their anionic form ZnONPs/PSS.

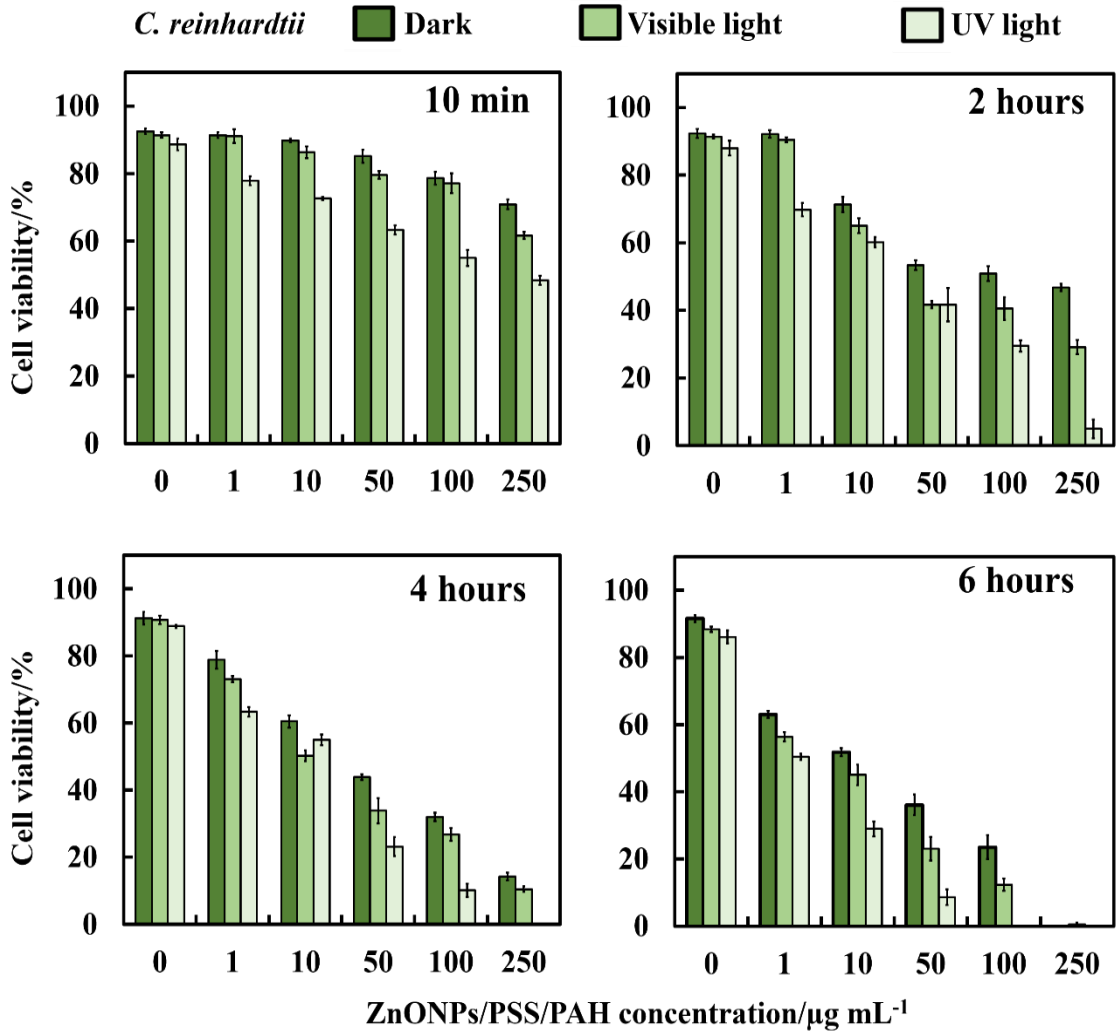


**Figure 4.13.** Comparison of the *C. reinhardtii* viability at various concentrations of the surface functionalized of ZnONPs with PSS and PAH in dark, visible, and UV light conditions at different incubation times.

Figure 4.14 shows SEM images of *C. reinhardtii* cells after incubation with ZnONPs coated with PSS and PAH layers. The SEM image in Figure 4.14A and 4.14B indirectly confirms lack of nanoparticle accumulation due to the electrostatic repulsion between the anionic ZnONPs/PSS and the negatively charged *C. reinhardtii* cell wall. Figure 4.14C and 4.14D show significant accumulation of PAH-surface-functionalized ZnONPs on the cell walls which corresponds to a much higher activity towards *C. reinhardtii*.

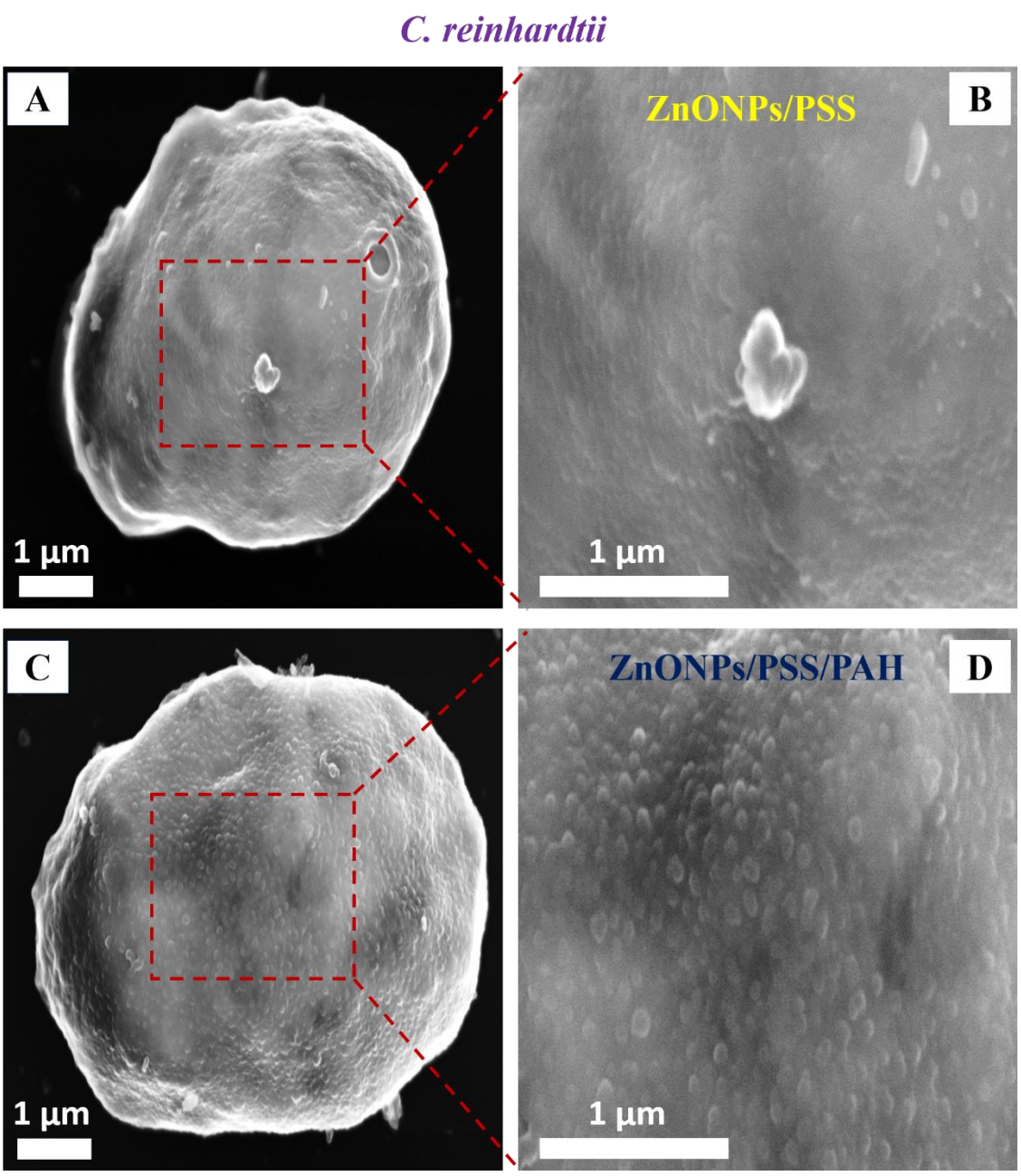


**Figure 4.14.** SEM images of *C. reinhardtii* after being incubated for 6 h to ZnONPs coated with PSS and PAH: (A and B) after treatment with ZnONPs/PSS, (C and D) after treatment with ZnONPs/PSS/PAH.

## 4.6 Anti-yeast activity of polyelectrolyte -coated ZnONPs

The anti-yeast activity of polyelectrolyte-coated ZnONPs toward *S.cerevisiae* cells was also determined. Figure 4.15 shows that at 10 minutes incubate time, the *S.cerevisiae* viability in dark and under visible and UV light condition was at the same level as the untreated sample. When the incubation time of ZnONP/PSS with cells increased to 2 h, no obvious toxic impact in the *S.cerevisiae* cell viability was observed up to 750 μg $mL^{-1}$. However, there was the impact of ZnONP/PSS observed at 1000 and 5000 μg $mL^{-1}$ in both dark, visible and UV light conditions. After 6 h incubation time, 100 μg $mL^{-1}$ ZnONPs/PSS concentration showed no anti-yeast activity in dark condition, visible and UV light while concentrations higher than 100 μg $mL^{-1}$, indicated decrease of cell viability under visible, UV light and dark conditions. These results require some discussion with regard to the conceivable factors that may contribute to the nanotoxicity of the coated ZnONPs on *S.cerevisiae* cells, which vary from their impact on the *C. reinhardtii* cells. Especially, *S.cerevisiae* cells have much thicker cell walls approximately 200 nm, higher than *C. reinhardtii* cell walls; the data suggests that it takes a much higher ZnONPs/PSS concentration to impact the *S.cerevisiae* cell viability. The results show that by coating the ZnONPs with an outer anionic polyelectrolyte layer their toxicity is greatly decreased for both *C. reinhardtii* and *S.cerevisiae* cells because of the electrostatic repulsion between the cells surface and the ZnONPs/PSS, which is seen for these samples by TEM and SEM (Figure 4.17A, B and Figure 4.18C).

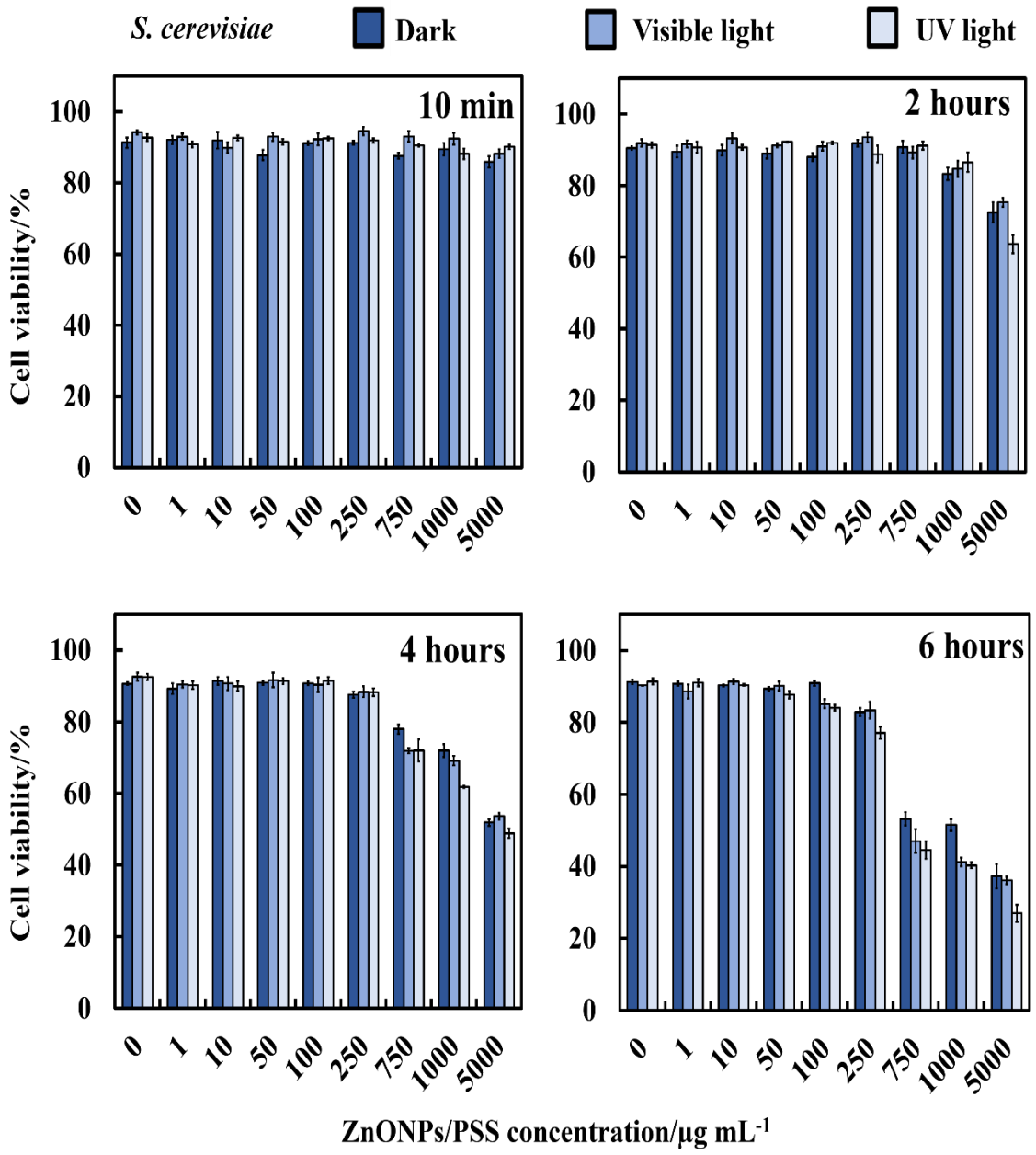


**Figure 4.15.** The antimicrobial activity of ZnONPs coated with one layer of PSS on *S.cerevisiae* cells at different particle concentrations. The *S.cerevisiae* was incubated with the PSS-surface-functionalized ZnONPs at 10 min., 2 h, 4 h, and 6 h.

Figure 4.16 shows the antimicrobial activity of coated ZnONPs with PSS and PAH polyelectrolytes at various ZnONPs/PSS/PAH concentrations on the number of viable *S.cerevisiae* cells. Figure 4.16 shows that after 6 h exposure times, the PAH-surface-functionalized ZnONPs showed excellent anti-yeast activity on cells even at lower particle concentrations in dark, and under visible light and UV light condition. A strong antimicrobial activity of the PAH-surface-functionalized ZnONPs on *S.cerevisiae* cells viability was discovered upon illumination with visible and UV light. The reason behind

that, upon illumination with visible light and UV light, the *S.cerevisiae* cell walls are probably to endure more damage from the ROS created in their vicinity which may facilitate further ZnONPs internalisation at higher concentrations of the ZnONPs/PSS/PAH and incubation times. In contrast, upon incubating the *S.cerevisiae* cell with the anionic nanoparticles (ZnONPs/PSS), no obvious difference between the number of viable *S.cerevisiae* cells until 250 µg $mL^{-1}$ particle concentration both in dark conditions, visible light and UV light for up to 6 h of exposure time. These results were also supported by TEM and SEM images of *S.cerevisiae* (Figure 4.17C, D and Figure 4.18D).

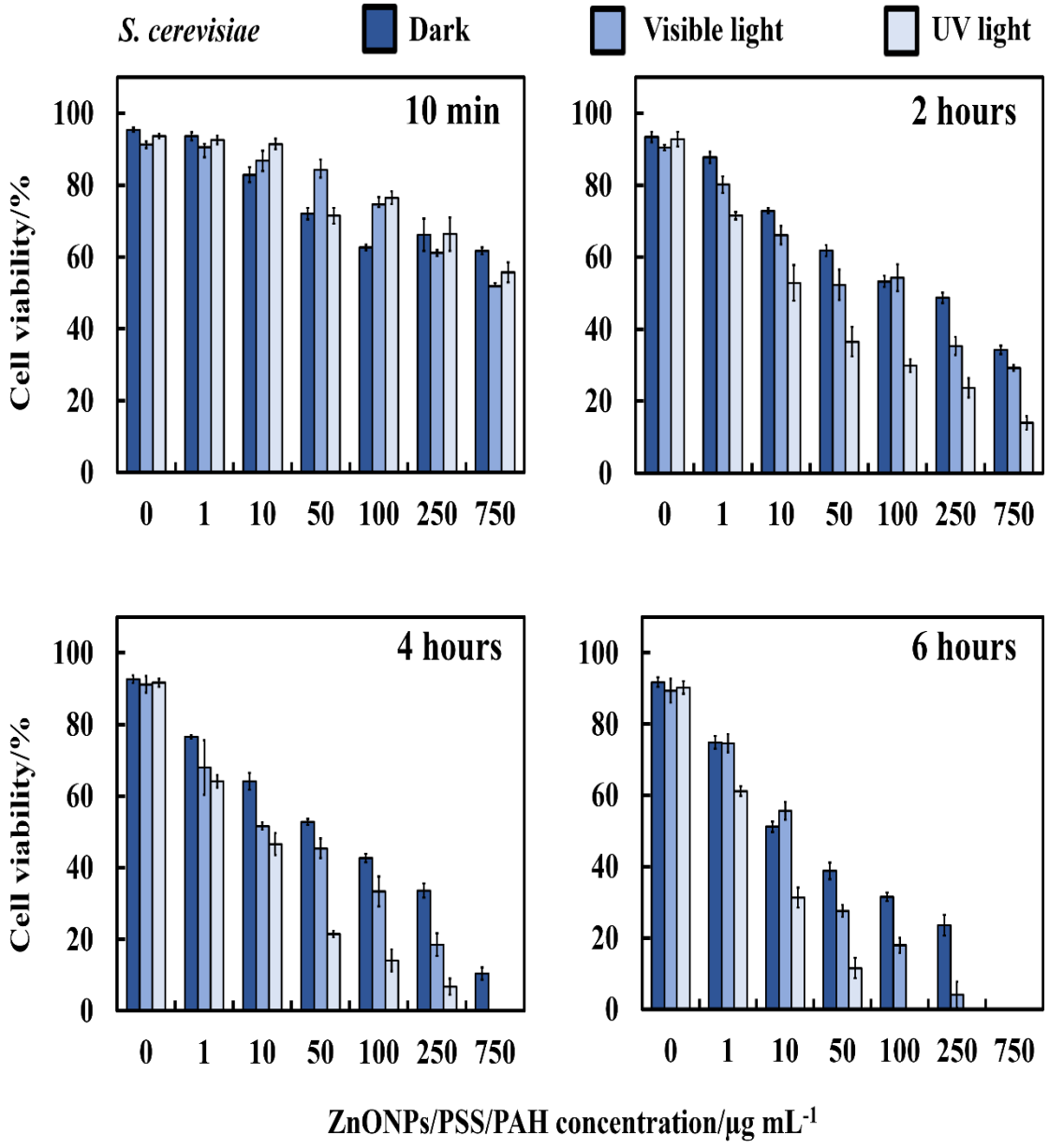


**Figure 4.16.** Comparison of the *S.cerevisiae* viability at various concentrations of the surface functionalized of ZnONPs with PSS and PAH in dark, visible and UV light conditions at different incubation times.

Figure 4.17 and Figure 4.18 shows TEM and SEM images of *S.cerevisiae* exposed into ZnONPs coated via various layers. The TEM and SEM image in Figure 4.17 A, B and Figure 4.18C encouraged all proposition that the electrostatic repulsion among the anionic nanoparticles ZnONPs/PSS and the negative charge of *S.cerevisiae* led to declined connection on the surface of *S.cerevisiae*. Figure 4.17 C, D and Figure 4.18D shows a great accumulation of PAH-surface-functionalized ZnONPs which led to the greater activity towards *S.cerevisiae* cells.

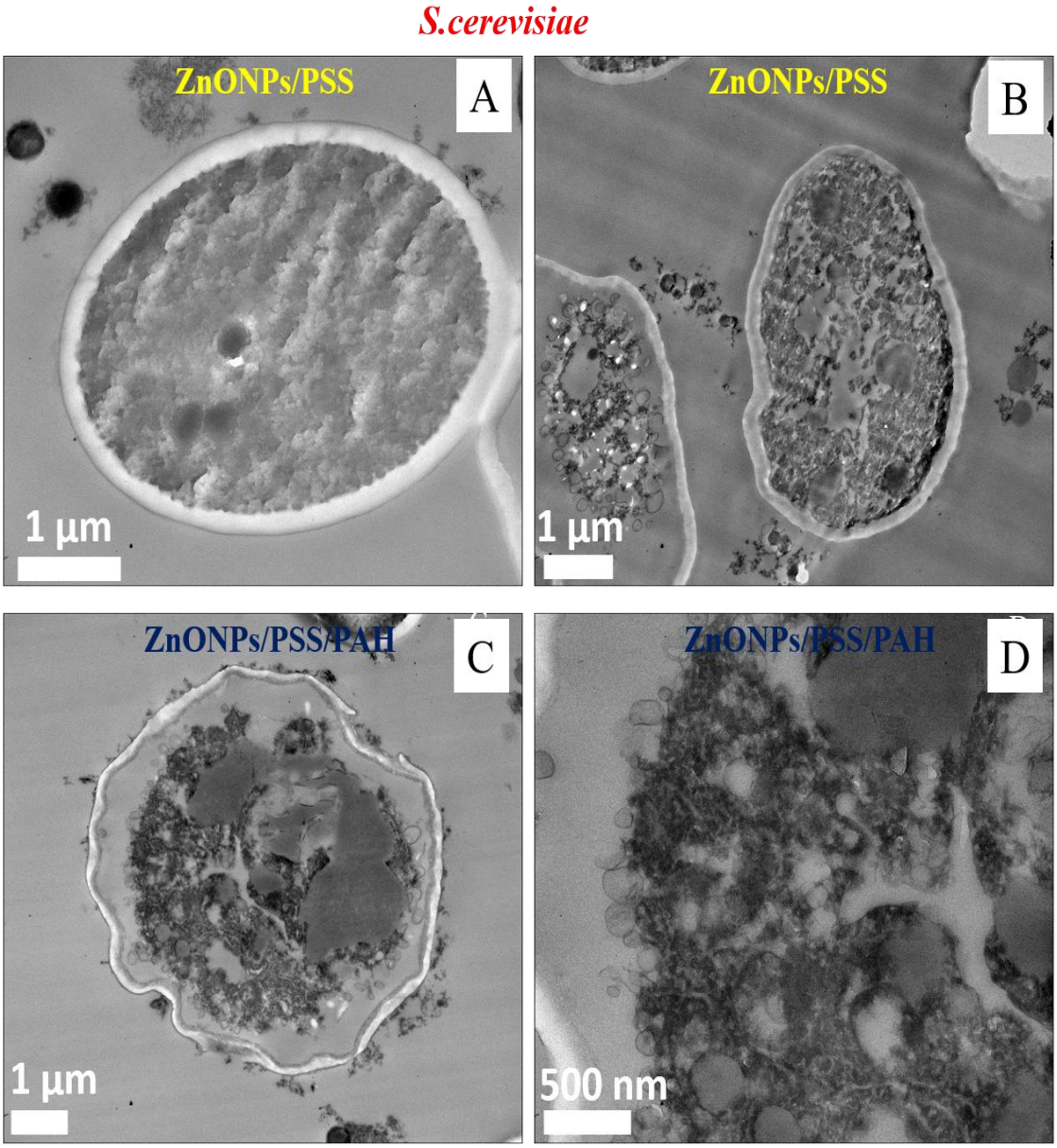


**Figure 4.17.** TEM images of *S.cerevisiae* after being exposed for 6 h with ZnONPs functionalized with PSS and PAH: (A) *S.cerevisiae* exposed to 250 µg $mL^{-1}$ ZnONPs/PSS (B) *S.cerevisiae* exposed to 5000 µg $mL^{-1}$ ZnONPs/PSS (C and D) *S.cerevisiae* exposed to 750 µg $mL^{-1}$ ZnONPs/PSS/PAH.

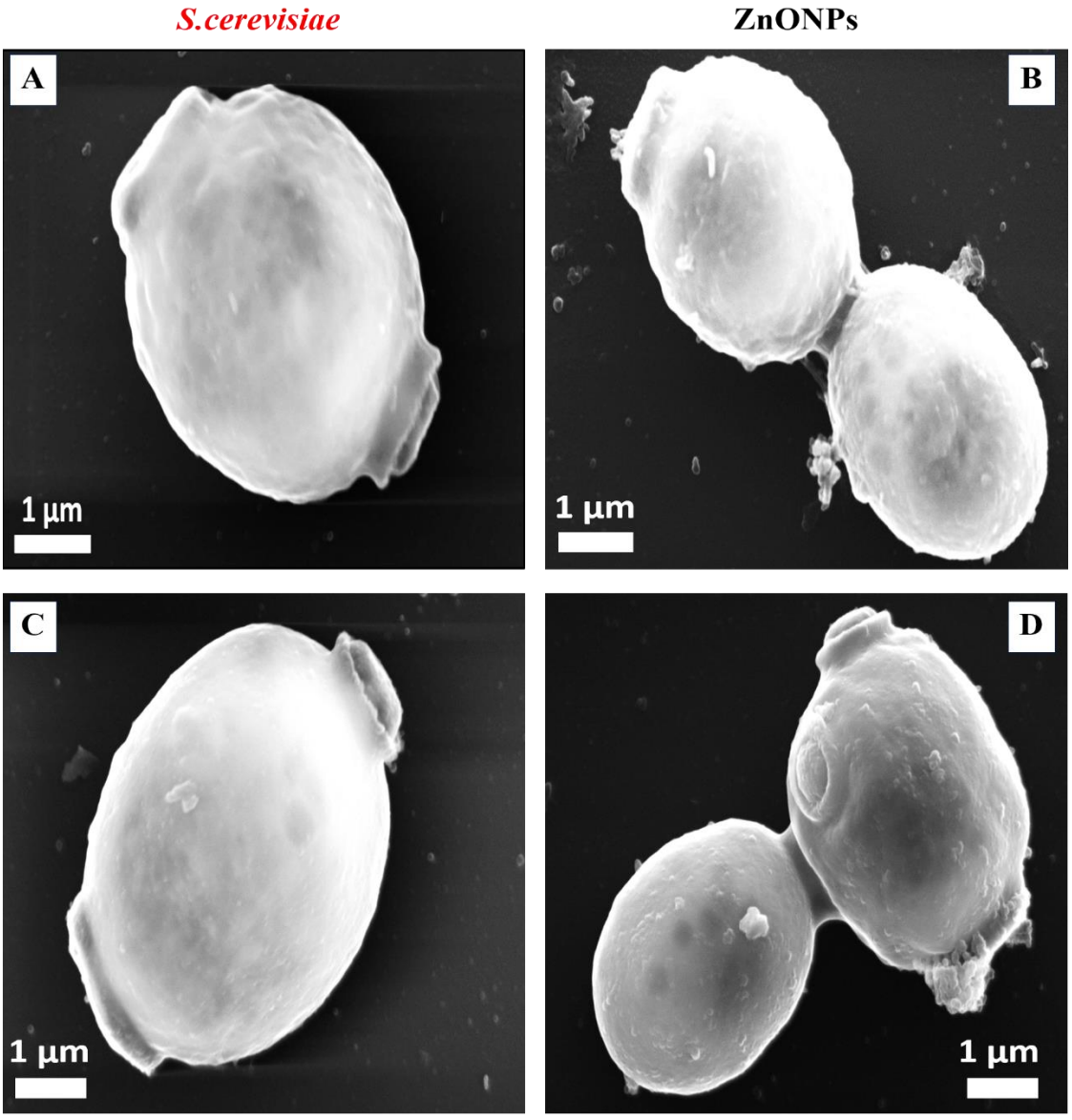


**Figure 4.18.** SEM images of *S.cerevisiae* after being incubated for 6 h into 750 µg $mL^{-1}$ bare and surface functionalized of ZnONPs: (A) an untreated sample without ZnONPs (B) *S.cerevisiae* incubated with ZnONPs (C) *S.cerevisiae* incubated with ZnONPs/PSS (D) *S.cerevisiae* incubated with ZnONPs/PSS/PAH.

## 4.7 Toxicity effect of silica-coated ZnONPs on *C. reinhardtii* and *S.cerevisiae*

The anti-algal and anti-yeast activity of ZnONPs coated with a layer of silica on the *C. reinhardtii* and *S.cerevisiae* cells viability was investigated at various exposure time (10 min., 2 h, 4 h, and 6 h). Cells were removed from the culture media by centrifugation, and a fixed amount of cells were incubated with dispersed ZnONPs/$SiO_2$ solutions of different

particle concentrations as shown in Figure 4.19 and Figure 4.20. The cells viability was then measured at various incubation times utilising an automatic cell counter by FDA cell viability assay. Figure 4.19 shows that there is no pronounced toxicity impact of ZnONPs/$SiO_2$ on the *C. reinhardtii* viability in dark, visible and UV light conditions at 10 minutes and 2 h incubation time. After 6 h of incubation with *C. reinhardtii* cells, no pronounced toxicity effect in the *C. reinhardtii* viability was observed up to 50 μg $mL^{-1}$ but there was a cytotoxic impact of ZnONP/$SiO_2$ measurable at 100 and 250 μg $mL^{-1}$ in dark, visible and UV light conditions. It was found that the toxicity impact of ZnONPs/$SiO_2$ on the *C. reinhardtii* viability at the same conditions is much lower than the one of the bare ZnONPs (see Figure 4.1). These results were also confirmed by SEM images (Figure 4.21A) of the treated *C. reinhardtii* cells with ZnONPs/$SiO_2$.

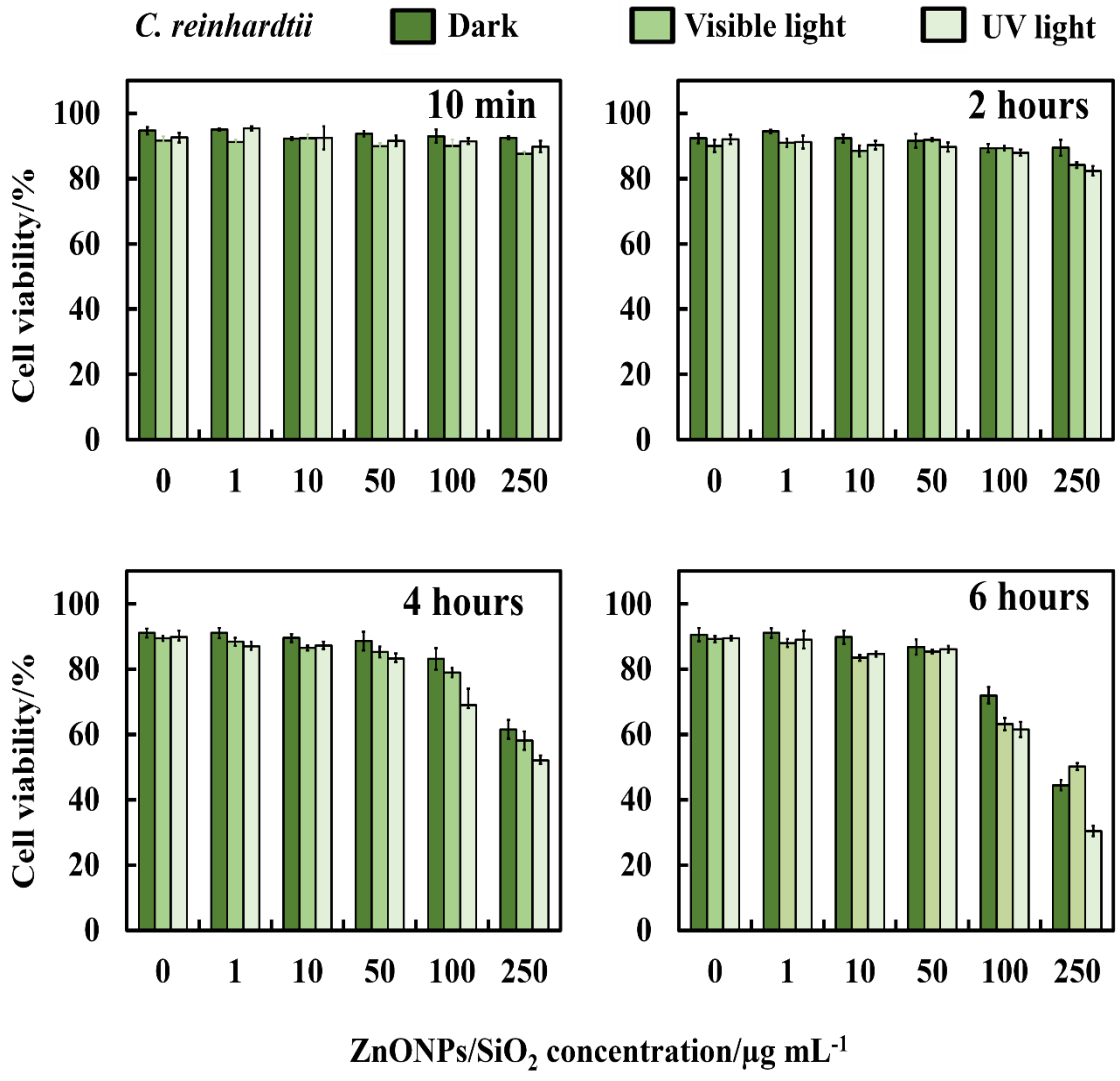


**Figure 4.19.** The effect of ZnONPs coated with layer of silica on the viability of *C. reinhardtii* at different particle concentrations. The cells were incubated with the $SiO_2$-surface-functionalized ZnONPs at 10 min., 2h, 4h, and 6 h of exposure times.

Figure 4.20 shows the toxicity effect on *S.cerevisiae* cells of different concentrations of ZnONPs/$SiO_2$. The data in Figure 4.20 shows that for exposure times at 10 minutes and 2 h, no measurable change in the *S.cerevisiae* viability was observed for ZnONPs/$SiO_2$ even at high particle concentrations, likewise important difference were not seen between the samples kept in dark or in visible and UV light conditions at the same ZnONPs/$SiO_2$ concentration. While for exposure times at 4 h, the ZnONPs/silica showed a toxic impact on *S.cerevisiae* viability at higher concentrations of ZnONPs/silica (750, 1000 and 5000 μg $ml^{-1}$), the impact was less at concentration 250 μg $ml^{-1}$. After 6 h incubation times, concentrations of 1-100 μg $mL^{-1}$ ZnONPs/$SiO_2$ had no impact, but at 250 μg $mL^{-1}$ there was a slightly decrease in the *S.cerevisiae* viability in the presence UV light compared to dark for the same conditions. The results in Figure 4.20 indicate that the anti-yeast activity of ZnONPs/$SiO_2$ under visible light, UV light as well as in dark conditions was less than the one of the uncoated ZnONPs (see Figure 4.10).

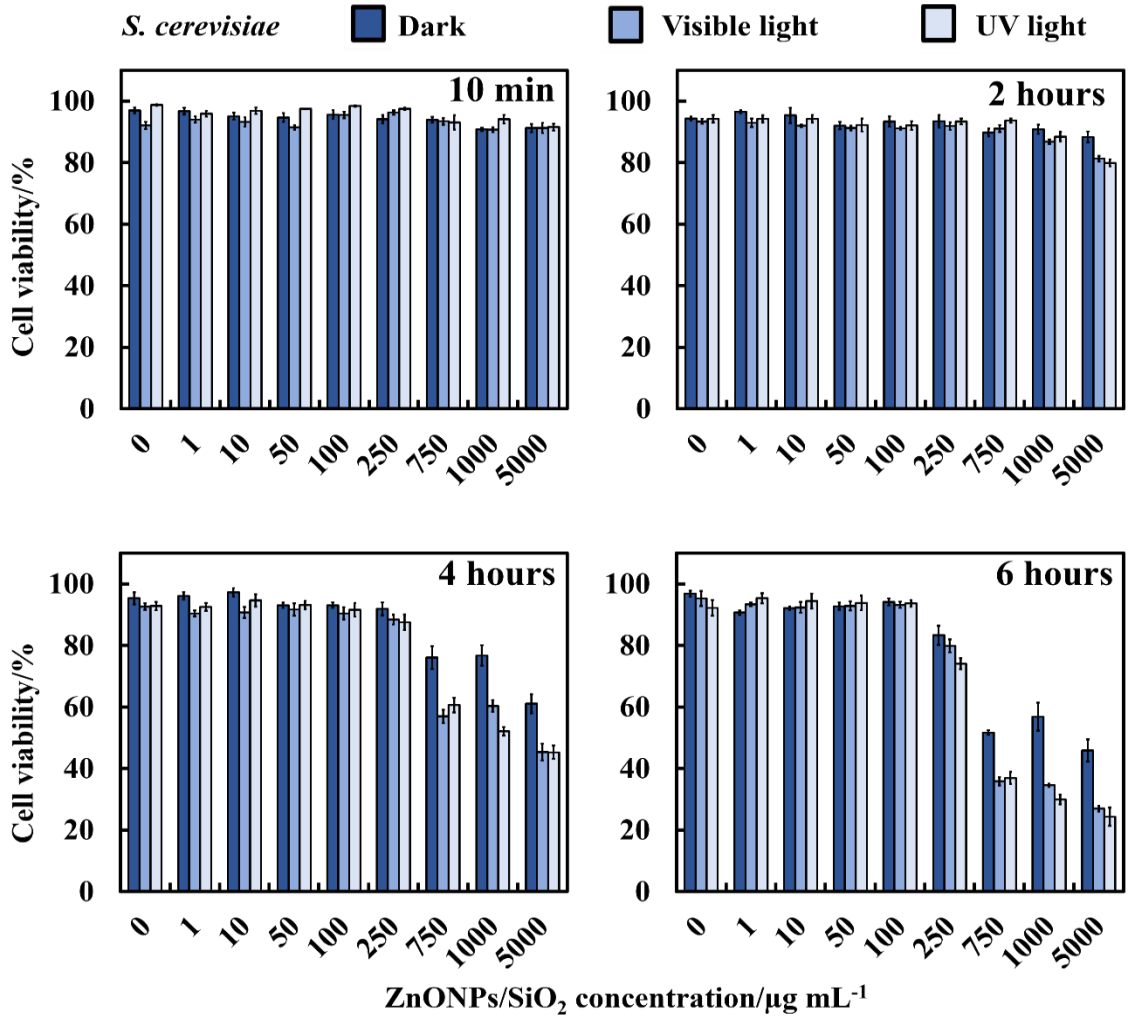


**Figure 4.20.** The effect of ZnONPs coated with one layer of silica on the viability of *S.cerevisiae* cells at different particle concentrations. The cells were incubated with the ZnONPs/$SiO_2$ at 10 min., 2 h, 4 h, and 6 h of exposure times.

The percentage of *S.cerevisiae* viability significantly decreased from 750 to 5000 µg $mL^{-1}$. It was discovered that at 5000 µg $mL^{-1}$ $SiO_2$-surface-functionalized ZnONPs concentration under UV light, a significant toxic impact occurred approximately 20 % in comparison with a control sample. A very similar impact was observed for ZnONPs/$SiO_2$ with ZnONPs/PSS (see Figure 4.12 and Figure 4.15) on the *C. reinhardtii* and *S.cerevisiae* cells due to the electrostatic repulsion as both of them have a negative surface charge, which leads to reducing toxicity. Figure 4.21B and 4.21C show SEM and TEM images of the *S.cerevisiae* cells after treatment with 750 µg $mL^{-1}$ $SiO_2$-surface-functionalized ZnONPs solution for 6 h.

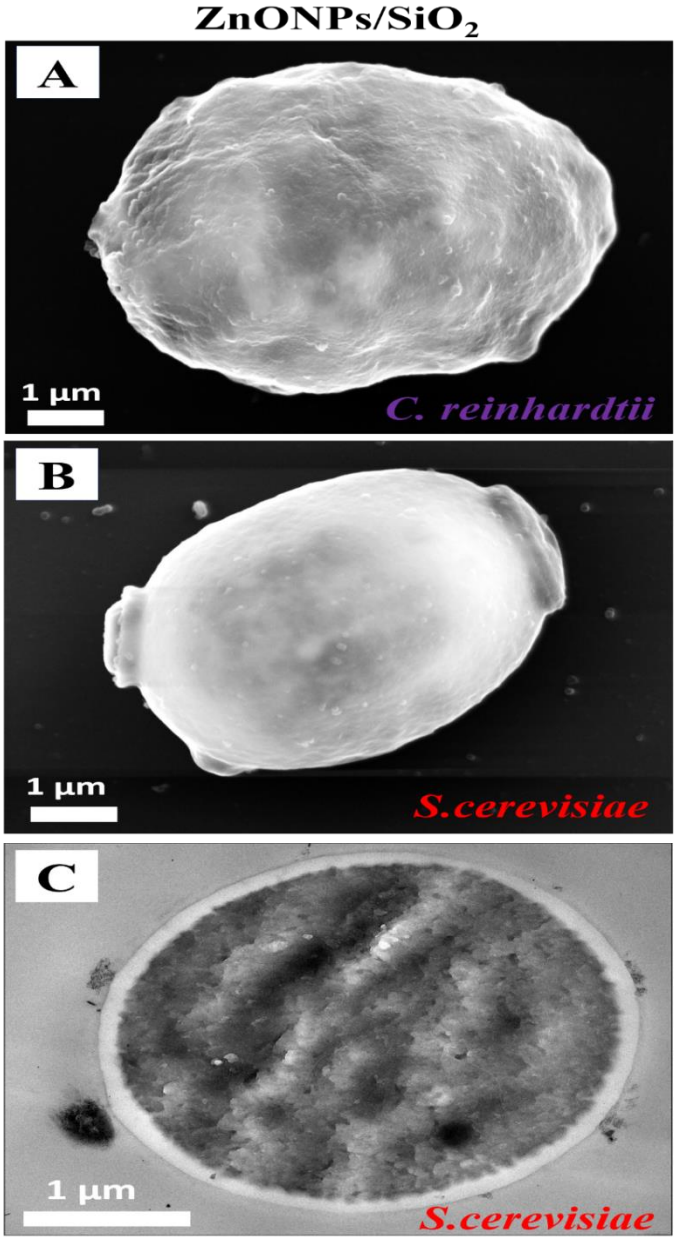


**Figure 4.21.** SEM images of (A) *C. reinhardtii*, (B) *S.cerevisiae* and TEM images of (C) *S.cerevisiae* after being incubated for 6 h with 750 µg $mL^{-1}$ surface functionalized of ZnONPs with $SiO_2$.

## 4.8 Toxicity effect of ZnS-coated ZnONPs on *C. reinhardtii* and *S.cerevisiae*

Figure 4.22 shows the cytotoxic impact of various particle concentrations of surface functionalized of ZnONPs with ZnS on the *C. reinhardtii* viability upon irradiation with visible and UV light or in dark conditions at various exposure time up to 6 h. We didn't observe the cytotoxic impact on the cell viability upon exposure with series of aqueous suspensions of various particle concentrations of ZnONPs/ZnS at room temperature and up to 2 h exposure time. The results were supported by SEM images of *C. reinhardtii* (Figure 4.24A). The toxicity impact at particle concentrations (50-250 µg $mL^{-1}$) of ZnONPs/ZnS on the *C. reinhardtii* viability irradiated with UV light for 6 h is more than that with the dark condition and visible light at the same concentrations.

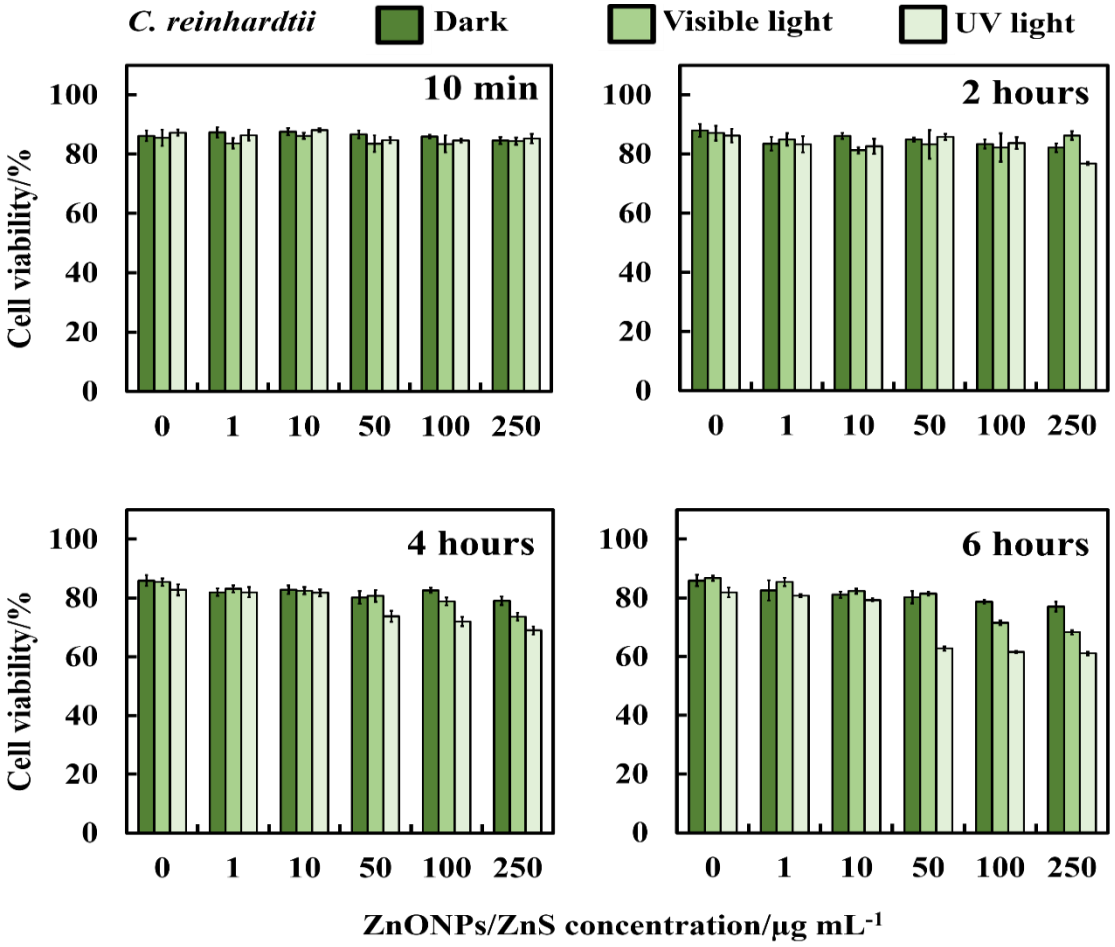


**Figure 4.22.** The effect of ZnONPs coated with layer of ZnS on the viability of *C. reinhardtii* at different particle concentrations (0, 1, 10, 50,100 and 250 µg $mL^{-1}$). The cells were incubated with the ZnONPs/ZnS at 10 min., 2 h, 4 h, and 6 h of exposure times.

Figure 4.23 shows that the *S.cerevisiae* cells are totally unaffected at 10 minutes incubation time in dark conditions which correspond with the results obtained when the

*S.cerevisiae* was irradiated with visible and UV light for the same period. After 2 h of incubation at higher particle concentration of ZnONPs/ZnS (5000 μg $mL^{-1}$), there was a remarkable decrease in the *S.cerevisiae* viability, but the impact disappeared at lower concentrations both in dark condition, visible and UV light. For the 6 h of exposure under visible and UV light, there was a considerable loss of viability for particle concentrations of 750 to 5000 μg $mL^{-1}$. However, in dark condition, there was a slight cytotoxic impact for ZnONPs/ZnS concentrations on the *S.cerevisiae* up to 5000 μg $mL^{-1}$ (Figure 4.23). The results show that at 5000 μg $mL^{-1}$ ZnONPs/ZnS concentration in presence UV light, a significant toxic impact occurred about 30% in comparison with a control sample of *S.cerevisiae*. This result may be explained by oxygen species released on the surface of the particle in the presence of UV light, which cause deadly damage to cells. However, the results indicated that the ZnONPs/ZnS have a weak effect on the cell viability. This was confirmed by both SEM and TEM images (Figure 4.24B and Figure 4.24C).

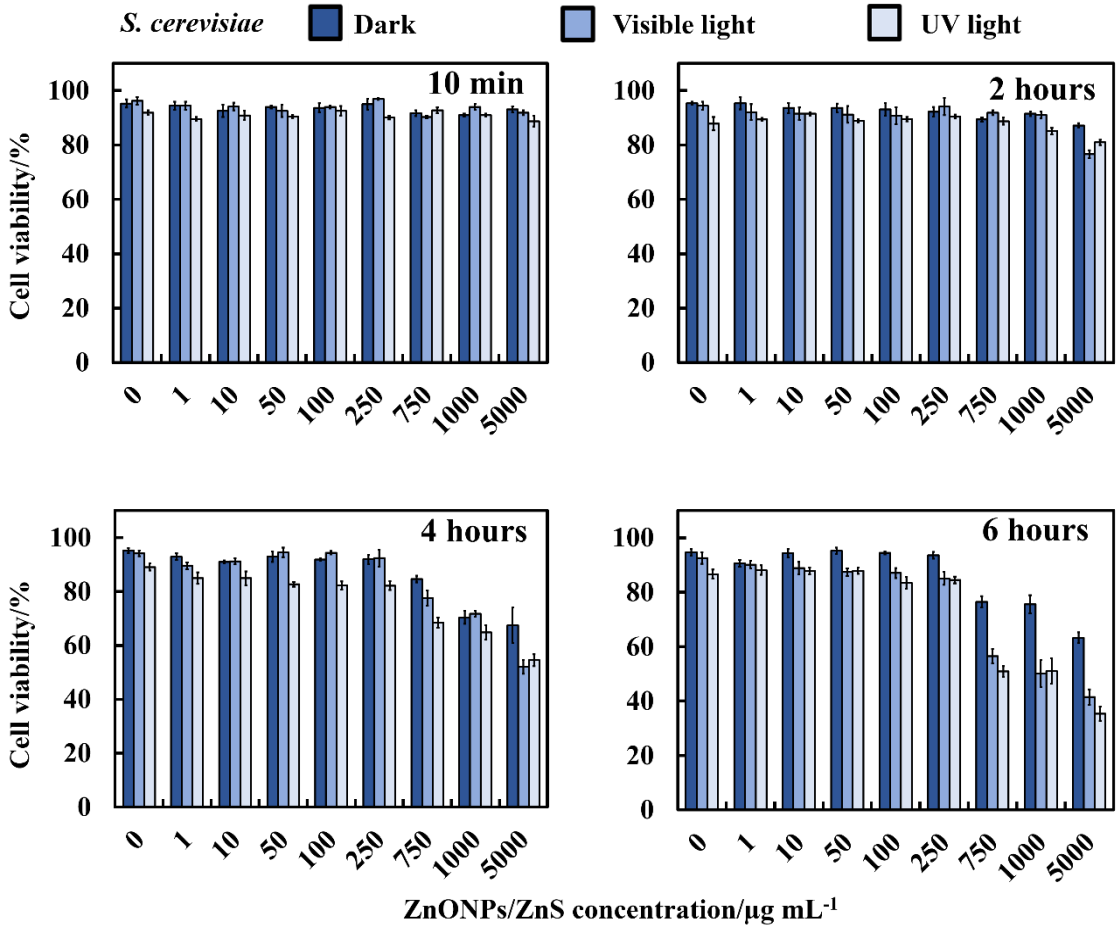


**Figure 4.23.** The effect of ZnONPs coated with one layer of ZnS on the viability of *S.cerevisiae* cells at different particle concentrations (0, 1, 10, 50,100, 250, 750, 1000 and 5000 μg $mL^{-1}$). The cells were incubated with the ZnONPs/ZnS at 10 min., 2 h, 4 h, and 6 h of exposure times in dark conditions, under visible and UV light.

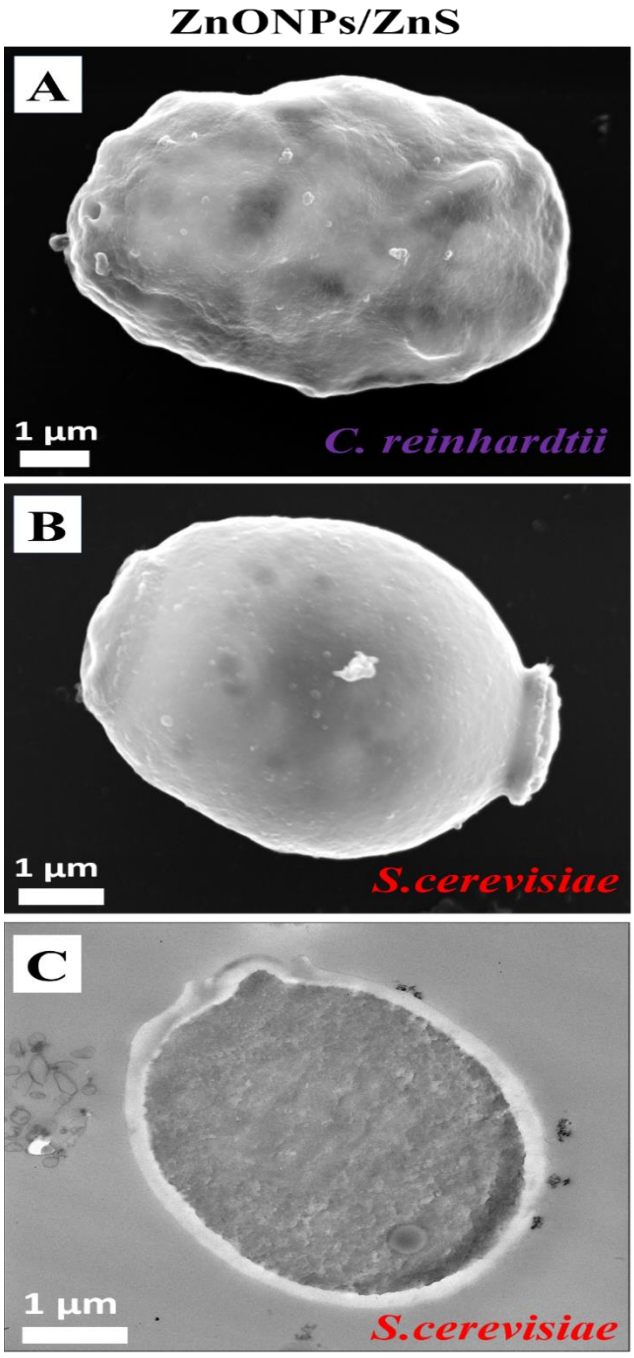


**Figure 4.24.** SEM images of (A) *C. reinhardtii*, (B) *S.cerevisiae* and TEM images of (C) *S.cerevisiae* after being incubated for 6 h with surface functionalized of ZnONPs with ZnS.

Figure 4.25 compares the toxicity of bare ZnONPs, ZnONPs/PSS, ZnONPs/$SiO_2$, ZnONPs/ZnS and ZnONPs/PSS/PAH on *C. reinhardtii* and *S.cerevisiae* cells under the same conditions at particle concentration 250 µg $mL^{-1}$ and after 6 hours exposure times. The results indicated that the bare ZnONPs and ZnONPs/PSS/PAH have a strong effect on the *C. reinhardtii* and *S.cerevisiae* cells viability at concentration 250 µg $mL^{-1}$ for 6 h of exposure time in dark, visible and UV light conditions. However, a very similar effect

was observed for ZnONPs/PSS, ZnONPs/$SiO_2$ and ZnONPs/ZnS on *S.cerevisiae* cells as shown in Figure 4.25A. These results show that the toxicity effect of the bare ZnONPs, ZnONPs/PSS, ZnONPs/$SiO_2$, ZnONPs/ZnS and ZnONPs/PSS/PAH on *S.cerevisiae* is much smaller than that of the *C. reinhardtii*.

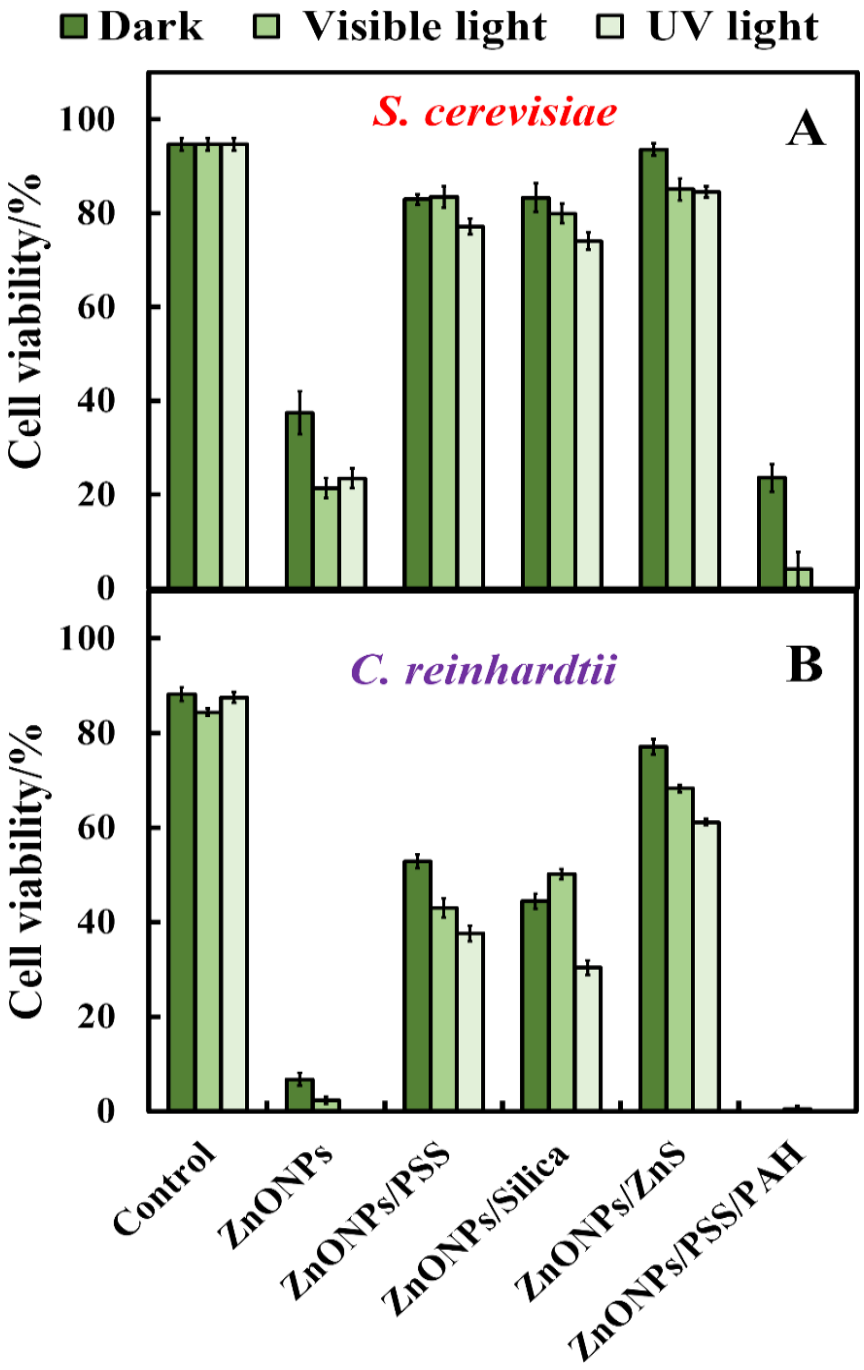


**Figure 4.25.** Comparison of the effect of bare ZnONPs, ZnONPs/PSS, ZnONPs/$SiO_2$, ZnONPs/ZnS and ZnONPs/PSS/PAH on the viability of (A) *S.cerevisiae* and (B) *C. reinhardtii* cells at particle concentration 250 µg $mL^{-1}$. The cells were incubated with the nanoparticles after 6 h exposure times in dark, visible and UV light conditions.

## 4.9 Effect of $ZnCl_2$ on *C. reinhardtii* cells

The aim of this experiment was to evaluate the toxicity of the ZnO nanoparticles for microalgae. The aqueous suspensions of ZnO nanoparticle in the lower concentration range were very toxic. This may be because of the possible emission of $Zn^{2+}$ ions from the ZnONPs in aqueous dispersions. To verify this, the toxic effect of $ZnCl_2$ was examined with various concentrations on *C. reinhardtii* cells in dark condition for the same period as shown in Figure 4.26. It should be noted that at low concentration there was no pronounced toxic impact for $ZnCl_2$ concentrations. At incubation times above 2 h, a sharp decline in the *C. reinhardtii* was observed for $ZnCl_2$ concentrations from 100-250 µg $ml^{-1}$. At 250 µg $ml^{-1}$ concentration of $ZnCl_2$ for 6 h incubation times all *C. reinhardtii* cells lost their viability. The results showed that all ZnONPs formulations have strong toxicity, the toxicity was due to solubilized Zn ions.[21]

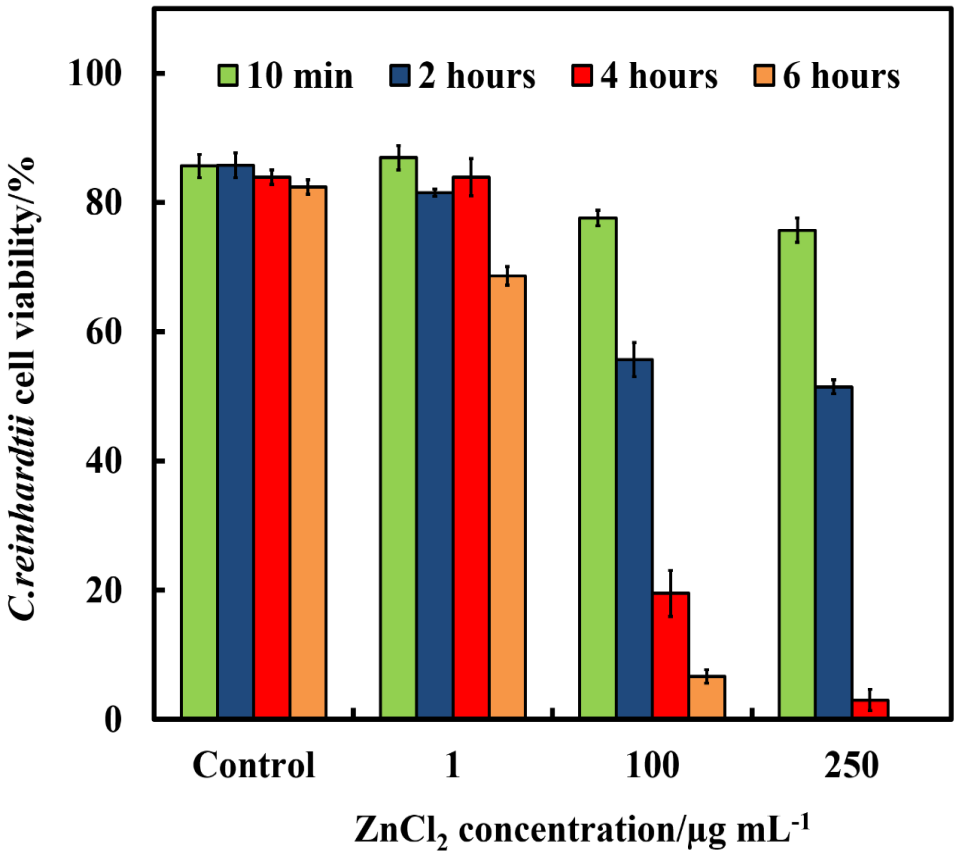


**Figure 4.26.** The effect of $ZnCl_2$ on the viability of *C. reinhardtii* at different concentrations (0, 1, 100 and 250 µg $mL^{-1}$). The cells were incubated with $ZnCl_2$ at 10 min., 2 h, 4 h and 6 h exposure times.

## 4.10 Conclusions

There is a lot of ongoing work on several classes of inorganic colloid particles of added functionality, which exhibit strong and universal antifungal, antibacterial and antiviral action towards which microbes have not been able to develop resistance. The mechanisms by which such ZnONPs attack microbial cells or inhibit their growth were discussed, which involve generation of reactive oxygen species (ROS) upon irradiation with UV light, cell membrane disruption due to the ZnONPs cationic surface, ROS scavenging, emission of heavy ions, as $Zn^{2+}$ on the cell surface, etc. Various ways to control the anti-algal and anti-yeast activity were studied of a range of bare and surface-modified ZnONPs on two different types of microbial cells: *C. reinhardtii* and *S. cerevisiae*. Results in present work indicate that bare ZnONPs had significant toxicity impact against *C. reinhardtii* and *S. cerevisiae* cells and the toxicity increased upon increasing the concentration of ZnONPs. The results also showed a decline in the chlorophyll content after 6 hours incubation to ZnONPs in dark, visible and UV light conditions. This showed that ZnONPs could not only damage the cell membranes as well as can interfere with the cell chloroplasts. The results from TEM and SEM analysis showed that direct contact between the ZnONPs and the cell membrane of *S. cerevisiae* and *C. reinhardtii* is very important for their effective anti-algal and anti-yeast action. In order to evaluate the role of the surface coating, a series of zinc sulfide or silica and polyelectrolyte-coated ZnONPs were likewise synthesised and their antimicrobial activity towards *S. cerevisiae* and *C. reinhardtii* was compared with that of bare ZnONPs. It was discovered that the anti-algal and anti-yeast activity of the coated ZnONPs alternates with their surface charge. The anionic nanoparticles (ZnONPs/ZnS, ZnONPs/$SiO_2$ and ZnONPs/PSS) have much lower anti-algal and anti-yeast activity than the cationic ones (ZnONPs/PSS/PAH and bare ZnONPs). In general, bare ZnONPs and PAH-coated ZnONPs showed remarkable anti-algal and anti-yeast activity and demonstrated a lethal effect against cells, even at low concentrations.

## 4.11 References


1. S. Fernando, T. Gunasekara and J. Holton, *Sri Lankan Journal of Infectious Diseases*, 2018, **8**.
2. L. Zhang, Y. Jiang, Y. Ding, M. Povey and D. York, *Journal of Nanoparticle Research*, 2007, **9**, 479-489.
3. Y.-W. Wang, A. Cao, Y. Jiang, X. Zhang, J.-H. Liu, Y. Liu and H. Wang, *ACS applied materials & interfaces*, 2014, **6**, 2791-2798.
4. A. Lipovsky, Y. Nitzan, A. Gedanken and R. Lubart, *Nanotechnology*, 2011, **22**, 105101.
5. A. F. Halbus, T. S. Horozov and V. N. Paunov, *Advances in colloid and interface science*, 2017, **249**, 134-148.
6. A. F. Halbus, T. S. Horozov and V. N. Paunov, *ACS applied materials & interfaces*, 2019, **11**, 12232–12243.
7. A. F. Halbus, T. S. Horozov and Vesselin N. Paunov, *Nanoscale Advances*, 2019, **1**, 2323 – 2336.
8. S. S. M. Al-Obaidy, A. F. Halbus, G. M. Greenway and V. N. Paunov, *Journal of Materials Chemistry B*, 2019, **7**, 3119-3133.
9. K. M. Reddy, K. Feris, J. Bell, D. G. Wingett, C. Hanley and A. Punnoose, *Applied physics letters*, 2007, **90**, 213902.
10. T. Dayakar, K. V. Rao, K. Bikshalu, V. Rajendar and S.-H. Park, *Materials Science and Engineering: C*, 2017, **75**, 1472-1479.
11. A. Marra, G. Rollo, S. Cimmino and C. Silvestre, *Coatings*, 2017, **7**, 29.
12. L. Ai, Y. Wang, G. Tao, P. Zhao, A. Umar, P. Wang and H. He, *Molecules*, 2019, **24**, 503.
13. K. Kasemets, A. Ivask, H.-C. Dubourguier and A. Kahru, *Toxicology in vitro*, 2009, **23**, 1116-1122.
14. H. Zhang, B. Chen, H. Jiang, C. Wang, H. Wang and X. Wang, *Biomaterials*, 2011, **32**, 1906-1914.
15. P. Nagarajan and V. Rajagopalan, *Science and Technology of Advanced Materials*, 2008, **9**, 035004.
16. M. Roselli, A. Finamore, I. Garaguso, M. S. Britti and E. Mengheri, *The Journal of nutrition*, 2003, **133**, 4077-4082.
17. R. Wahab, A. Mishra, S.-I. Yun, Y.-S. Kim and H.-S. Shin, *Applied microbiology and biotechnology*, 2010, **87**, 1917-1925.
18. P. Espitia, *Food Bioprocess Technol*, 2012, **5**, 1447.
19. L. K. Adams, D. Y. Lyon and P. J. Alvarez, *Water research*, 2006, **40**, 3527-3532.
20. K. Hirota, M. Sugimoto, M. Kato, K. Tsukagoshi, T. Tanigawa and H. Sugimoto, *Ceramics International*, 2010, **36**, 497-506.
21. M. Heinlaan, A. Ivask, I. Blinova, H.-C. Dubourguier and A. Kahru, *Chemosphere*, 2008, **71**, 1308-1316.

# Chapter 5

# 5. Characterisation of surface modified magnesium hydroxide nanoparticles

## 5.1 Introduction

Magnesium hydroxide nanoparticles have recently attracted much attention due to their wide applications as environmentally friendly antimicrobial nanomaterials, with potentially low toxicity and low fabrication cost. Surface modification of magnesium hydroxide nanoparticles is vital for controlling their properties and interactions with molecules and ligands of relevance for biomedical applications, in addition to their susceptibility to undergo a transformation in environmental and biological systems. Considerable efforts have been devoted to the development of surface modifiers that can offer not only stability but also better control of the interaction between nanoparticles and biological membranes to obtain more biocompatible materials.[1-4]

In this Chapter, magnesium hydroxide was synthesised via the direct precipitation method. The synthesis and characterisation of a range of surface modified $Mg(OH)_2$NPs were described including particle size distribution, crystallite size, zeta potential, isoelectric point, X-ray diffraction, dynamic light scattering, scanning electron microscopy, thermogravimetric analysis, energy dispersive X-ray analysis, Fourier transform infrared spectroscopy, and transmission electron microscopy.

The mean hydrodynamic diameter and zeta potential of the $Mg(OH)_2$NPs in deionized water were measured by dynamic light scattering instrument of suspensions prepared by dispersing 0.025 g of $Mg(OH)_2$NPs sample in 100 mL of deionized water by a digital sonicator. The average hydrodynamic diameter of $Mg(OH)_2$NPs was found to be 69±10 nm and their zeta potential was +30±6 mV as shown in Figure 5.1 and Figure 5.2.

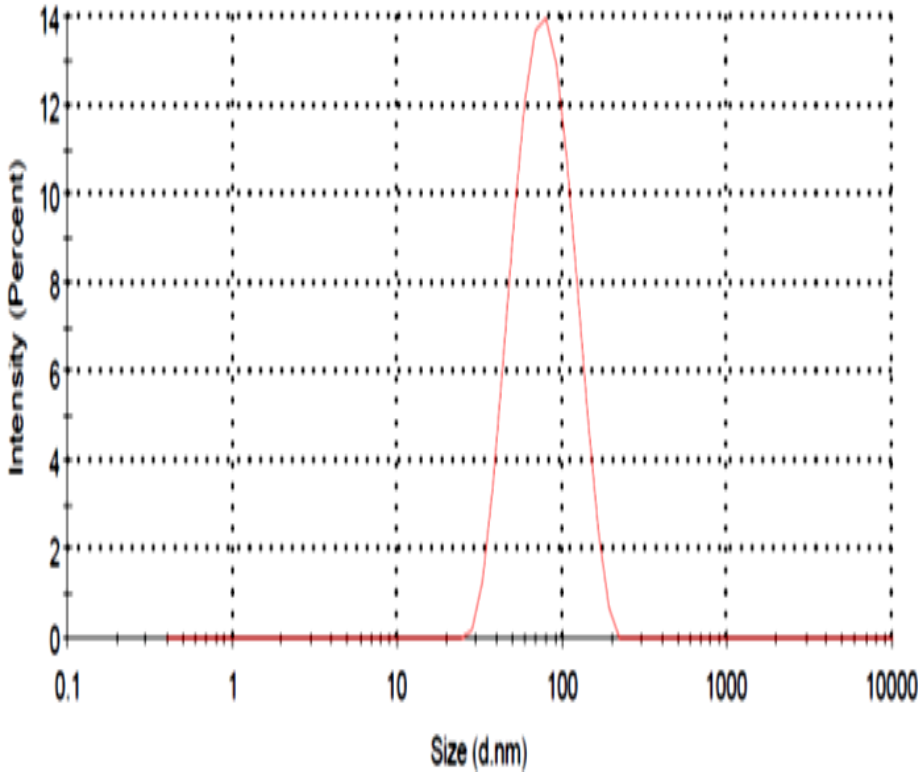


**Figure 5.1.** The particles size of $Mg(OH)_2$NPs made from a magnesium chloride at 75°C.

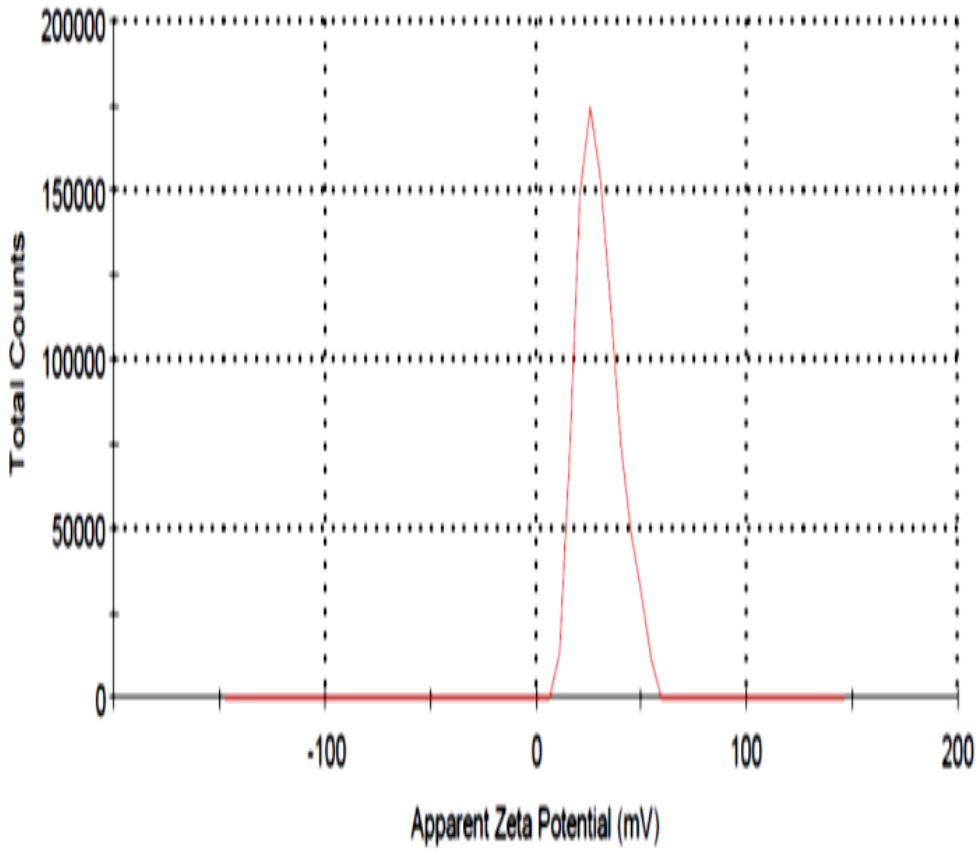


**Figure 5.2.** The zeta potential of $Mg(OH)_2$NPs made from a magnesium chloride at 75°C.

## 5.2 Thermogravimetric analysis (TGA) of $Mg(OH)_2$NPs

Thermo gravimetric analysis carried out between 50 and 1000 $^oC$, as shown in Figure 5.3, indicated that the $Mg(OH)_2$ sample was stable up to 270 $^oC$. Then, the endothermic peak corresponding to the removal of the adsorbed water molecules takes place between 270-300 $^oC$ as also reported by other authors.[5] The major weight loss step is found in the temperature range of 300 - 450 $^oC$, which is due to the transition phase, corresponding to the decomposition of $Mg(OH)_2$NPs to MgO. The TGA curve exhibits a total mass loss equal to 29.46 %, which is slightly lower than the calculated mass loss (30.8%) attributed to the complete dehydroxylation process of $Mg(OH)_2$. This result also agrees with a previous work.[5-7]

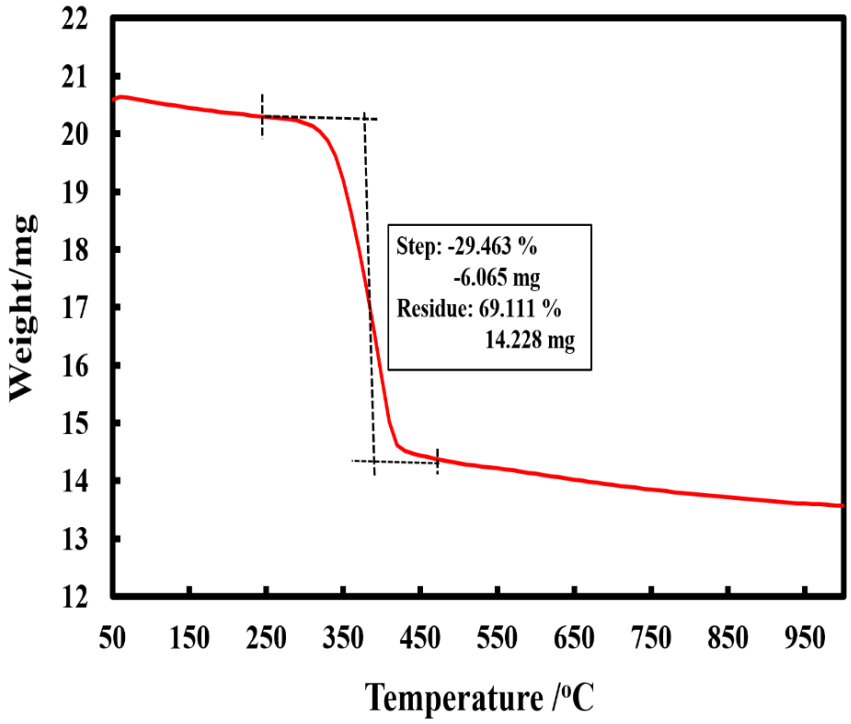


**Figure 5.3.** Thermal gravimetric analysis pattern of $Mg(OH)_2$NPs powder.

## 5.3 EDX analysis of $Mg(OH)_2$NPs

Energy dispersive X-ray Diffraction analysis was carried out on the synthesised $Mg(OH)_2$NPs to verify the elemental composition. The EDX data in Figure 5.4 confirm the presence of magnesium and oxygen signals in the $Mg(OH)_2$NPs sample. The elemental analysis of the $Mg(OH)_2$NPs yielded 36.59 % of magnesium and 59.94 % of oxygen which indicates that the formed $Mg(OH)_2$NPs was in its highly purified form and in agreement with previous studies.[8]

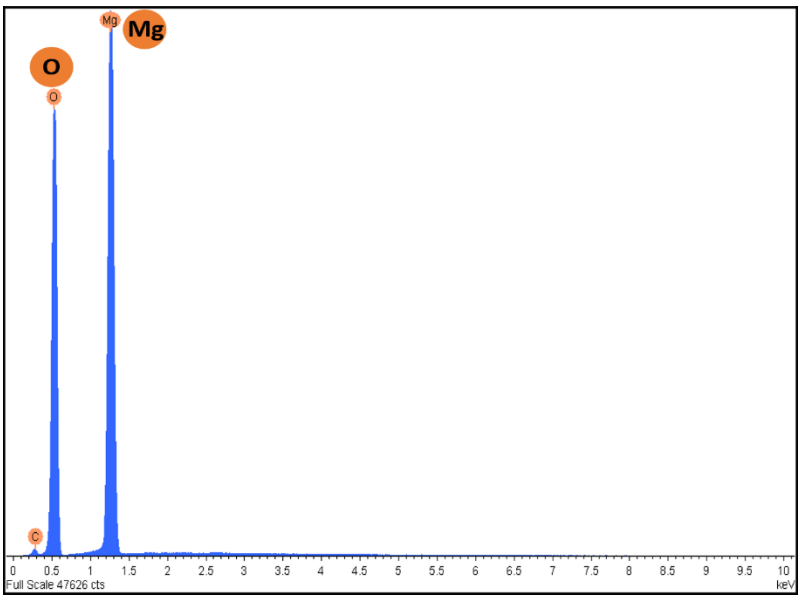


**Figure 5.4.** The EDX spectra of the uncoated $Mg(OH)_2$NPs.

## 5.4 The zeta potential and particle size of $Mg(OH)_2$NPs at different pH

The zeta potential and particle size of the $Mg(OH)_2$NPs produced was measured at pH in the range 3-12 and the results are shown in Figure 5.5. The isoelectric point of non-coated $Mg(OH)_2$NPs was approximately at pH 11.7, i.e. the bare $Mg(OH)_2$NPs are cationic at neutral pH. As it can be seen from Figure 5.5, the zeta potential decreases and the particle size increases upon increasing of pH. The aggregation of $Mg(OH)_2$NPs occurs above pH 8.5.

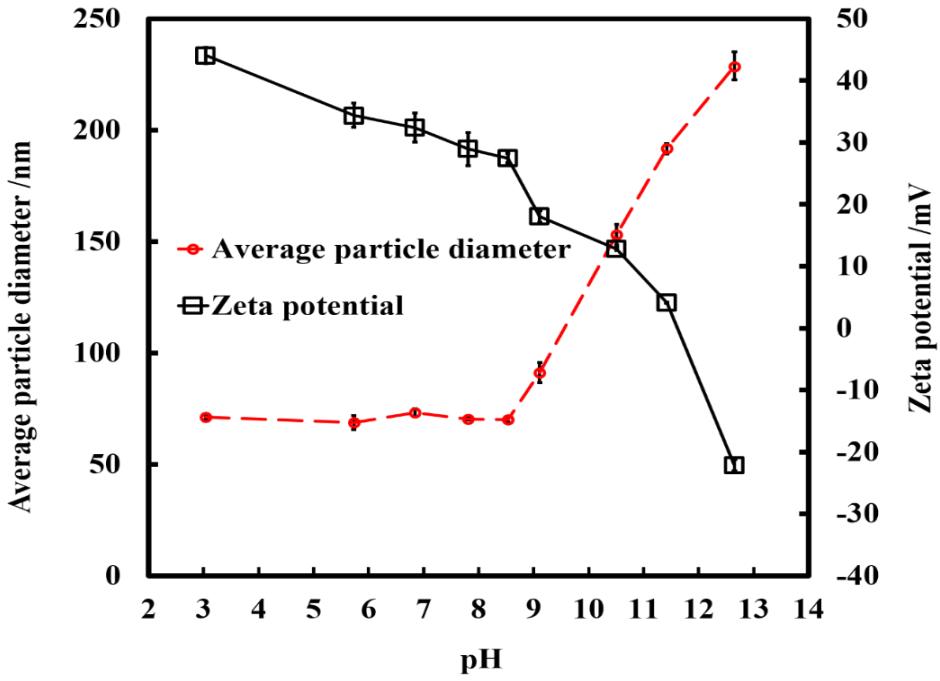


**Figure 5.5.** Variations in particle size and zeta potential of $Mg(OH)_2$NPs suspensions with pH.

## 5.5 FTIR spectrum of $Mg(OH)_2$NPs

The FTIR spectrum of the $Mg(OH)_2$NPs synthesized using a magnesium chloride solution at different reaction temperatures is shown in Figure 5.6. The sharp and intense 3700 $cm^{-1}$ FTIR peak corresponds to the $Mg(OH)_2$ asymmetric O–H stretching. The band at 1400 $cm^{-1}$ is due to the water O–H stretch. The strong and wide 570 $cm^{-1}$ peak is due to Mg−O stretching. No other absorption peaks from impurities were detected. This result indicates that the $Mg(OH)_2$ obtained had higher purity and is also in agreement with previous studies.[9, 10]

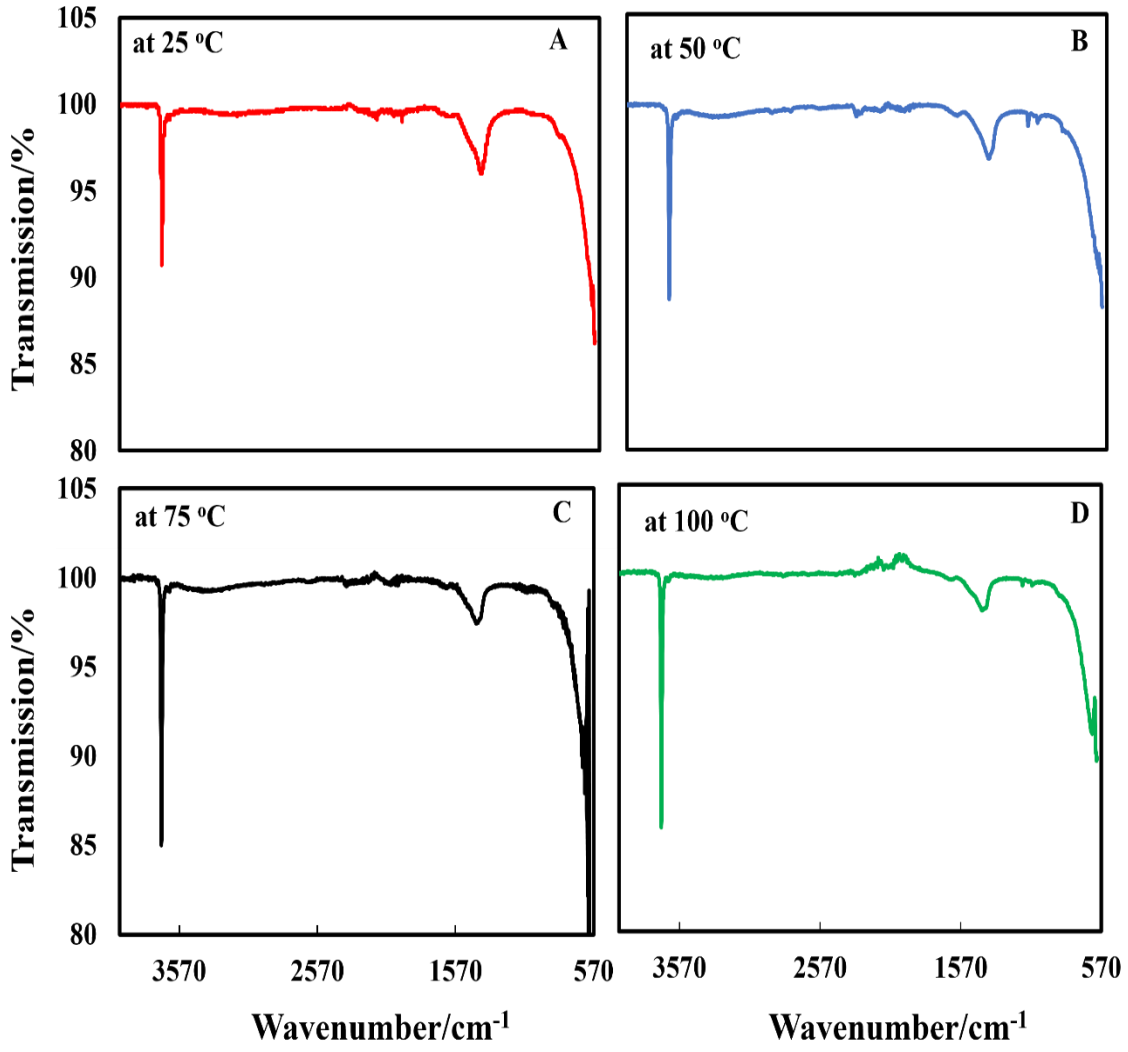


**Figure 5.6.** FTIR spectra of the as prepared $Mg(OH)_2$NPs at different reaction temperatures; (A) 25 °C, (B) 50 °C,(C) 75 °C and (D) 100 °C.

## 5.6 Effect of the precipitation temperature on the particle size of $Mg(OH)_2$NPs

The effect of precipitation temperature on the particle size of $Mg(OH)_2$NPs for the synthesis done at various reaction temperature (25°C, 50°C, 75°C and 100°C) was studied. Figure 5.7 shows the impact of the temperature of the reaction mixture on the size of $Mg(OH)_2$NPs for one hour. $Mg(OH)_2$NPs of lower average size were produced at 75°C and 100°C, while larger particles were created at 25°C and 50°C. Therefore, 75°C and 100°C were the optimal temperatures for the production of $Mg(OH)_2$NPs.

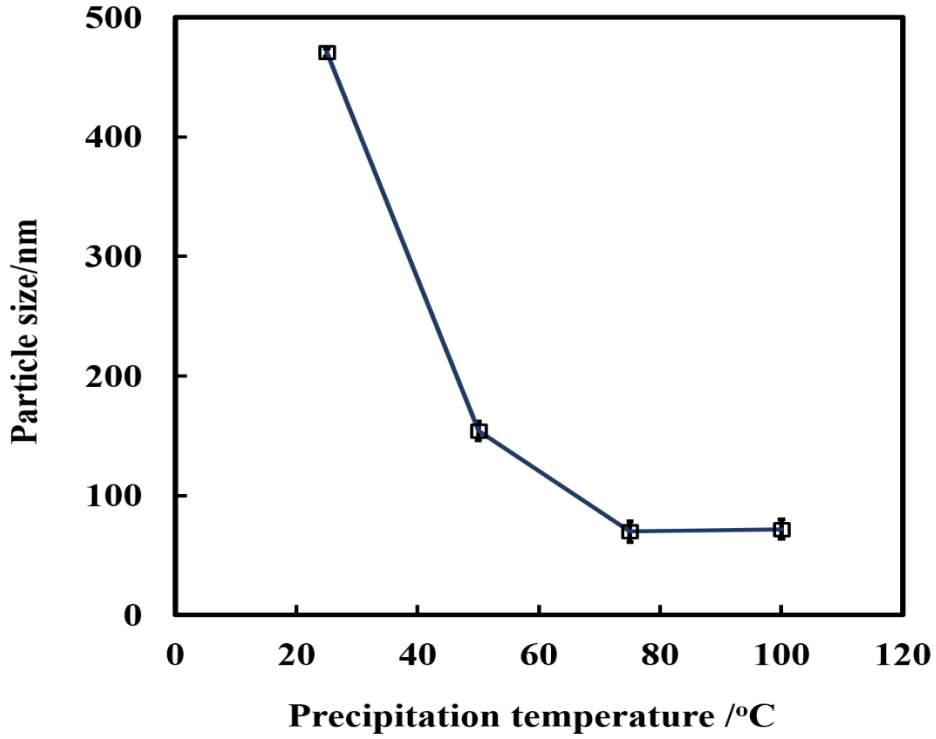


**Figure 5.7.** The impact of reaction temperature on the size of the produced $Mg(OH)_2$NPs.

## 5.7 Effect of the precipitation temperature on crystallite size of the synthesized $Mg(OH)_2$NPs

Figure 5.8 shows the XRD pattern of $Mg(OH)_2$NPs samples obtained at various reaction temperatures 25 °C, 50 °C,75 °C and 100 °C using magnesium chloride as a precursor. The diffraction peaks are in agreement with the hexagonal structure of $Mg(OH)_2$NPs according to Joint Committee on Powder Diffraction Standards **(**JCPDS) Card No. 00-044-1482, which indicates that no apparent impurities are detected. The average crystallite size of $Mg(OH)_2$NPs was calculated using the Scherrer equation, $D=K\lambda/\beta\cos\theta$,

were *D* is the crystallite size in nm, *K* is a dimensionless shape constant taken as 0.94, *2θ* is the diffraction angle, λ is the wavelength of the X-ray radiation (CuKα = 0.15406 nm), and *β* is the full width at half-maximum (FWHM) of the diffraction peak.

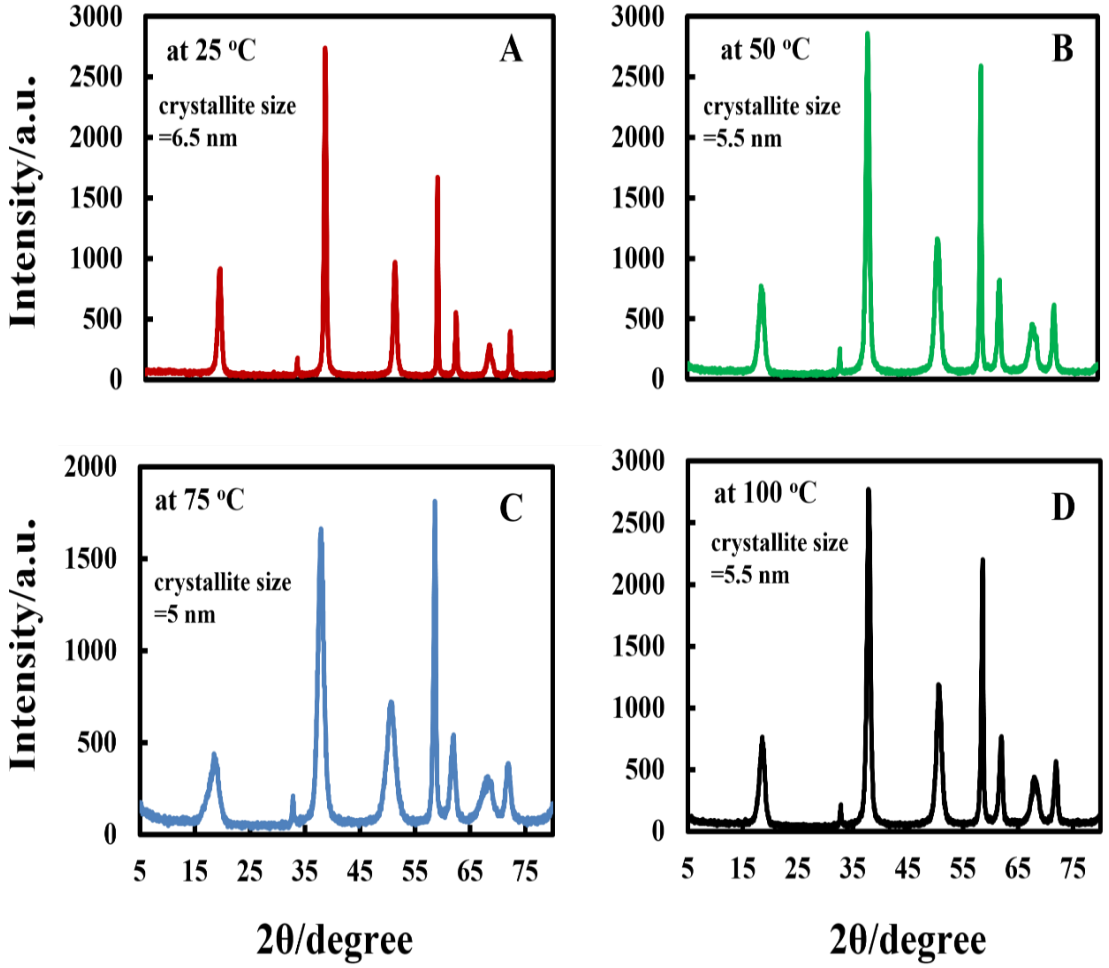


**Figure 5.8.** Comparison of X-ray pattern of $Mg(OH)_2$NPs precipitated at 25°C (A), 50°C (B), 75°C (C) and 100°C (D).

## 5.8 Polyelectrolyte-functionalized $Mg(OH)_2$NPs

The particle size of 69 nm $Mg(OH)_2$NPs was coated with two subsequent layers of PSS and PAH via the procedures explained in chapter two.[11, 12] Figure 5.9 shows the zeta potential of the coated $Mg(OH)_2$NPs as a function of the number of polyelectrolyte layers. The zeta potential of the $Mg(OH)_2$NPs changed from approximately +30 mV to -36 mV for $Mg(OH)_2$NPs/PSS (Figures 5.11B). Further coating with PAH yielded positively charged $Mg(OH)_2$NPs/PSS/PAH with a zeta potential of +51 mV (Figures 5.11D). As expected, the particle surface charge alternates with the addition of oppositely charged polyelectrolyte layer. Figure 5.10 shows that the coated NPs size increases after every

subsequent polyelectrolyte coating due to partial aggregation (also see Figures 5.11A and 5.11C).

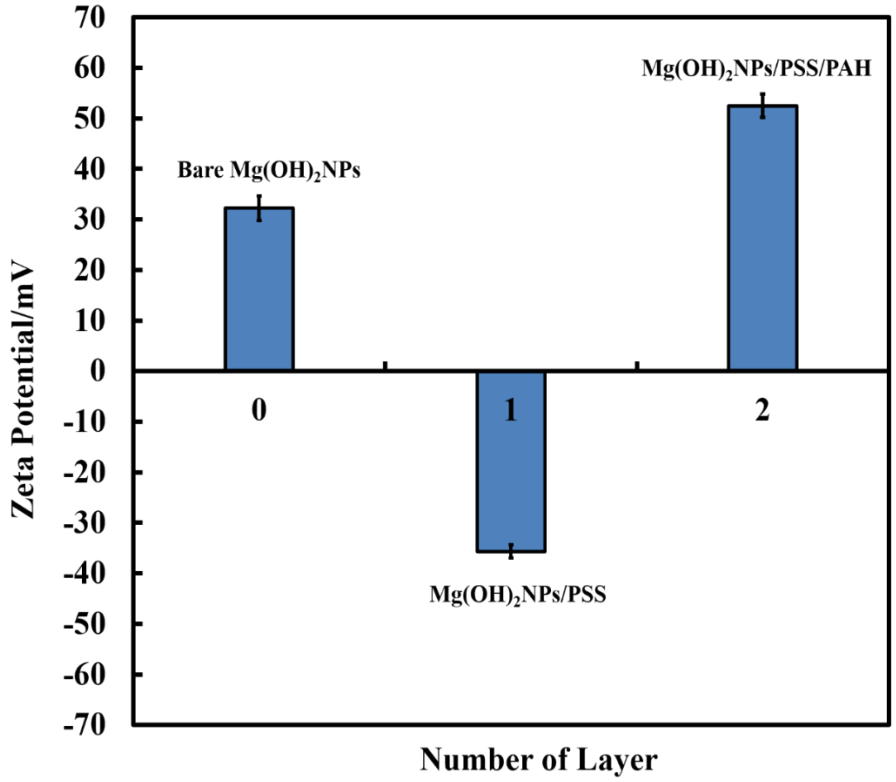


**Figure 5.9.** The zeta potential of bare-and polyelectrolyte-coated $Mg(OH)_2$NPs.

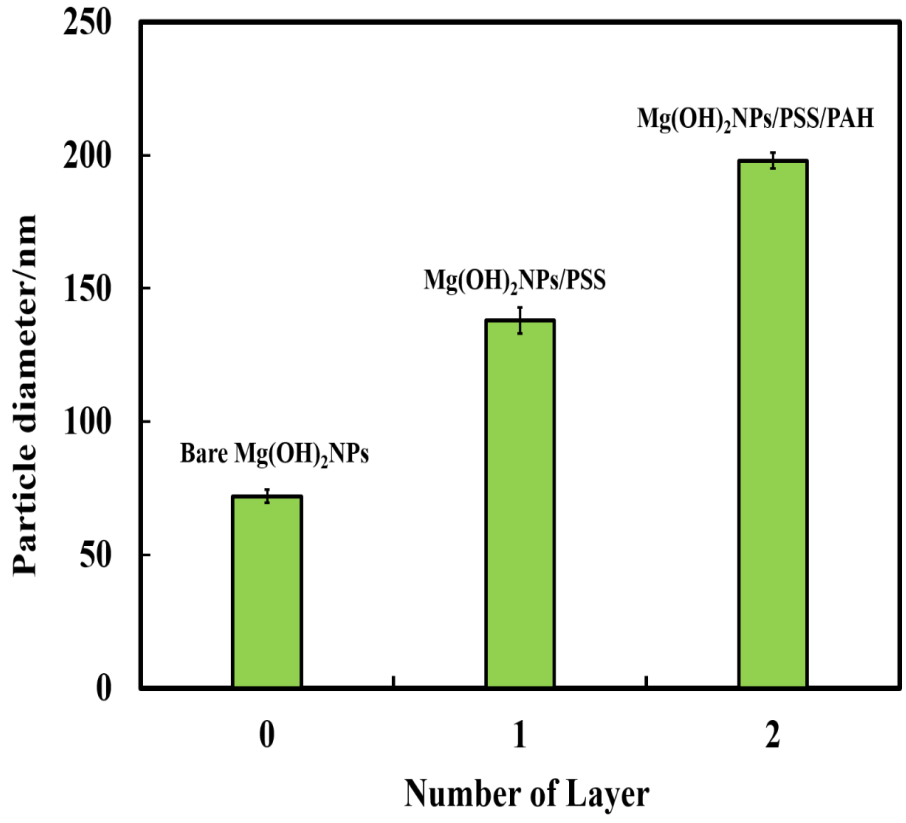


**Figure 5.10.** The particle size of bare-and polyelectrolyte-coated $Mg(OH)_2$NPs.

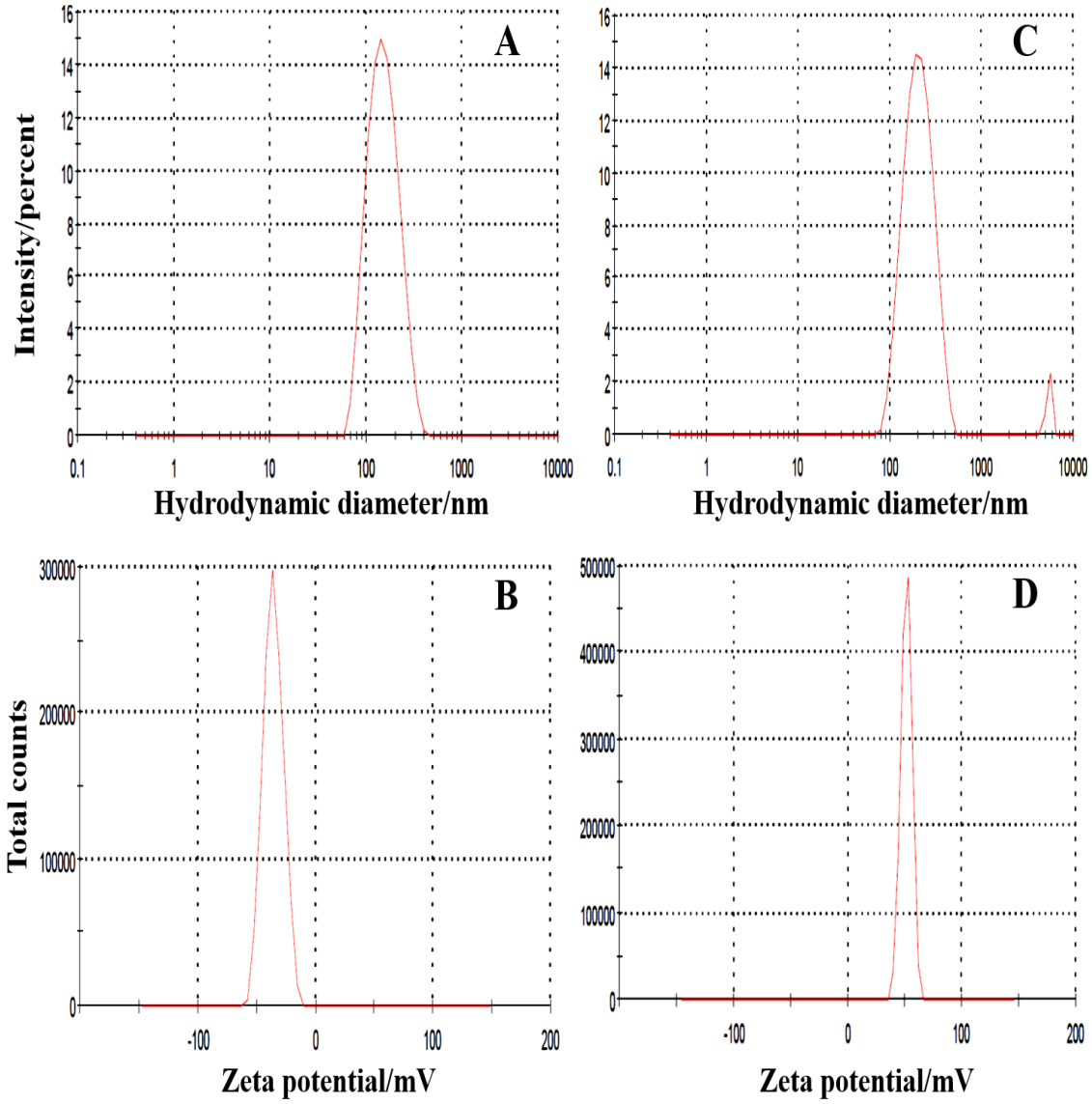


**Figure 5.11.** (A) The particle size and (B) zeta potential of $Mg(OH)_2$NPs/PSS. (C) The particle size and (D) zeta potential of $Mg(OH)_2$NPs/PSS/PAH using dropwise addition of particles suspension with ultra-sonication.

## 5.9 Conclusions

$Mg(OH)_2$NPs were prepared by the direct precipitation method. Synthesis and antibacterial effects of $Mg(OH)_2$NPs were undertaken and factors contributing to the formation of well-defined nanoparticles were explored. A simple and cost effective method to obtain nanoparticles with narrow size dispersion was established in this Chapter. Here, the synthesis and characterisation of a range of surface modified $Mg(OH)_2$NPs were investigated, including particle size distribution, zeta potential, thermogravimetric analysis (TGA), energy dispersive X-ray analysis (EDX), isoelectric point, Fourier transform infrared spectroscopy (FTIR) and X-ray diffraction (XRD). The hydrodynamic diameter and zeta potential of the $Mg(OH)_2$NPs were found to be 69±10 nm and their zeta potential was +30±6 mV. The TGA results indicated that the major weight loss step is found in the temperature range of 300 - 450 $^oC$, which is due to the transition phase, corresponding to the decomposition of $Mg(OH)_2$ to MgO. The elemental analysis of the $Mg(OH)_2$ yielded 36.59 % of magnesium and 59.94 % of oxygen which indicates that the formed $Mg(OH)_2$NPs was in its highly purified form. The isoelectric point of non-coated $Mg(OH)_2$NPs was approximately at pH 11.7. Magnesium hydroxide was found to be positively charged at all pH values less than the isoelectric point. The XRD results showed that the obtained $Mg(OH)_2$ has a crystalline structure with the hexagonal structure of $Mg(OH)_2$NPs according to Joint Committee on Powder Diffraction Standards **(**JCPDS) Card No. 00-044-1482. A series of polyelectrolyte-coated $Mg(OH)_2$NPs with two subsequent layers of PSS and PAH were likewise synthesised while using the layer by-layer technique. The results showed that the zeta potential of the $Mg(OH)_2$NPs changed from approximately +30 mV to −36 mV for $Mg(OH)_2$NPs/PSS. Further coating with PAH yielded positively charged $Mg(OH)_2$NPs/PSS/PAH with a zeta potential of +51 mV. The experiment also showed that the coated $Mg(OH)_2$NPs size increases after every subsequent polyelectrolyte coating due to partial aggregation. The $Mg(OH)_2$NPs coated with anionic or cationic polyelectrolytes will use in the next Chapter to be incubated with individual microorganisms such as *E.coli*, *C. reinhardtii* and *S. cerevisiae* to study the antimicrobial effect of coated $Mg(OH)_2$NPs.

## 5.10 References


1. A. F. Halbus, T. S. Horozov and V. N. Paunov, *ACS Applied Materials & Interfaces*, 2019, **11**, 12232–12243.
2. A. F. Halbus, T. S. Horozov and Vesselin N. Paunov, *Nanoscale Advances*, 2019, **1**, 2323 – 2336.
3. A. F. Halbus, T. S. Horozov and V. N. Paunov, *Advances in colloid and interface science*, 2017, **249**, 134-148.
4. S. S. M. Al-Obaidy, A. F. Halbus, G. M. Greenway and V. N. Paunov, *Journal of Materials Chemistry B*, 2019, **7**, 3119-3133.
5. J. C. Yu, A. Xu, L. Zhang, R. Song and L. Wu, *The Journal of Physical Chemistry B*, 2004, **108**, 64-70.
6. H. Dhaouadi, H. Chaabane and F. Touati, *Nano-Micro Letters*, 2011, **3**, 153-159.
7. F. Meshkani and M. Rezaei, *Powder Technology*, 2009, **196**, 85-88.
8. C. Dong, J. Cairney, Q. Sun, O. L. Maddan, G. He and Y. Deng, *Journal of Nanoparticle Research*, 2010, **12**, 2101-2109.
9. H. Pang, G. Ning, W. Gong, J. Ye and Y. Lin, *Chemical Communications*, 2011, **47**, 6317-6319.
10. X.-F. Wu, G.-S. Hu, B.-B. Wang and Y.-F. Yang, *Journal of crystal Growth*, 2008, **310**, 457-461.
11. M. J. Al-Awady, G. M. Greenway and V. N. Paunov, *RSC Advances*, 2015, **5**, 37044-37059.
12. A. F. Halbus, T. S. Horozov and V. N. Paunov, *Biomimetics*, 2019, **41**, 1-20.

# Chapter 6

# 6. Controlling the antimicrobial action of surface modified magnesium hydroxide nanoparticles

## 6.1 Introduction

The increased proliferation of infectious illnesses caused by microorganisms found in food packaging, medical devices, water treatment systems and domestic appliances has elicited increased interest. [1-7] The increased resistance of microorganisms against current biocides has caused a great concern particularly for individuals of compromised immune systems. This has prompted expanded efforts to investigate new types of nanomaterials as antibacterial agents [8] which do not rely on the existing pathways of antimicrobial resistance. Recent studies have been concentrated on antibacterial inorganic nanoparticles, for example, metal oxide nanoparticles, like ZnO, MgO, CuO, $Cu_2O$, $Al_2O_3$, $TiO_2$,$CeO_2$ and $Y_2O_3$; metals, e.g. copper, silver, gold etc., metal hydroxides such as $Mg(OH)_2$ as well as colloids made from biodegradable materials, such as chitosan, lignin and dextran, loaded with antibacterial agents. [6] $Mg(OH)_2$NPs have successfully been deployed as antifungal and antibacterial agents towards different microorganisms [9-11] and there are indications that they can be highly effective. [12]

In this chapter, the role of the polymer coating in the antimicrobial activity of $Mg(OH)_2$ nanoparticles synthesized by the direct precipitation method was investigated. Three different types of microorganisms, *C. reinhardtii*, *S.cerevisiae* cells and Gram-negative *E.coli* were used to examine the antimicrobial activity of the surface modified $Mg(OH)_2$NPs. The relationship between antifungal and antibacterial effect of the particle size, surface charge, in addition to their adhesion to the microbial cell wall was explored. The size of the $Mg(OH)_2$NPs is likewise essential for their potential activity, as smaller particles have higher portability to relocate between biological compartments. [13] Moreover, the surface charge of the $Mg(OH)_2$NPs determines their ability to electrostatically interact with the biological membranes. The present study investigates the impact of the $Mg(OH)_2$NPs concentration, their zeta potential and particle size on the viability of *C. reinhardtii, S.cerevisiae* and *E.coli* at different exposure times. The antimicrobial activity and the nanoparticle internalisation between *C. reinhardtii, S.cerevisiae* and *E.coli* was explored. In our experiments with surface functionalized

$Mg(OH)_2$NPs on microbial cells, done systematically on *C. reinhardtii*, *S.cerevisiae* and *E.coli*, we have tested their effect in the absence of growth media whose components may potentially interfere with the particle surface charge. This would lead to ambiguity in the results depending on the media composition and concentration. To avoid this we remove the microbial cells from the media prior to testing the effect of the surface functionalized $Mg(OH)_2$NPs on them. The antibacterial activity of $Mg(OH)_2$NPs coated with anionic and cationic polyelectrolytes was investigated. The working hypothesis is that coating the $Mg(OH)_2$NPs with cationic polyelectrolytes may enhance their antimicrobial activity while coating them with anionic polyelectrolytes as an outer layer may lead to decreased antibacterial activity because of their electrostatic repulsion from the bacterial cell wall (Figure 6.1).

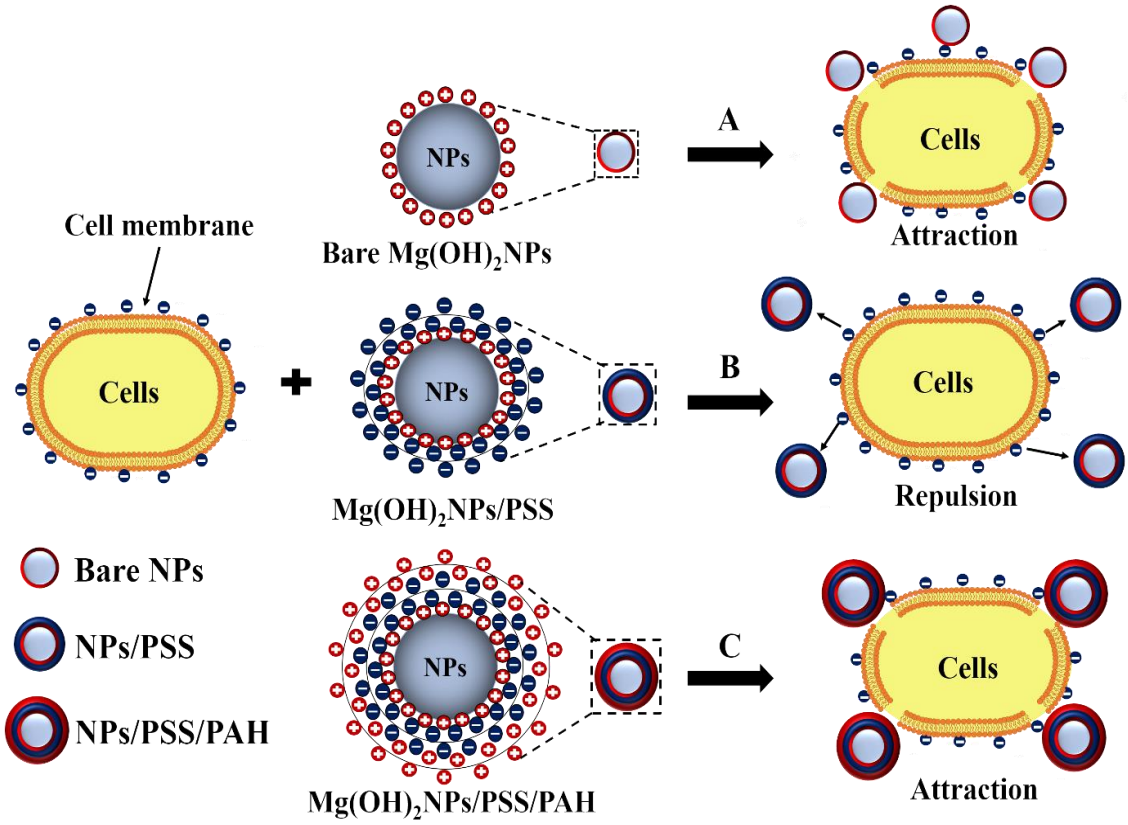


**Figure 6.1.** Schematic diagram showing the various contacting patterns between the bare and polyelectrolyte-coated $Mg(OH)_2$NPs on cells. (A and C) The adhesion of the uncoated and cationic polyelectrolyte-coated $Mg(OH)_2$NPs to the cell wall surfaces is favoured due to their opposite surface charges. (B) The interaction between the anionic outer surface of the cell membrane and the $Mg(OH)_2$NPs coated with anionic polyelectrolyte is repulsive. The cationic $Mg(OH)_2$NPs and $Mg(OH)_2$NPs/PSS/PAH nanoparticles are expected to be more effective against the microbial cells than the anionic $Mg(OH)_2$NPs/PSS particles.

## 6.2 Cytotoxicity assay of bare $Mg(OH)_2$NPs on *S.cerevisiae* cells

The antimicrobial activity of bare $Mg(OH)_2$NPs on *C. reinhardtii*, *S. cerevisiae* and *E. coli* was compared and Figure 6.2 shows the cell viability. Samples of *S.cerevisiae* cells were incubated with dispersed $Mg(OH)_2$NPs at different particle concentrations (0, 250, 500, 1000, 2500 and 5000 µg $mL^{-1}$) for different periods of time up to one day. Then, an aliquot of every sample was taken to examine the number of viable *S.cerevisiae* cells using an automatic cell counter by FDA cell viability assay. Figure 6.2 shows the percentage of viable *S.cerevisiae* cells at various incubation time (10 min., 6 h, 12 h and 24 h). One can see that the percentage of viable *S.cerevisiae* after 10 minutes incubation is at the same level as in the untreated sample. After 6 h of incubation, no measurable antimicrobial effect is noticed up to 500 µg $mL^{-1}$ $Mg(OH)_2$NPs, however, antimicrobial activity is observed at 1000, 2500 and 5000 µg $mL^{-1}$ $Mg(OH)_2$NPs. After 12 h, the viability of *S.cerevisiae* sharply decreases at particle concentrations in the range 500 – 5000 µg $mL^{-1}$. After one day of incubation concentrations higher than 250 µg $mL^{-1}$ bare $Mg(OH)_2$NPs it showed measurable antimicrobial activity towards *S.cerevisiae*. Optical microscopy examination of these samples suggests that the *S.cerevisiae* cells aggregate at a high particle concentration. Our results indicate a strong decline of the *S.cerevisiae* cell viability at concentrations above 1000 µg $mL^{-1}$ bare $Mg(OH)_2$NPs.

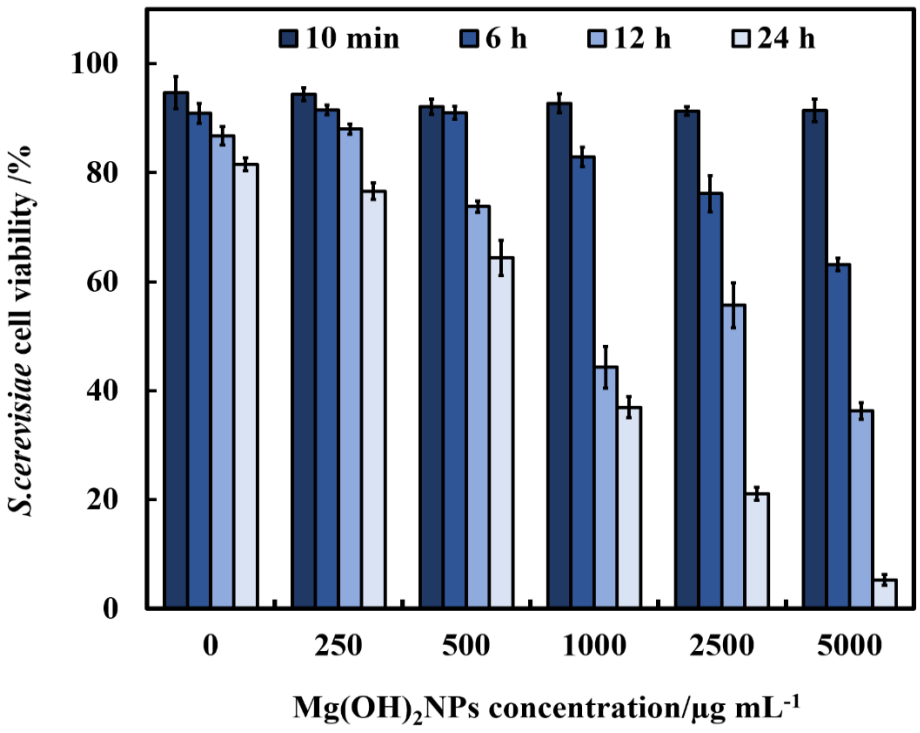


**Figure 6.2.** The antimicrobial activity of bare $Mg(OH)_2$NPs on *S.cerevisiae* cells at various particle concentrations. The cells were incubated with the $Mg(OH)_2$NPs at different periods of time shown.

The data on Figure 6.2 suggest that at high concentrations of bare $Mg(OH)_2$NPs they electrostatically adhere to the negatively charged cell membranes, subsequently killing the cells. The attachment of $Mg(OH)_2$NPs to the cells was also examined by TEM imaging. Figure 6.3A and 6.3C show TEM images of the *S.cerevisiae* cells before and after treatment with 1000 µg $mL^{-1}$ $Mg(OH)_2$NPs solution for 24 h. Those are compared with the untreated samples of *S.cerevisiae* shown in Figure 6.3A and 6.3B. The TEM images show that before the treatment (Figure 6.3A), the membrane of the *S.cerevisiae* cells is regular and smooth, the treatment with 1000 µg $mL^{-1}$ $Mg(OH)_2$NPs leads to a significant accumulation of $Mg(OH)_2$NPs on the external wall of *S.cerevisiae* at such a high particle concentration (Figure 6.3C).

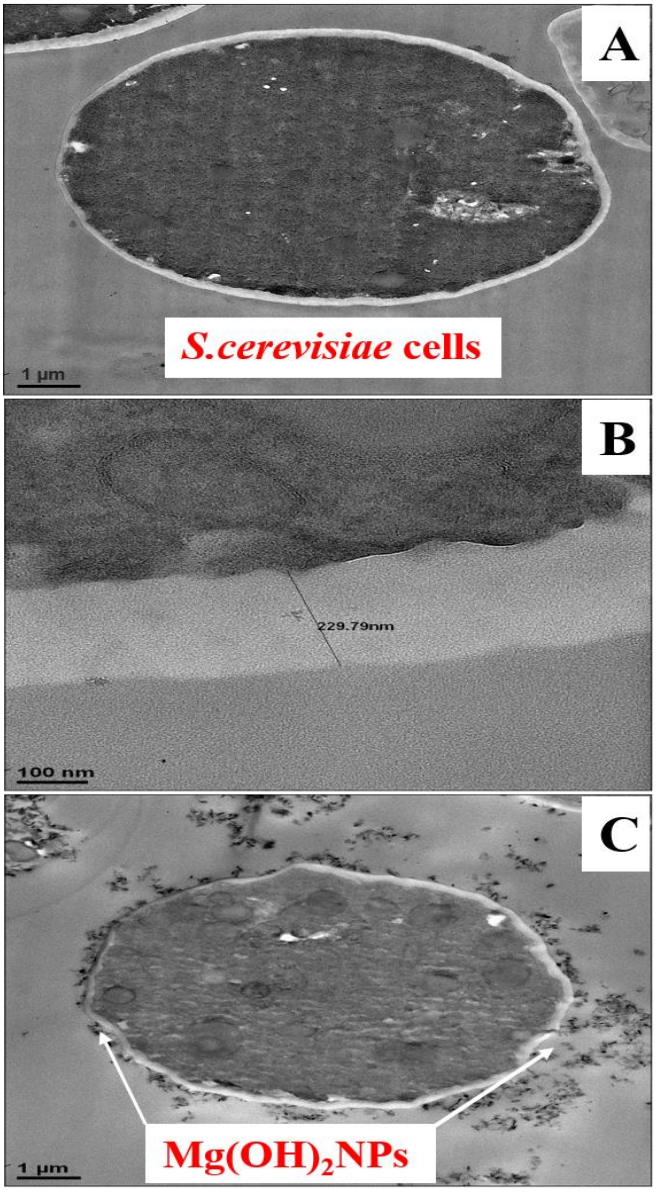


**Figure 6.3.** TEM images of *S.cerevisiae* after being incubated for one day with bare $Mg(OH)_2$NPs: (A) A control sample without $Mg(OH)_2$NPs. (B) A high-resolution TEM

image of the *S.cerevisiae* wall without $Mg(OH)_2$NPs. (C) *S.cerevisiae* cells incubated with 1000 µg $mL^{-1}$ $Mg(OH)_2$NPs showing the attachment of $Mg(OH)_2$NPs to the outer cell surface.

These results were also confirmed by EDX of the treated *S.cerevisiae* cells which showed the presence of Mg on the outer part of the cell membrane (Figure 6.4). Although the exposure of the *S.cerevisiae* cells to bare $Mg(OH)_2$NPs at concentration 1000 µg $mL^{-1}$ caused a cytotoxicity effect (Figure 6.3C) it did not cause an internalisation of $Mg(OH)_2$NPs as the cell wall of *S.cerevisiae* cells is very thick (200 nm, Figure 6.3B) compared to other microbial cells . Two probable mechanisms for the antimicrobial effect of $Mg(OH)_2$NPs on yeast were envisaged. Due to their cationic nature at neutral pH, there is a significant accumulation of $Mg(OH)_2$NPs on the cell membranes. As these particles have very irregular morphology and consist of smaller crystallites, their adhesion to the cell membrane in large amounts can potentially cause its dislocation and cracking. Although we do not observe a straight permeation of $Mg(OH)_2$NPs to the *S.cerevisiae* wall, local damage of the membrane may lead to cell viability loss. Another possible mechanism of membrane damage can be caused by the counter-ion atmosphere of the $Mg(OH)_2$NPs which consists of highly concentrated hydroxyl ions ($OH^-$) of very high local pH which can cause lipid hydrolysis on the membrane surface and killing the cell. Some of these mechanisms have been commented on by other authors for uncoated $Mg(OH)_2$NPs.[14-16]

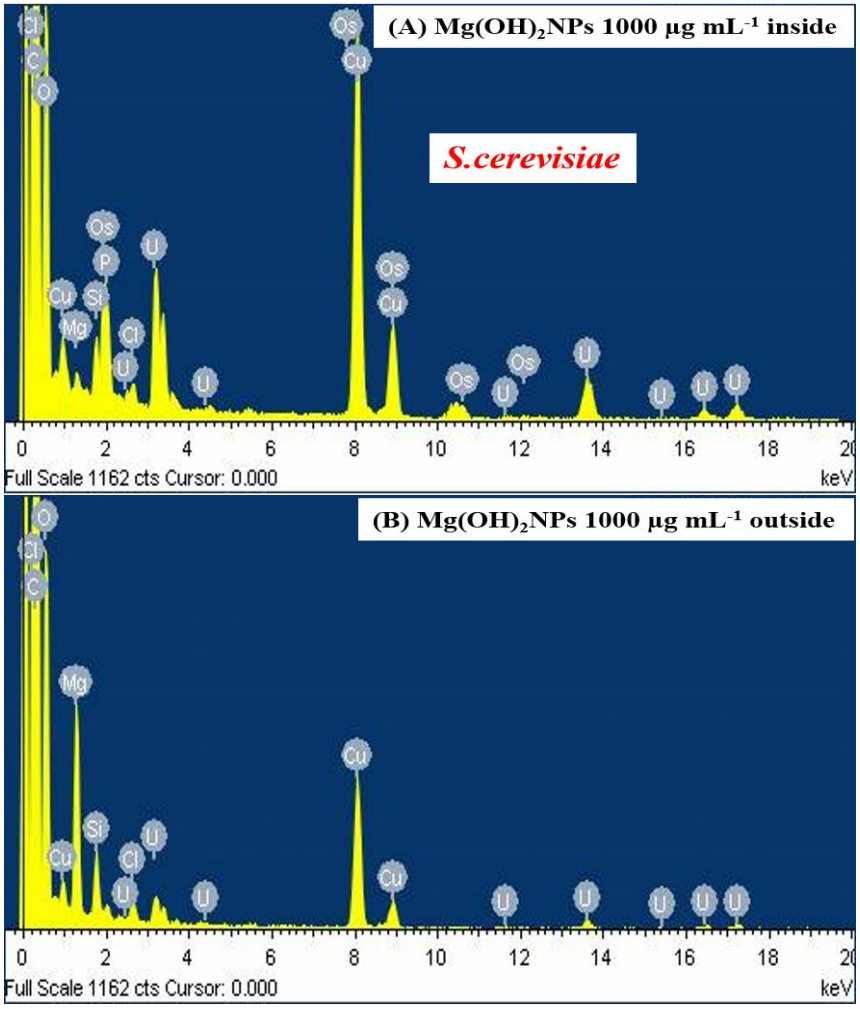


**Figure 6.4.** EDX diagram of *S.cerevisiae* cells at 1000 µg $mL^{-1}$: (A) the inside membrane of *S.cerevisiae* and (B) the outside membrane of *S.cerevisiae*. The data indicate the existence of $Mg(OH)_2$NPs on the outside part of the cell membrane.

## 6.3 Cytotoxicity assay of bare $Mg(OH)_2$NPs on *C. reinhardtii* cells

The antimicrobial activity of $Mg(OH)_2$NPs towards *C. reinhardtii* under similar conditions for various exposure times was also examined as shown in Figure 6.5. At a 10 minutes exposure time, all *C. reinhardtii* were viable at the similar level as the untreated sample. After two hours of incubation, the *C. reinhardtii* viability declined for $Mg(OH)_2$NPs concentrations from 250 µg $mL^{-1}$ to 1000 µg $mL^{-1}$. After 4 h the *C. reinhardtii* viability was reduced to 40% at 1000 µg $mL^{-1}$ of $Mg(OH)_2$NPs, while after 6 h, it sharply declined for 250 µg $mL^{-1}$ to 1000 µg $mL^{-1}$ concentrations of $Mg(OH)_2$NPs, leading to complete loss of cell viability at concentrations above 750 µg $mL^{-1}$ $Mg(OH)_2$NPs.

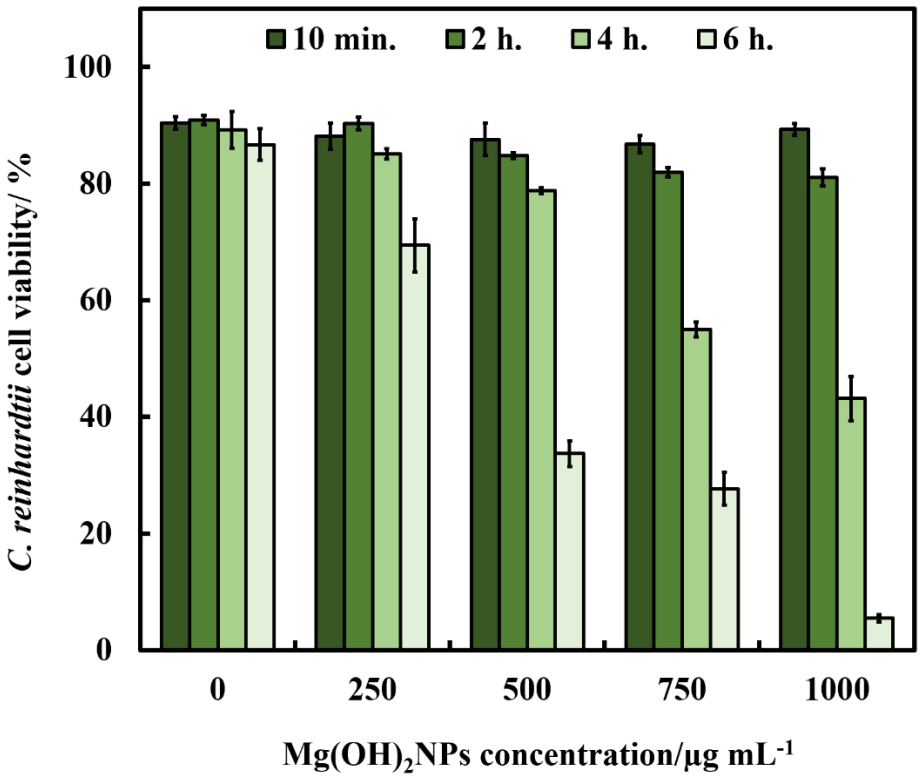


**Figure 6.5.** The antimicrobial activity of bare $Mg(OH)_2$NPs on *C. reinhardtii* cells at various particle concentrations. The cells were incubated with the $Mg(OH)_2$NPs at different periods of time shown.

Figure 6.6 shows TEM images of *C. reinhardtii* exposed to $Mg(OH)_2$NPs at various concentrations. TEM images of the *C. reinhardtii* after 6 h of incubation with $Mg(OH)_2$NPs indicate the localization of the $Mg(OH)_2$NPs with respect to the cell membrane. One can see that the outer cell wall of *C. reinhardtii* has a thick layer of associated NPs after treatment with 750 µg $mL^{-1}$, 1000 µg $mL^{-1}$ and 5000 µg $mL^{-1}$ concentrations of $Mg(OH)_2$NPs (Figure 6.6C, 6.6D, 6.6E and 6.6F). Internalization of $Mg(OH)_2$NPs in the *C. reinhardtii* was not observed even at 5000 µg $mL^{-1}$ $Mg(OH)_2$NPs as shown in Figures 6.7 and 6.8. The EDX shows the absence of Mg in the inside of *C. reinhardtii* but confirms its presence on the outer wall.

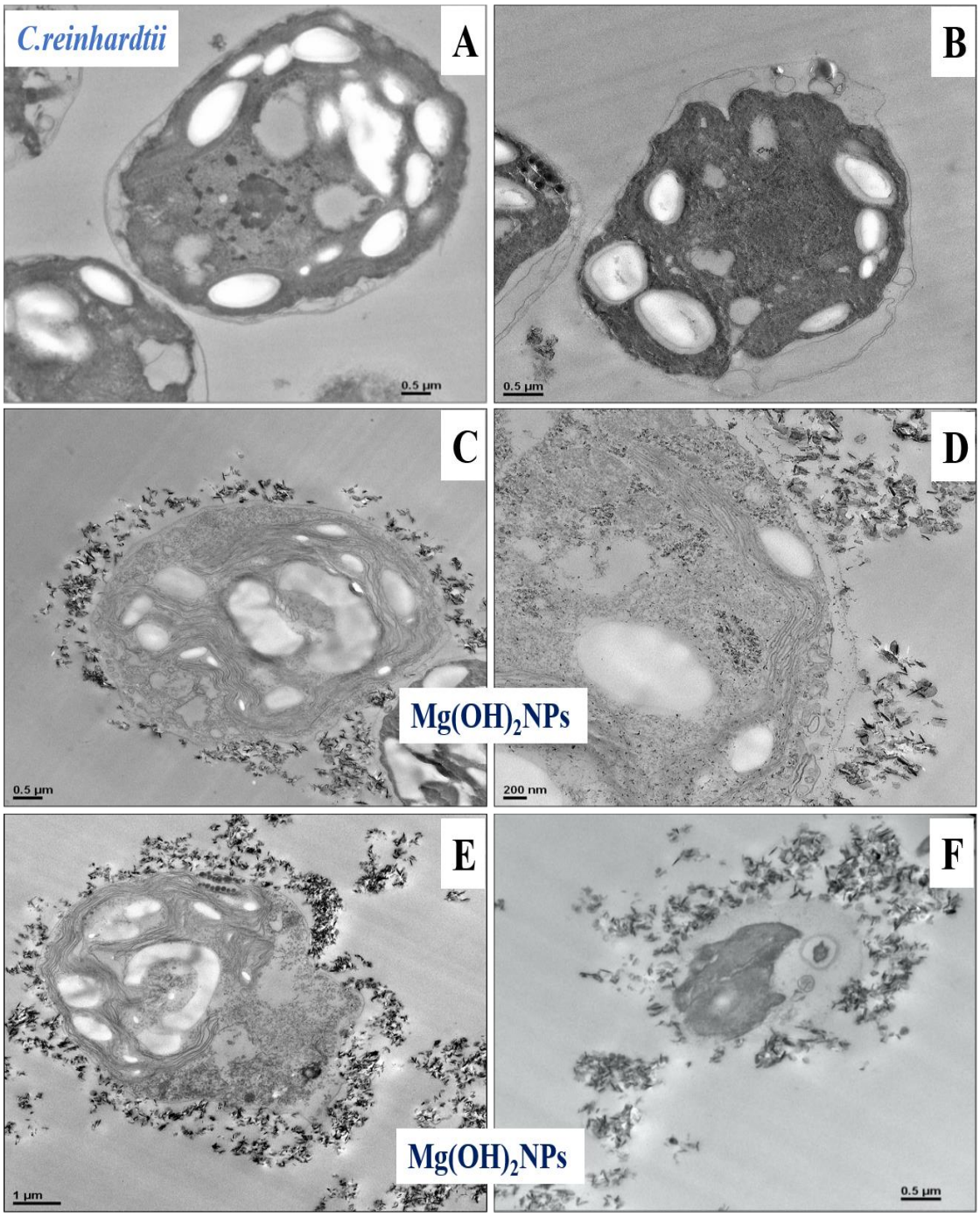


**Figure 6.6.** TEM images of *C. reinhardtii* after being exposed to 0, 250, 750, 1000 and 5000 µg $mL^{-1}$ $Mg(OH)_2$NPs for six hours (fixed, embedded in resin and sectioned). (A) An untreated sample without $Mg(OH)_2$NPs; (B) *C. reinhardtii* treated with 250 µg $mL^{-1}$ $Mg(OH)_2$NPs; (C) and (D) *C. reinhardtii* incubated with 750 µg $mL^{-1}$ $Mg(OH)_2$NPs at different magnifications. (E) and (F) *C. reinhardtii* treated with 1000 µg $mL^{-1}$ and 5000 µg $mL^{-1}$ $Mg(OH)_2$NPs, respectively.

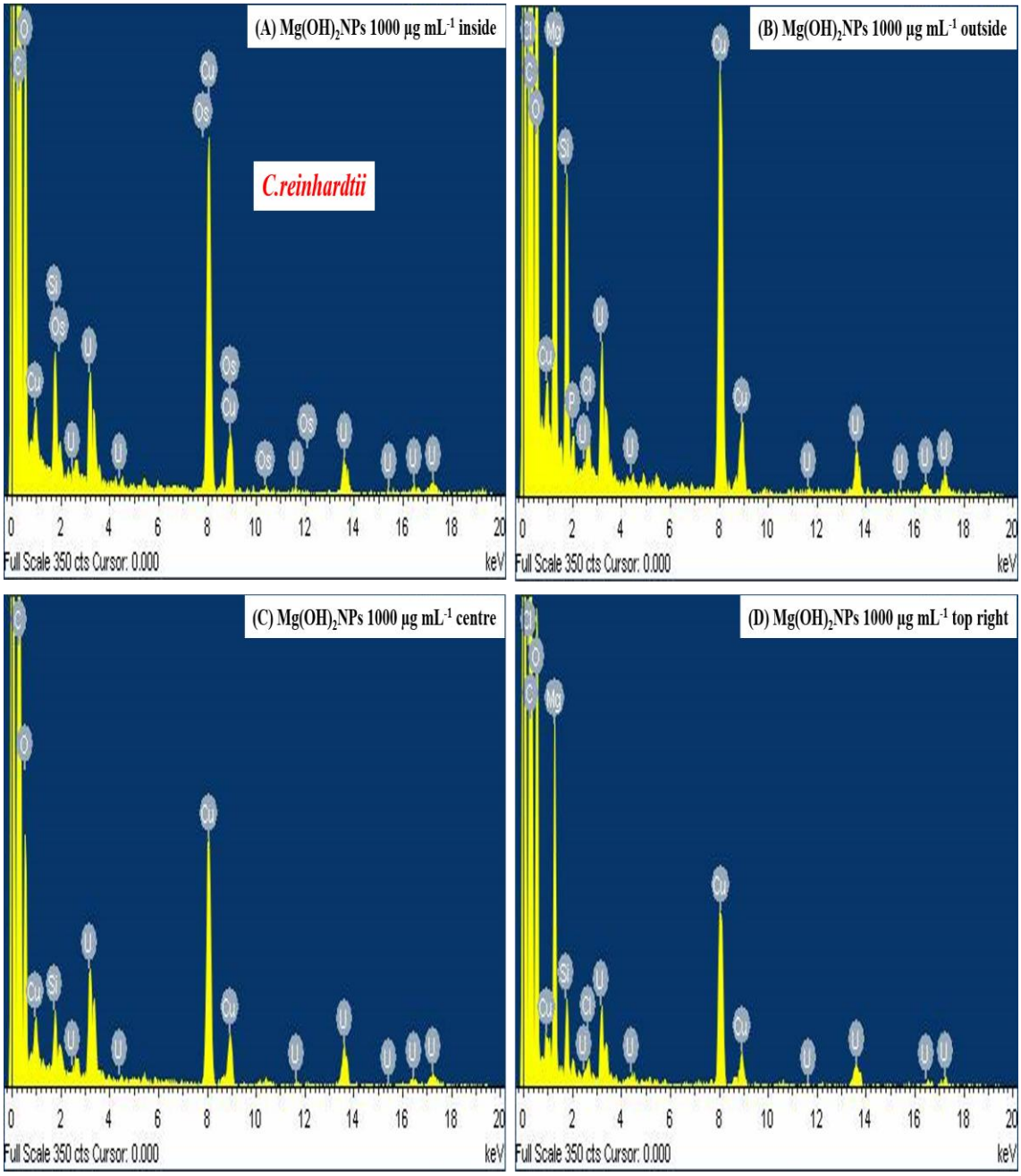


**Figure 6.7.** EDX chart of the *C. reinhardtii* with $Mg(OH)_2$NPs at 1000 µg $mL^{-1}$: (A) inside membrane of *C. reinhardtii* and (B) outside membrane of *C. reinhardtii* ; (C) centre cell and (D) top right. This demonstrates the lack of internalised $Mg(OH)_2$NPs in *C. reinhardtii* even at NPs concentration 1000 µg $mL^{-1}$.

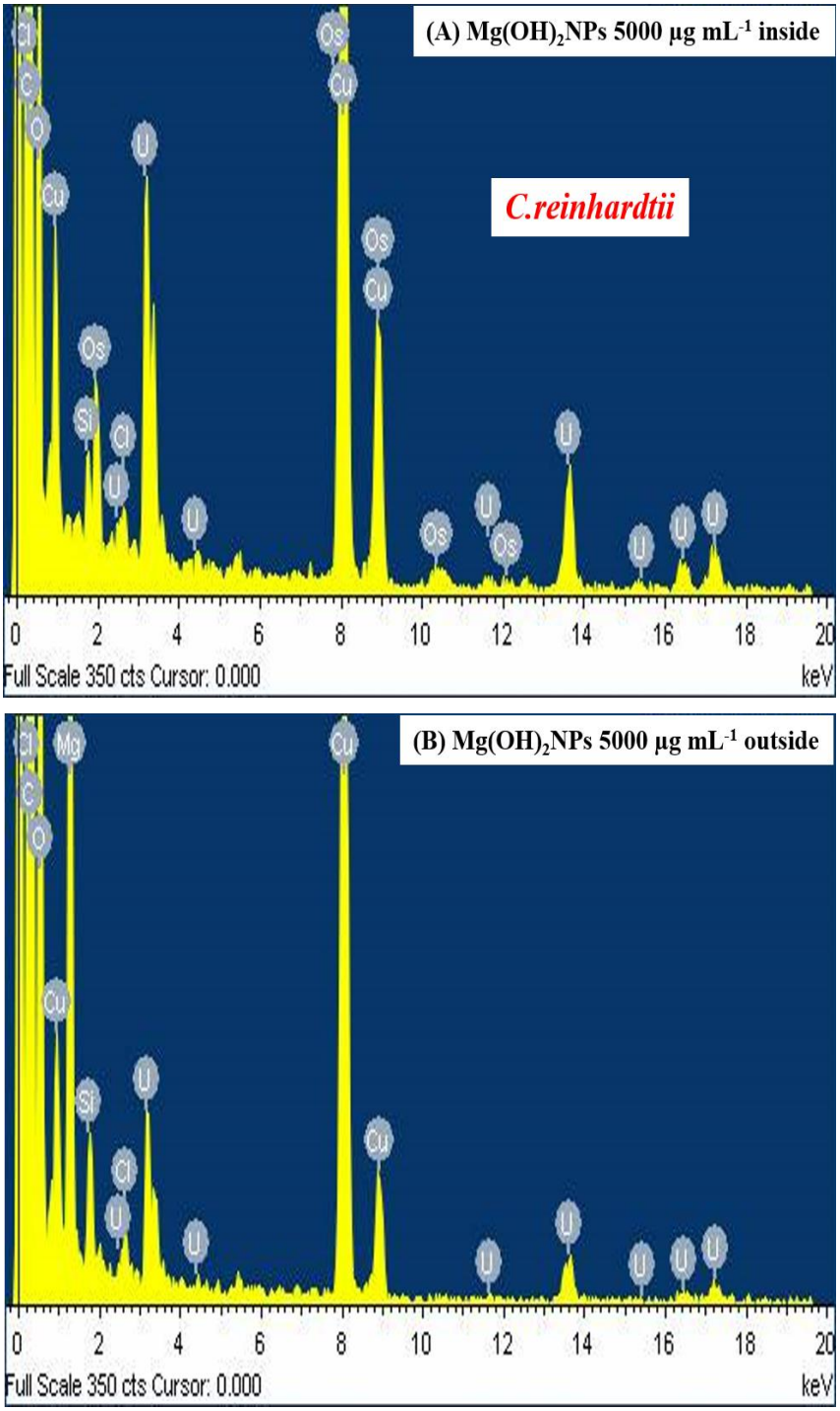


**Figure 6.8.** EDX chart of the *C. reinhardtii* with $Mg(OH)_2$NPs at 5000 µg $mL^{-1}$: (A) inside the membrane of the *C. reinhardtii* and (B) outer the membrane of the *C. reinhardtii*.

## 6.4 Cytotoxicity assay of bare $Mg(OH)_2$NPs on *E. coli*

Figure 6.9 shows the results for the effect of bare $Mg(OH)_2$NPs towards *E.coli* at various incubation times. The data demonstrate that the bare $Mg(OH)_2$NPs have an excellent antimicrobial effect on the *E. coli* at 6000 µg $mL^{-1}$ for one day. The *E. coli* viability decreases sharply for treatment with 6000 µg $mL^{-1}$ $Mg(OH)_2$NPs after four hours of

exposure. The viability decreases further after six hours, and after one day it resulted in approximately 97% loss of viability.

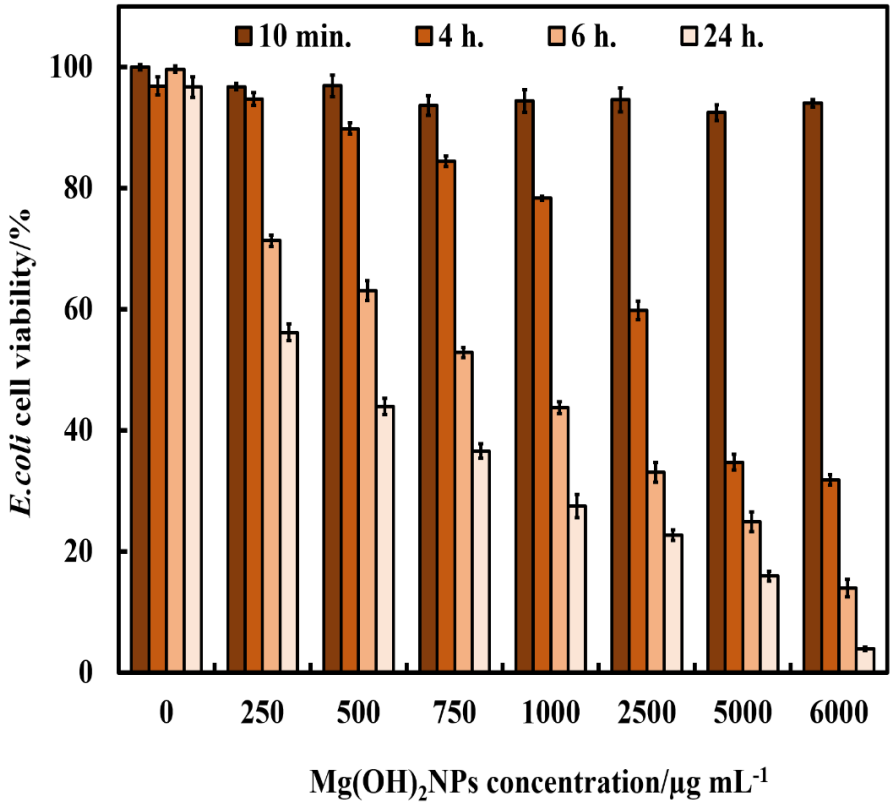


**Figure 6.9.** The antibacterial activity of bare $Mg(OH)_2$NPs on *E. coli* at various particle concentrations. The cells were incubated with the $Mg(OH)_2$NPs at different periods of time shown.

Past research suggested that the antibacterial effect might be credited to the multiple factors: (i) the cellular internalization of NPs where they could potentially interfere with the bacterial DNA and cellular organelles [17-19]; (ii) immediate contacts with the bacterial cell wall [15, 20]; and (iii) the increased local dissolution of metal ions of the nanoscale metal oxide.[21, 22] Usually, the antimicrobial impact is dependent on the size of the nanoparticles and a better antimicrobial effect is achieved with smaller nanoparticles.[14, 23, 24] The $Mg(OH)_2$NPs with the smallest size (about 70 nm) had the highest antimicrobial activity. We did TEM imaging and EDX analysis to examine the location of magnesium in the *E.coli* after treating them with non-coated $Mg(OH)_2$NPs. Magnesium was not detected by the EDX in many randomly selected regions inside the *E.coli* but it was primarily found on the outer side of the cell wall as shown in Figure 6.11. This showed that the dissolved magnesium ions and $Mg(OH)_2$NPs did not go to the inside of *E.coli*. Nevertheless, evident

changes of the *E.coli* cell structure were seen after incubation with $Mg(OH)_2$NPs. Figure 6.10D shows image of untreated *E.coli* where the bacteria have preserved the integrity of their cell walls. After incubation with 2500 µg $mL^{-1}$ (Figure 6.10E) and 5000 µg $mL^{-1}$ (Figure 6.10F) $Mg(OH)_2$NPs for one day, the cell profile became fussy and the walls of *E.coli* appear disintegrated. Therefore, the antimicrobial activity of $Mg(OH)_2$NPs might be expressed more via their adsorption on the outer side of the cell wall rather than through internalization in the cell, which leads to the decay of the cell walls of *E.coli*. Furthermore, SEM imaging was used to study the presence of $Mg(OH)_2$NPs on the surfaces of the bacteria. Figure 6.10A, 6.10B and 6.10C show *E.coli* samples after being treated with 2500 µg $mL^{-1}$ and 5000 µg $mL^{-1}$ $Mg(OH)_2$NPs for one day. They indicate that the cell wall has a build-up of a dense layer of nanoparticles. Moreover, EDX indicated that the samples contain magnesium, and confirm that the $Mg(OH)_2$NPs have ability to adhere on the bacterial cell wall with occasional penetration on the inside. Consequently, the *E.coli* lack of viability is associated with the compromised integrity of bacteria walls, which is seen for these samples by SEM and TEM. This is consistent with the mechanisms outlined above which indicates that the antimicrobial action of $Mg(OH)_2$NPs on the cells is likely to be due to the cationic character of $Mg(OH)_2$NPs that adsorb on the negatively charged bacterial cell wall by electrostatic attraction. The adsorbed $Mg(OH)_2$NPs disrupt the integrity of the bacterial cell wall which then increase its permeability and kills the bacteria.

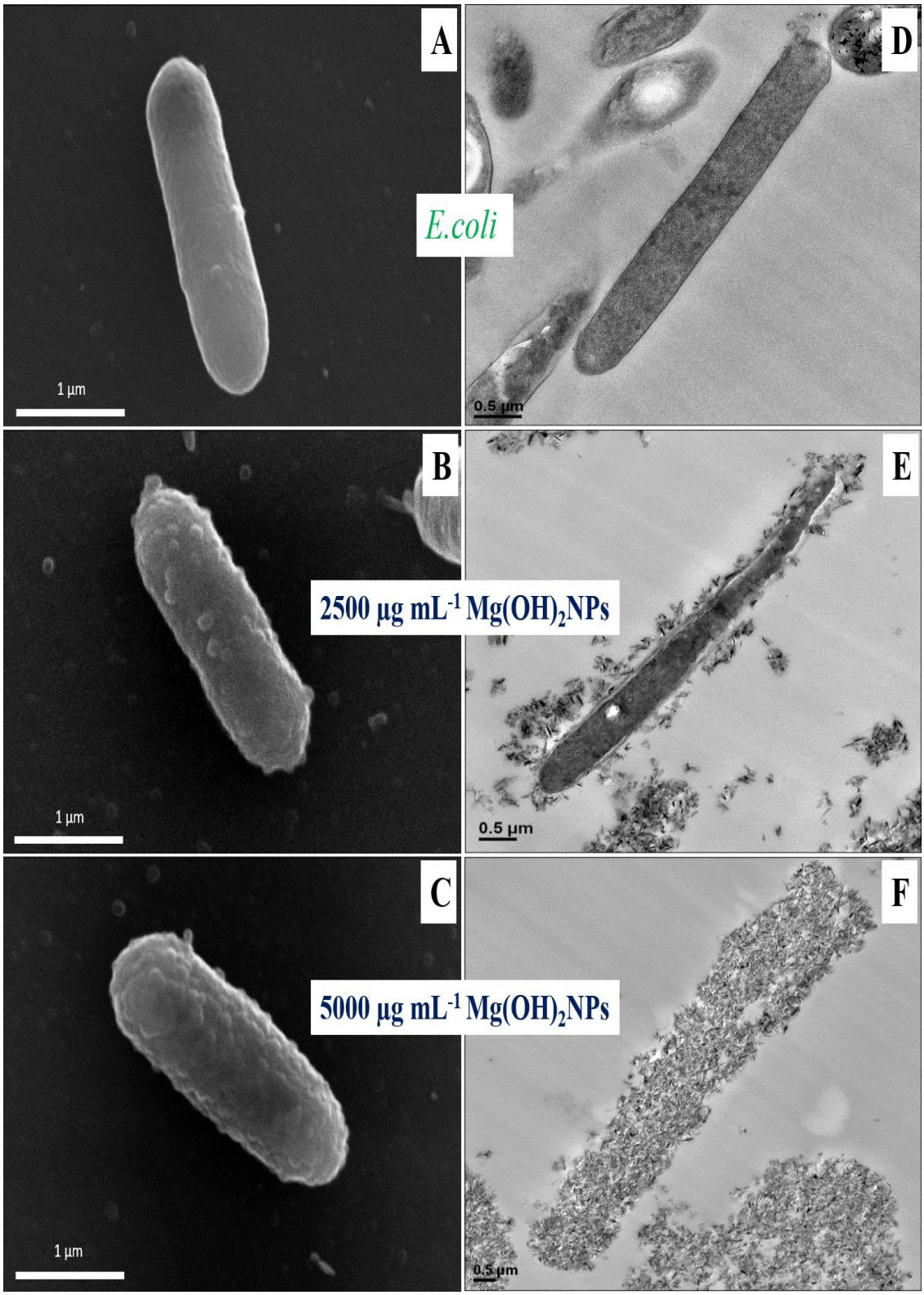


**Figure 6.10.** SEM and TEM images of *E.coli* after being incubated for 24 h with a suspension of bare $Mg(OH)_2$NPs : (A) SEM and (D) TEM images of an untreated sample. (B) SEM and (E) TEM images of *E.coli* incubated with 2500 µg $mL^{-1}$ $Mg(OH)_2$NPs . (C) SEM and (F) TEM images of *E.coli* incubated with 5000 µg $mL^{-1}$ $Mg(OH)_2$NPs.

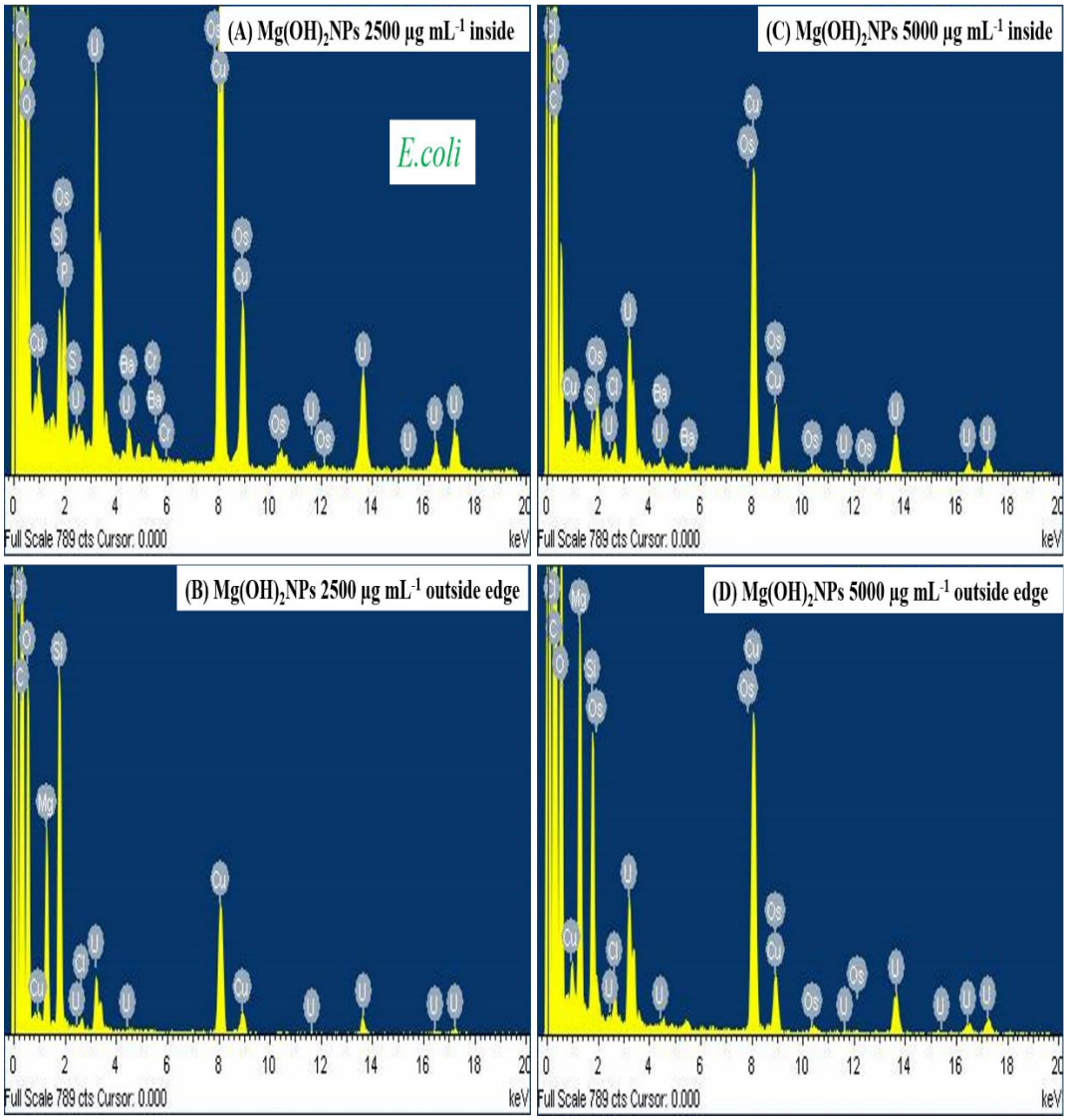


**Figure 6.11.** EDX diagram of *E.coli* cells incubated with $Mg(OH)_2$NPs at 2500 µg $mL^{-1}$ and 5000 µg $mL^{-1}$: (A) *E.coli* inside wall and (B) *E.coli* outer wall areas. (C) *E.coli* inside wall and (D) *E.coli* outer wall areas. The data indicate the existence of $Mg(OH)_2$NPs on the external part of the cell membrane.

## 6.5 Zeta potential measurements of cells after treatment with $Mg(OH)_2$NPs

The effect of the particles attachment on the outer cell wall was further explored as it may play a significant role on their antimicrobial action.[14-16] The zeta potential of the *S.cerevisiae, C. reinhardtii* and *E.coli* after treatment with $Mg(OH)_2$NPs in solution was studied. The cells were incubated with $Mg(OH)_2$NPs suspensions at different particle concentrations. Then, an aliquot of every suspension was taken to examine the cells average zeta potential value by a Zetasizer. It was found that $Mg(OH)_2$NPs have an average zeta potential of +30 ± 6 mV. Upon incubation with bare $Mg(OH)_2$NPs, the

*S.cerevisiae* cells, which are negatively charged (zeta potential of -12 ± 5 mV), still showed negative but significantly reduced by magnitude zeta potential due to a build–up of cationic NPs, as shown in Figure 6.12. Note that the zeta potential of treated cells does not vary much with the duration of the treatment.

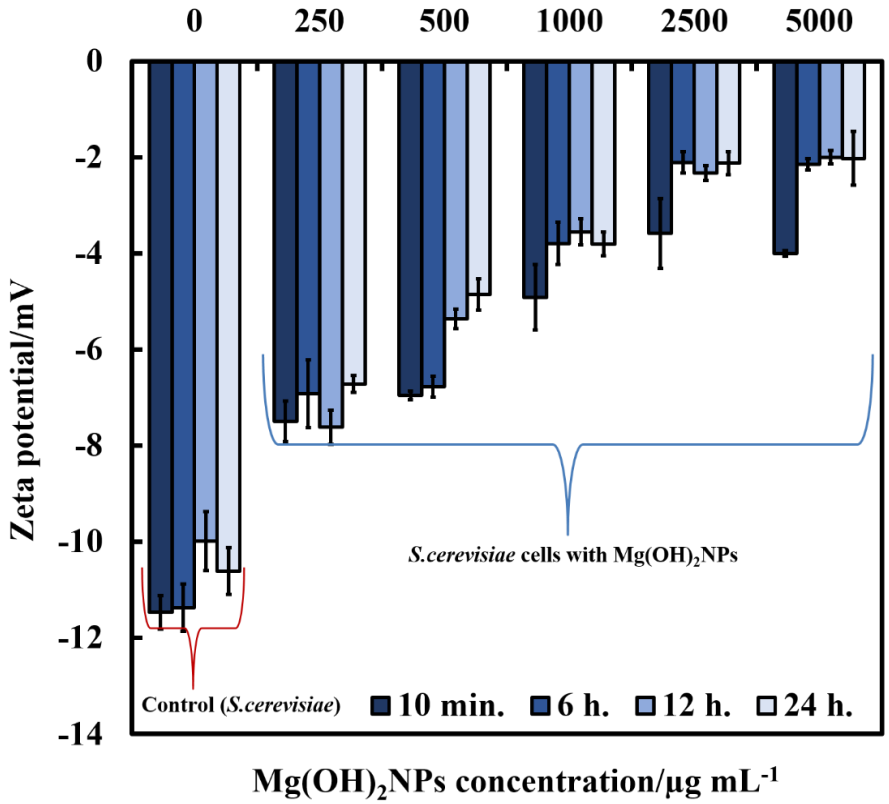


**Figure 6.12.** The zeta potential of *S.cerevisiae* cells treated with different concentrations of $Mg(OH)_2$NP suspensions at various incubation times.

The *C. reinhardtii* cells which have a negative zeta potential of -18 ± 5mV, also reduced their zeta potential by a magnitude after treatment with the cationic $Mg(OH)_2$NPs but did not charge reverse even at high particle concentrations, as presented in Figure 6.13. Figure 6.14 shows the impact of bare $Mg(OH)_2$NPs on the *E.coli* zeta potential. *E.coli* cells, which carried negative charge (zeta potential -41 ± 5 mV), remained negatively charged when treated with up to 100 µg $mL^{-1}$ $Mg(OH)_2$NPs. At higher $Mg(OH)_2$NPs concentration, the zeta potential of *E. coli* cells turned positive when exposed to 500 µg $mL^{-1}$ to 6000 µg $mL^{-1}$ $Mg(OH)_2$NPs. These results show that the adhesion of $Mg(OH)_2$NPs to cells might indeed be primarily driven by electrostatic interactions.[14, 25] It can be concluded that the positive charge of $Mg(OH)_2$NPs might have a high impact on the adsorption of particles on the cells membrane. This was confirmed by both the SEM and TEM images (Figure 6.10).

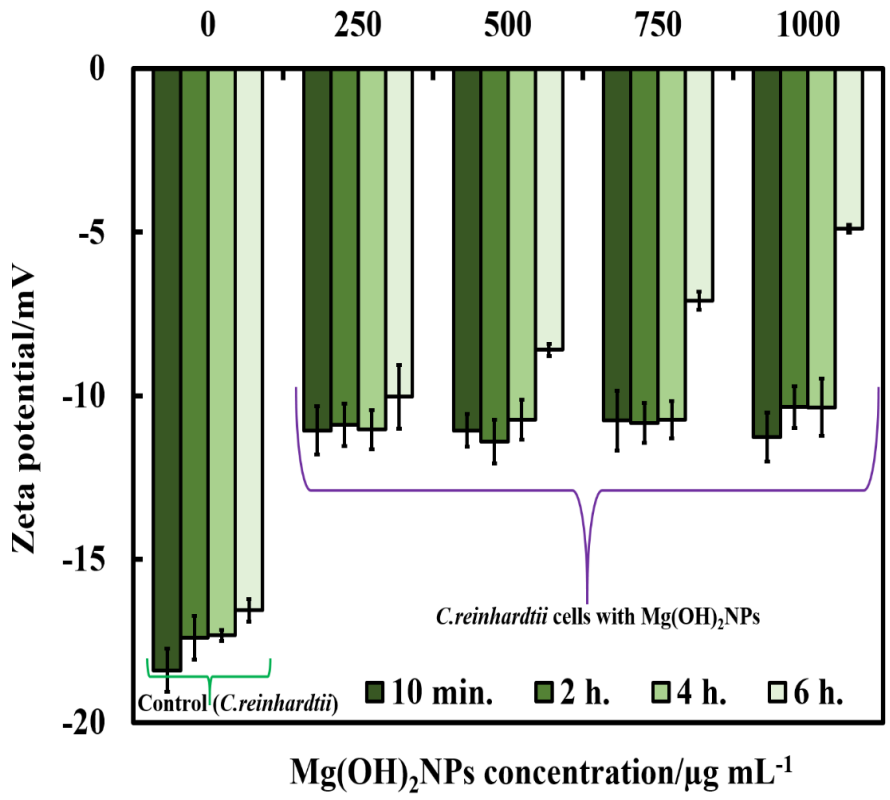


**Figure 6.13.** The zeta potential of *C. reinhardtii* cells treated with different concentrations of $Mg(OH)_2$NP suspensions at various incubation times.

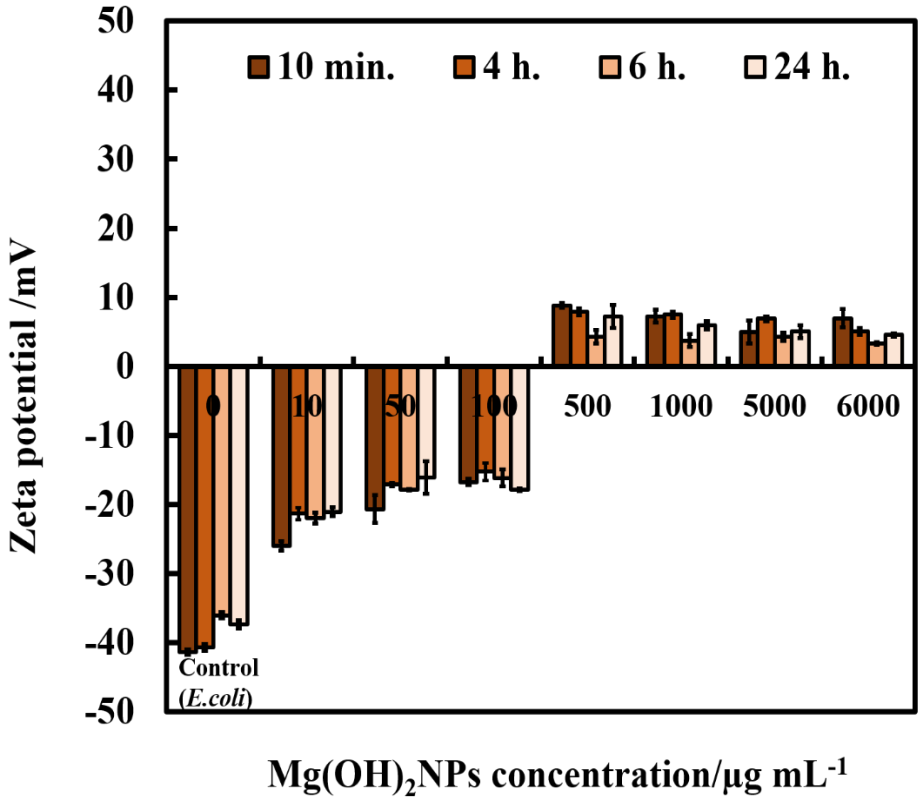


**Figure 6.14.** The zeta potential of *E.coli* treated with different concentrations of $Mg(OH)_2$NP suspensions at various incubation times.

## 6.6 Cytotoxicity assay of polyelectrolyte-coated $Mg(OH)_2$NPs on *S.cerevisiae*.

The antimicrobial activity of $Mg(OH)_2$NPs coated with multilayers of polyelectrolytes on *S.cerevisiae, C. reinhardtii* and *E.coli* was studied. In order to control the electrostatic interaction, we functionalized $Mg(OH)_2$NPs with PSS and PAH and compared their antimicrobial effect with that of the bare $Mg(OH)_2$NPs. Aqueous suspensions of *S.cerevisiae* were incubated with $Mg(OH)_2$NPs/PSS and $Mg(OH)_2$NPs/PSS/PAH suspensions at various particle concentrations (0, 250, 500, 1000, 2500 and 5000 μg $mL^{-1}$) for up to one day (Figure 6.15).

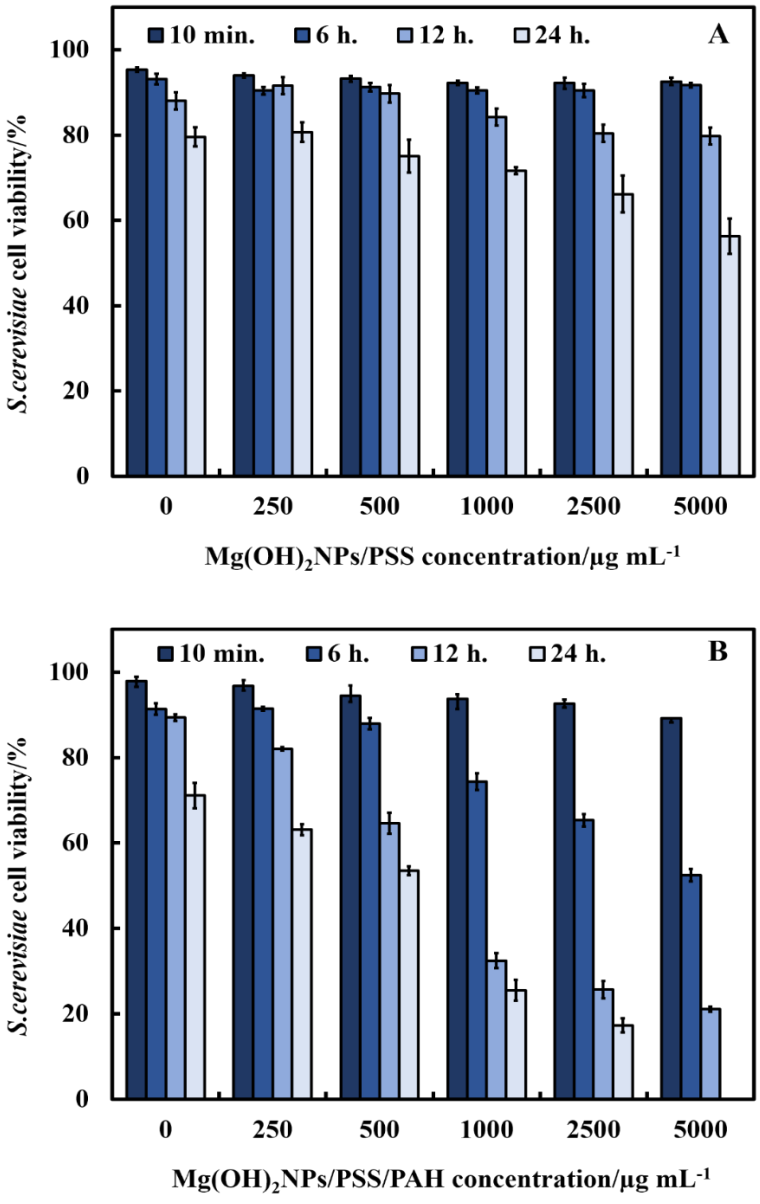


**Figure 6.15.** *S.cerevisiae* cell viability as a function of nanoparticle concentration after incubation for up to 24 hours with (A) $Mg(OH)_2$NPs/PSS and (B) $Mg(OH)_2$NPs/PSS/PAH.

The results represented in Figure 6.15A show that the anionic $Mg(OH)_2$NPs/PSS have a lower antimicrobial activity on *S.cerevisiae* compared to the cationic bare $Mg(OH)_2$NPs (c.f. Figure 6.2). At incubating times up to six hours, no change in the *S.cerevisiae* viability was registered for $Mg(OH)_2$NPs/PSS even at high particle concentrations. The same treatment with the cationic $Mg(OH)_2$NPs/PSS/PAH showed a significant antimicrobial activity on *S.cerevisiae* at particle concentrations of 1000, 2500 and 5000 μg $mL^{-1}$ as shown in Figure 6.15B. A very strong effect of the $Mg(OH)_2$NPs/PSS/PAH on *S.cerevisiae* viability was observed upon their incubation with high particle concentrations of 5000 μg $mL^{-1}$ for up to 24 h. In contrast, upon incubation with the anionic $Mg(OH)_2$NPs/PSS at high particle concentrations of 5000 μg $mL^{-1}$, it was observed a moderate impact on *S.cerevisiae* viability for up to one day of incubation (Figure 6.15B). Hence, by coating the $Mg(OH)_2$NPs with an outer layer of anionic polyelectrolyte their antimicrobial activity is significantly decreased because of the electrostatic repulsion between the anionic $Mg(OH)_2$NPs/PSS and the anionic surface of *S.cerevisiae* cells. Figure 6.16B, 6.16C and 6.16D show TEM images of *S.cerevisiae* cells after their incubation with $Mg(OH)_2$NPs coated with PSS and PAH layers. The TEM image in Figure 6.16B indirectly confirms lack of nanoparticle accumulation due to the electrostatic repulsion among the anionic $Mg(OH)_2$NPs/PSS and the negatively charged *S.cerevisiae* cell wall. Figure 6.16C and 6.16D show a great accumulation of $Mg(OH)_2$NPs/PSS/PAH on the cell walls which corresponds to a much higher activity towards *S.cerevisiae*. One can conclude that coating $Mg(OH)_2$NPs with PSS as an external layer significantly diminishes their ability to attach on the treated cells as shown in Figure 6.16B. *S.cerevisiae* cell viability tests revealed that $Mg(OH)_2$NPs/PSS were much less effective in killing the cells than the $Mg(OH)_2$NPs/PSS/PAH or bare $Mg(OH)_2$NPs, which strongly accumulate on the cell membrane due to electrostatic attraction. These results were also supported via TEM images of *S.cerevisiae*. The antimicrobial activity of each type of nanoparticles on the *S.cerevisiae* cells follow the order: $Mg(OH)_2$NPs/PSS/PAH > $Mg(OH)_2$NPs> $Mg(OH)_2$NPs/PSS (Figure 6.17).

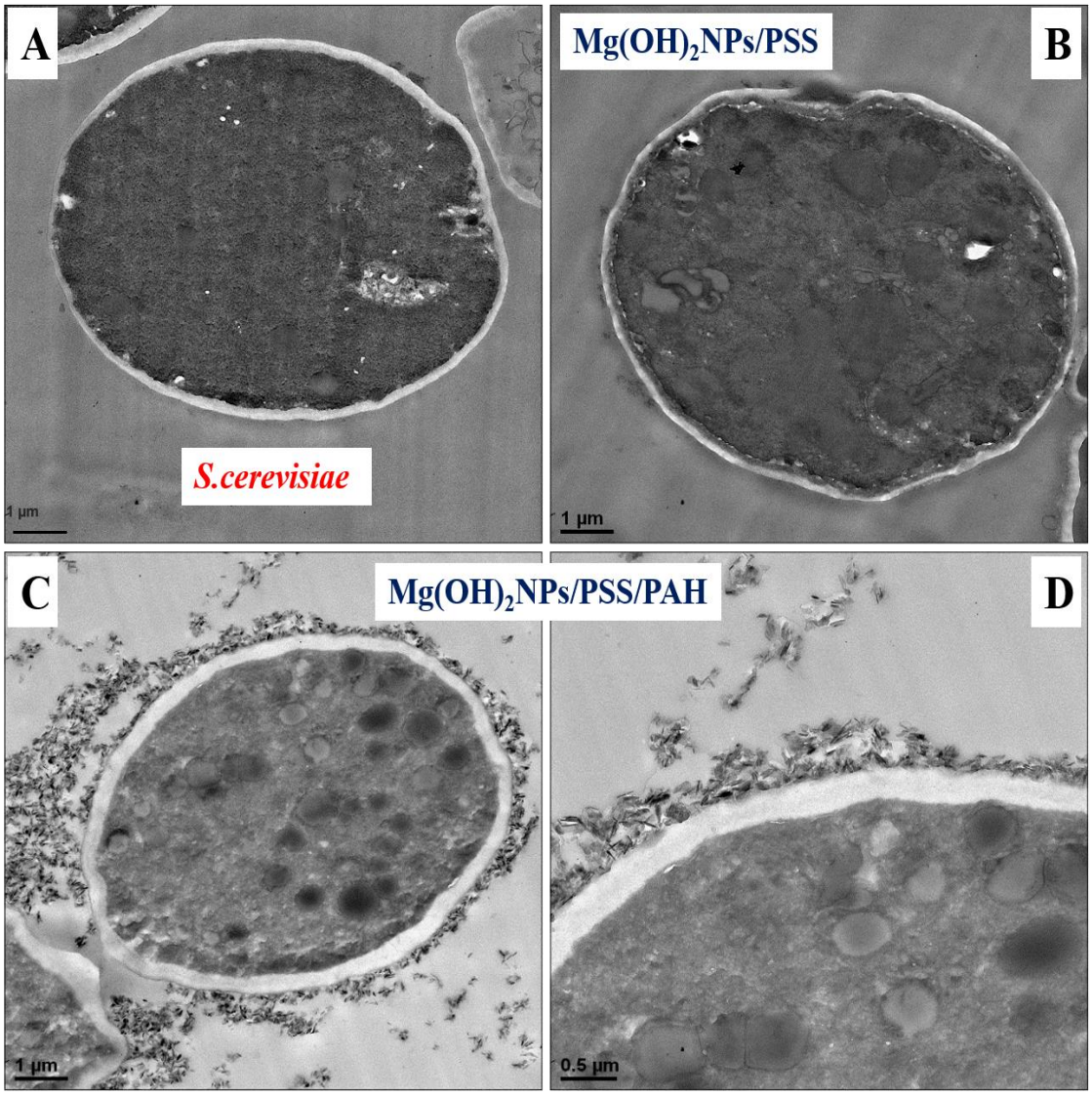


**Figure 6.16.** TEM images of *S.cerevisiae* cells incubated for one day with $Mg(OH)_2$NPs coated by polyelectrolytes: (A) an untreated sample without $Mg(OH)_2$NPs. (B) $Mg(OH)_2$NPs/PSS. (C and D) $Mg(OH)_2$NPs/PSS/PAH at different magnifications.

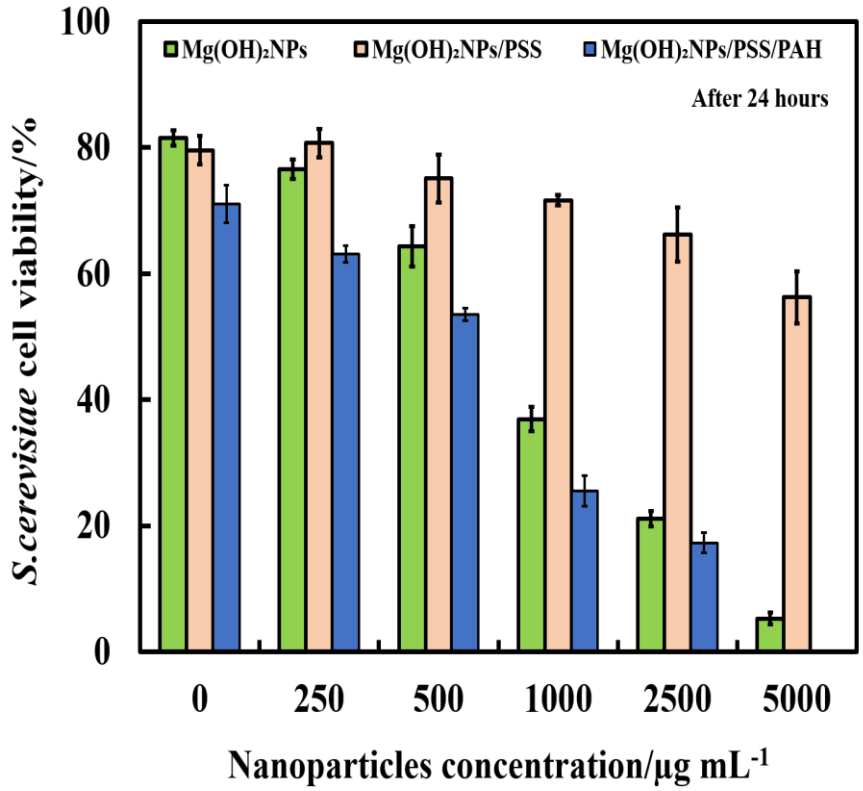


**Figure 6.17.** *S.cerevisiae* cell viability after incubation as a function of nanoparticle concentration for up to 24 hours with uncoated and polyelectrolyte-coated $Mg(OH)_2$NPs.

## 6.7 Cytotoxicity assay of polyelectrolyte-coated $Mg(OH)_2$NPs on *C. reinhardtii* cells

Figure 6.18A and Figure 6.18B compares the antimicrobial activity of multilayer-coated $Mg(OH)_2$NPs with PSS and PAH polyelectrolytes at various NPs concentrations on the *C. reinhardtii*. Figure 6.18A shows that, for incubation times up to 6 h, no measurable variation in the C. *reinhardtii* cell viability was detected for $Mg(OH)_2$NPs/PSS even at high particle concentrations. However, at similar conditions, the cationic $Mg(OH)_2$NPs/PSS/PAH displayed an marked antimicrobial activity on *C. reinhardtii* even at 250 µg $mL^{-1}$. A very strong effect of the $Mg(OH)_2$NPs/PSS/PAH on the *C. reinhardtii* cells viability was observed for exposure times up to six hours at 1000 µg $mL^{-1}$ particle concentrations (Figure 6.18B).

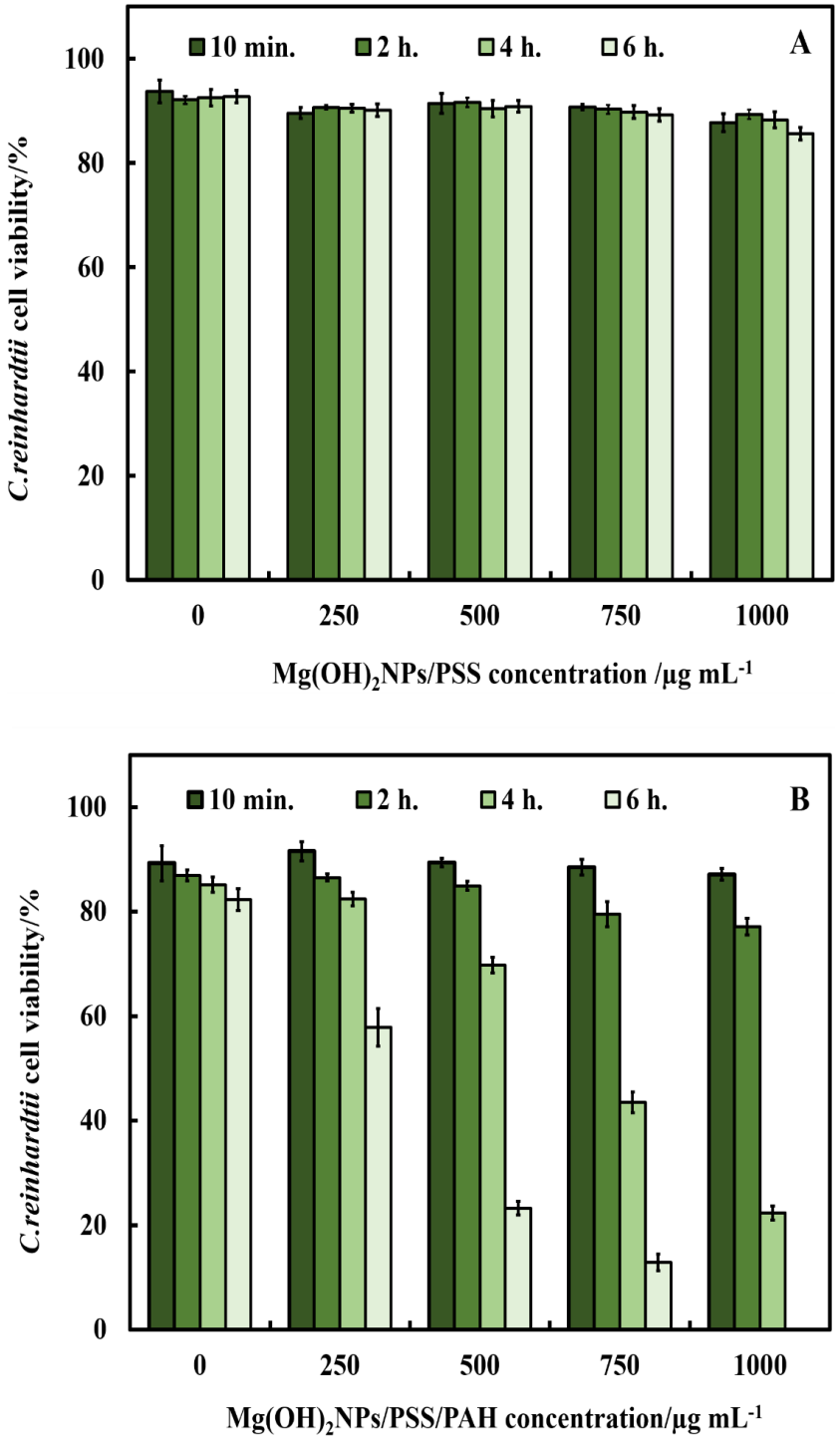


**Figure 6.18.** *C. reinhardtii* cell viability as a function of nanoparticle concentration after incubation for up to 6 h with (A) $Mg(OH)_2$NPs/PSS and (B) $Mg(OH)_2$NPs/PSS/PAH.

One can conclude that by coating the $Mg(OH)_2$NPs with an external layer of anionic polyelectrolyte, their antimicrobial activity decreased for both *S.cerevisiae* and *C. reinhardtii* because of the electrostatic repulsion among the $Mg(OH)_2$NPs/PSS and the cells walls (see Figure 6.20). Figure 6.19A, 6.19B and 6.19C confirm this hypothesis with TEM images of *C. reinhardtii* exposed into the polyelectrolyte-coated $Mg(OH)_2$NPs.

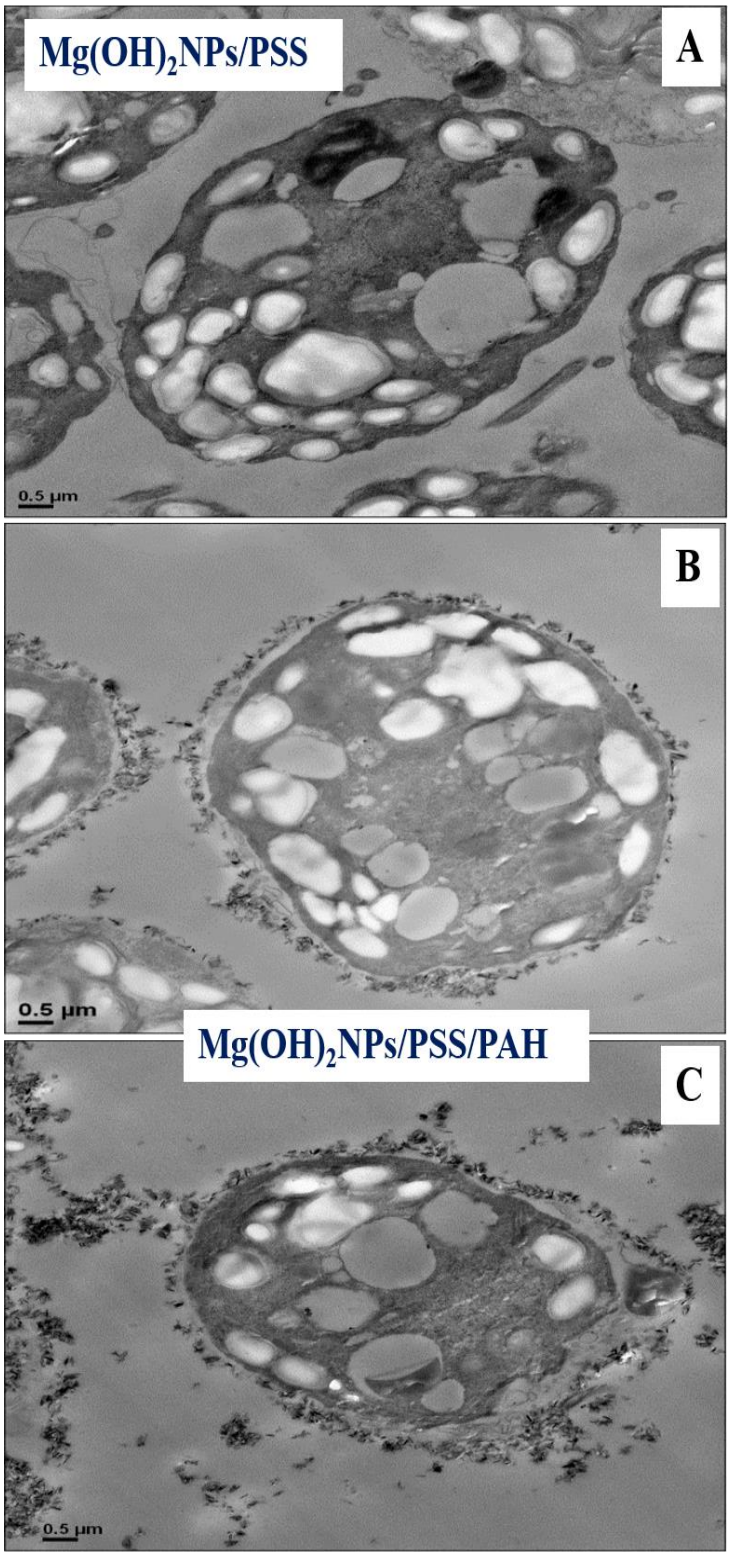


**Figure 6.19.** TEM images of *C. reinhardtii* after being incubated for 6 h with (A) 1000 µg $mL^{-1}$ $Mg(OH)_2$NPs/PSS, (B) 750 µg $mL^{-1}$ $Mg(OH)_2$NPs /PSS/PAH and (C) 1000 µg $mL^{-1}$ of $Mg(OH)_2$NPs /PSS/PAH.

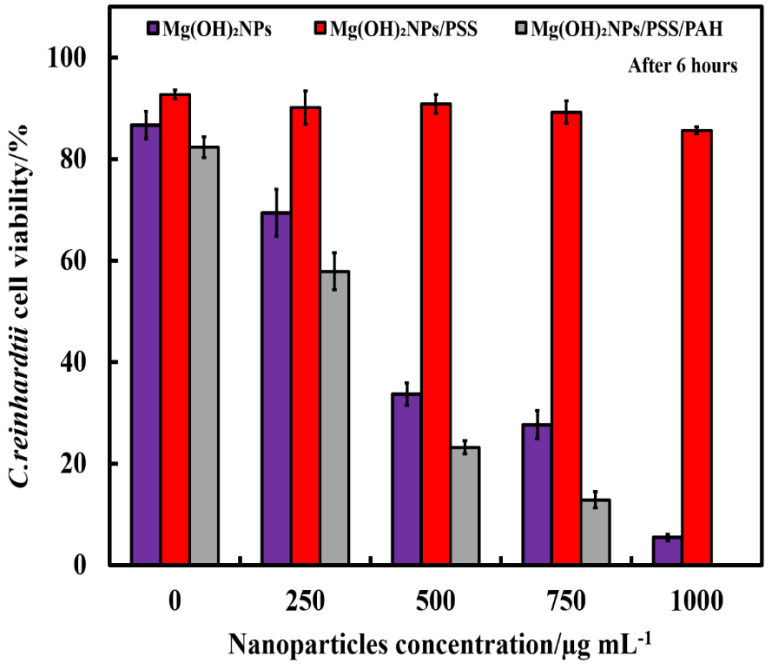


**Figure 6.20.** The anti-algal activity of free $Mg(OH)_2$NPs and polyelectrolyte-coated $Mg(OH)_2$NPs.

Figure 6.21 compares the antimicrobial activity of bare $Mg(OH)_2$NPs, $Mg(OH)_2$NPs/PSS and $Mg(OH)_2$NPs/PSS/PAH on *C. reinhardtii* and *S.cerevisiae* cells. The anti-algal and anti-yeast action of the $Mg(OH)_2$NPs coated with PSS and PAH follow the order: *C. reinhardtii* > *S.cerevisiae*.

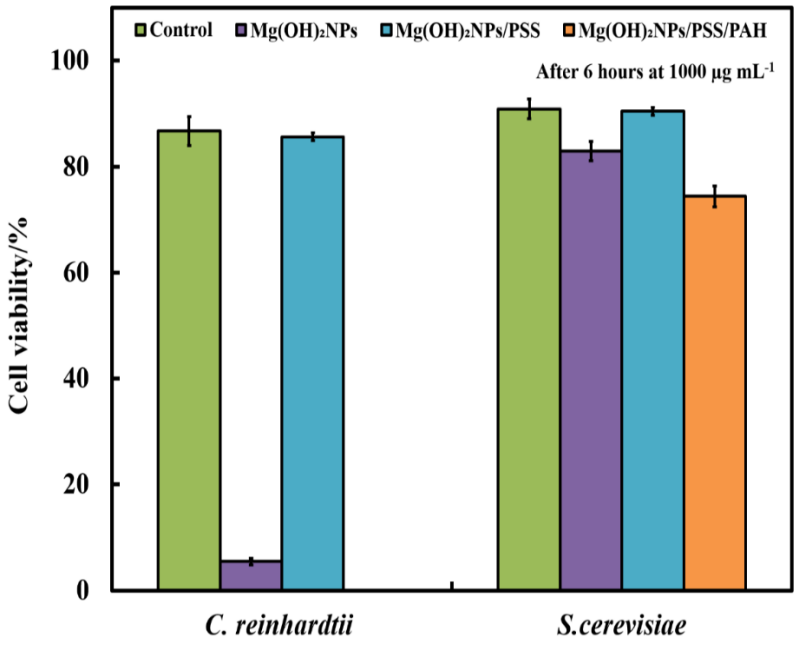


**Figure 6.21.** The anti-algal and anti-yeast activity of uncoated and polyelectrolyte-coated $Mg(OH)_2$NPs on *C. reinhardtii* and *S.cerevisiae* cells at particle concentration 1000 µg $mL^{-1}$. The cells were incubated with nanoparticles for 6 h.

## 6.8 Antibacterial activity of polyelectrolyte-coated $Mg(OH)_2$NPs on *E.coli*

It was also conducted similar tests with Gram-negative bacteria (*E.coli*) and polyelectrolyte-coated $Mg(OH)_2$NPs when the bacterial cells were removed from their culture media. Figure 6.22A and 6.22B show the effect of polyelectrolyte multilayer-coated $Mg(OH)_2$NPs against *E.coli*. Similarly to *S.cerevisiae* and *C. reinhardtii* we found no pronounced antibacterial effect of $Mg(OH)_2$NPs/PSS on *E.coli* for various exposure times. Figure 6.22A shows that the antibacterial activity of $Mg(OH)_2$NPs/PSS against *E.coli* is also much lower than the one of the bare $Mg(OH)_2$NPs. We envisage that this result is due to similar decrease of the NPs accumulation on the bacterial cell wall after functionalization of the $Mg(OH)_2$NPs with anionic PSS layer (see Figure 6.23A, 6.23B, 6.23D and 6.23E). The subsequent deposition of a cationic polyelectrolyte layer of PAH, yields $Mg(OH)_2$NPs/PSS/PAH which showed excellent antibacterial properties against *E.coli*, as seen in Figure 6.22B. Note that the PAH-coated NPs have even stronger antibacterial activity than the uncoated $Mg(OH)_2$NPs towards *E.coli*. Hence the antibacterial activity of the polyelectrolyte coated $Mg(OH)_2$NPs appears to alternate with their surface charge. The *E. coli* Gram-negative cell wall is composed of an organized triple membrane containing a thin inner layer of peptidoglycan between an outer membrane consisting of porins [17], phospholipids molecules, lipopolysaccharides (LPS), lipoproteins, surface proteins, and a cytoplasmic membrane consisting of phospholipids molecules and porins (see Figure 6.24).[17]

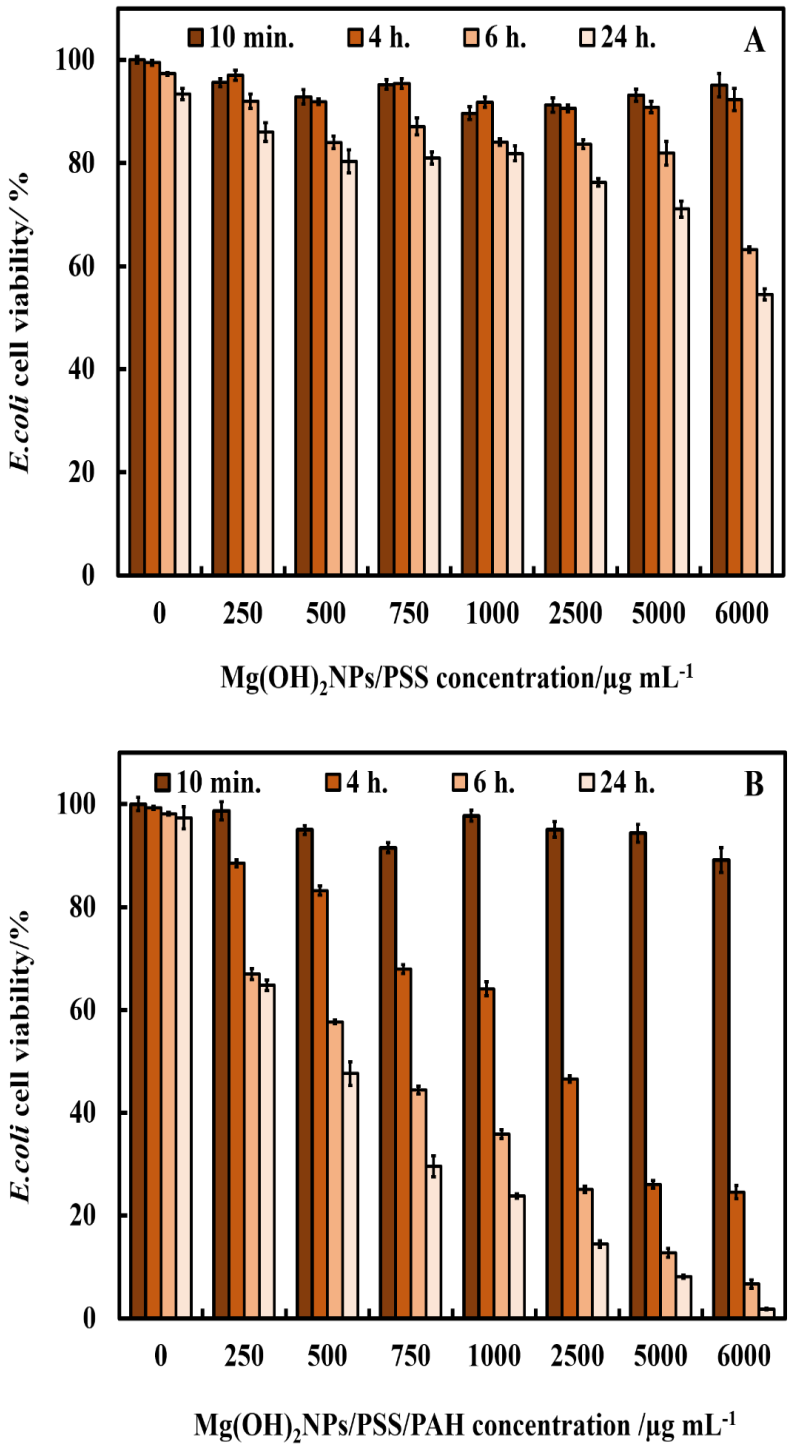


**Figure 6.22.** The *E.coli* cell viability after treatment with (A) $Mg(OH)_2$NPs/PSS and (B) $Mg(OH)_2$NPs/PSS/PAH for various incubation times as a function of the nanoparticle concentration.

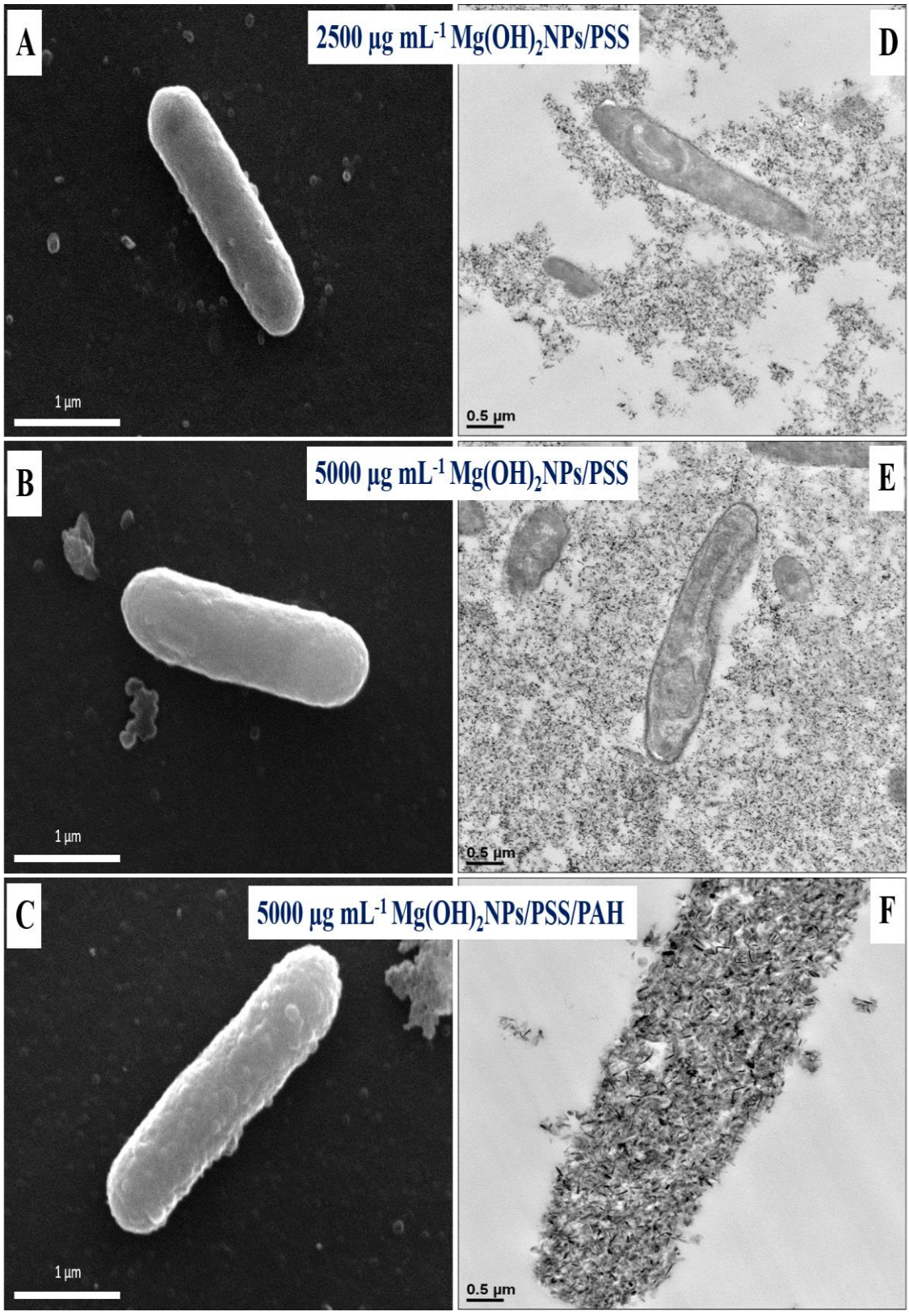


**Figure 6.23.** (A) SEM and (D) TEM images of *E.coli* after incubation with 2500 µg $mL^{-1}$ $Mg(OH)_2$NPs/PSS; (B) SEM and (E) TEM images of *E.coli* after incubation with 5000 µg $mL^{-1}$ $Mg(OH)_2$NPs/PSS; (C) SEM and (F) TEM images of *E.coli* after incubation with 5000 µg $mL^{-1}$ $Mg(OH)_2$NPs/PSS/PAH. The cells were removed from the particle suspension before the sample preparation for TEM and SEM imaging.

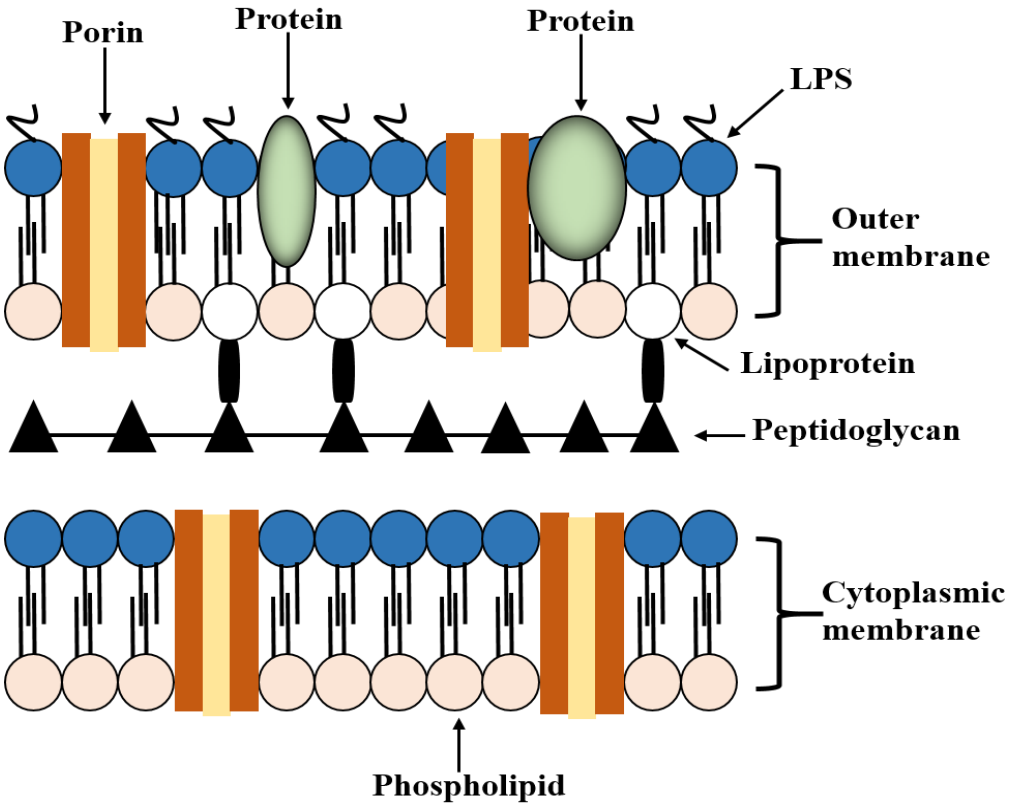


**Figure 6.24.** Schematic overview of the cell wall. Redrawn from ref.[17]

Figure 6.23A-6.23F show SEM and TEM images of *E.coli* after treatment for 24 h with $Mg(OH)_2$NPs coated with a single layer of PSS and ones with additional layer of PAH. Note that there are a very few $Mg(OH)_2$NPs/PSS attached to the bacteria as shown in Figure 6.23A, 6.23B, 6.23D and 6.23E. On the other hand, we found a significant accumulation of $Mg(OH)_2$NPs/PSS/PAH onto the surface of the bacteria as shown in Figure 6.23C and 6.23F. These SEM and TEM images are consistent with the antibacterial activity profile of the polyelectrolyte-coated $Mg(OH)_2$NPs against *E.coli* as reported in Figure 6.22B. It can be argued that the weak attachment of the anionic particles $Mg(OH)_2$NPs/PSS to the bacteria, as supported via the SEM and TEM images, causes a little damage of the bacteria wall. Figure 6.10B, 6.10C, 6.10E and 6.10F for the bare $Mg(OH)_2$NPs and Figure 6.23C and 6.23F for the $Mg(OH)_2$NPs/PSS/PAH, show that there is a substantial build-up of cationic NPs (uncoated and PAH-coated $Mg(OH)_2$NPs) onto the anionic bacterial cell surface which corresponds to greater local increase of the NPs concentration that successively disrupts the bacteria (also see Figure 6.25). In order to investigate if this is due to higher local concentration of $Mg^{2+}$ ions we

also examined the antibacterial activity of $MgCl_2$ solutions of various concentrations for 24 h on *E.coli*, where the bacterial cells were extracted from the culture media in a similar processes as explained above for the $Mg(OH)_2$NPs treatment with *E.coli*. It was found that $MgCl_2$ did not have significant antibacterial action compared to the $Mg(OH)_2$NPs even at high concentrations, as shown in Figure 6.26. Similar is the effect of the pH on the bacterial cell viability – it was found that the incubation of bacteria with NaOH solution of pH 10.4 (corresponding to the pH of bare $Mg(OH)_2$NPs suspension) did not produce a comparable effect. Hence the analysis of these results suggests that magnesium ions in the $Mg(OH)_2$NPs and the basic pH of 10.4 is unlikely to be responsible for killing *E.coli*. [16] The most likely explanation is the rough surface morphology of the clustered $Mg(OH)_2$NPs which when electrostatically attracted towards the cell membrane cause membrane disruptions which kill the bacteria.

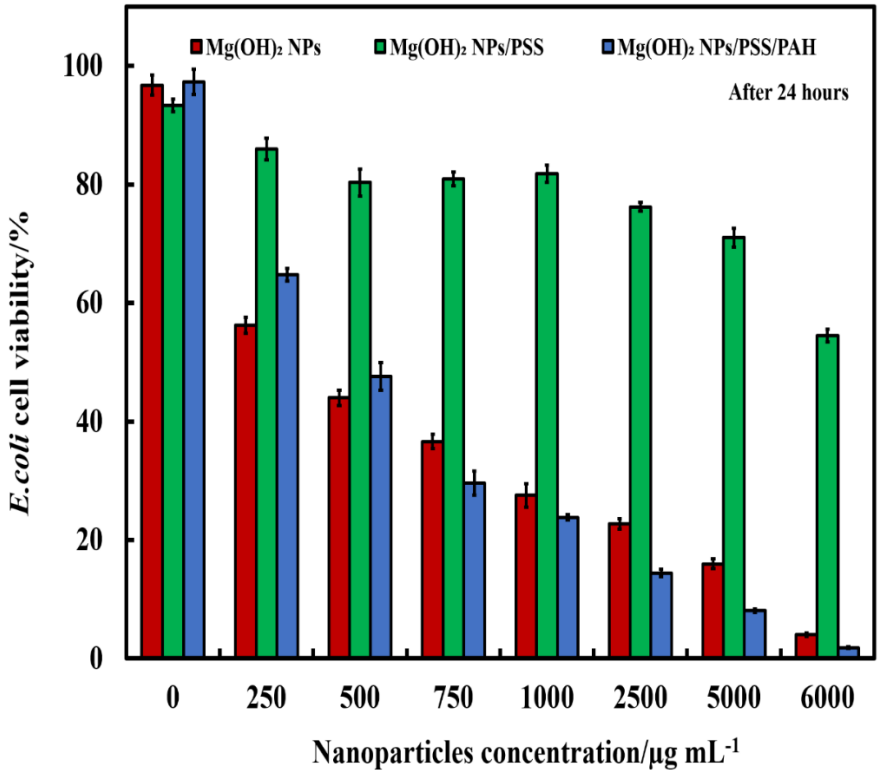


**Figure 6.25.** Relationship between the antibacterial efficiency of bare and polyelectrolyte-coated $Mg(OH)_2$NPs on the viability of *E.coli*. *E. coli* was incubated for one day to 0, 250, 500,750, 1000, 2500, 5000 and 6000 μg $mL^{-1}$ of different types of nanoparticles.

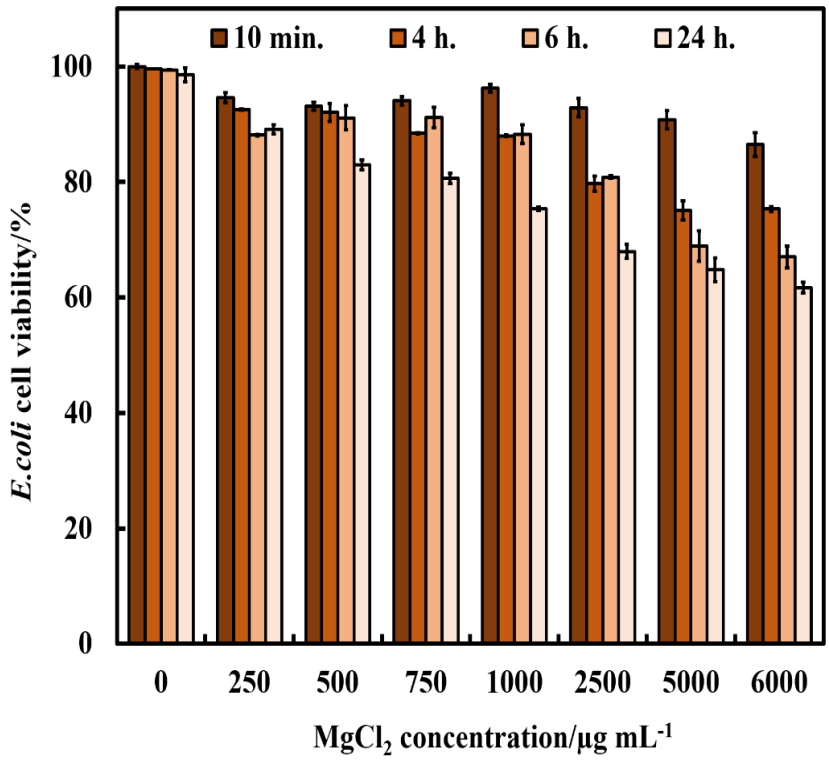


**Figure 6.26.** The antibacterial impact of various concentration of $MgCl_2$ towards *E. coli* for various exposure times. The experiment was achieved via incubated of *E. coli* with $MgCl_2$ for one day.

Note that neither $Mg^{2+}$ ions nor reactive oxygen species (ROS) generation can explain the antimicrobial properties of the $Mg(OH)_2$NPs. The solubility of $Mg(OH)_2$NPs is too low for the free $Mg^{2+}$ ions to have any measurable cytotoxic effect as their concentration is limited by the solubility product of $Mg(OH)_2$NPs ($1.8 \times 10^{-11}$ $M^3$). The $Mg(OH)_2$NPs are not a photoactive material which means that it is not producing ROS upon illumination. Hence, the antimicrobial effect is likely coming from the surface roughness of the $Mg(OH)_2$NPs, which sticks onto the negatively charged microbial cells electrostatically due to their cationic character and pierces their cell membrane. The effect is also amplified by the high concentration of $OH^-$ ions in their electric double layers which they bring in close contact with the microbial cell surface upon adhesion. This can potentially lead to partial hydrolysis of the lipids in their cell membranes and cell death.

The minimum inhibitory concentration (MIC) of free $Mg(OH)_2$NPs and PSS/PAH-coated $Mg(OH)_2$NPs on *E. coli*, *S. cerevisiae* and *C. reinhardtii* was determined. It was found that at the same conditions, the MIC of the PSS/PAH-coated $Mg(OH)_2$NPs is 2 times lower than this of free $Mg(OH)_2$NPs (see Table 6.1).

**Table 6.1.** Minimum inhibitory concentration (MIC) of bare $Mg(OH)_2$NPs and PSS/PAH-coated $Mg(OH)_2$NPs against *C. reinhardtii*, *S. cerevisiae* and *E. coli*.

| | **$Mg(OH)_2$NPs** | **PSS/PAH-coated $Mg(OH)_2$NPs** |
|---|---|---|
| | **MIC** | **MIC** |
| ***C. reinhardtii*** | 1000 μg $mL^{-1}$ | 750 μg $mL^{-1}$ |
| ***S.cerevisiae*** | 5000 μg $mL^{-1}$ | 2500 μg $mL^{-1}$ |
| ***E.coli*** | 5000 μg $mL^{-1}$ | 2500 μg $mL^{-1}$ |

Figure 6.27 shows the cytotoxicity assay of the free PAH on *S. cerevisiae*, *C. reinhardtii* and *E.coli* for up to 6 hours for *C. reinhardtii* and 24 hours for *S. cerevisiae* and *E.coli* of exposure. Both runs were done at the varying overall PAH concentration and different incubation times. One can see a very small effect on the presence of free PAH on the *cells* viability. One can conclude that the free PAH does not measurably impact the cell viability up to 5000 μg $mL^{-1}$ for *S. cerevisiae,* 1000 μg $mL^{-1}$ for *C. reinhardtii* and 6000 μg $mL^{-1}$ for *E.coli*. Note that in our $Mg(OH)_2$NPs/PSS/PAH nanoparticles there is not any free PAH and free PSS as the particles have undergo multiple washing/centrifugation cycles after their surface functionalization. However, at these concentrations of the PAH-coated on $Mg(OH)_2$NPs, the effect of the $Mg(OH)_2$NPs on *S. cerevisiae*, *C. reinhardtii* and *E.coli* is very significant. Therefore, one may conclude that the PAH- coated on $Mg(OH)_2$NPs shows excellent anti-yeast, anti-algal and antibacterial properties with these cells which is not related to free PAH.

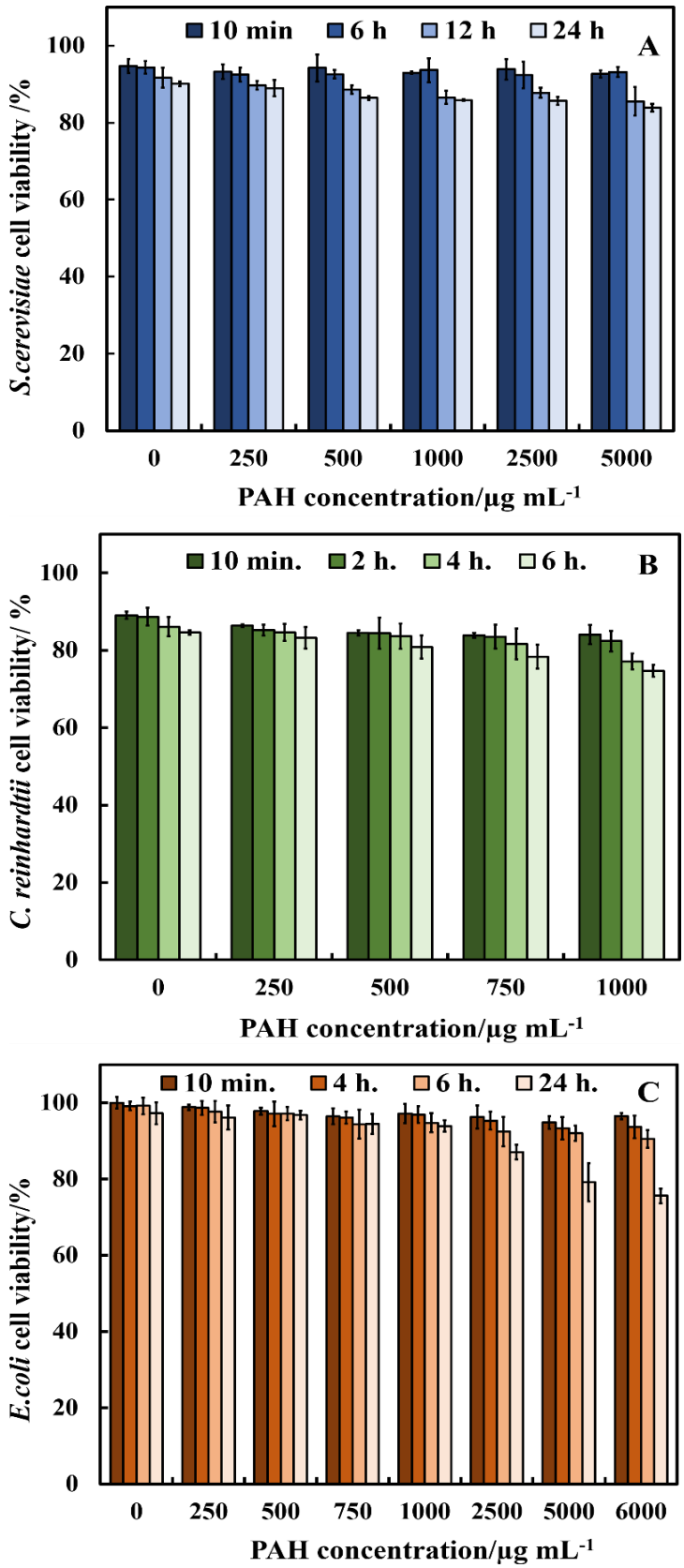


**Figure 6.27.** The anti-yeast, anti-algal and antibacterial of free PAH at various concentrations on (A) *S. cerevisiae*, (B) *C. reinhardtii* (C) *E.coli*. The cells were incubated with the free PAH at different times of exposure before being washed and tested for their cell viability.

Figure 6.28 shows the cytotoxicity assay of the free $Mg(OH)_2$NPs and $Mg(OH)_2$NPs/PSS/PAH on human embryonic kidney cells (HEK 293 cell line) for up to 24 h of exposure. The data in Figure 6.28 shows a very small effect on the presence of free $Mg(OH)_2$NPs and $Mg(OH)_2$NPs/PSS/PAH on the cell viability over a period of up to 24 h. It was found that the control sample of HEK 293 cells have lost a minor fraction of their viability over this period of time due to depletion of the culture media. One can conclude that the nanoparticle does not measurably impact the cell viability up to 2500 µg $mL^{-1}$. However, at these concentrations of free $Mg(OH)_2$NPs and $Mg(OH)_2$NPs/PSS/PAH, the effect on yeast, algae and *E.coli* is very significant – see Figure 6.2, 6.5 and 6.9, respectively. Therefore, one may conclude that the $Mg(OH)_2$NPs show excellent biocompatibility with these human cell line. More research will be conducted in the future on the effects of the nanoparticles on different type of other cell lines.[26]

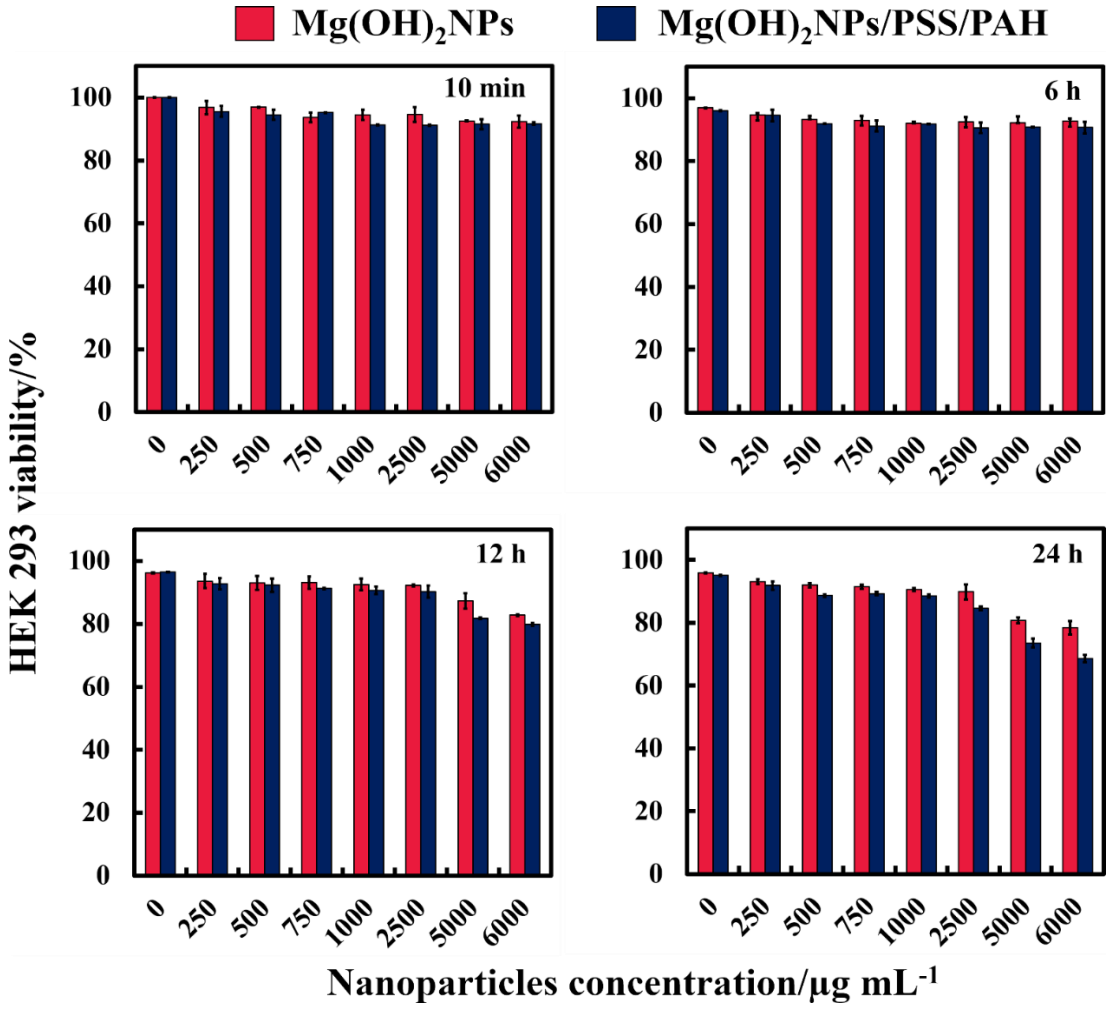


**Figure 6.28.** Comparison of the cell viability of human embryonic kidney cells (HEK 293 cell line) upon incubation as a function of nanoparticle concentration for up to 24 h at with bare $Mg(OH)_2$NPs and $Mg(OH)_2$NPs/PSS/PAH.

## 6.9 Conclusions

Compared with other inorganic nanoparticles studied in the literature, $Mg(OH)_2$NPs have high antimicrobial activity at moderate to high particle concentrations. However since $Mg(OH)_2$NPs are nontoxic materials and have been broadly used in medical industries and food, the $Mg(OH)_2$NPs have great application potential as a new antimicrobial agents. Various ways to control the antimicrobial activity and cytotoxicity of a range of bare and surface-modified $Mg(OH)_2$NPs were studied on three different types of microbial cells: microalgae, yeast and bacteria. The antimicrobial activity of the $Mg(OH)_2$NPs on *S. cerevisiae*, *C. reinhardtii* and *E.coli* was examined. This work suggests that bare $Mg(OH)_2$NPs are effective antimicrobial agents. The results from TEM and SEM analysis showed that direct contact between the $Mg(OH)_2$NPs and the cell membrane of *S. cerevisiae*, *C. reinhardtii* and *E.coli* is very important for their effective antimicrobial action. In order to evaluate the role of the surface coating, a series of polyelectrolyte-coated $Mg(OH)_2$NPs were likewise synthesised using the layer by-layer technique and their antimicrobial activity towards *S. cerevisiae*, *C. reinhardtii* and *E.coli* was compared with that of bare $Mg(OH)_2$NPs. It was discovered that the antimicrobial activity of the coated $Mg(OH)_2$NPs alternates with their surface charge. The anionic nanoparticles ($Mg(OH)_2$NPs/PSS) have much lower antibacterial activity than the cationic ones ($Mg(OH)_2$NPs/PSS/PAH and bare $Mg(OH)_2$NPs). These can bring important insights how the antimicrobial properties of $Mg(OH)_2$NPs and other inorganic nanoparticles can be controlled by designing nanoparticle surface coatings that promote their adhesion to the microbial cell walls as well as by taking into account the nanoparticles surface morphology. $Mg(OH)_2$NPs have been studied for their antimicrobial properties by other but no effect of the surface charge of the particles have been examined on their efficiency. As $Mg(OH)_2$NPs is a cationic material of IEP 11.7, it is positively charged over a very wide range of pH. Therefore here the toxicity of $Mg(OH)_2$NPs was explored against three different microorganisms after surface modification with different polyelectrolytes to examine this dependence. This has never been done before for $Mg(OH)_2$NPs nor has the mechanism of antimicrobial action been commented for different surface charge of the particles, as it was done in this Chapter.

## 6.10 References


1. D. Lee, R. E. Cohen and M. F. Rubner, *Langmuir*, 2005, **21**, 9651-9659.
2. L.-A. B. Rawlinson, S. M. Ryan, G. Mantovani, J. A. Syrett, D. M. Haddleton and D. J. Brayden, *Biomacromolecules*, 2009, **11**, 443-453.
3. A. Muñoz-Bonilla and M. Fernández-García, *Progress in Polymer Science*, 2012, **37**, 281-339.
4. A. F. Halbus, T. S. Horozov and V. N. Paunov, *ACS applied materials & interfaces*, 2019, **11**, 12232–12243.
5. A. F. Halbus, T. S. Horozov and V. N. Paunov, *Nanoscale Advances*, 2019, **1**, 2323 – 2336.
6. A. F. Halbus, T. S. Horozov and V. N. Paunov, *Advances in colloid and interface science*, 2017, **249**, 134-148.
7. S. S. M. Al-Obaidy, A. F. Halbus, G. M. Greenway and V. N. Paunov, *Journal of Materials Chemistry B*, 2019, **7**, 3119-3133.
8. B. Vatsha, P. Tetyana, P. M. Shumbula, J. C. Ngila, L. M. Sikhwivhilu and R. M. Moutloali, *Journal of Biomaterials and Nanobiotechnology*, 2013, **4**, 365.
9. H. Zhang, B. Chen and J. F. Banfield, *The Journal of Physical Chemistry C*, 2010, **114**, 14876-14884.
10. J. Liu, D. M. Aruguete, M. Murayama and M. F. Hochella Jr, *Environmental science & technology*, 2009, **43**, 8178-8183.
11. Y. Zhang, Y. Chen, P. Westerhoff, K. Hristovski and J. C. Crittenden, *Water research*, 2008, **42**, 2204-2212.
12. A. R. Petosa, D. P. Jaisi, I. R. Quevedo, M. Elimelech and N. Tufenkji, *Environmental science & technology*, 2010, **44**, 6532-6549.
13. A. Hoshino, K. Fujioka, T. Oku, M. Suga, Y. F. Sasaki, T. Ohta, M. Yasuhara, K. Suzuki and K. Yamamoto, *Nano Letters*, 2004, **4**, 2163-2169.
14. X. Pan, Y. Wang, Z. Chen, D. Pan, Y. Cheng, Z. Liu, Z. Lin and X. Guan, *ACS applied materials & interfaces*, 2013, **5**, 1137-1142.
15. C. Dong, J. Cairney, Q. Sun, O. L. Maddan, G. He and Y. Deng, *Journal of Nanoparticle Research*, 2010, **12**, 2101-2109.
16. C. Dong, G. He, W. Zheng, T. Bian, M. Li and D. Zhang, *Materials Letters*, 2014, **134**, 286-289.
17. R. Brayner, R. Ferrari-Iliou, N. Brivois, S. Djediat, M. F. Benedetti and F. Fiévet, *Nano Letters*, 2006, **6**, 866-870.

18. W. Lin, Y. Xu, C.-C. Huang, Y. Ma, K. B. Shannon, D.-R. Chen and Y.-W. Huang, *Journal of Nanoparticle Research*, 2009, **11**, 25-39.
19. I. Sondi and B. Salopek-Sondi, *Journal of colloid and interface science*, 2004, **275**, 177-182.
20. C. Dong, D. Song, J. Cairney, O. L. Maddan, G. He and Y. Deng, *Materials Research Bulletin*, 2011, **46**, 576-582.
21. N. M. Franklin, N. J. Rogers, S. C. Apte, G. E. Batley, G. E. Gadd and P. S. Casey, *Environmental science & technology*, 2007, **41**, 8484-8490.
22. M. Heinlaan, A. Ivask, I. Blinova, H.-C. Dubourguier and A. Kahru, *Chemosphere*, 2008, **71**, 1308-1316.
23. O. Choi and Z. Hu, *Environmental science & technology*, 2008, **42**, 4583-4588.
24. Y. Pan, S. Neuss, A. Leifert, M. Fischler, F. Wen, U. Simon, G. Schmid, W. Brandau and W. Jahnen-Dechent, *Small*, 2007, **3**, 1941-1949.
25. P. Chen, B. A. Powell, M. Mortimer and P. C. Ke, *Environmental science & technology*, 2012, **46**, 12178-12185.
26. A. F. Halbus, T. S. Horozov and V. N. Paunov, *Biomimetics*, 2019, **41**, 1-20.

# Chapter 7

# 7. Characterisation of the surface functionalized CuONPs

## 7.1 Introduction

Non-coated CuONPs have positive surface charge at neutral pH and can electrostatically adhere to the negatively charged cell walls.[1-3] The average size of CuONPs is likewise essential for their potential anti-bacterial, anti-yeast and anti-algal activity, as smaller nanoparticles have higher portability between biological compartments. However, the electrostatic interactions can be potentially modified and disrupted by the presence of another type of anionic species in the media such as surfactants, polymers, proteins and others. This can result in the formation of carbohydrates and protein corona which may change and even reverse the positive surface charge of the nanoparticles and render them ineffective as anti-bacterial, anti-yeast and antialgal agents. In order to address this problem here CuONPs with a special coating containing terminal boronic acid surface groups was engineered. These were designed to provide a non-electrostatic mechanism for their attachment to the bacteria, algae and yeast which was expected to enhance their accumulation on the cell walls even in the presence of anionic species in the media. Our idea is that the hydroxy phenyl boronic acid groups on the CuONPs will be able to covalently bind to various glycoproteins and carbohydrates that are abundant on the cell walls, thus forming boronic ester bonds with diols.[4, 5]

Such boronic acid (BA) surface functionality has been used to prepare chemosensors for sugar groups[6] and it is known that the BA that make them very effective for biomedical applications due to their low toxicity.[7, 8] Although this approach has been used for sensing and quantification of bacteria whose membranes contain various polysaccharides with diol groups,[9-14] this is the first report where this functionality is used in the development of more effective anti-bacterial, anti-algal and anti-yeast nanoparticles.

Here the mean particle hydrodynamic diameter and zeta potential of bare and functionalized CuONPs were studied. The results for the non-functionalized particles are presented in Figures 7.1 and 7.2. The bare CuONPs average particle hydrodynamic diameter was about 93 nm while their average zeta potential was around +37 mV, i.e. the non-functionalized (bare) CuO nanoparticles are cationic at pH 6.

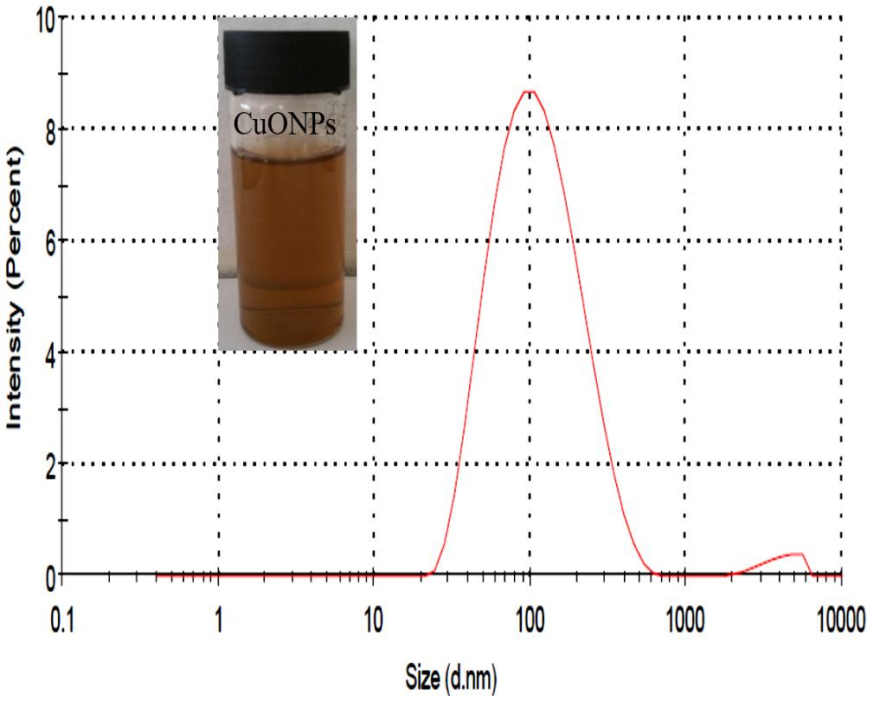


**Figure 7.1.** The particle size distribution of CuONPs produced by annealing at 100 °C.

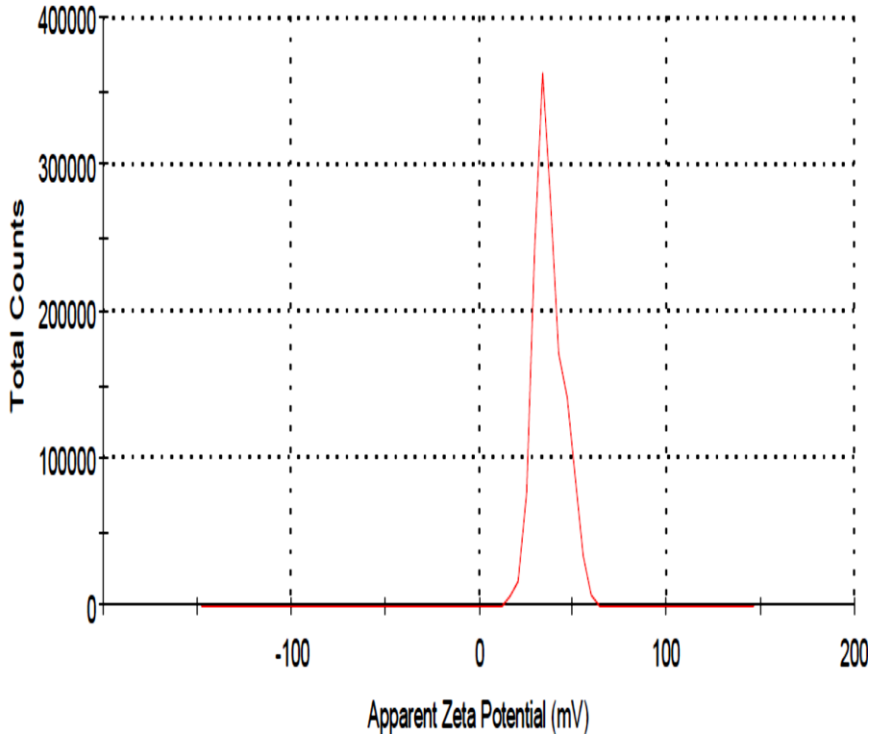


**Figure 7.2.** The zeta potential distribution of CuONPs produced by annealing at 100 °C.

## 7.2 X-RAY Diffraction of CuONPs

The crystalline nature of CuONPs was studied by X-ray diffraction (XRD). Figure 7.3 shows XRD pattern of CuONPs obtained by direct precipitation method using a copper chloride solution after annealing at 100 ºC, 200 ºC, 300 ºC, 400 ºC, 500 ºC and 600 ºC. The diffraction peaks agree very well with the hexagonal structure of CuO according to

the Joint Committee on Powder Diffraction Standards (JCPDS no.01-077-7716). This indicates that are no apparent impurities, suggesting that CuO of high purity has been prepared. The average crystal size of CuONPs calculated from XRD data using the Scherrer equation was 13 nm (see Figure 7.3A), i.e. much smaller than the hydrodynamic diameters of the CuONPs dispersed in deionized water. This indicates that the CuONPs in aqueous dispersions are aggregates of smaller crystallites. The data in Figure 7.3 also shows that the crystal size for CuONPs annealed at 600$^{o}$C was highest and for CuONPs annealed at 100$^{o}$C the value was the lowest. It was also detected that with increasing the annealing temperature, the intensity of the diffraction peaks became sharper and the size of crystallinity of CuONPs was also increased.

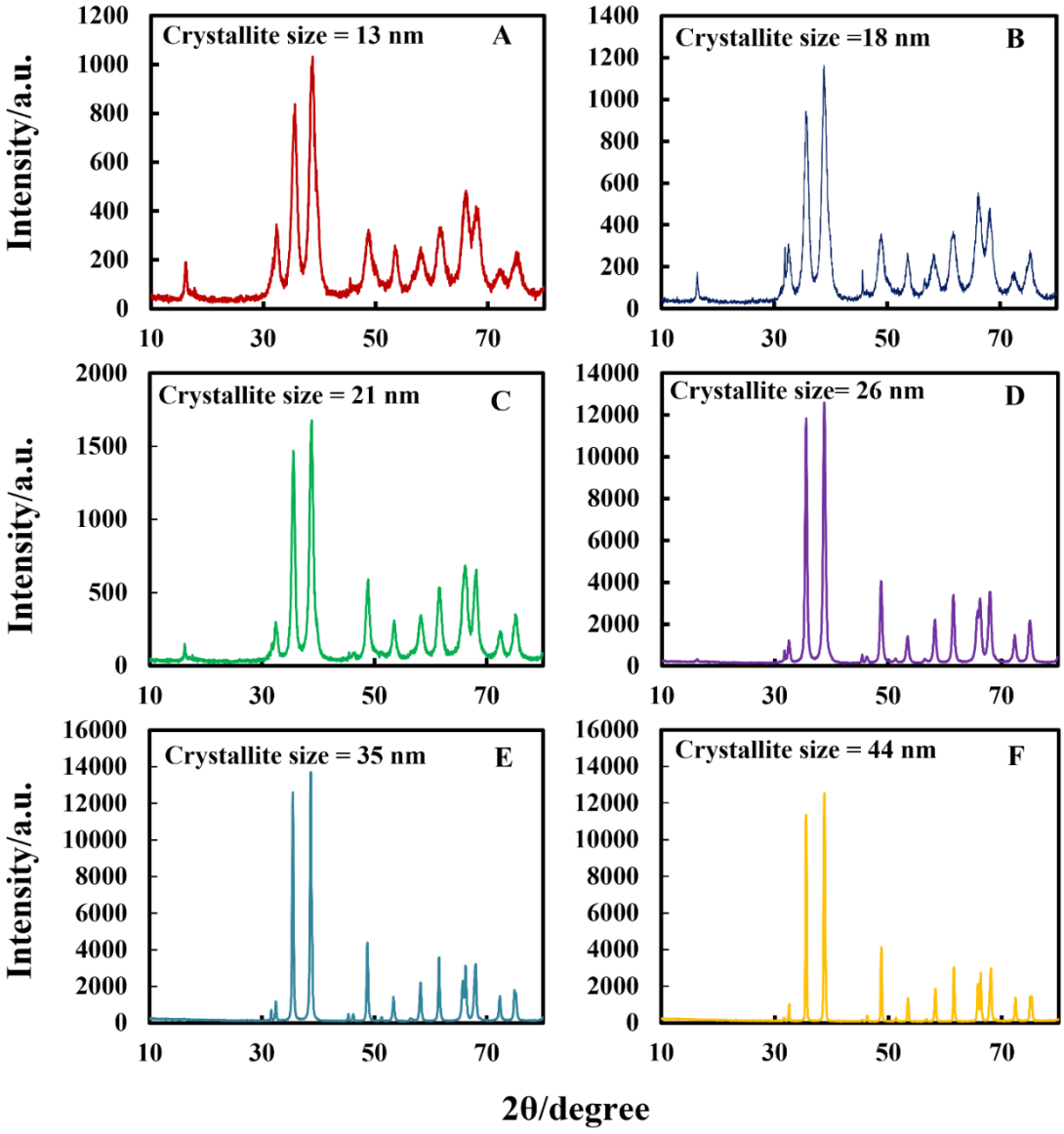


**Figure 7.3.** XRD pattern of CuONPs annealed at (A) 100 °C, (B) 200 °C, (C) 300 °C, (D) 400 °C, (E) 500 °C and (F) 600 °C with different crystallite size. The largest peak in the XRD results was used to determine the crystallite size.

## 7.3 Energy dispersive X-ray Diffractive (EDX) of CuONPs

Figure 7.4 shows the EDX analysis data obtained at 10 keV from CuONPs annealed at 100 $^{o}$C. The results reveal the presence of copper (Cu) and oxygen (O) without other detectable elemental impurities in the EDX spectra. Note that there is a small peak of carbon due to the carbon coating of the sample prepared for SEM imaging. The elemental analysis confirmed that the synthesized sample was CuO, which is in good agreement with the results of XRD and the literature.[15, 16]

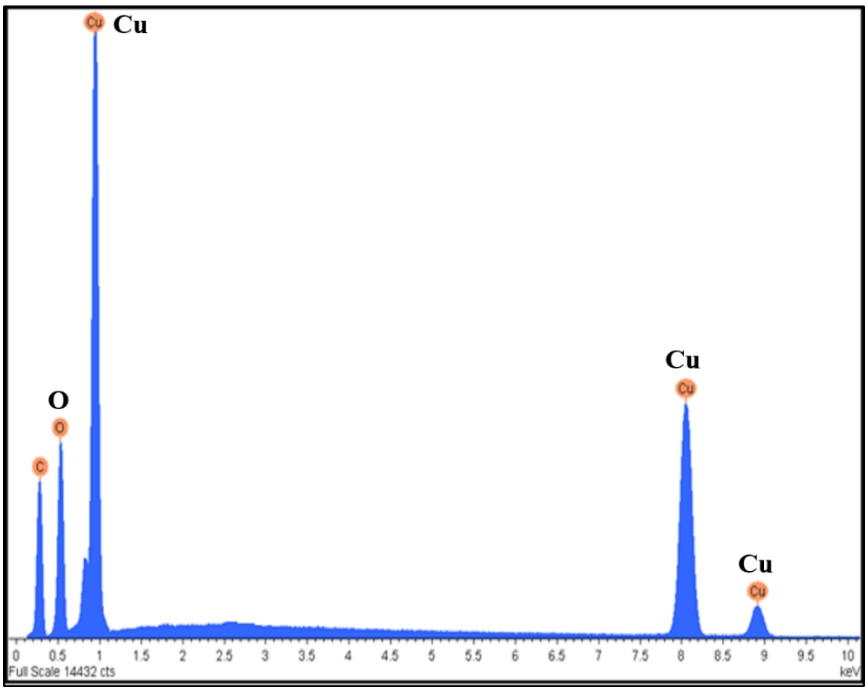


**Figure 7.4.** EDX spectrum of CuONPs.

## 7.4 Effect of the annealing temperature on the particle size and zeta potential of the CuONPs

The particle size and zeta potential of CuONPs were examined at different calcination temperature as shown in Figure 7.5 and Figure 7.6. The results in Figure 7.5 show that the hydrodynamic diameter is increasing with increasing of the annealing temperature. Therefore, it was found that CuONPs with same crystal type but various particle size could be obtained by changing the calcination temperature and also these results were in agreement with the previous studies.[16] These results may be explained that at higher calcination temperatures, agglomeration of CuONPs begin to occur and hence the particle size increased. The zeta potential was tested for every calcined sample of CuONPs, and

it can be seen from the Figure 7.6 that at 100°C, the zeta potential was +37 mV which means it was a highly stable, in contrast, at 600°C the zeta potential was -4 mV.

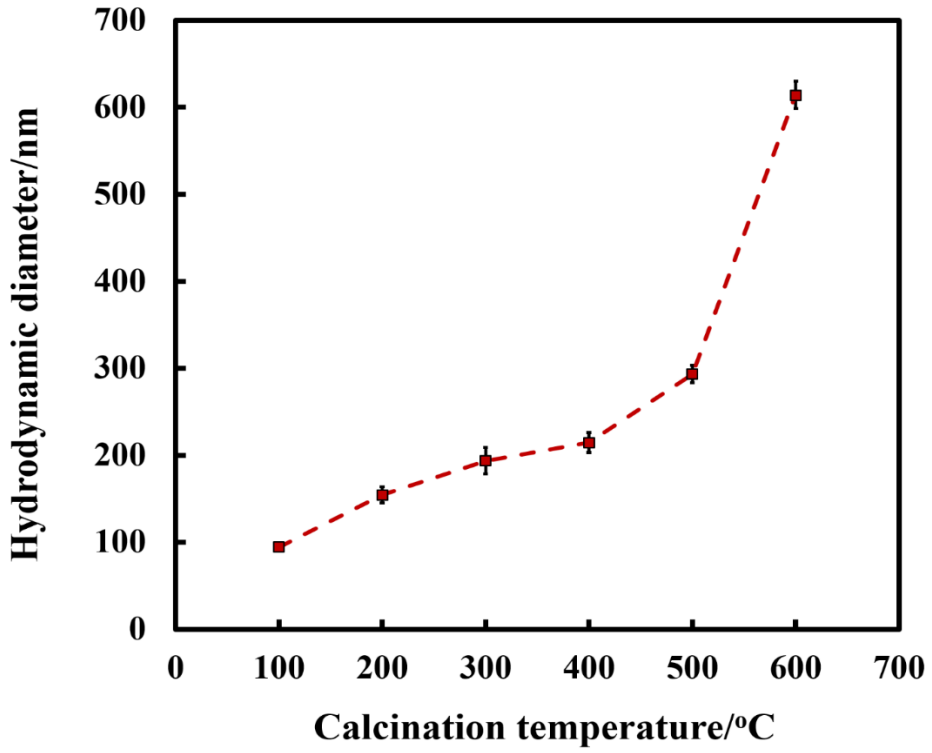


**Figure 7.5.** The hydrodynamic diameter of CuONPs annealed at various temperatures.

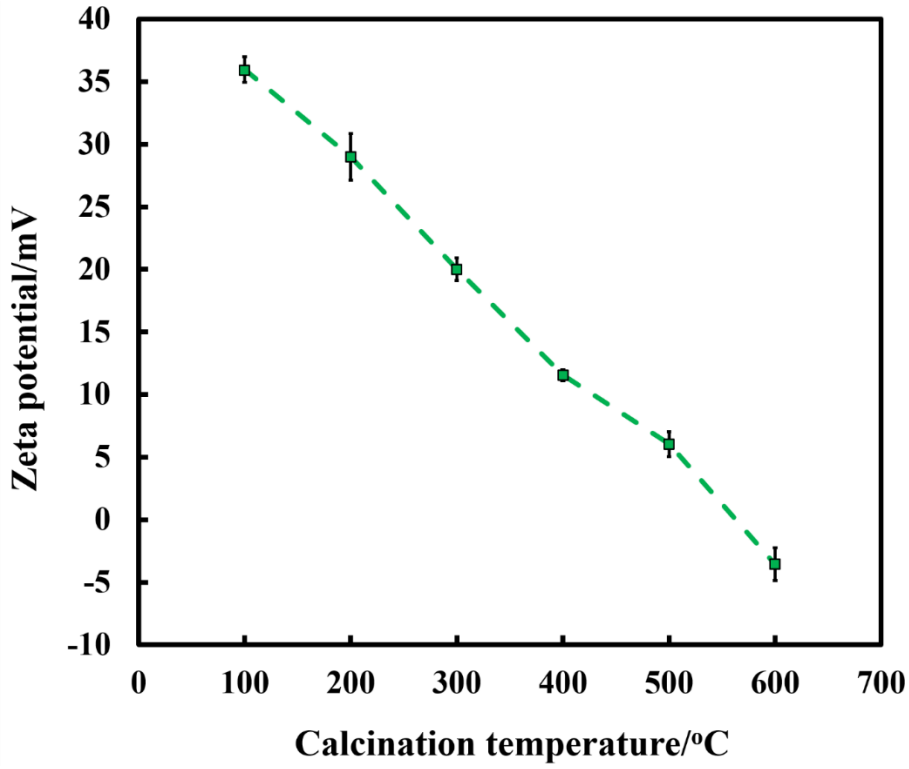


**Figure 7.6.** The zeta potential of CuONPs annealed at different temperatures.

## 7.5 FTIR analysis of CuONPs annealed at various temperatures.

Figure 7.7 shows the FTIR spectra of CuONPs annealed at 100°C, 200°C, 300°C, 400°C, 500°C and 600°C. The broad absorption peak at about 3445.89 $cm^{-1}$ was caused by the adsorbed water molecules. Because nano crystalline materials possess a high surface to volume ratio, they can absorb moisture. Similar peak at 3434 $cm^{-1}$ in the FTIR spectra of CuONPs are described.[16, 17] The peaks at 1632.77 might be for the Cu-O symmetrical stretching. [16, 18] The two infrared absorption peaks observed the vibrational modes of CuONPs in the range of 500 - 700 $cm^{-1}$. These peaks were detected at 533.33 $cm^{-1}$ and 585.41 $cm^{-1}$, respectively. The peak at 533.33 $cm^{-1}$ could be because of stretching of Cu-O.[19] The two peaks at 533.33 $cm^{-1}$ and 585.41 $cm^{-1}$ showed the creation of the CuONPs. These two peaks provision the existence of monoclinic phase. No other IR active modes are detected in the range of 500- 700 $cm^{-1}$, which completely rules out the presence of $Cu_2O$. Two peaks at 525 $cm^{-1}$ and 580 $cm^{-1}$ in the FTIR spectra described for CuONPs which closely matches with our results.[20] Thus, the metal-oxygen frequencies observed for CuONPs are in near agreement with that of literature values.[16]

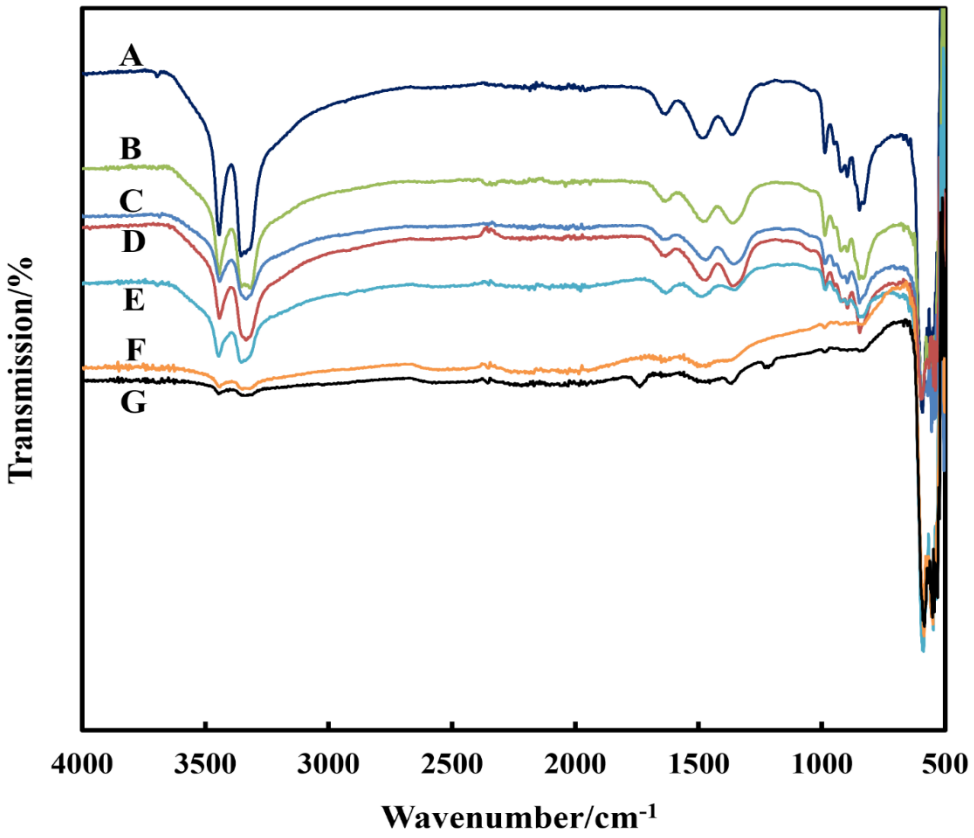


**Figure 7.7.** FTIR spectra of prepared CuONPs at different calcination temperatures (A) $Cu(OH)_2$ without calcinated , (B) 100 °C, (C) 200 °C, (D) 300 °C, (E) 400°C, (F) 500°C and (G) 600°C in the range of 500– 4000 $cm^{-1}$.

## 7.6 The zeta potential and particle size of CuONPs at different pH

The zeta potential of bare CuONPs as a function of pH is shown in Figure 7.8. The isoelectric point (IEP) of the CuONPs (corresponding to the pH where the CuONPs have zero zeta potential) is at pH 9. It was found that at pH values above the IEP, the CuONPs partially lost their colloid stability and formed larger aggregates (500 nm or bigger). To avoid the ambiguity related to the particle surface charge being influenced by pH, the antibacterial tests were carried at pH between 5 and 6 (away from the IEP) to ensure that the particle size is around 100 nm.

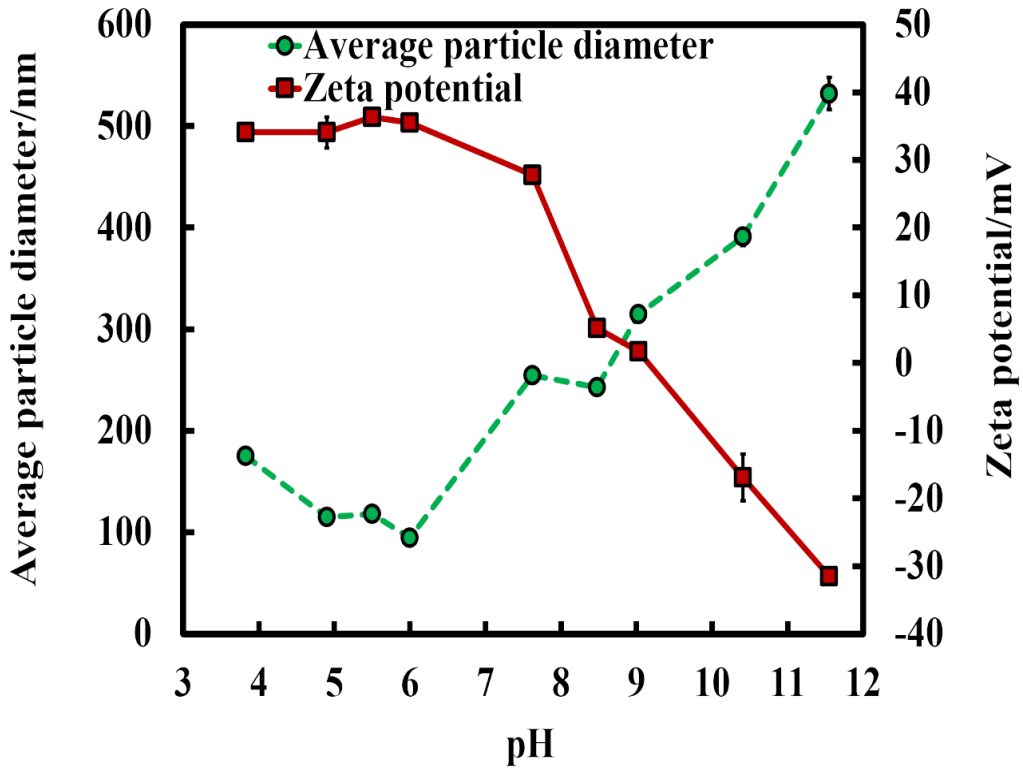


**Figure 7.8.** Zeta potential and particle diameter of bare CuONPs versus pH of the aqueous suspension.

## 7.7 Polyelectrolytes and their antibacterial activity on *E. coli*

The purpose of these experiments was to examine what impact coating CuONPs with two various polyelectrolytes, had on their zeta potential and particle size. CuONPs were coated in two various polyelectrolytes the first coated with alternating layers of anionic (PSS) polyelectrolyte to create CuONPs/PSS and the second coated with cationic (PAH) polyelectrolyte to form CuONPs/PSS/PAH. Figure 7.9 shows the PSS and PAH can reverse the surface charges of the particles.

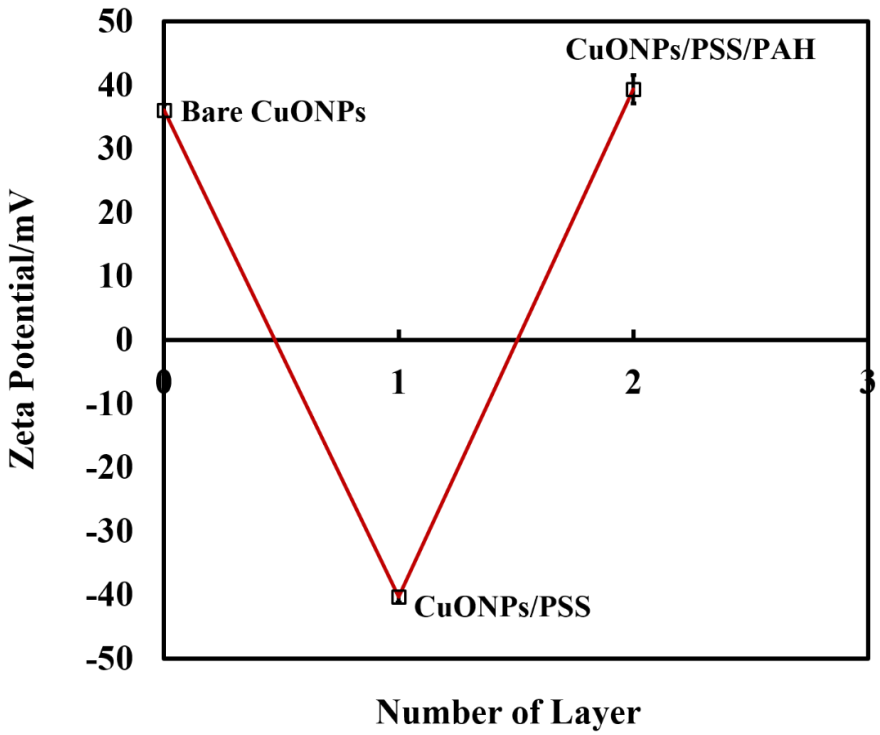


**Figure 7.9. The zeta potential of uncoated and polyelectrolyte-coated CuONPs.**

The zeta potential of uncoated and polyelectrolyte-coated CuONPs was a significant part in the killing of microorganisms. The utilization of the polyelectrolytes formed stable nanoparticles when coated with anionic polyelectrolyte PSS as the zeta potential was observed to be -41 mV (Figure 7.12) and after that coated with cationic polyelectrolyte PAH created stable nanoparticles with a zeta potential about +40 mV as shown in Figure 7.14. It was noticed that the anionic nanoparticles (CuONPs/PSS) were unstable and the zeta potential was -5 mV which was more than estimated and it is likely that the most of the PSS had been washed away. This problem was overcome via utilizing 0.5 M sodium chloride in the washing of the nanoparticles to form stable coated CuONPs. Additionally, the average particle size of these nanoparticles has been measured after each polyelectrolyte coating as shown in Figure 7.10. It can be seen from Figures 7.10, 7.11 and 7.13 that the particles size of CuONPs increased with the number of coating layers.

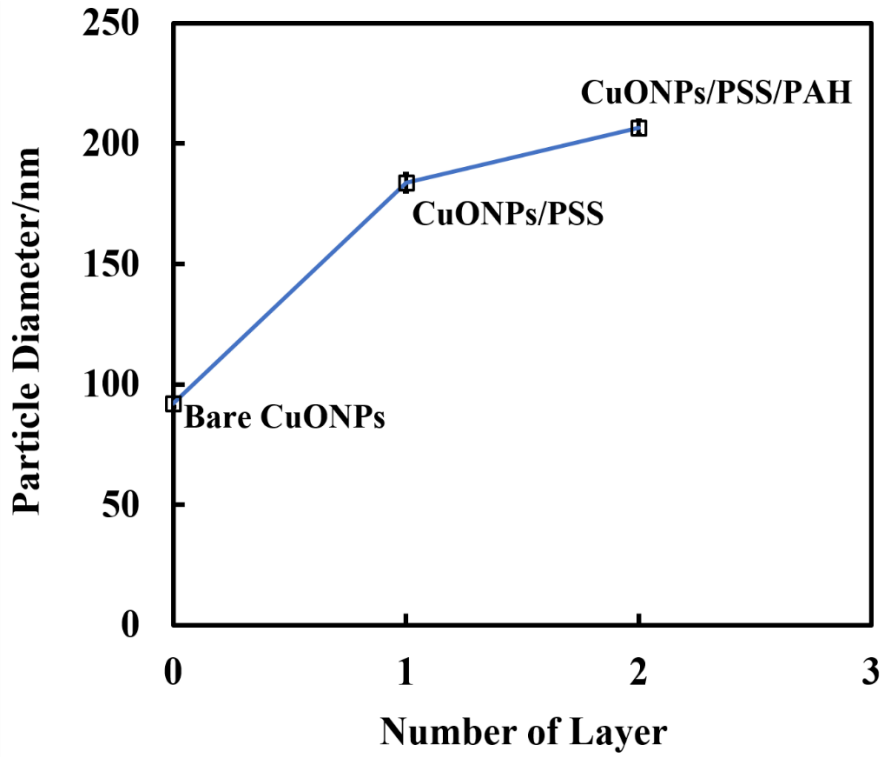


**Figure 7.10. The particle size of uncoated and polyelectrolyte-coated CuONPs.**

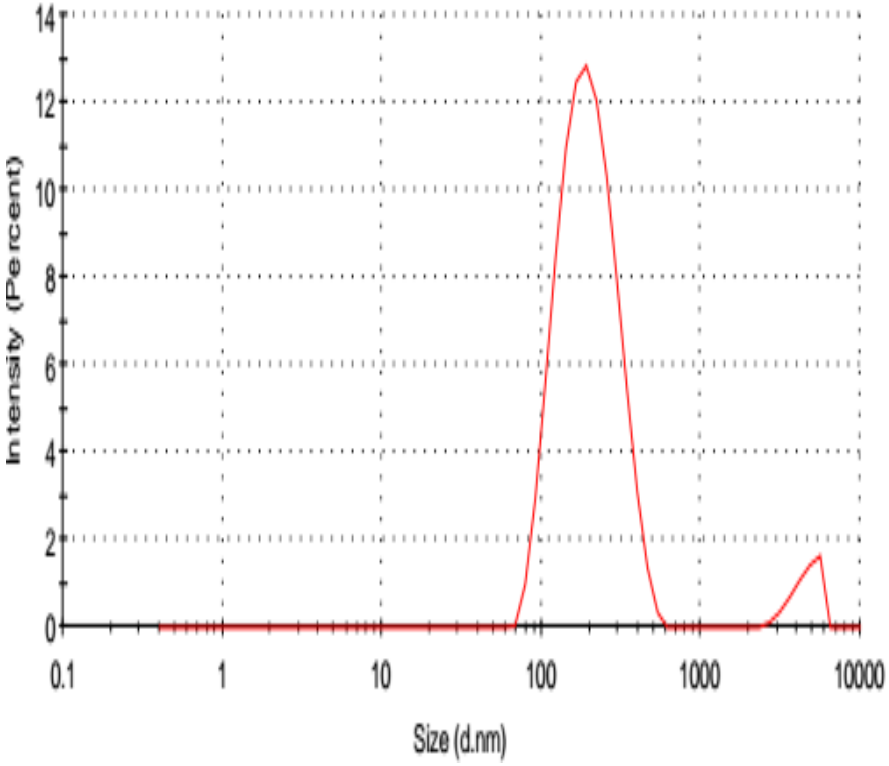


**Figure 7.11.** The particle size of CuONPs/PSS using dropwise addition with ultra-sonication.

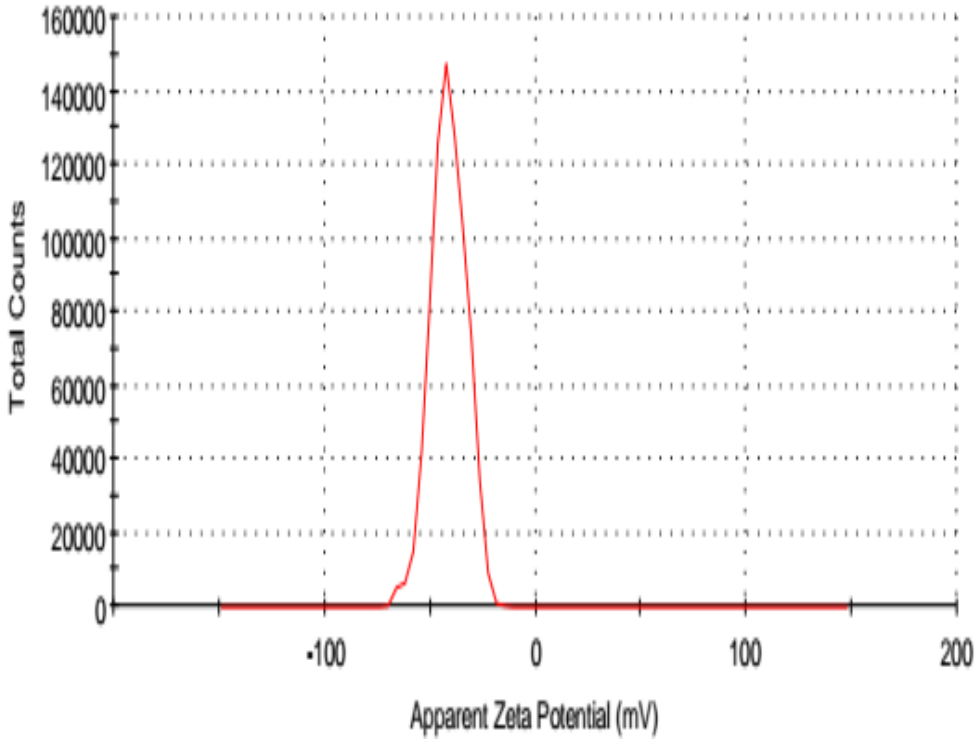


**Figure 7.12.** The zeta potential of CuONPs/PSS using dropwise addition with ultrasonication.

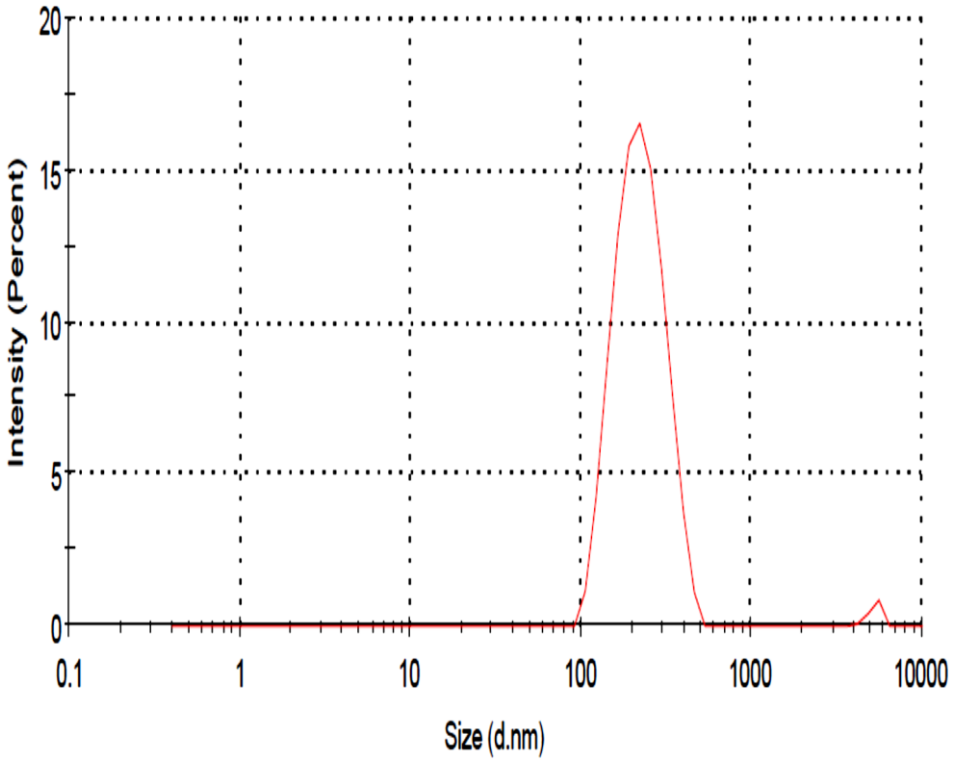


**Figure 7.13.** The particle size of CuONPs/PSS/PAH using dropwise addition with ultrasonication.

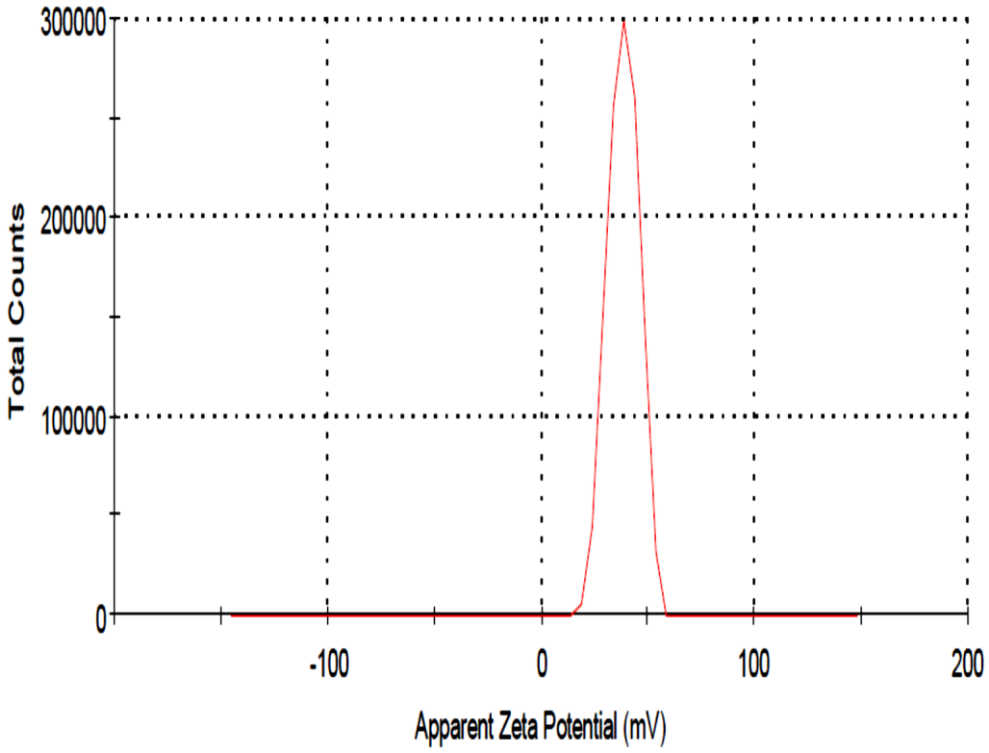


**Figure 7.14.** The zeta potential of CuONPs/PSS/PAH using dropwise addition with ultra-sonication.

## 7.8 Surface modification of CuONPs by APTES and 4-FPBA

Organic silane compounds suitable in our work are silane derivatives having at least one organic radical per molecule connected to silicon by a Si–C bond. Usual of the helpful silane are those with functional groups as APTES. The adhesion between the CuONPs surface and the silane could be covalent bond or adsorption. The beginning stage is copper oxide surface containing OH groups to which silane molecules could be physisorbed or chemisorbed. It is well known that various metal oxides will hydrolyse in the existence of water to procedure hydroxide layers at the surface. Water molecules may be both chemically and physically adsorbed onto the surface of the CuONPs. An hydroxide or oxide surface can become charged by reacting with $H^+$ or $OH^-$ ions because of surface amphoteric reactions depending on the isoelectric point (IP) of the CuONPs. The IP of CuONPs found to be at around pH 9.03. Below the IP, hydroxide surfaces adsorb protons to form positively charged surfaces. Above the IP, they lose protons to form negatively charged surfaces.[21] In the present work, CuONPs/APTES nanoparticles functionalized with 4-formylphenylboronic acid groups was studied. The amine group in CuONPs/APTES nanoparticles was reacted with 4- formylphenylboronic acid to procedure imine linkages via Schiff base chemistry (see Figure 7.15).[22-24]

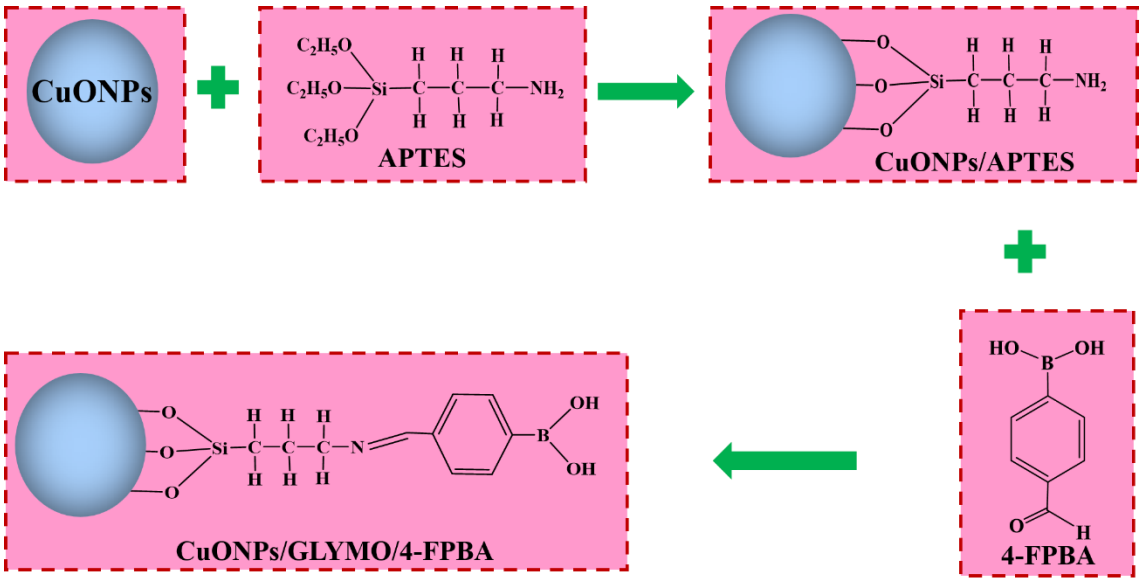


**Figure 7.15.** Surface functionalization and modification of the CuONPs support using APTES and 4-FPBA.

Surface modification of CuONPs was achieved by successive covalent bond formation reactions (Figure 7.15). First, APTES was introduced to the surface of CuONPs through silanization (Cu-O-Si oxane bond formation), which is a general method for metal oxide surface treatment. Then, reactions between the amine of APTES and the 4-formylphenylboronic acid creates a stable conjugation between 4-formylphenylboronic acid and CuONPs (Figure 7.15). The zeta potential (see Figure 7.16) and the average particle size (see Figure 7.17) of CuONPs before surface treatment were determined to be +37 mV and 93 nm, respectively. Figure 7.16 shows there were no significant differences between the zeta potential of bare CuONPs and surface modified ones.

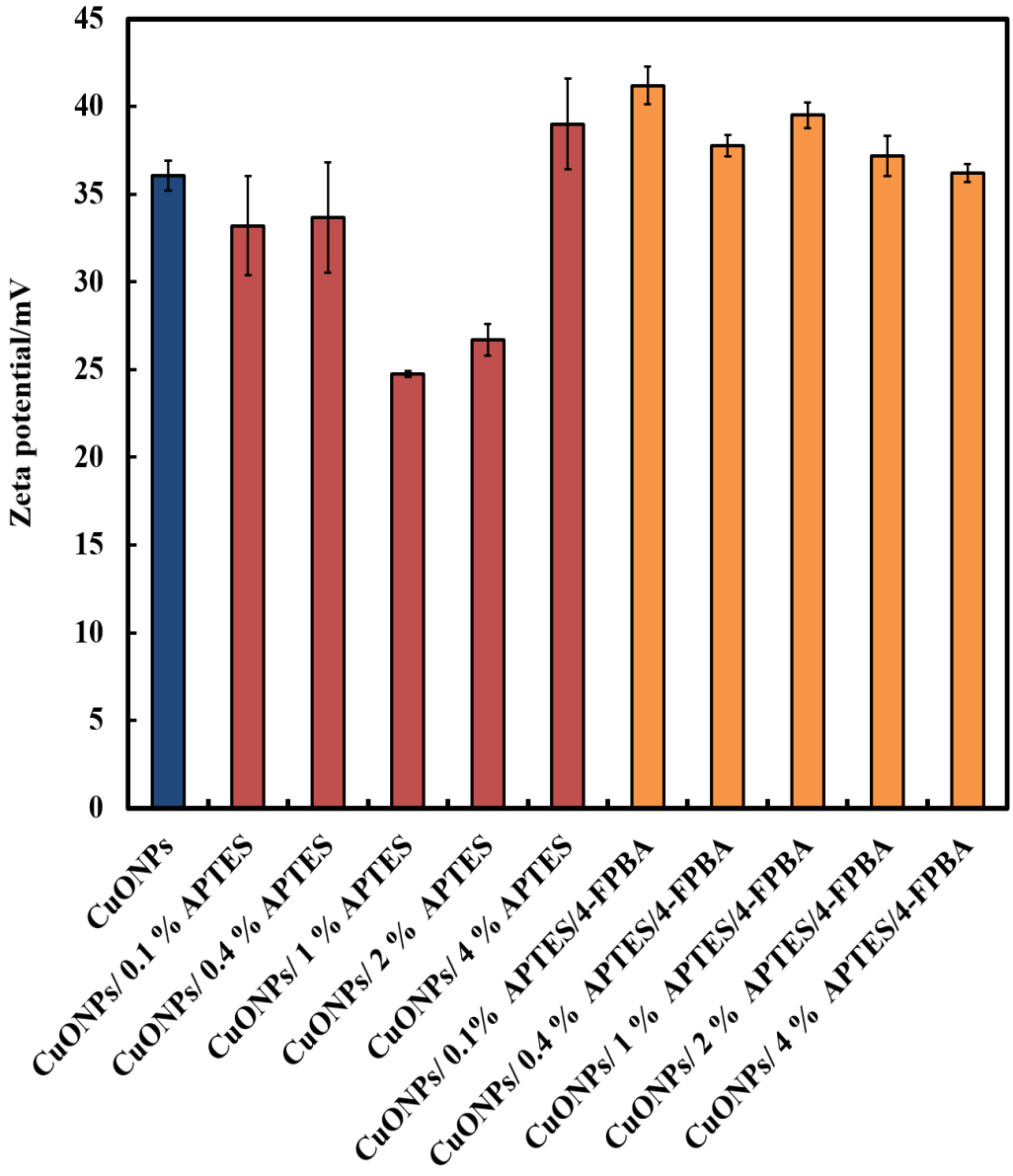


**Figure 7.16.** The zeta potential of unmodified CuONPs and CuONPs modified with APTES and 4-FPBA.

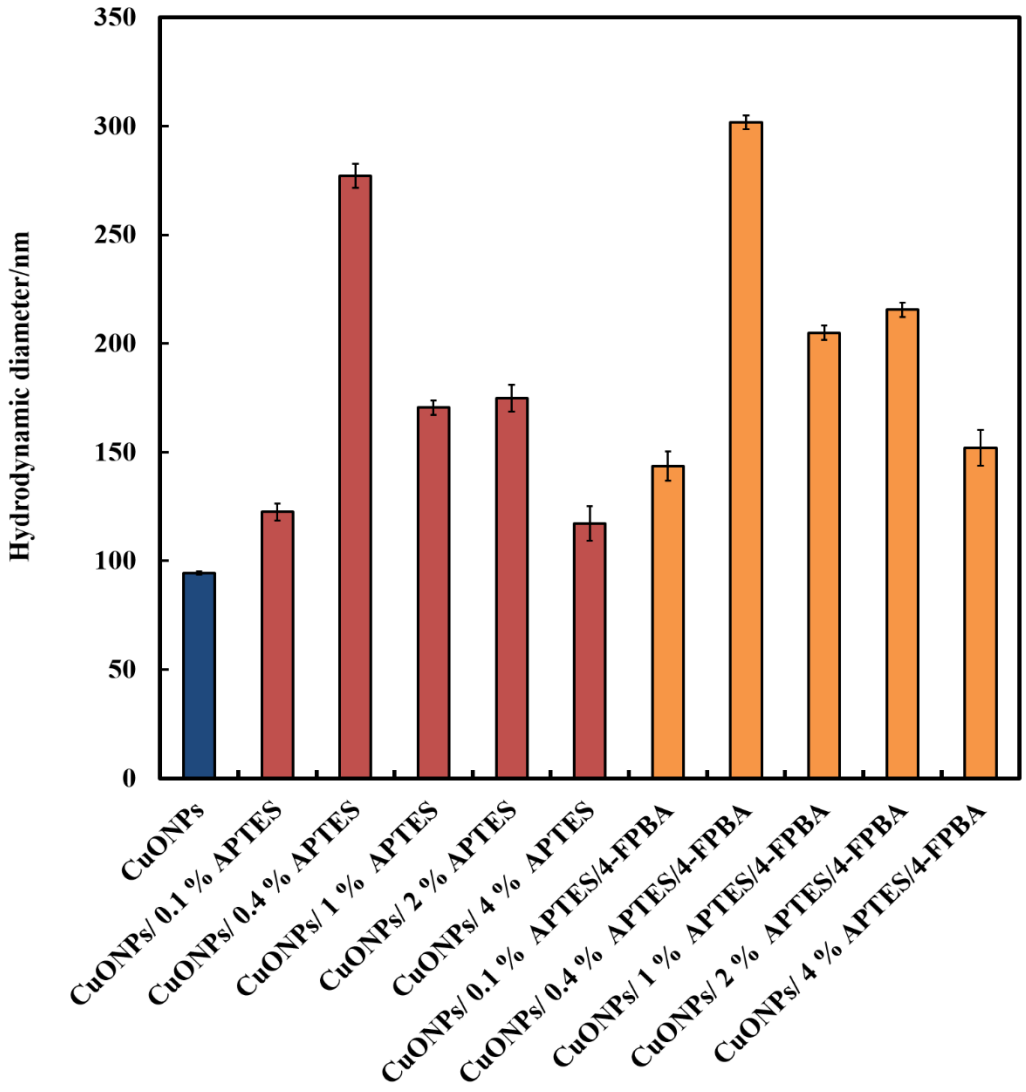


**Figure 7.17.** The particle size of unmodified CuONPs and CuONPs modified with APTES and 4-FPBA.

## 7.8.1 FTIR analysis of unmodified CuONPs and CuONPs modified with APTES and 4-FPBA.

To confirm the functionalized of the CuONPs surface through the silylation reaction, an FTIR spectrum of the functionalized-CuONPs was obtained (Figure 7.19). The characteristic absorption bands of the Cu–O bond of the functionalized CuONPs shifted to higher wavenumbers 628.7 $cm^{-1}$ compared to the non-functionalized CuONPs (in 621.4 $cm^{-1}$). This phenomenon can be explained by the formation of Cu–O–Si bonds. The Cu–O–H groups on the nanoparticle surface are replaced by Cu–O–Si(O–)$_2$–R as shown in Figure 7.19. Figure 7.18 shows the FTIR of (A) free APTES and (B) free 4-FPBA.The greater electronegativity of–Si(O–) compared to H leads to an enhancement of the bond

forces for the Cu–O bonds, shifting the absorption bands to high wavenumbers.[25, 26] Surface modification by alkoxysilanes is a complex process because it does not involve a single mechanism and several experimental parameters influence the system. Si–O stretching and Si–O–H bending vibrations at 960 and 869 $cm^{-1}$ were observed for all of the samples. For the APTES- functionalized CuONPs, the stretching Cu–O–Si was verified at 1150-1100 $cm^{-1}$.[27] The presence of amino groups associated with the 3-aminopropyl of the alkoxysilanes was observed. The absorption bands at 1325 and 2920-2850 $cm^{-1}$ are ascribed to the C–N and C–H stretching vibrations, respectively. A broad band at 1628 $cm^{-1}$ can be ascribed to the N–H stretching vibration, which is indicative of the free amino group. A small shoulder at 3370 $cm^{-1}$ corresponds to the N–H asymmetric stretching of the amine H-bonds, indicating a possible $NH_2$ interaction toward the CuONPs surface.[27] The bending aromatic C=C groups could be also observed at (1490–1650 $cm^{-1}$). Also the sharp peaks at around 1343 $cm^{-1}$ and 1090 $cm^{-1}$ could be assigned to the stretching vibrations B–O and C–B groups (Figure 7.20).[28, 29]

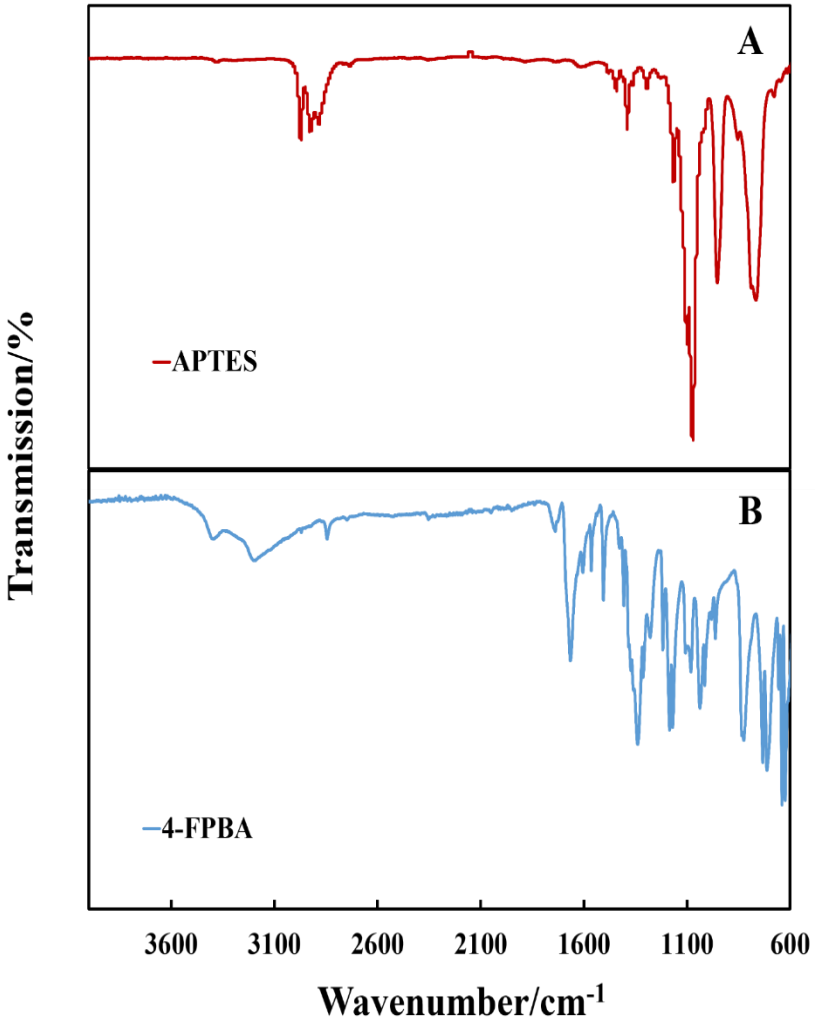


**Figure 7.18.** The FTIR spectra of (A) APTES and (B) 4-FPBA.

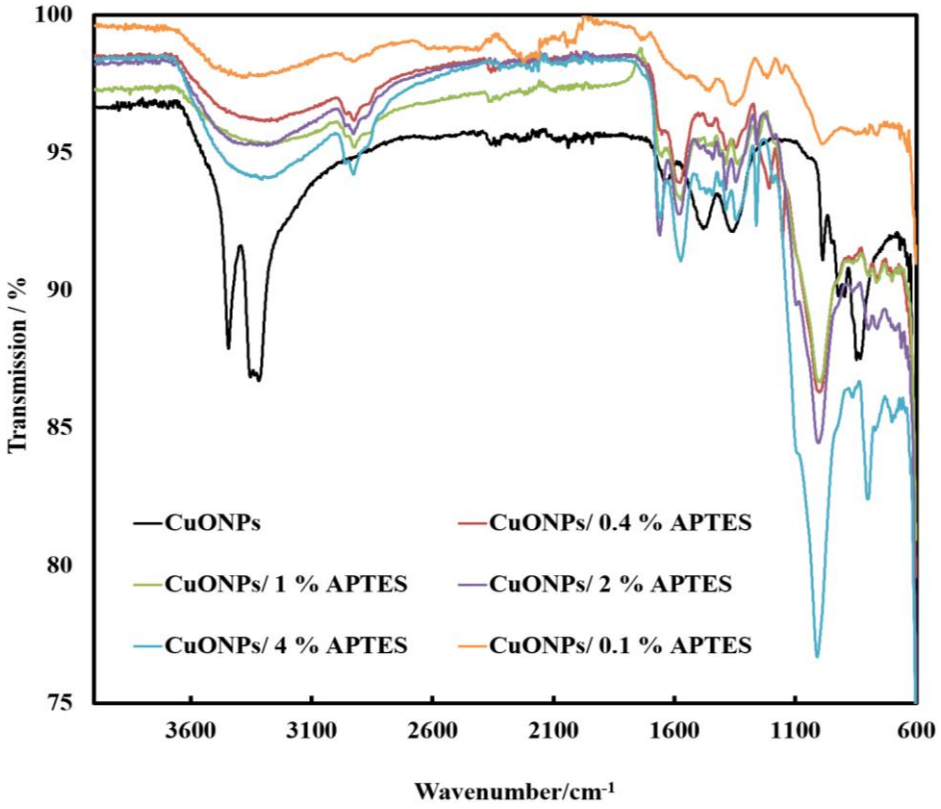


**Figure 7.19.** The FTIR spectra of the unmodified and modified CuONPs with APTES.

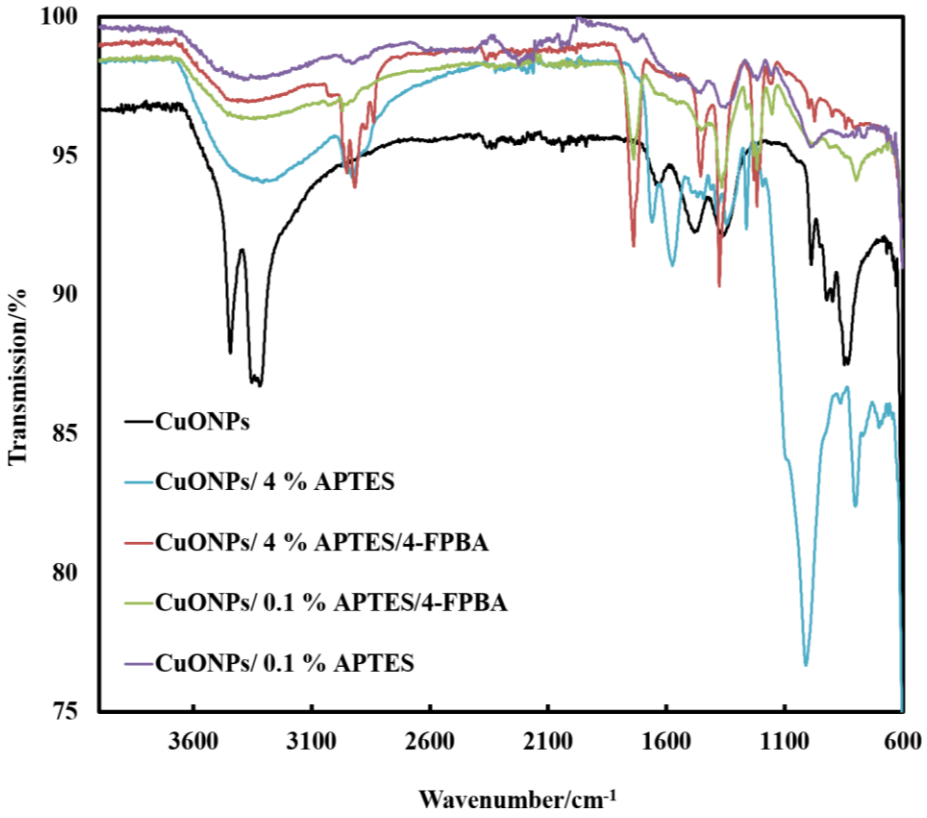


**Figure 7.20.** The FTIR spectra of the unmodified and modified CuONPs with APTES and 4-FPBA.

## 7.9 Characterization of the CuONPs surface functionalized with GLYMO and 4-HPBA or 4-TPBA

For synthesizing the boronic-acid functionalized CuONPs, a two-step of the method was adopted (Figure 7.21). GLYMO was reacted to prepare GLYMO bonded CuONPs (denoted as CuONPs/GLYMO). 4-HPBA or 4-TPBA was mixed with of CuONPs/GLYMO solution. The final product of boronic acid functionalized CuONPs, denoted as CuONPs/GLYMO/4-HPBA or CuONPs/GLYMO/4-TPBA.

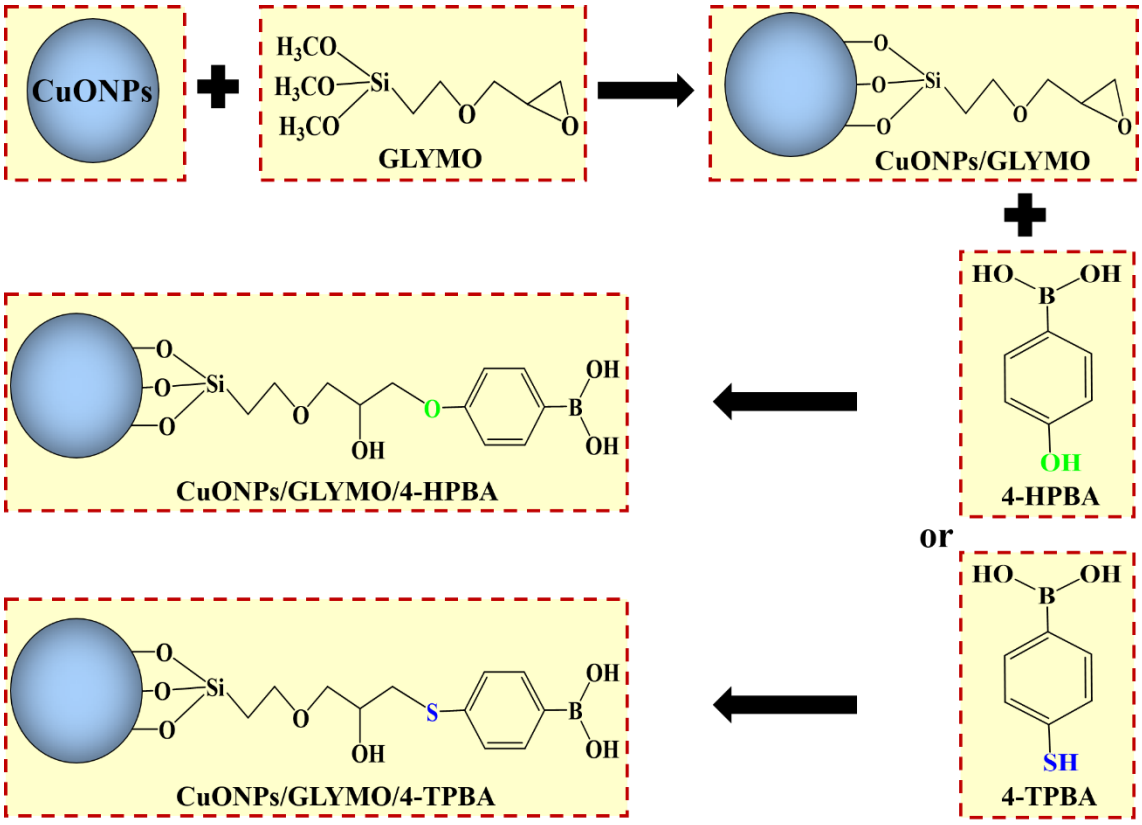


**Figure 7.21.** The schematic of the surface functionalized of CuONPs with GLYMO and 4-HPBA or 4-TPBA.

The zeta potentials and hydrodynamic diameters of bare and functionalized CuONPs determined at pH 6 are compared in Figure 7.22. One can see that the bare CuONPs dispersed in deionized water have the smallest hydrodynamic diameter (93±3 nm), while the diameter of surface-modified CuONPs varied between 106±6 nm (for CuONPs/GLYMO), 121±4 nm (for CuONPs/GLYMO/4-HPBA) and 156±6 nm (for CuONPs/GLYMO/4-TPBA).The zeta potential of bare CuONPs was positive while the two types of surface-modified CuONPs had small but negative zeta potential, ranging

from around -3±2 mV (CuONPs/GLYMO) to -10±2 mV (CuONPs/GLYMO/4-HPBA) and -5±1 mV (CuONPs/GLYMO/4-TPBA) (see Figure 7.22).

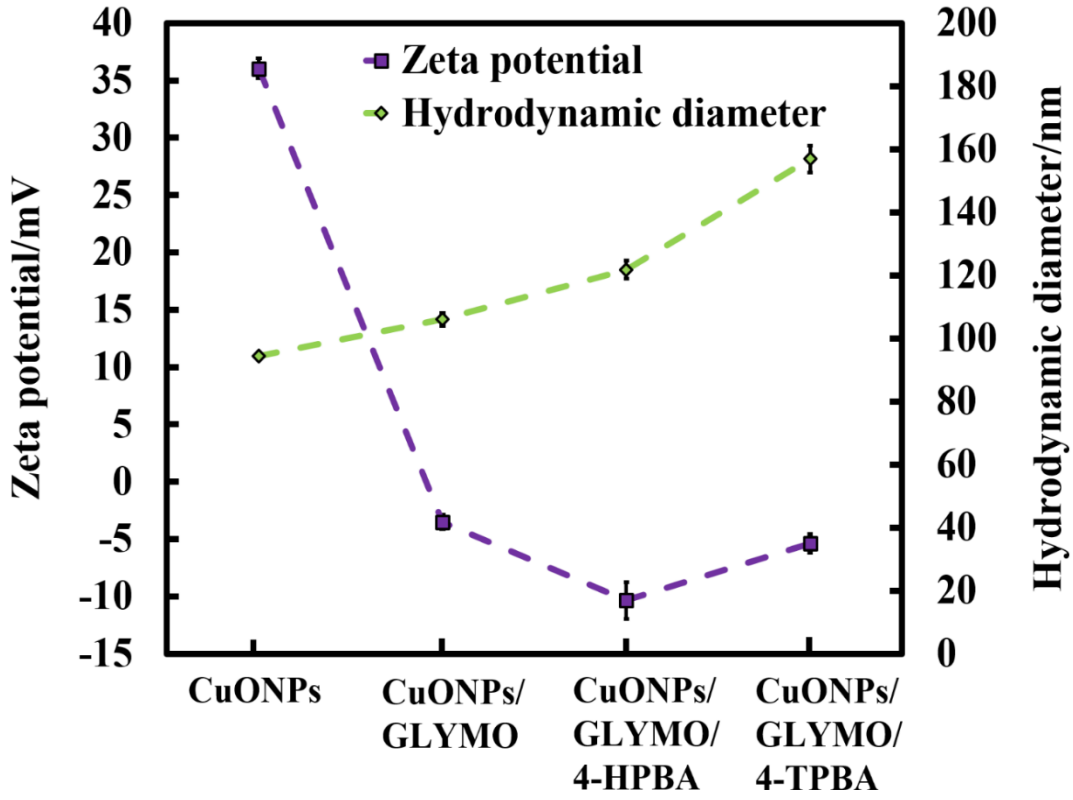


**Figure 7.22.** Zeta potential and hydrodynamic diameter of the bare and surface modified CuONPs with GLYMO and 4-HPBA or 4-TPBA, measured at room temperature at pH 6 (error bars are standard deviations).

Since the CuONPs are photoactive, there was a concern that the GLYMO/HPBA functionality can potentially be affected by oxidation under the action of UV light. In order to check the stability of this coating against oxidation, we measured periodically the zeta potential of the CuONPs/GLYMO/4-HPBA over the course of 3 days while the samples were exposed to UV light. The results, presented in Figure 7.23 indicate that the zeta-potential of the functionalized CuONPs does not change, i.e. the coating is not prone to oxidation at these conditions and hence the particles preserve their functionality and antibacterial action.

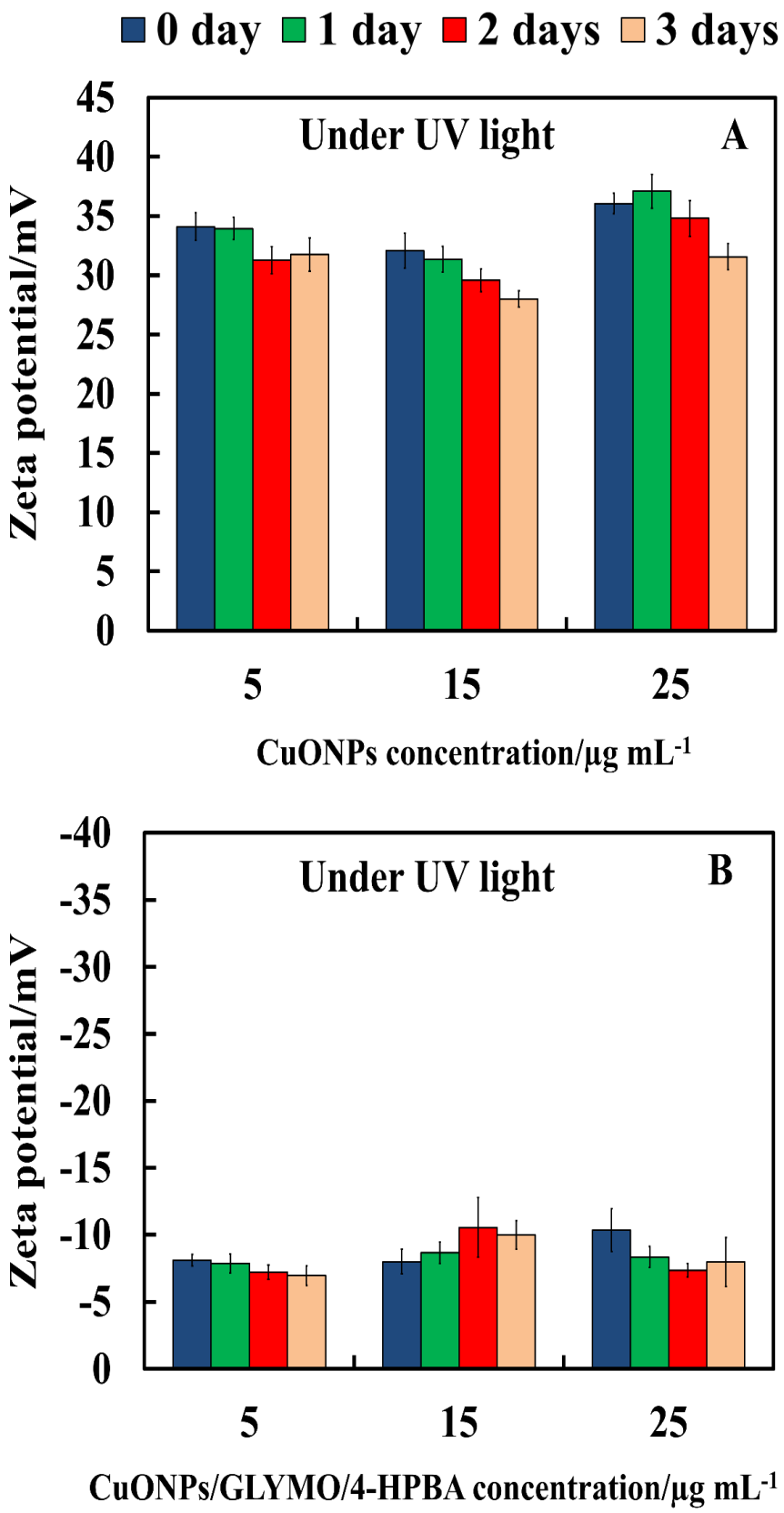


**Figure 7.23.** The zeta potential of (A) bare CuONPs and (B) CuONPs functionalized with GLYMO and 4-HPBA at different concentrations (5, 15 and 25 µg $mL^{-1}$) after exposure to UV light for 0 day, 1 day, 2 days and 3 days.

### 7.9.1 FTIR of the surface functionalized of CuONPs with GLYMO and 4-HPBA

The efficiency of the alkoxysilane-mediated functionalization with GLYMO (and latter with 4-HPBA) on CuONPs was examined by FTIR. The OH groups on the surface of the CuO nanoparticles are the reactive sites for the reaction with alkoxy silane groups of GLYMO. Figures 7.24A, 7.24B and 7.24C show normalized FTIR spectra of the bare CuONPs and those, surface modified with GLYMO or GLYMO/4-HPBA. In the spectra of all CuONPs, the broad band between 400 and 800 $cm^{-1}$ corresponds to Cu-O-Cu. GLYMO contains two functional groups: epoxy and methoxysilyl, which can both hydrolyze and condensate. One can see that the epoxy band in FTIR spectra (Figure 7.24A) is preserved, while the intensity of Si-O-Me band is decreased. Moreover, the two bands of OH groups appear at ~3300 and ~1640 $cm^{-1}$ because of the hydrolysis of Si-O-Me groups.

Also a peak at 1050 $cm^{-1}$ appears, which can be assigned to the formation of Si-O-Si groups. The comparison of the FTIR spectra of the bare and functionalized CuONPs samples show some new characteristic absorption peaks.

Figure 7.24C (CuONPs/GLYMO) shows a peak at ~1200 $cm^{-1}$ which refers to Si-O-Me groups.[30] In the FTIR spectrum of the CuONPs/GLYMO/4-HPBA, the peak at about 3300 $cm^{-1}$ could be attributed to the stretching vibration of O–H groups. The peaks at ~2500 $cm^{-1}$ were assigned to the stretching and bending vibrations of C–H groups. The bending of the aromatic C=C groups could be also observed at 1490–1650 $cm^{-1}$. The sharp peaks at around 1343 $cm^{-1}$ and 1090 $cm^{-1}$ could be assigned to the stretching vibrations B–O and C–B groups (Figure 7.24C).[28, 29]

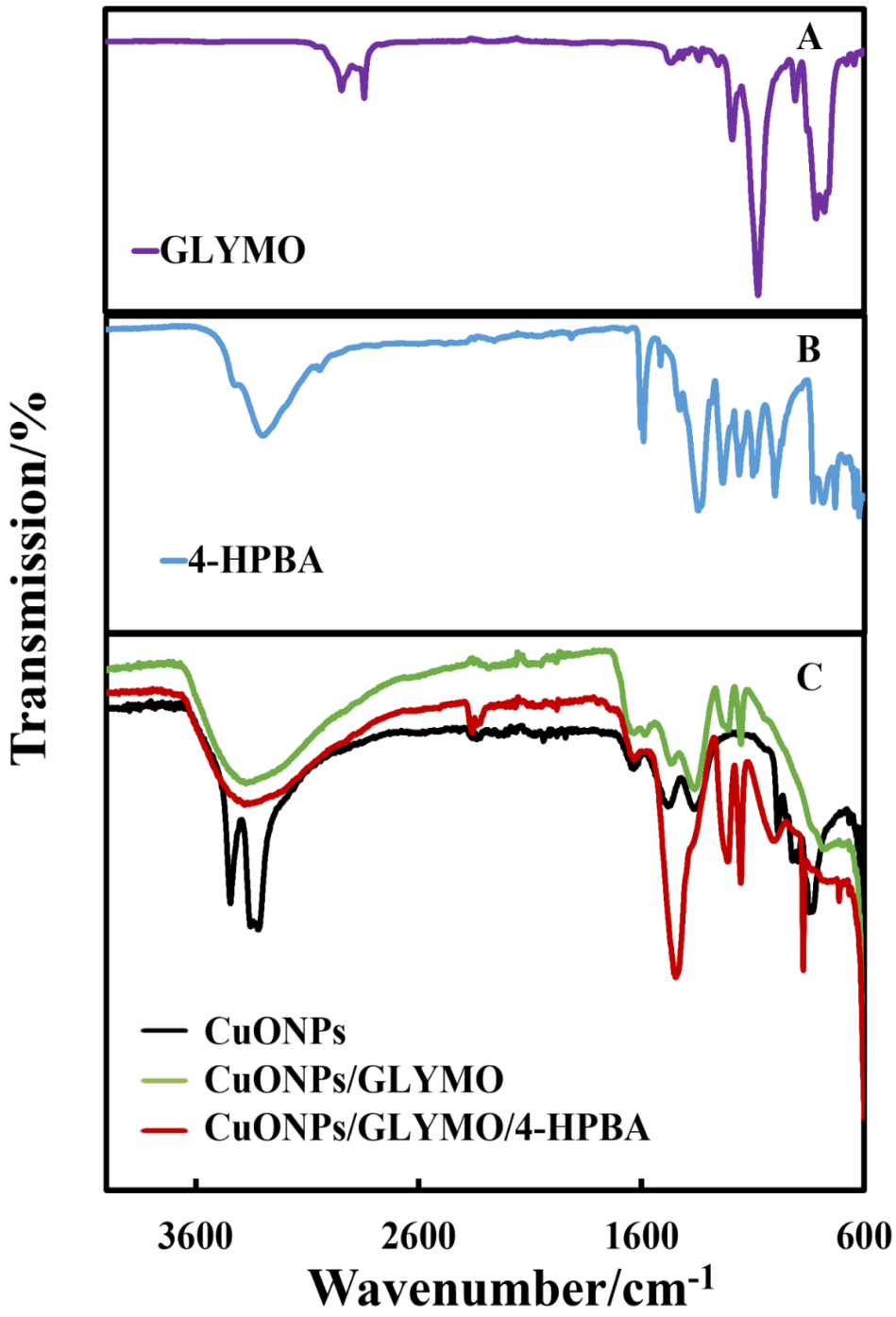


**Figure 7.24.** The FTIR spectra of (A) pure GLYMO, (B) pure 4-HPBA and (C) the bare and functionalized CuONPs.

## 7.10 Surface modified of CuONPs by 4-CPBA

CuONPs were modified with phenylboronic acid by using 4-carboxyphenylboronic acid (4-CPBA). 4-CPBA was chosen because it contains carboxylate groups, which can coordinate to the surface of CuONPs (Figure 7.25). Furthermore, it is well known that the phenylboronic acid moieties of 4-CPBA can covalently bond to cis-diol moieties in a

reversible fashion; this makes it an ideal ligand for highly efficient, selective recognition of the sialic acid groups that are overexpressed on the surface of cells. The zeta potential and hydrodynamic size of CuONPs/4-CPBA were characterized by using the Malvern Zetasizer NanoZS system. The characterization results discovered a zeta potential of around +7 mV (Figure 7.26) and average particle size of about 119 nm (Figure 7.27).

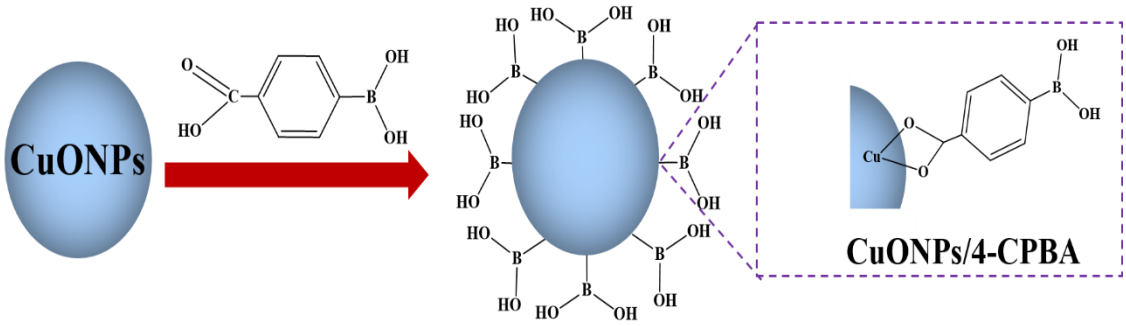


**Figure 7.25.** Schematic illustration of the modified reaction of CuONPs with 4-CPBA.

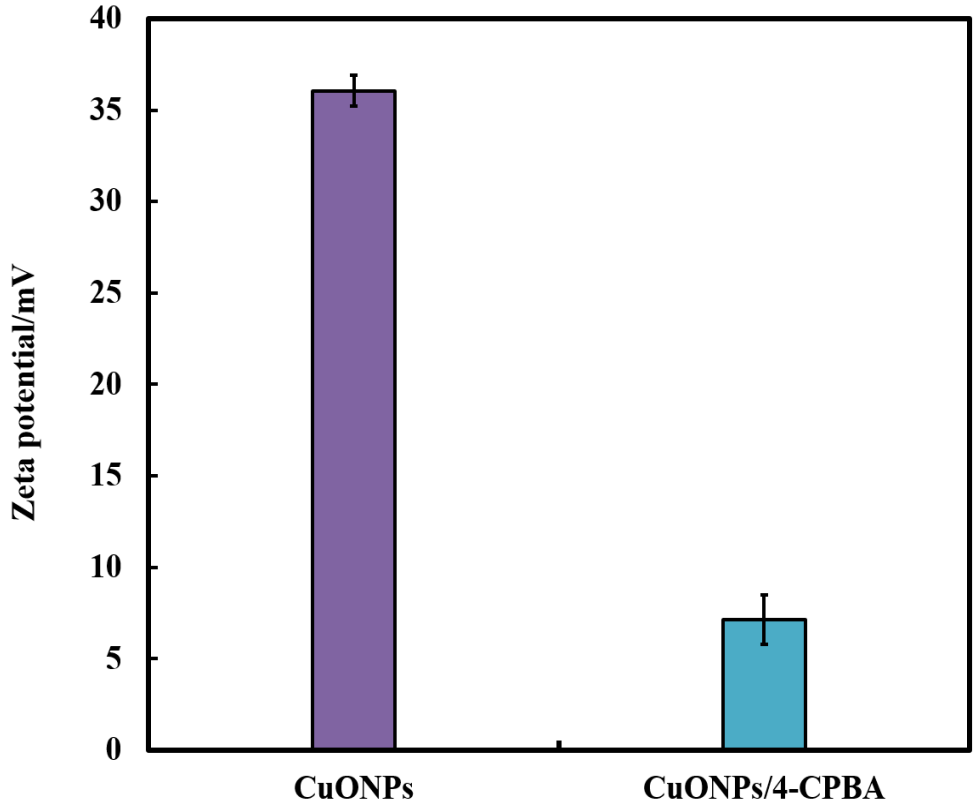


**Figure 7.26.** The zeta potential of CuONPs and CuONPs/ 4-CPBA.

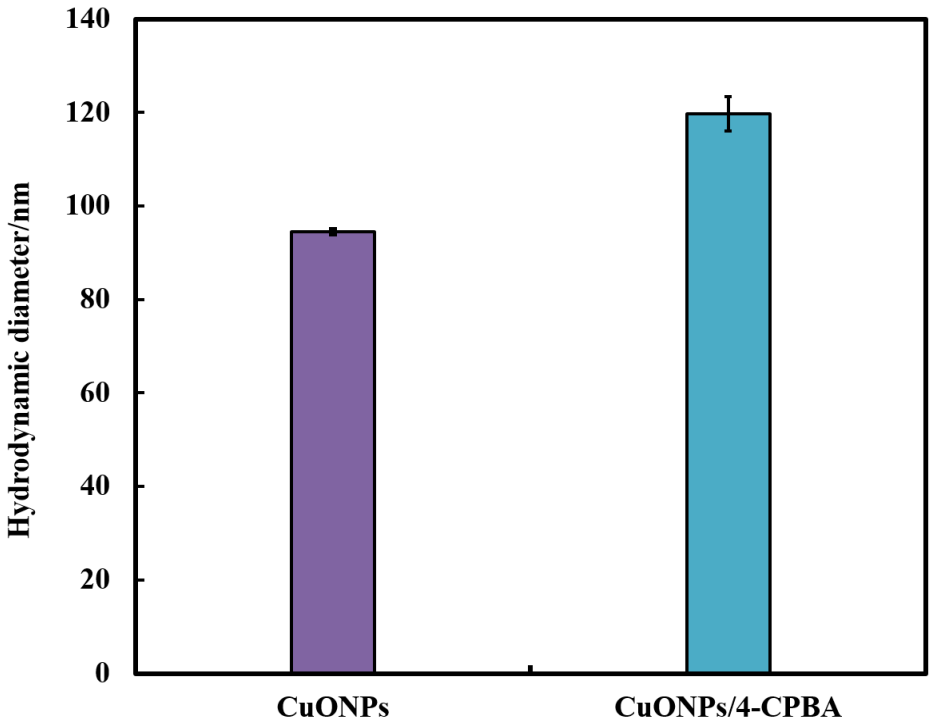


**Figure 7.27.** The particle size of CuONPs and CuONPs/ 4-CPBA.

### 7.10.1 The FTIR spectra of the surface modified of CuONPs with 4-CPBA.

FTIR spectra of CuONPs, 4-CPBA, and CuONPs/4-CPBA are shown in Figure 7.28. As compared with the spectrum of CuONPs, a characteristic band (1,340 $cm^{-1}$), which is ascribed to the B–O bond, can be observed from the spectrum of CuONPs/4-CPBA. As compared with 4-CPBA, CuONPs/4-CPBA do not display the characteristic band of COOH at 1,710 $cm^{-1}$. These results provide strong evidence for the attachment of the carboxyl group of 4-CPBA to CuONPs and indicate the success of using 4-CPBA for particle modification.[31]

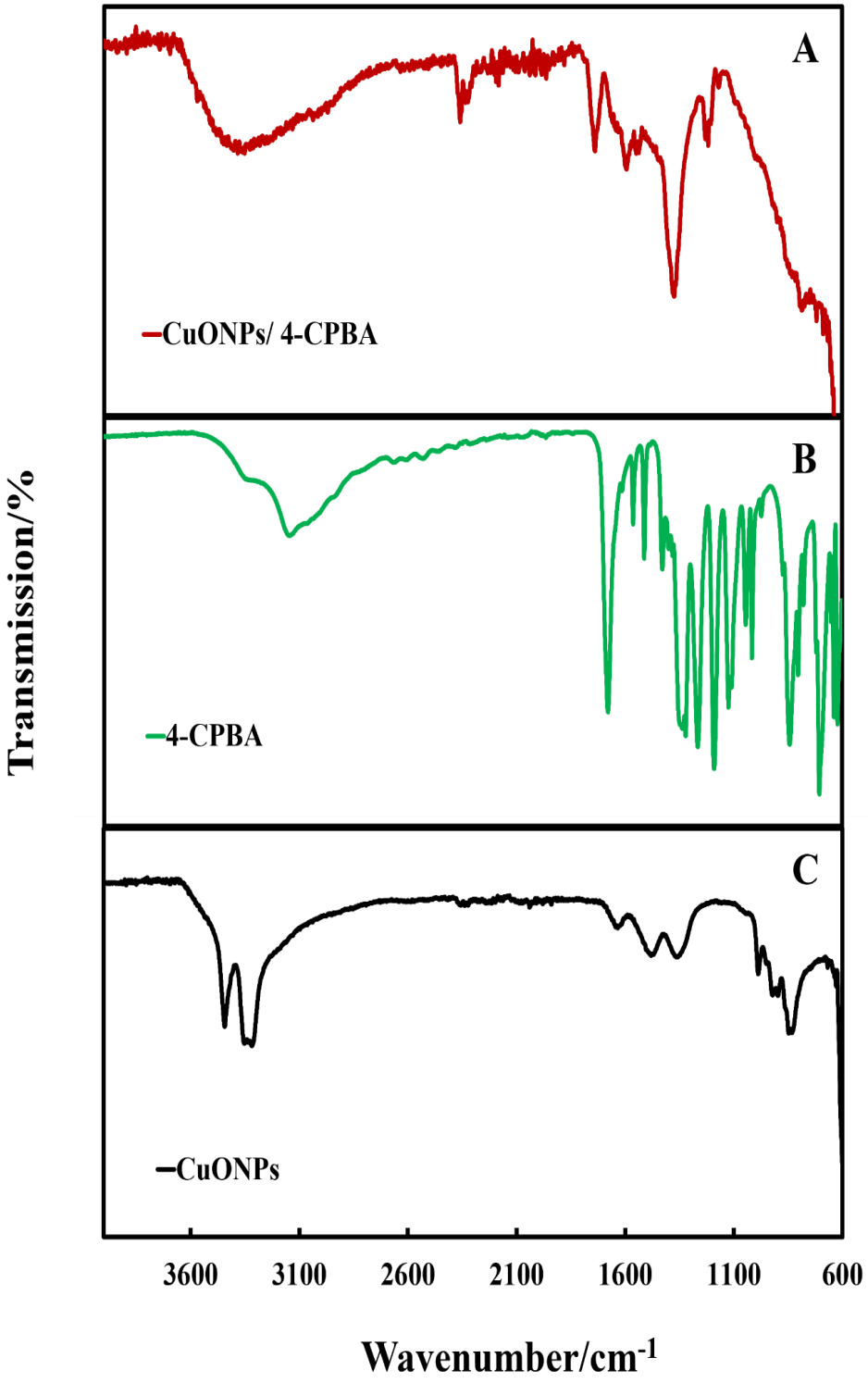


**Figure 7.28.** The FTIR spectra of (A) the CuONPs modified with 4-CPBA, (B) 4-CPBA and (C) unmodified CuONPs. The absorption peaks at ~1,345 $cm^{-1}$ and at ~1,710 $cm^{-1}$ are assigned to the carboxyl group, indicating that 4-CPBA was successfully functionalized onto the CuONPs.

## 7.11 Conclusions

It can be concluded that the synthesis of CuONPs requires no expensive ingredients and complicated equipment's. The method is easy, less time-consuming and flexible. The developed nanoparticles were characterized by XRD, EDX, FTIR, zeta potential and DLS measurements. XRD spectra confirmed the formation of single phase CuONPs. Crystallite size was found to increase with the increase in annealing temperature. Minimum crystallite size of 13 nm was observed in the case of CuONPs annealed at 100°C. The average crystal size of CuONPs calculated from XRD data using the Scherrer equation was much smaller than the hydrodynamic diameters of the CuONPs dispersed in deionized water. This indicates that the CuONPs in aqueous dispersions are aggregates of smaller crystallites. The elemental quantification and stoichiometry ratio of CuONPs were confirmed by EDX analysis. The FTIR spectra confirmed the presence of metal-oxygen bond. The bare CuONPs average particle hydrodynamic diameter was 93 nm while their average zeta potential was +37 mV, i.e. the non-functionalized (bare) CuO nanoparticles are cationic at pH 6. The isoelectric point of the CuONPs (corresponding to the pH where the CuONPs have zero zeta potential) was at pH 9. In this Chapter, a novel type of modified CuONPs has been developed by functionalizing the CuONPs with GLYMO, APTES, 4-FPBA, 4-TPBA, 4-CPBA and 4-HPBA to produce an antibacterial agent of much higher efficiency than bare CuONPs. Surface modification and characterization of CuONPs were investigated. FTIR analysis shows that grafting of GLYMO and 4-HPBA on the CuONPs has occurred successfully. The results showed that the zeta potential of bare CuONPs was positive while the two types of surface-modified CuONPs had small but negative zeta potential, ranging from around -3 ± 2 mV (CuONPs/GLYMO) to -10 ± 2 mV (CuONPs/GLYMO/4-HPBA) and -5 ± 1 mV (CuONPs/GLYMO/4-TPBA). Previous work in the literature has shown the possibility of preparing the APTES functionalization of other inorganic nanoparticles, but in this Chapter, GLYMO brings epoxy-ring as a terminal group. This functionality has not been reported before for CuONPs.

## 7.12 References


1. A. F. Halbus, T. S. Horozov and V. N. Paunov, *ACS applied materials & interfaces*, 2019, **11**, 12232–12243.
2. A. F. Halbus, T. S. Horozov and V. N. Paunov, *Advances in colloid and interface science*, 2017, **249**, 134-148.
3. A. F. Halbus, T. S. Horozov and Vesselin N. Paunov, *Nanoscale Advances*, 2019, **1**, 2323 – 2336.
4. P. C. Trippier and C. McGuigan, *MedChemComm*, 2010, **1**, 183-198.
5. J. Yan, G. Springsteen, S. Deeter and B. Wang, *Tetrahedron*, 2004, **60**, 11205-11209.
6. A. P. De Silva, H. N. Gunaratne, T. Gunnlaugsson, A. J. Huxley, C. P. McCoy, J. T. Rademacher and T. E. Rice, *Chemical reviews*, 1997, **97**, 1515-1566.
7. K. Lacina, P. Skládal and T. D. James, *Chemistry Central Journal*, 2014, **8**, 60.
8. M. V. Kuzimenkova, A. E. Ivanov, C. Thammakhet, L. I. Mikhalovska, I. Y. Galaev, P. Thavarungkul, P. Kanatharana and B. Mattiasson, *Polymer*, 2008, **49**, 1444-1454.
9. O.-W. Lau, B. Shao and M. T. Lee, *Analytica chimica acta*, 2000, **403**, 49-56.
10. P. Ertl and S. R. Mikkelsen, *Analytical chemistry*, 2001, **73**, 4241-4248.
11. R. Wannapob, P. Kanatharana, W. Limbut, A. Numnuam, P. Asawatreratanakul, C. Thammakhet and P. Thavarungkul, *Biosensors and Bioelectronics*, 2010, **26**, 357-364.
12. S. Liu, U. Wollenberger, J. Halámek, E. Leupold, W. Stöcklein, A. Warsinke and F. W. Scheller, *Chemistry–A European Journal*, 2005, **11**, 4239-4246.
13. B. Elmas, M. Onur, S. Şenel and A. Tuncel, *Colloid and Polymer Science*, 2002, **280**, 1137-1146.
14. N. DiCesare and J. R. Lakowicz, *Analytical biochemistry*, 2001, **294**, 154-160.
15. R. Manimaran, K. Palaniradja, N. Alagumurthi, S. Sendhilnathan and J. Hussain, *Applied Nanoscience*, 2014, **4**, 163-167.
16. I. Z. Luna, L. N. Hilary, A. S. Chowdhury, M. Gafur, N. Khan and R. A. Khan, *Open Access Library Journal*, 2015, **2**, 1.
17. A. A. Radhakrishnan and B. B. Beena, *Indian Journal of Advances in Chemica l Science*, 2014, **2**, 158-161.
18. I. Markova-Deneva, *J. Univ. Chem. Technol. Metall*, 2010, **45**, 351-378.
19. K. Karthik, N. V. Jaya, M. Kanagaraj and S. Arumugam, *Solid State Communications*, 2011, **151**, 564-568.

20. V. V. T. Padil and M. Černík, *International Journal of Nanomedicine*, 2013, **8**, 889.
21. F. Grasset, N. Saito, D. Li, D. Park, I. Sakaguchi, N. Ohashi, H. Haneda, T. Roisnel, S. Mornet and E. Duguet, *Journal of Alloys and Compounds*, 2003, **360**, 298-311.
22. V. J. Cunningham, A. M. Alswieleh, K. L. Thompson, M. Williams, G. J. Leggett, S. P. Armes and O. M. Musa, *Macromolecules*, 2014, **47**, 5613-5623.
23. J.-L. DiFlavio, R. Pelton, M. Leduc, S. Champ, M. Essig and T. Frechen, *Cellulose*, 2007, **14**, 257-268.
24. R. M. Issa, A. M. Khedr and H. Rizk, *Journal of the Chinese Chemical Society*, 2008, **55**, 875-884.
25. M. Ma, Y. Zhang, W. Yu, H.-y. Shen, H.-q. Zhang and N. Gu, *Colloids and Surfaces A: Physicochemical and Engineering Aspects*, 2003, **212**, 219-226.
26. R. A. Bini, R. F. C. Marques, F. J. Santos, J. A. Chaker and M. Jafelicci, *Journal of Magnetism and Magnetic Materials*, 2012, **324**, 534-539.
27. L. D. White and C. P. Tripp, *Journal of Colloid and Interface Science*, 2000, **232**, 400-407.
28. Y. Guo, Y. Chen, F. Cao, L. Wang, Z. Wang and Y. Leng, *RSC Advances*, 2017, **7**, 48386-48393.
29. M. Arslan, B. Kiskan and Y. Yagci, *Scientific reports*, 2017, **7**, 5207.
30. P. T. PREMAZU, *Materiali in tehnologije*, 2012, **46**, 19-24.
31. N. Sun, C. Deng, G. Ge and Q. Xia, *Biotechnology letters*, 2015, **37**, 211-218.

# Chapter 8

# 8. Self-grafting copper oxide nanoparticles show a strong enhancement of their antibacterial, anti-algal and anti-yeast action

## 8.1 Introduction

Spreading of antimicrobial resistance among common bacterial pathogens, bacterial infections, including antibiotic-resistant infections, has recently drawn much attention.[1-4] A range of colloidal particles are being extensively studied in various antimicrobial applications due to their small size to volume ratio and ability to exhibit a wide spectrum of antibacterial action.[5-8] Antibacterial NPs could bypass the increasing rates of antibiotic resistance by attacking and destroying the bacteria in other ways.[9] Surface functionalization of nanoparticles is vital for controlling their properties and interactions with molecules and ligands of relevance for biomedical applications, in addition to their susceptibility to undergo a transformation in environmental and biological systems.[10, 11] Considerable efforts have been devoted to the development of surface modifiers that can offer not only stability but also better control of the interaction between nanoparticles and biological membranes in order to obtain more biocompatible materials.[12] Perreault and co-workers have shown that polymer coated (polystyrene-co-butyl acrylate) CuONPs display increased cellular uptake and toxicity in the green alga *C. reinhardtii*. The ascorbate and citrate surface layers are well known for their anti-oxidant properties and are used as reducing agents as well as negatively charged stabilizers of nanoparticles synthesis and dispersion.[13] Líbalová *et al*. have evaluated the cytotoxicity of a panel of CuONPs with various surface modifications such as cationic polyethylenimine (PEI), neutral polyvinylpyrrolidone (PVP), sodium ascorbate (ASC) and anionic sodium citrate (CIT), versus the pristine bare CuONPs, using a murine macrophage cell line. The results from their work suggest that the PEI-coated CuONPs were found to be the most cytotoxic. Líbalová *et al*. have also reported that the ascorbate-coated CuONPs, which were found to be the least cytotoxic, produced lower levels of ROS in comparison to bare nanoparticles.[11]

CuONPs have been widely used as a dopant for semiconductors, chemical sensors, supported heterogeneous nano-catalysts, coating material and in anti-cancer treatments but their functional properties have been proven essential for their applications in

biological research.[14, 15] The bare CuONPs are cationic at neutral pH and can adhere to the negatively charged bacterial cell walls only by electrostatic interactions.[5, 14, 15]

The average size of CuONPs is also essential for their potential antimicrobial activity, as smaller nanoparticles have higher portability and ability to potentially penetrate and relocate between the bacterial cell compartments. This makes them very effective antimicrobial agents. However, electrostatic adhesion can be easily disabled by the presence of another type of anionic substances in the solution, e.g. organic acids, albumins, surfactants, polymers and others. It impacts the nanoparticle interactions with different biomolecules, for example, carbohydrates and proteins which can be adsorbed on the particles and form a corona of different surface properties to that of the original nanoparticles. This is the likely reason why CuONPs can quickly lose their antimicrobial activity in biological fluids as well as in formulations that contain anionic polyelectrolytes and surfactants.

Here CuONPs with boronic acid surface functionality were engineered in an attempt to design a non-electrostatic mechanism for their attachment to the bacteria which was expected to amplify their accumulation on the cell walls despite the presence of other anionic species. This is shown schematically in Figure 8.1. Our idea here is to introduce boronic acid (BA) surface groups on the CuONPs which are able to covalently bind to various glycoproteins and carbohydrates that are abundant on the bacterial cell walls.

Boronic acid has been used before in chemosensor applications due to its high sensitivity for sugar determination.[16] An attractive feature of the BA surface functionality that makes it very effective for biomedical applications is their perceived absence of toxicity[17] despite its ability to form reversible covalent complexes with diols.[18, 19] The binding of BA to sugars is very sensitive to the sugar concentration, however, it is undiscriminating and will therefore bind to any diol containing compounds.[20] BA has also been discussed as a promising tools for the quantification of the total content of bacteria.[21-23] BA surface groups can covalently bind to saccharides and form boronic esters.[24-26]

*R. rhodochrous*, *E.coli*, *C. reinhardtii* and *S. cerevisiae* were used as model bacteria and cells species to examine the antibacterial, anti-algal and anti-yeast activity of the 4-HPBA functionalized CuONPs. The current work was carried out with CuONPs, CuONPs/GLYMO, CuONPs/GLYMO/4-HPBA, CuONPs/PSS, CuONPs/PSS/PAH, CuONPs/APTES and CuONPs/APTES/4-FPBA to investigate the impact of (i) the nanoparticle concentration, and (ii) the zeta potential and particle size on the viability of microorganisms at different exposure times. The novelty of work is that the antibacterial, anti-algal and anti-yeast activity of CuONPs functionalized with 4-HPBA is not based on

electrostatic adhesion to the bacterial cells and therefore could potentially be used in complex biological environment. Significantly, the functionalization of the CuONPs with 4-HPBA groups as an outer monolayer should lead to their covalent attachment on the sugar (OH) groups on the membrane surface, thus bringing the CuONPs in very close proximity to the bacterial cell membrane and increasing their efficiency (Figure 8.1A and 8.1B). The toxicity of both bare CuONPs and functionalized CuONPs on human keratinocytes was also examined.

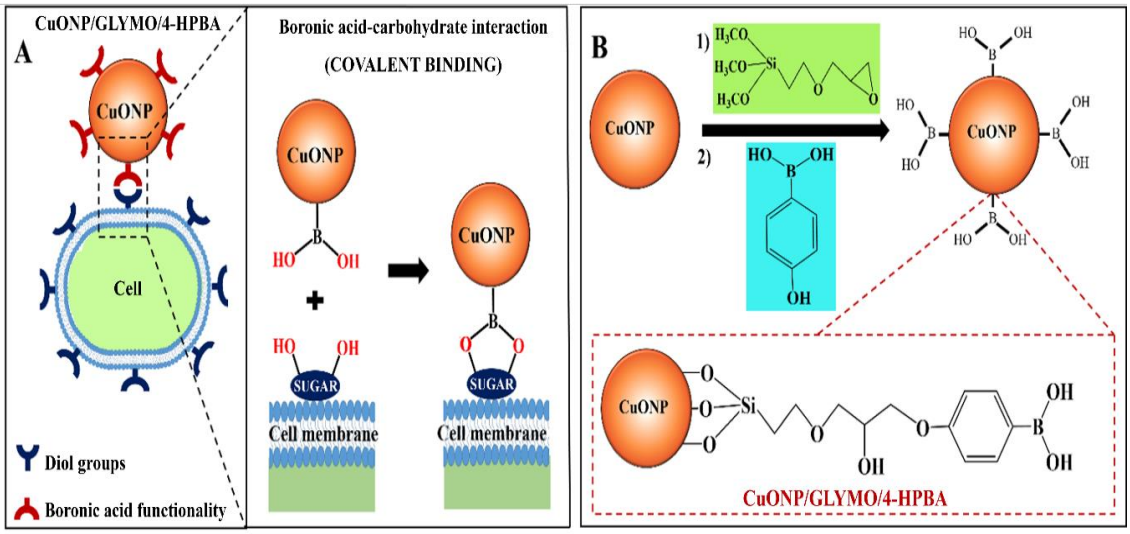


**Figure 8.1.** (A) Schematics showing the mechanism of self-grafting/covalent attachment of HPBA-functionalized CuONPs and the cell membrane. (B) The schematic of the synthesis method of CuONPs/GLYMO/4-HPBA by sequential grafting of GLYMO and 4-HPBA on CuONPs in an aqueous suspension.

## 8.2 Antibacterial activity of polyelectrolyte- coated CuONPs on *E. coli*

Figure 8.2 shows the antibacterial activity of uncoated and polyelectrolyte-coated CuONPs at various particle concentrations towards *E.coli* bacteria. It should be noted in Figure 8.2 (D, E and F) that after incubation times up to 6 hours, no variation in the number of viable *E.coli* was detected for CuONPs/PSS even at 250 µg $mL^{-1}$ particle concentrations. The antibacterial activity of CuONPs/PSS under visible light, UV light as well as in dark conditions was less than the one of the uncoated CuONPs. The variance among the number of *E.coli* in dark conditions and UV light (Figures 8.2F) is solely because of the photo activity of the CuONPs. The results indicate that the functionalization of the CuONPs with anionic polyelectrolyte decreased its antibacterial activity perhaps due to the electrostatic repulsion of the coated CuONPs from the cell surface of *E.coli* as both of them have a negative surface charge. Nevertheless, in Figure

8.2G, 8.2H and 8.2I where a next layer of PAH has included the number of *E.coli* in dark conditions, visible light and UV light decreases considerably. In fact, it is close to antibacterial activity to the *E.coli* as the uncoated CuONPs. At lower CuONPs/PSS/PAH concentrations (5 µg $mL^{-1}$) these cationic coated particles have even higher antibacterial activity than the uncoated CuONPs irrespective of the time of incubate in dark, visible light and UV light conditions. Moreover, the cationic nanoparticles (the uncoated CuONPs and CuONPs/PSS/PAH) have higher antibacterial activity than the anionic nanoparticles (CuONPs/PSS).

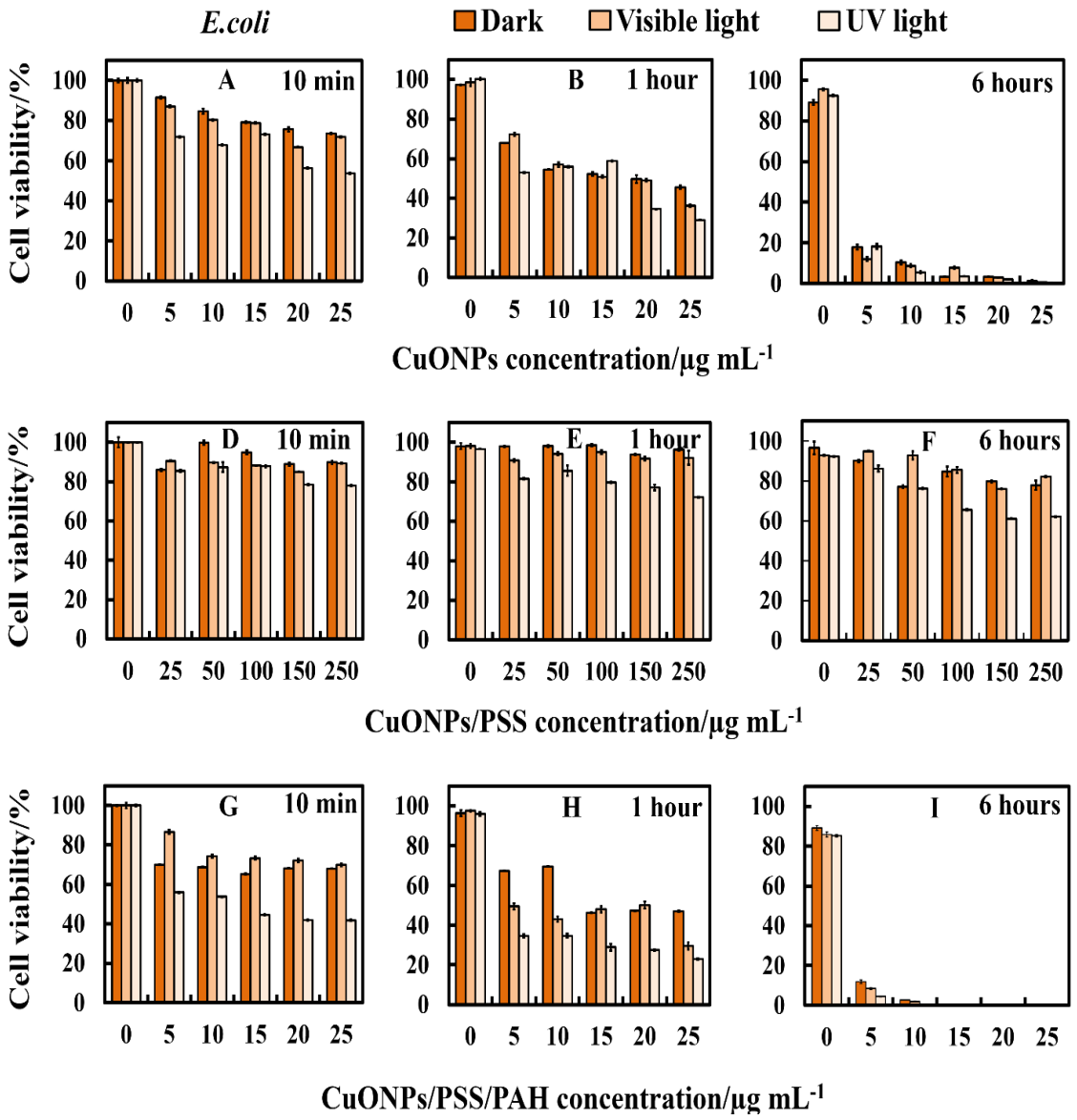


**Figure 8.2.** Comparison of the *E.coli* viability using various concentrations of bare CuONPs and the surface coated of CuONPs with PSS and PAH in dark, visible and UV light conditions at 10 minutes, 1 h, and 6 h of incubation times in comparison with an untreated sample of *E.coli*.

Furthermore, to see better the interactions among the CuONPs and *E.coli* we utilized SEM and TEM to study the surface of *E.coli* which were incubated with CuONPs for 6 hours as shown in Figure 8.3. The result was also confirmed via EDX chart of *E.coli* with CuONPs which revealed the existence of Cu on the external part of the *E.coli* surface (Figure 8.4).

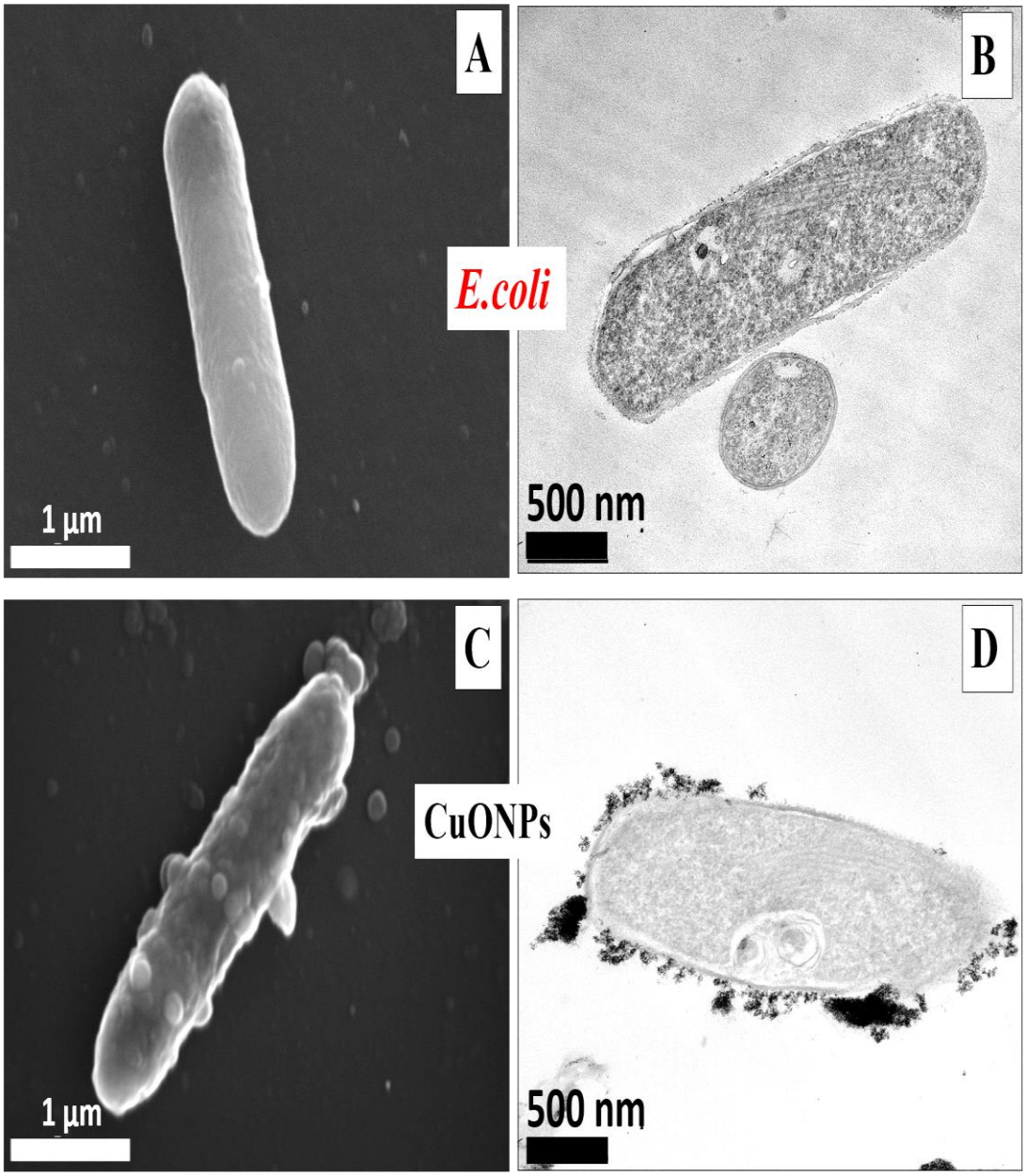


**Figure 8.3.** SEM and TEM image of *E.coli* after being exposed for 6 hours with uncoated CuONPs: (A and B) SEM and TEM image of an untreated sample without CuONPs. (C and D) SEM and TEM image of *E.coli* incubated with 25 µg $mL^{-1}$ CuONPs.

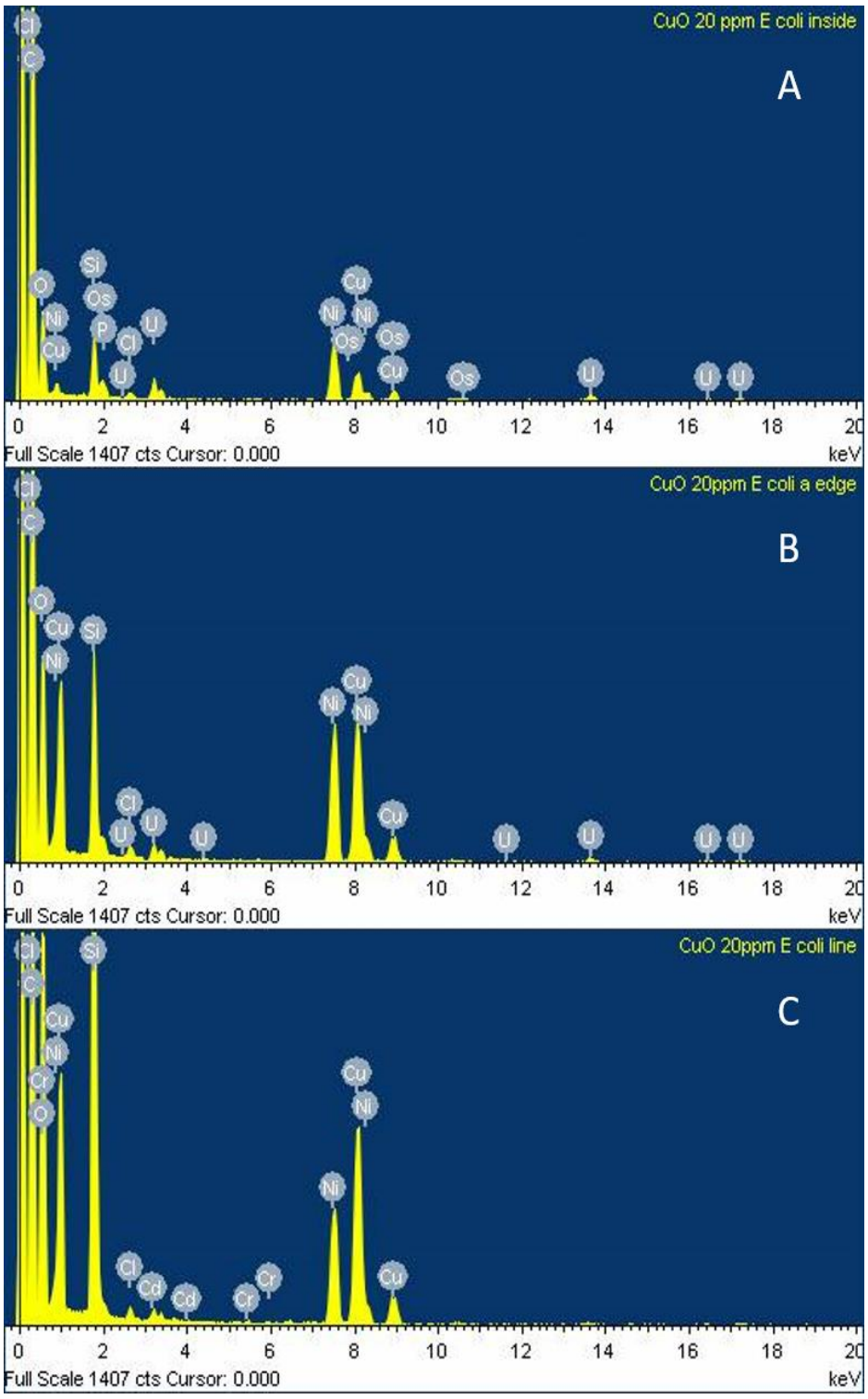


**Figure 8.4.** EDX diagram of *E.coli* cells with CuONPs at 20 µg $mL^{-1}$: (A) *E.coli* inside membrane and (B) *E.coli* edge membrane areas and (C) *E.coli* outside membrane areas. The result shows the existence of CuONPs on the inner and outer part of the cell membrane.

*E. coli* was incubated with PSS suspensions of different concentrations of polyelectrolyte. The cells were removed from the culture media to avoid any interaction between the PSS

and the components of the culture media. Cell viability assay does not indicate any measurable cytotoxic impact of the PSS on *E. coli* for a wide range of PSS concentrations at room temperature and up to 6 hours of incubation (Figure 8.5). Additionally, to study the accumulation of CuONPs on the *E.coli* surface, the *E.coli* was incubated with polyelectrolyte-coated CuONPs and then their extract from the CuONPs solution after a constant time of incubating. The bacteria suspension were sectioned and imaged with TEM. Figure 8.6 shows TEM images of *E.coli* for CuONPs coated with a layer of PSS and next layer of PAH for 6 hours of incubating time in dark conditions.

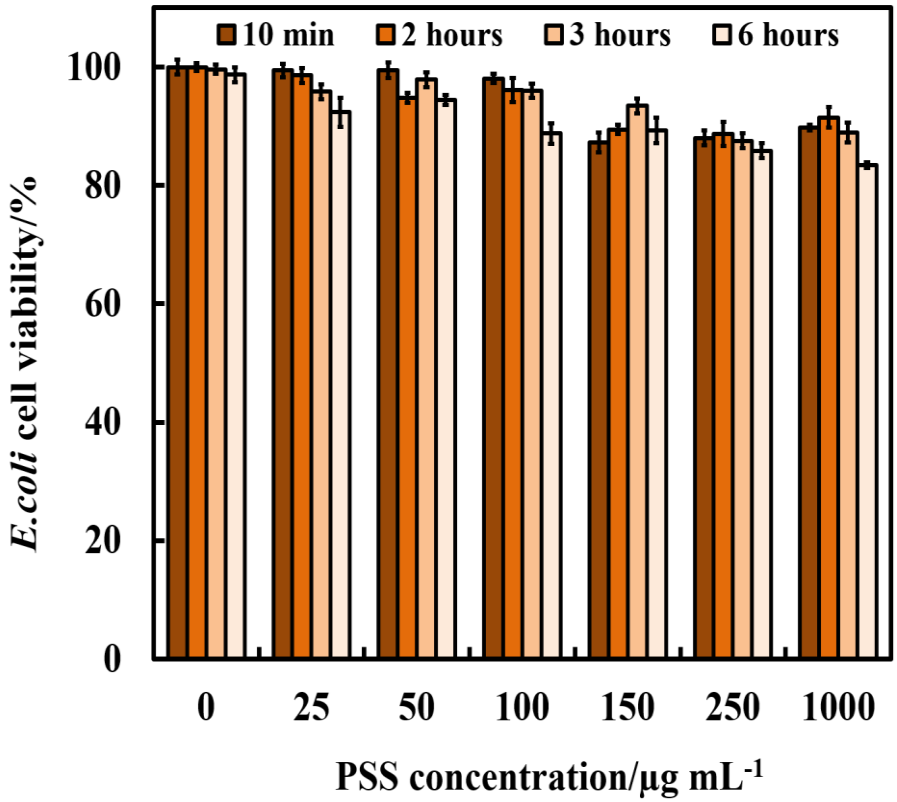


**Figure 8.5.** The antibacterial activity of free PSS on *E.coli*. The bacteria were incubated with PSS for at 10 min., 2 h, 3 h and 6 h of incubating times.

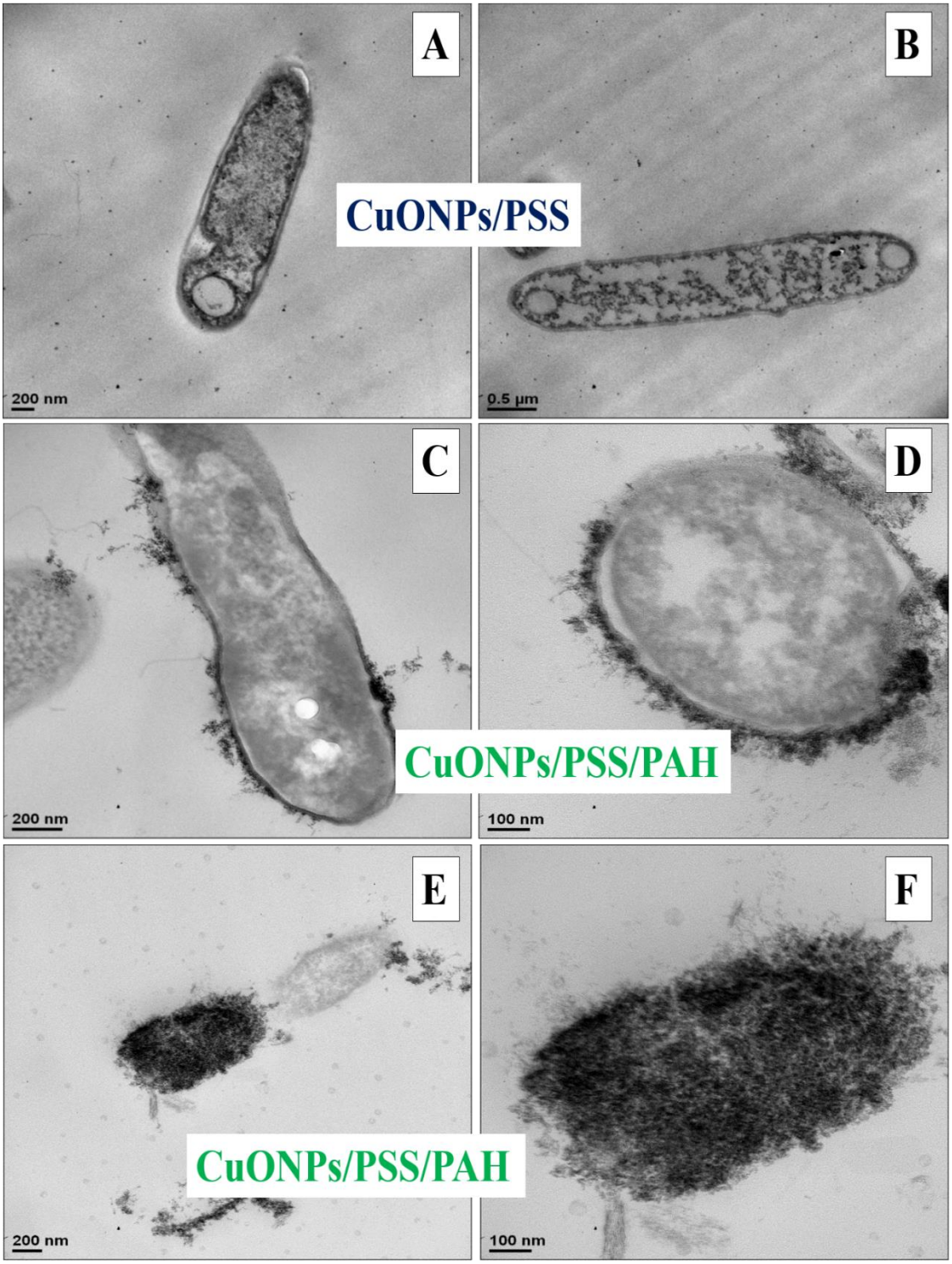


**Figure 8.6.** TEM images of *E.coli* after being incubated for 6 h into CuONPs coated with various layers of polyelectrolyte in dark condition: (A and B) TEM image of *E.coli* incubated with 250 µg $mL^{-1}$ CuONPs/PSS. (C and D) TEM images of *E.coli* incubated with 20 µg $mL^{-1}$ CuONPs/PSS/PAH. (E and F) TEM images of *E.coli* incubated with 25 µg $mL^{-1}$ CuONPs/PSS/PAH.

## 8.3 Antibacterial activity of APTES- and 4-FPBA-grafted CuONPs on *E. coli*

The surface functionalized CuONPs were obtained using 3-aminopropytriethoxysilane (APTES) and 4-formylphenylboronic acid (4-FPBA). In the first step, the ethoxy groups of the APTES reacted with the surface hydroxyl groups of the CuONPs. Next, the amino groups of APTES reacted with the aldehyde groups of 4-FPBA, and then the modified surface of the APTES functionalized CuONPs with boronic acid groups was formed (CuONPs/APTES/4-FPBA). Owing to the low cytotoxicity of boronic acid,[27, 28] it was important to verify the innocuous nature of CuONPs/APTES/4-FPBA conjugates in the present work. A series of experiments were carried out to evaluate the antibacterial activity of CuONPs, CuONPs/APTES and CuONPs/APTES/4-FPBA. Figure 8.7 shows the results of the antibacterial activity of nanoparticles on *E.coli*. The date in Figure 8.7, CuONPs/APTES (D, E and F) and CuONPs/APTES/4-FPBA (G, H and I) nanoparticles showed low antibacterial activity on *E.coli* within 1 hour and 6 hours. The low antibacterial activity of these nanoparticles was shown by using the concentration of 4% APTES. A possible mechanism for these is that higher concentration of APTES covered the CuONPs, thus reducing the interaction between nanoparticles and the cells. However, in Figure 8.8G, 8.8H and 8.8I where a lower concentration of 0.1% APTES the CuONPs/APTES/4-FPBA is included the viability of the *E.coli* reduce considerably. It is exciting that at lower CuONPs/0.1% APTES/4-FPBA concentrations (5 μg $mL^{-1}$) these particles have even more antibacterial activity than the bare CuONPs irrespectively of the time of exposure in both dark, visible and UV light conditions (Figure 8.8G).

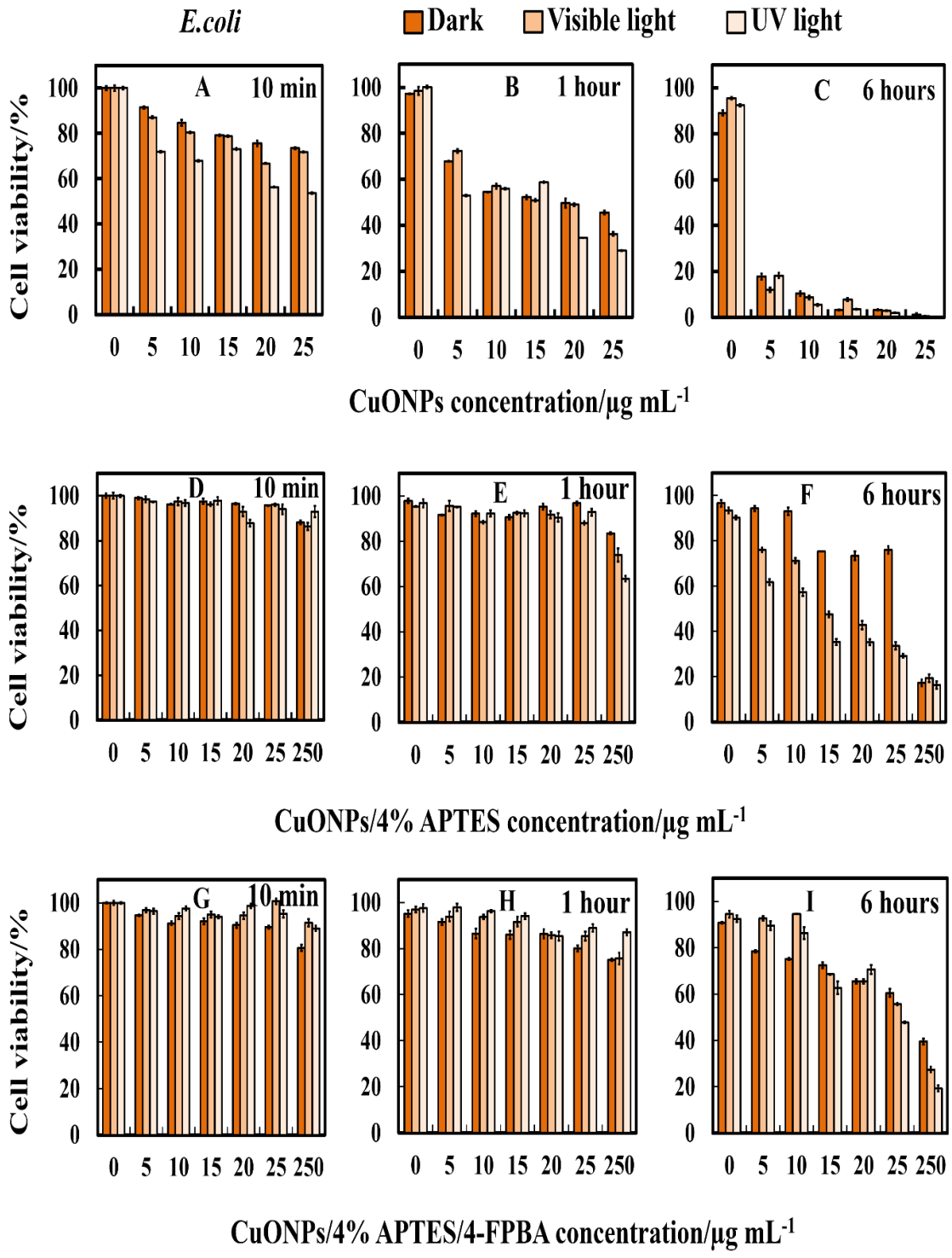


**Figure 8.7.** The impact of CuONPs functionalized with 4% APTES and 4-FPBA on the viability of *E.coli* at different particle concentrations (0, 5, 10, 15, 20, 25 and 250 µg $mL^{-1}$). The bacteria was incubated with the CuONPs for at 10 min, 1 h and 6 h exposure times in dark, visible and in UV light conditions, respectively. The antibacterial activity on the *E.coli* cells was evaluated for: (A, B and C) bare CuONPs; (D, E and F) CuONPs/4% APTES and (G, H and I) CuONPs/4% APTES/4-FPBA at different nanoparticle concentrations and exposure times.

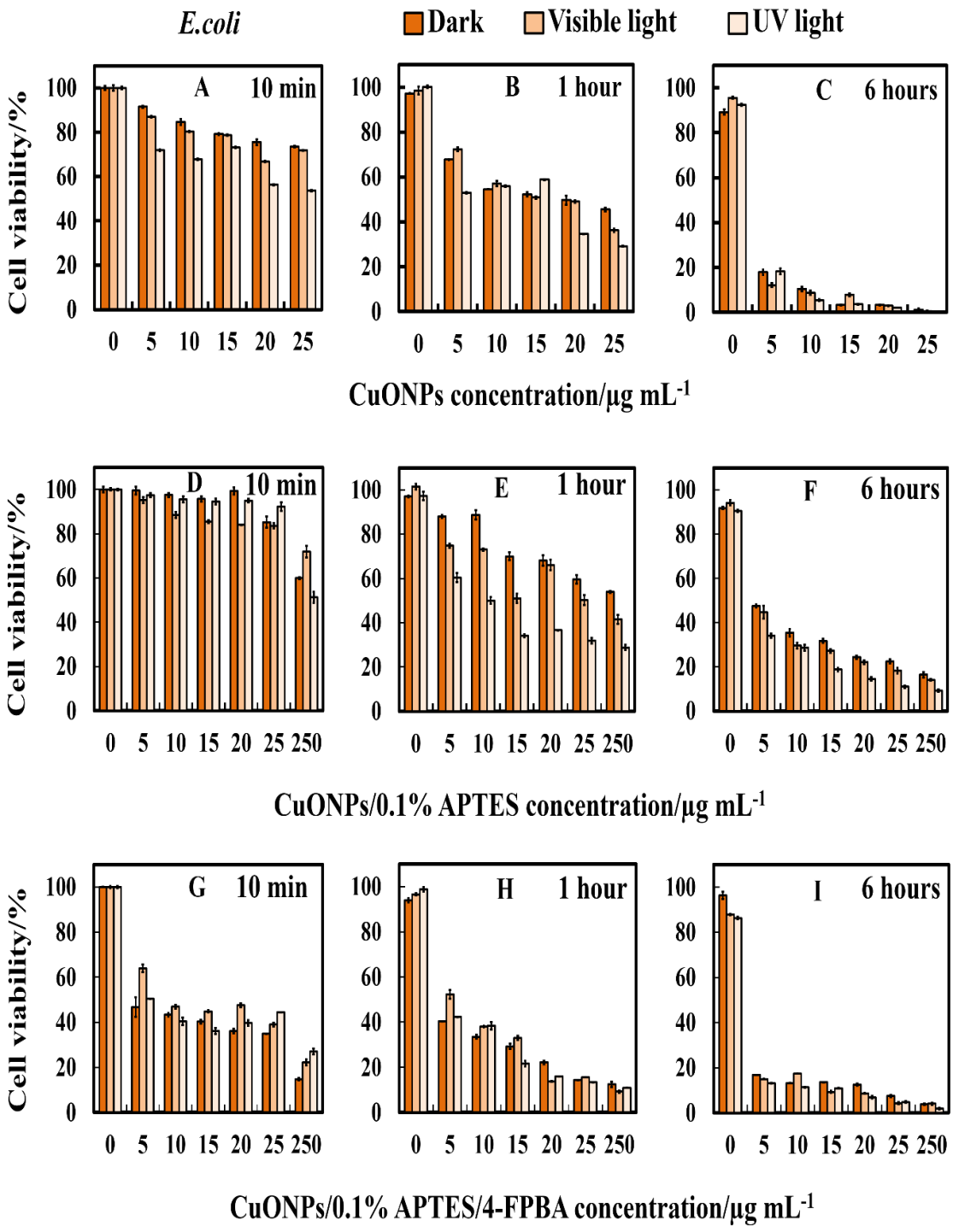


**Figure 8.8.** The impact of CuONPs functionalized with 0.1% APTES and 4-FPBA on the viability of *E.coli* at different particle concentrations (0, 5, 10, 15, 20,25 and 250 µg $mL^{-1}$). The bacteria was incubated with the CuONPs for at 10 min, 1 h and 6 h exposure times in dark, visible and in UV light conditions, respectively. The antibacterial activity on the *E.coli* cells was evaluated for: (A, B and C) bare CuONPs; (D, E and F) CuONPs/0.1%

APTES and (G, H and I) CuONPs/0.1% APTES/4-FPBA at different nanoparticle concentrations and exposure times.

It was likewise conducted similar assessments with *E.coli* and free 4-FPBA where the bacteria were removed from their culture media (see Figure 8.9). It should be observed in Figure 8.9 that there is no pronounced antibacterial activity of free 4-FPBA on the *E.coli* in dark conditions at the range of concentrations irrespectively of the time of exposure.

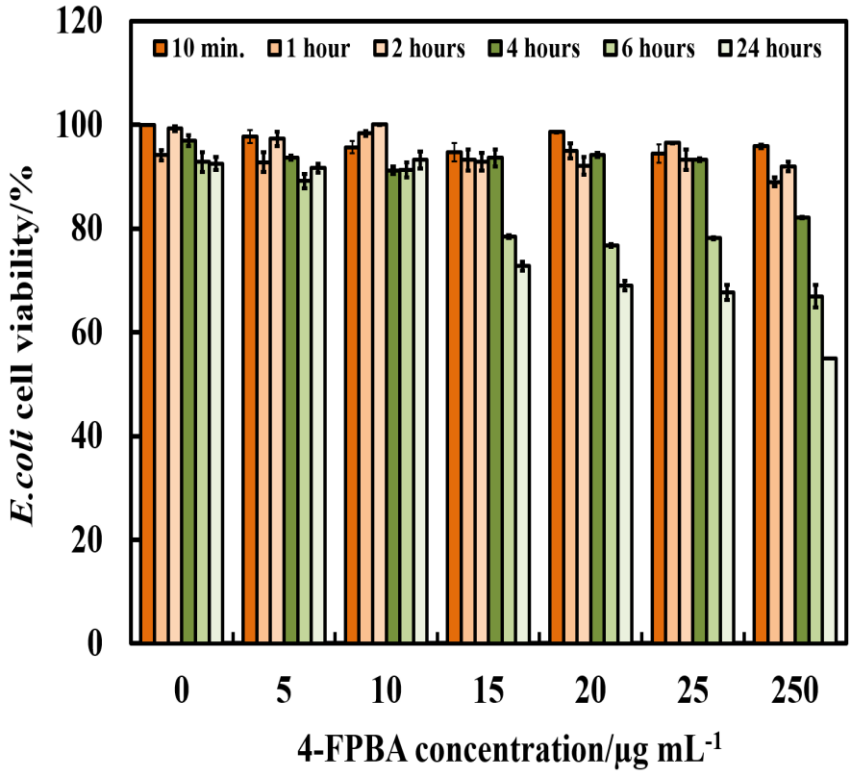


**Figure 8.9.** The antibacterial activity of free 4-FPBA on *E.coli* at various 4-FPBA concentrations (0, 5, 10, 15, 20, 25 and 250 µg $mL^{-1}$). The *E.coli* was incubated with the 4-FPBA at 10 min., 1 h, 2 h, 4 h, 6 h and 24 h of exposure times.

In order to study the build-up of CuONPs/APTES and CuONPs/APTES/4-FPBA on the *E.coli* cell surface we incubated them with the same range of free CuONPs followed by their removal from the nanoparticle suspension after a fixed time of exposure. The cell samples were sectioned and imaged with SEM as explained in chapter two. Figure 8.10 shows SEM images of *E.coli* with CuONPs/APTES (Figure 8.10A and 8.10C) and CuONPs/APTES/4-FPBA (Figure 8.10B and 8.10D) after incubation for up to 6 hours.

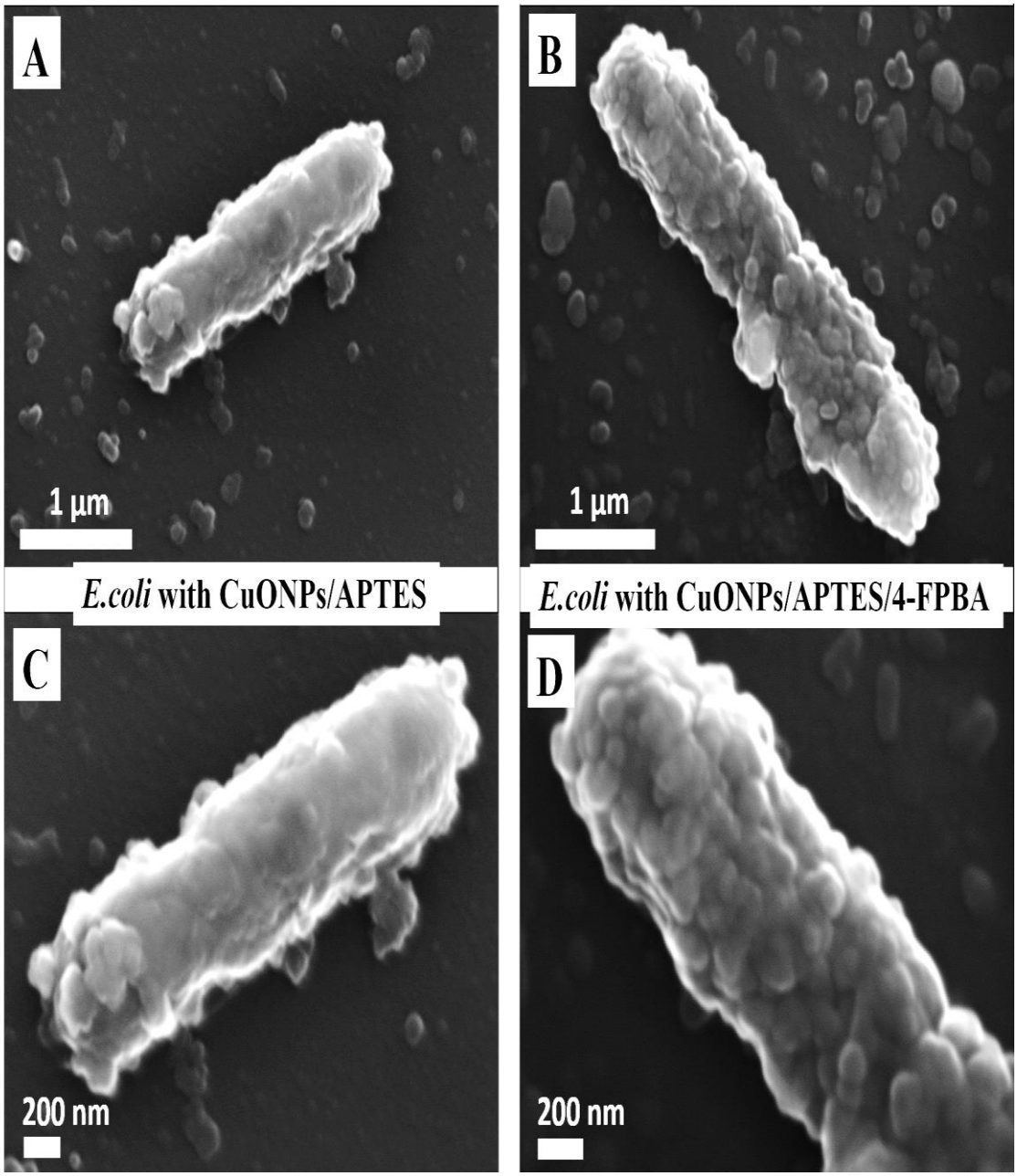


**Figure 8.10.** SEM images of *E.coli* after being exposed with CuONPs functionalized with APTES and 4-FPBA. *E.coli* incubated for 6 h with 25 µg $mL^{-1;}$ (A and C) CuONPs/0.1% APTES and (B and D) CuONPs/0.1% APTES/4-FPBA.

From Figure 8.10 it should be observed that there are very few CuONPs/APTES attached to the *E.coli* (Figures 8.10A and 8.10C) while we note a significant build-up of CuONPs/APTES/4-FPBA on the cell wall (Figure 8.10B and 8.10D). These results are consistent with the antibacterial activity pattern of the CuONPs functionalized with APTES and 4-FPBA on *E.coli* presented in Figure 8.8. The reason is attributed to the interaction between *E.coli* surface and the 4-FPBA-functionalized CuONPs because of

the reaction of CuONPs/APTES/4-FPBA with sugar on the cell surface by covalent interactions and kill cells.

## 8.4 Antibacterial activity of surface functionalized CuONPs against *E.coli*.

The antibacterial activity of CuONPs surface functionalized with GLYMO and 4-HPBA on *E.coli* at pH 6 was examined. Although the bare CuONPs are cationic below pH 9, their functionalization with GLYMO resulted in weakly negatively charged CuONPs/GLYMO. Further functionalization with 4-HPBA also yielded negatively charged CuONPs/GLYMO/4-HPBA. The *E.coli* cells were extracted from the growth media and re-dispersed in deionized water and aliquots of this *E. coli* cultures were incubated with fixed concentration of the nanoparticles (i) under UV light, (ii) under visible light and (iii) in dark conditions.

The *E.coli* culture was incubated with CuONPs at different particle concentrations (0, 5, 10, 15, 20 and 25 μg $mL^{-1}$) for various durations (10 minutes, 1 hour and 6 hours). The viability of *E.coli* after this treatment in dark, visible and UV light conditions is shown in Figure 8.11 at various incubation times. It was noticed that immediately after exposure (10 minutes), the fraction of viable *E.coli* declined in the presence of bare CuONPs and CuONPs/GLYMO/4-HPBA concentrations over 5 μg $mL^{-1}$. After 1 hour of such treatment in dark, visible light and UV light conditions, the viability of *E.coli* in the presence of nanoparticles was further reduced. After 6 hours incubation with 5-25 μg $mL^{-1}$ CuONPs/GLYMO/4-HPBA, all *E.coli* lost completely their viability. Figures 8.11A, 8.11B and 8.11C show that the CuONPs had excellent antibacterial activity towards *E. coli*. There are many various mechanisms discussed in the literature about how CuONPs kill *E.coli* and their antibacterial action might be a mixture of all of them. One mechanism is based on the photoactive nature of these nanoparticles which in the presence of oxygen from air and visible or UV light, form reactive oxygen species (ROS) which are free radicals and lead to peroxidation of lipids from the bacterial cell membrane. [5, 6, 8, 29]

The cell wall of *E.coli* is negatively charged while the un-functionalized (bare) CuONPs is positively charged (below pH 9). Therefore, the un-functionalized CuONPs were able to electrostatically adhere on the bacterial cell surface which led to damage of their cell membrane. When the free CuONPs attach to the cell, the ROS created locally can interact directly with the cell organelles which can amplify the cell damage. The ROS generation begins from a chain of free radical reactions inside the bacteria. Lipid peroxidation is a type of oxidative stress for the bacteria, which leads to its deactivation.

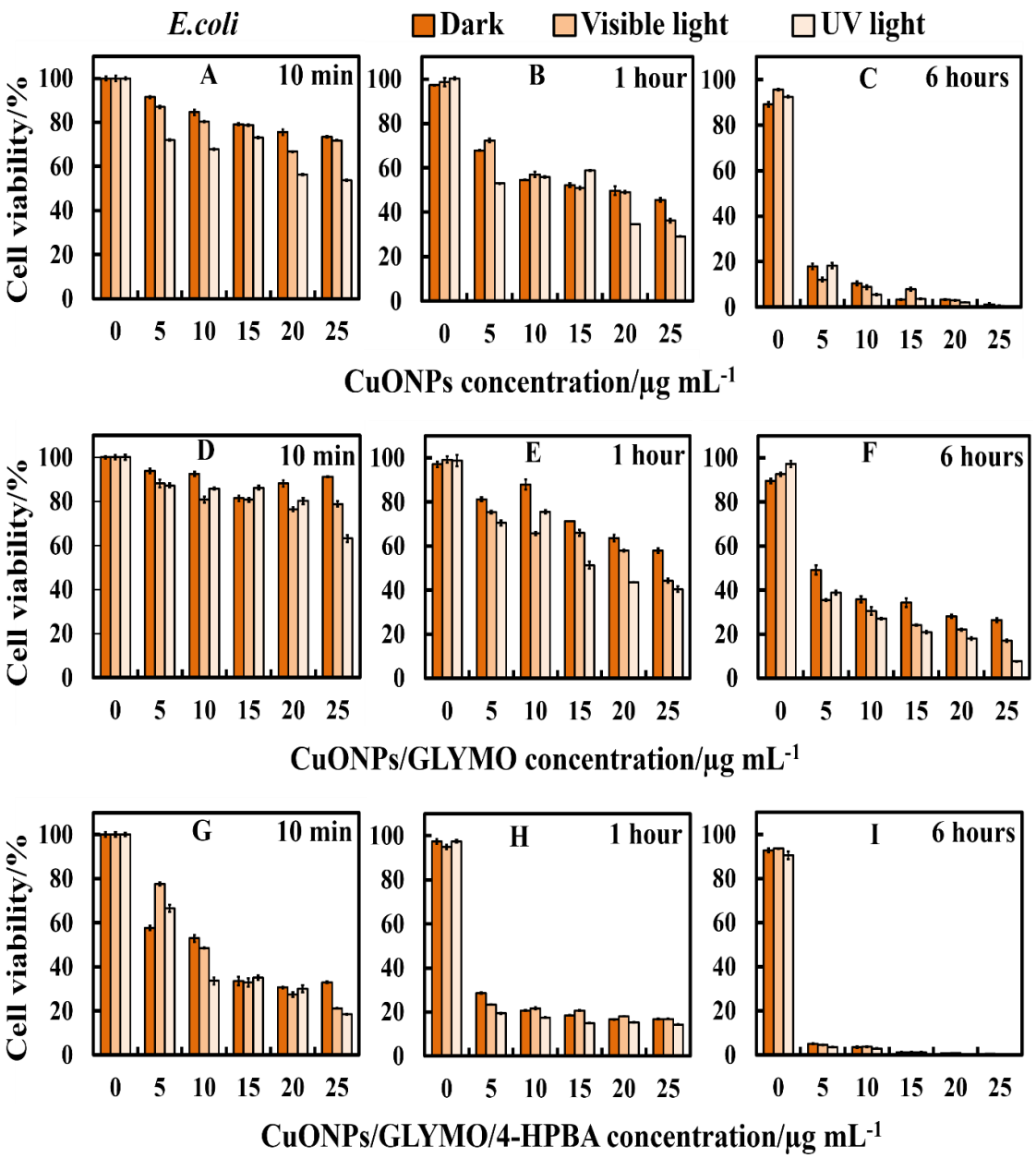


**Figure 8.11.** Comparison of the *E.coli* viability at various concentrations of the bare CuONPs (A - C), and surface functionalized of CuONPs with GLYMO (D - F) and 4-HPBA (G - I) in dark, visible and UV light conditions at different incubation times (shown).

However, Figure 8.11 shows that the antibacterial activity of 25 μg $mL^{-1}$ CuONPs towards *E.coli* under UV light for 1 hour is slightly higher than that under dark conditions. This suggests that the ROS generation under UV light has only a minor effect on the antibacterial action of CuONPs.

Another possible antimicrobial mechanism is the release of free $Cu^{2+}$ ions from the CuONPs which may interfere with the cell membrane proteins. However, the

concentration of free $Cu^{2+}$ ions in the aqueous solution around the CuONPs is negligible due to its very small solubility. The values of the CuO solubility varies with pH but in pure water it is approximately $3\times10^{-5}$ M.[30] This is not sufficient to explain the antimicrobial effect of CuONPs, which increases with their concentration, while the CuO solubility is constant at fixed pH and temperature. The working hypothesis is that the strong antimicrobial action can be explained by the direct attraction of the cationic CuONPs with the anionic bacterial cell walls. As CuONPs are aggregates of rough surface, a likely explanation is that their adhesion to the membrane causes its rupture and this is the main contributing factor to the cell death – see below.

It was also found that the antibacterial effect of CuONPs/GLYMO (Figure 8.11D, 8.11E and 8.11F) is lower than the one of the bare CuONPs and CuONPs/GLYMO/4-HPBA. Note that CuONP/GLYMO are anionic at this pH and therefore lack electrostatic adhesion to the bacterial cell walls. Nevertheless, the introduction of a secondary functionalization of these anionic nanoparticles by conjugation of 4-HPBA made the produced CuONPs/GLYMO/4-HPBA much more effective against *E.coli* than the bare CuONPs. The later effect can be seen in Figure 8.11G, 8.11H and 8.11I. It is interesting that at lower CuONPs/GLYMO/4-HPBA concentrations (5 μg $mL^{-1}$) these anionic particles are several times more effective than the bare CuONPs and CuONPs/GLYMO irrespectively of the time of exposure in dark, visible or UV light conditions. These results require some discussion with respect to the possible factors that may contribute to the antibacterial activity of the CuONPs/GLYMO/4-HPBA. It has been shown that ligands with BA-functionality can covalently bind with diol compounds, like nucleotides, glycate-protein and saccharide.[24, 25, 31] Note that despite their negative surface charge, the anionic nanoparticles CuONPs/GLYMO/4-HPBA are showing a very significant antibacterial effect on *E.coli* even at lower particle concentrations than the bare CuONPs due to their covalent binding to the bacterial membrane. *E. coli* is surrounded by an outer membrane containing lipopolysaccharides (LPSs) with many diol-groups.[31-34] The strong (covalent) interactions between the boronic acid terminal group of the CuONPs/GLYMO/4-HPBA particles and the diol-groups from the LPS layer leads to the particle build-up on their cell membranes. In contrast, the adhesion of the bare CuONPs to the bacterial cell membrane is largely driven by electrostatic interactions while the CuONPs/GLYMO/4-HPBA bind to the surface saccharides through formation of boronic ester (see Figure 8.1). There are many examples in the literature where this effect has been utilized for sensing sugars [29, 31, 35-38] but to our best knowledge this is the first time this idea is applied for antibacterial nanoparticle attachment to their targets.

The *E.coli* samples were sectioned and imaged with SEM and TEM as described in the methods section. Figure 8.12 and Figure 8.13 show TEM and SEM images of *E. coli* cells after incubation with CuONPs functionalized with GLYMO and 4-HPBA for up to 6 hours. The images clearly show the adherent layer of nanoparticles which bind to the bacteria. The result was also confirmed via EDX chart of *E.coli* with CuONPs which revealed the presence of Cu on the external part of the *E.coli* surface (Figure 8.4).

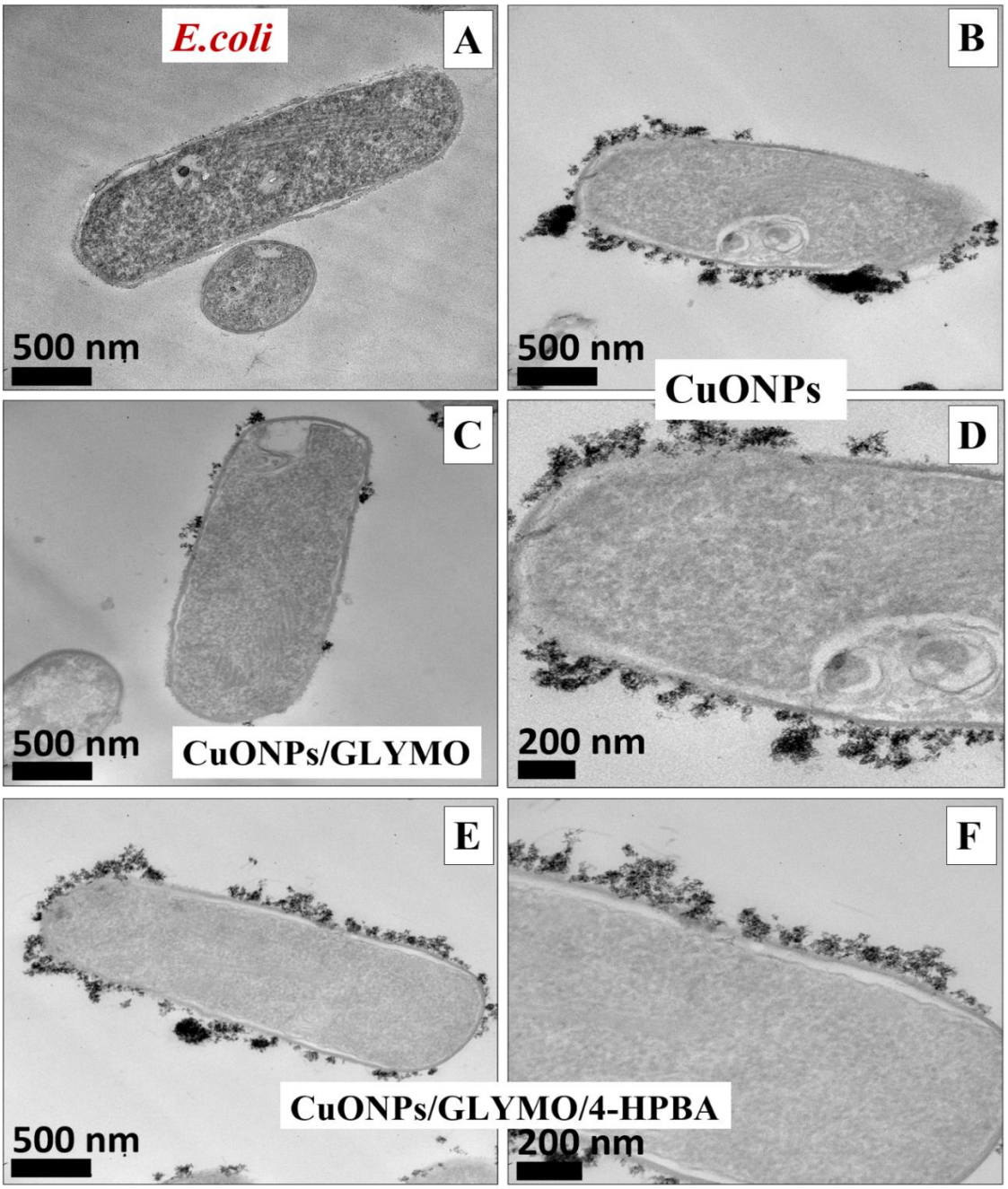


**Figure 8.12.** TEM images of *E.coli* at different magnifications: (A) before treatment, and (B, D) after treatment with 25 µg $mL^{-1}$ bare CuONPs, (C) 25 µg $mL^{-1}$ CuONPs/GLYMO and (E, F) 25 µg $mL^{-1}$ CuONPs/GLYMO/4-HPBA, all for 6 h.

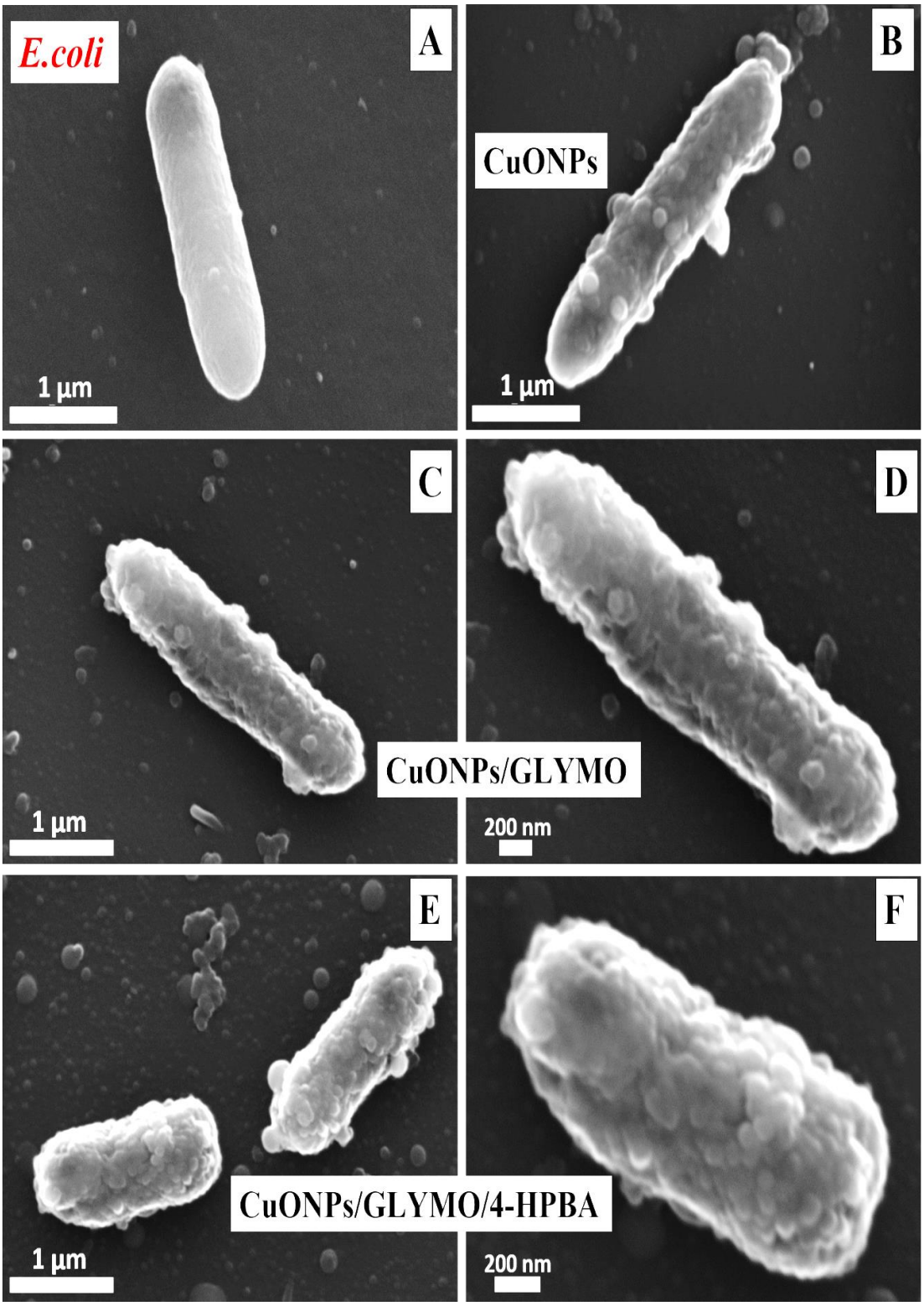


**Figure 8.13.** SEM images of *E.coli* after being incubated for 6 h with bare CuONPs and CuONPs functionalized with GLYMO or 4-HPBA: (A) *E.coli* before treatment, (B) *E.coli* incubated with 25 µg $mL^{-1}$ CuONPs, (C and D) *E.coli* incubated with 25 µg $mL^{-1}$ CuONPs/ GLYMO at different magnifications. (E and F) *E.coli* incubated with 25 µg $mL^{-1}$ CuONPs/GLYMO/4-HPBA at different magnifications. Note the extensive build-up of (B) CuONPs and (E, F) CuONPs/GLYMO/4-HPBA on the *E. coli* cell walls.

An additional confirmation for the mechanism of attachment of the CuONPs/GLYMO/4-HPBA to bacterial cells is presented in Figure 8.14, where we compared the zeta-potential of *E. coli* after being treated with bare CuONPs and CuONPs/GLYMO/4-HPBA of different particle concentrations. Note that when the bacterial cells are treated with bare CuONPs, which are cationic at neutral pH, the zeta potential of the bacteria is reduced by absolute value (Figure 8.14A) due to the partial deposition of the cationic CuONPs on the negatively charged bacterial cell wall. However, the incubation of the bacterial cells with CuONPs/GLYMO/4-HPBA does not incur measurable change in their zeta-potential despite their adsorption on the bacterial cell wall (Figure 8.14B). This is an additional confirmation that the attachment of the CuONPs/GLYMO/4-HPBA to the bacteria is not electrostatic and as Figures 8.12 and 8.13 indicate, the BA-functionalized CuONPs bind to the bacteria despite their negative surface charge. This result is easy to understand as the CuONPs/GLYMO/4-HPBA particles are anionic. SEM and TEM images confirm the particle deposition of the *E.coli* outer membrane.

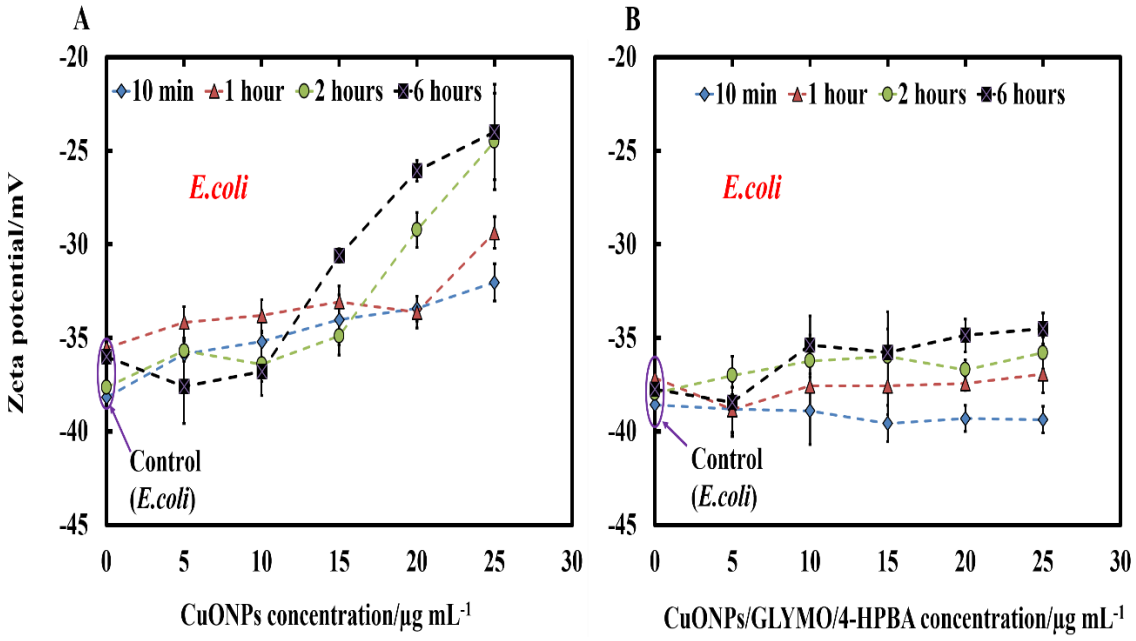


**Figure 8.14.** The zeta potential of *E. coli* in aqueous suspensions treated with various concentration of (A) bare CuONPs and (B) CuONPs/GLYMO/4-HPBA at various exposure times. Error bars indicate standard deviations of means.

The occasional build-up of more than one layer of CuONPs/GLYMO/4-HPBA particles on the bacteria can also be a result of partial particle aggregation before they bind to the bacterial cell wall. The zeta-potential of the CuONPs is low by magnitude and such partial

particle coagulation may take place at various stages of the sample preparation. However, the CuONPs/GLYMO/4-HPBA particles adhere to the negatively charged bacterial cell walls by covalent interactions despite their negative zeta potentials as they dominate the weaker electrostatic repulsion. We confirmed the result by performing EDX on sectioned *E. coli* and compared between bare CuONPs and 4-HPBA functionalized CuONPs which showed presence of Cu on the outer part of the cell membrane as CuONPs/GLYMO/4-HPBA much higher than the bare CuONPs ones as shown in Figure 8.15. Our results show higher Cu concentration on the bacteria outer cell wall for the functionalized CuONPs compared with the bare ones.

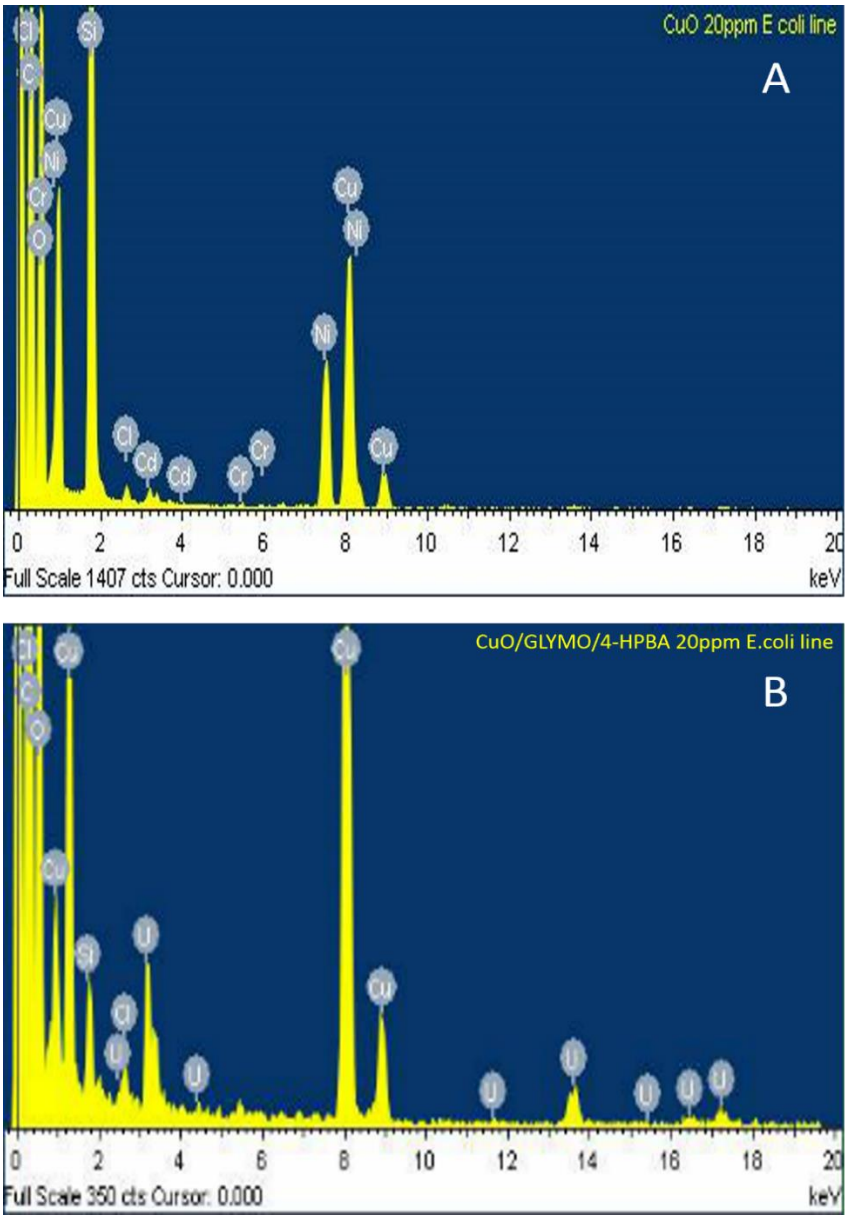


**Figure 8.15.** EDX diagram of *E.coli* outside membrane areas with (A) bare CuONPs and surface functionalized of CuONPs with GLYMO and (B) 4-HPBA at 20 µg $mL^{-1}$. The result shows the existence of CuONPs on the outer part of the cell membrane.

## 8.5 Anti-algal activity of APTES- and FPBA-grafted CuONPs.

The anti-algal activity of non-functionalized and 4-FPBA-functionalized CuONPs with *C. reinhardtii* was also examined by incubation of solutions of a different concentration of non-functionalized and 4-FPBA-functionalized CuONPs with a fixed amount of *C. reinhardtii* cells (see Figure 8.16). Figure 8.16G displays that at 10 minutes incubation time, the viability of the *C. reinhardtii* had severely reduced to 20% at 25 μg $mL^{-1}$. While the Figure 8.16A illustrations that there was no noticeable anti-algal activity for bare CuONPs concentrations at 10 minutes. Nevertheless, a good anti-algal activity was seen after 1 hour and 2 hours of incubation (Figure 8.16B and 8.16C). The comparison between the non-functionalized and the 4-FPBA-functionalized CuONPs upon incubation with *C. reinhardtii* cells can be seen in Figure 8.16G, H, I. 4-FPBA-functionalized CuONPs showed enhanced anti-algal activity in comparison with the same concentration of non-functionalized CuONPs and APTES functionalized CuONPs which appeared to have a low anti-algal activity of the cells were viable after 1 hour at 5 μg $mL^{-1}$ Figure 8.16 (B, E, H). This is described by the very good adhesion of the CuONPs/APTES/ 4-FPBA to the *C. reinhardtii* surface because of the fact that the boronic acid binds reversibly to diols to procedure a cyclic boronic ester in aqueous media. Especially, 4-FPBA functionalized CuONPs led to attach strongly (covalently) on the sugar (OH) groups on the *C. reinhardtii* surface, thus bringing the CuONPs in very close proximity to the membrane causing cell death.

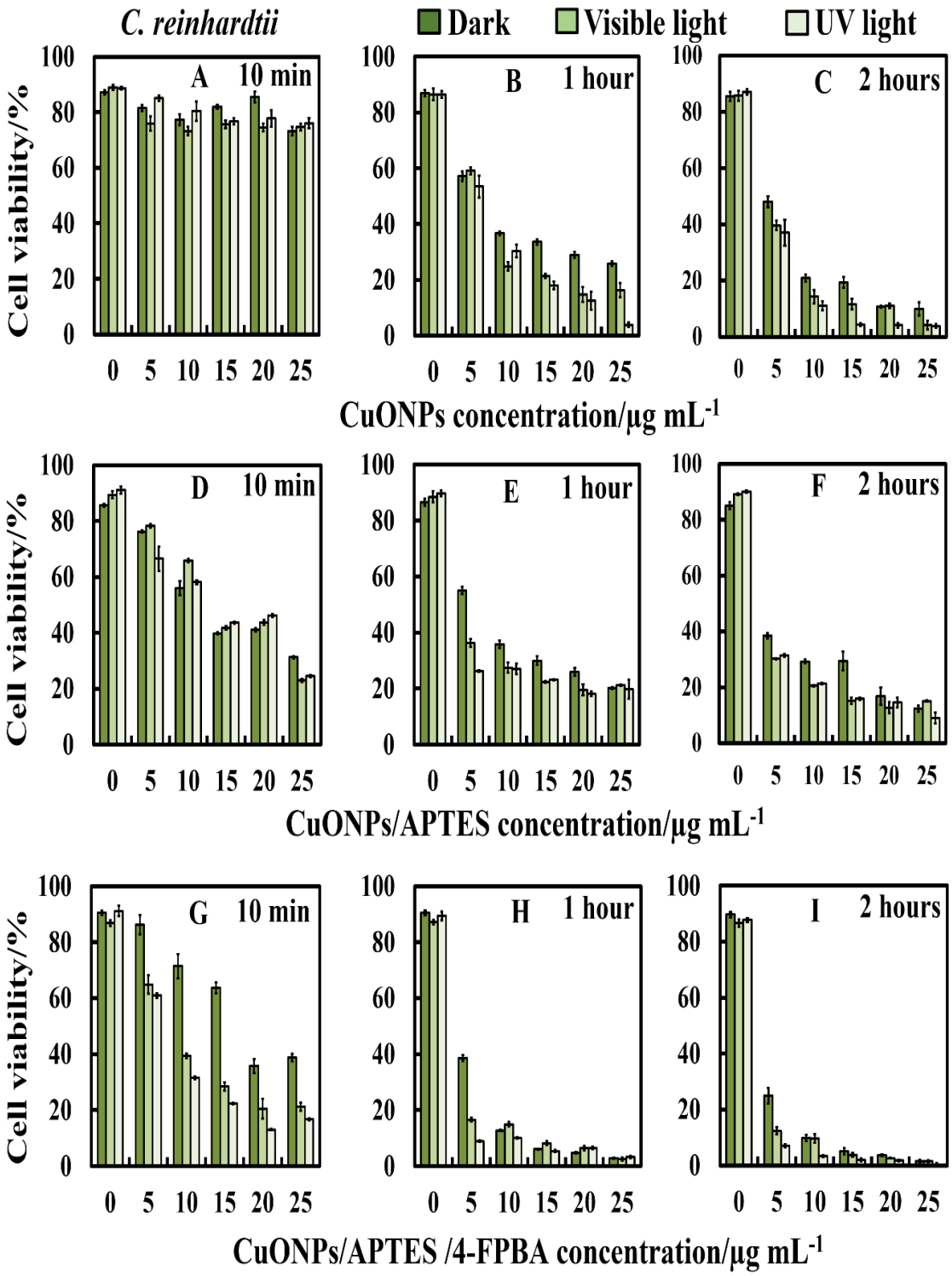


**Figure 8.16.** The comparison between the anti-algal activity of non-functionalized CuONPs, 0.1% APTES functionalized CuONPs and 4-FPBA functionalized 0.1% APTES and CuONPs on *C. reinhardtii* at various nanoparticle concentrations (0, 5, 10, 15, 20 and 25 µg $mL^{-1}$). The *C. reinhardtii* was incubated with the nanoparticles at 10 min, 1 h and 2 h of exposure times in dark conditions, under visible and UV light.

## 8.6 Anti-algal activity of GLYMO- and HPBA-grafted CuONPs.

The HPBA- grafted CuONPs with *C. reinhardtii* were tested after removing the cells from their culture media. Figure 8.17 compares the effect of bare CuONPs and surface-grafted CuONPs with GLYMO and 4-HPBA at different particle concentrations on the *C. reinhardtii* viability. During the first 10 min of exposure, the cells were not affected by both the bare CuONPs and CuONPs/GLYMO up to a concentration of 25 μg $mL^{-1}$ (see Figure 8.17A and 8.17D). However, the CuONPs/GLYMO/4-HPBA or CuONPs/GLYMO/4-TPBA nanoparticles showed a significant impact on the algal cell viability even at this short exposure time (Figure 8.17G and 8.17J). In this case, the algal cell viability decreased more than 5-fold upon exposure from 5 μg $mL^{-1}$ to 25 μg $mL^{-1}$ CuONPs/GLYMO/HPBA compared to the bare CuONPs. This can be attributed to several factors. First, *C. reinhardtii* cell walls consist of polysaccharides, glycoproteins, and cellulose, which provide multiple binding sites for the cationic CuONPs via nonspecific electrostatic interactions with the anionic surface of the cells. It is widely discussed in the literature that CuONPs appeared to create ROS under UV light due to their pronounced photocatalytic properties in aqueous solution.[5] Since the pore sizes in the plant cell walls are commonly in the range 5−20 nm,[39] the CuONPs (93 nm in diameter) adsorbed onto the algal surfaces-as confirmed by the TEM (Figure 8.18B and 8.18C) and SEM imaging (Figure 8.19B and 8.19D) are unlikely to permeate through the *C. reinhardtii* cell walls. Nevertheless, accumulation of nanoparticles could impact mechanically the *C. reinhardtii* cell membranes where CuONPs are clustered as a rough aggregate which could cause braking of the membrane and discharge of the *C. reinhardtii* cell content to the extracellular space as shown in the EDX analyses (Figure 8.20). Moreover, the accumulation of densely packed CuONPs on the *C. reinhardtii* cell membrane could also block nutrient uptake, thus altering the photosynthetic efficiency of algae as evidenced in the previous studies. [39] In extreme cases, this process can distort algal cell walls as implied by the severely wrinkled and deformed *C. reinhardtii* cell shown in TEM (Figure 8.18B and 8.18C) and SEM images (Figure 8.19B, 8.19D, 8.19E and 8.19F).

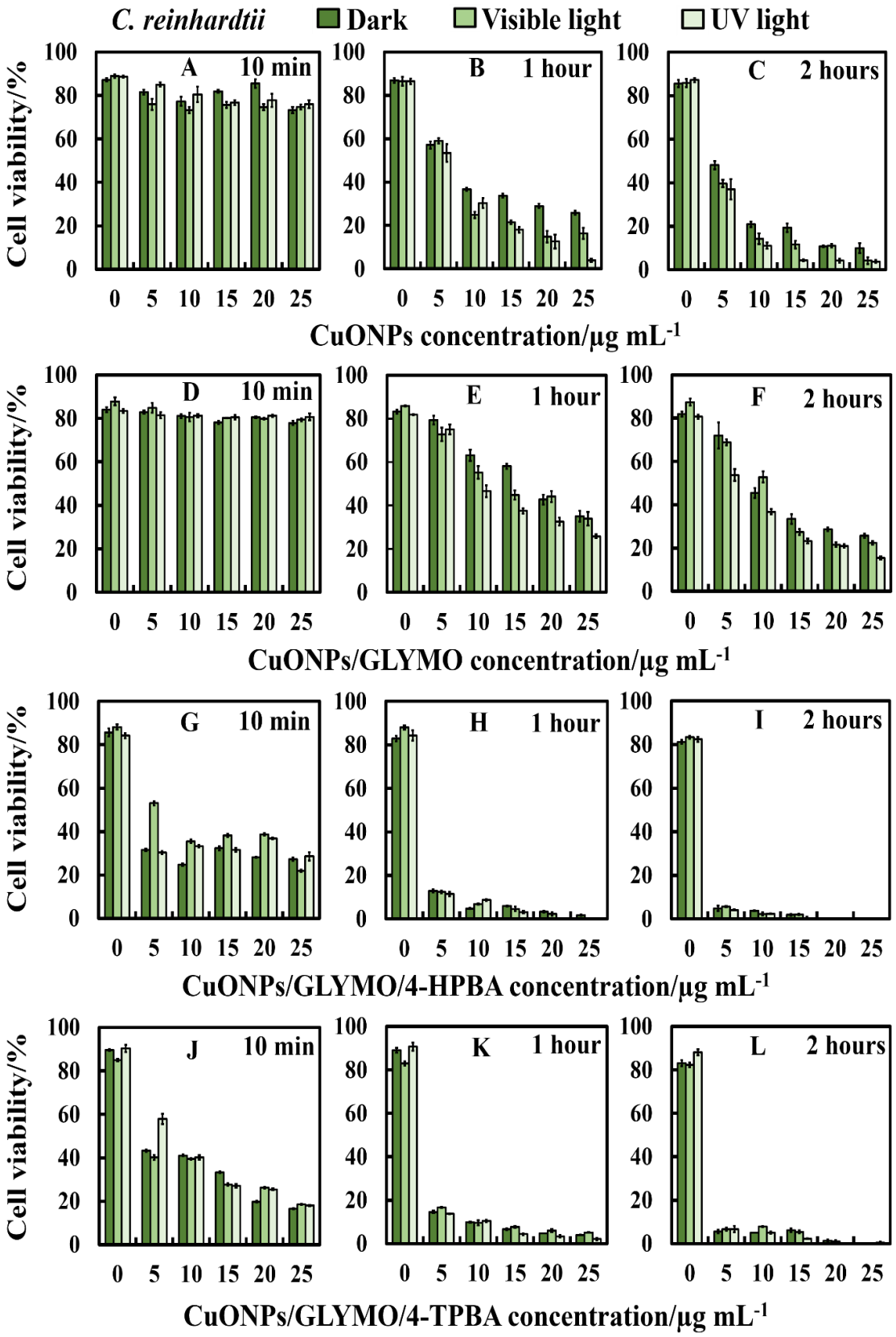


**Figure 8.17.** The antimicrobial activity of bare, GLYMO or 4-HPBA-GLYMO-, 4-TPBA-GLYMO-functionalized CuONPs at various concentrations (0, 5, 10, 15, 20 and 25 µg $mL^{-1}$) on *C. reinhardtii*. The *C. reinhardtii* was incubated with the nanoparticles at

10 min, 1 h and 2 h of exposure times in dark conditions, under visible and UV light. Statistical analysis of these data is enclosed in Table 1.

**Table 8.1.** Time-Kill assay statistical analysis on the data in Figure 8.17 between bare, GLYMO or 4-HPBA-GLYMO-functionalized CuONPs at various concentrations (0, 5, 10, 15, 20 and 25 μg $mL^{-1}$) on *C. reinhardtii* at 10 min, 1 hour and 2 hours of exposure times in dark conditions, under visible and UV light. Data were expressed as average values ± standard deviations of the mean. P-values of less than 0.05 were considered significant.

| Species | Multiple Comparison | P-value | Significance |
|---|---|---|---|
| ***C. reinhardtii*** | 10 min bare CuONPs vs 10 min 4-HPBA-GLYMO-functionalized CuONPs in dark | 0.000000039 | *** |
| | 1 hour bare CuONPs vs 1 hour 4-HPBA-GLYMO-functionalized CuONPs in dark | 0.000746407 | *** |
| | 2 hours bare CuONPs vs 2 hours 4-HPBA-GLYMO-functionalized CuONPs in dark | 0.022429609 | * |
| | 10 min bare CuONPs vs 10 min 4-HPBA-GLYMO-functionalized CuONPs under visible light | 0.000068264 | *** |
| | 1 hour bare CuONPs vs 1 hour 4-HPBA-GLYMO -functionalized CuONPs under visible light | 0.030751950 | * |
| | 2 hours bare CuONPs vs 2 hours 4-HPBA-GLYMO-functionalized CuONPs under visible light | 0.051276850 | * |
| | 10 min bare CuONPs vs 10 min 4-HPBA-GLYMO-functionalized CuONPs under UV light | 0.000000020 | *** |
| | 1 hour bare CuONPs vs 1 hour 4-HPBA-GLYMO -functionalized CuONPs under UV light | 0.065300820 | - |
| | 2 hours bare CuONPs vs 2 hours 4-HPBA-GLYMO-functionalized CuONPs under UV light | 0.133708000 | - |
| | 10 min GLYMO-functionalized CuONPs vs 10 min 4-HPBA-GLYMO-functionalized CuONPs in dark | 0.000000001 | *** |
| | 1 hour GLYMO-functionalized CuONPs vs 1 hour 4-HPBA-GLYMO-functionalized CuONPs in dark | 0.000251755 | *** |
| | 2 hours GLYMO-functionalized CuONPs vs 2 hours 4-HPBA-GLYMO-functionalized CuONPs in dark | 0.001793596 | ** |

| | | |
|---|---|---|
| 10 min GLYMO-functionalized CuONPs vs 10 min 4-HPBA-GLYMO-functionalized CuONPs under visible light | 0.000025410 | *** |
| 1 hour GLYMO-functionalized CuONPs vs 1 hour 4-HPBA-GLYMO-functionalized CuONPs under visible light | 0.000186613 | *** |
| 2 hours GLYMO-functionalized CuONPs vs 2 hours 4-HPBA-GLYMO-functionalized CuONPs under visible light | 0.004923197 | ** |
| 10 min GLYMO-functionalized CuONPs vs 10 min 4-HPBA-GLYMO-functionalized CuONPs under UV light | 0.000000005 | *** |
| 1 hour GLYMO-functionalized CuONPs vs 1 hour 4-HPBA-GLYMO-functionalized CuONPs under UV light | 0.002375242 | ** |
| 2 hours GLYMO-functionalized CuONPs vs 2 hours 4-HPBA-GLYMO-functionalized CuONPs under UV light | 0.003316280 | ** |
| 10 min bare CuONPs vs 10 min GLYMO-functionalized CuONPs in dark | 0.940036000 | - |
| 1 hour bare CuONPs vs 1 hour GLYMO-functionalized CuONPs in dark | 0.078833000 | - |
| 2 hours bare CuONPs vs 2 hours GLYMO-functionalized CuONPs in dark | 0.116148000 | - |
| 10 min bare CuONPs vs 10 min GLYMO-functionalized CuONPs under visible light | 0.105017000 | - |
| 1 hour bare CuONPs vs 1 hour GLYMO-functionalized CuONPs under visible light | 0.060348000 | - |
| 2 hours bare CuONPs vs 2 hours GLYMO-functionalized CuONPs under visible light | 0.081441000 | - |
| 10 min bare CuONPs vs 10 min GLYMO-functionalized CuONPs under UV light | 0.298251000 | - |
| 1 hour bare CuONPs vs 1 hour GLYMO-functionalized CuONPs under UV light | 0.140810000 | - |
| 2 hours bare CuONPs vs 2 hours GLYMO-functionalized CuONPs under UV light | 0.092962000 | - |

< 0.05 is considered significant. *P <0.05, **P <0.01, ***P <0.001

Various mechanisms have been discussed in the literature about how CuONPs kill algal cells and their antibacterial action might be a mixture of all of them. One mechanism is based on the photoactive nature of these nanoparticles which in the presence of oxygen from air and visible or UV light, form reactive oxygen species (ROS) which are free radicals and lead to peroxidation of lipids from the bacterial cell membrane.[5, 6, 8, 29] The cell wall of the microalgae is negatively charged while the non-functionalized (bare) CuONPs are positively charged (below pH 9). Therefore, the bare CuONPs were able to electrostatically adhere on the bacterial cell surface which led to damage of their cell membrane. When the bare CuONPs attach to the cell, the ROS created locally can interact directly with the cell membrane and organelles which can amplify the cell damage. The ROS generation can start a chain of free radical reactions inside the algae. Lipid membrane peroxidation is a type of oxidative stress for the algal cells, which leads to their loss of viability. On the other hand, Figure 8.17 shows that the anti-algal activity of 25 μg $mL^{-1}$ CuONPs under UV light for 1 hour is only slightly higher than that under dark conditions. This suggests that the ROS generation under UV light has only a little effect on the anti-algal action of CuONPs.

Another possible antimicrobial mechanism is the release of free $Cu^{2+}$ ions from the CuONPs which may interfere with the cell membrane proteins. However, the concentration of free $Cu^{2+}$ ions in the aqueous solution around the CuONPs is negligible due to its very low solubility at pH 5-6.

In order to investigate the effect of the presence of $Cu^{2+}$ ions emitted from the CuONPs in aqueous solution on the viability of the *C. reinhardtii* microalgae, we tested a range of $CuCl_2$ concentrations 0-100 μg $mL^{-1}$. One can see from the results presented in Figure 8.21 that the effect of the $Cu^{2+}$ ions on the microalgae viability is ~2 times smaller than the CuONPs/GLYMO/HPBA. The CuO solubility varies with pH but in deionized water at pH 6-6.5 it is approximately $2.5\text{-}3\times10^{-5}$ M.[30] Thus the presence of $Cu^{2+}$ is not sufficient to explain the anti-algal effect of CuONPs, which increases with their concentration, while the CuO solubility is constant at fixed pH and temperature. Our current understanding is that the strong anti-algal action can be explained by the attraction between the cationic bare CuONPs with the anionic algal cell membrane. As the CuONPs are nano-aggregates with a rough surface, a likely explanation of the strong anti-algal effect is that their adhesion to the cell membrane causes its rupture and this is the main contributing factor to the cell death.

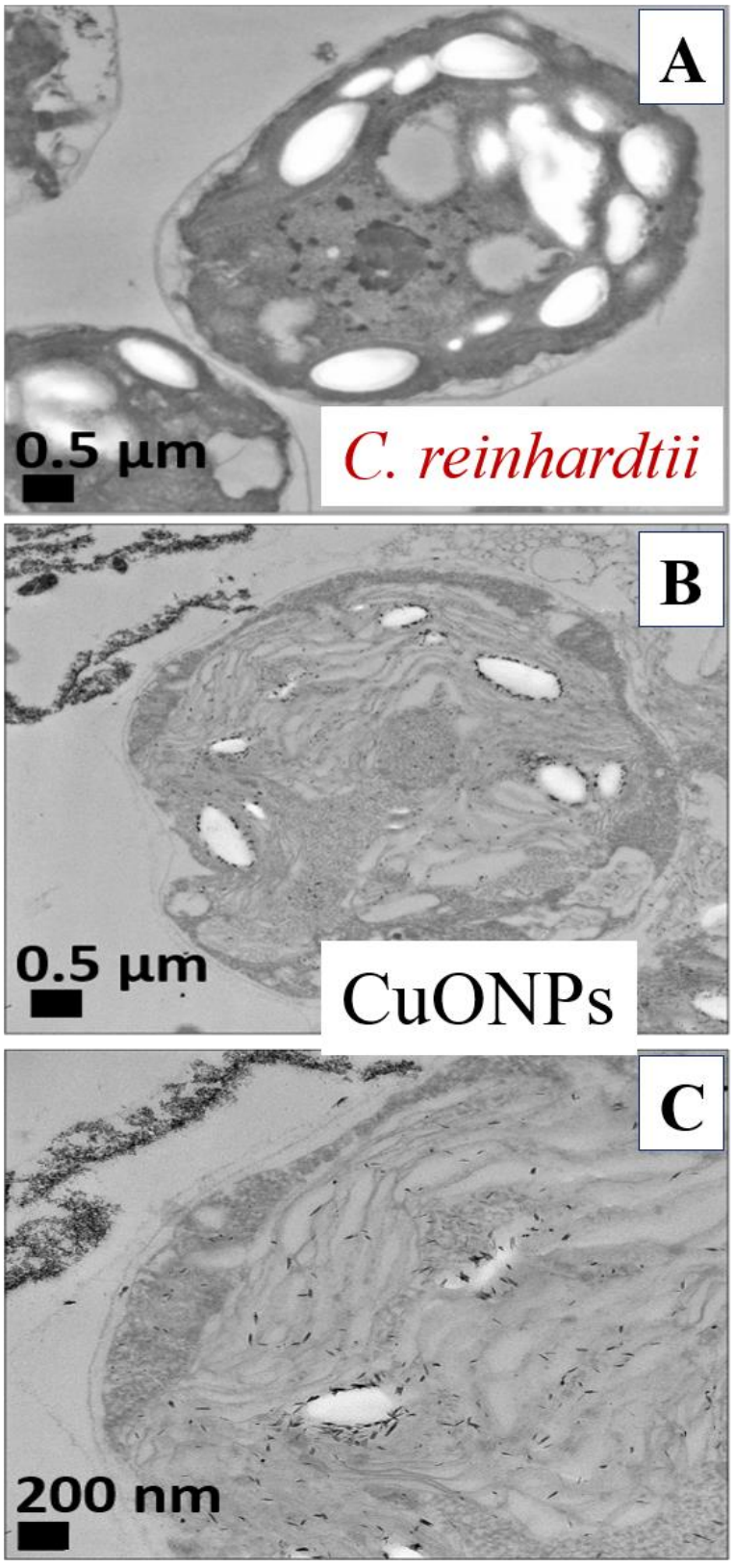


**Figure 8.18.** TEM images of *C. reinhardtii* after being exposed for 2 h to CuONPs: (A) control of *C. reinhardtii* before treatment with CuONPs (B and C) *C. reinhardtii* after treatment with 25 µg $mL^{-1}$ of CuONPs at different magnifications.

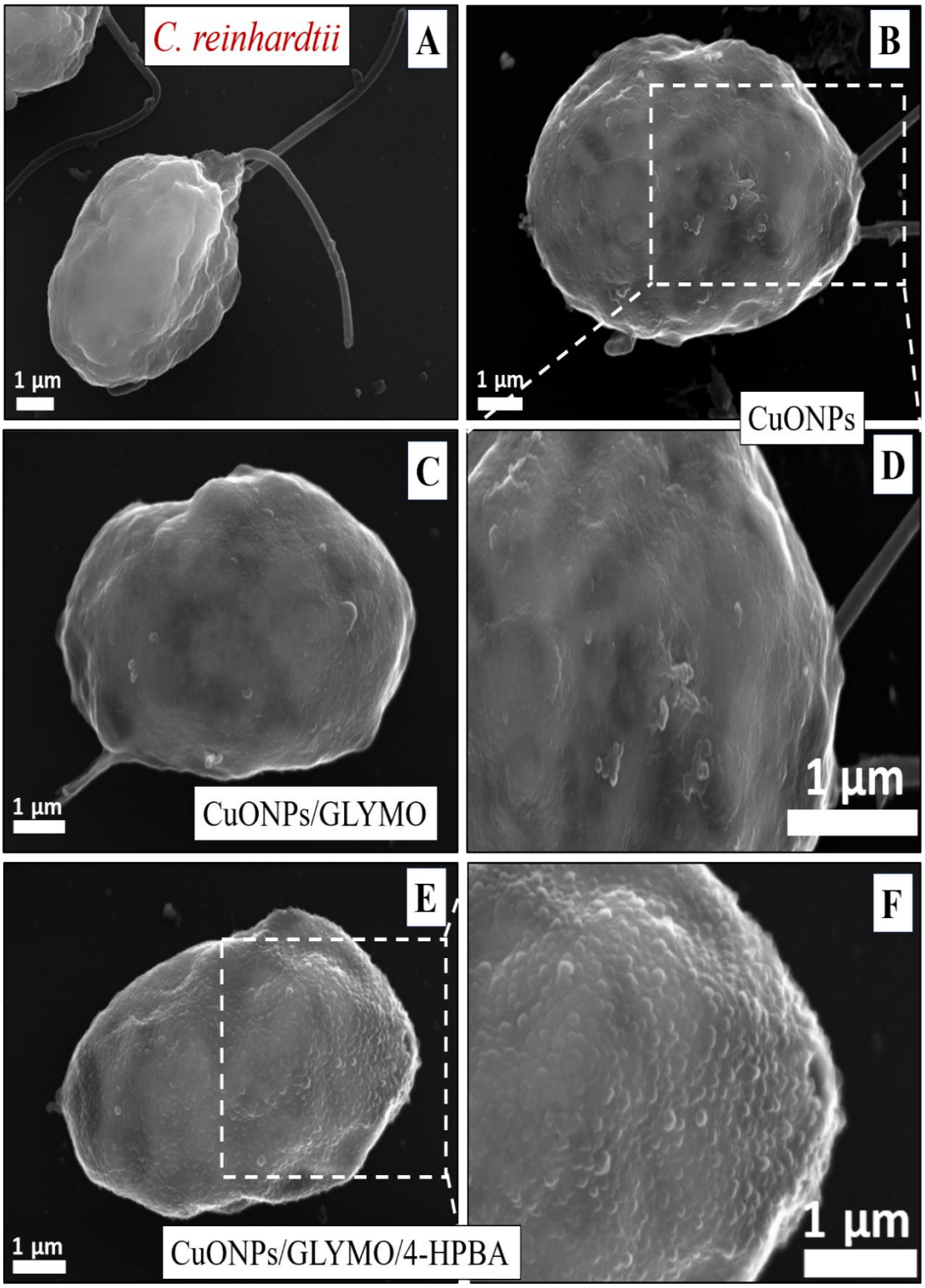


**Figure 8.19.** SEM images of *C. reinhardtii* after being exposed for 2 h to nanoparticles: (A) control of *C. reinhardtii* before treatment with CuONPs, (B and D) *C. reinhardtii* after treatment with 25 µg $mL^{-1}$ of CuONPs, (C) *C. reinhardtii* after treatment with 25 µg $mL^{-1}$ of CuONPs/GLYMO, (E and F) *C. reinhardtii* after treatment with 25 µg $mL^{-1}$ of CuONPs/GLYMO/4-HPBA.

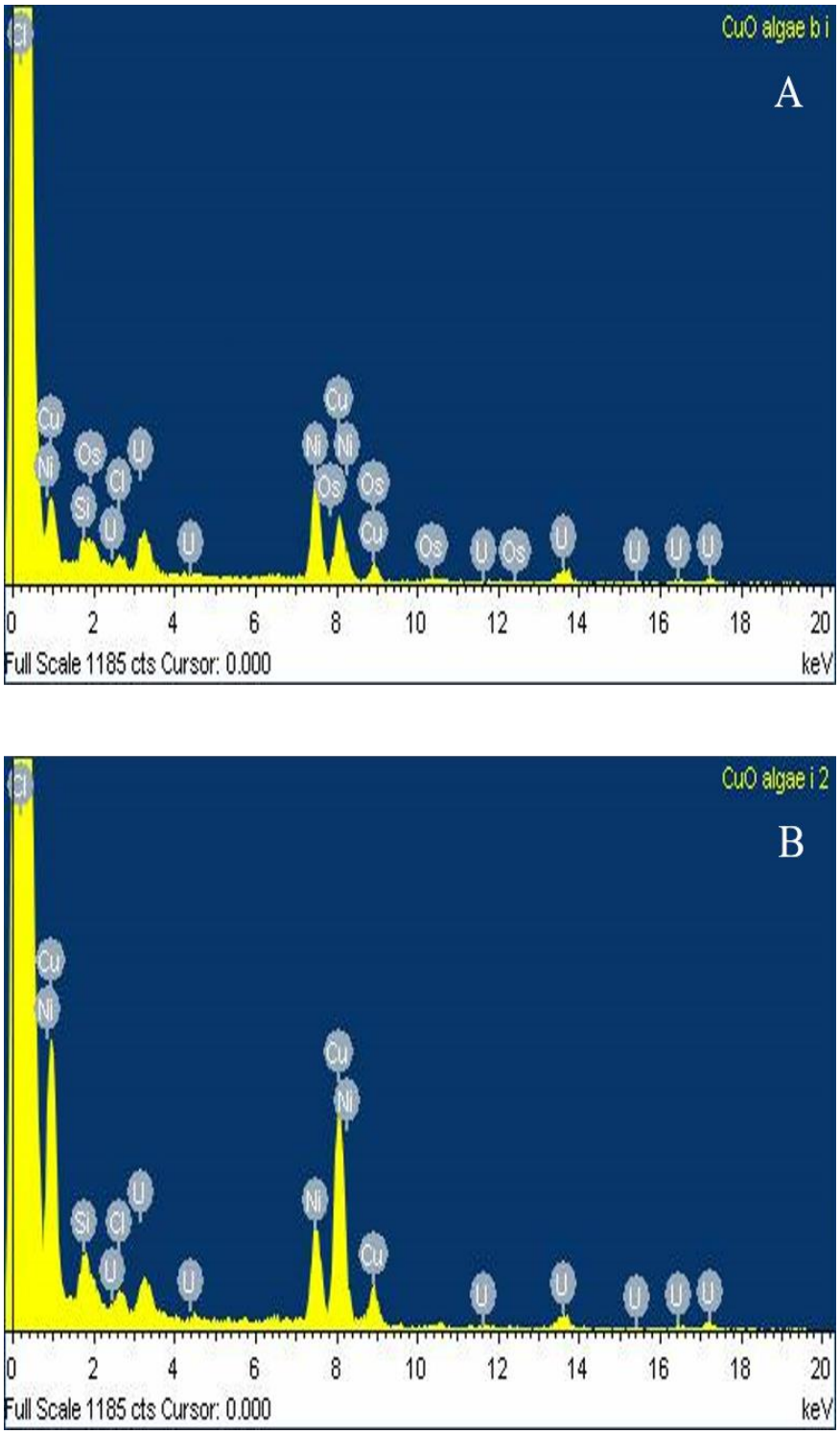


**Figure 8.20.** EDX diagram of *C. reinhardtii* cells treatment with CuONPs at 25 µg $mL^{-1}$: (A) *C. reinhardtii* inside membrane and (B) *C. reinhardtii* outside membrane areas. The result shows the existence of CuONPs on the inner and outer part of the cell membrane.

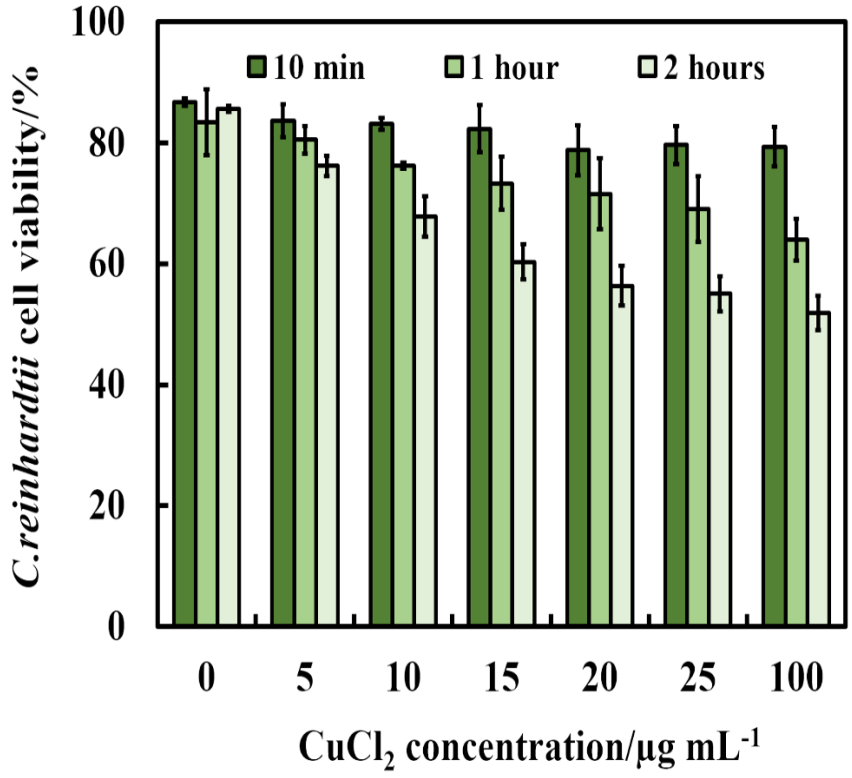


**Figure 8.21.** The *C. reinhardtii* cell viability after incubation with $CuCl_2$ as a function of $CuCl_2$ concentration for up to 2 h.

## 8.7 Anti-yeast activity of GLYMO- and HPBA-grafted CuONPs.

There are varying levels of anti-yeast activity for non-functionalized CuONPs and their functionalized versions, CuONPs/GLYMO, and CuONPs/GLYMO/4-HPBA or CuONPs/GLYMO/4-TPBA. To investigate this effect on *S. cerevisiae*, cells were incubated with bare CuONPs, GLYMO- and TPBA or HPBA-surface grafted CuONPs at varying concentrations (0 – 25 µg $mL^{-1}$). The results for the *S. cerevisiae* cell viability are presented in Figure 8.22A-8.22L and indicate lower viability upon increasing the CuONPs concentration. For this study, the *S. cerevisiae* presented a level of resistance to CuONPs/GLYMO, whereas both bare CuONPs and CuONPs/GLYMO/4-HPBA or CuONPs/GLYMO/4-TPBA showed a much higher activity when introduced to *S. cerevisiae*. In particular the CuONPs/GLYMO/4-HPBA and CuONPs/GLYMO/4-TPBA proved to be far more effective when the concentration was between 20 and 25 µg $mL^{-1}$ (Figure 8.22I and 8.22L).

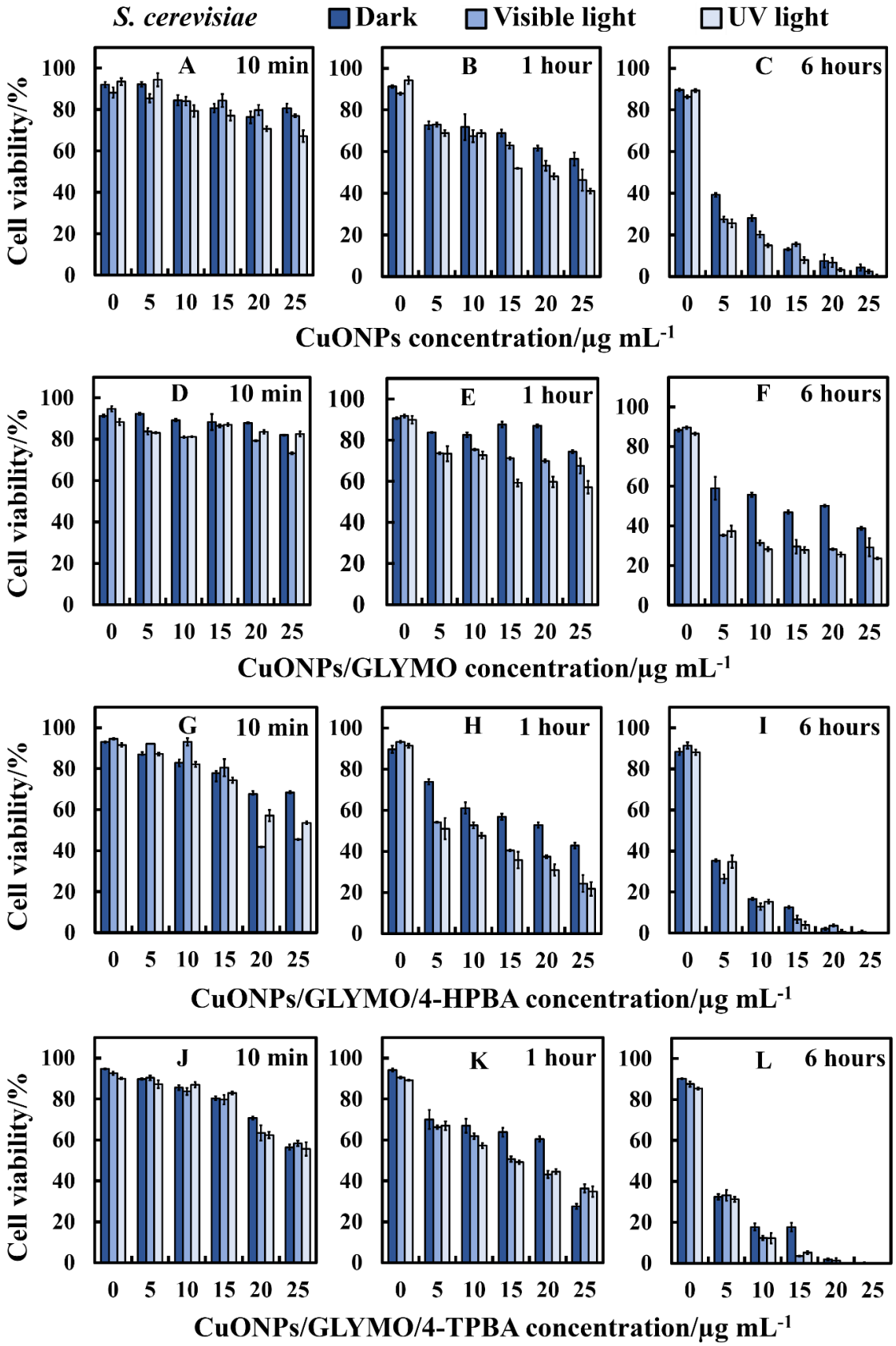


**Figure 8.22.** Representative cell viability of *S. cerevisiae* cells upon incubation of bare and HPBA-surface grafted CuONPs of different particle concentrations (0, 5, 10, 15, 20 and 25 µg $mL^{-1}$) in dark, visible and UV light conditions. The *S. cerevisiae* cells were incubated with: (A-C) bare CuONPs; (D-F) CuONPs/GLYMO, (G-I)

CuONPs/GLYMO/4-HPBA and (J-L) CuONPs/GLYMO/4-TPBA at 10 min, 1 h and 6 h exposure times. Data are means ± SD of three independent replicates.

Many different studies on cells have also demonstrated that copper exposure rapidly prompts membrane alterations before DNA degradation.[40, 41] All these investigations concluded that the antimicrobial effect of copper was related to its ability to discharge copper ions and their damaging impact on the cell membrane. Other mechanisms for the antimicrobial effect of CuONPs have also been discussed which involve adhesion of CuONPs to cells by electrostatic interactions, similar to that in the algal studies. CuONPs/GLYMO/4-HPBA can form reversible boronic ester interactions with cis-diol-containing carbohydrate and glycoproteins molecules which are abundant on the yeast cell wall.[42]

Figure 8.23 shows the TEM and SEM image of *S. cerevisiae* cells incubated with bare CuONPs as well as ones surface-grafted with GLYMO and 4-HPBA. Sectioned samples of the *S. cerevisiae* exposed to CuONPs were analysed with EDX (Figure 8.25) and revealed that CuONPs accumulate predominantly on the outer side of the cell membrane. TEM images (Figure 8.23G and Figure 8.24) and SEM images (Figure 8.23H) demonstrated an extracellular accumulation of CuONPs/GLYMO/4-HPBA which leads to cell death due to membrane damage. There are many studies suggesting that 'contact killing' is started by the dissolved $Cu^{2+}$ ions discharged from the copper surfaces by the culture medium and causing cell damage by interacting with enzymes and DNA.[43, 44] However, as discussed earlier, the concentration of $Cu^{2+}$ supported by CuONPs is apparently too low to produce this effect. Comparison of the anti-yeast activity of CuONPs/GLYMO and of CuONPs/GLYMO/HPBA indicate that the difference can be attributed to their cell binding ability rather than the $Cu^{2+}$ ions, as they both emit the same concentration of $Cu^{2+}$, determined by CuO solubility product.

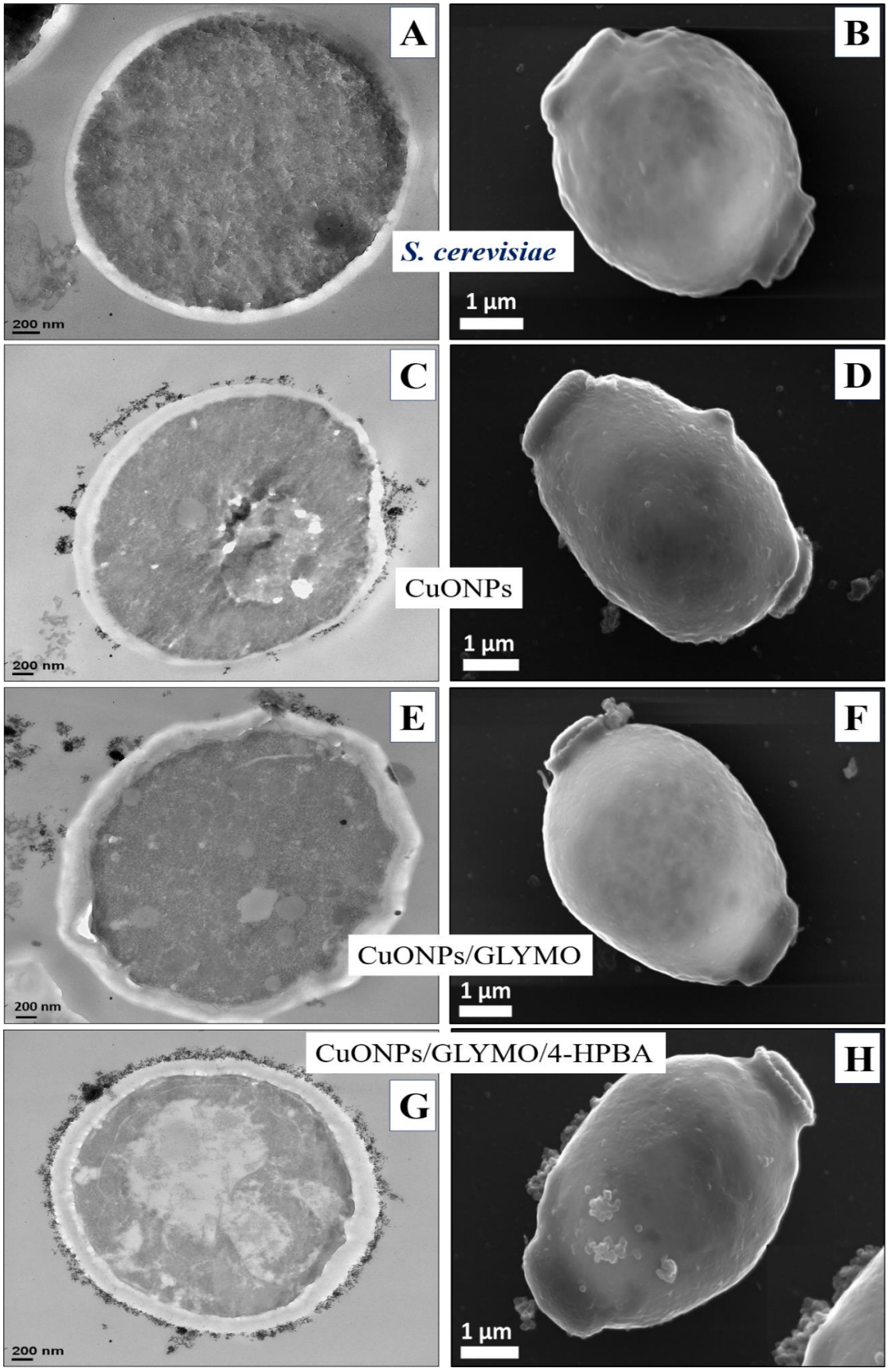


**Figure 8.23.** TEM and SEM image of *S. cerevisiae* cells with (A) and (B) being the control sample of untreated *S. cerevisiae*, (C) and (D) samples of *S. cerevisiae* after incubation in a suspension of 25 µg $mL^{-1}$ CuONPs for 6 h, (E) and (F) after incubation

with 25 µg $mL^{-1}$ CuONPs/ GLYMO and (G) and (H) after incubation with 25 µg $mL^{-1}$ CuONPs/ GLYMO/4-HPBA.

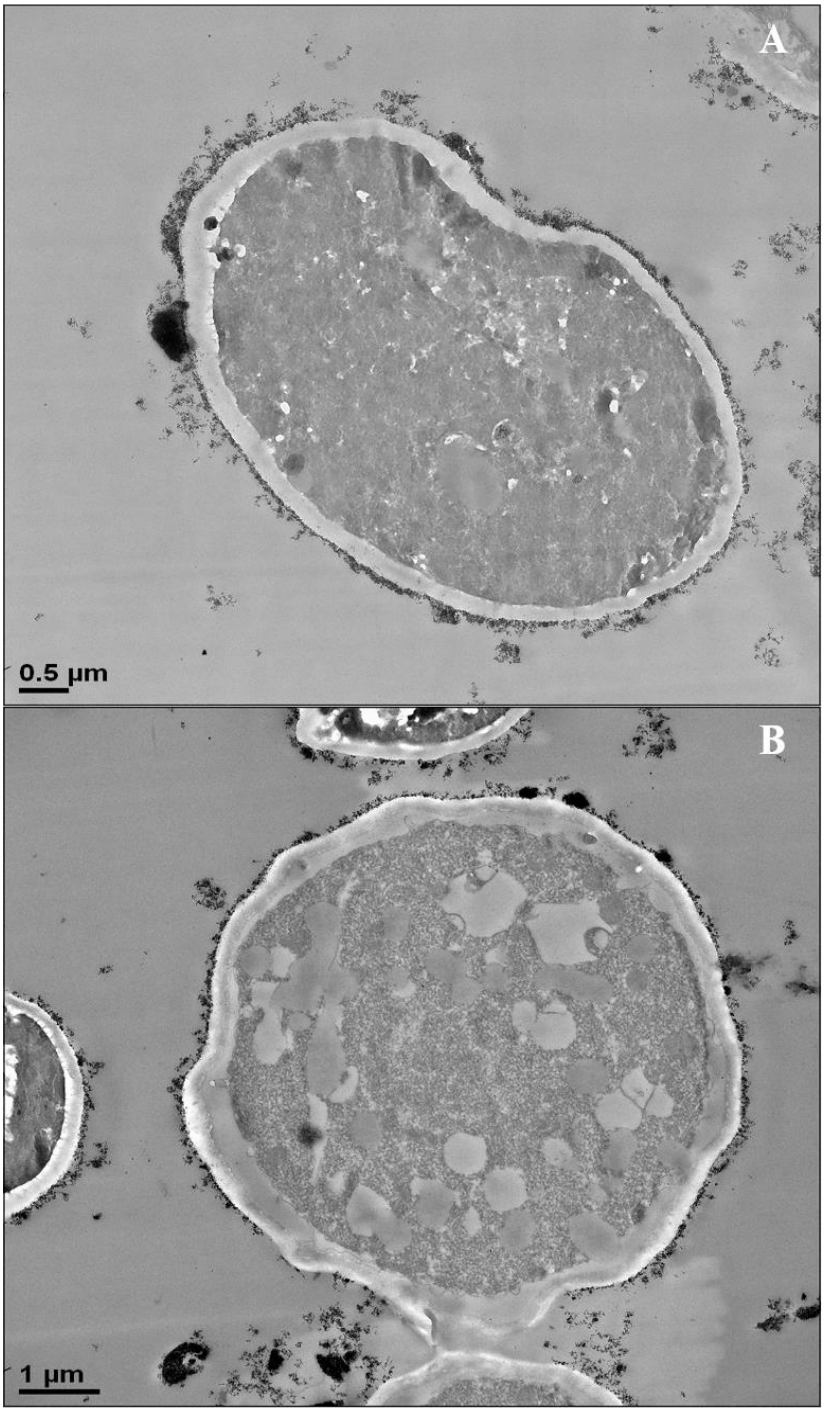


**Figure 8.24.** TEM images of *S. cerevisiae* after being incubated for 6 h with CuONPs functionalized with GLYMO and 4-TPBA at 25 µg $mL^{-1}$ at different magnifications.

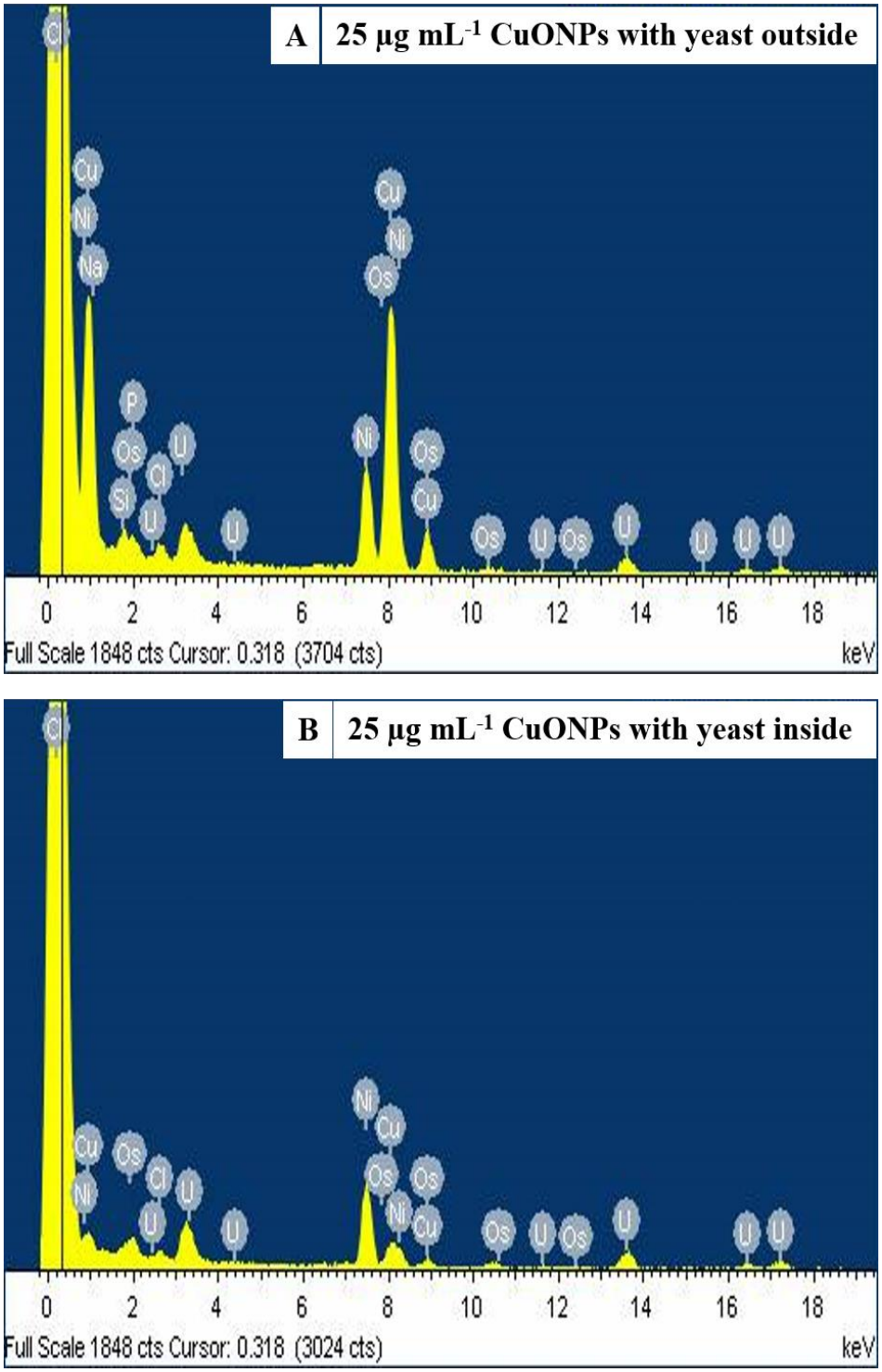


**Figure 8.25.** EDX diagram of *S. cerevisiae* cells with CuONPs at 25 µg $mL^{-1}$: (A) *S. cerevisiae* outside membrane and (B) *S. cerevisiae* inside membrane areas. The result shows the existence of CuONPs on the inner and outer part of the cell membrane.

Figures 8.26A, 8.26B, 8.27A and 8.27B show the zeta potential of algae and yeast cells after being treated with bare CuONPs and CuONPs/GLYMO/4-HPBA at different particle concentrations. The zeta potential of both types of cells treated with bare CuONPs, which are cationic at neutral pH, is reduced by absolute value (Figure 8.26A and 8.27A) due to the partial deposition of the cationic CuONPs on the negatively charged cells wall. However, the incubation of both types of cells with CuONPs/GLYMO/4-HPBA does not incur measurable change in their zeta-potential despite their adsorption on the cells wall (Figure 8.26B and 8.27B). This is an additional confirmation that the attachment of the CuONPs/GLYMO/4-HPBA to both algae and yeast cells is not based on electrostatic attraction and the HPBA grafted CuONPs bind to the cells despite their negative surface charge. Apparently, the negatively charged GLYMO-grafted CuONPs do not bind the cells although their surface charge is very similar to that of the CuONPs/GLYMO/4-HPBA. This indicates that the covalent binding is the main reason for the build-up of CuONPs/GLYMO/4-HPBA on the cells surface, as confirmed by the TEM and SEM images in Figures 8.18, 8.19 and 8.23.

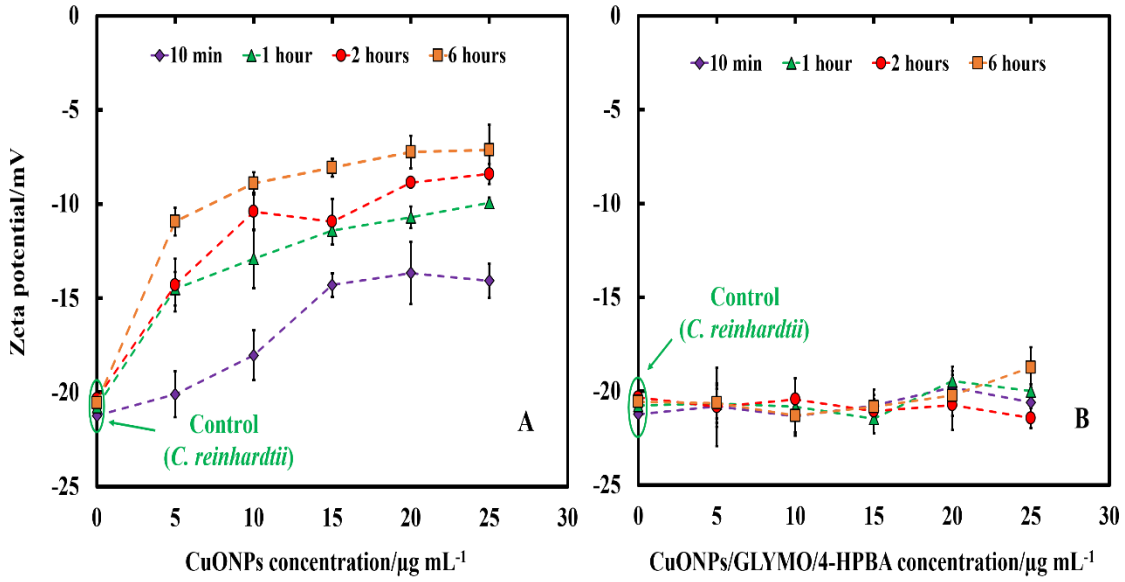


**Figure 8.26.** The zeta potential of *C. reinhardtii* suspensions treated with of various concentration of (A) bare CuONPs and (B) CuONPs/GLYMO/4-HPBA at various exposure times. Error bars indicate standard deviations of means.

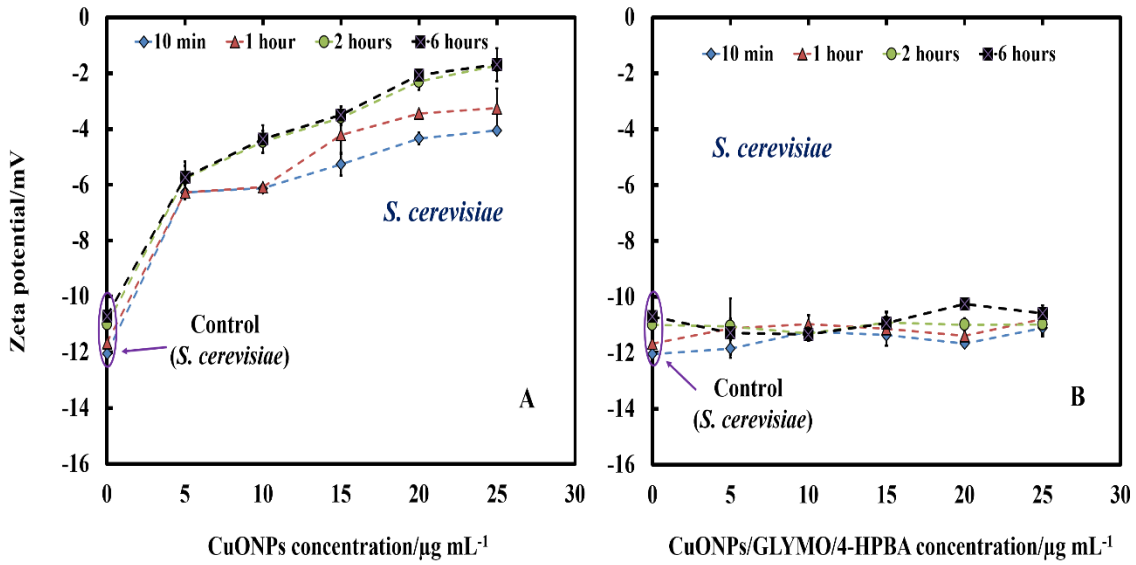


**Figure 8.27.** The zeta potential of *S. cerevisiae* in aqueous suspensions treated with various concentration of (A) bare CuONPs and (B) CuONPs/GLYMO/4-HPBA at various exposure times. Error bars indicate standard deviations of means.

## 8.7 Anti-algal and anti-fungal activity of HPBA-grafted CuONPs in the presence of glucose.

The anti-algal and antifungal activity of GLYMO- and HPBA-grafted CuONPs were studied towards *C. reinhardtii* and *S. cerevisiae* in the presence of different concentrations of glucose at 25 µg $mL^{-1}$ nanoparticle concentration (Figure 8.28). Glucose was added to the cell suspension before particle addition to the cells. It was discovered that the cells apparently lose their viability in the presence of bare CuONPs after 6 hours not only upon exposure to lower concentrations of glucose, but also upon incubation with higher concentrations of glucose. It was also found that the cell viability in the presence of CuONPs/GLYMO/4-HPBA nanoparticles increases with an increase of the glucose concentration. A possible mechanism for this could be that the hydroxyl groups of the 4-Hydroxyphenylboronic acid on the surface of CuONPs/GLYMO/4-HPBA nanoparticles interact with the glucose, thus reducing the interaction between 4-HPBA-groups and the carbohydrates on the algal and yeast cell membranes.

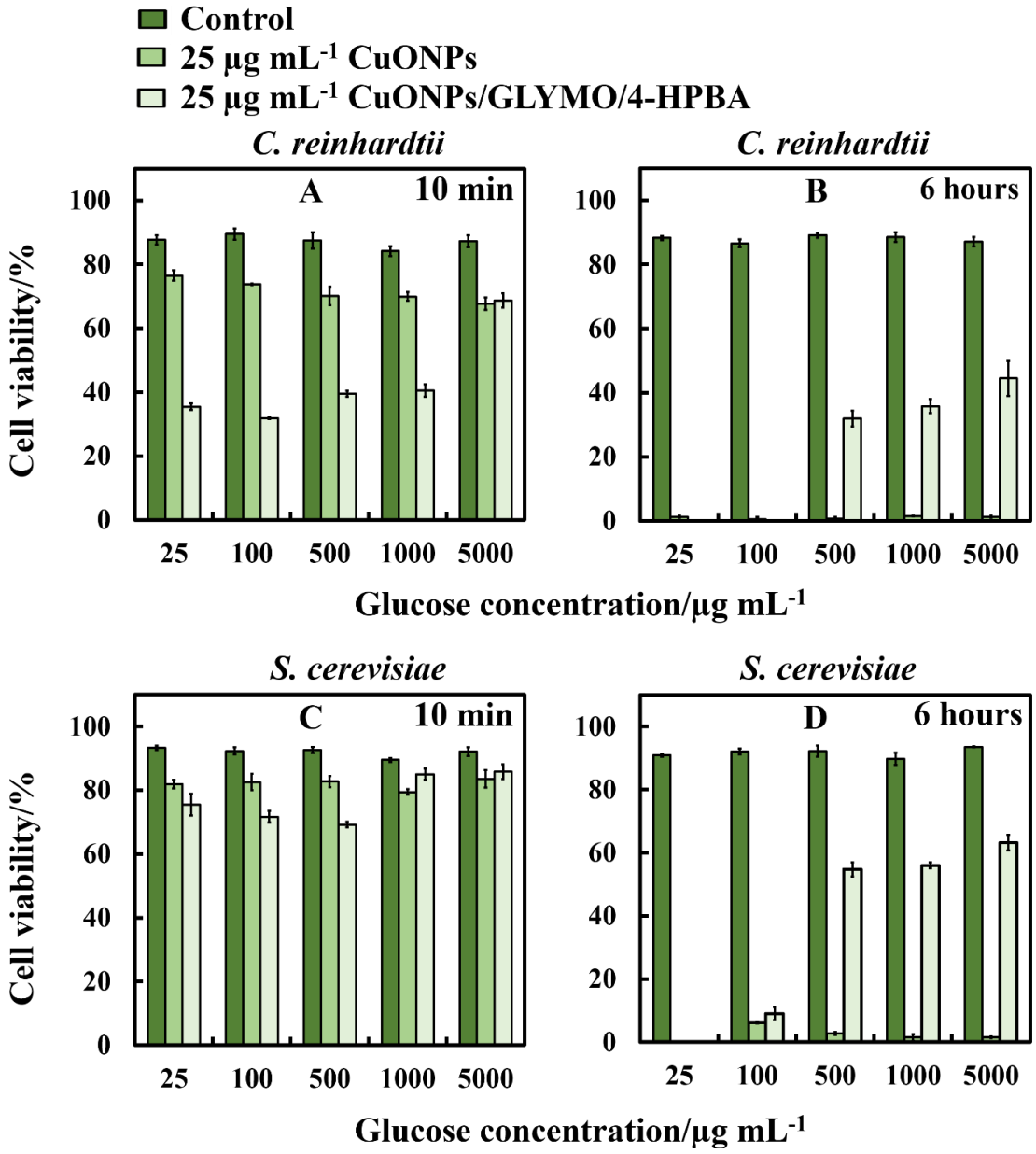


**Figure 8.28.** The cell viability after incubation as a function of nanoparticle concentration for 6 h at various glucose concentrations. (A and B) *C. reinhardtii* and (C and D) *S. cerevisiae* cells.

## 8.8 Anti-algal and anti-yeast activity of free GLYMO and 4-HPBA.

Figure 8.29 and Figure 8.30 shows the cytotoxicity assay of the free GLYMO and 4-HPBA on *C. reinhardtii* and *S. cerevisiae* for up to 2 hours for *C. reinhardtii* and 6 hours for *S. cerevisiae* of exposure. Both runs were done at the varying overall GLYMO and 4-HPBA concentration and different incubation times. One can see a very small effect on the presence of free GLYMO on the *C. reinhardtii* viability over a period of up to 2 hours (Figure 8.29A). One can conclude that the free GLYMO and 4-HPBA does not measurably impact the cell viability up to 25 µg $mL^{-1}$. Note that in our

CuONPs/GLYMO/HPBA nanoparticles there is not any free HPBA and free GLYMO as the particles have undergone multiple washing/centrifugation cycles after their surface functionalization. However, at these concentrations of the HPBA- grafted on CuONPs, the effect of the CuONPs on *C. reinhardtii* and *S. cerevisiae* is very significant – see Figure 8.17 and Figure 8.22, respectively. Therefore, one may conclude that the HPBA-grafted CuONPs shows excellent anti-algal and anti-yeast activity which is not related to the presence of free HPBA.

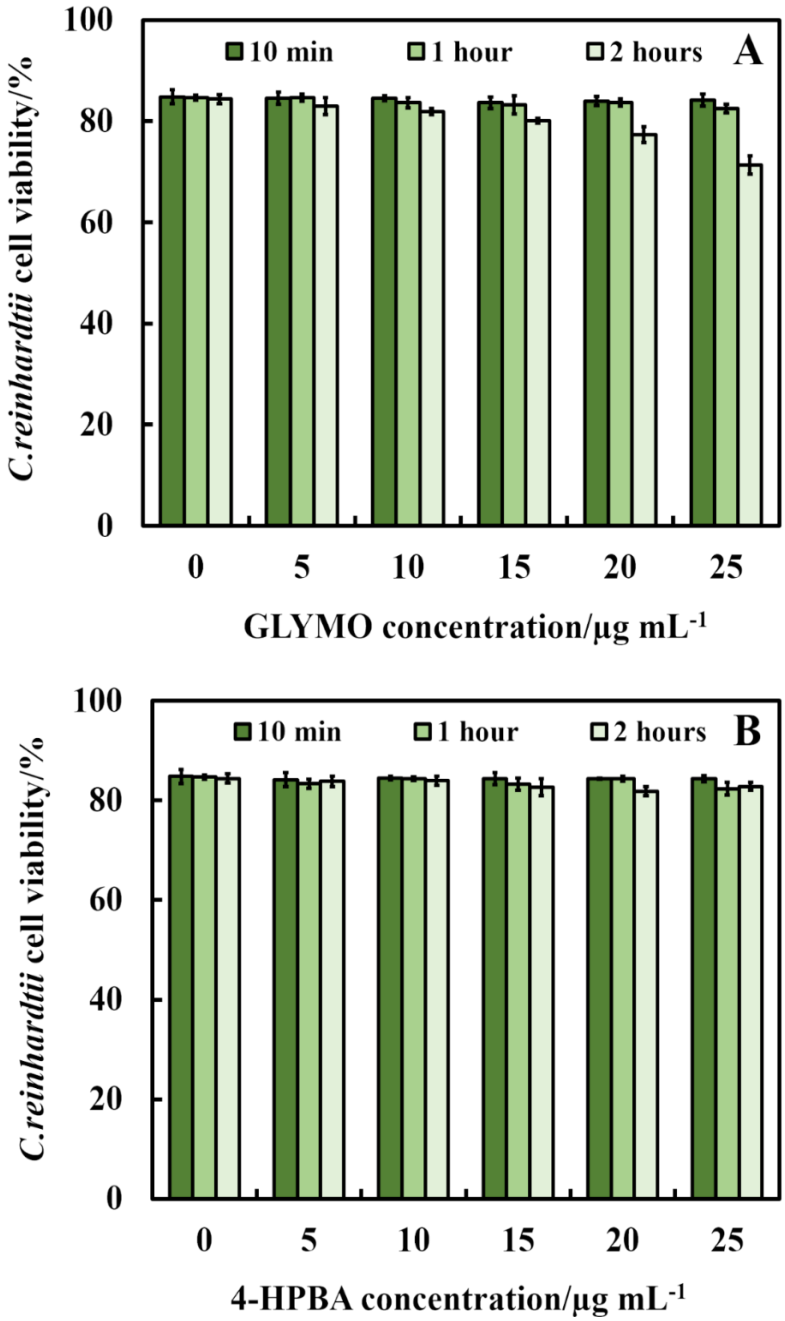


**Figure 8.29.** The anti-algal activity of (A) free GLYMO and (B) free 4-HPBA at various concentrations (0, 5, 10, 15, 20 and 25 μg $mL^{-1}$) on *C. reinhardtii*. The *C. reinhardtii* was

incubated with the GLYMO and 4-HPBA at 10 min, 1 h and 2 h of exposure before being washed and tested for their cell viability.

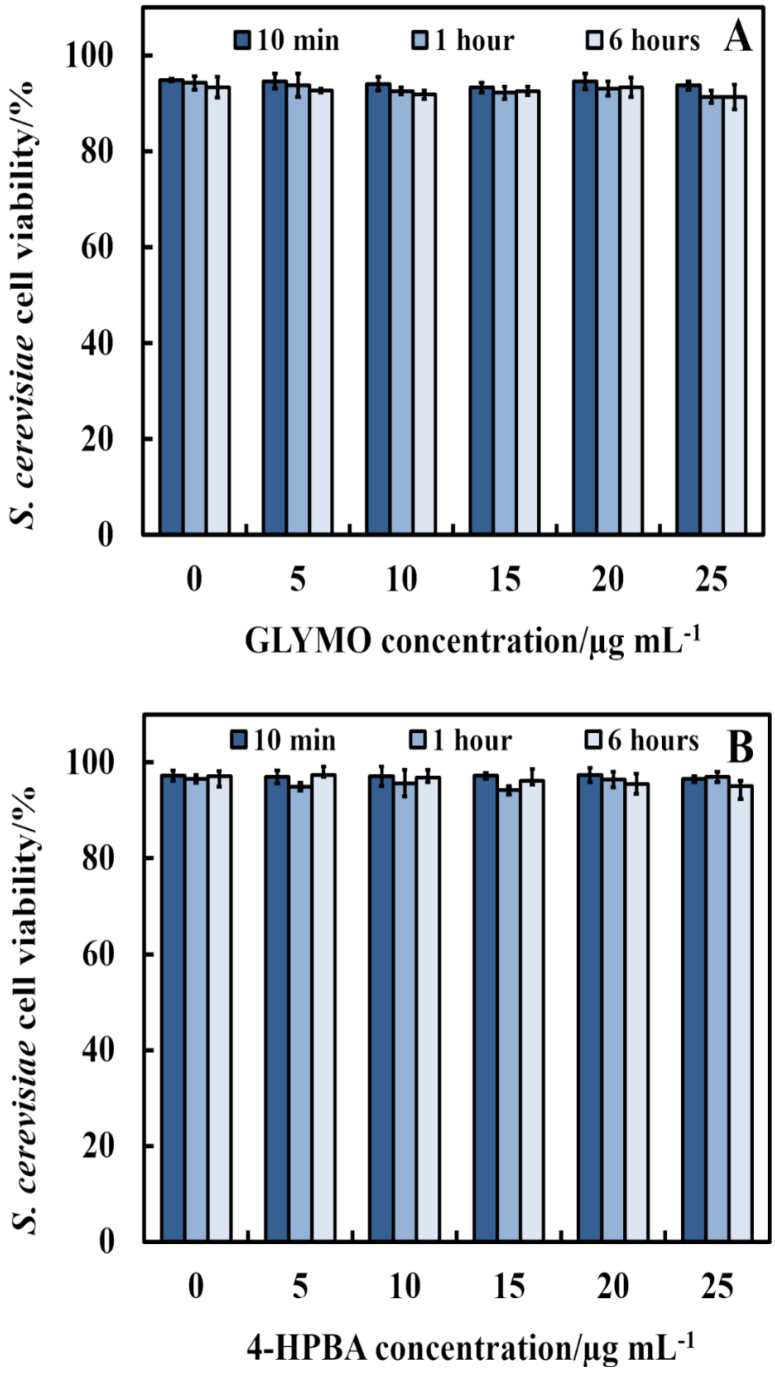


**Figure 8.30.** The anti-yeast activity of (A) free GLYMO and (B) free 4-HPBA at various concentrations (0, 5, 10, 15, 20 and 25 μg $mL^{-1}$) on *S. cerevisiae*. The *S. cerevisiae* was incubated with solutions of free GLYMO and free 4-HPBA at 10 min, 1 h and 6 h of exposure before being washed and tested for their cell viability.

## 8.9 Antifungal and antibacterial activity of 4-CPBA functionalized CuONPs on *S.cerevisiae* and *R. rhodochrous*

Copper oxide nanoparticles functionalized with 4-carboxyphenylboronic acid (4-CPBA) (designated as CuONPs/4-CPBA) were developed as antifungal and antibacterial activity on *S.cerevisiae* and *R. rhodochrous*. 4-CPBA was chosen because it contains carboxylate groups, which can coordinate to the surface of CuONPs (Figure 8.31). The antifungal and antibacterial activity of 4-CPBA functionalized CuONPs towards *S.cerevisiae* and *R. rhodochrous* was examined at room temperature for a 2 hours incubation period as presented in Figure 8.32 and Figure 8.33.

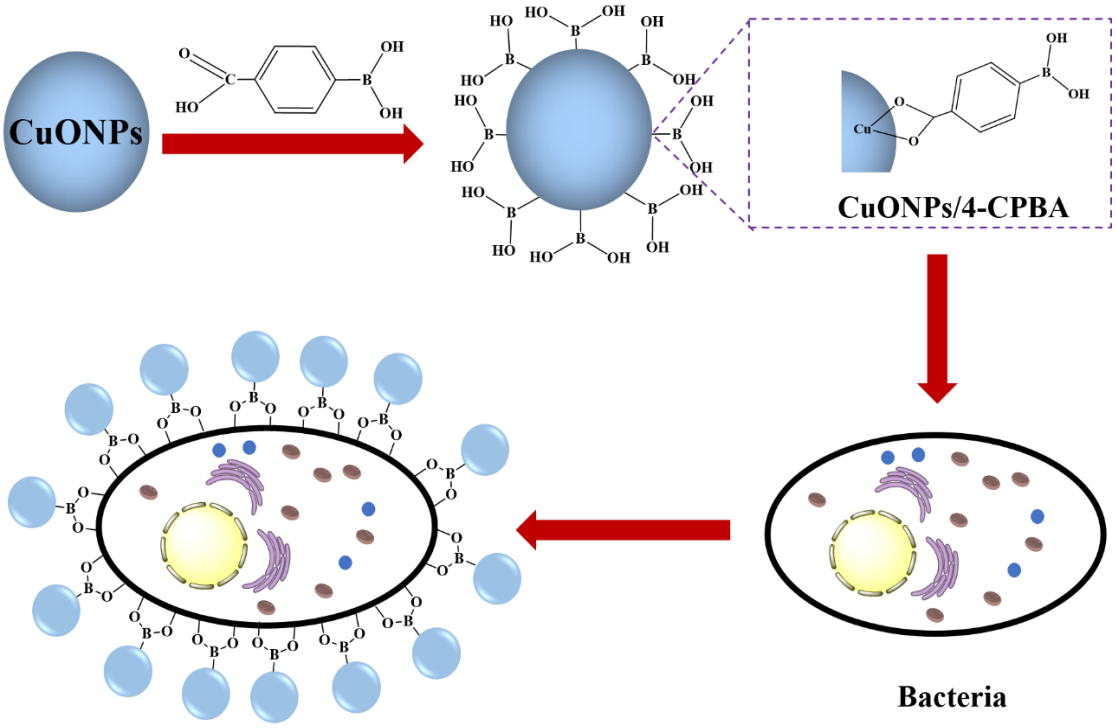


**Figure 8.31.** Schematic representation of the formation of the carboxylic acid-terminated 4-CPBA, the coupling of CuONPs/4-CPBA and the binding of cells via cyclic boronic ester formation.

It can be noted that the viability of *S.cerevisiae* cells declined to 25% at 25 µg $mL^{-1}$ concentration under UV light while it was about 65% at 5 µg $mL^{-1}$ concentration at 10 minutes incubation. In the case of the *R. rhodochrous*, there was no pronounced antibacterial impact for the incubation of *R. rhodochrous* with each individual concentration at 10 minutes, a reduction was seen for 250 µg $mL^{-1}$ concentrations. After 2 hours, 4-CPBA functionalized CuONPs had been the most active killing all cells because of the attraction between 4-CPBA functionalized CuONPs and the cell surface for both *S.cerevisiae* and *R. rhodochrous*. This is explained by the cell surfaces containing

saccharide groups in the form of glycolipids and glycoproteins. It has been demonstrated that bacteria can be attached by their surface sugar groups to boronic acids functionality in CuONPs/4-CPBA which causes the death of cells.[45-47] Figure 8.34 shows a great accumulation of 4-CPBA functionalized CuONPs which led to the greater activity towards *R. rhodochrous*.

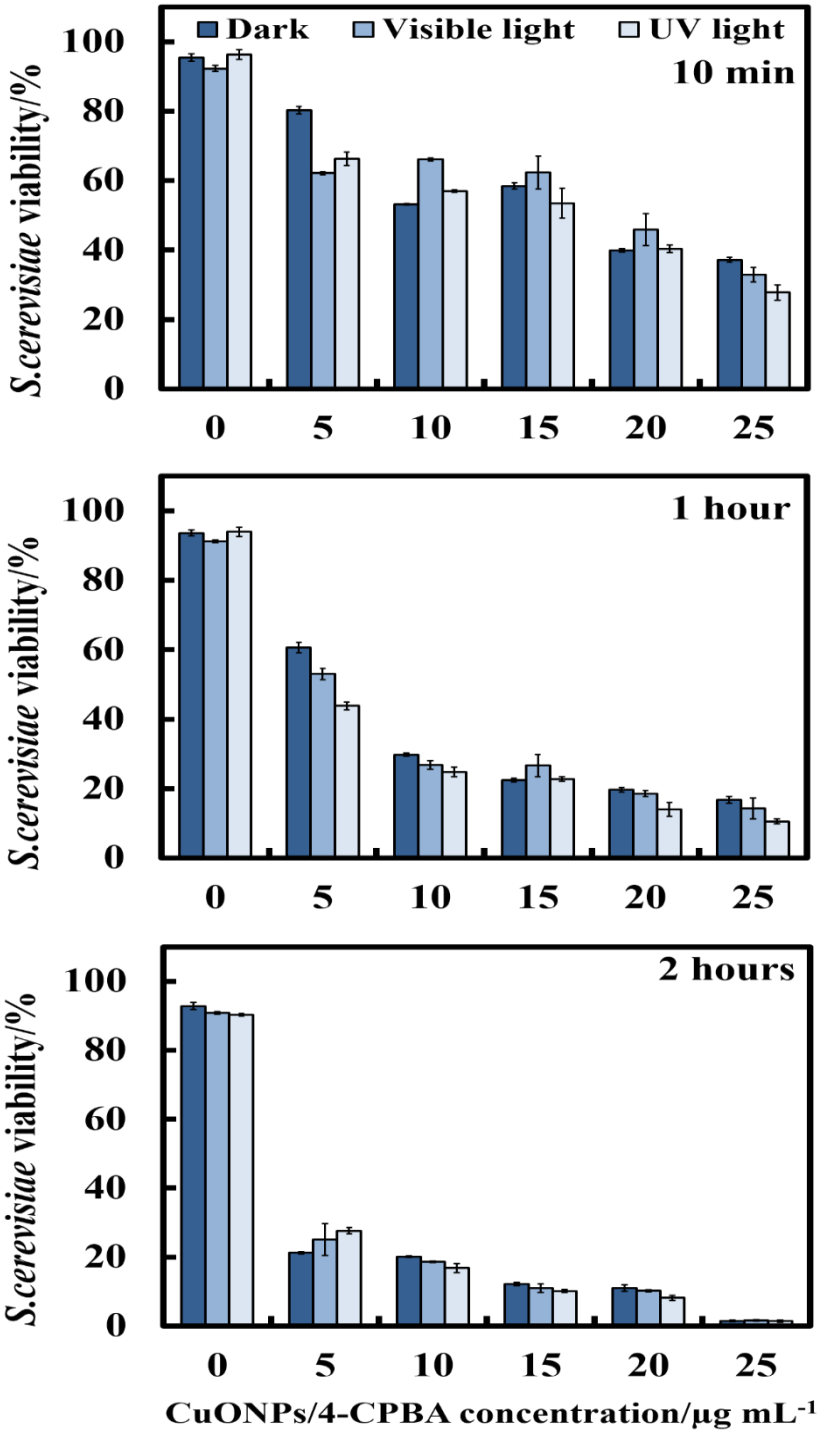


**Figure 8.32.** The antifungal activity of 4-CPBA functionalized CuONPs on *S.cerevisiae* at various CuONPs/4-CPBA concentrations. The *S.cerevisiae* was incubated with the

CuONPs/4-CPBA at 10 minutes, 1 h and 2 h of exposure times in dark, under visible and UV light.

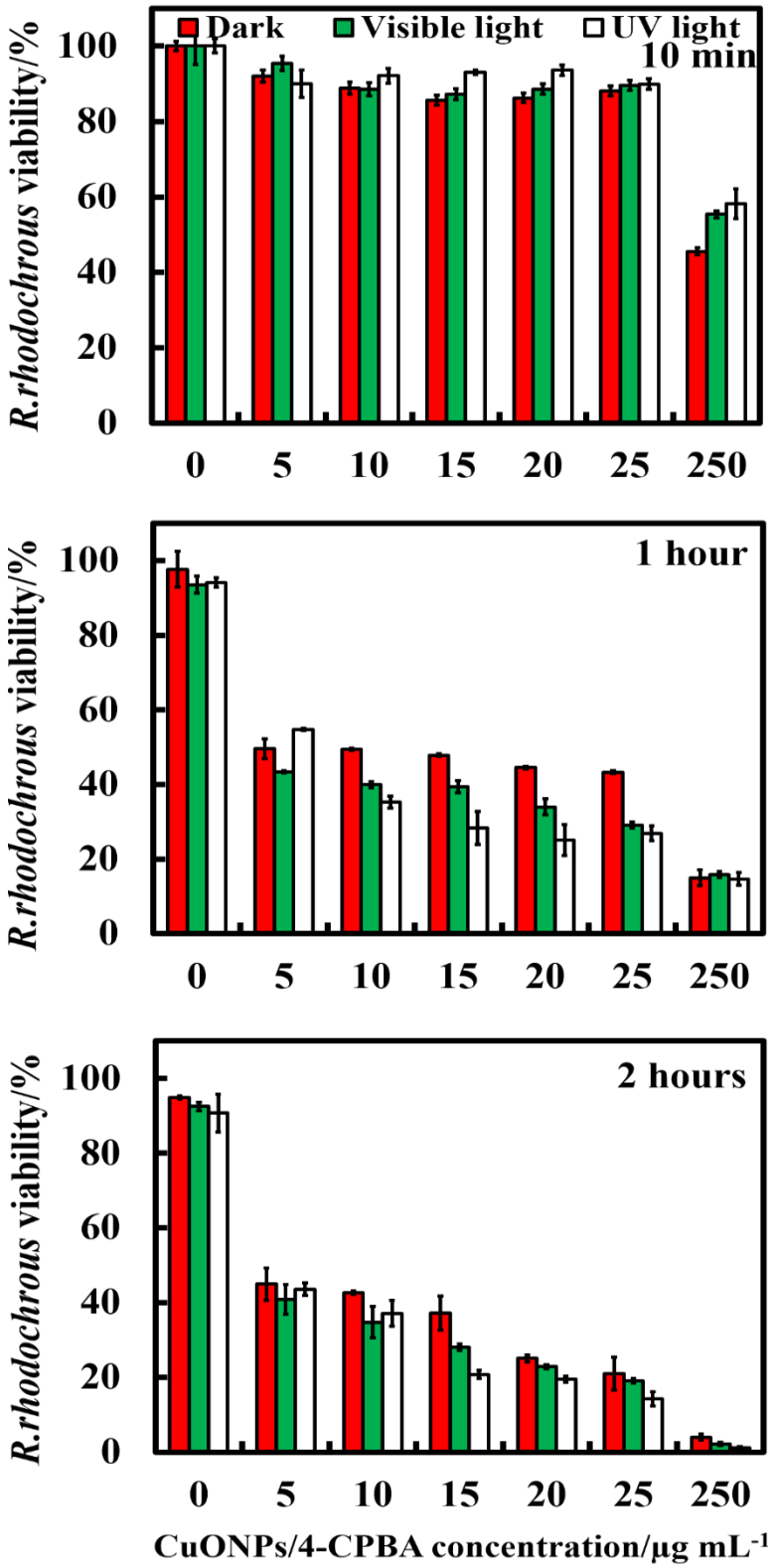


**Figure 8.33.** The antibacterial activity of CuONPs/4-CPBA on *R. rhodochrous* at various nanoparticles concentrations. The *R. rhodochrous* was incubated with the CuONPs/4-CPBA at 10 min., 1 h and 2 h of exposure times in dark, under visible and UV light.

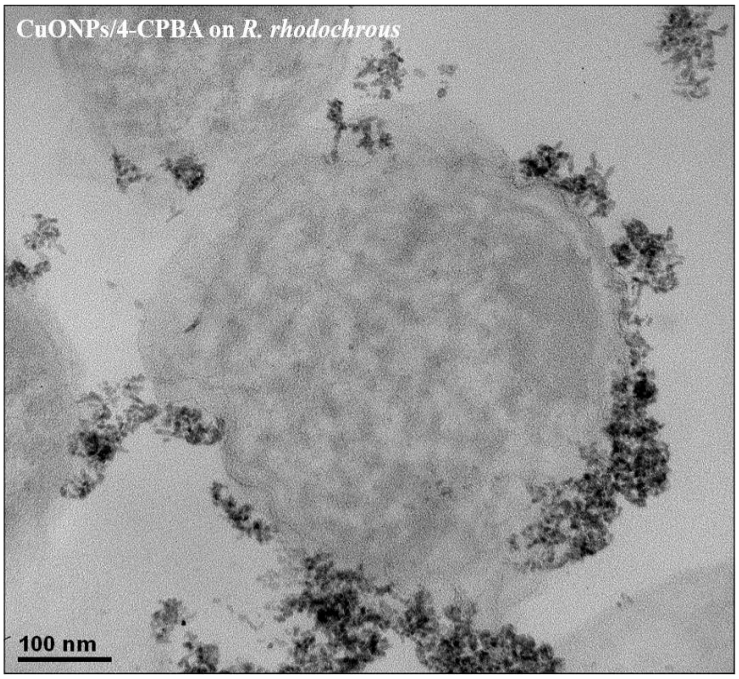


**Figure 8.34.** TEM images of *R. rhodochrous* after being incubated for 2 h into 25 μg $mL^{-1}$ 4-CPBA-functionalized CuONPs.

## 8.10 Antibacterial properties of HPBA-surface functionalized CuONPs on *R. rhodochrous*.

The antibacterial properties of the HPBA-modified CuONPs against Gram-positive bacteria were also tested. Figure 8.35 presents the antibacterial assay of *R. rhodochrous* where the control samples of untreated bacteria were compared with the ones treated with bare CuONPs, CuONPs/GLYMO and CuONPs/GLYMO/4-HPBA. Note that the cationic bare CuONPs are showing an antibacterial effect on *R. rhodochrous* even at moderate CuONPs concentrations (Figure 8.35B). It was discovered that even at very low concentrations of CuONPs/GLYMO/4-HPBA they are several times more effective against *R. rhodochrous* (Figures 8.35H and 8.35I) than the bare CuONPs (Figure 8.35B and 8.35C) and CuONPs/GLYMO (Figure 8.35E and 8.35F). A strong effect of the bare CuONPs on *R. rhodochrous* viability was observed only after 6 hours of exposure time (Figure 8.35C). The charge of the bare CuONPs is an important factor to interact with *R. rhodochrous* membranes, which contribute to their high antibacterial activity.

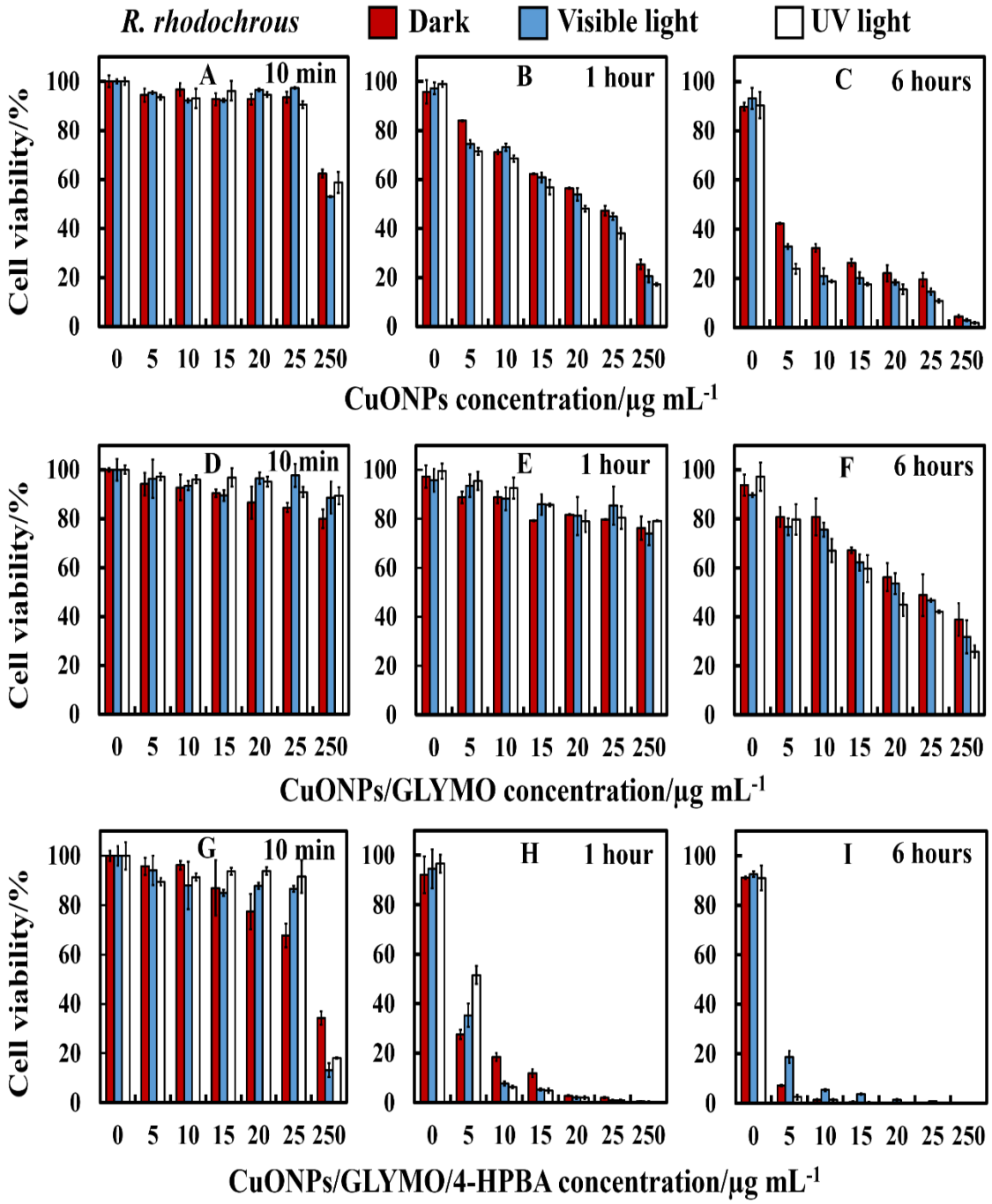


**Figure 8.35.** Cell viability of *R. rhodochrous* upon incubation of bare and surface functionalized of CuONPs of different particle concentrations (0, 5, 10, 15, 20, 25 and 250 µg $mL^{-1}$) in dark, visible and UV light conditions. The *R. rhodochrous* cells were incubated with: (A-C) bare CuONPs; (D-F) CuONPs/GLYMO and (G-I) CuONPs/GLYMO/4-HPBA at 10 min, 1 h and 6 h exposure times.

Note that for exposure times up to 10 minutes and 1 hour (Figure 8.35D and E), no measurable change in the *R. rhodochrous* viability was detected for CuONPs/GLYMO even at high particle concentrations. This also confirms that potential release of $Cu^{2+}$ ions is not the main factor in the antibacterial activity of these particles, as CuONPs/GLYMO

would support the similar concentration of $Cu^{2+}$ as the bare CuONPs. We also did not see a significant difference between the samples kept in dark, visible or in UV light conditions at the same CuONPs/GLYMO concentration. TEM imaging shows that the surfaces of *R. rhodochrous* cells accumulate a significant number of deposited nanoparticles after treatment for 6 hours with bare CuONPs (Figure 8.36B) and CuONPs/GLYMO/4-HPBA nanocomposites (Figure 8.36D). In contrast, the untreated (Figure 8.36A) and CuONPs/GLYMO treated *R. rhodochrous* (Figure 8.36C) show smooth and intact *R. rhodochrous* cell membranes. These results suggest that the 4-HPBA functional group in the modified CuONPs/GLYMO/4-HPBA particles has a significant role in promoting adhesion to the *R. rhodochrous* membranes. The strong covalent attachment of the CuONPs/GLYMO/4-HPBA with the *R. rhodochrous* cell membrane is likely to be the main contributor towards the bacterial cell membrane disruption and damage which makes it a very efficient antibacterial agent.[31]

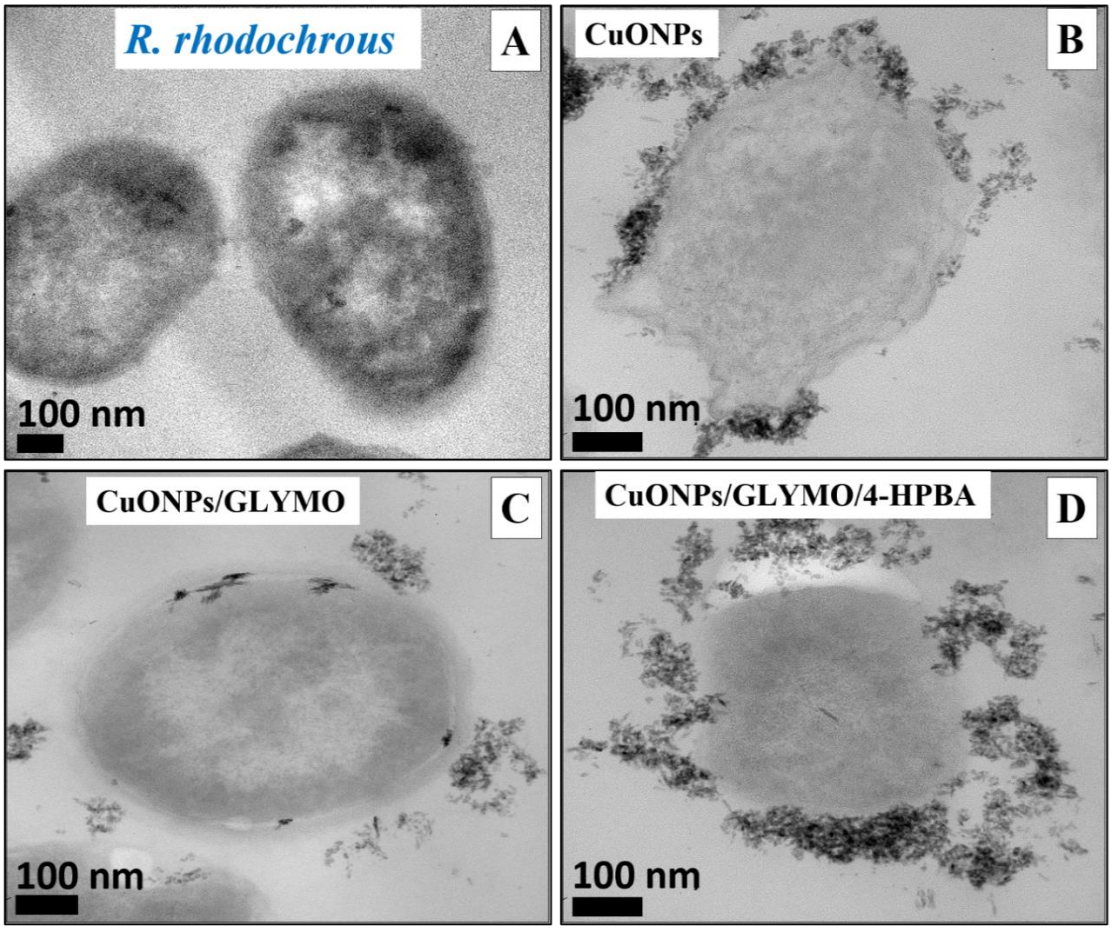


**Figure 8.36.** TEM images of *R. rhodochrous* after being incubated for 6 hours into 25 µg $mL^{-1}$ bare and surface functionalized of CuONPs: (A) an untreated sample without CuONPs (B) *R. rhodochrous* incubated with CuONPs (C) *R. rhodochrous* incubated with CuONPs/GLYMO (D) *R. rhodochrous* incubated with CuONPs/GLYMO/4-HPBA.

Direct CFU/mL measurements (see Tables 8.2 and 8.3) also confirm the same trends for the effect of the CuONPs/GLYMO/4-HPBA compared to CuONPs for both *E.coli* and *R. rhodochrous*.

**Table 8.2.** Experimental data for the CFU/mL for *E.coli* after treatment with various concentrations of CuONPs, CuONPs/GLYMO and CuONPs/GLYMO/HPBA (0, 5, 10, 15, 20, 25 μg $mL^{-1}$) in dark conditions for 10 min, 1 h and 6 h, respectively. CFU $mL^{-1}$ were calculated as (no. of colonies per plate × dilution factor) / volume of culture plate (mL). The dilution factor is 10000 and the volume of culture plate 0.1 mL.

| ***E.coli*** | | | | | | | |
|---|---|---|---|---|---|---|---|
| **Time** | **NPs conc. (μg $mL^{-1}$)** | **CuONPs** | | **CuONPs/GLYMO** | | **CuONPs/GLYMO/4-HPBA** | |
| | | **Average (CFU $mL^{-1}$)** | **Log (CFU $mL^{-1}$)** | **Average (CFU $mL^{-1}$)** | **Log (CFU $mL^{-1}$)** | **Average (CFU $mL^{-1}$)** | **Log (CFU $mL^{-1}$)** |
| **10 min** | **0** | **66 ± 5 × $10^5$** | **6.823** | **66 ± 5 × $10^5$** | **6.823** | **66 ± 5 × $10^5$** | **6.823** |
| | **5** | **58 ± 2 × $10^5$** | **6.765** | **66 ± 3 × $10^5$** | **6.821** | **40 ± 4 × $10^5$** | **6.605** |
| | **10** | **53 ± 3 × $10^5$** | **6.729** | **64 ± 2 × $10^5$** | **6.806** | **28 ± 2 × $10^5$** | **6.452** |
| | **15** | **52 ± 4 × $10^5$** | **6.721** | **64 ± 5 × $10^5$** | **6.808** | **23 ± 4 × $10^5$** | **6.367** |
| | **20** | **43 ± 3 × $10^5$** | **6.640** | **66 ± 8 × $10^5$** | **6.819** | **22 ± 2 × $10^5$** | **6.348** |
| | **25** | **43 ± 2 × $10^5$** | **6.633** | **58 ± 4 × $10^5$** | **6.768** | **15 ± 2 × $10^5$** | **6.176** |
| **1 hour** | **0** | **72 ± 2 × $10^5$** | **6.857** | **72 ± 2 × $10^5$** | **6.857** | **72 ± 2 × $10^5$** | **6.857** |
| | **5** | **49 ± 6 × $10^5$** | **6.693** | **59 ± 3 × $10^5$** | **6.773** | **15 ± 3 × $10^5$** | **6.185** |
| | **10** | **35 ± 2 × $10^5$** | **6.544** | **56 ± 2 × $10^5$** | **6.753** | **8 ± 2 × $10^5$** | **5.937** |
| | **15** | **27 ± 2 × $10^5$** | **6.431** | **55 ± 7 × $10^5$** | **6.740** | **6 ± 1 × $10^5$** | **5.801** |
| | **20** | **23 ± 2 × $10^5$** | **6.361** | **50 ± 4 × $10^5$** | **6.698** | **5 ± 3 × $10^5$** | **5.753** |
| | **25** | **19 ± 3 × $10^5$** | **6.293** | **44 ± 3 × $10^5$** | **6.646** | **3 ± 2 × $10^5$** | **5.477** |
| **6 hours** | **0** | **80 ± 2 × $10^5$** | **6.903** | **80 ± 2 × $10^5$** | **6.903** | **80 ± 2 × $10^5$** | **6.903** |
| | **5** | **21 ± 3 × $10^5$** | **6.329** | **47 ± 7 × $10^5$** | **6.672** | **7 ± 5 × $10^5$** | **5.845** |
| | **10** | **14 ± 2 × $10^5$** | **6.146** | **47 ± 3 × $10^5$** | **6.675** | **3 ± 2 × $10^5$** | **5.477** |
| | **15** | **11 ± 3 × $10^5$** | **6.054** | **40 ± 5 × $10^5$** | **6.602** | **0** | **0** |
| | **20** | **2 ± 2 × $10^5$** | **5.301** | **37 ± 5 × $10^5$** | **6.575** | **0** | **0** |
| | **25** | **0** | **0** | **37 ± 2 × $10^5$** | **0** | **0** | **0** |

**Table 8.3.** Experimental data for the CFU/mL for *R.rhodochrous* after treatment with various concentrations of CuONPs, CuONPs/GLYMO and CuONPs/GLYMO/HPBA (0, 5, 10, 15, 20, 25 and 250 μg $mL^{-1}$) in dark conditions for 10 min, 1 h and 6 h, respectively. CFU $mL^{-1}$ were calculated as (no. of colonies per plate × dilution factor) / volume of culture plate (mL). The dilution factor is 10000 and the volume of culture plate 0.1 mL.

| *R.rhodochrous* | | | | | | | |
|---|---|---|---|---|---|---|---|
| Time | NPs conc. (μg $mL^{-1}$) | CuONPs | | CuONPs/GLYMO | | CuONPs/GLYMO/4-HPBA | |
| | | Average (CFU $mL^{-1}$) | Log (CFU $mL^{-1}$) | Average (CFU $mL^{-1}$) | Log (CFU $mL^{-1}$) | Average (CFU $mL^{-1}$) | Log (CFU $mL^{-1}$) |
| 10 min | 0 | $51 \pm 3 \times 10^5$ | 6.713 | $51 \pm 3 \times 10^5$ | 6.713 | $51 \pm 3 \times 10^5$ | 6.713 |
| | 5 | $50 \pm 5 \times 10^5$ | 6.701 | $49 \pm 3 \times 10^5$ | 6.693 | $47 \pm 4 \times 10^5$ | 6.675 |
| | 10 | $50 \pm 2 \times 10^5$ | 6.701 | $49 \pm 6 \times 10^5$ | 6.693 | $44 \pm 2 \times 10^5$ | 6.643 |
| | 15 | $50 \pm 5 \times 10^5$ | 6.698 | $50 \pm 2 \times 10^5$ | 6.698 | $47 \pm 2 \times 10^5$ | 6.678 |
| | 20 | $48 \pm 4 \times 10^5$ | 6.687 | $45 \pm 3 \times 10^5$ | 6.659 | $45 \pm 3 \times 10^5$ | 6.653 |
| | 25 | $44 \pm 2 \times 10^5$ | 6.649 | $50 \pm 2 \times 10^5$ | 6.698 | $44 \pm 3 \times 10^5$ | 6.646 |
| | 250 | $39 \pm 3 \times 10^5$ | 6.598 | $48 \pm 2 \times 10^5$ | 6.681 | $30 \pm 5 \times 10^5$ | 6.486 |
| 1 hour | 0 | $52 \pm 2 \times 10^5$ | 6.716 | $52 \pm 2 \times 10^5$ | 6.716 | $52 \pm 2 \times 10^5$ | 6.716 |
| | 5 | $44 \pm 3 \times 10^5$ | 6.649 | $50 \pm 2 \times 10^5$ | 6.698 | $25 \pm 2 \times 10^5$ | 6.397 |
| | 10 | $39 \pm 8 \times 10^5$ | 6.591 | $48 \pm 2 \times 10^5$ | 6.681 | $17 \pm 3 \times 10^5$ | 6.247 |
| | 15 | $34 \pm 4 \times 10^5$ | 6.539 | $46 \pm 4 \times 10^5$ | 6.662 | $11 \pm 2 \times 10^5$ | 6.041 |
| | 20 | $31 \pm 2 \times 10^5$ | 6.491 | $45 \pm 2 \times 10^5$ | 6.656 | $7 \pm 5 \times 10^5$ | 5.845 |
| | 25 | $26 \pm 5 \times 10^5$ | 6.420 | $47 \pm 2 \times 10^5$ | 6.675 | 0 | 0 |
| | 250 | $16 \pm 6 \times 10^5$ | 6.213 | $37 \pm 5 \times 10^5$ | 6.572 | 0 | 0 |
| 6 hours | 0 | $53 \pm 5 \times 10^5$ | 6.724 | $53 \pm 5 \times 10^5$ | 6.724 | $53 \pm 5 \times 10^5$ | 6.724 |
| | 5 | $30 \pm 1 \times 10^5$ | 6.486 | $45 \pm 2 \times 10^5$ | 6.653 | $14 \pm 2 \times 10^5$ | 6.156 |
| | 10 | $29 \pm 4 \times 10^5$ | 6.467 | $43 \pm 3 \times 10^5$ | 6.640 | $3 \pm 2 \times 10^5$ | 5.522 |
| | 15 | $23 \pm 3 \times 10^5$ | 6.374 | $36 \pm 4 \times 10^5$ | 6.564 | 0 | 0 |
| | 20 | $19 \pm 5 \times 10^5$ | 6.278 | $31 \pm 4 \times 10^5$ | 6.491 | 0 | 0 |
| | 25 | $10 \pm 3 \times 10^5$ | 6.028 | $27 \pm 1 \times 10^5$ | 6.436 | 0 | 0 |
| | 250 | $0.3 \pm 5 \times 10^5$ | 4.522 | $27 \pm 3 \times 10^5$ | 6.441 | 0 | 0 |

## 8.11 Effect of the presence of glucose on the antibacterial activity of HPBA-functionalized CuONPs towards *E.coli* and *R. rhodochrous*.

Figure 8.37 shows the antibacterial activity of the HPBA-surface functionalized CuONPs towards *E.coli* and *R. rhodochrous* at different concentrations of glucose and fixed nanoparticle concentration of 25 μg $mL^{-1}$. Note that all bacteria apparently lost their viability in the presence of bare CuONPs after 6 hours independently of the concentration of glucose in the solution. However, the bacteria viability in the presence of CuONPs/GLYMO/4-HPBA increased with increasing of the glucose concentration. A

possible mechanism for this could be that in the presence of glucose the boronic acid functional groups of the CuONPs/GLYMO/4-HPBA nanoparticles bind to the free glucose in solution thus reducing the interaction between 4-HPBA terminal group and the bacterial membranes. This also confirms that the mechanism of attachment of the CuONPs/GLYMO/4-HPBA to the bacteria is based on binding to sugar groups.

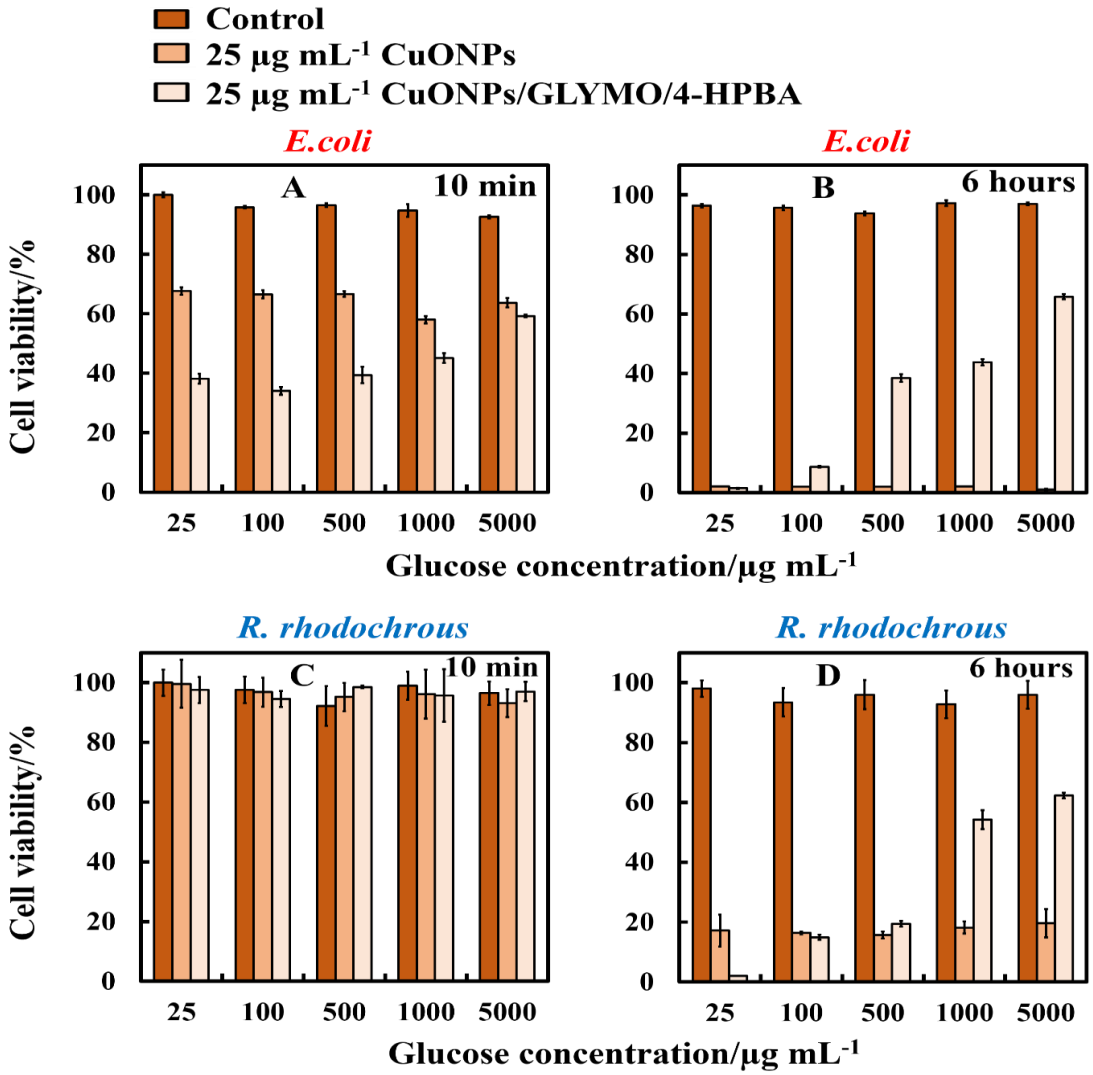


**Figure 8.37.** Bacterial cell viability after incubation as a function of nanoparticle concentration for 6 h at various glucose concentrations (A and B) *E.coli* and (C and D) *R.rhodochrous*.

## 8.12 Cytotoxicity of bare and HPBA-functionalized CuONPs on human keratinocytes.

Figure 8.38 shows the cytotoxicity assay of CuONPs and CuONPs/GLYMO/HPBA on HaCaT cells for up to several hours of exposure. The results confirm that CuONPs/GLYMO/HPBA have negligible toxic effect on these cells while bare CuONPs

have some low level of toxicity compared with the control sample. These results are obtained with particle concentrations where they are showing very strong antibacterial effect on *E.coli* and *R. rhodochrous* while leaving the keratinocyte cells unaffected. We took SEM images of dehydrated HaCaT cells after being treated with bare and HPBA-functionalized CuONPs and compared them with SEM images of the control sample (no treatment). The results are presented in Figure 8.39. In both cases, we did not observe significantly different build-up of CuONPs on these images which does not allow directly to differentiate the mechanism of their potential cytotoxic action on keratinocytes. One possible explanation why the skin cells are unaffected by both the bare and the functionalized CuONPs could be that their membrane is easier to bend around the adhering rough nanoparticles and is less prone to dislocation and rupture than the rigid membranes of bacteria.[9] This result is reassuring that such antimicrobial particles can potentially find application in wound care formulations as an alternative to antimicrobial delivery vehicles.[37, 38]

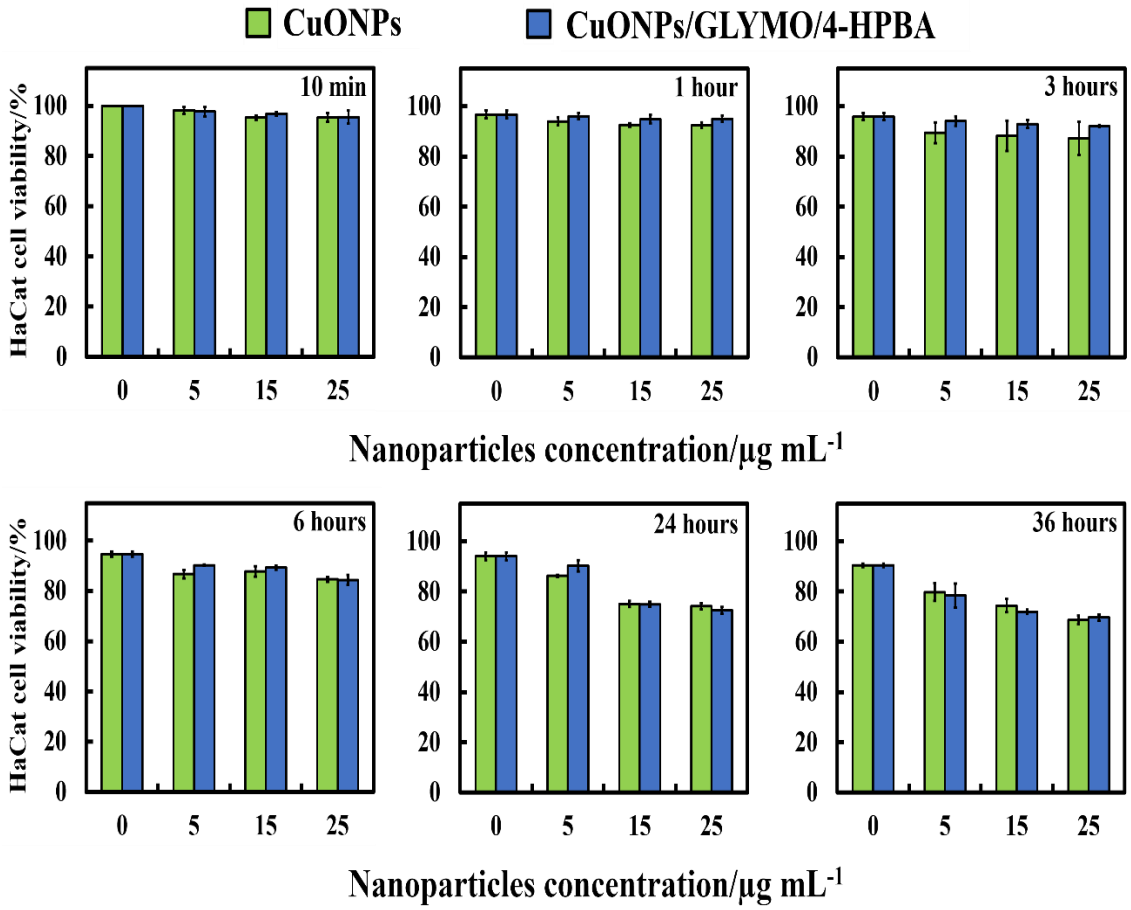


**Figure 8.38.** HaCaT cell viability after incubation as a function of nanoparticle concentration for up to 36 h with bare CuONPs and CuONPs/GLYMO/4-HPBA.

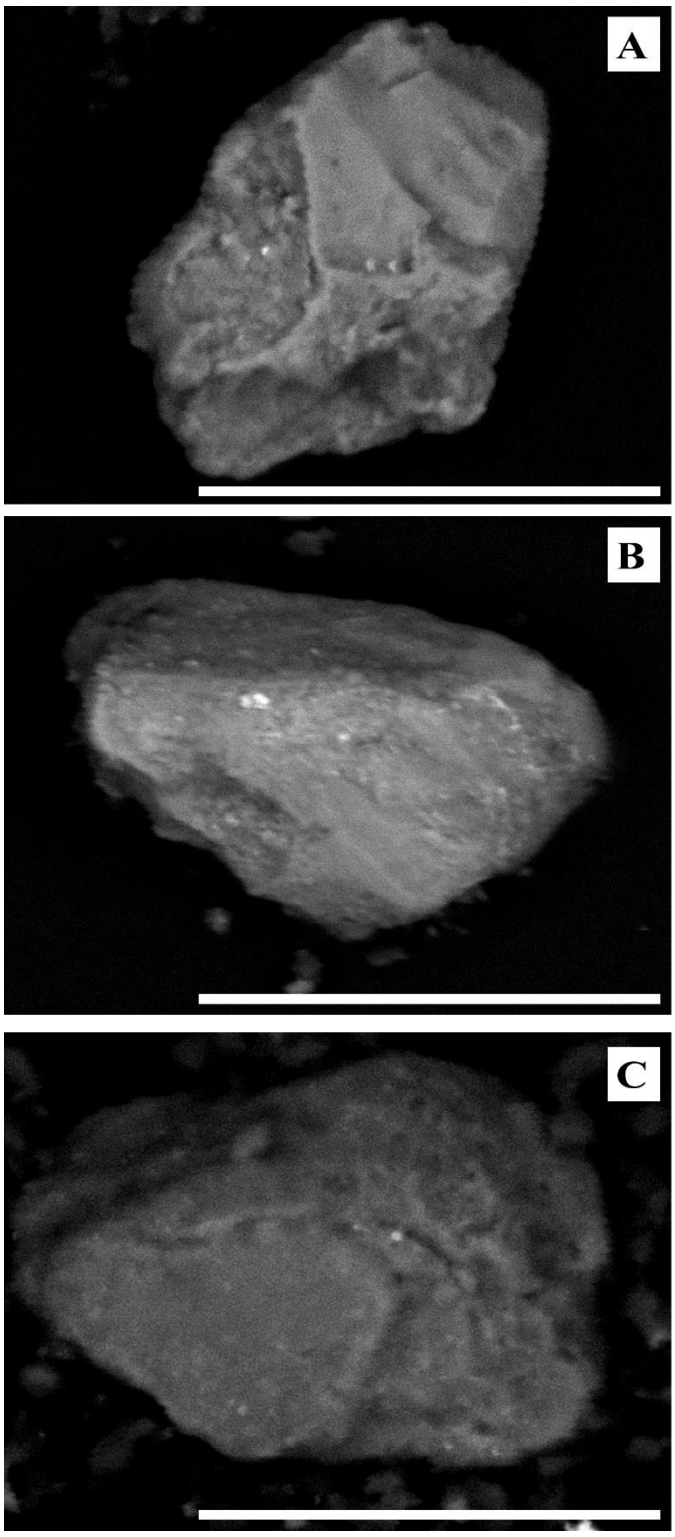


**Figure 8.39.** SEM images of HaCaT cells after being incubated for 36 h with bare CuONPs and CuONPs functionalized with 4-HPBA: (A) HaCaT cell before treatment, (B) HaCaT cells incubated with 25 μg $mL^{-1}$ CuONPs and (C) HaCaT cells incubated with 25 μg $mL^{-1}$ CuONPs/GLYMO/4-HPBA and the scale bars are 30 μm.

## 8.13 Toxicity of bare- and HPBA-grafted CuONPs on human cells.

Some preliminary studies on the cytotoxicity of the HPBA-grafted CuONPs on representative samples of human cells were conducted. Figure 8.40 shows the results on cytotoxicity assay of CuONPs and CuONPs/GLYMO/HPBA on HEK 293 cells human embryonic kidney cell line) for up to several hours of exposure. The results confirm that CuONPs/GLYMO/HPBA had no measurable toxicity on these cells while with bare CuONPs some low level of toxicity was measured compared with the control sample (no CuONPs) for the duration of their exposure. These results were obtained with particle concentrations where they show very strong anti-algal and anti-yeast effect, respectively. This result is reassuring that such functionalized CuONPs particles can potentially find applications in anti-algal formulation at much lower concentration without potentially harmful effect to the environment and human health.

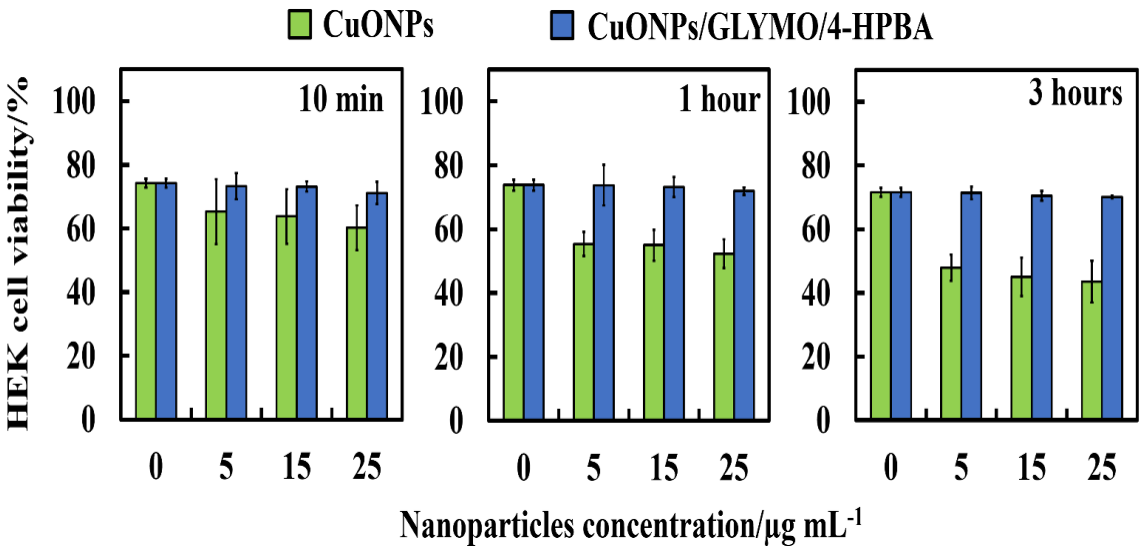


**Figure 8.40.** Comparison of the cell viability of human embryonic kidney cells (HEK 293) upon incubation as a function of nanoparticle concentration for up to 3 h with bare CuONPs and CuONPs/GLYMO/4-HPBA under dark conditions.

## 8.14 Antibacterial activity of $CuCl_2$ on *E.coli* and *R. rhodochrous*

To address the question of whether the toxicity of nanoparticles is unique, it is critical to conduct direct comparisons between nanoparticles and their ionic under similar conditions. For metallic nanoparticles, some researchers have proposed that the toxicity of the nanoparticles is because of dissolved metal ions.[48, 49] To check the antibacterial effect of copper ions ($CuCl_2$) assay was performed on both *E. coli* is a Gram-negative and *R. rhodochrous* is a Gram-positive bacterium as shown in Figure 8.41 and Figure 8.42.

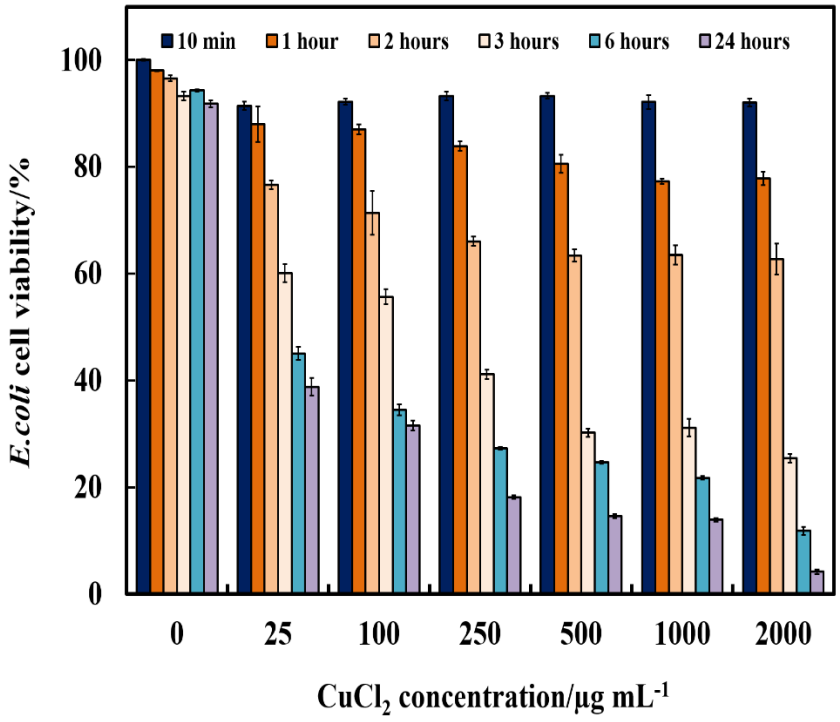


**Figure 8.41.** The antibacterial activity of $CuCl_2$ on *E.coli* at different concentrations. The *E.coli* was incubated with the $CuCl_2$ at 10 min, 1 h, 2 h, 3 h, 6 h and 24 h of exposure times.

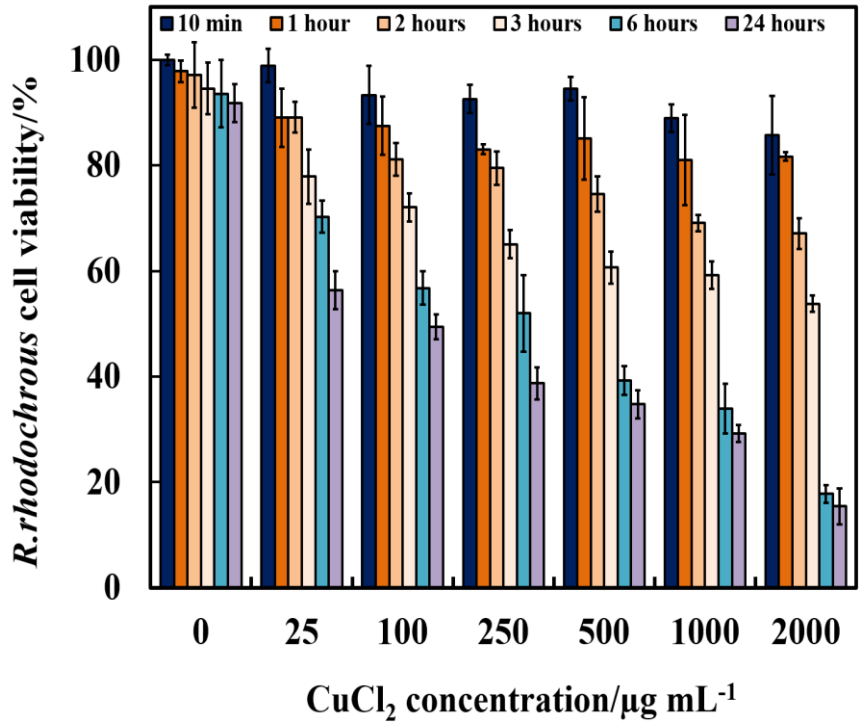


**Figure 8.42.** The antibacterial activity of $CuCl_2$ on *R. rhodochrous* at different concentrations. The *R. rhodochrous* was incubated with the $CuCl_2$ at 10 min, 1 h, 2 h, 3 h, 6 h and 24 h of exposure times.

From Figure 8.41 and Figure 8.42, it can be indicated that $CuCl_2$ have antibacterial activity towards *E.coli* and *R. rhodochrous*. Correspondingly, reports as to whether copper nanoparticles are toxic simply because they release copper ions or whether they can exhibit nonspecific toxicity have been a subject of discussion in the literature. Bondarenko *et al.* have reported toxicity investigations comparing nano CuO to $CuSO_4$ and microsized CuO at the exposure concentration of 0.001-10000 mg/L in *E. coli*.[50] On the basis of their results, they proposed that nano CuO was toxic because of the Cu ion discharged into the solution because all three Cu species resulted in biotic generation of reactive oxygen species (ROS) and single-stranded DNA damage.[50]

## 8.15 Conclusions

In conclusion, it was demonstrated that by surface grafting of GLYMO and 4-Hydroxy phenyl boronic acid (HPBA) on CuONPs formulations can be produced which are several times more effective against *R. rhodochrous, E.coli*, algae and yeast compared to bare CuONPs at the same conditions and particle concentration. The HPBA coating produces a surface functionality that allows the CuONPs particles to reversibly form covalent bonds with the diol groups from glycoproteins and carbohydrates expressed on the cell wall of both *R. rhodochrous*, *E.coli*, yeast and algae. The results show the profound differences in the surface properties of the bare CuONPs and the CuONPs/GLYMO/4-HPBA particles which have opposite surface charge at pH 5-6. The zeta potential of non-functionalized CuONPs, GLYMO-grafted CuONPs and HPBA-grafted CuONPs was +37 mV, -3 mV and -10 mV, respectively. Antibacterial tests showed that the anionic CuONPs/GLYMO/4-HPBA showed much higher antibacterial, anti-algal and anti-yeast action than the cationic bare CuONPs. This is explained by the strong covalent binding of the anionic particles CuONPs/GLYMO/4-HPBA to the cell walls due to formation of boronic ester bonds between 4-Hydroxyphenylboronic acid and diol groups from carbohydrates on the cell surface. SEM and TEM images of both sectioned *R. rhodochrous*, *E.coli*, *C. reinhardtii* and *S. cerevisiae* cells exposed to CuONPs/GLYMO/4-HPBA confirmed the significant accumulation of these nanoparticles on the cell membrane. Control experiments proved that the binding ability of the CuONPs/GLYMO/4-HPBA to algae, yeast, *R. rhodochrous* and *E.coli* can be adjusted and reversed by adding glucose in the media which competes for the HPBA groups of the CuONPs surface and reduces their ability to attach to the cell membrane. This effect allows direct control over their antibacterial, anti-algal and anti-yeast action. The experiments of incubation of the CuONPs/GLYMO/4-HPBA with human embryonic kidney cells were also studied which surprisingly showed no measurable cytotoxicity. This suggests that this type of surface coating can potentially be applied to a range of inorganic nanoparticles, as ZnONPs, $TiO_2$NPs, $Ag_2$ONPs, $Cu_2$ONPs and others which would lead to fabrication of superior and environmentally friendly antibacterial, anti-algal and antifungal agents at significantly reduced particle concentration. This chapter is the first report of a novel type of modified CuONPs has been developed by functionalizing the NPs with GLYMO and 4-HPBA. Previous work in the literature has used the GLYMO functionalization of other inorganic nanoparticles. No other study in the present literature

has demonstrated such an antimicrobial action of functionalized CuONPs with GLYMO and 4-HPBA as in this Chapter.

## 8.16 References


1. A. F. Halbus, T. S. Horozov and V. N. Paunov, *ACS applied materials & interfaces*, 2019, **11**, 12232–12243.
2. S. S. M. Al-Obaidy, A. F. Halbus, G. M. Greenway and V. N. Paunov, *Journal of Materials Chemistry B*, 2019, **7**, 3119-3133.
3. G. Mi, D. Shi, M. Wang and T. J. Webster, *Advanced healthcare materials*, 2018, **7**, 1800103.
4. A. F. Halbus, T. S. Horozov and Vesselin N. Paunov, *Nanoscale Advances*, 2019, **1**, 2323 – 2336.
5. A. F. Halbus, T. S. Horozov and V. N. Paunov, *Advances in colloid and interface science*, 2017, **249**, 134-148.
6. P. Yuan, X. Ding, Y. Y. Yang and Q. H. Xu, *Advanced healthcare materials*, 2018, **7**, 1701392.
7. E. Alpaslan, B. M. Geilich, H. Yazici and T. J. Webster, *Scientific reports*, 2017, **7**, 45859.
8. J. T. Seil and T. J. Webster, *International journal of nanomedicine*, 2012, **7**, 2767.
9. J. Penders, M. Stolzoff, D. J. Hickey, M. Andersson and T. J. Webster, *International journal of nanomedicine*, 2017, **12**, 2457.
10. G. V. Lowry, K. B. Gregory, S. C. Apte and J. R. Lead, *Journal*, 2012.
11. H. Líbalová, P. M. Costa, M. Olsson, L. Farcal, S. Ortelli, M. Blosi, J. Topinka, A. L. Costa and B. Fadeel, *Chemosphere*, 2018, **196**, 482-493.
12. K. L. Chen and G. D. Bothun, *Journal*, 2013.
13. F. Perreault, A. Oukarroum, S. P. Melegari, W. G. Matias and R. Popovic, *Chemosphere*, 2012, **87**, 1388-1394.
14. M. E. Grigore, E. R. Biscu, A. M. Holban, M. C. Gestal and A. M. Grumezescu, *Pharmaceuticals*, 2016, **9**, 75.
15. M. Ahamed, H. A. Alhadlaq, M. Khan, P. Karuppiah and N. A. Al-Dhabi, *Journal of Nanomaterials*, 2014, **2014**, 17.
16. A. P. De Silva, H. N. Gunaratne, T. Gunnlaugsson, A. J. Huxley, C. P. McCoy, J. T. Rademacher and T. E. Rice, *Chemical reviews*, 1997, **97**, 1515-1566.
17. K. Lacina, P. Skládal and T. D. James, *Chemistry Central Journal*, 2014, **8**, 60.
18. P. C. Trippier and C. McGuigan, *MedChemComm*, 2010, **1**, 183-198.
19. J. Yan, G. Springsteen, S. Deeter and B. Wang, *Tetrahedron*, 2004, **60**, 11205-11209.
20. M. V. Kuzimenkova, A. E. Ivanov, C. Thammakhet, L. I. Mikhalovska, I. Y. Galaev, P. Thavarungkul, P. Kanatharana and B. Mattiasson, *Polymer*, 2008, **49**, 1444-1454.
21. O.-W. Lau, B. Shao and M. T. Lee, *Analytica chimica acta*, 2000, **403**, 49-56.
22. P. Ertl and S. R. Mikkelsen, *Analytical chemistry*, 2001, **73**, 4241-4248.
23. R. Wannapob, P. Kanatharana, W. Limbut, A. Numnuam, P. Asawatreratanakul, C. Thammakhet and P. Thavarungkul, *Biosensors and Bioelectronics*, 2010, **26**, 357-364.
24. S. Liu, U. Wollenberger, J. Halámek, E. Leupold, W. Stöcklein, A. Warsinke and F. W. Scheller, *Chemistry–A European Journal*, 2005, **11**, 4239-4246.
25. B. Elmas, M. Onur, S. Şenel and A. Tuncel, *Colloid and Polymer Science*, 2002, **280**, 1137-1146.
26. N. DiCesare and J. R. Lakowicz, *Analytical biochemistry*, 2001, **294**, 154-160.
27. W. Yang, X. Gao and B. Wang, *Medicinal Research Reviews*, 2003, **23**, 346-368.

28. Z. Wu, S. Zhang, X. Zhang, S. Shu, T. Chu and D. Yu, *Journal of pharmaceutical sciences*, 2011, **100**, 2278-2286.
29. M. J. Al-Awady, G. M. Greenway and V. N. Paunov, *RSC Advances*, 2015, **5**, 37044-37059.
30. L. A. McDowell and H. L. Johnston, *Journal of the American Chemical Society*, 1936, **58**, 2009-2014.
31. R. Amin and S. A. Elfeky, *Spectrochimica Acta Part A: Molecular and Biomolecular Spectroscopy*, 2013, **108**, 338-341.
32. M. Tümer, H. Köksal, M. K. Sener and S. Serin, *Transition Metal Chemistry*, 1999, **24**, 414-420.
33. M. Imran, J. Iqbal, S. Iqbal and N. Ijaz, *Turkish journal of biology*, 2007, **31**, 67-72.
34. A. P. F. Maillard, P. R. Dalmasso, B. A. L. de Mishima and A. Hollmann, *Colloids and Surfaces B: Biointerfaces*, 2018, **171**, 320-326.
35. S. L. Wiskur, J. J. Lavigne, H. Ait-Haddou, V. Lynch, Y. H. Chiu, J. W. Canary and E. V. Anslyn, *Organic letters*, 2001, **3**, 1311-1314.
36. J. H. Hartley, T. D. James and C. J. Ward, *Journal of the Chemical Society, Perkin Transactions 1*, 2000, 3155-3184.
37. M. J. Al-Awady, A. Fauchet, G. M. Greenway and V. N. Paunov, *Journal of Materials Chemistry B*, 2017, **5**, 7885-7897.
38. M. J. Al-Awady, P. J. Weldrick, M. J. Hardman, G. M. Greenway and V. N. Paunov, *Materials Chemistry Frontiers*, 2018.
39. P. Chen, B. A. Powell, M. Mortimer and P. C. Ke, *Environmental science & technology*, 2012, **46**, 12178-12185.
40. C. E. Santo, E. W. Lam, C. G. Elowsky, D. Quaranta, D. W. Domaille, C. J. Chang and G. Grass, *Applied and environmental microbiology*, 2011, **77**, 794-802.
41. S. Warnes, V. Caves and C. Keevil, *Environmental microbiology*, 2012, **14**, 1730-1743.
42. V. L. Dhadge, A. Hussain, A. M. Azevedo, R. Aires-Barros and A. C. Roque, *Journal of The Royal Society Interface*, 2014, **11**, 20130875.
43. G. Grass, C. Rensing and M. Solioz, *Applied and environmental microbiology*, 2011, **77**, 1541-1547.
44. C. E. Santo, D. Quaranta and G. Grass, *Microbiologyopen*, 2012, **1**, 46-52.
45. M. D. Mager, V. LaPointe and M. M. Stevens, *Nature chemistry*, 2011, **3**, 582.
46. L. Lapinsonnière, M. Picot, C. Poriel and F. Barrière, *Electroanalysis*, 2013, **25**, 601-605.
47. A. Stephenson-Brown, S. Yong, M. H. Mansor, Z. Hussein, N.-C. Yip, P. M. Mendes, J. S. Fossey and F. J. Rawson, *Chemical Communications*, 2015, **51**, 17213-17216.
48. Z.-m. Xiu, Q.-b. Zhang, H. L. Puppala, V. L. Colvin and P. J. Alvarez, *Nano letters*, 2012, **12**, 4271-4275.
49. C. Kaweeteerawat, C. H. Chang, K. R. Roy, R. Liu, R. Li, D. Toso, H. Fischer, A. Ivask, Z. Ji and J. I. Zink, *ACS nano*, 2015, **9**, 7215-7225.
50. O. Bondarenko, A. Ivask, A. Käkinen and A. Kahru, *Environmental pollution*, 2012, **169**, 81-89.

# Chapter 9

# 9. 'Ghost' Silica Nanoparticles of 'Host'-Inherited Antibacterial Action

## 9.1 Introduction

Nanoparticles have been extensively explored for a range of biomedical applications, as contrast agents for medical imaging, labelling of cells, targeting of tumors and therapeutic drug delivery. [1-5] The optical, photoactive, electronic, catalytic and thermal properties can be greatly influenced by the specific particle morphology (sphere, cube, rod, etc.) and size. [6-8] Often the nanoparticle shape and size can be easily controlled with a high degree of accuracy during their synthesis procedure. [9-18] Nanoparticles have been heavily researched in recent years for their potential nanotoxicity and promising antimicrobial capabilities due to their high surface area to volume ratios,[4, 19-21] and nanoparticles of different metal oxides[22] as titanium dioxide,[23] zinc oxide[24] iron oxides[25] silver and copper oxides have been investigated. Antibacterial action includes the disruption of the bacterial membrane integrity leading to the leakage of intracellular components [26], creation of reactive oxygen species (ROS) harming bacterial cell constituents[27] as well as metal ions leaching from the nanoparticles interfering with the bacterial metabolism.[28] These mechanisms are found to depend on the particle shape, size, surface charge, chemical functionalities and composition.[29-37]

Silica nanoparticles ($SiO_2$NPs) have been explored as good candidates for drug delivery vehicles, biosensor applications and biomedical imaging due to their relatively low toxicity against mammalian cells, their biocompatibility and their easy surface modifications.[38, 39] $SiO_2$NPs modified with either photosensitizing molecules or antibiotics, or anchored to hybrid materials are promising in both bacterial detection[40] and antibacterial action.[41] Despite this great potential, the effects of the surface morphology of $SiO_2$NPs on the interactions with bacteria are not well documented in the literature.[34] SBA-15 mesoporous silica sieve with uniform hexagonal pores, a narrow pore size distribution and a tunable pore diameter of between 5 and 15 nm have been used by Molina-Manso and co-workers to encapsulate 3 various antimicrobial agents such as rifampicin, linezolid and vancomycin.[42] Yu *et al.* have studied the use of poly(N-isopropylacrylamide)-gated $Fe_3O_4/SiO_2$ core shell nanoparticles for the temperature

triggered release of antibacterial enzyme lysozyme.[43] Ruiz-Rico and others have stated the antimicrobial effect of caprylic acid incorporated in mesoporous silica particles against *Escherichia coli*, *Salmonella enterica*, *Staphylococcus aureus* and *Listeria monocytogenes*. They discovered that bacteria treatment with the caprylic acid-loaded silica nanoparticles produced disruption of cell envelope and leakage of cytoplasmic content, which resulted in cell death.[44]

Design and synthesis of surface-rough nanoparticles have attracted much attention due to their special structure and wide applications.[45] Here we explore the role of the silica particle surface roughness on their antimicrobial action. We prepared the surface-rough $SiO_2$NPs by using mesoporous shaped CuONPs as templates (host), which are reported to have strong antimicrobial action.[2, 3] In order to explore the effect of the particle surface roughness and morphology we effectively created 'ghost' $SiO_2$NPs which copy the morphology of the templated 'host' CuONPs. The CuO was removed from the composite $CuO/SiO_2$ nanoparticles by dissolving the CuO with nitric acid and additional cleaning with EDTA which left mesoporous $SiO_2$NPs with similar size and morphology as the host nanoparticle but free of any copper content. However, since the original CuONPs are cationic at neutral pH and naturally adhere to bacteria, we needed to engineer similar attraction between bacteria and the rough and mesoporous 'ghost' $SiO_2$NPs. For this reason, we functionalized the 'ghost' $SiO_2$NPs with boronic acid surface groups in an attempt to design a non-electrostatic mechanism for their attachment to bacteria surfaces which is expected to accumulate them on the cell walls despite the presence of other anionic species in the aqueous solution. This is shown schematically in Figure 9.1.

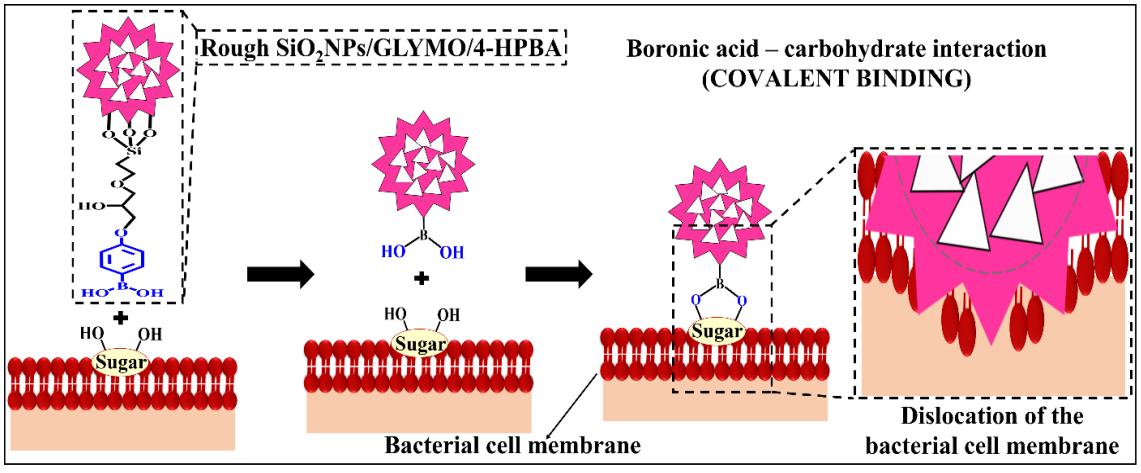


**Figure 9.1.** Schematics showing the mechanism of self-grafting/covalent attachment of HPBA-functionalized surface-rough $SiO_2$NPs and the sugar groups on the surface of the bacterial cell membrane.

The boronic acid (BA) groups on the surface-rough $SiO_2$NPs which are able to covalently bind to various glycoproteins and carbohydrates that are abundant on the bacterial cell walls. BA-functionality has been used before in chemosensor applications due to its high sensitivity for sugar determination[46] and the antimicrobial properties of BA-functionalized CuONPs particles have been recently reported.[2, 3] The BA-surface functionalization of the $SiO_2$NPs was done using GLYMO and further conjugation with phenylboronic acid.[2, 3] For comparison, we used smooth $SiO_2$NPs of similar size surface functionalized in the same way as the 'ghost' $SiO_2$NPs/GLYMO/4-HPBA in order to compare their antibacterial action and evaluate the effect of the particles surface roughness (Figure 9.1).

*R. rhodochrous* as model bacteria species was used to examine the antibacterial activity of the 4-HPBA functionalized smooth and rough $SiO_2$NPs. The present study was carried out with $SiO_2$NPs, $SiO_2$NPs/GLYMO and $SiO_2$NPs/GLYMO/4-HPBA (see Figure 9.2) to investigate the impact of the nanoparticle concentration, the zeta potential and particle size on the viability of *R. rhodochrous* at different exposure times. Significantly, the functionalization of the rough $SiO_2$NPs with 4-HPBA groups as an outer monolayer should lead to their covalent attachment on the sugar (OH) groups on the membrane surface, thus bringing the rough $SiO_2$NPs in very close proximity to the bacterial cell membrane and increasing their antibacterial efficiency.

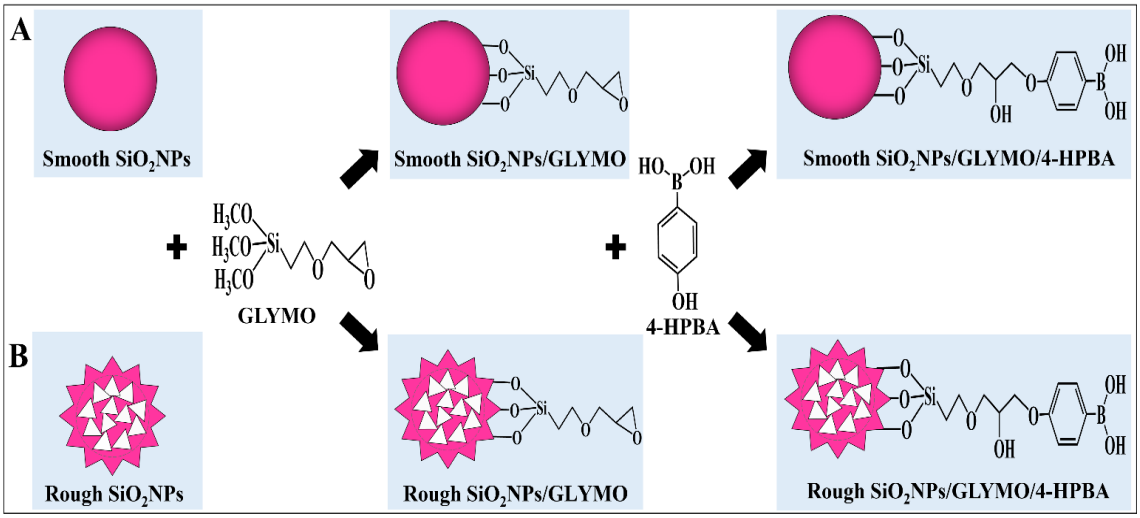


**Figure 9.2.** The schematic of the synthesis method of (A) a surface-smooth $SiO_2$NPs/GLYMO/4-HPBA and (B) a surface-rough $SiO_2$NPs/GLYMO/4-HPBA by sequential grafting of GLYMO and 4-HPBA on $SiO_2$NPs in an aqueous suspension.

Figure 9.3 shows that the 'ghost' $SiO_2$NPs were fabricated by using composite mesoporous copper oxide nanoparticles ('host' CuONPs) as templates which allowed the $SiO_2$NPs to copy their surface morphology. The 'host' CuONPs used here as templates, however, had a very high antibacterial effect, with or without functionalization. Composite CuONPs/$SiO_2$ were dispersed in the $HNO_3$ and EDTA solution to remove templates exhaustively.

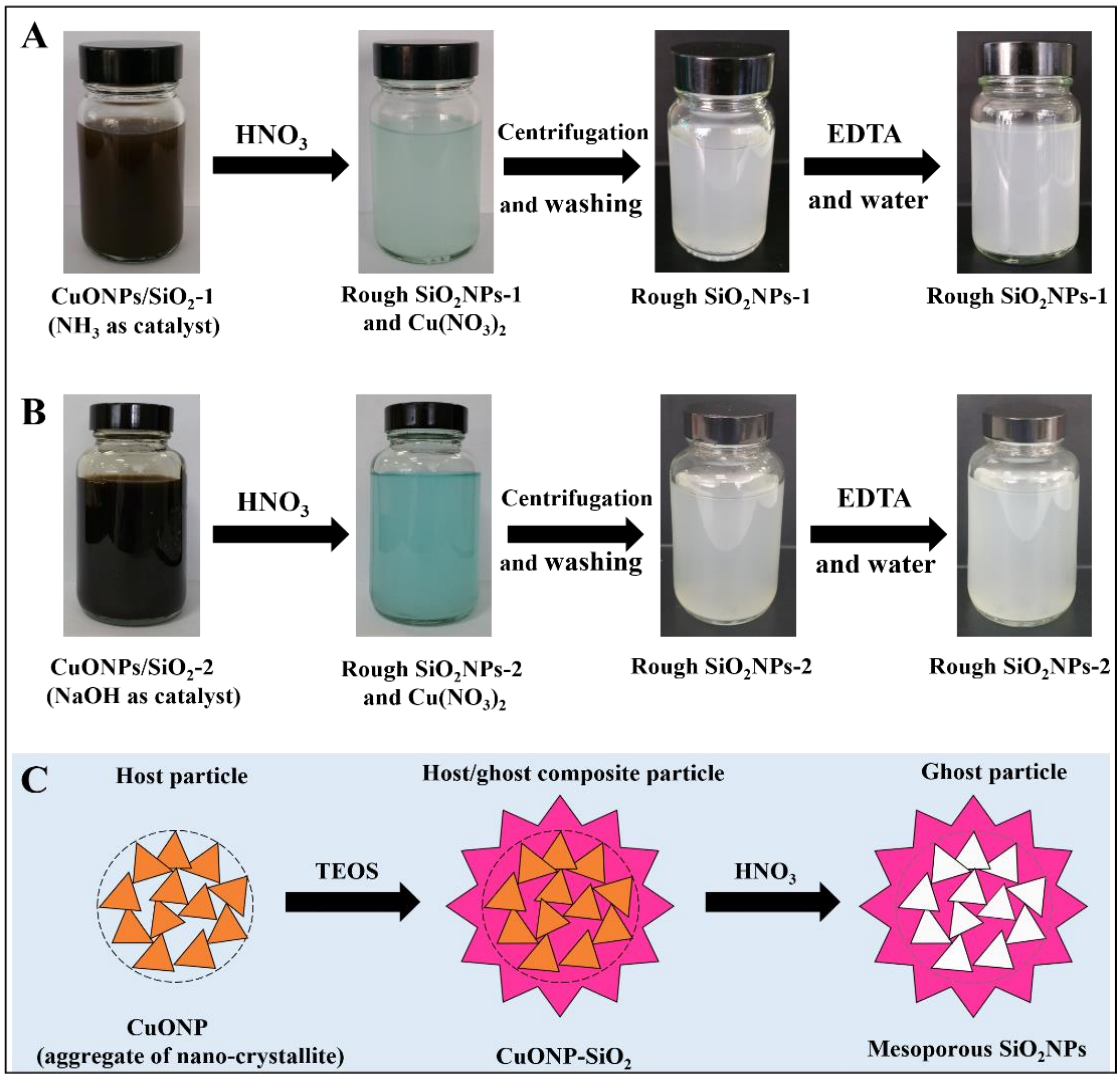


**Figure 9.3.** Schematics to show the synthesis of (A) a surface-rough $SiO_2$NPs-1 ($NH_3$ as a catalyst), (B) a surface-rough $SiO_2$NPs-2 (NaOH as a catalyst) from CuONPs/$SiO_2$ and (C) the schematic of the synthesis method of CuONPs/$SiO_2$ and a surface-rough $SiO_2$NPs.

## 9.2 Surface modification of CuONPs with $SiO_2$, GLYMO and 4-HPBA.

Figures 9.4A and 9.4D show the TEM images of CuONPs produced by annealing at 100 °C and further sonication. Silica-coated copper oxide nanoparticles were prepared based on base hydrolysis of tetraethyl orthosilicate in the presence of CuONPs. This functionality has been characterized by dynamic light scattering instrument and TEM. TEM analysis showed that the silica was coated CuONPs (Figures 9.4B, 9.4E). A typical TEM image of the obtained CuONPs/$SiO_2$ showed that the copper particles (darker) were coated with a uniform silica (light gray) - see also Figure 9.5A and 9.5B.

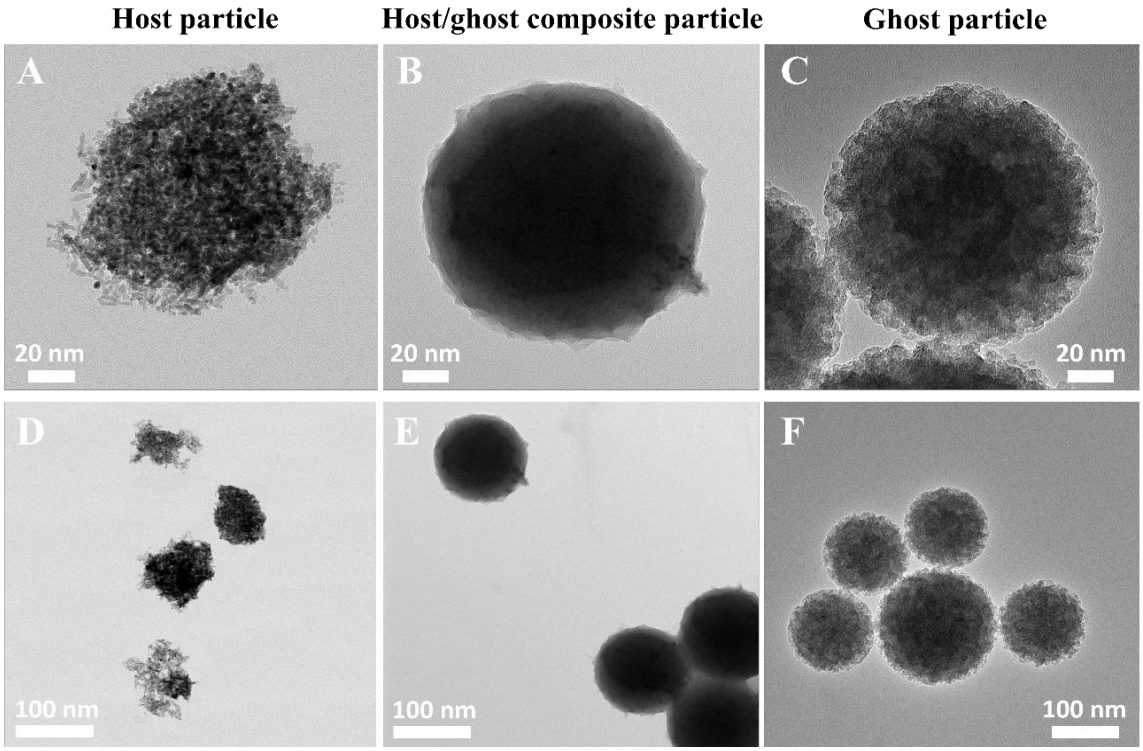


**Figure 9.4.** TEM images of (A, D) bare CuONPs aggregate of nano-crystallites (host), (B, E) $SiO_2$-coated CuONPs producing a surface-rough $SiO_2$NPs (host/ghost composite), (C, F) mesoporous surface-rough 'ghost' $SiO_2$NPs.

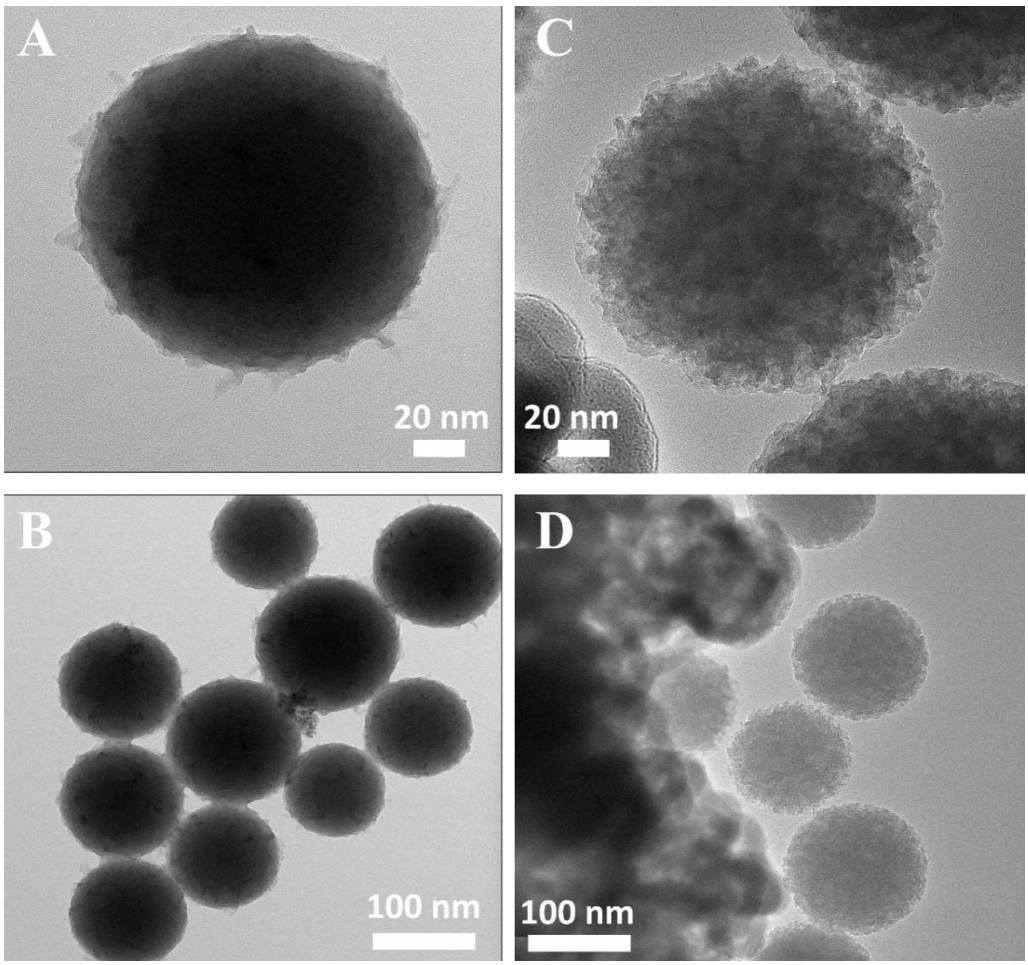


**Figure 9.5.** TEM images of (A and B) $SiO_2$-coated CuONPs producing a surface-rough $SiO_2$NPs-2 and (C and D) mesoporous ghost $SiO_2$NPs-2 at different magnifications.

After coating with $SiO_2$ layer, the average hydrodynamic diameter of CuONPs/$SiO_2$ was increased, corresponding to a 25 ± 5 nm thick $SiO_2$ layer on the CuONPs, and the surface of CuONPs/$SiO_2$ became rough. These nanoparticles were treated with $HNO_3$ to remove the CuO templates completely, producing mesoporous and surface rough 'ghost' $SiO_2$NPs as shown in Figure 9.4C, which copies certain surface roughnes features from the original host particles. The zeta potential curve for the nanoparticles suggests a changing surface for the uncoated CuONPs, with the zeta potential ranging from positive values +37 ± 3 mV to negative values - 44 ± 7 mV after the surface modification of the CuONPs with $SiO_2$ layer, GLYMO and 4-HPBA as shown in Figure 9.6A. The negative charge of silica layer contributes to a reduction in the total charge of the composite nanoparticles. Dynamic light scattering analysis indicated that the size of the CuONPs has increased after coating with $SiO_2$ and functionalized with GLYMO and 4-HPBA (Figure 9.6B).

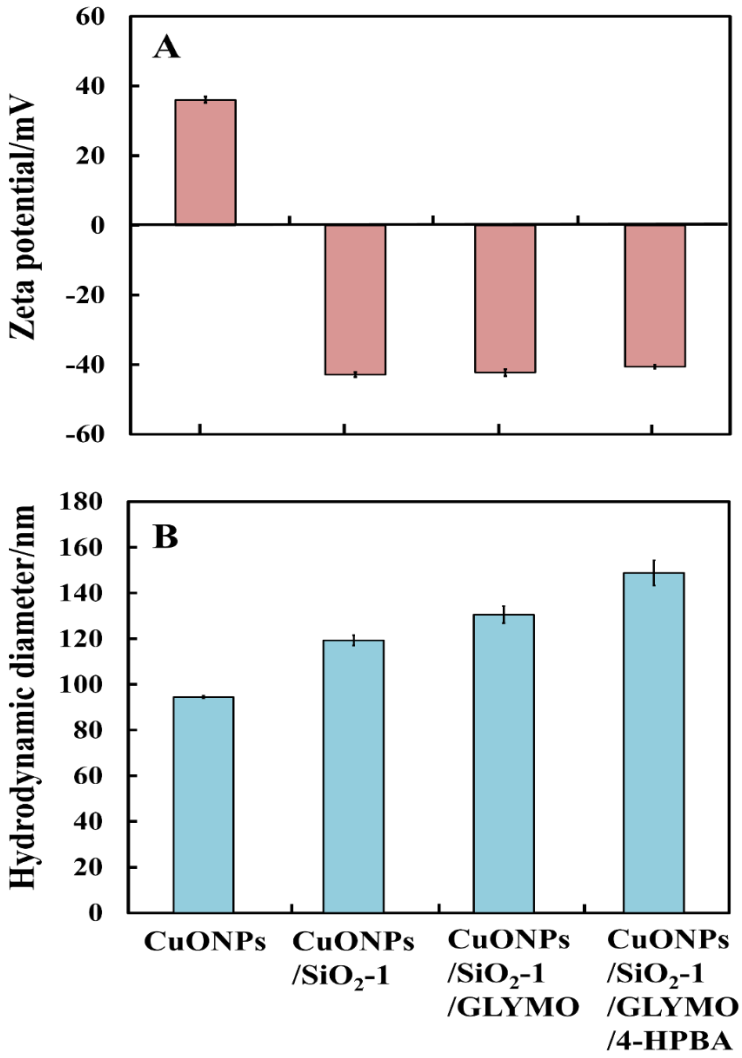


**Figure 9.6.** The (A) zeta potential and (B) particle size of bare CuONPs, CuONPs/$SiO_2$, CuONPs/$SiO_2$/GLYMO and CuONPs/$SiO_2$/GLYMO/4-HPBA.

## 9.3 Surface modification of the mesoporous surface-rough $SiO_2$NPs.

The rough $SiO_2$NPs were prepared by using shaped CuONPs as templates. CuONPs was first synthesized in aqueous solution, silica layer was then coated on CuONPs to achieve CuONPs/$SiO_2$ nanocomposite. CuONPs/$SiO_2$ nanocomposite were dispersed in the $HNO_3$ and EDTA solution to remove templates exhaustively. Figure 9.7A and 9.7C show the TEM images of the resultant surface rough $SiO_2$NPs and an analogous surface smooth $SiO_2$NPs, respectively. The images in Figure 9.4A and 9.7A show that the rough surface morphology of the original CuONPs clusters is reflected in the produced rough $SiO_2$NPs. Thus, rough $SiO_2$NPs with the size of 115 ± 10 nm were successfully fabricated from CuONPs.

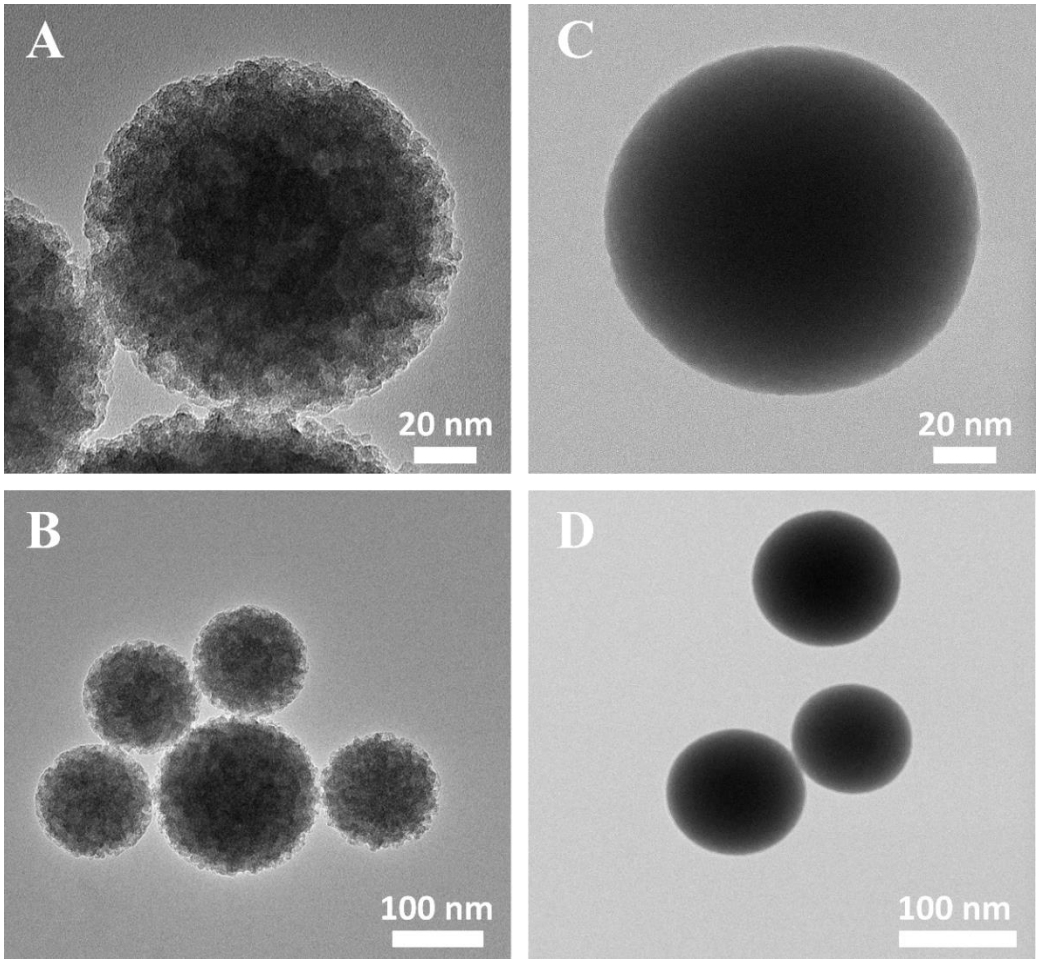


**Figure 9.7.** TEM images of (A, B) mesoporous surface-rough 'ghost' $SiO_2$NPs, (C, D) smooth $SiO_2$NPs of similar particle size.

Figure 9.5C and 9.5D shows the TEM images of a surface-rough $SiO_2$NPs at different magnifications produced with NaOH catalyst in the Stöber process instead of ammonia. Figure 9.8A and 9.8B shows EDX analysis of the CuONPs/$SiO_2$ nanoparticles before and after treatment with $HNO_3$ and EDTA solution. Figure 9.8A shows that the presence of Cu, Si and O before the treatment. Figure 9.8B shows the absence of CuONPs trapped inside the silica after treatment with $HNO_3$, indicating complete removal of CuONPs. The EDX data shows only two main peaks consisting of Si and O components with no peaks of copper. Hence the 'ghost' $SiO_2$NPs are free of copper oxide and $Cu^{2+}$ residues. Since they have negative surface charge, one could expect them not to have antimicrobial action. The surface-rough $SiO_2$NPs were modified using a GLYMO and 4-HPBA and further characterized using the DLS measurement. The data in Figure 9.8C and Figure 9.9A shows that the zeta potential of all the nanoparticles remained negative, which would offer a good opportunity for studying negatively charged cell membranes and negatively

charged for the bare rough $SiO_2$NPs and rough $SiO_2$NPs/GLYMO/4-HPBA. The hydrodynamic size of bare rough $SiO_2$NPs was 115 ± 10 nm, rough $SiO_2$NPs/GLYMO and rough $SiO_2$NPs/GLYMO/4-HPBA possessed the slightly larger size, as shown in Figure 9.8D and Figure 9.9B.

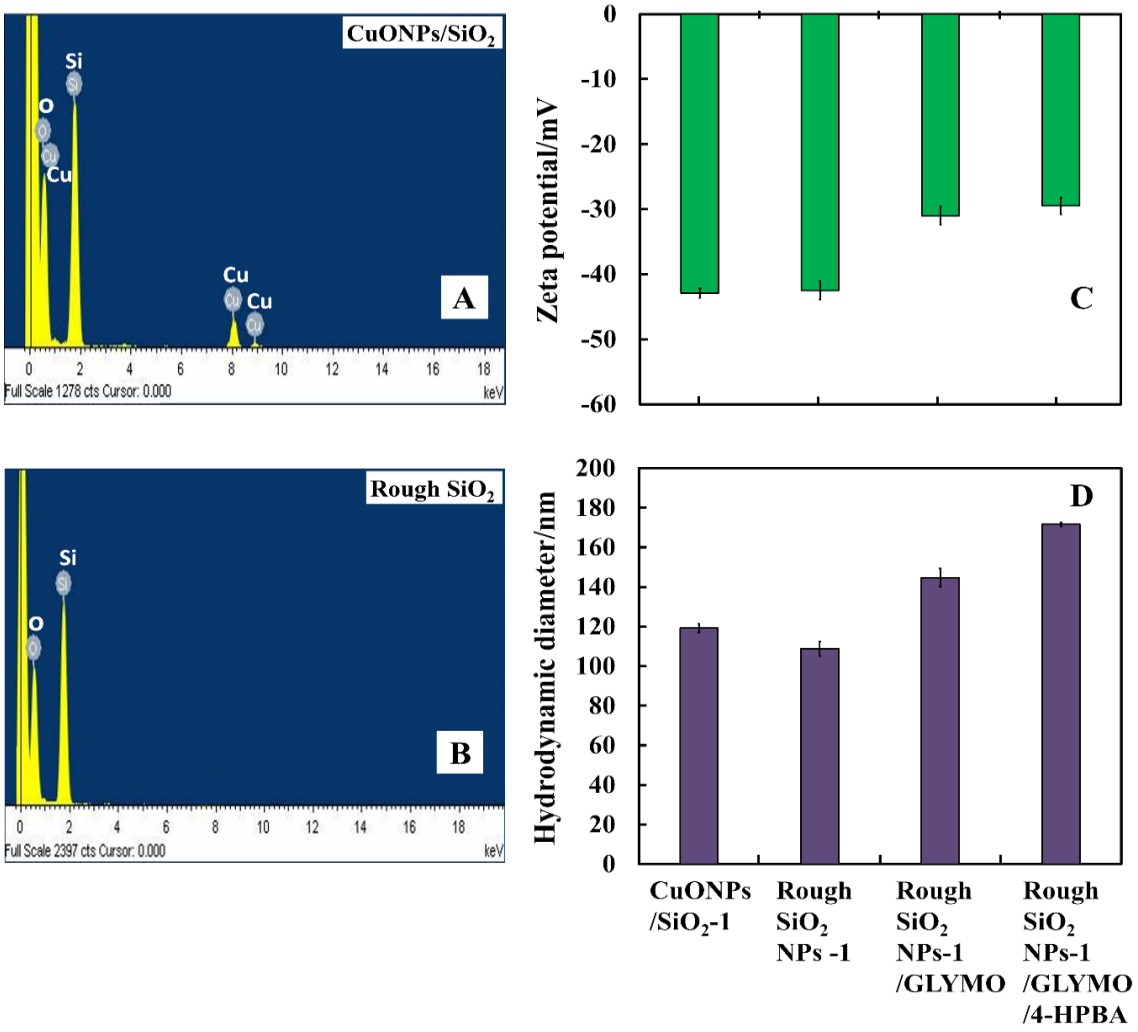


**Figure 9.8.** EDX spectrum of the CuONPs/$SiO_2$ nanoparticles before (A) and after (B) treatment with $HNO_3$ and EDTA solution. (C) The zeta potential and (D) the particle hydrodynamic diameter of CuONPs/$SiO_2$, rough $SiO_2$NPs, rough $SiO_2$NPs/GLYMO and rough $SiO_2$NPs/GLYMO/4-HPBA at pH 7.

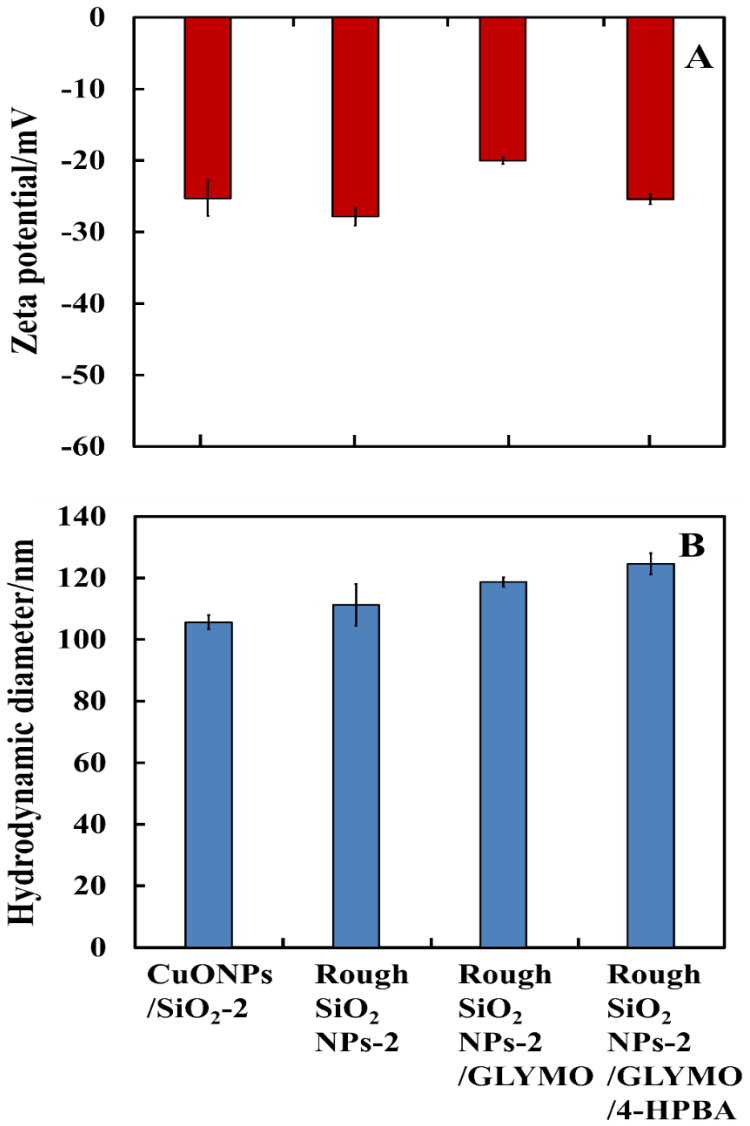


**Figure 9.9.** The (A) zeta potential and (B) particle size of CuONPs/$SiO_2$-2, rough $SiO_2$NPs-2, rough $SiO_2$NPs-2/GLYMO and rough $SiO_2$NPs-2/GLYMO/4-HPBA.

## 9.4 Surface modification of smooth $SiO_2$NPs by GLYMO and 4-HPBA.

At first, the silica nanoparticles were dispersed in deionized water. And then, the $SiO_2$NPs were functionalized with GLYMO for boronic acid immobilization. According to the method, GLYMO was attached to the silica walls by reaction between the hydroxyl and silanol groups. The easy reaction between the epoxy group of GLYMO and hydroxyl groups of 4-HPBA. Figure 9.10 C shows TEM images of smooth $SiO_2$NPs before the functionalizing process. DLS measurement of functionalized nanoparticles was taken using a Malvern Zetasizer Nano ZS system. Diameter distribution of smooth $SiO_2$NPs is shown in Figure 9.10D. The average diameter of the bare smooth $SiO_2$NPs is

107 ± 10 nm, which is in consistent with the result shown in Figure 9.10B. The zeta potential of smooth $SiO_2$NPs slightly changed after modification with GLYMO and 4-HPBA (Figure 9.10A).

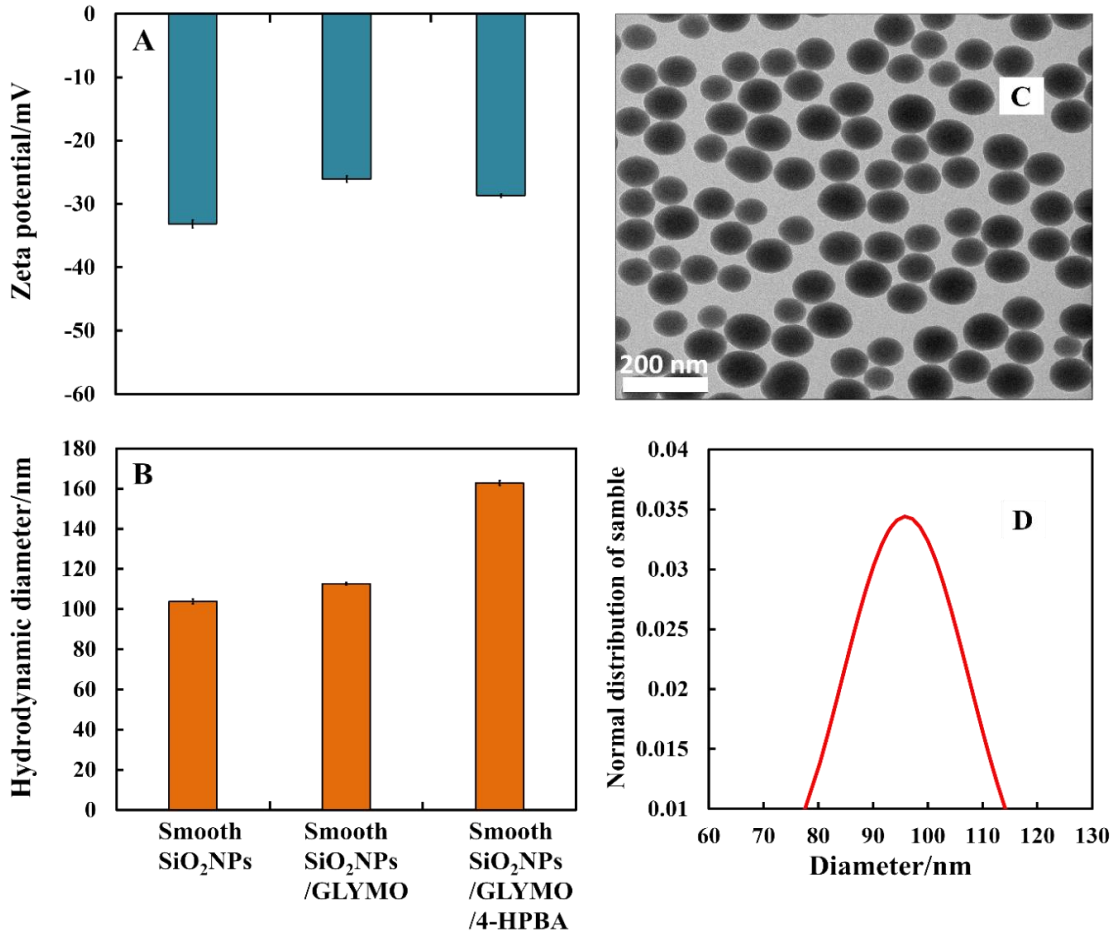


**Figure 9.10.** (A) The zeta potential and (B) the particle hydrodynamic diameter of smooth $SiO_2$NPs, $SiO_2$NPs/GLYMO and $SiO_2$NPs/GLYMO/4-HPBA at pH 7. (C) TEM image of the smooth $SiO_2$NPs and (D) their size distribution.

## 9.5 Antibacterial activity of surface functionalized CuONPs by $SiO_2$, GLYMO and 4-HPBA on *R.rhodochrous*.

Silica-coated copper oxide nanoparticles (labelled as CuONPs/$SiO_2$) were prepared. Then, GLYMO and 4-HPBA functionalization of CuONPs/$SiO_2$ was also prepared as previously described. This leads to the formation of CuONPs/$SiO_2$/GLYMO and CuONPs/$SiO_2$/GLYMO/4-HPBA nanoparticles. However, we needed to test the antibacterial activity of these nanoparticles on the selected bacteria by incubating bacteria with solutions of various concentrations of these nanoparticles to its threshold of antibacterial impact on *R.rhodochrous*. Figure 9.11 shows the antibacterial impact of

suspensions of bare CuONPs, composite CuONPs/$SiO_2$, CuONPs/$SiO_2$/GLYMO and CuONPs/$SiO_2$/GLYMO/4-HPBA of various concentrations on *R.rhodochrous*. In this case **(**Figure 9.11), the CuONPs crystallites are still inside the composite NPs and have not yet been removed. The data in Figure 9.11 indicate that the bare CuONPs has an extremely strong antibacterial impact in a wide range of concentrations ranged from 5 µg $mL^{-1}$ to 250 µg $mL^{-1}$ after 6 h of incubation (see Figure 9.11B). Figure 9.11D and 9.11F shows the antibacterial impact of the CuONPs/$SiO_2$ and CuONPs/$SiO_2$/GLYMO on *R.rhodochrous* cells after up to 6 h incubation time at room temperature. In this case, there was no pronounced antibacterial impact for the incubation of *R.rhodochrous* with each individual concentration. The antibacterial impact of CuONPs/$SiO_2$ and CuONPs/$SiO_2$/GLYMO in dark and under UV light is much lower than the one of the bare CuONPs. One may conclude that the functionalization of the CuONPs with $SiO_2$ and GLYMO reduced its nanotoxicity. This is probably due to the electrostatic repulsion of the CuONPs/$SiO_2$ and the functionalized CuONPs/$SiO_2$/GLYMO from the *R.rhodochrous* surface as both of them have a negative surface charge. However, in Figure 9.11G and 9.11H where a third functionalizing of the 4-HPBA is included (CuONPs/$SiO_2$/GLYMO/4-HPBA) the viability of the *R.rhodochrous* reduce considerably. In fact, it is close to the antibacterial impact of the bare CuONPs. This is explained by the boronic acids functionality in CuONPs/$SiO_2$/GLYMO/4-HPBA can selectively bind with carbohydrates on the bacteria surface by covalent interactions.

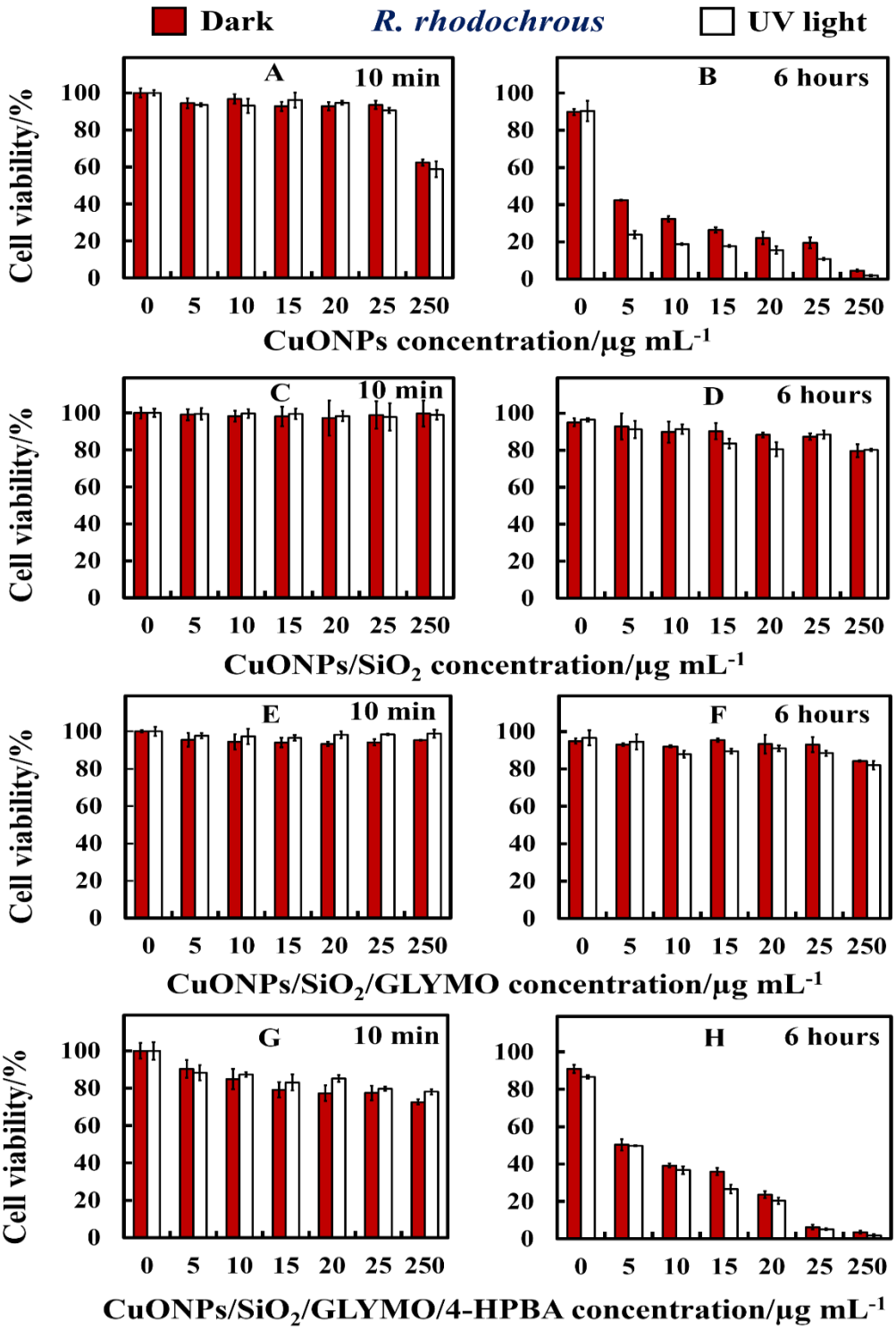


**Figure 9.11.** Cell viability of *R. rhodochrous* upon incubation of bare and surface functionalized of CuONPs of different particle concentrations in dark and UV light conditions. The *R. rhodochrous* cells were incubated with: (A, B) bare CuONPs; (C, D) CuONPs/$SiO_2$, (E, F) CuONPs/$SiO_2$/GLYMO and (G, H) CuONPs/$SiO_2$/GLYMO/4-HPBA at 10 min and 6 h exposure times.

TEM imaging shows that the outer cell walls of *R.rhodochrous* accumulate a significant number of deposited bare CuONPs (Figure 9.12B) and CuONPs/$SiO_2$/GLYMO/4-HPBA nanocomposites (Figure 9.12E and 9.12F) over 6 h. In contrast, the untreated (Figure 9.12A), CuONPs/$SiO_2$ (Figure 9.12C) and CuONPs/$SiO_2$/GLYMO (Figure 9.12D) treated bacterial cells show smooth and intact cell membranes. These results (Figure 9.12E and 9.12F) suggest that the 4-HPBA functional group in the modified CuONPs/$SiO_2$/GLYMO/4-HPBA particles has a significant role in promoting adhesion to the bacterial cell membranes. The strong covalent attachment of the CuONPs/$SiO_2$/GLYMO/4-HPBA with the cell membrane is likely to be the main contributor towards the bacterial cell membrane disruption and damage which makes it a very efficient antibacterial agent.

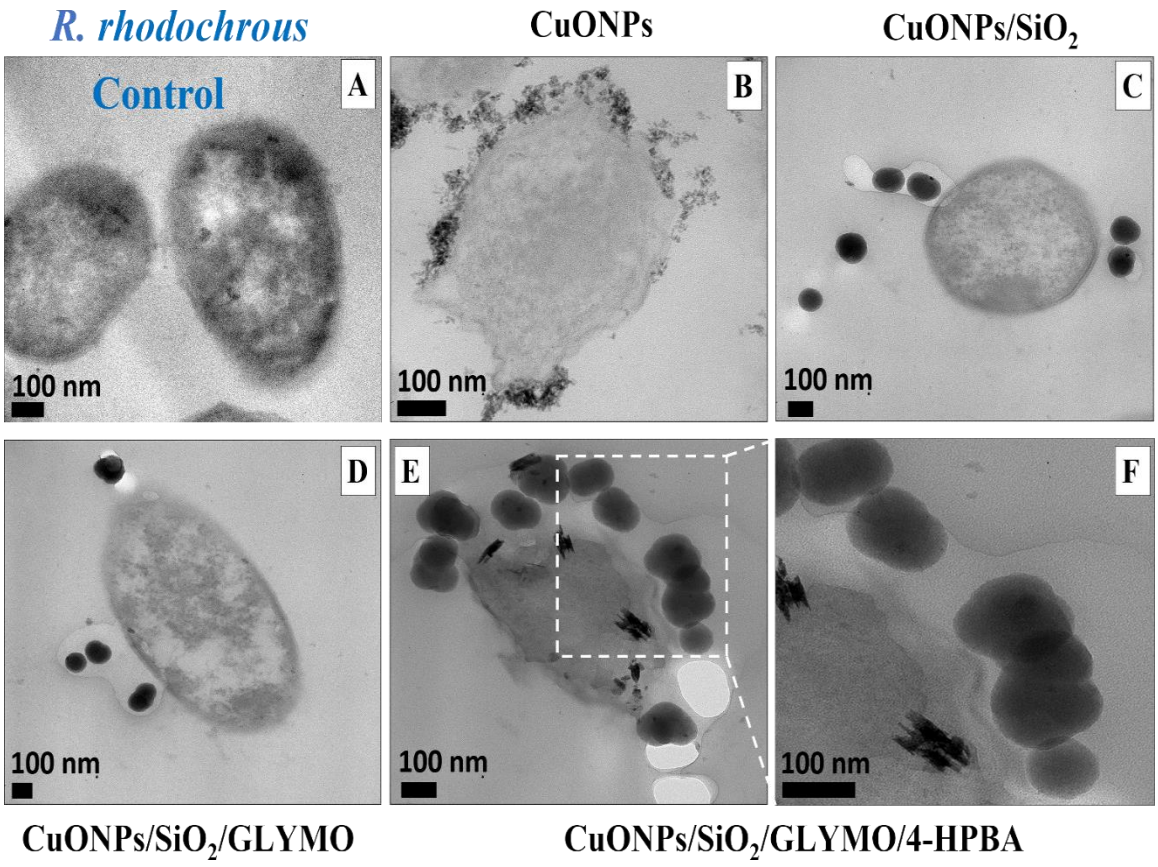


**Figure 9.12.** TEM images of *R. rhodochrous* after being incubated for 6 h into 25 µg $mL^{-1}$ bare and surface functionalized of CuONPs: (A) an untreated sample without CuONPs (B) *R. rhodochrous* incubated with CuONPs (C) *R. rhodochrous* incubated with CuONPs/$SiO_2$ (D) *R. rhodochrous* incubated with CuONPs/$SiO_2$/GLYMO and (E and F) *R. rhodochrous* incubated with CuONPs/$SiO_2$/GLYMO/4-HPBA.

## 9.6 Antibacterial activity of surface functionalized smooth $SiO_2$NPs against *R. rhodochrous.*

Antibacterial activity experiments were conducted through the incubation of suspensions of various particle concentrations of smooth $SiO_2$NPs, smooth $SiO_2$NPs/GLYMO and smooth $SiO_2$NPs/GLYMO/4-HPBA with *R. rhodochrous.* The data in Figure 9.13A-9.13D show a very low antibacterial activity on the *R. rhodochrous* cells upon incubation with series of suspensions of various particle concentrations of bare $SiO_2$NPs, $SiO_2$NPs/GLYMO and $SiO_2$NPs/GLYMO/4-HPBA at room temperature. At 6-24 hours exposure time, the percentage of *R. rhodochrous* viability was reduced in the case of smooth $SiO_2$NPs/GLYMO/4-HPBA particles at concentrations in the range 25-2000 µg $mL^{-1}$. In contrast, the *R. rhodochrous* viability with bare $SiO_2$NPs and $SiO_2$NPs/GLYMO was higher than that for $SiO_2$NPs/GLYMO/4-HPBA for the same concentrations and exposure times. These results indicate that surface-smooth silica nanoparticles (see Figure 9.7C and 9.7D) do not apparently affect the viability of the *R. rhodochrous* for the duration of these incubation experiments. This was also confirmed by the TEM images (Figure 9.14A and 9.14B).

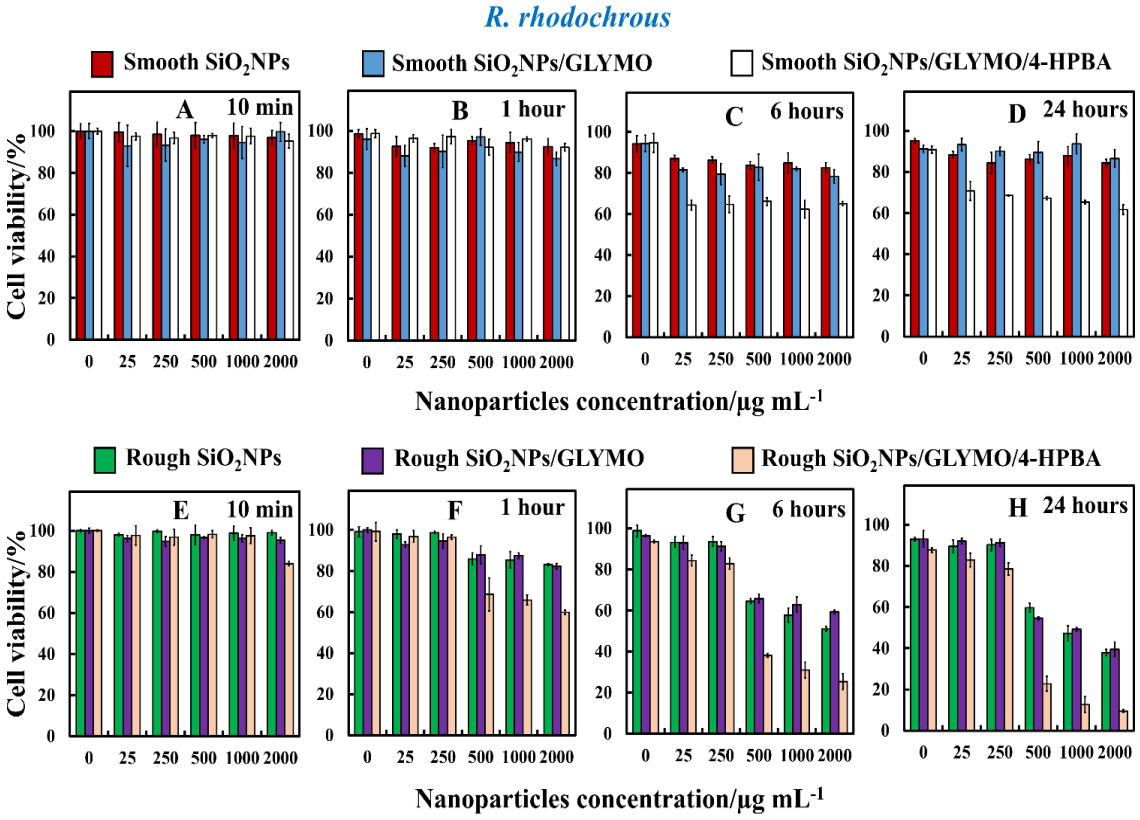


**Figure 9.13.** Cell viability of *R. rhodochrous* as a function of nanoparticle concentration with (A-D) smooth $SiO_2$NPs, $SiO_2$NPs/GLYMO and $SiO_2$NPs/GLYMO/4-HPBA. (E-H)

Cell viability of *R. rhodochrous* upon incubation of bare and surface functionalized rough $SiO_2$NPs of different particle concentrations. The incubation times were (A, E) 10 min, (B,F) 1 h, (C,G) 6 h and (D, H) 24 h, respectively.

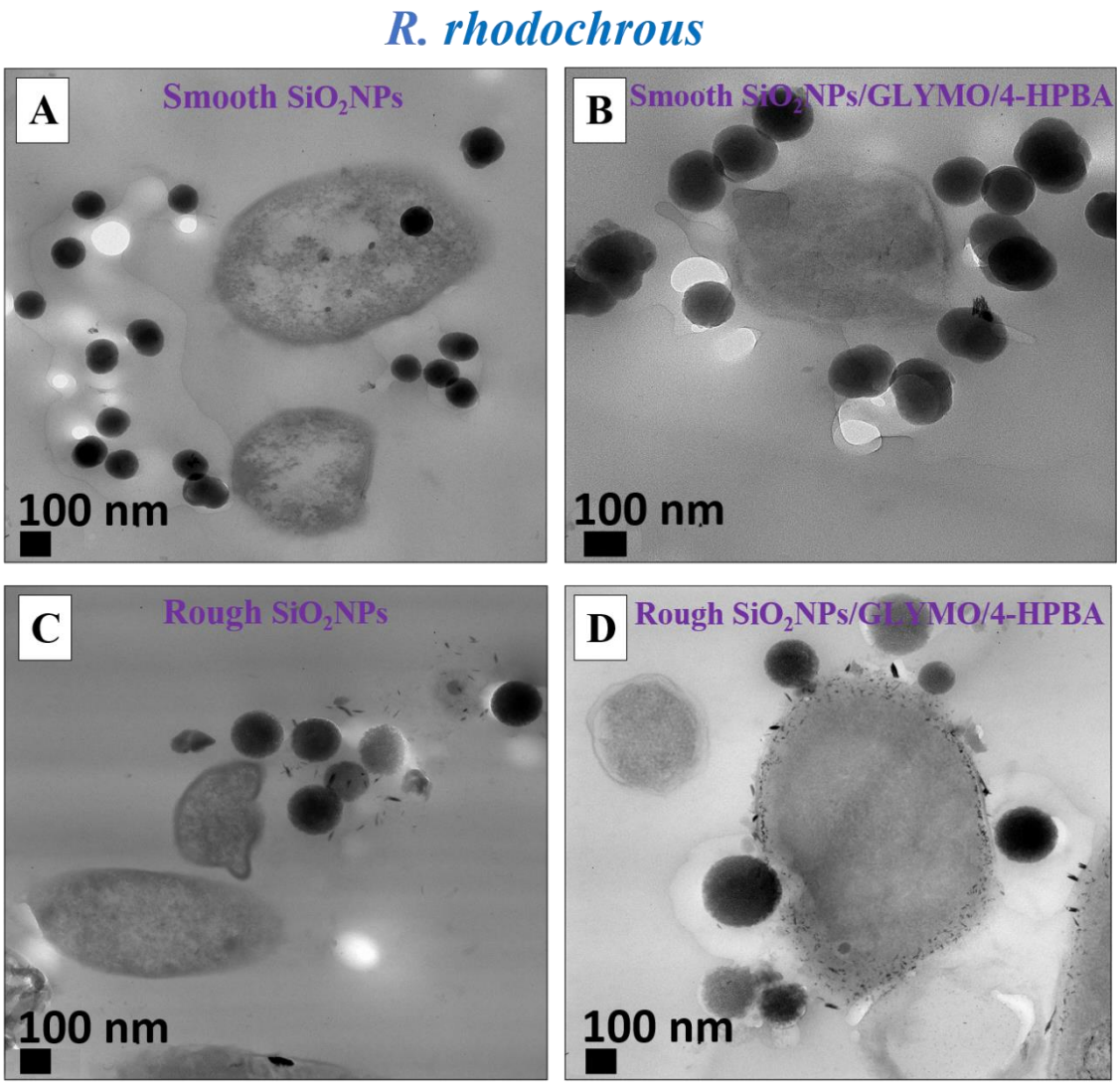


**Figure 9.14.** TEM images of *R. rhodochrous* after being incubated for 6 h into bare and surface functionalized of $SiO_2$NPs: (A) *R. rhodochrous* after treatment with 500 µg $mL^{-1}$ of smooth $SiO_2$NPs (B) *R. rhodochrous* after treatment with 500 µg $mL^{-1}$ of smooth $SiO_2$NPs/GLYMO/4-HPBA (C) *R. rhodochrous* after treatment with 500 µg $mL^{-1}$ of mesoporous surface-rough 'ghost' $SiO_2$NPs and (D) *R. rhodochrous* after treatment with 500 µg $mL^{-1}$ of 'ghost' $SiO_2$NPs/GLYMO/4-HPBA.

## 9.7 Antibacterial activity of surface functionalized rough $SiO_2$NPs and smooth $SiO_2$NPs on *R.rhodochrous*.

The viability of the *R. rhodochrous* was studied after treatment with surface functionalized rough $SiO_2$NPs produced using two different catalysts, $NH_4OH$ and NaOH, in the Stöber process, respectively. Figure 9.13E-9.13H compares the effect of bare rough $SiO_2$NPs and surface-functionalized rough $SiO_2$NPs with GLYMO and 4-HPBA at different particle concentrations on the *R. rhodochrous* viability. Both functionalized $SiO_2$NPs particles in this experiment were produced using $NH_4OH$ as catalyst. We incubated samples of *R. rhodochrous* with dispersed rough $SiO_2$NPs (bare and functionalized with GLYMO and GLYMO/4-HPBA) at fixed particle concentrations (0, 25, 250, 500, 1000 and 2000 μg $mL^{-1}$) for different periods of exposure up to 24 h. The data in Figure 9.13E-9.13H reveal that no measurable change in the *R. rhodochrous* cell viability was observed for both rough $SiO_2$NPs and rough $SiO_2$NPs/GLYMO at 250 μg $mL^{-1}$ particle concentrations. We did not detect significant difference between the rough $SiO_2$NPs and rough $SiO_2$NPs/GLYMO at the same particle concentration. For longer incubation times, however, the rough $SiO_2$NPs/GLYMO/4-HPBA showed significant antibacterial activity on *R. rhodochrous* at 500, 1000, 2000 μg $mL^{-1}$ particle concentrations (Figure 9.13F-9.13H). The attachment of rough $SiO_2$NPs/GLYMO/4-HPBA to the bacteria was examined by TEM imaging (Figure 9.14D). The TEM images confirm that the nanoparticles do not transfer in to the bacteria, rather than accumulate on their cell walls. However, the estimates show that at the silica NPs concentration of 500 μg $mL^{-1}$ and $10^6$ bacteria per mL, where the antibacterial effect of the ghost nanoparticles starts to manifests itself, the ratio between NPs and cells is nearly ~430,000, i.e. vastly in favor of the NPs. Hence not all NPs attach to the bacteria. The revealed mechanism of action, however, implies that even a single rough silica NP can pierce the bacterial cell membrane. The antibacterial activity of 4-HPBA-functionalized rough $SiO_2$NPs (made with NaOH as a catalyst) on *R. rhodochrous* was also tested as shown in Figure 9.15.

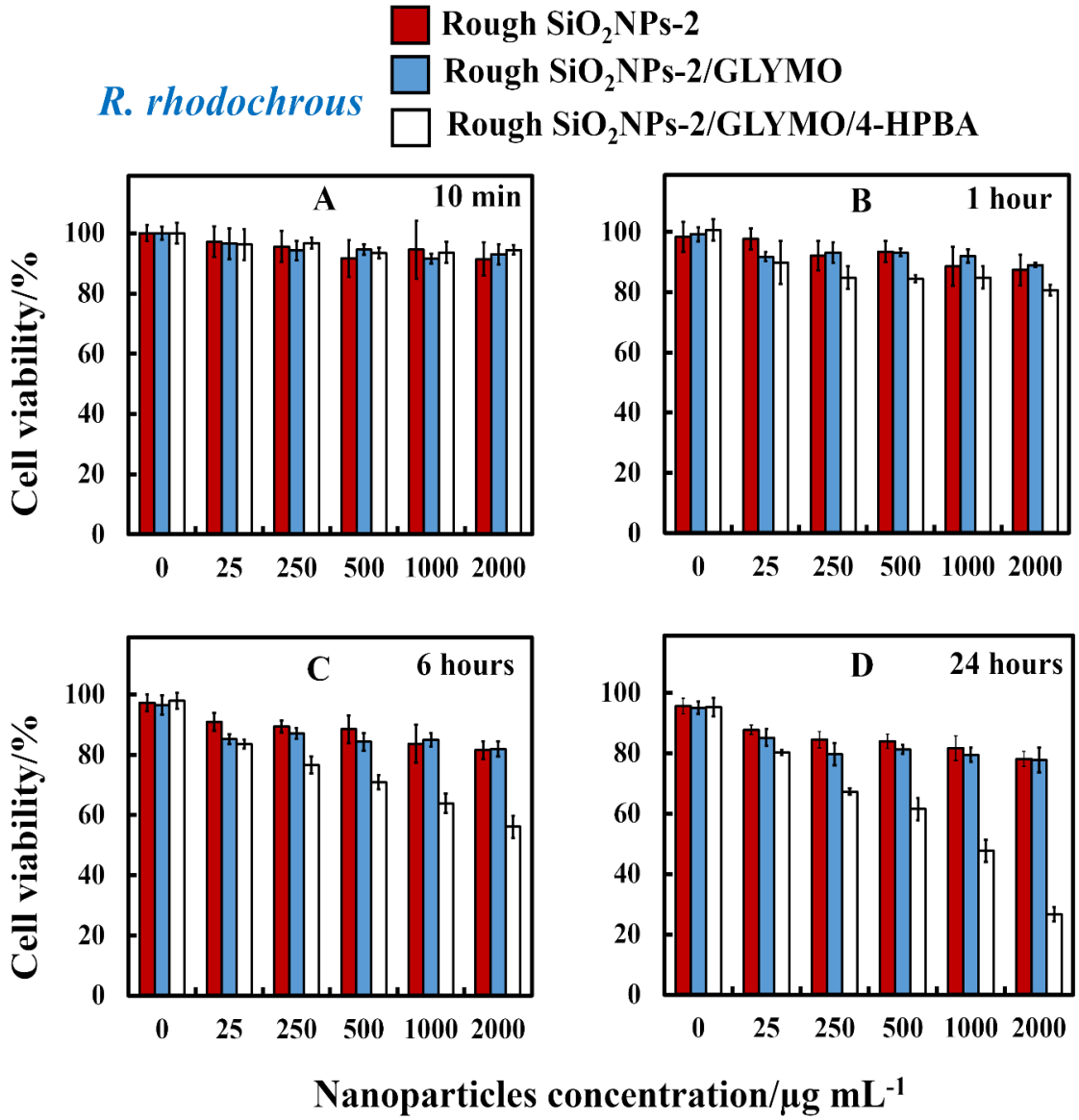


**Figure 9.15.** Representative the cell viability of *R. rhodochrous* upon incubation of bare and surface functionalized of rough $SiO_2$NPs-2 of different particle concentrations. The *R. rhodochrous* cells were incubated with the rough $SiO_2$NPs-2, rough $SiO_2$NPs-2/GLYMO and rough $SiO_2$NPs-2/GLYMO/4-HPBA at 10 min, 1 hour, 6 hours and 24 hours of exposure times.

The data in Figure 9.15 show similar antibacterial trends to those observed with rough $SiO_2$NPs prepared with ammonia as a catalyst (Figure 9.13E-9.13H). They also show that the rough $SiO_2$NPs/GLYMO/4-HPBA has a strong antibacterial effect on *R. rhodochrous* at 2000 µg $mL^{-1}$ particle concentration. A plausible explanation for this result is that the surface morphology of the rough $SiO_2$NPs/GLYMO/4-HPBA forces the cell membrane of the bacteria to closely follow its topology due to formation of covalent bonds between

the cis-diols groups on the cell membrane surface and the 4-hydroxyphenylboronic acid terminal groups on the particle surface. The adhesion of the rough nanoparticles to the cells due to formation of strong reversible boronic esters with carbohydrates and glycoprotein molecules which are abundant on the *R. rhodochrous* cell wall leads to dislocation of the bacterial membrane which kills the bacteria. Note also, that the free GLYMO or 4-HPBA reagents do not show any antibacterial activity at concentrations up to 2000 μg $mL^{-1}$ (see Figure 9.16).

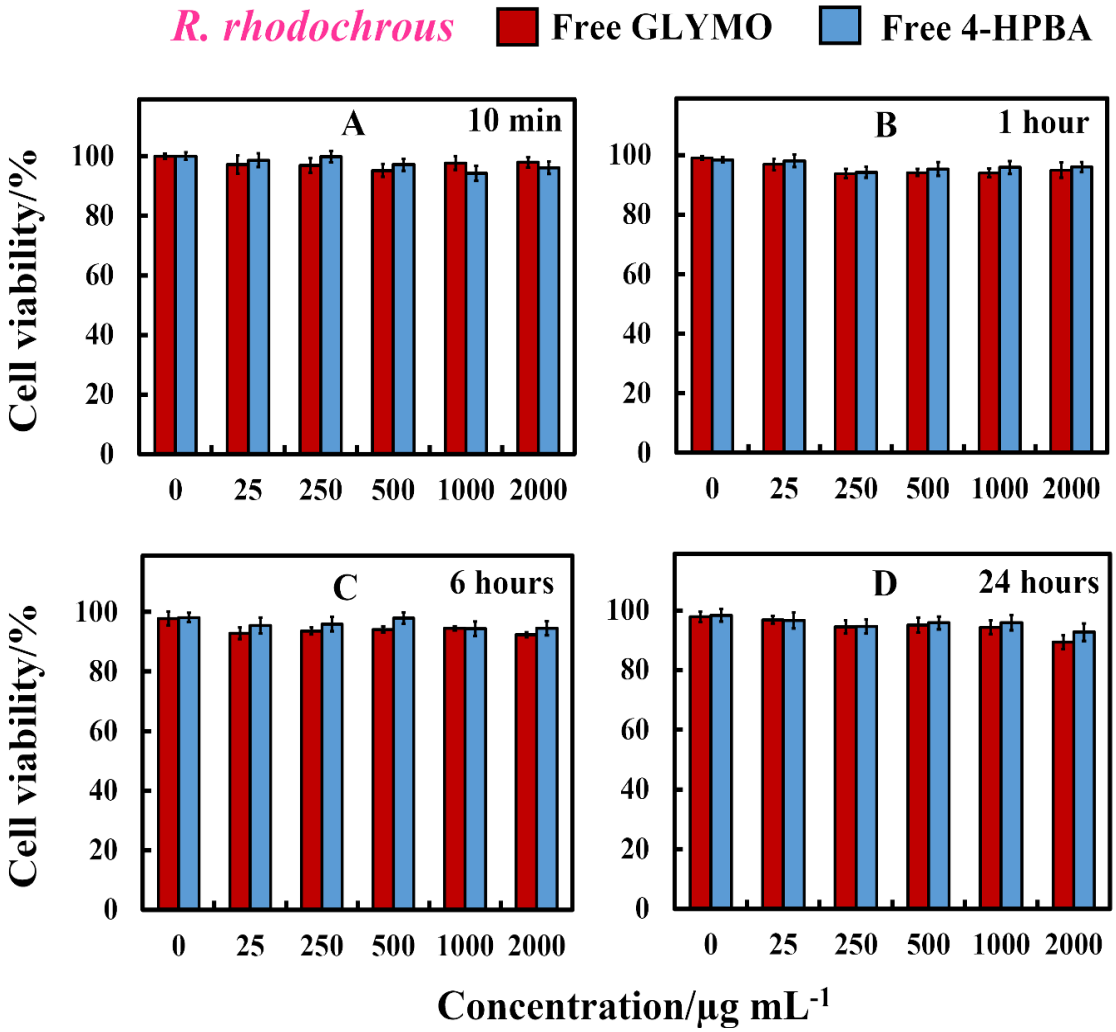


**Figure 9.16.** The antibacterial activity of free GLYMO and 4-HPBA at various concentrations (0, 25, 250, 500, 1000 and 2000 μg $mL^{-1}$) on *R. rhodochrous*. The *R. rhodochrous* was incubated with the GLYMO and 4-HPBA at 10 min, 1 h, 6 h and 24 h of exposure before being washed and tested for their cell viability.

The antibacterial activity of both bare (non-functionalized) and surface functionalized smooth and rough $SiO_2$NPs with GLYMO and 4-HPBA on *R. rhodochrous* was compared

in order to determine whether the surface roughness of the 'ghost' $SiO_2$NPs, that mimics the one of the original (host) CuONPs, could enhance their antibacterial activity. Figure 9.17 compares the *R. rhodochrous* viability upon incubation with HPBA-functionalized $SiO_2$NPs and bare $SiO_2$NPs with the same concentration of nanoparticles. The HPBA-functionalized rough $SiO_2$NPs shows much higher antibacterial efficiency against *R. rhodochrous* than both the bare $SiO_2$NPs and GLYMO-functionalized $SiO_2$NPs at the same conditions. The reason behind this is the rough surface morphology of the $SiO_2$NPs which when covalent bonding between rough $SiO_2$NPs/GLYMO/4-HPBA and the cell membrane cause membrane disruptions which kill the *R. rhodochrous*.

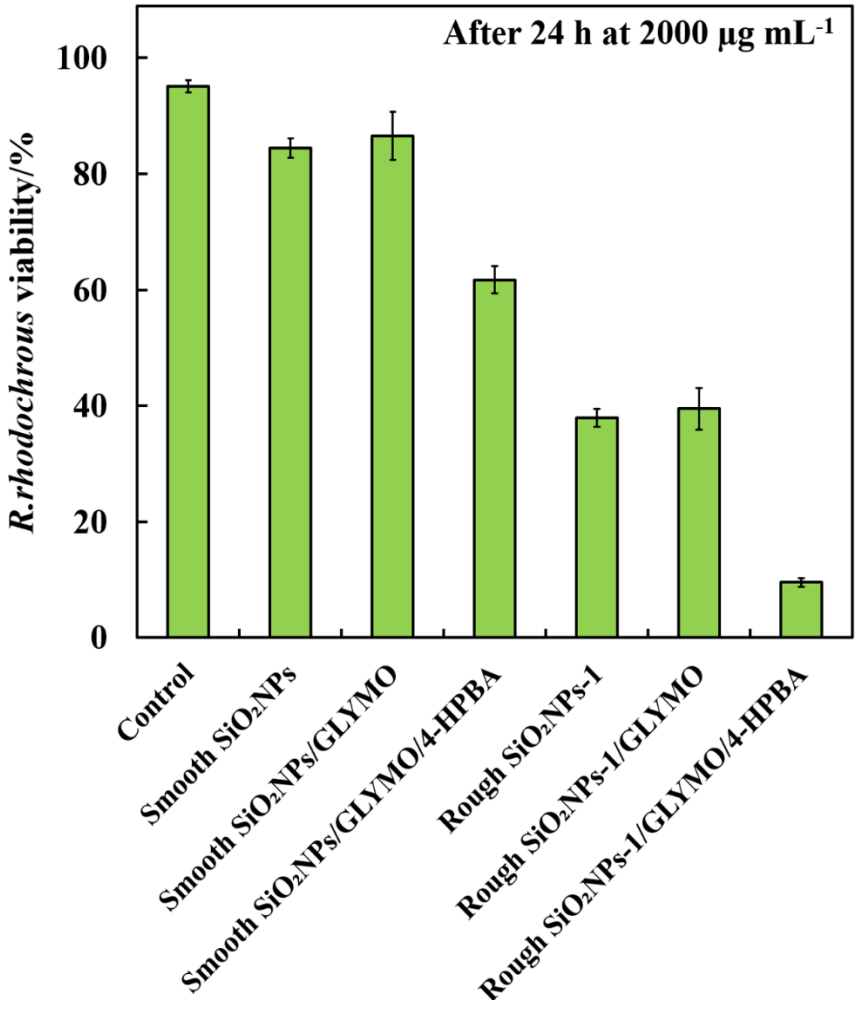


**Figure 9.17.** Comparison of the *R. rhodochrous* viability at 2000 µg $mL^{-1}$ concentration of the bare and surface functionalized smooth and rough $SiO_2$NPs with GLYMO and 4-HPBA at 24 h of exposure time.

## 9.8 Cytotoxicity of bare and HPBA-functionalized $SiO_2$NPs on human keratinocytes.

The action of HPBA-functionalized $SiO_2$NPs towards human keratinocyte cell was tested. Figure 9.18 shows the cytotoxicity assay of smooth and rough $SiO_2$NPs and $SiO_2$NPs/GLYMO/HPBA on HaCaT cells for up to 24 hours of exposure. The results confirm that bare $SiO_2$NPs and $SiO_2$NPs/GLYMO/HPBA have negligible toxic effect on these cells irrespective of the particle roughness. These results are obtained with particle concentrations where they are showing very strong antibacterial effect on *R. rhodochrous* (see Figure 9.17) while leaving the keratinocyte cells unaffected. One possible explanation why the skin cells are unaffected by both the bare and the functionalized $SiO_2$NPs could be that their membrane is easier to bend around the adhering rough nanoparticles and is less prone to dislocation and rupture than the rigid membranes of bacteria.[47] This result is reassuring that such antimicrobial particles can potentially find application in wound care formulations as an alternative to antimicrobial delivery vehicles.[35, 36]

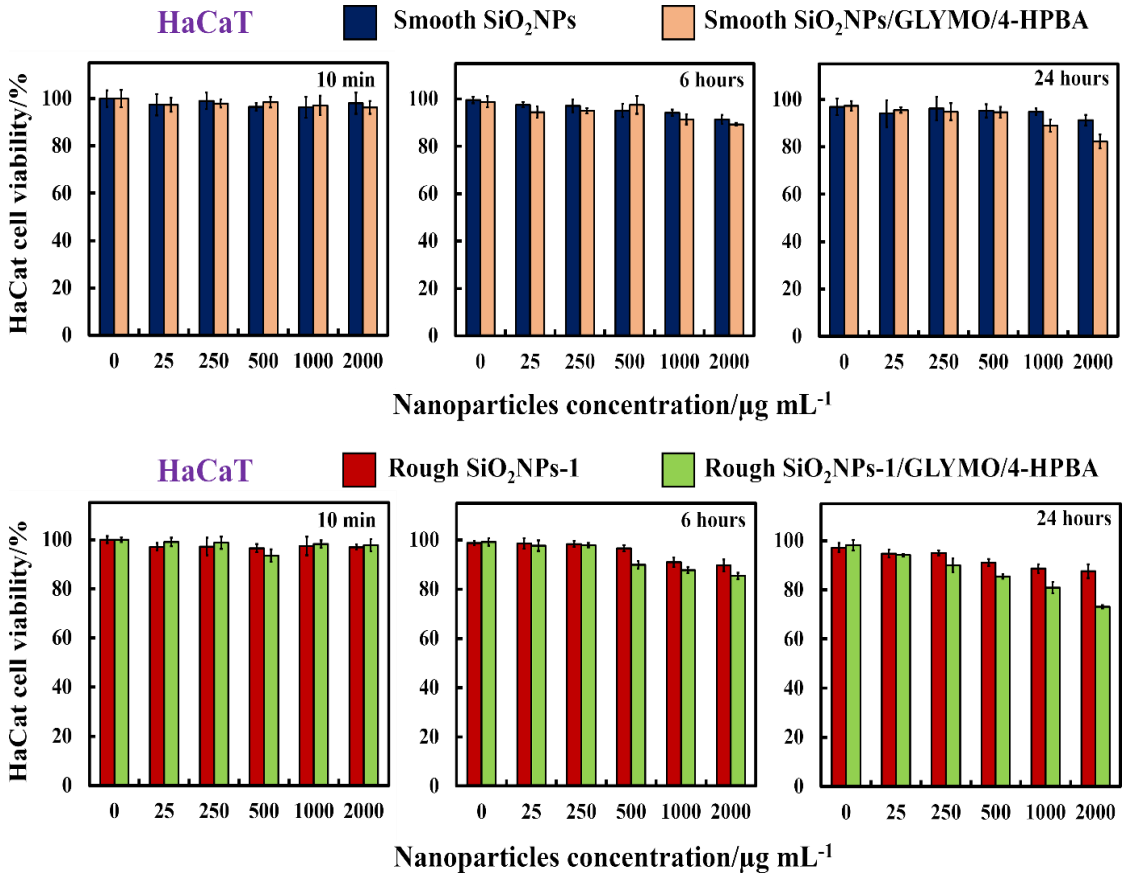


**Figure 9.18.** HaCaT cell viability after incubation as a function of nanoparticle concentration for up to 24 hours at with bare and surface functionalized $SiO_2$NPs with GLYMO and 4-HPBA.

## 9.9 Conclusions

Controlling the surface morphology of silica particles at the nanoscale has been a challenge in the field of nanotechnology. Here, a method to create a rough silica layer was developed on the CuONPs as templates. The results from TEM analysis confirmed that the silica layer was coated on the CuONPs. The diameter of CuONPs/$SiO_2$ was increased, corresponding to a 25 ± 5 nm thick $SiO_2$ layer on the CuONPs, and the surface of CuONPs/$SiO_2$ became rough. CuONPs/$SiO_2$ were dispersed in the $HNO_3$ and EDTA solution to remove templates exhaustively. EDX results showed that the absence of CuONPs trapped inside the silica after treatment with $HNO_3$, indicating complete removal of CuONPs. EDX data showed only two main peaks consisting of Si and O components with no peaks of copper. It was demonstrated that by surface grafting of GLYMO and 4-HPBA on surface-rough $SiO_2$NPs can produce formulations which are several times more effective against *R. rhodochrous* compared to bare $SiO_2$NPs at the same conditions and particle concentration. The 4-HPBA coating produces a surface functionality that allows the $SiO_2$NPs particles to reversibly form covalent bonds with the diol groups from glycoproteins and carbohydrates expressed on the cell wall of *R. rhodochrous*. Antibacterial tests showed that the anionic surface-rough $SiO_2$NPs/GLYMO/4-HPBA have much higher antibacterial action than the bare smooth and rough $SiO_2$NPs. This is explained by the strong covalent binding of the anionic particles surface-rough $SiO_2$NPs/GLYMO/4-HPBA to the cell walls due to formation of boronic ester bonds between 4- Hydroxyphenylboronic acid and diol groups from carbohydrates on the cell surface. In this Chapter, a brand new family of antibacterial property made from biocompatibility material ($SiO_2$NPs) were reported which has totally different compared with the CuONPs described in the previous Chapter. The results imply that the combination of adhesive particle-cell interactions with surface-rough morphology transferred from the "host" CuONPs to the apparently benign $SiO_2$NPs by templating produced "ghost" $SiO_2$NPs with significant "host-intertied" antibacterial effect. No other study in the present literature has demonstrated such a universal action of surface roughness 'ghost' $SiO_2$NPs functionalized with GLYMO and 4-HPBA as in this Chapter. The incubation of the HPBA-functionalized $SiO_2$NPs with human keratinocytes was also studied which surprisingly showed no measurable cytotoxicity. This type of functionality showed good antibacterial activity against *R. rhodochrous*; thus, surface grafting of GLYMO and 4-HPBA on surface-rough $SiO_2$NPs could be used as an antibacterial agent in many fields.

## 9.10 References


1. H. Palza, *International journal of molecular sciences*, 2015, **16**, 2099-2116.
2. A. F. Halbus, T. S. Horozov and V. N. Paunov, *ACS Applied Materials & Interfaces*, 2019, **11**, 12232–12243.
3. A. F. Halbus, T. S. Horozov and Vesselin N. Paunov, *Nanoscale Advances*, 2019, **1**, 2323 – 2336.
4. A. F. Halbus, T. S. Horozov and V. N. Paunov, *Advances in colloid and interface science*, 2017, **249**, 134-148.
5. S. S. M. Al-Obaidy, A. F. Halbus, G. M. Greenway and V. N. Paunov, *Journal of Materials Chemistry B*, 2019, **7**, 3119-3133.
6. R. Brayner, S. A. Dahoumane, C. Yepremian, C. Djediat, M. Meyer, A. Coute and F. Fievet, *Langmuir*, 2010, **26**, 6522-6528.
7. H. Zhang, B. Chen and J. F. Banfield, *The Journal of Physical Chemistry C*, 2010, **114**, 14876-14884.
8. J. Liu, D. M. Aruguete, M. Murayama and M. F. Hochella Jr, *Environmental science & technology*, 2009, **43**, 8178-8183.
9. Y. Zhang, Y. Chen, P. Westerhoff, K. Hristovski and J. C. Crittenden, *Water research*, 2008, **42**, 2204-2212.
10. A. R. Petosa, D. P. Jaisi, I. R. Quevedo, M. Elimelech and N. Tufenkji, *Environmental science & technology*, 2010, **44**, 6532-6549.
11. K. Tiede, M. Hassellöv, E. Breitbarth, Q. Chaudhry and A. B. Boxall, *Journal of Chromatography A*, 2009, **1216**, 503-509.
12. V. H. Grassian, *The Journal of Physical Chemistry C*, 2008, **112**, 18303-18313.
13. Z. Abbas, C. Labbez, S. Nordholm and E. Ahlberg, *The Journal of Physical Chemistry C*, 2008, **112**, 5715-5723.
14. C. Rao, G. Kulkarni, P. J. Thomas and P. P. Edwards, *Chemistry–A European Journal*, 2002, **8**, 28-35.
15. J.-P. Jolivet, C. Froidefond, A. Pottier, C. Chanéac, S. Cassaignon, E. Tronc and P. Euzen, *Journal of Materials Chemistry*, 2004, **14**, 3281-3288.
16. Q. Zhao, T. Xie, L. Peng, Y. Lin, P. Wang, L. Peng and D. Wang, *The Journal of Physical Chemistry C*, 2007, **111**, 17136-17145.
17. S. E. McNeil, *Journal of Leukocyte Biology*, 2005, **78**, 585-594.
18. S.-W. Bian, I. A. Mudunkotuwa, T. Rupasinghe and V. H. Grassian, *Langmuir*, 2011, **27**, 6059-6068.

19. S. Parham, D. H. Wicaksono, S. Bagherbaigi, S. L. Lee and H. Nur, *Journal of the Chinese Chemical Society*, 2016, **63**, 385-393.
20. G. Fu, P. S. Vary and C.-T. Lin, *The Journal of Physical Chemistry B*, 2005, **109**, 8889-8898.
21. S. Makhluf, R. Dror, Y. Nitzan, Y. Abramovich, R. Jelinek and A. Gedanken, *Advanced Functional Materials*, 2005, **15**, 1708-1715.
22. C. Kaweeteerawat, A. Ivask, R. Liu, H. Zhang, C. H. Chang, C. Low-Kam, H. Fischer, Z. Ji, S. Pokhrel and Y. Cohen, *Environmental science & technology*, 2015, **49**, 1105-1112.
23. M. J. Al-Awady, G. M. Greenway and V. N. Paunov, *RSC Advances*, 2015, **5**, 37044-37059.
24. K. M. Reddy, K. Feris, J. Bell, D. G. Wingett, C. Hanley and A. Punnoose, *Applied physics letters*, 2007, **90**, 213902.
25. C. Lee, J. Y. Kim, W. I. Lee, K. L. Nelson, J. Yoon and D. L. Sedlak, *Environmental science & technology*, 2008, **42**, 4927-4933.
26. P. Sahoo, P. S. Murthy, S. Dhara, V. Venugopalan, A. Das and A. Tyagi, *Journal of nanoparticle research*, 2013, **15**, 1841.
27. K.-Y. Yoon, J. H. Byeon, J.-H. Park and J. Hwang, *Science of the Total Environment*, 2007, **373**, 572-575.
28. G. Singh, E. M. Joyce, J. Beddow and T. J. Mason, *The Journal of Microbiology, Biotechnology and Food Sciences*, 2012, **2**, 106.
29. C. M. Goodman, C. D. McCusker, T. Yilmaz and V. M. Rotello, *Bioconjugate chemistry*, 2004, **15**, 897-900.
30. T. Silva, L. R. Pokhrel, B. Dubey, T. M. Tolaymat, K. J. Maier and X. Liu, *Science of the total environment*, 2014, **468**, 968-976.
31. A. Simon-Deckers, S. Loo, M. Mayne-L'hermite, N. Herlin-Boime, N. Menguy, C. Reynaud, B. Gouget and M. Carriere, *Environmental science & technology*, 2009, **43**, 8423-8429.
32. X. Xiao, G. A. Montaño, T. L. Edwards, A. Allen, K. E. Achyuthan, R. Polsky, D. R. Wheeler and S. M. Brozik, *Langmuir*, 2012, **28**, 17396-17403.
33. Y. Roiter, M. Ornatska, A. R. Rammohan, J. Balakrishnan, D. R. Heine and S. Minko, *Langmuir*, 2009, **25**, 6287-6299.

34. M. Mathelié-Guinlet, L. Béven, F. Moroté, D. Moynet, C. Grauby-Heywang, I. Gammoudi, M.-H. Delville and T. Cohen-Bouhacina, *Advances in colloid and interface science*, 2017, **245**, 81-91.
35. M. J. Al-Awady, A. Fauchet, G. M. Greenway and V. N. Paunov, *Journal of Materials Chemistry B*, 2017, **5**, 7885-7897.
36. M. J. Al-Awady, P. J. Weldrick, M. J. Hardman, G. M. Greenway and V. N. Paunov, *Materials Chemistry Frontiers*, 2018.
37. S. S. Al-Obaidy, G. M. Greenway and V. N. Paunov, *Nanoscale Advances*, 2019.
38. W. Tan, K. Wang, X. He, X. J. Zhao, T. Drake, L. Wang and R. P. Bagwe, *Medicinal research reviews*, 2004, **24**, 621-638.
39. Y. Wang, Q. Zhao, N. Han, L. Bai, J. Li, J. Liu, E. Che, L. Hu, Q. Zhang and T. Jiang, *Nanomedicine: Nanotechnology, Biology and Medicine*, 2015, **11**, 313-327.
40. M. T. Pham, T. Van Nguyen, T. D. V. Thi, H. L. N. Thi, K. T. Tong, T. T. Tran, V. H. Chu, J.-C. Brochon and H. N. Tran, *Advances in Natural Sciences: Nanoscience and Nanotechnology*, 2012, **3**, 045013.
41. Z. Guo, J. Xue, T. Liu, X. Song, Y. Shen and H. Wu, *Micro & Nano Letters*, 2014, **9**, 210-214.
42. D. Molina-Manso, M. Manzano, J. C. Doadrio, G. Del Prado, A. Ortiz-Pérez, M. Vallet-Regí, E. Gómez-Barrena and J. Esteban, *International journal of antimicrobial agents*, 2012, **40**, 252-256.
43. E. Yu, I. Galiana, R. Martínez-Máñez, P. Stroeve, M. D. Marcos, E. Aznar, F. Sancenón, J. R. Murguía and P. Amorós, *Colloids and Surfaces B: Biointerfaces*, 2015, **135**, 652-660.
44. M. Ruiz-Rico, C. Fuentes, É. Pérez-Esteve, A. I. Jiménez-Belenguer, A. Quiles, M. D. Marcos, R. Martínez-Máñez and J. M. Barat, *Food Control*, 2015, **56**, 77-85.
45. X. Du and J. He, *ACS applied materials & interfaces*, 2011, **3**, 1269-1276.
46. A. P. De Silva, H. N. Gunaratne, T. Gunnlaugsson, A. J. Huxley, C. P. McCoy, J. T. Rademacher and T. E. Rice, *Chemical reviews*, 1997, **97**, 1515-1566.
47. J. Penders, M. Stolzoff, D. J. Hickey, M. Andersson and T. J. Webster, *International journal of nanomedicine*, 2017, **12**, 2457.

# Chapter 10

# 10. Summary of the thesis and future work

## 10.1 Summary of the thesis

Nanotechnology offers unconventional approaches for fighting microbes that do not rely on the existing pathways of antibiotic action. This makes possible to address the challenge of antimicrobial resistance by using nanoparticles with engineered antimicrobial action designed to target specific pathogens. There is a lot of ongoing work on several classes of inorganic colloid particles of added functionality, which exhibit strong and universal antibacterial, antifungal and antiviral action towards which microbes have not been able to develop resistance. The mechanisms by which such nanoparticles attack microbial cells or inhibit their growth include the generation of reactive oxygen species (ROS) upon irradiation with UV light, cell membrane disruption due to the NPs cationic surface, ROS scavenging, emission of heavy ions, as $Cu^{2+}$ on the cell surface, etc. Various strategies have recently been pursued in search of antimicrobial agents based on natural as well as synthetic nanoparticles. The latter include nanoparticles synthesised from various metals oxides, e.g. copper, zinc, as well as low soluble metal hydroxides, as $Mg(OH)_2$. These inorganic nanoparticles have very different mechanisms of antimicrobial activity and can retain their antimicrobial action in a range of adverse conditions. Smaller nanoparticles usually show greater antimicrobial activity due to larger surface-to-volume ratio in suspension and greater area of contact with targeted microbial cells. However, significant research effort is needed to carefully test their side effects, environmental impact and potential nanotoxicity before nanoparticles can be safely and broadly used as efficient substitutes of conventional antimicrobials. The work presented in the thesis contributes to this field as summarised below.

In Chapter 3 and 4, a range of zinc oxide nanoparticles of various crystallite size was prepared via direct precipitation method after calcining at various temperatures ranging from 100-600$^{o}$C and characterised in terms of their surface charge and average hydrodynamic diameter in aqueous suspensions. The toxicity impact of the ZnONPs on microalgae and yeast was examined. Results in present work indicate that ZnONPs had substantial toxicity impact against yeast and microalgae cells and the toxicity increased upon increasing the concentration of ZnONPs. In addition, illumination of the microalgae

and yeast cells under visible and UV light had a bigger effect on their viability in the presence of ZnONPs compared with the same experiments carried out in dark conditions. It can be concluded that ZnONPs at concentrations above 1 μg $mL^{-1}$ for 6 hours exposure time noticeably impact the microalgae viability while ZnONPs concentrations more than 100 μg $mL^{-1}$ led to complete damage of cells. The results also demonstrated a decline in the chlorophyll content after 6 hours incubation to ZnONPs in visible and UV light conditions. This showed that ZnONPs could not only damage the cell membranes as well as can interfere with the cell chloroplasts. Zinc sulfide, silica and polyelectrolyte-coated ZnONPs of alternating charge were also produced and their nanotoxicity on microalgae and yeast was studied. It was found that ZnONPs/ZnS, ZnONPs/$SiO_2$ and anionic nanoparticles as ZnONPs/PSS showed much lower nanotoxicity than the cationic bare ZnONPs and ZnONPs/PSS/PAH, respectively. This can be explained that the weak adhesion of the ZnONPs/ZnS, ZnONPs/PSS and ZnONPs/$SiO_2$ to the cell walls because of their electrostatic repulsion while in the case of cationic ZnONPs or PAH-modified ZnONPs was the strong adhesion between the particle and cell membranes, which cause damage to cells. These results were supported by SEM and TEM images of sectioned cells.

Chapter 5 and 6 consider $Mg(OH)_2$NPs which, according to the literature, have high antimicrobial activity at moderate to high particle concentrations. Since $Mg(OH)_2$ is a nontoxic material which has been broadly used in medical and food industries, the $Mg(OH)_2$NPs have great application potential as a new antimicrobial agent. Various ways to control the antimicrobial activity and cytotoxicity of a range of bare and surface-modified $Mg(OH)_2$NPs were studied on three different types of microbial cells: microalgae, yeast and bacteria. The antimicrobial activity of the $Mg(OH)_2$NPs on *S. cerevisiae*, *C. reinhardtii* and *E.coli* was examined. This work confirms that bare $Mg(OH)_2$NPs are effective antimicrobial agents. The results from TEM and SEM analysis showed that direct contact between the $Mg(OH)_2$NPs and the cell membrane of *S. cerevisiae*, *C. reinhardtii* and *E.coli* is very important for their effective antimicrobial action. In order to evaluate the role of the surface coating, a series of polyelectrolyte-coated $Mg(OH)_2$NPs were likewise synthesised using the layer by-layer technique and their antimicrobial activity towards *S. cerevisiae*, *C. reinhardtii* and *E.coli* was compared with that of bare $Mg(OH)_2$NPs. It was discovered that the antimicrobial activity of the coated $Mg(OH)_2$NPs alternates with their surface charge. The anionic nanoparticles ($Mg(OH)_2$NPs/PSS) have much lower antibacterial activity than the cationic ones

($Mg(OH)_2$NPs/PSS/PAH and bare $Mg(OH)_2$NPs). These can bring important insights how the antimicrobial properties of $Mg(OH)_2$NPs and other inorganic nanoparticles can be controlled by designing nanoparticle surface coatings that promote their adhesion to the microbial cell walls as well as by taking into account the nanoparticles surface morphology. $Mg(OH)_2$NPs have been studied for their antimicrobial properties by other but no effect of the surface charge of the particles have been examined on their efficiency. As $Mg(OH)_2$NPs is a cationic material of IEP 11.7, it is positively charged over a very wide range of pH. Therefore here the toxicity of $Mg(OH)_2$NPs was explored against three different microorganisms after surface modification with different polyelectrolytes to examine this dependence. This has never been done before for $Mg(OH)_2$NPs nor has the mechanism of antimicrobial action been commented for different surface charge of the particles, as it was done in Chapter 5 and 6.

In Chapter 7 and 8, a novel type of modified CuONPs has been developed by functionalizing the NPs with GLYMO and 4-HPBA (CuONPs/GLYMO/4-HPBA) to produce an antibacterial agent of much higher efficiency than bare CuONPs. This novel coating with boronic acid functionality allows the antimicrobial particles to form covalent bonds with the diol groups from carbohydrates expressed on the cell wall of both Gram-positive, Gram–negative, *C.reinhardtii* and *S. cerevisiae* cells. The profound differences in the surface properties of the bare CuONPs and the CuONPs/GLYMO/4-HPBA particles were demonstrated which at neutral pH have a different surface charge. The zeta potential of non-functionalized CuONPs, GLYMO-functionalized CuONPs and 4-HPBA-functionalized CuONPs at pH 6 was +37 mV, -3 mV and -10 mV, respectively. Antibacterial assays showed that the anionic nanoparticles as CuONPs/GLYMO/4-HPBA have much higher antibacterial action than the cationic ones non-functionalized CuONPs for both Gram-positive, Gram-negative, *C.reinhardtii* and *S. cerevisiae* cells. This is explained by the strong adhesion of the anionic particles CuONPs/GLYMO/4-HPBA to the cell walls due to their covalent interactions between the terminal 4-Hydroxyphenylboronic acid group and carbohydrates on the cell surface. SEM and TEM images of *R. rhodochrous, E.coli, C.reinhardtii* and *S. cerevisiae* cells exposed to 4-HPBA functionalized CuONPs confirmed the formation of a significant build-up of these nanoparticles on the bacterial cell outer membrane. Control experiments proved that the binding ability of the modified CuONPs/GLYMO/4-HPBA to bacteria can be adjusted and reversed by adding glucose in the media which engages the boronic acid groups of the CuONPs surface and lessens their ability to attach to bacteria. This effect allows for

a direct control over their antimicrobial action. Preliminary experiments of incubation of the HPBA-functionalized CuONPs with human keratinocytes showed no measurable cytotoxicity. In general, it can be envisaged that this type of functionality can be successfully applied to a range of inorganic nanoparticles, as ZnONPs, $TiO_2$NPs, $Ag_2$ONPs, $Cu_2$ONPs and others which would lead to fabrication of superior antimicrobial agents at significantly lower particle concentration.

The role of the nanoparticle surface morphology and roughness in the antimicrobial activity has been investigated in Chapter 9. A method to create a rough silica layer has been developed on the CuONPs as templates. The results from TEM analysis confirmed that the CuONPs were coated with a layer of silica. As a result, the diameter of CuONPs/$SiO_2$ has increased due to a 25 ± 5 nm thick $SiO_2$ layer on the CuONPs, and the surface of CuONPs/$SiO_2$ became rough. CuONPs/$SiO_2$ were dispersed in $HNO_3$ and EDTA solutions to remove templates exhaustively. EDX data showed only two main peaks consisting of Si and O components with no peaks of copper, indicating the complete removal of the CuONP core. It has been demonstrated that by surface grafting of GLYMO and 4-HPBA on the surface-rough $SiO_2$NPs can produce formulations which are several times more effective against *R. rhodochrous* compared to bare $SiO_2$NPs at the same conditions and particle concentration. Antibacterial tests showed that the anionic surface-rough $SiO_2$NPs/GLYMO/4-HPBA have much higher action than the bare smooth and rough $SiO_2$NPs. This is explained by the strong covalent binding of the anionic particles surface-rough $SiO_2$NPs/GLYMO/4-HPBA to the cell walls due to formation of boronic ester bonds between 4- Hydroxyphenylboronic acid and diol groups from carbohydrates on the cell surface. The results imply that the combination of adhesive particle-cell interactions with surface-rough morphology transferred from the "host" CuONPs to the apparently benign $SiO_2$NPs by templating produced "ghost" $SiO_2$NPs with significant "host-intertied" antibacterial effect. One can say is that the surface roughness of the ghost $SiO_2$NPs is on the same scale as the CuONPs templates and their particles sizes match closely. This, combined with similar surface functionalization with 4-HPBA yielded significant antimicrobial effect, although $SiO_2$ is usually benign to bacteria. Interestingly this effect does not depend on the presence of copper as it has already been removed. No other study in the present literature has demonstrated such a universal antibacterial action of the combination of surface roughness and adhesion of 'ghost' $SiO_2$NPs functionalized with GLYMO and 4-HPBA as it is done for the first time in this Chapter. This result has huge implications for many other nanoparticles systems and it is a very novel and original

finding. It was also showed that the cytotoxicity of the 'ghost' $SiO_2$NPs/GLYMO/4-HPBA on human keratinocyte cells is practically negligible in the range of concentrations which kill *R. rhodochrous* bacteria. This type of functionality showed good antibacterial activity against *R. rhodochrous*; thus, surface grafting of GLYMO and 4-HPBA on surface-rough $SiO_2$NPs could be used as an antibacterial agent in many fields. Finally, it was found that the antimicrobial effect of the nanoparticles towards cells follows the order: CuONPs > ZnONPs > $Mg(OH)_2$NPs > $SiO_2$NPs.

## 10.2 Future work

Possible directions for future research are outline below. Those may include the following:

1. Examination the toxicity impacts of bare and functionalized zinc oxide nanoparticles with (3-glycidyloxypropyl)-trimethoxysilane to allow further covalent coupling of 4-hydroxyphenylboronic acid upon incubation with cells such as *R. rhodochrous, E. coli, C. reinhardtii* and *S. cerevisiae* in dark and in the presence of visible and UV light conditions at various exposure times.

2. Synthesis and evaluation of the antibacterial, anti-algal and anti-yeast properties of surface modified magnesium hydroxide nanoparticles with (3-glycidyloxypropyl)-trimethoxysilane and 4-hydroxyphenylboronic acid.

3. Synthesis of other nanoparticles such as $Cu_2O$ nanoparticles and characterise their properties. Also, examination of toxic effects of these nanoparticles on *R. rhodochrous, C. reinhardtii, S. cerevisiae, E.coli,* and *B. subtilis*.

4. Study the anti-algal and anti-yeast activity of surface-rough $SiO_2$NPs on *C. reinhardtii* and *S. cerevisiae* cells.

5. Study the action of bare and functionalized ZnONPs towards human keratinocyte cell.